

The Development of Rab27-Effector Protein Interaction Inhibitors for Treatment of Cancer Cell Invasion and Proliferation

Raghdan Zeki Al-Saad

MSc, DipClinPharm, BPharm

Thesis submitted to the University of Nottingham for the degree of Doctor of Philosophy

July 2017

Abstract

There are more than 60 Rab proteins in mammals constituting the largest family among the Ras superfamily of GTPases. Rab proteins are essential components of the intracellular secretory machinery, regulating transport and exocytosis of various intracellular organelles including secretory granules. Rab-regulated secretory functions are exerted by interaction with their downstream effector proteins, preferentially when they are activated into their GTP-bound state. Accordingly, Rab proteins can switch from active to inactive states through cycling from GTP- and GDP- bound forms, respectively.

The Rab27 subfamily consists of Rab27a/b isoforms that have similar but not identical functions. Those functions include the regulation of trafficking, docking and fusion of various lysosome-related organelles and secretory granules; such as melanosomes in melanocytes and lytic granules in cytotoxic T lymphocytes. Rab27a/b exert their specific and versatile functions by interacting with eleven effector proteins, preferentially in their GTP-bound state. In recent years, a number of studies have identified roles for Rab27 proteins and their effectors in cancer cell invasion and metastasis, immune response, inflammation and allergic responses. These findings suggest that Rab27-effector protein interaction inhibitors could contribute to the development of effective strategies to treat these diseases. However, there has been very little research reported on the development and identification of such inhibitors.

The foremost aim of the present study was to identify and develop candidate inhibitors of Rab27-effector protein interactions. To this end, fluorescent GST-pull down and FRET-based protein-protein interaction assays were developed to be used as in vitro read-outs for Rab27-effector interactions. In addition, a melanosome clustering assay was used as an indirect read-out for Rab27-effector protein interactions in living cells. The binding affinity of Slp1 and Slp2 effectors was determined using those in vitro assays. Furthermore, essential determinants of Rab27-Slp2 effector interaction were characterised and used to develop Slp2 super-effectors. The findings of this study suggest that the development of Rab27 super-effectors is an effective strategy to inhibit Rab27-effector interactions.

Contents

Acknowledgements ..... **xvi**

Declaration ..... **xvii**

Abbreviations ..... **xviii**

1 Introduction **1**

1.1 The Ras superfamily 2

1.1.1 Structure of the GTPase domain 3

1.1.2 Lipid modification of the Ras superfamily 4

1.2 The Rab proteins family 7

1.2.1 Structural characteristics of the Rab family 10

1.2.2 Mechanism of activation of Rab proteins 13

1.2.3 Functions of Rab proteins 18

1.3 Rab27 subfamily proteins 24

1.3.1 Regulators of Rab27 GTP-GDP cycle 25

1.3.2 Functions and tissue expression of Rab27a/b proteins 27

1.3.3 Rab27-related diseases 30

1.4 Rab27 effector proteins 33

1.4.1 Functions and distinct features of Rab27 effectors 37

1.4.2 Rab27-effector protein interaction disrupting mutations 47

1.5 Rab27-related cancer cell invasion and proliferation 49

1.6 Inhibitors of small GTPases protein-protein interactions 54

1.7 Aims and objectives 55

2 Methods **56**

2.1 Molecular Biology techniques 57

2.1.1 Plasmid DNA preparation Techniques 57

2.1.2 Bacterial cell culture techniques 67

2.1.3 Generating plasmid DNA constructs 69

2.2 Protein production and purification techniques 82

2.2.1 Small-scale protein production 82

2.2.2 Large-scale protein production 82

2.2.3 Purification of recombinant proteins 83

2.2.4 Electrophoresis 86

2.2.5 Western blot analysis 89

2.2.6 Imaging 90

2.2.7 Determination of protein concentrations 90

2.2.8 Mass spectrometry analysis 91

2.3 Protein-protein interaction assays 91

2.3.1 Fluorescent GST-pull down protein-protein interaction assay experiments 91

2.3.2 FRET-based protein-protein interaction assay experiments 94

2.4 Tissue culture and microscopy techniques 96

2.4.1 Maintenance of growth of mammalian cell lines 96

2.4.2 Generating adenoviruses and transfection of HEK 293A cells using adenoviral vectors 97

2.4.3 Infection of melan-a melanocytes using adenoviruses 99

2.4.4 Live-cell Microscopy 99

2.4.5 The cellular melanosome clustering assay 100

2.5 Molecular dynamics simulation of Rab27-Slp2-a effector protein interaction 100

2.6 Small molecule inhibitors 102

2.7 Sequence alignments 102

2.8 Statistical analysis 102

3 Development of the fluorescent GST-pull down assay as an in vitro measure of the binding affinity of Rab27 to its effectors 104

3.1 Introduction 105

3.2 Aims 108

3.3 Results 109

3.3.1 Generation of 6x Histidine-m.Cherry-hRab27b recombinant proteins 109

3.3.2 Generation of 6x Histidine-Rab recombinant proteins 113

3.3.3 Generation of GST-mSlp1 and GST-mSlp2 recombinant proteins 115

3.3.4 Optimising the conditions of the fluorescent GST-pull down assay experiments 117

3.3.5 Determination of Rab27b binding affinity to mSlp1 and mSlp2 effector proteins using the fluorescent GST-pull down assay 121

3.3.6 Disruption of Rab27b-effector protein binding using unlabelled Rab27a/b 122

3.4 Discussion 126

3.5 Conclusions 128

4 Determining the Rab27-effector protein binding affinity using a FRET-based assay 129

4.1 Introduction 130

4.2 Aims 133

4.3 Results 134

4.3.1 Generation of 6x Histidine-[GFP-mSlp1-(1-116), GFP-mSlp2-(3-80) and GFP] recombinant proteins 134

4.3.2 Establishing and optimising the FRET-based protein-protein interaction assay experiments 136

4.3.3 Slp1 and Slp2 have different binding affinities to Rab27 141

4.3.4 Specificity of the FRET based protein-protein interaction assay .. 146

4.4 Discussion 149

4.5 Conclusions 152

5 Identification of the key determinants of the functional effects of Rab27-effector interactions on melanosome transport 153

5.1 Introduction..... 154

5.2 Aims..... 155

5.3 Results 156

5.3.1 Identifying the key determinants of Rab27a-Slac2-a interaction-dependent melanosome transport 156

5.3.2 mSlp2-(3-80) disrupts Rab27a-Slac2-a interaction-dependent melanosome transport..... 157

5.3.3 Testing of the effects of introducing different point mutations into mSlp2-(3-80)..... 160

5.3.4 mSlp2-(R32W) mutant partially disrupts Rab27a-Slac2-a interaction-dependent melanosome transport 162

5.3.5 Testing of the inhibitory effects of different mSlp2 fragments on Rab27a-Slac2-a interaction-dependent melanosome transport 164

5.3.6 mSlp2-(3-67) is comparable to mSlp2-(3-80) in terms of inducing melanosome clustering 168

5.3.7 mSlp1-(1-116) disrupts Rab27a-Slac2-a interaction-dependent melanosome transport..... 172

5.3.8 mSlac2-a-(1-146) is not comparable to mSlac2-a-(1-266) in terms of disrupting Rab27a-Slac2-a interaction-dependent melanosome transport 175

5.3.9 Generation of GST-mSlp2-(3-41) and GST-mSlp2-(3-56) recombinant proteins 178

5.4 Discussion..... 179

5.5 Conclusions 184

6 Designing and development of Rab27-effector protein interaction inhibitors..... 185

6.1 Introduction..... 186

6.2 Aims..... 187

6.3 Results 188

6.3.1 Molecular dynamics simulation studies of Rab27-Slp2 interaction 188

6.3.2 Development of Rab27 super-effectors based on molecular dynamics simulation of Rab27-Slp2 effector protein interaction 197

6.3.3 Testing the inhibitory effects of the mutated mSlp2-(3-56) super-effector protein using the FRET-based assay 208

6.3.4 Testing of Hesperidin and BMD-20 as candidate small molecule inhibitors 213

6.4 Discussion 219

6.5 Conclusions 225

7 Summary 226

8 Appendix 232

References 266

List of Figures

1.1. Human genes of the Ras superfamily. 3
1.2. Cartoon presentation of 3-D structure of Ras superfamily GTPases. 4
1.3. The classical and alternative pathways of Rab geranylgeranylation. 7
1.4. Phylogenetic analysis of mammalian Rab family proteins. 9
1.5. Activation-inactivation model of Rab. 10
1.6. Structural features of Rab GTPases. 13
1.7. The Rab activation and membrane association cycle. 15
1.8. Structure of Rab7-REP interaction complex. 17
1.9. Structure of the doubly prenylated Rab (Ypt1)-GDI interaction complex. 18
1.10. The intracellular distribution of Rab proteins. 19
1.11. Intracellular secretory granules trafficking. 20
1.12. Amino acid sequence homology of mouse Rab27a, Rab27b and Rab3a. 25
1.13. Regulation of Rab27 GTP-GDP cycle during exocytosis of secretory granules. 27
1.14. A schematic representation of mouse Rab27 effectors 35
1.15. Carton representation of Rab–effector interaction specificity. 36
1.16. Structure of Rab27a in complex with Slp2-a. 42
1.17. Structure of Rab27b in a complex with Slac2-a. 44
1.18. Structure of Slac2-a domains. 45
1.19. Cellular transport of melanosomes in epidermal melanocytes. 47
1.20. A schematic representation of Rab27-regulated exocytosis in invasive cancers. 50
2.1. Magnet used to collect glutathione magnetic beads using Eppendorf tubes. 93
2.2. Magnet used to collect glutathione magnetic beads using a 96-well microplate. 94
2.3. A schematic representation of the dispersed and clustered melanocyte phenotypes. 100
2.4. BMD-20 chemical structure. 102
3.1. Comparison of the fluorescent GST-pull down and co-immunoprecipitation assays. 107

3.2. Small scale induction of the 6x Histidine-m.Cherry-hRab27b (1-218; T23N) recombinant protein production. 110
3.3. Production and purification profile of the 6x Histidine-m.Cherry-hRab27b-(1-218; T23N) recombinant protein. 111
3.4. Western blot analysis of different 6x Histidine-m.Cherry-hRab27b recombinant proteins. 112
3.5. Production and purification profile of the 6x Histidine-rRab27a-(1-221) recombinant protein. 114
3.6. Western blot analysis profile of different 6x Histidine-Rab recombinant proteins. 115
3.7. Production and purification profile of the GST protein. 116
3.8. Effect of incubation time and GTP concentration on the binding between m.Cherry-hRab27b and GST-mSlp1-(1-201). 118
3.9. Effect of GTP and glutathione magnetic beads concentration on the binding between m.Cherry-hRab27b and GST-mSlp1-(1-201). 119
3.10. Effect of using different GTP concentrations on the binding between m.Cherry-hRab27b and GST-mSlp1-(1-201). 120
3.11. Comparison of the binding of the full length and C-terminal truncated hRab27b to mSlp1 effector protein (1-201). 121
3.12. The binding affinity profile of hRab27b to mSlp1 and mSlp2 effector proteins. 122
3.13. Amino acid sequence alignment of Rab27a/b proteins. 123
3.14. Disrupting hRab27b binding to either mSlp1 or mSlp2 effector proteins. 125
4.1. A schematic representation of the FRET-based protein-protein interaction assay. 133
4.2. Small scale induction of the 6x Histidine-GFP-mSlp1-(1-116) recombinant protein production. 135
4.3. Western blot analysis of the 6x Histidine-GFP-mSlp1-(1-116) recombinant protein. 136
4.4. FRET profile of m.Cherry-hRab27b and GFP-mSlp1 binding. 138
4.5. Effect of GTP concentration on the binding between GFP-mSlp1-(1-116) and m.Cherry-hRab27b after 2 hours incubation. 140

4.6. Effect of the incubation time on the binding between GFP-mSlp1-(1-116) and m.Cherry-hRab27b. 141
4.7. The binding affinity profile of mSlp1 and mSlp2 effector proteins to 0.6 μM hRab27b. 142
4.8. The binding affinity profile of mSlp1 and mSlp2 effector proteins to 0.3μM hRab27b. 143
4.9. The binding affinity profile of mSlp1 and mSlp2 effector proteins to 0.15μM hRab27b. 144
4.10. Comparison of the binding of mSlp1 and mSlp2 to the full length and C-terminal truncated hRab27b. 145
4.11. The binding affinity profile of mSlp1 and mSlp2 effector proteins to 0.15μM hRab27a. 146
4.12. Disruption of hRab27b interaction with either mSlp1 or mSlp2 effector proteins using different unlabelled Rabs. 148
5.1. The cellular melanosome clustering assay as a read-out for Rab27a-Slac2-a interaction-dependent melanosome transport. 157
5.2. Amino acid sequence alignment of human and mouse Slp2-a. 158
5.3. Effects of mSlp2-(3-80), mSlp2-(3-80; D3A) and mSlp2-(3-79) on Rab27a-Slac2-a interaction-dependent melanosome transport. 160
5.4. The introduced point mutations into mSlp2-(3-80). 161
5.5. Introducing different point mutations into mSlp2-(3-80) does not affect the induced melanosome clustering. 162
5.6. R32W mutation partially inhibits mSlp2-(3-80)-induced melanosome clustering. 163
5.7. Sequence alignment of Slp2/Exophilin4-Rab27a binding interface with other Rab27 effector proteins. 164
5.8. mSlp2-(10-41), mSlp2-(10-50) and mSlp2-(10-56) do not inhibit Rab27a-Slac2-a interaction-dependent melanosome transport. 165
5.9. mSlp2-(3-56) partially inhibits Rab27a-Slac2-a interaction-dependent melanosome transport. 166
5.10. Testing the effects of GST-mSlp2-(3-41) and GST-mSlp2-(3-56) on hRab27b-mSlp1 interaction. 168
5.11. Sequence alignment of mSlac2-a-mRab27b binding interface with other Rab27 effector proteins. 169

5.12. Testing of the inhibitory effects of mSlp2-(3-67) and mSlp2-(10-67) on Rab27a-Slac2-a interaction-dependent melanosome transport. 171
5.13. Amino acid sequence alignment of human and mouse Slp1. 172
5.14. mSlp1-(1-116) is comparable to mSlp2-(3-80) in terms of disrupting Rab27a-Slac2-a interaction-dependent melanosome transport. 174
5.15. Amino acid sequence alignment of human and mouse Slac2-a. 175
5.16. mSlac2-a-(1-146) does not completely disrupt Rab27a-Slac2-a interaction-dependent melanosome transport. 177
5.17. Production and purification profile of the GST-mSlp2-(3-41) recombinant protein. 178
6.1. Free energy of binding of Rab27a-Slp2 interaction. 190
6.2. Three-dimensional structure of Rab27a-Slp2 proposed mutations. 194
6.3. Full three-dimensional structure of Rab27a-Slp2 proposed mutations. .. 196
6.4. Effects of introducing different mutations into mSlp2-(3-56) on Rab27a-Slac2-a interaction-dependent melanosome transport. 199
6.5. Effects of introducing different mutations into mSlp2-(3-67) on Rab27a-Slac2-a interaction dependent melanosome transport. 201
6.6. Effects of introducing different mutations into mSlp2-(10-56) and mSlp2-(10-67) on Rab27a-Slac2-a interaction-dependent melanosome transport. ... 203
6.7. Effects of introducing single mutations into mSlp2-(3-56) on Rab27-Slac2-a interaction-dependent melanosome transport. 206
6.8. Molecular dynamics simulation studies of Rab27a-Slp2 207
6.9. Separation profile of different 6x Histidine-mSlp2 recombinant proteins. 209
6.10. Western blot analysis profile of different 6x Histidine-mSlp2 recombinant proteins. 210
6.11. The inhibitory effect of the mutated mSlp2-(3-56) super-effector protein on hRab27b-mSlp1 effector interaction. 212
6.12. The inhibitory effect of the mutated mSlp2-(3-56) super-effector protein on hRab27b-mSlp2 effector interaction. 213
6.13. Model of hesperidin docking on Slac2-a structure. 214
6.14. Proposed model of BMD-20 interaction with Slac2-a. 215
6.15. Testing the proposed inhibitory effects of BMD-20 and hesperidin on hRab27b-effector protein interaction. 216

6.16. Hesperidin and BMD-20 treated cells. 218
6.17. Molecular docking of Nexinhib20 on Rab27a structure..... 224
8.1. A schematic representation of the pETDuet-1-m.Cherry-hRab27b vector generation steps. 233
8.2. pETDuet-1-m.Cherry-hRab27b-(1-218; T23N) vector map. 234
8.3. PCR amplification of hRab27b-(1-218; T23N). 234
8.4. An ethidium bromide stained 1% TBE agarose gel showing NotI restriction enzyme digests of different pETDuet-1-m.Cherry-hRab27b vectors. 235
8.5. Amino acid sequence alignment of the pETDuet-1-m.Cherry-hRab27b-(1-218; T23N) vector sequencing data. 236
8.6. Amino acid sequence alignment of the pETDuet-1-m.Cherry-hRab27b-(1-218) vector sequencing data. 237
8.7. Amino acid sequence alignment of the pETDuet-1-m.Cherry-hRab27b-(1-218; Q78L) vector sequencing data. 237
8.8. Amino acid sequence alignment of the pETDuet-1-m.Cherry-hRab27b-(1-200) vector sequencing data. 238
8.9. The proteomic analysis and amino acid sequence alignment of the 6x histidine m.Cherry-Rab27b-(1-218) recombinant protein. 238
8.10. Amino acid sequence alignment of the pET-14b-rRab27a-(1-221) vector sequencing data. 239
8.11. Amino acid sequence alignment of the pET-15b-hRab27b-(1-218) vector sequencing data. 239
8.12. Amino acid sequence alignment of the pET-14b-hRab5a-(1-216) vector sequencing data. 240
8.13. Amino acid sequence alignment of pGEX-4T1-mSlp1-(1-201) vector sequencing data. 240
8.14. pGEX-4T1-mSlp2-(3-80) vector map. 241
8.15. Amino acid sequence alignment of the pGEX-4T1-mSlp2-(3-80) vector sequencing data. 241
8.16. Amino acid sequence alignment of the pETDuet-1-GFP-mSlp1-(1-116)-m.Cherry-hRab27a-(1-221) vector sequencing data. 242
8.17. Amino acid sequence alignment of the pETDuet-1-GFP-mSlp1-(1-116) vector sequencing data. 242
8.18. pETDuet-1-GFP-mSlp2-(3-80) vector map. 243

8.19. An ethidium bromide stained 1% TBE agarose gel showing BamHI and NotI digests of different pETDuet-1 vectors. 243
8.20. Amino acid sequence alignment of the pETDuet-1-GFP-mSlp2-(3-80) vector sequencing data. 244
8.21. pENTR-EGFP-C2-mSlp2-(3-80) vector map. 244
8.22. Amino acid sequence alignment of the pENTR-EGFP-C2-mSlp2-(3-80) vector sequencing data. 245
8.23. Amino acid sequence alignment of the pENTR-EGFP-C2-mSlp2-(3-80; D3A) vector sequencing data. 245
8.24. Amino acid sequence alignment of the pENTR-EGFP-C2-mSlp2-(3-79) vector sequencing data. 246
8.25. Amino acid sequence alignment of the pENTR-EGFP-C2-mSlp2-(3-80; R32W) vector sequencing data. 246
8.26. Amino acid sequence alignment of the pENTR-EGFP-C2-mSlp2-(3-80; K58A) vector sequencing data. 246
8.27. Amino acid sequence alignment of the pENTR-EGFP-C2-mSlp2-(3-80; R61A) vector sequencing data. 247
8.28. Amino acid sequence alignment of the pENTR-EGFP-C2-mSlp2-(3-80; H62A) vector sequencing data. 247
8.29. Amino acid sequence alignment of the pENTR-EGFP-C2-mSlp2-(3-80; G68I) vector sequencing data. 247
8.30. Amino acid sequence alignment of the pENTR-EGFP-C2-mSlp2-(3-80; D70A) vector sequencing data. 248
8.31. Amino acid sequence alignment of the pENTR-EGFP-C2-mSlp2-(3-80; I71A) vector sequencing data. 248
8.32. Amino acid sequence alignment of the pENTR-EGFP-C2-mSlp2-(3-80; R73A) vector sequencing data. 248
8.33. Amino acid sequence alignment of the pENTR-EGFP-C2-mSlp2-(3-80; S75A) vector sequencing data. 249
8.34. pENTR-EGFP-C2-mSlp1-(1-116) vector map. 249
8.35. Amino acid sequence alignment of the pENTR-EGFP-C2-mSlp1-(1-116) vector sequencing data. 249
8.36. Amino acid sequence alignment of the pENTR-EGFP-C2-mSlac2-a-(1-146) vector sequencing data. 250

8.37. Amino acid sequence alignment of the pENTR-EGFP-C2-mSlp2-(10-41) vector sequencing data. 250
8.38. Amino acid sequence alignment of the pENTR-EGFP-C2-mSlp2-(10-50) vector sequencing data. 250
8.39. Amino acid sequence alignment of the pENTR-EGFP-C2-mSlp2-(10-56) vector sequencing data. 250
8.40. Amino acid sequence alignment of the pENTR-EGFP-C2-mSlp2-(10-56; K26R, A28R, Q44R, N48I) vector sequencing data. 251
8.41. Amino acid sequence alignment of the pENTR-EGFP-C2-mSlp2-(10-56; K26R, A28R, Q44R, N48I, E56F) vector sequencing data. 251
8.42. Amino acid sequence alignment of the pENTR-EGFP-C2-mSlp2-(10-56; K26R, A28R, Q44R, N48I, G51L, E56F) vector sequencing data. 251
8.43. Amino acid sequence alignment of the pENTR-EGFP-C2-mSlp2-(3-41) vector sequencing data. 252
8.44. Amino acid sequence alignment of the pENTR-EGFP-C2-mSlp2-(3-56) vector sequencing data. 252
8.45. Amino acid sequence alignment of the pENTR-EGFP-C2-mSlp2-(3-56; K26R) vector sequencing data. 252
8.46. Amino acid sequence alignment of the pENTR-EGFP-C2-mSlp2-(3-56; A28R) vector sequencing data. 253
8.47. Amino acid sequence alignment of the pENTR-EGFP-C2-mSlp2-(3-56; K26R, A28R) vector sequencing data. 253
8.48. Amino acid sequence alignment of the pENTR-EGFP-C2-mSlp2-(3-56; K26R, A28R, Q44R) vector sequencing data. 253
8.49. Amino acid sequence alignment of the pENTR-EGFP-C2-mSlp2-(3-56; Q44R) vector sequencing data. 254
8.50. Amino acid sequence alignment of the pENTR-EGFP-C2-mSlp2-(3-56; K26R, A28R, Q44R, N48I) vector sequencing data. 254
8.51. Amino acid sequence alignment of the pENTR-EGFP-C2-mSlp2-(3-56; N48I) vector sequencing data. 254
8.52. Amino acid sequence alignment of the pENTR-EGFP-C2-mSlp2-(3-56; Q44R, N48I) vector sequencing data 255
8.53. Amino acid sequence alignment of the pENTR-EGFP-C2-mSlp2-(3-56; K26R, A28R, Q44R, N48I, G51L) vector sequencing data. 255

8.54. Amino acid sequence alignment of the pENTR-EGFP-C2-mSlp2-(3-56; K26R, A28R, Q44R, N48I, G51L, E56F) vector sequencing data. 255
8.55. Amino acid sequence alignment of the pENTR-EGFP-C2-mSlp2-(3-56; K26R, A28R, Q44R, N48I, E56F) vector sequencing data. 256
8.56. Amino acid sequence alignment of the pENTR-EGFP-C2-mSlp1-(1-74) vector sequencing data. 256
8.57. Amino acid sequence alignment of the pENTR-EGFP-C2-mSlp1-(70-116) vector sequencing data. 256
8.58. Amino acid sequence alignment of the pENTR-m.Cherry-mSlp1-(1-74) vector sequencing data. 257
8.59. Amino acid sequence alignment of the pENTR-EGFP-C2-mSlp2-(3-67) vector sequencing data. 257
8.60. Amino acid sequence alignment of the pENTR-EGFP-C2-mSlp2-(3-67; K26R, A28R) vector sequencing data. 257
8.61. Amino acid sequence alignment of the pENTR-EGFP-C2-mSlp2-(3-67; K26R, A28R, Q44R) vector sequencing data. 258
8.62. Amino acid sequence alignment of the pENTR-EGFP-C2-mSlp2-(3-67; K26R, A28R, Q44R, N48I) vector sequencing data. 258
8.63. Amino acid sequence alignment of the pENTR-EGFP-C2-mSlp2-(3-67; K26R, A28R, Q44R, N48I, G51L) vector sequencing data. 258
8.64. Amino acid sequence alignment of the pENTR-EGFP-C2-mSlp2-(3-67; K26R, A28R, Q44R, N48I, G51L, E56F) vector sequencing data. 259
8.65. Amino acid sequence alignment of the pENTR-EGFP-C2-mSlp2-(3-67; K26R, A28R, Q44R, N48I, G51L, E56F, H62R, R63F) vector sequencing data. 259
8.66. Amino acid sequence alignment of the pENTR-EGFP-C2-mSlp2-(10-67) vector sequencing data. 259
8.67. Amino acid sequence alignment of the pENTR-EGFP-C2-mSlp2-(10-67; K26R, A28R, Q44R, N48I) vector sequencing data. 260
8.68. Amino acid sequence alignment of the pENTR-EGFP-C2-mSlp2-(10-67; K26R, A28R, Q44R, N48I, E56F, H62R, R63F) vector sequencing data. 260
8.69. Amino acid sequence alignment of the pENTR-EGFP-C2-mSlp2-(10-67; K26R, A28R, Q44R, N48I, G51L, E56F, H62R, R63F) vector sequencing data. 260

8.70. Amino acid sequence alignment of the pGEX-4T1-mSlp2-(3-41) vector sequencing data. 261
8.71. Amino acid sequence alignment of the pGEX-4T1-mSlp2-(3-56) vector sequencing data. 261
8.72. pETDuet-1- mSlp2-(3-80) vector map. 262
8.73. BamHI and NotI digests of the pETDuet-1-mSlp2-(3-80) vector. 262
8.74. Amino acid sequence alignment of the pETDuet-1-mSlp2-(3-80) vector sequencing data. 263
8.75. Amino acid sequence alignment of the pETDuet-1-mSlp2-(3-80; K26R, A28R) vector sequencing data. 263
8.76. Amino acid sequence alignment of the pETDuet-1-mSlp2-(3-80; K26R, A28R, Q44R) vector sequencing data. 263
8.77. Amino acid sequence alignment of the pETDuet-1-mSlp2-(3-80; K26R, A28R, Q44R, N48I) vector sequencing data. 264
8.78. Amino acid sequence alignment of the pETDuet-1-mSlp2-(3-56) vector sequencing data. 264
8.79. Amino acid sequence alignment of the pETDuet-1-mSlp2-(3-56; K26R, A28R, Q44R, N48I) vector sequencing data. 264
8.80. Amino acid sequence alignment of the pETDuet-1-mSlp2-(3-67) vector sequencing data. 265

List of Tables

1.1 Comparison of Rab27a/b tissue expression……30

1.2 Griscelli syndrome types…….33

1.3. Putative functions of Rab27 effectors……..40

2.1. Simple PCR reaction Conditions……57

2.2. List of PCR primers used to perform simple PCR in this study……59

2.3. Site-directed mutagenesis reaction Conditions……...60

2.4. List of PCR primers used to perform site-directed mutagenesis in this study……..64

2.5. A list of the restriction enzymes and buffers used in this study...…….65

2.6. Components of 10% (v/v) SDS-PAGE gel……..87

2.7. A list of the antibodies used in this study…..……90

2.8. Volumes used for passaging melan-a and HEK293A cells……..96

6.1. A list of Slp2 proposed mutations..…….....191

6.2. Reasons behind the proposed Slp2 mutations……192

6.3. Consensus of Slp2 proposed mutations with corresponding residues in other Rab27 effectors…….....208

Acknowledgements

First and foremost I would like to thank my supervisor, Dr Alistair Hume, for his support, guidance, reading my thesis and valuable input during conducting this project. I would like also to thank my second supervisor, Dr Ian Kerr, for his valuable advice during the supervision meetings.

I would like to thank Dr David Tooth for his assistance and guidance on electrophoresis and western blot analysis of proteins and also for performing mass spectrometry analysis.

I would like to thank Dr Charles Laughton and Mohammed Tumbi for their collaboration and helpful discussions regarding the development of Rab27 super-effectors and also for performing molecular dynamics simulation studies.

Thanks to Dr Steven Charlton and David Sykes for allowing me to use the CLARIOstar microplate reader in their Lab.

Thanks to Dr Michael Stocks for synthesing BMD-20 and performing related NMR analysis.

Thanks to Paolo Sanzà for his wonderful collaboration and help.

Thanks to Dalila Zanette and Deborah Briggs for their practical help during the first year of my study.

I would like to thank my sponsor, the Iraqi Ministry of Higher Education and Scientific Research and the Iraqi Cultural Attaché in London, for their support.

I deeply thank my wife, Asseel, for her continuous support, encouragement and endless patience.

Thanks to my family, especially my parents and my brother Ahmed, for their unending encouragement and support.

Thanks for everyone who helped me during conducting this project, but I forgot to mention here.

Declaration

I declare that the following thesis and the data presented in it are my own work, under the supervision of Dr Alistair Hume at the University of Nottingham, unless otherwise indicated below or stated in the text.

• Spectrophotometry analysis in chapter 3 was performed by Dr David Tooth (Centre for Biomolecular Sciences, University of Nottingham).

• m.Cherry and m.Cherry-Rab27a proteins used in Chapters 3 and 4 were kind gifts from Dr Alistair Hume.

• GFP and GFP-Slac2-a-(1-266) adenoviral constructs used in Chapter 5 were kind gifts from Dr Alistair Hume.

• Molecular dynamics simulation studies and related homology modelling in chapter 6 were performed by Mohammed Tumbi under supervision of Dr Charles Laughton (The University of Nottingham, Centre for Biomolecular Sciences).

• Synthesis of BMD-20 and related NMR analysis (used in chapter 6) were performed by Dr Michael Stocks (The University of Nottingham, Centre for Biomolecular Sciences).

• The used vectors are referenced accordingly (if they were not generated by myself).

Raghdan Z. Al-Saad, July 2017.

Abbreviations

ABD – Actin Binding Domain

ANOVA – Analysis of Variance

AP – Autophagosome

APS – Ammonium Persulphate

Arf – ADP-ribosylation Factor

aSyn – Alpha-Synuclein

ATP1a1 – α-subunit of Na+, K+ -ATPase isoform 1

A.U. – Arbitrary Unit

BME – β-Mercaptoethanol

BP – Base Pair

BR-MyoVa – Brain-spliced isoform of Myosin-Va

BSA – Bovine Serum Albumin

C – m.Cherry

CBR – C-terminus Binding Region

CC – Coiled-Coil

CHM – Choroideremia

CHML – Choroideremia Like

CI-MPR – Cation Independent-MPR

CLIC3 – Chloride Intracellular Channel Protein 3

COP – Coat Protein

CRMP-2 – Collapsing Response Mediator Protein-2

DMEM – Dulbeco's Modified Eagle Medium

DMSO – Dimethyl Sulphoxide

DTT – Dithiothreitol

EDTA – Ethylenediaminetetraacetic Acid

EE – Early Endosome

EEA1 – Early Endosome Antigen 1

EFBD – Exon F-Binding Domain

EGFP – Enhanced Green Fluorescent Protein

ER – Endoplasmic Reticulum

ERGIC – ER-Golgi Intermediate Compartment

FBS – Foetal Bovine Serum

FGF1 – Fibroblast Growth Factor 1

FGFR – Fibroblast Growth Factor Receptor

FHL – Familial Hemophagocytic Lymphohistiocytosis

FRET – Fluorescence Resonance Energy Transfer

FTase – Farnesyltransferase

GAP – GTPase-Activating Protein

GDF – GDI-Displacement Factor

GDI – Guanine-nucleotide Dissociation Inhibitor

GEF – Guanine-nucleotide Exchange Factor

GFP – Green Fluorescent Protein

GGPP – Geranylgeranylpyrophosphate

GGTase I – Geranylgeranyltransferase I

GLUT4 – Glucose Transporter type 4

GS – Griscelli Syndrome

GSH – Glutathione

GST – Glutathione-S-Transferase

GTBD – Globular Tail-Binding Domain

H – Human

HEK – Human Embryonic Kidney

HOPS – Homotypic Vacuole Fusion and Protein Sorting

HSC70 – Heat Shock Cognate 70 Protein

HSP90 – Heat-Shock Protein 90

HVD – Hypervariable C-terminal Domain

IMAC – Immobilized Metal Affinity Chromatography

IPTG – Isopropyl β-D-1-thiogalactopyranoside

KO – Knockout

Kpsi – Kilo-pound-force Per Square Inch

LB – Lysogeny Broth

LD – Lipid Droplet

LE – Late Endosome

L/V – Lysosome/Vacuole

M – Mouse

MBD – Myosin-Va Binding Domain

MDCK II – Madin–Darby Canine Kidney II

MEL – Mobile Effector Loop

MHDs – Munc13 Homology Domains

Mlph – Melanophilin

MMP – Matrix Metalloproteinase

MPR – Mannose-6-Phosphate Receptor

mRFP1 – Monomeric Red Fluorescent Protein 1

MST1 – Mammalian Sterile 20–like Kinase 1

MyRIP – Myosin-VIIa and Rab27 Interacting Protein

NEXINHIB20 – Neutrophil Exocytosis Inhibitor20

NF-κB – Nuclear Factor-κB

NMDARs – N-methyl-D-Aspartate Receptors

OCRL1 – Lowe Oculocerebrorenal Syndrome Protein1

OD_{600} – Optical $Density_{600}$

PAS – Preautophagosomal Structure

PBS – Phosphate Buffered Saline

PCR – Polymerase Chain Reaction

PDB – Protein Data Bank

PKA – Protein Kinase A

PMA – Phorbyl 12-myristate 13-acetate

PVDF – Polyvinyldifluoride

R – Rat

Rab – Ras-like In Brain

RabCDRs – Rab Complementary-Determining Regions

RabF – Rab Family

Rab11-FIP2 – Rab11 Family Interacting Protein 2

Rab3GEP – Rab3 Guanine-nucleotide Exchange Protein

RabSF – Rab Subfamily

Ran – Ras-like nuclear

RANKL – Receptor Activator of NF-KB Ligand

Ras – Rat sarcoma

RBD – Rab27 Binding Domain

RBL-2H3 – Rat Basophilic Leukemia-2H3

RBP – Rab Binding Platform

RCP – Rab Coupling Protein

RE – Recycling Endosome

REP – Rab Escort Protein

RGGT – Rab geranylgeranyltransferase

Rho – Ras homology

RILP – Rab Interacting Lysosomal Protein

RPMI – Roswell Park Memorial Institute

SCRs – Sequence Conserved Regions

SDS-PAGE – Sodium Dodecyl Sulphate - Polyacrylamide Gel Electrophoresis

SEM – Standard Error of the Mean

SHD – Slp Homology Domain

SHH – Sonic Hedgehog

shRNA – Short Hairpin RNA

siRNA – Small Interfering RNA

Slac2 – Slp Homologue Lacking C2 Domains

Slp – Synaptotagmin-Like Protein

SNARE – Soluble N-ethylmaleimide–Sensitive Factor Attachment Protein Receptor

SOS – Son Of Sevenless

StRIP3 – Stabilized α-Helical Domain of Rab6 Interacting Protein1-3

SV – Secretory Vesicles/granules

TBC – Tre-2/Bub2/Cdc16

TBE – Tris/Borate/EDTA

TE – Tris/EDTA

TEMED – N,N,N,N'-Tetramethyethylene-diamine

TGN – Trans-Golgi Network

TNFα – Tumour Necrosis Factor α

TSAP – Thermosensitive Alkaline Phosphatase

UTR – Untranslated Region

VAMP – Vesicle-Associated Membrane Protein

V-ATPase – Vacuolar H(+)-ATPase

ZnF – Zinc Finger Motif

Chapter 1

Introduction

1.1 The Ras superfamily

The Rat sarcoma (Ras) superfamily are small monomeric G proteins (GTPases) that exert their actions by cycling between GTP- and GDP-bound active and inactive states, respectively (Oxford and Theodorescu, 2003; Wennerberg et al., 2005).

In general, the Ras superfamily can be classified into five families: Ras, Ras homology (Rho), Ras-like in brain (Rab), ADP-ribosylation factor (Arf) and Ras-like nuclear (Ran) (Pereira-Leal and Seabra, 2000; Wennerberg et al., 2005) (Figure 1.1).

The Ras proteins control many intracellular compartments by translating the extracellular signals into wide range of specific intracellular events that organise the cellular growth and survival mechanisms in the cell (Ehrhardt et al., 2002; Mitin et al., 2005; Omerovic et al., 2007; Reuther and Der, 2000). In addition, Ras proteins have been implicated in the oncogenesis of human tumours (Rajalingam et al., 2007; Yan et al., 2015). Rho GTPases play an important role in regulating and maintaining cell-cell junctions (Arnold et al., 2017). Also, Rho GTPases act as key regulators of actin dynamics, regulating cell migration (Blom et al., 2017). Interestingly, during an attempt to identify members of the Ras family, Touchot and co-workers were able to isolate four genes from rat brain which encoded four novel Ras-like GTPases named Rab l, -2, -3 and -4 (Touchot et al., 1987). The Rab GTPases represent the largest family among the Ras superfamily of GTPases and function as essential regulators of membrane trafficking of different intracellular organelles (Stenmark and Olkkonen, 2001; Zerial and McBride, 2001). Arf GTPases, like Rabs regulate intracellular membrane trafficking (Donaldson et al., 2016). In addition, they have been involved in cancer cell invasion and migration by promoting cell spreading and migration of primary tumours (Casalou et al., 2016). The Ran family (comprising only Ran) is involved in the regulation of cycling of the nuclear contents (import and export) (Reiner and Lundquist, 2016). It has also been implicated in the regulation of cell signalling pathways related to cell adhesion, migration and invasion (Yuen et al., 2016).

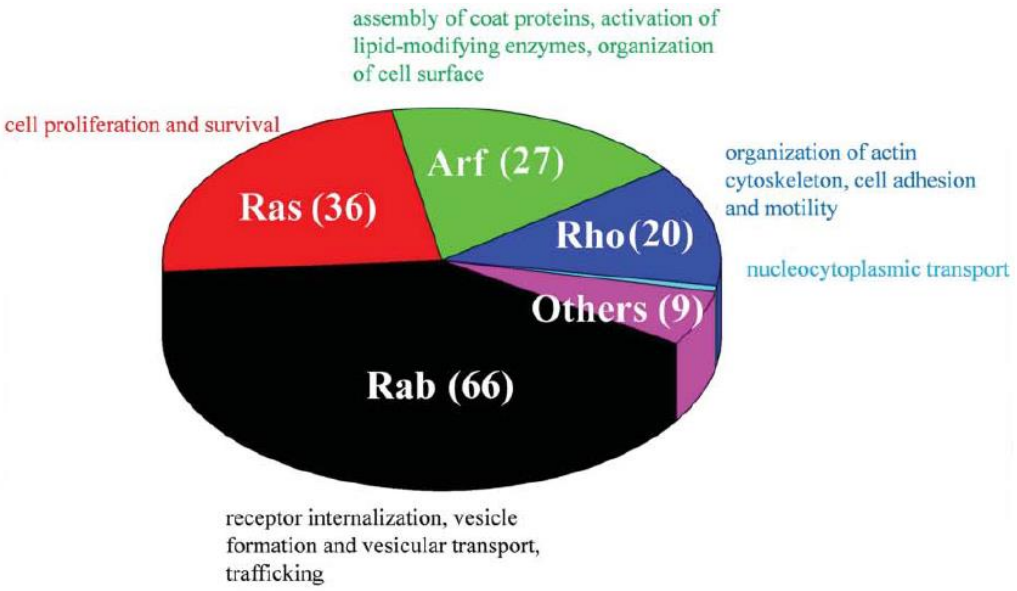


Figure 1.1. Human genes of the Ras superfamily. The Ras GTPases superfamily human genes with their essential functions; Ras, Rho, Rab, Arf and Ran are shown in red, blue, black, green and cyan, respectively. Other Ras GTPases are shown in purple. Reproduced from (Prakash and Gorfe, 2016).

1.1.1 Structure of the GTPase domain

All Ras GTPases contain a GTPase domain, consisting of six β sheet strands surrounded by five α helices and connected by ten loops. The GTPase domain comprises five conserved motifs (G1-G5) clustered in loops, surrounding the nucleotide-binding site (Bourne et al., 1991; Colicelli, 2004; Vetter, 2014; Vetter and Wittinghofer, 2001) (Figure 1.2). The G1 motif (also called Walker A motif) (GXXXXGKS/T) contains two glycine residues responsible for phosphate-binding, therefore it is also known as P-loop. In addition, it contains lysine residue, interacting with the β- and γ-phosphate oxygens. Serine or threonine hydroxyl groups are crucial for making contacts with β-phosphate oxygen and the magnesium ion. The G2 or the switch I region is implicated in effector binding as its conformation changes following GTP-GDP exchange, thus it is also termed effector region. The presence of the GTP γ-phosphate can be sensed by a conserved threonine residue in G2 domain, in addition threonine residue makes contacts with $Mg2^{+}$. The G3 or the Walker B motif (DXXG) is in close proximity to the switch II region near aspartic acid contact with $Mg2^{+}$. Switch II region is implicated in sensing the presence of the γ-phosphate and effector binding by regulating GTP-GDP exchange. In the G4 motif (N/TKXD), aspartic acid forms hydrogen bonds with the nitrogen atoms of the GTP guanine ring,

and asparagine can bind the oxygen of the purine. In addition, both asparagine and lysine can stabilise the GTP binding domain. The sequence of the G5 motif (SAK) is not highly conserved; it stabilises the asparagine and aspartic residues in the G4 motif.

Upon binding with GTP γ-phosphate, the switch I and switch II regions adopt a more defined (less flexible) structure, preferentially triggering effector protein binding. Whereas, upon release of GTP γ-phosphate (GDP-bound state), the switch I and switch II regions become more flexible (open), conferring a lower affinity to effector protein (Vetter, 2014; Vetter and Wittinghofer, 2001). But the idea of the existence of the switch I and switch II regions in close and open states is further complicated by discovering that H-Ras (GTP-bound) exists in two conformational states, suggesting that further investigations need to be done accordingly (Shima et al., 2010; Zhao et al., 2017).

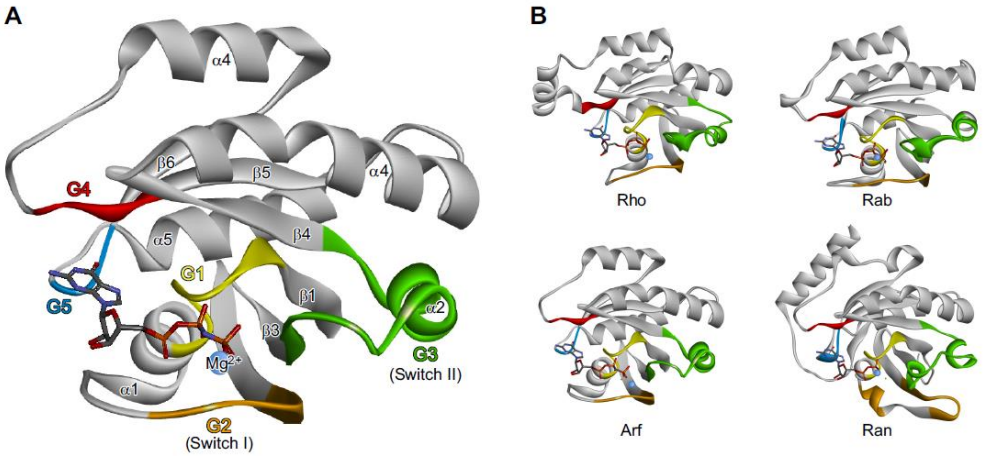


Figure 1.2. Cartoon presentation of 3-D structure of Ras superfamily GTPases. A) 3-D structure of H-Ras-GTP complex, it consists of six β sheet strands flanked by five α helices. Conserved G1–G5 motifs are presented. B) 3-D structure of Rho, Arf, Rab and Ran GTPases. Reproduced from (Loirand et al., 2013).

1.1.2 Lipid modification of the Ras superfamily

Lipid modification of proteins is required for membrane association and regulation of various cellular processes; such as intracellular membrane trafficking and signal transduction cascades (Casey and Seabra, 1996; Prakash and Gorfe, 2016). Therefore, to mediate protein association with phospholipid

bilayers, lipophilic moieties are added to their C-terminus by prenylation (Wright and Philips, 2006).

Farnesyltransferase (FTase) and geranylgeranyltransferase I (GGTase I) enzymes recognise the CAAX motif (C; Cysteine, A; aliphatic residue and X; any residue) and add farnesyl (15 carbon) or geranylgeranyl (20 carbon) isoprenoid groups at the C-terminus of Ras and Rho proteins, respectively (Reiss et al., 1990; Seabra et al., 1991; Shinde and Maddika, 2017). The X residue plays significant role in determining enzyme selectivity: glycine, alanine, serine, threonine, histidine, asparagine, glutamine and cysteine serve as substrates for FTase enzyme. GGTase I enzyme works selectively on leucine, whereas valine, isoleucine, phenylalanine and methionine serve as substrates for both enzymes. Proline, tyrosine, tryptophan, lysine, arginine, aspartic acid and glutamic acid are very weak substrates for prenylation (Moores et al., 1991). Although FTase and GGTase I enzymes have their own preferences when interacting with their protein substrates (as described above), they can work on the same substrate; reviewed in (Wang and Casey, 2016).

Rab proteins are modified by Rab geranylgeranyltransferase (RGGT) enzyme. This enzyme was first separated from rat brain cytosol as a multi-component enzyme (components A and B) (Seabra et al., 1992a; Seabra et al., 1992b). Rab prenylation motifs contain either one or two cysteine residues; i.e. CXC, XCC, CCXX, CCXXX, CCX and CXXX (Magee and Seabra, 2003; Pereira-Leal et al., 2001). Component A, also called Rab escort protein (REP), binds unprenylated Rabs, presenting them to component B (Andres et al., 1993). Component B is required for enzyme catalytic activity by recognising REP-unprenylated Rab complex, attaching geranylgeranyl groups onto Rabs (details of Rab geranylgeranylation described in section 1.1.2.1) (Anant et al., 1998; Seabra et al., 1992b).

Arf proteins are modified by N-terminal myristoylation (Donaldson and Jackson, 2011; Jackson and Bouvet, 2014). In contrast to other Ras GTPases, Ran protein is characterised by nuclear localization and lacking of carboxyl terminal sequence required for posttranslational lipid modification, instead, it contains an acidic carboxyl terminus (Rush et al., 1996).

1.1.2.1 Rab geranylgeranylation pathways

There are two pathways for Rab geranylgeranylation (Figure 1.3). The classical pathway involves first binding of unprenylated Rab protein to REP, forming a stable complex (Alexandrov et al., 1999; Andres et al., 1993), this complex then becomes a substrate for RGGT enzyme and geranylgeranylation reaction occurs by adding two geranylgeranyl pyrophosphate (GGPP) molecules to Rab C-terminus without prior dissociation of REP (Desnoyers and Seabra, 1998; Thoma et al., 2001c). The binding of new GGPP molecules to the Rab-REP-RGGT complex then stimulates the dissociation of the ternary complex, releasing REP-prenylated Rab (Thoma et al., 2001b). REP can then deliver the newly prenylated Rab to its intracellular target membrane (Alexandrov et al., 1994; Shen and Seabra, 1996).

In the alternative pathway, GGPP increases the binding affinity between REP and RGGT, forming REP-RGGT complex. This complex then associates with unprenylated protein, leading to Rab prenylation (Thoma et al., 2001a). Baron and Seabra found that over-expression of REP (wild-type and mutants) in human embryonic kidney (HEK) 293 cells failed to form stable complexes with endogenous unprenylated Rabs. In addition, intracellular GGPP stabilises REP–RGGT complexes in cells, suggesting the superiority of the alternative over the classical pathway in the mechanism of Rab prenylation (Baron and Seabra, 2008).

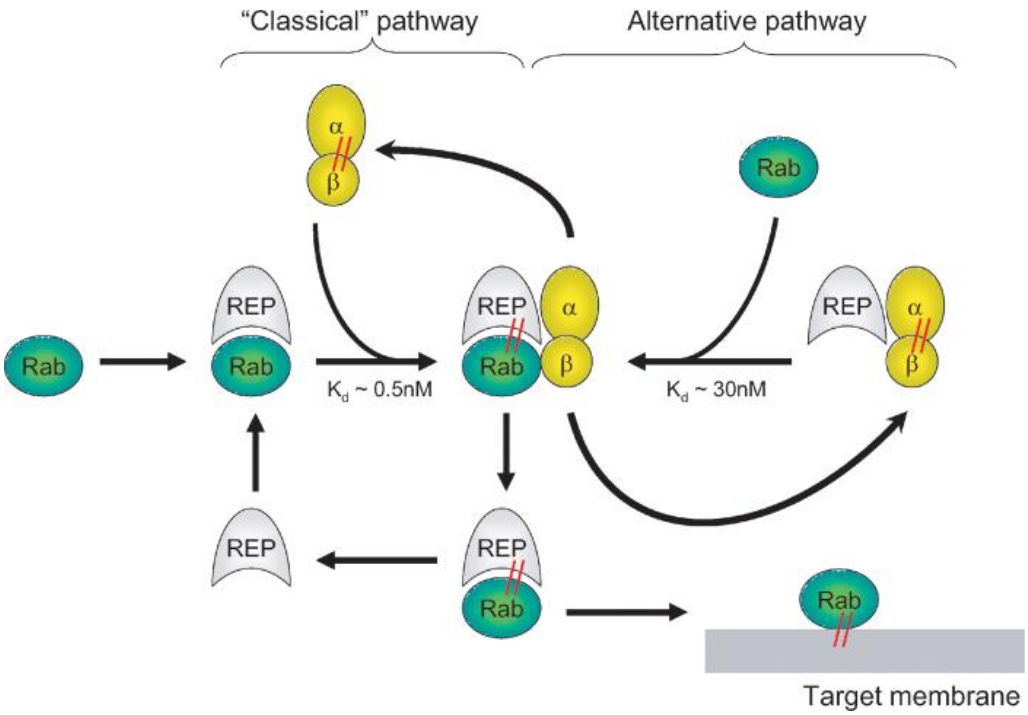


Figure 1.3. The classical and alternative pathways of Rab geranylgeranylation. In the classical pathway, REP interacts with the newly synthesised Rab, this complex then serves as a substrate for GGPP-RGGT (α- and β-subunits), promoting geranylgeranylation reaction and adding geranylgeranyl groups to C-terminal cysteines of the Rab protein. This is followed by RGGT dissociation from REP-Rab complex, REP remains associated with prenylated Rab protein until delivered to the target membrane and REP is then directed to the cytosol to start a new prenylation cycle. In the alternative pathway, GGPP triggers the binding between RGGT and REP and subsequent binding with unprenylated Rab takes place, leading to the formation of prenylated Rab. This is followed by dissociation of RGGT and REP delivers prenylated Rab to the target membrane as described in the classical pathway. Reproduced from (Leung et al., 2006).

1.2 The Rab proteins family

So far, there are more than 60 Rab proteins identified in mammals, representing the largest family among Ras superfamily of GTPases (Figure 1.4) (Hutagalung and Novick, 2011; Li and Marlin, 2015; Pereira-Leal and Seabra, 2000). In comparison, the number of Rab proteins in Saccharomyces cerevisiae (yeast), Drosophila melanogaster (fly) and Caenorhabditis elegans (worm) are 11, 26 and 31, respectively (Bock et al., 2001; Gallegos et al., 2012), suggesting that the number of Rab proteins increases based on the complexity of the species.

Rab proteins play specific functions in regulating intracellular membrane trafficking, transport, docking, exocytosis and fusion of various intracellular organelles including secretory granules. Rab proteins exert their functions by interacting with specific effector proteins, thereby each interaction gives individual Rabs their function (Diekmann et al., 2011; Grosshans et al., 2006b; Izumi et al., 2003; Pfeffer, 2013; Seabra et al., 2002; Stenmark, 2009; Zerial and McBride, 2001).

Rab GTPases interact with their effector proteins preferentially when they are activated into their GTP-bound state. Therefore, once Rab GTPases are transformed from the GTP- into GDP-bound state, the effector protein dissociates from interaction with its Rab GTPase (Figure 1.5). Therefore, the GTP- and GDP-bound reversible states represent a molecular switch mechanism from active to inactive states, respectively (Goody et al., 2017; Hammer and Wu, 2002; Li and Marlin, 2015; Ostermeier and Brunger, 1999).

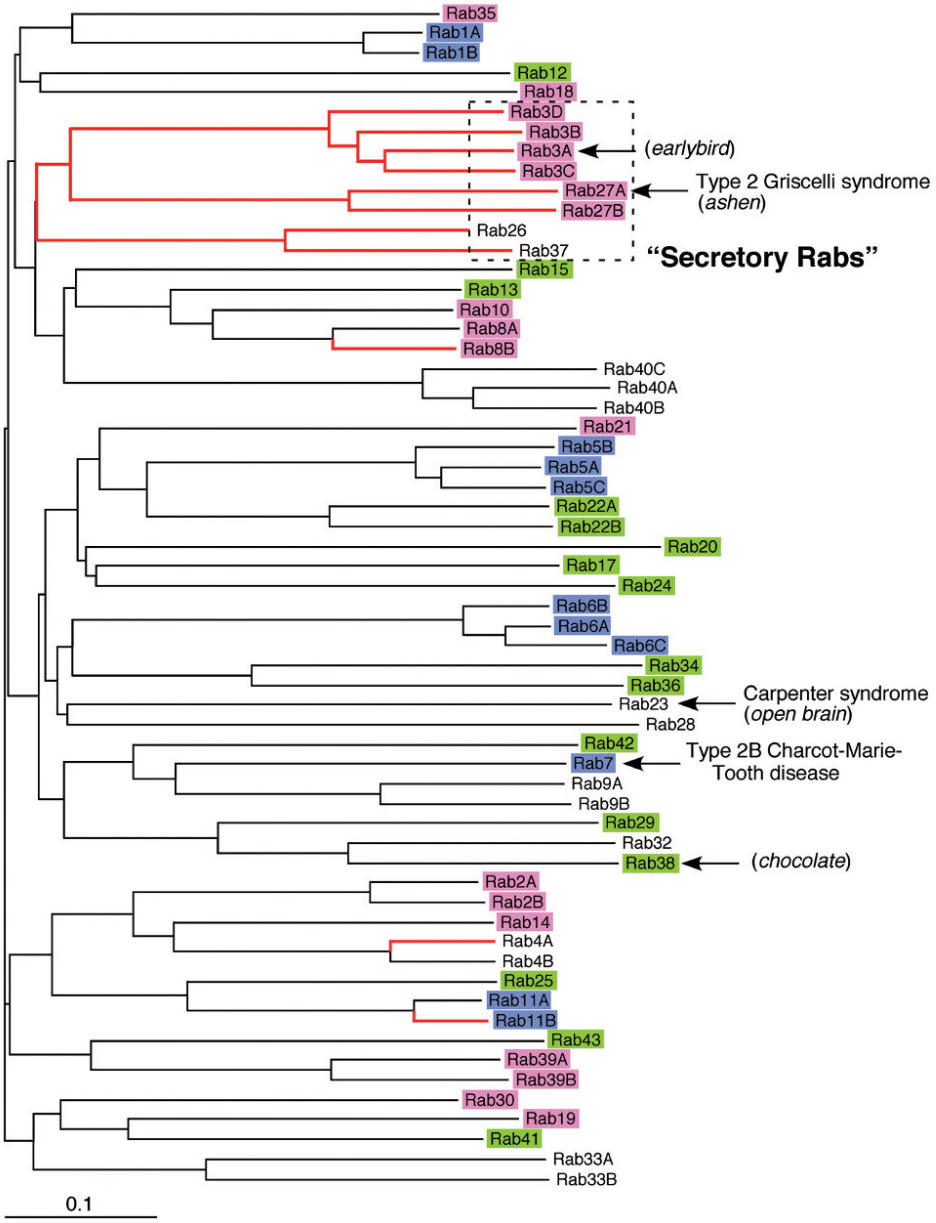


Figure 1.4. Phylogenetic analysis of mammalian Rab family proteins. The blue background represents the conserved Rabs from yeasts to humans; the magenta background represents shared Rabs among C. elegans, Drosophila, mice and humans; the green background represents vertebrate Rabs. Red lines represent Rabs implicated in regulating intracellular membrane trafficking; such as Rab3, Rab26, Rab27 and Rab37 (dotted box). The indicated arrows represent Rab-associated disease states. Reproduced from (Fukuda, 2008).

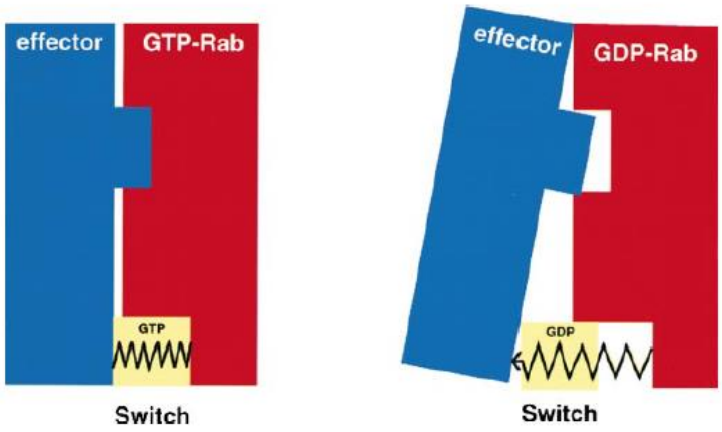


Figure 1.5. Activation-inactivation model of Rab. The Rab associates with its effector in its GTP-bound state. Once the Rab is transformed into its GDP-bound state, the effector protein dissociates from interaction with Rab. Reproduced from (Ostermeier and Brunger, 1999).

1.2.1 Structural characteristics of the Rab family

As part of the Ras superfamily, the Rab family group of proteins shares some of the structural characteristics with other members of the Ras superfamily, including the GTPase domain (as described in section 1.1.1). In addition, Rab proteins family consists of a C-terminal Rab prenylation motif, containing either one or two cysteine residues (Khosravi-Far et al., 1991) (as described in section 1.1.2) and a hypervariable C-terminal domain (HVD) proposed to serve as a targeting signal, directing Rabs to their target membranes (Chavrier et al., 1991). However, it was found that not only the HVD can determine Rab targeting (Stenmark et al., 1994), for instance other regions within the Rab family (RabF) and Rab subfamily (RabSF) motifs (details of these motifs discussed below) are implicated in Rab27a and Rab5a targeting to melanosomes and endosomes, respectively (Ali et al., 2004). Furthermore, substituting HVD with synthetic polyethylene glycol in Rab1 and Rab5 does not affect membrane targeting, suggesting that HVD is not the only determinant for membrane targeting and may partially act in this respect (Li et al., 2014a).

Interestingly, by performing sequence alignment of large number of mammalian Rabs, Pereira-Leal and Seabra identified five specific Rab motifs of conserved

residues, termed RabF1-RabF5 (Pereira-Leal and Seabra, 2000). RabF1 (IGVDF; loop 2, β2) is in the switch I motif, the other RabFs including RabF2 (KLQIW; β3), RabF3 (RFRSIT; loop 4), RabF4 (YYRGA; α2, loop 5) and RabF5 (LVYDIT; β4, loop 6) are in the Switch II domain. Interestingly, the WDTAGQE motif within the Switch II domain of Rab7B and Rab28 (WDIGGQT) is characterised by double double-glycine residues, equivalent to the highly-conserved glycine-glycine residues in the Arf GTPase family (Lee et al., 2008).

Furthermore, four RabSF regions were identified by Pereira-Leal and Seabra as described below: The already identified, highly conserved regions within Rab subfamilies (Moore et al., 1995) were verified by Pereira-Leal and Seabra, and termed RabSF2, RabSF3 and RabSF4. Notably, RabSF4 is identified in the HVD (a region with high sequence variability), indicating a high homology of this region among mammalian Rabs; on average, the identity of the HVD region and the Rab subfamily regions among Rabs are 14.4% and 58.4 %, respectively. In addition, the already identified 3D structure of Rab3a interaction with rabphilin-3a (effector protein) (Ostermeier and Brunger, 1999) demonstrated that three regions within the N-terminus of Rab3a participate in the binding to rabphilin-3a. These regions were termed Rab complementary-determining regions (RabCDRs): RabCDRI-RabCDRIII. RabCDRs are one of the key determinants of the specificity of binding of Rab proteins to their effectors as these regions have variable sequences among Rab proteins. RabCDRII and RabCDRIII correspond to RabSF3 and RabSF4, whereas RabCDRI is considered as an indicator of a conserved Rab subfamily and named RabSF1 (for further details see Figure 1.6).

Interestingly, mapping of RabF and RabSF regions onto the 3D structure of Rab3a, revealed two subfamily specific surfaces (Pereira-Leal and Seabra, 2000). The first one consists of RabSF1, RabSF3 and RabSF4, forming the interacting surface with rabphilin3-a effector protein (Ostermeier and Brunger, 1999). RabSF2 locates on the opposite side (near or within the switch I region), forming the second subfamily specific surface which might act as interacting surface with other effectors. This suggests that RabSF regions confer a specificity for Rab-effector protein interaction as the same effector protein might

interact with different Rab isoforms (as they share the same subfamily specific regions) (Pereira-Leal and Seabra, 2000). The 3D structure of Rab27a in complex with its effector protein Slp2-a, revealed that specific interaction with Slp2-a is mediated by RabF1, RabF2, RabF3, RabSF1 and RabSF4 regions (Chavas et al., 2008).

In addition, Rab proteins contain three hydrophobic conserved residues termed the invariant hydrophobic triad. This triad lies in the interface between switch I and switch II regions (Merithew et al., 2001). It was suggested that the hydrophobic interface between the switch regions, including the invariant hydrophobic triad, stabilises the active conformation of Rab3a (Dumas et al., 1999). In Rab3a, this triad (F59, W76, Y91) determines the specificity of the binding between Rab3a switch regions and its effector, rabphilin3-a (Ostermeier and Brunger, 1999). However, the conformation of the invariant hydrophobic triad represents the major determinant of the effector protein recognition and specificity. This can be exemplified by abrogating the interaction between Rab5c and rabphilin3-a caused by changing the conformation of the invariant hydrophobic triad of Rab5c (F58, W75, Y90) (Merithew et al., 2001). Rab4a and Rab5a share the same effector protein, rabaptin5, but with different binding sites. This is related to a slight difference in the conformation of the invariant hydrophobic triad motif and the presence of V43, F70, V73 and S76 residues in Rab4a that adopt different surface topology and charge distribution to bind rabaptin5, thereby preventing the overlapping of Rab4a with the Rab5a-rabaptin5 binding site; i.e. Rab4a and Rab5a interact with rabaptin5 at different binding sites (Huber and Scheidig, 2005).

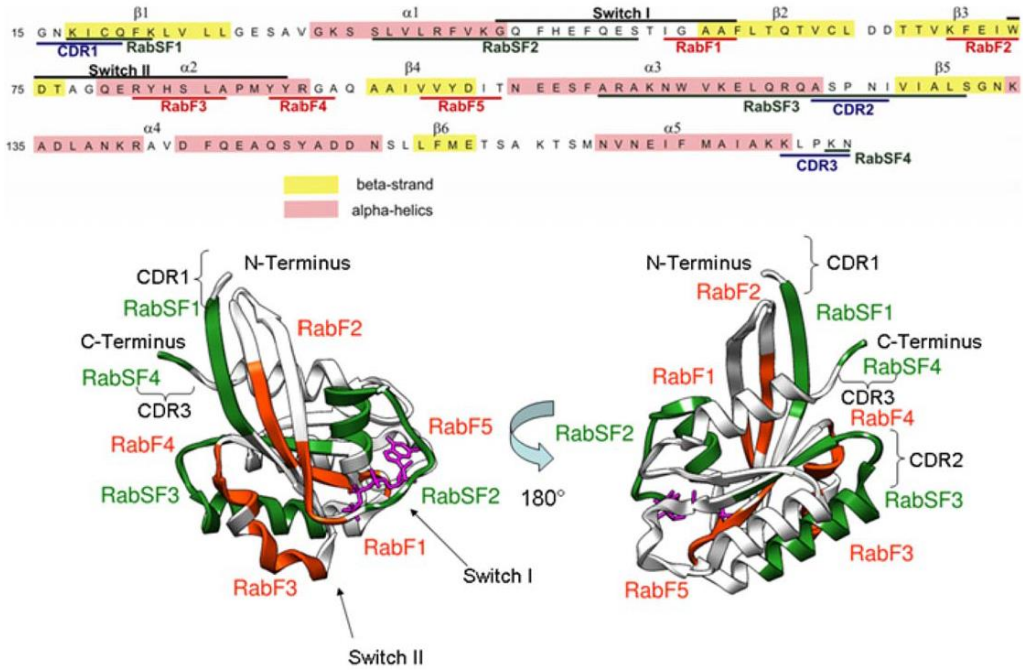


Figure 1.6. Structural features of Rab GTPases. Sequence of Rab specific regions including (RabF1-RabF5), (RabSF1-RabSF4) and CDRI-CDRIII are mapped onto human Rab5a-GTP 3D structure (shown in orange-red). Characteristic Rab regions with high sequence identity (RabSF1-RabSF3) shown in green. The nucleotide displayed in pink. Reproduced from (Stein et al., 2012).

1.2.2 Mechanism of activation of Rab proteins

As mentioned before, the Rab effector proteins interact preferentially with the GTP-bound state of Rab proteins, therefore thorough understanding of the mechanisms of Rab switching from GTP-bound active state into GDP-bound inactive state provides clues to disclose Rab protein functional pathways in the future (Fukuda, 2013). The switching between these two conformations (active and inactive conformations) involves the switch I and switch II regions that change their conformation during binding with GTP or GDP, therefore they play a considerable role during downstream signalling by allowing effector protein binding (Pfeffer, 2005).

In general, activation of Rab proteins (Figure 1.7) requires Rab association and targeting to their specific intracellular membranes and organelles. This is accomplished by prenylation of Rab carboxyl terminal as described in section 1.1.2.1 (Gomes et al., 2003; Pfeffer, 2001; Zhang et al., 2000). In addition, REP presents the GDP-bound form of Rab to RGGT, since REP has a higher affinity

to bind Rab in its GDP bound form (Seabra, 1996) (as mentioned in the classical pathway for geranylgeranyl prenylation of Rabs; section 1.1.2.1). Accordingly, REP interacts with Rab to form 1:1 complex and this binding involves ionic bonds interaction rather than depending on the presence of the two C-terminal cysteine residues in the Rab. (Anant et al., 1998; Andres et al., 1993; Hutagalung and Novick, 2011). This is followed by dissociation of Rab-REP complex from RGGT and delivering of Rab-GDP protein to its intracellular target membrane by REP (Alexandrov et al., 1994). Rab guanine-nucleotide dissociation inhibitor (GDI) then recognises the Rab-GDP bound form and redirects Rab from the membrane into its original site of distribution in the cytosol (Dirac-Svejstrup, 1995; Muller and Goody, 2017; Pfeffer et al., 1995; Soldati et al., 1993; Ullrich et al., 1993). Furthermore, the GDI-displacement factor (GDF) plays additional role with GDI by re-targeting Rab-GDP to its specific membrane (Segev, 2001). GDF mediates Rab dissociation from GDI, promoting Rab association with its specific intracellular membranes (Dirac-Svejstrup et al., 1997). Interestingly, it was reported that human Yip3/PRA1, a Rab-interacting protein (Bucci et al., 1999), has a proven GDF activity by catalysing the dissociation of GDI from Rab-GDI complexes (Muller and Goody, 2017; Sivars et al., 2005; Sivars et al., 2003). In addition, the formation of chaperone complex consisting of heat-shock protein 90 (HSP90), heat shock cognate 70 protein (HSC70) and cysteine string protein displays some GDF activity by mediating membrane association of Rab-GDI complex (Sakisaka et al., 2002).

As described previously, the activation of Rab proteins occurs by cycling between the GTP and GDP forms, and this process is activated by guanine-nucleotide exchange factor (GEF), releasing GDP and catalysing GTP binding (Barr and Lambright, 2010; Chavrier and Goud, 1999; Deneka et al., 2003).

Once the Rab reaches its target membrane and interacts with its specific effector protein, it may be converted into its GDP-bound state by the action of GTPase-activating protein (GAP) by catalysing the low intrinsic Rab GTPase activity (Cherfils and Zeghouf, 2013; Deneka et al., 2003; Pan et al., 2006; Segev, 2001) thereby releasing the Rab from effector interaction. This is followed by recycling of Rab-GDP from the membrane into the cytosol by GDI and a new cycle commences again.

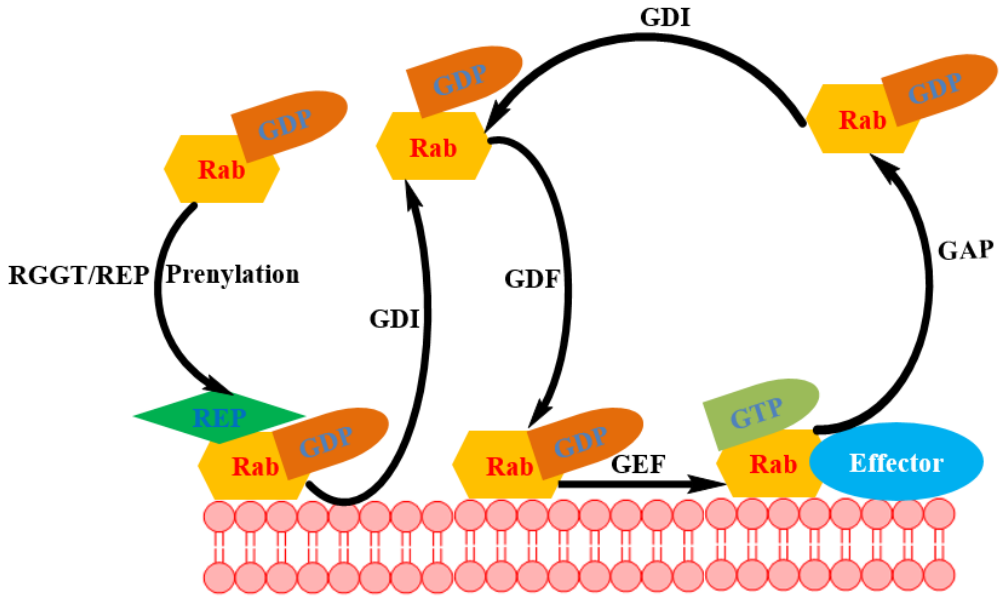


Figure 1.7. The Rab activation and membrane association cycle. After synthesis of Rab (GDP) in the cytoplasm, RGGT binds Rab (GDP)-REP complex, catalysing Rab prenylation by adding two geranylgeranyl groups to the C-terminal cysteine residues; REP directs Rab (GDP) to its specific membrane. Next, Rab (GDP)-REP complex dissociates from RGGT association and GDI then recognises the Rab (GDP) (after REP dissociation) and redirects the Rab into its original site of distribution in the cytosol. Then GDF, targets Rab (GDP) into its specific site at the target membrane, allowing GEF to activate the Rab (GDP) into Rab (GTP), mediating the interaction of the Rab (GTP) with its downstream effector protein. Thereafter, GAP catalyses Rab GTPase intrinsic activity, converting Rab from the GTP- into GDP-bound conformation. GDI then recycles Rab (GDP) from the membrane into the cytosol and a new cycle can start again.

1.2.2.1 REP and GDI proteins

REP and GDI are required for regulation of Rab GTP-GDP cycle by binding to GDP-bound form of Rabs and displaying several functional similarities (Alory and Balch, 2003; Wu et al., 2007). In addition, they are structurally related by sharing several conserved motifs (Alory and Balch, 2000). REP can bind both prenylated and unprenylated Rabs. In comparison, GDI displays higher affinity for prenylated Rabs (in their GDP bound state) mainly (Pylypenko and Goud, 2012; Pylypenko et al., 2006; Wu et al., 2007). There are two REP isoforms in mammals: REP1 (Choroideremia; CHM) and REP2 (Choroideremia like; CHML) with 72% amino acid identity (Cremers et al., 1994; Cremers et al., 1992; Desnoyers et al., 1996; Wu et al., 1996). Furthermore, two GDI isoforms have been identified in mammals: GDIα and GDIβ isoforms are structurally

related and share similar functions, including the recycling of Rabs from membranes to the cytosol. They interact with Rab (GDP-bound) proteins in a proportion related to their relative cellular expression (Araki et al., 1995; Nishimura et al., 1994; Shisheva et al., 1994; Yang et al., 1994).

REP and GDI share five regions of high sequence homology termed sequence conserved regions (SCRs): 1A, 1B, 2, 3A and 3B (Pylypenko et al., 2003; Schalk et al., 1996). In addition, analysis of the 3D structure of bovine α-GDI demonstrated that GDI consists of two domains: domain I (the Rab binding platform) comprises SCR1 and 3B; domain II (the mobile effector loop; MEL) consists of SCR 2 and 3A. SCRs consisting of 1, 3B and 3A are implicated in GDI recycling of Rab proteins (Luan et al., 2000; Schalk et al., 1996). Upon binding of GDI to the Rab, MEL adopts different conformation (a closed state), retrieving Rab from the membrane (An et al., 2003).

Intriguingly, switch I and more likely switch II regions of Rab are significantly involved in the binding to the Rab binding platform (RBP) located in domain I of GDI (Sultana et al., 2011). In addition, mutational analysis revealed that conserved residues including glutamine-236, arginine-240 and threonine-248 are implicated in binding to Rab1a and Rab3a (Wu et al., 1998a). Shisheva et al. found that the 18-residue segment in the C-terminal variable region of GDIβ is not crucial for retrieving GDP-loaded Rabs (Rab2, Rab4, Rab5, Rab8, Rab9 and Rab11). Furthermore, introduction of M250Y mutation within the SCR 3B region abrogated GDI retrieval activity for all the previously mentioned Rabs. (Shisheva et al., 1999). For further details of Rab interaction with REP and GDI, see Figures 1.8 and 1.9.

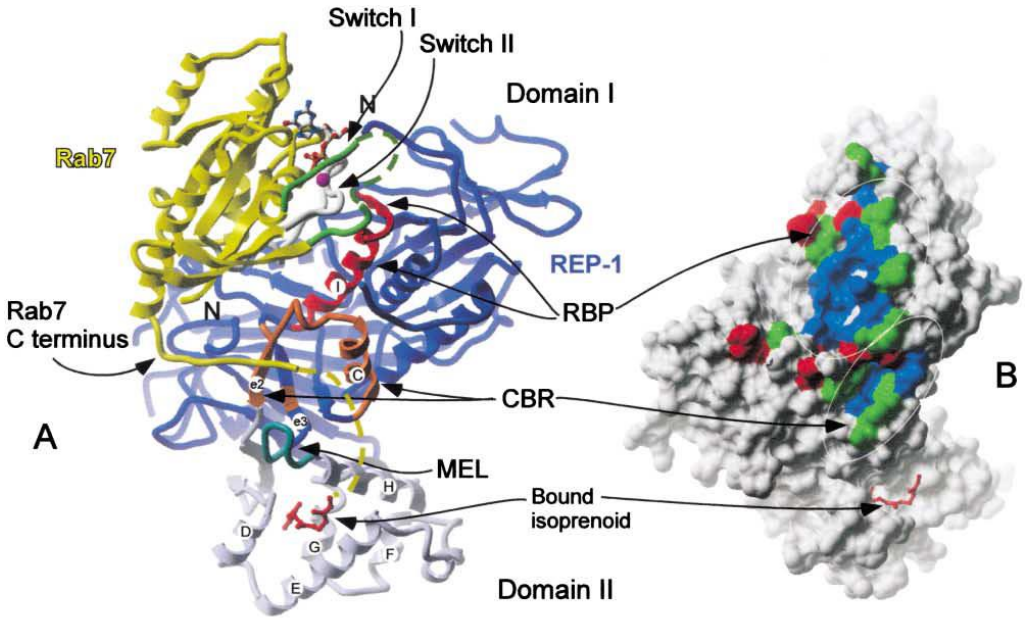


Figure 1.8. Structure of Rab7-REP interaction complex. A) Ribbon diagram representation of REP-1 (blue) in complex with Rab7 (yellow). Domain I, domain II and the RBP of REP-1 are highlighted in dark blue, light blue and red, respectively. The C-terminus binding region (CBR) and MEL of REP-1 are shown in dark orange and sky blue, respectively. Rab7 geranylgeranyl groups are displayed as ball-and-stick models. The switch I (grey) and II (green) regions of Rab7 are highlighted. None-visible part of the switch I region of Rab7 are shown as dashed green line. The GDP (atomic colours) and $Mg2^{+}$ ion are displayed as ball-and-stick and space filling models, respectively. B) REP-1 binding residues to Rab7. REP-1 is shown in grey; REP residues involved in the binding to Rab7 are shown based on the degree of conservation between RGDI and REP: blue, green and red represent invariant residues, conserved residues and REP specific residues, respectively. Rab7 geranylgeranyl groups are shown as in A. Reproduced from (Rak et al., 2004).

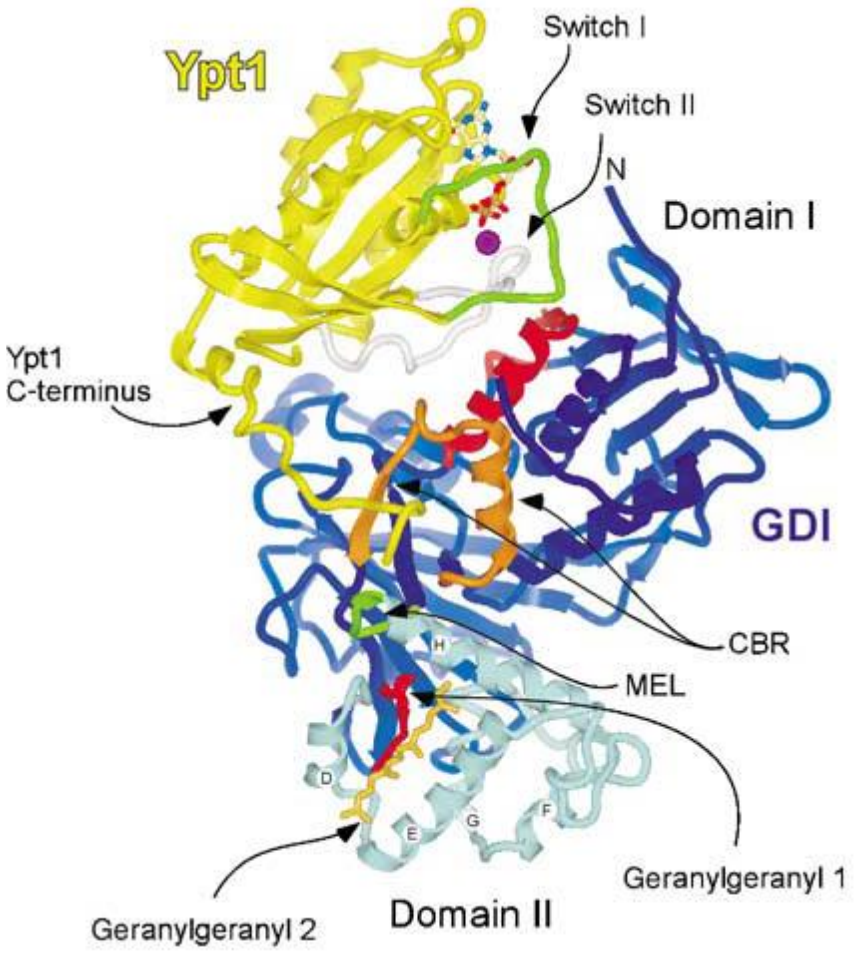


Figure 1.9. Structure of the doubly prenylated Rab (Ypt1)-GDI interaction complex. Ribbon diagram representation of GDI (blue) in complex with Ypt1 (yellow). Domain I, domain II, the RBP, CBR and MEL of GDI are highlighted in dark blue, light blue, red, gold and green, respectively. The switch I (green) and II (grey) regions of Ypt1 are highlighted. Domain II comprising helices of GDI are indicated by letters. The isoprenoid moieties 1 and 2 are shown in red and dark yellow ball-and-stick models, respectively. The GDP (atomic colours) and $Mg2^{+}$ ion are displayed as ball-and-stick and space filling models, respectively. Reproduced from (Pylypenko et al., 2006).

1.2.3 Functions of Rab proteins

The specific and versatile functions of Rab proteins can be exemplified by their wide range intracellular distribution (Figure 1.10) which enables them to exert these specific roles (Zerial and McBride, 2001). In addition, the diversity and complexity of Rab proteins functions correlate with the degree of development and specialization of eukaryotic organs or tissues (Fukuda, 2013).

Furthermore, Rab proteins regulate many of the cellular endocytic pathways, participating effectively in the regulation of the host defence mechanisms against exogenous pathogens (Seabra et al., 2002). Notably, certain members of the Rab

family have specific roles in controlling the secretory functions of various secretory cells and granules; such as Rab3a/b/c/d, Rab4a, Rab8b, Rab11b, Rab26, Rab27a/b and Rab37 (Fukuda, 2008). Rab proteins regulation of membrane trafficking involves cargo sorting and vesicle formation, vesicle and organelle transport, vesicle tethering/docking and vesicle fusion (Kelly et al., 2012) (Figure 1.11) as described in the subsequent sections.

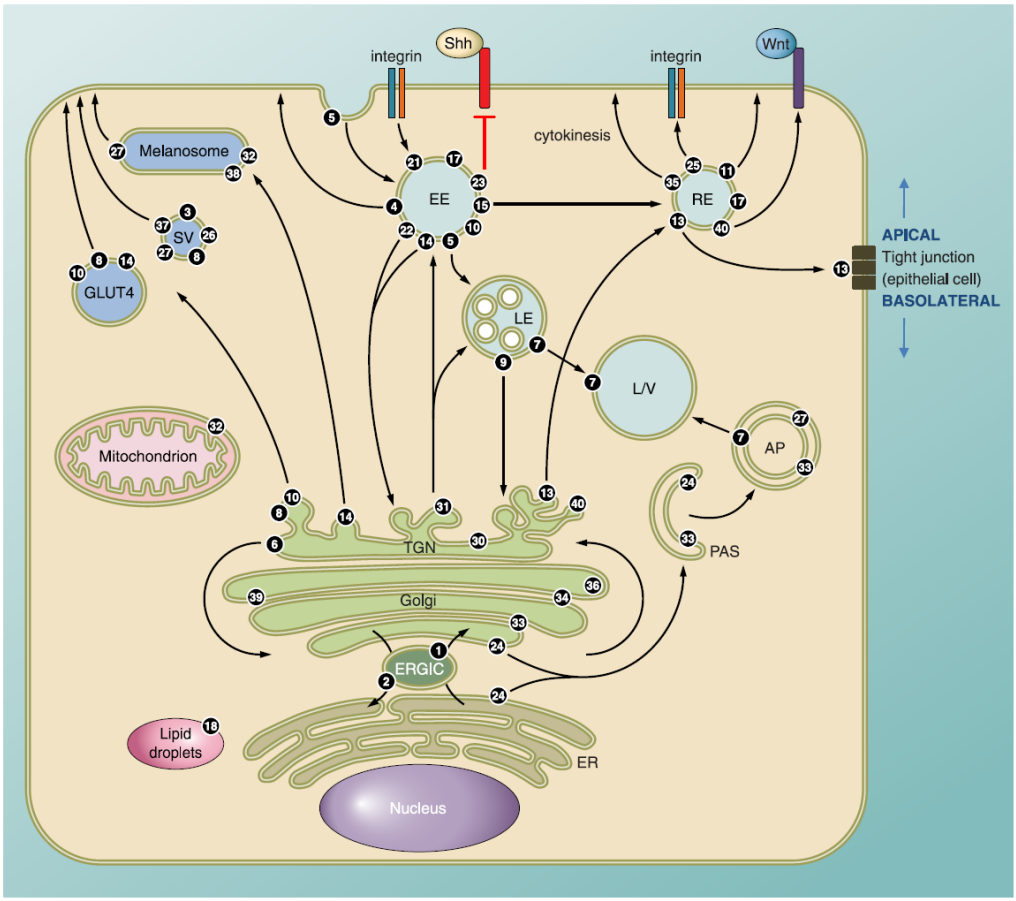


Figure 1.10. The intracellular distribution of Rab proteins. Rab1 and Rab2 are implicated in the regulation of endoplasmic reticulum (ER)-Golgi transport and retrograde transport from Golgi and the ER-Golgi intermediate compartment (ERGIC) back to the ER. Intra-Golgi traffic is regulated by Rab6. The biosynthetic transport of the glucose transporter type 4 (GLUT4) containing vesicles from the trans-Golgi network (TGN) to the plasma membrane is regulated by Rab8, Rab10, and Rab14. Rab3, Rab26, Rab27 and Rab37 are involved in the exocytosis of several secretory vesicles/granules (SV). In addition, Rab27, Rab32 and Rab38 are involved in melanosome transport. Rab5 mediates the formation of the early endosome (EE), while trafficking towards the lysosome for degradation is mediated by Rab7. Directing of the membrane traffic from the early endosome to the recycling endosome (RE) is mediated by Rab15. The regulation of the fast and slow endocytic recycling is driven by Rab4 and Rab11, respectively. Rab18 mediates the regulation of specialised functions, including regulation of lipid droplets (LD) and intracellular lipid storage

compartments. The formation of the preautophagosomal structure (PAS) is mediated by Rab24 and Rab33, this is followed by the formation of the autophagosome (AP) which is then targeted to the lysosome/vacuole (L/V). The transport of integrins is regulated by Rab21 and Rab25, controlling cell adhesion and cytokinesis. The formation of tight junctions in polarized epithelial cells is regulated by Rab13. The sonic hedgehog (Shh) signalling pathway is negatively regulated by Rab23. Rab40 regulates Wnt signaling by recruiting components of the ubiquitination machinery. Rab34 Rab35 and Rab39 are classified as poorly characterized Rabs. The regulation of the plasma membrane recycling of an essential factor in cytokinesis is driven by Rab35, while Rab34 and Rab39 are localised in the Golgi with uncharacterised functions. LE; late endosome. Reproduced from (Hutagalung and Novick, 2011).

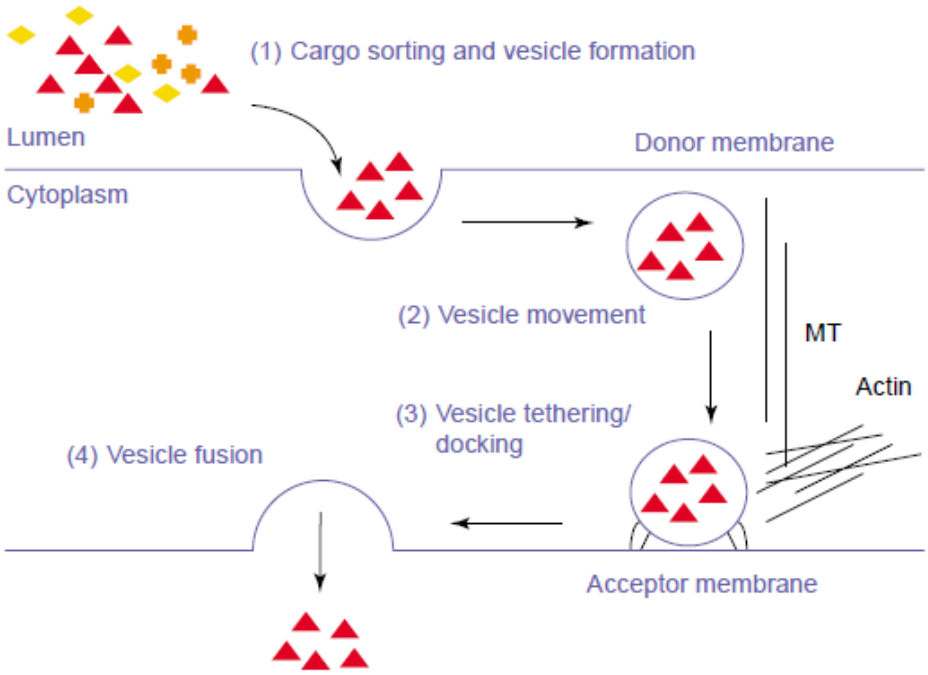


Figure 1.11. Intracellular secretory granules trafficking. Firstly, the transported molecules are assembled in a specific region of the donor membrane and encapsulated in vesicles, this is followed by detachment of the budding vesicle from the donor membrane (Rab1, Rab2, Rab5 and Rab9 are involved in this process). Secondly, the formed vesicles transport through the cytoplasm along the microtubules and/or actin filaments (Sec4, Rab5, Rab6 and Rab27 are involved in this process). Thirdly, these vesicles associate with the acceptor membrane by a process termed docking/tethering (Ypt1, Ypt7, Sec4, Rab1 and Rab5 are involved in this process). Fourthly, these vesicles undergo fusion process with the target membrane, releasing their contents into the target site. Reproduced from (Seabra et al., 2002).

1.2.3.1 Cargo sorting and vesicle formation (budding)

Vesicle formation requires vesicle coating protein complexes such as coat protein (COP) I, COPII or clathrin and selection of cargo components. Several

Rab proteins have been implicated in this process (Hutagalung and Novick, 2011). For instance, Rab9 has been shown to be involved in the regulation of the mannose-6-phosphate receptor (MPR) transport between late endosomes and TGN (Lombardi et al., 1993; Riederer et al., 1994; Shapiro et al., 1993). Rab9 exerts its function by interaction with its effector TIP47, inducing the interaction between MPR and TIP47 and budding of the late endosomes (Aivazian et al., 2006; Carroll et al., 2001; Ganley et al., 2004). Interestingly, it has recently been shown that the constitutively active mutant of Rab9 (Q66L) is involved in the transport of cation independent-MPR (CI-MPR) from the TGN to endosomes (Kucera et al., 2016).

In addition, it has been reported that Rab5 and Rab7 are implicated in the recruitment of the retromer associated trimer, Vps26-Vps29-Vps35 which is important for cargo binding, enhancing traffic of transmembrane proteins from endosomes to the TGN (Rojas et al., 2008). Furthermore, the interaction of Rab1b with its effector GBF1, enhances COPI recruitment, thereby regulating cargo sorting (Garcia et al., 2011). Also, many Rab proteins are involved in cancer progression and development, for instance Rab25 has been implicated in the regulation of activated α5β1 integrins sorting toward the chloride intracellular channel protein 3 (CLIC3)-positive late endosomes/lysosomes in A2780-Rab25 human ovarian carcinoma cell line (Dozynkiewicz et al., 2012).

1.2.3.2 Vesicle transport

Rab proteins regulate vesicle and organelle transport by interacting with effectors that recruit motor proteins, driving vesicle traffic along microtubules or actin filaments. The most prominent example of Rab regulation of vesicle transport is the Rab27-regulated melanosome transport mediated by interaction of Rab27a with its effector Slac2-a/melanophilin (Mlph), coupling Rab27a to myosin-Va motor protein, thereby transporting melanosomes to the plasma membrane in melanocytes (Hume et al., 2001; Hume et al., 2006; Hume et al., 2007; Strom et al., 2002; Wu et al., 2001). In addition, plasma membrane recycling of endosomes is regulated by interaction of Rab11 with its downstream effector, Rab11 family interacting protein 2 (Rab11-FIP2) which serves as a linker protein with myosin-Vb motor protein (Hales et al., 2002; Schafer et al., 2014). Also, the association of Rab11 with its effector, Rab coupling protein

(RCP), regulates the trafficking of the axonal β1 integrins in adult dorsal root ganglion neurons and differentiated PC12 cells (Eva et al., 2010). Depletion of Rab11a and Rab11b mediated by small interfering RNA (siRNA) reduces the intracellular recycling of the fibroblast growth factor 1 (FGF1) and the fibroblast growth factor receptor (FGFR) 4 in in U2OS cells stably expressing FGFR4 (Haugsten et al., 2014).

It has been reported that Rab6 is involved in the regulation of the retrograde transport between endosomes, Golgi and the ER (Del Nery et al., 2006; Iwanami et al., 2016; Martinez et al., 1997; Storrie et al., 2012). In addition, Rab6 regulates the exocytosis to the plasma membrane, for instance the association of Rab6 with the kinesin-1 motor protein directs the exocytotic vesicles along the microtubules towards the plasma membrane (Grigoriev et al., 2007). The Rab6 effector proteins, Bicaudal D1/D2 couple Rab6 with the dynein-dynactin motor complex, driving microtubule minus-end-directed traffic of the Rab6-containing vesicles (Matanis et al., 2002). Intriguingly, the interaction of Rab7 with the Rab interacting lysosomal protein (RILP) recruits the dynein-dynactin motor complex, trafficking late endosomes towards centrosomes and the lysosomes (Cantalupo et al., 2001; Guerra and Bucci, 2016; Johansson et al., 2007; Jordens et al., 2001; Wu et al., 2005a). In Drosophila, Rab4 directly interacts with kinesin-2 motor protein, directing Rab4-containing vesicles towards the synapse (Dey et al., 2017). It has been reported that Rab14 interacts directly with the kinesin-3 motor, KIF16B, transporting the FGFR 2 containing vesicles from Golgi towards the plasma membrane of mouse fibroblast during early stages of embryonic development (Ueno et al., 2011).

1.2.3.3 Vesicle docking/tethering

Fusion of membranes is commonly preceded by docking and tethering of intracellular vesicles. Vesicle docking/tethering involves Rab-mediated docking steps, this is followed by fusion of the docked vesicles by means of formation of the soluble N-ethylmaleimide–sensitive factor attachment protein receptor (SNARE) complex (Kummel and Ungermann, 2014). By using liposome–liposome tethering assay, it was found that homotypic vacuole fusion and protein sorting (HOPS) complex binds the Rab7-like Ypt7, tethering the liposomes

containing liposomes carrying 1,2-dioleoyl-sn-glycero-3-[(N-(5-amino-1carboxypentyl) iminodiacetic acid) succinyl] (Lurick et al., 2017).

Early endosome antigen 1 (EEA1), a Rab5 effector protein, has been implicated in the early endosomes tethering. This is accomplished by association with endosomes through the phosphatidylinositol 3-phosphate binding region and interacting with syntaxin 6 SNARE protein (Christoforidis et al., 1999; Lawe et al., 2002; Mills et al., 2001; Simonsen et al., 1999; Simonsen et al., 1998). In addition, the Ypt1 Rab protein regulates tethering via recruiting its effector, the conserved oligomeric Golgi (COG) which serves as a tethering agent (Suvorova et al., 2002). For instance, direct interaction of COG complex with Sec1/Munc18 (SM) protein Sly1, mediates the colocalisation of the t-SNARE, Syntaxin5 and the v-SNARE, GS15, thereby regulating intra-Golgi transport (Laufman et al., 2009). Many of the Rab27-effector protein interactions have been shown to be involved in the regulation of tethering of secretory granules. For instance, direct interaction of Rab27a with Munc13-4 is necessary for docking of secretory lysosomes at the plasma membrane of rat basophilic leukemia-2H3 (RBL-2H3) cells (Elstak et al., 2011). Moreover, Rab27a interaction with its effector, Slp2-a mediates docking of Rab27a-containing vesicles to the plasma membrane in several secretory cells (Menasche et al., 2008; Mrozowska and Fukuda, 2016; Yasuda et al., 2015b; Yasuda et al., 2012).

1.2.3.4 Vesicle Fusion

Rab proteins regulate vesicle fusion by directly interacting with SNARE proteins or indirectly via interaction with SNARE regulating proteins (Hutagalung and Novick, 2011). For instance, Sec4, a yeast Rab, interacts with its effector Sro7p, mediating Sro7p binding to Sec9p SNARE protein and forming a ternary complex consisting of Sec4, Sro7p and Sec9p, thereby regulating SNARE function (Grosshans et al., 2006a; Grosshans and Novick, 2008; Lehman et al., 1999). Intriguingly, the Rab27 effector, Slp1 has been involved in insulin secretion by mediating fusion of undocked granules to the plasma membrane via association of its C2A domain with the plasma membrane phospholipids (Wang et al., 2013). Furthermore, Rab7 recruits its effector, the vici syndrome protein EPG5, mediating the assembly of trans-SNARE complexes and EPG5 binding to LC3/LGG-1 and assembled STX17-SNAP29 Qabc SNARE complexes, thus

promoting fusion of autophagosomes with the late endosomes (Wang et al., 2016).

1.3 Rab27 subfamily proteins

There are two Rab27 isoforms (Rab27a and Rab27b) that share similar but not identical functions (Izumi, 2007). The type of the interacting effector protein represents the main determinant of their specific functions, especially the regulation of the exocytosis of various intracellular secretory granules and organelles (Fukuda, 2013; Itzen and Goody, 2008; Izumi et al., 2003; Stenmark, 2009; Yamaoka et al., 2015). Although the Rab27 proteins are widely distributed among metazoans, no Rab27 proteins have been identified yet in yeasts and plants (Diekmann et al., 2011).

It has been reported that amino acid and DNA sequence homology between mouse Rab27a and human Rab27a are 96% and 88%, respectively, whereas amino acid and DNA sequence homology between mouse Rab27a and human Rab27b are 72% and 67%, respectively (Ramalho et al., 2001). Furthermore, amino acid sequence similarity between human Rab27a and Rab27b is 81% (Chen et al., 1997). Notably, amino acid sequence alignment of Rab27a and Rab27b demonstrated that most of the Rab27 interacting residues with their effectors are conserved between them (Kukimoto-Niino et al., 2008) (for further details see Figure 1.12). This suggests that tissue expression of these isoforms might determine their functional specificity as both Rab27a/b can bind the same effectors and share most of the interacting residues with their downstream effectors.

Notably, the Rab3 subfamily is closely related to Rab27a/b subfamily (Izumi, 2007) as both subfamilies have moderate amino acid sequence homology (41-44%) (Chen et al., 1997) (for further details of sequence homology see Figure 1.12). This might explain why both subfamilies share some effector proteins and sequence differences confer interaction specificity with their downstream effectors as described in sections 1.4, 1.4.1.3 and 1.4.2. Remarkably, Rab27a/b exhibit the slowest prenylation rate among many Rab proteins in vivo and in cells (Kohnke et al., 2013).

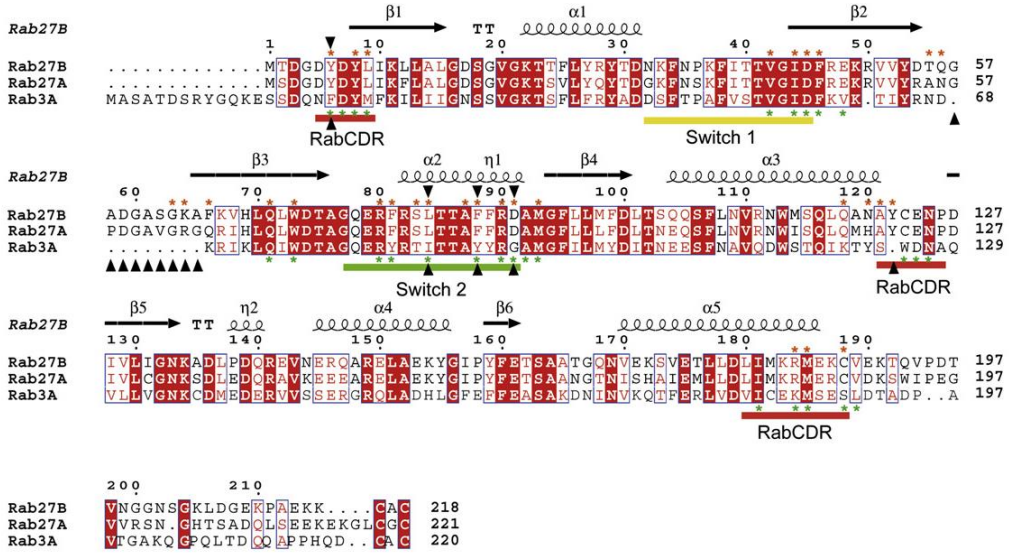


Figure 1.12. Amino acid sequence homology of mouse Rab27a, Rab27b and Rab3a. Mouse Rab27a and Rab3a sequences were aligned with the mouse Rab27b sequence in complex with Slac2-a. Switch I, switch II and RabCDRs are presented as yellow, green and red bars, respectively. The interacting residues of Rab27b with Slac2-a and those of Rab3a with rabphilin are indicated by orange and green asterisks, respectively. The arrowheads indicate mutated or inserted Rab27a and Rab3a residues tested by Kukimoto-Niino and colleagues. Reproduced from (Kukimoto-Niino et al., 2008).

Intriguingly, it has been demonstrated that overexpression of the active Rab27a-(Q78L) GTPase deficient mutant in melan-a cells (Menasche et al., 2003a) and in B16 melanoma cells (Bahadoran et al., 2003) induced significant perinuclear clustering of melanosomes. Further investigations revealed that the induced perinuclear clustering of melanosomes in melan-a cells caused by this Rab27a mutant is due to inability of this mutant to localise Rab27a on mature melanosomes (Rab27a is dispersed throughout the cytosol), thus disrupting Rab27a-dependent melanosome transport by competing with endogenous Rab27a for Slac2-a binding. This finding was confirmed by overexpression of Rab27a-(C219A, C221A) mutant, causing mutation of the geranylgeranylation sites and defective Rab27a attachment to the mature melanosomes, thereby inducing significant perinuclear clustering of melanosomes (Ishida et al., 2014).

1.3.1 Regulators of Rab27 GTP-GDP cycle

As members of the Rab family, Rab27 proteins functions are regulated by cycling between GTP- (active) and GDP- bound (inactive) states, and the main regulators of this process are GEF and GAP enzymes (for further details see

sections 1.2.2 and 1.2.2.1). So far, there are one Rab27 GEF termed Rab3 guanine-nucleotide exchange protein (Rab3GEP) as it also acts on Rab3 protein (Figueiredo et al., 2008; Imai et al., 2013; Tarafder et al., 2011; Wada et al., 1997). Silencing of RAB3GEP using siRNA induced perinuclear clustering of melanosomes in melan-ink4a melanocytes caused by reduction in localisation of Rab27a to melanosomes, indicating that Rab3GEP is required for Rab27 targeting to melanosomes (Tarafder et al., 2011).

On the other hand, there are two Rab27-GAP enzymes, a Tre-2/Bub2/Cdc16 (TBC)-domain proteins: Rab27-GAPα/EPI64/TBC1D10A and Rab27-GAPβ/FLJ13130/TBC1D10B (Fukuda, 2011; Hou et al., 2013; Imai et al., 2011; Ishibashi et al., 2009; Itoh and Fukuda, 2006). However, EPI64 and FLJ13130 cannot be considered as specific Rab27 GAPs as they can act on several Rab, Ras and Arf proteins; e.g. Rab3a, Rab35, Rab8a, H-Ras and Arf6 (Chaineau et al., 2013; Hanono et al., 2006; Hokanson and Bretscher, 2012; Hsu et al., 2010; Ishibashi et al., 2009; Nagai et al., 2013). It has also been reported that Rab27-GAP might promote Rab27a binding to its GDP-Rab27 effector, Coronin 3, regulating the endocytosis of the insulin secretory membrane in the pancreatic β-cell line MIN6 (Kimura et al., 2008; Kimura et al., 2010). Interestingly, stimulation of platelets by thrombin decreased Rab27-GTP, whereas Rab27-GDP was increased and this might be due to activation of Rab27-GAP (Kondo et al., 2006). Notably, overexpression of Rab27-GAPα/EPI64 enhanced exosome secretion in human lung adenocarcinoma A549 cells by interacting specifically with Rab27a, but not Rab27b (Li et al., 2014b). Furthermore, it was found that parotid acinar cells stimulation by isoproterenol induced secretory granule exocytosis (amylase release) by promoting Rab27-GAPα/EPI64 activity, thereby reducing the endogenous levels of Rab27-GTP (Imai et al., 2011). Furthermore, overexpression of Rab27-GAPα/EPI64 and Rab27-GAPβ/FLJ13130 caused perinuclear clustering of melanosomes in melan-a melanocytes by activating the intrinsic Rab27a GTPase activity, thereby transforming Rab27a into its GDP-bound inactive form and inhibiting Slac2-a binding activity (Itoh and Fukuda, 2006) (for further details of the Rab27 GTP-GDP cycle regulation see Figure 1.13).

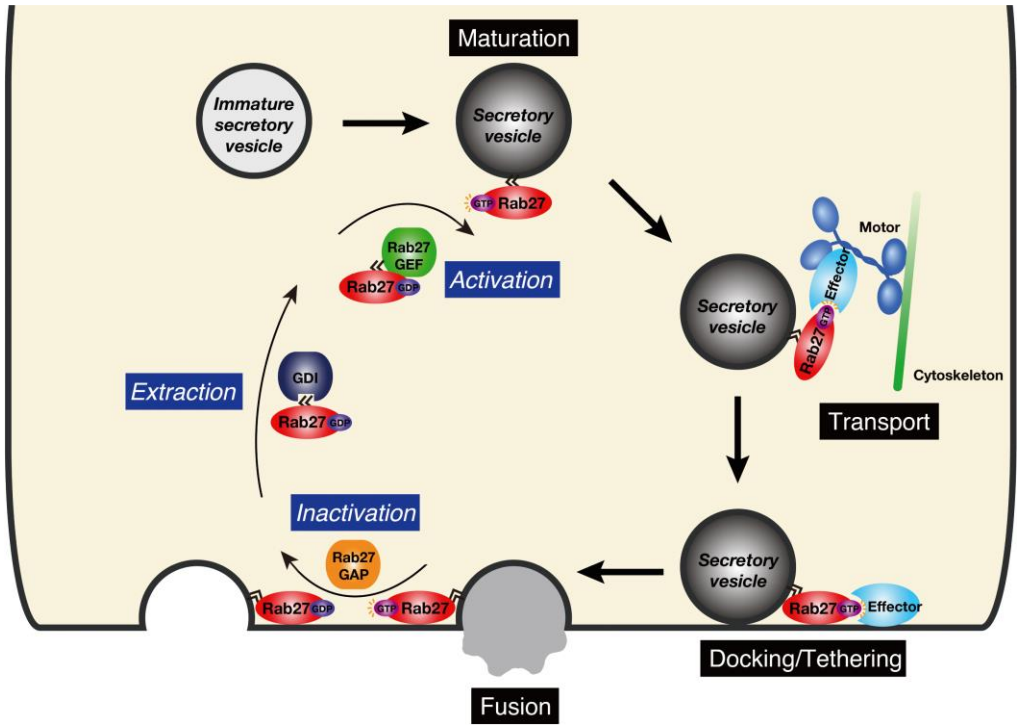


Figure 1.13. Regulation of Rab27 GTP-GDP cycle during exocytosis of secretory granules. The exocytosis of secretory granules by parotid acinar cells was used as a model to depict the Rab27 GTP-GDP cycle. The Rab27 GTP-bound form localises to the secretory vesicles, upon binding to Rab27 effectors, the secretory vesicles are anchored/tethered to the plasma membrane. Upon exposure to extracellular stimulus, the Rab27–effector complex(s) then mediates the exocytosis of secretory vesicles, followed by inactivation of Rab27 at the plasma membrane by the effect of the Rab27-GAP EPI64 and the inactive Rab27 form (GDP-bound) is then detached from the plasma membrane by GDI. The Rab27-GEF then activates the GDP-bound form of Rab27 into its GTP-bound state (active form) and Rab27 localises again to the secretory vesicles in the cytosol to start a new cycle. Reproduced from (Fukuda, 2013).

1.3.2 Functions and tissue expression of Rab27a/b proteins

Rab27 subfamily proteins are tissue specific Rabs (Pereira-Leal and Seabra, 2001), therefore their tissue expression determines their specific and versatile functions. In general, Rab27a and Rab27b share the same effector proteins, and Rab27b could compensate for loss of function caused by Rab27a deficiency. For instance, ubiquitous transgenic expression of Rab27b in the *ashen* mice (see section 1.3.3) compensates for Rab27a loss of function by restoring peripheral melanosomes distribution in melanocytes and thus curing the coat colour defects

in the *ashen* mice, indicating that there is functional redundancy between Rab27a/b isoforms (Barral et al., 2002).

Rab27a/b isoforms are widely expressed in various cell types and tissues, but the tissue expression of Rab27b appears to be more specific, less abundant than Rab27a and restricted to specific cell types (Itzen and Goody, 2008; Ramalho et al., 2001) (see Table 1.1).

Rab27a can be detected in mouse melanocyte cell lines: melan-a, melan-b and melan-c, but not Rab27b (Ramalho et al., 2001). It has also been shown that Rab27a is highly expressed in promyelocytic leukemia HL-60, chronic myelogenous leukemia K-562, Hela and melanoma (G361) cells, whereas Rab27b can be expressed in in Hela cells only (Chen et al., 1997).

Rab27 protein has a significant role in the regulation of immune functions, for instance Rab27a is expressed abundantly and more highly than Rab27b, in human peripheral blood neutrophils, and functions by mediating the secretion of tertiary and specific granules (Herrero-Turrion et al., 2008). Rab27a has also been involved in the regulation of neutrophil migration by mediating elastase secretion from azurophilic granules at the rear of bone marrow polymorphonuclear leukocytes (Singh et al., 2012). Moreover, it has been suggested that Rab27b regulates neutrophil chemotaxis, probably by regulating primary granule exocytosis (Singh et al., 2014). In neutrophil-like differentiated HL60 cells, Rab27a functions a substantial role in neutrophil extracellular traps formation (Kawakami et al., 2014). It has also been reported that Rab27a is involved in the delivery of lytic granules to the plasma membrane and also it participates in the regulation of lytic granules movement in the cytosol of natural killer cells (Liu et al., 2010).

In *ashen* mice pancreatic acinar cells, although the total Rab27b expression was increased by 32.5%, the Rab27b-GTP active form was unchanged, suggesting that Rab27b could not compensate for Rab27a deficiency, causing a reduction in the amylase release in acinar cells (Hou et al., 2015). This suggests that Rab27a has a substantial role in the amylase release in acinar cells. However, Rab27b has also been shown to localise to zymogen granules and is involved in the regulation of the exocytosis of pancreatic acinar cells (Chen et al., 2004). In

addition, in the Rab27b knockout (KO) mouse model, the size of zymogen granules is decreased with a moderate decrease in amylase release by acinar cells (Hou et al., 2016), suggesting an additional role for Rab27b with Rab27a in amylase release. Interestingly, Rab27b is involved in the regulation of secretory vesicle formation and release by lacrimal gland acinar cells (Chiang et al., 2012; Chiang et al., 2011).

Rab27a has a specific role in the regulation of dense-core vesicles docking to the plasma membrane in PC12 cells and the silencing of RAB27A using siRNA significantly reduced the docking of dense-core vesicles to the plasma membrane (Tsuboi and Fukuda, 2006a). In cystinosis, a lysosomal storage disorder, overexpression of the constitutively active, Q78L mutant of Rab27a in cystinotic fibroblasts, restores normal lysosomal transport and reduces endoplasmic reticulum stress, suggesting that Rab27a plays an essential role in the regulation of the intracellular lysosomal trafficking (Johnson et al., 2013).

Early research conducted by Hume and colleagues revealed that overexpression of dominant negative Rab27a mutants, T23N and N133I, equivalent to the dominant negative Ras mutants S17N and N116I, respectively induced perinuclear clustering of melanosomes in melan-a cells, indicating an essential role of Rab27a in melanosome transport in melanocytes (Hume et al., 2001) (as described in section 1.4.1.3). Moreover, Rab27a and Rab27b play a substantial role in the regulation of dense granule exocytosis in platelets (Novak et al., 2002; Tolmachova et al., 2007). Notably, Rab27a deficiency in *ashen* mice bone-marrow macrophages caused multi-nucleation and giant cell formation during osteoclasts differentiation, suggesting that Rab27 plays an essential role in the regulation of lysosome-related organelles transport in osteoclasts (Shimada-Sugawara et al., 2015).

In addition, Rab27a is essential for the establishment of an immediately releasable pool and determining the readily releasable pool size of insulin-containing secretory granules in pancreatic β-cells (Cazares et al., 2014). Intriguingly, Rab27a acts as a negative regulator of angiogenesis in endothelial cells by stabilising membrane-localised vascular endothelial growth factor

receptor-1via regulation of palmitoylating enzyme DHHC3 trafficking (Boucher et al., 2017).

Rab27a tissue expression	Rab27b tissue expression
• Eye, stomach, small intestine, large intestine, spleen, lung, platelets, kidney, liver, testis, prostate, ovary, oocytes, pituitary, leukocytes, skin, sebaceous glands and keratinocytes, but not in the brain (Barral et al., 2002; Chen et al., 1997; Kasai et al., 2005; Seabra et al., 1995; Tolmachova et al., 2004; Yi et al., 2002). • Exocrine glands; such as serous and mucous acinar cells (Tolmachova et al., 2004). • Endocrine organs such as α, β, δ pancreatic cells, adrenal medulla and cortex and thyroid gland (Merrins and Stuenkel, 2008; Tolmachova et al., 2004; Yi et al., 2002; Yu et al., 2007). • Ciliated and Clara cells of the murine bronchiolar epithelium (Bolasco et al., 2011)	• Brain, stomach, small intestine, large intestine, spleen, liver, pancreatic exocrine cells, testis, pituitary, urinary bladder, kidney, lung, submandibular salivary glands and eye (Chen et al., 1997; Gomi et al., 2007; Hendrix et al., 2012; Ramalho et al., 2001; Zhao et al., 2002). • Rab27b is highly expressed in platelets with less expression in the gastrointestinal tract, but not in melanocytes or cytotoxic T lymphocytes, indicating that Rab27b could compensate for Rab27a functions in platelets, but not for those functions in melanocytes or cytotoxic T lymphocytes (Barral et al., 2002). • Ciliated and Clara cells of the murine bronchiolar epithelium (Bolasco et al., 2011). • Eosinophils of the parenchyma of the lung mice (Bolasco et al., 2011).

Table 1.1. Comparison of Rab27a/b tissue expression.

1.3.3 Rab27-related diseases

Rab27 and its effectors are involved in the regulation of various intracellular secretory functions and any defect in those functions is often associated with diseases. The most well documented Rab27-related disease is Griscelli syndrome (GS) (Griscelli et al., 1978) which can be classified into three types (see Table 1.2). GS type I occurs due to mutations within the MYO5A gene encoding myosin-Va motor protein (Pastural et al., 1997) and is characterised by albinism and neurological, but no immunological defects (Dessinioti et al.,

2009). GS type I is the human equivalent to the *dilute* mouse model (Mercer et al., 1991).

GS type II is caused by mutations in the gene encoding Rab27a, leading to albinism, immune deficiency and some neurological defects (Anikster et al., 2002; Isikay, 2014; Menasche et al., 2000) and is similar to the *ashen* mouse model (Wilson et al., 2000). Three missense mutations within RAB27A gene: W73G, L130P and A152P have been identified in GS type II patients and found to cause defective cytotoxic T cell lytic granule exocytosis (Menasche et al., 2000). Furthermore, it has been shown that Rab27a loses its GTP-GDP-binding ability upon introduction of the L130P and A152P mutations, possibly by impairing protein folding, whereas the W73G Rab27a mutant retains its GTP-GDP-binding ability. Notably, the W73G, W73L and W73S Rab27a mutants lack the intrinsic GTP hydrolysis activity, probably by causing conformational changes at the P-Loop or the switch regions, impairing Slac2-a effector protein binding activity, pointing out the importance of W73 in maintaining Rab27a interaction with Slac2-a (Menasche et al., 2003a). It has also been reported that K22R, I44T, F46I, G43S, A87P and K134E missense mutations within RAB27A gene can also cause GS type II (Mamishi et al., 2008; Masri et al., 2008; Mishra et al., 2014; Ohbayashi et al., 2010; Westbroek et al., 2008; Zur Stadt et al., 2006). In addition, it has been demonstrated that the G43S mutation located in the switch I region of Rab27a lacks Slac2-a binding ability in vitro and overexpression of this Rab27a mutant failed to restore normal melanosomes distribution in primary melanocytes from patients with GS type II (Westbroek et al., 2008). Furthermore, 2 heterozygote RAB27A missense mutations (L70P and A76V) and a homozygous RAB27A nonsense mutation (Q118X) have been identified in GS type II patients and found to disrupt Slp2-a effector protein binding in vitro (Menasche et al., 2008). Intriguingly, R82C has been identified as a novel mutation in Rab27a and causes immunodeficiency with normal pigmentation, completely disrupting the interaction of Rab27a with Munc13-4 effector protein, but only partially inhibiting the interaction with Slac2-a (Netter et al., 2016). Notably, Munc13-4 (Rab27 effector protein) dysfunction causes type 3 familial hemophagocytic lymphohistiocytosis (FHL) which is characterised by defective cytotoxicity of cytotoxic T lymphocytes (Feldmann

et al., 2003; Yamamoto et al., 2004). In addition, it has been reported that deletion of R141, replacement of V142 by isoleucine or (A76V, Y159C, S163R) Rab27a missense mutations cause type 3 FHL without albinism and found to disrupt the interaction of Rab27a with Munc13-4 (Cetica et al., 2015).

GS type III is caused by mutations within the MLPH gene encoding melanophilin/Slac2-a effector protein and is characterised by only albinism without any neurological or immunological defects (Menasche et al., 2003b; Tomita and Suzuki, 2004), and is the human equivalent to the *leaden* mouse model (Matesic et al., 2001). It has also been reported that the deletion of the REEERLQ motif (31-37 aa) from Slac2-a in *leaden* mice resulted in defective Slac2-a function (Matesic et al., 2001) and completely abolished Rab27a-binding activity (Fukuda, 2002b). It has also been shown that the R35W mutation in Slac2-a causes GS type III (Menasche et al., 2003b; Nouriel et al., 2015), since this slac2-a mutant lacks the ability to interact with Rab27a (Menasche et al., 2003b). In addition, it has been shown that primary epidermal melanocytes from patients with GS type III display a perinuclear clustering of melanosomes pattern, indicating that this mutation disrupts Rab27a-Slac2-a binding, thereby affecting melanosome transport in melanocytes and causing only hypopigmentation (Westbroek et al., 2012).

It has also been shown that the Rab27a and Slp2-a are compensatory induced in dysferlin-deficient patients suffering from limb girdle muscular dystrophy 2B, thereby promoting vesicle trafficking pathways, but probably upregulating endocytotic vesicle release and causing subacute inflammatory response (Kesari et al., 2008). Recently, various mutations in Slac2-b (Rab27 effector protein) have been identified and found to cause inherited skin fragility (Liu et al., 2014; Malchin et al., 2016; McGrath et al., 2012; Turcan et al., 2016).

Rab prenylation defects can be caused by mutations within the RGGT and REP genes, for instance RGGT dysfunction leads to the gunmetal mice phenotype, which is characterised by hypopigmentation and platelet coagulation defects (Detter et al., 2000; Novak et al., 1995; Swank et al., 1993). Whereas, REP dysfunction results in Rab underprenylation defects in the retinal pigment

epithelium, causing choroideremia which is characterised by progressive blindness and retinal degeneration (Seabra et al., 1995).

GS type	Mouse phenotype	Mutated gene	Mutated protein	Pathological features
I	*dilute*	MYO5A	myosin-Va	Albinism and neurological defects
II	*ashen*	RAB27A	Rab27a	Albinism, immune deficiency and some neurological defects
III	*leaden*	MLPH	melanophilin/Slac2-a	Albinism

Table 1.2. Griscelli syndrome types.

1.4 Rab27 effector proteins

So far, there are eleven distinct Rab27 effector proteins in human and mouse that interact preferentially with Rab27 in its GTP-bound state (Fukuda, 2005; Fukuda, 2013) (Figure 1.14). Rab27 effector proteins can be sub-classified structurally into three major groups. The first group consists of the synaptotagmin-like protein (Slp) family (Kuroda et al., 2002a) and rabphilin3-a (Fukuda, 2003a; Fukuda et al., 2004). Thus far, five distinct Slp proteins: Slp1, Slp2-a, Slp3-a, Slp4-a/b and Slp5 have been identified in mammals (Fukuda and Mikoshiba, 2001; Fukuda et al., 2001; Kuroda et al., 2002b). These Rab27 effectors share two conserved, N-terminal α-helical Rab27 binding domains termed Slp homology domain (SHD) 1 and 2 (Fukuda, 2002a; Fukuda and Mikoshiba, 2001; Fukuda et al., 2001). However, there is a zinc finger motif between SHD1 and SHD2 of Slp3-a, Slp4-a, Slp5 and rabphilin3-a, while SHD1 and SHD2 of Slp1 and Slp2-a are linked directly; i.e. they lack the zinc finger motif (Fukuda, 2005; Fukuda et al., 2001). The other characteristic feature of this group is the presence of two C-terminal tandem C2 domains termed A and B and these tandem C2 domains bind to membrane phospholipids (Fukuda, 2002a). A linker sequence of various lengths connects the SHD and C2 domains. The C2 domains are phospholipids binding domains which are found in many calcium–dependent protein kinases C (α, βI, βII and γ), phospholipases C and GAPs (Ponting and Parker, 1996). In addition, it has been reported that there are

four Slp2 isoforms (Slp2-a-d) and two Slp3 isoforms (Slp3-a-b) and only A isoforms act as Rab27 effectors as other Slp isoforms lack the SHD domains (Fukuda et al., 2001).

The second group of Rab27 effector proteins consists of Slac2 (Slp homologue lacking C2 domains) family (Slac2-a, Slac2-b and Slac2-c) (El-Amraoui et al., 2002; Fukuda and Kuroda, 2002; Fukuda et al., 2002; Kuroda et al., 2002a; Matesic et al., 2001; Strom et al., 2002; Wu et al., 2002) and Noc2 (Fukuda, 2003a; Fukuda et al., 2004). Members of this group share the N-terminal SHD with Slp family, but lack the C2 tandem domains. In addition, Slac2-b lacks the zinc finger motif. Notably, SHD1 serves as a main Rab27-binding site, whereas SHD2 and the zinc finger motifs stabilise the whole SHD structure and determine Rab27 binding affinity and specificity (Fukuda, 2002b; Fukuda, 2003b). The C-terminal regions of Slac2-a (amino acids 400–590) and Slac2-c (amino acids 670–856) are involved in actin binding (Fukuda and Kuroda, 2002). Interestingly, it has been reported that SHD of Slp1, Slp2-a, Slp3-a, Slac2-a and Slac2-b specifically co-immunoprecipitated with Rab27a in COS-7 cells, indicating that these effectors are specific Rab27effectors, whereas SHD of Slp4-a and rabphilin3-a co-immunoprecipitated with Rab3a, Rab8 and Rab27a, indicating that Slp4-a and rabphilin3-a are not specific Rab27 effectors (Kuroda et al., 2002a).

The third group contains Munc13-4 only which can be considered as a new category of Rab27 effector proteins as the Rab27 binding domain (RBD) differs from that of Slp and Slac2 families (it does not contain SHD). The region between the C2A domain and MUN domain represents the RBD of Munc13-4 (Elstak et al., 2011; Neeft et al., 2005; Shirakawa et al., 2004).

Remarkably, Rab27 effectors can be sub-classified based on their Rab27 binding affinity into a high affinity binding group: Slp1, Slp2-a, Slp4-a, Slp5, Slac2-b, rabphilin and Noc2 and a low affinity binding group: Slp3-a, Slac2-a and Slac2-c (Fukuda, 2006).

In addition to these Rab27-GTP binding effectors, Coronin 3, a Rab27-GDP binding effector, has been identified recently and found to have distinct functions in the regulation of the endocytosis of the insulin secretory membrane by

interacting with Rab27a-GDP through its N-terminal domain, thereby promoting F-actin assembly in pancreatic β-cells (Kimura et al., 2008; Kimura and Niki, 2011; Kimura et al., 2010).

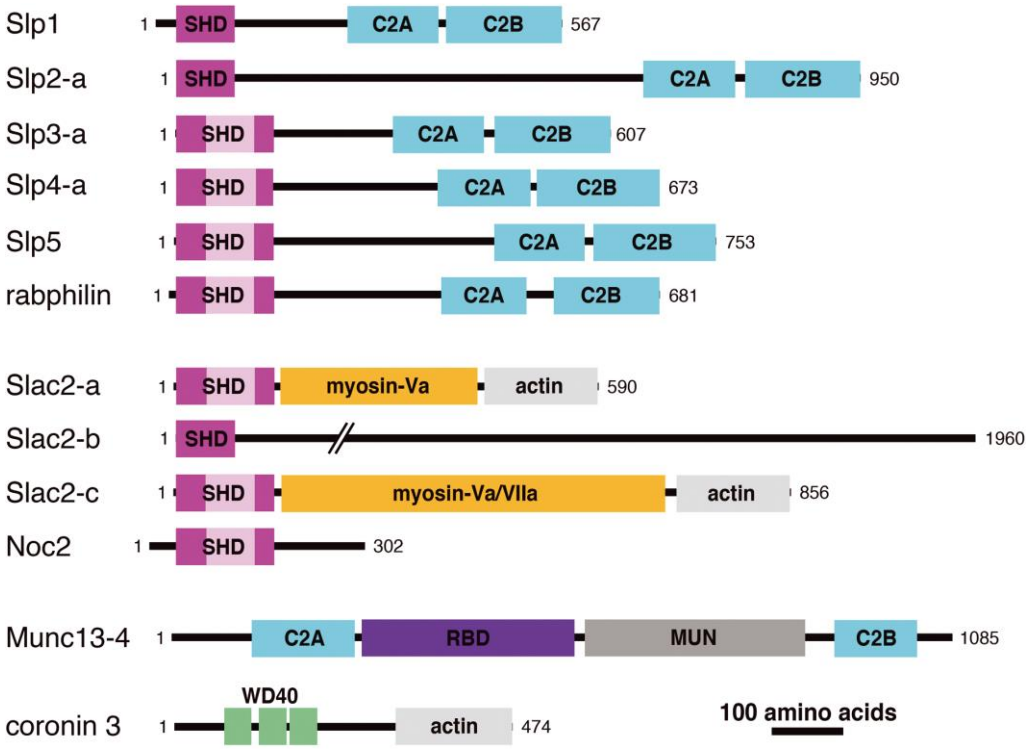


Figure 1.14. A schematic representation of mouse Rab27 effectors structure. Synaptotagmine homology like domain (SHD) (dark purple) represents the Rab27-GTP binding domain of Slp family (Slp1-5 and rabphilin) and Slac2 family (Slac2a-c and Noc2). Most of these Rab27-binding domains consist of two SHD domains connected by Zn^{2+}-binding motif (light purple). The Rab27-GTP-binding domain (RBD) of Munc13-4 differs from that of Slp and Slac2 families. Coronin 3 interacts with Rab27a-GDP through its N-terminal domain. Myosin-Va-, myosin-Va/VIIa-, actin-, C2A- and C2B- binding domains are depicted. Reproduced from (Fukuda, 2013).

Interestingly, in order to investigate the key determinates of the specificity of Rab27 interaction with its effectors, Itzen and Goody compared the structures of the complexes of interaction of Rab27b with Slac2-a and Slp2-a and Rab3a with rabphilin (Figure 1.15). They argue that Y6, F88 and D91 residues confer Rab27 certain degree of specificity in terms of binding to Slac2-a, Slp2-a and rabphilin, whereas the equivalent Rab3a residues (F19, Y91 and G94) shift Rab3a binding

specificity to rabphilin only (Itzen and Goody, 2008) (see also sections 1.4.1.3 and 1.4.2).

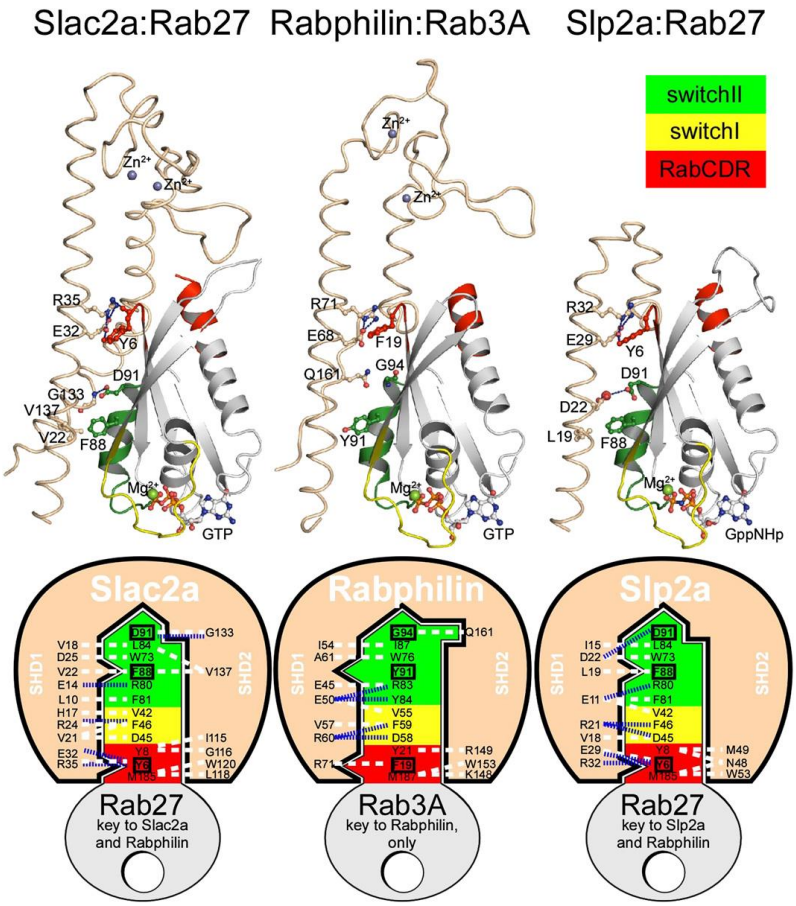


Figure 1.15. Carton representation of Rab–effector interaction specificity. The 3D structures of Rab27b-Slac2-a (left), Rab3a-rabphilin (middle) and Rab27b-Slp2 (right) complexes are depicted. In the top panel, the key residues: Y6 (Rab27)/F19(Rab3a), F88(Rab27)/Y91(Rab3a) and D91(Rab27)/G94(Rab3a) together with their binding partners are depicted as a ball-and-stick models. In addition, Rab proteins are displayed as cartoon models; the effectors are shown inside ribbon representation. In the bottom panel, a schematic representation of the conserved interacting residues between Rab proteins and their effectors are depicted. The key binding residues in Rab27b:Slac2-a, Rab3a:rabphilin and Rab27a:Slp2-a complexes are displayed as boxes. Y6, F88 and D91 Rab27 residues allow binding to Slac2-a, Slp2-a and rabphilin, whereas F19, Y91 and G94 Rab3a residues permit binding to rabphilin only. Polar and hydrophobic interactions are shown as blue and white dashes, respectively. Water molecules are displayed as red spheres. SHD represents Slp homology domains 1 and 2. Reproduced from (Itzen and Goody, 2008).

1.4.1 Functions and distinct features of Rab27 effectors

As mentioned previously, Rab27 proteins exert their specific and versatile function by interacting with their downstream effectors. Occasionally, Rab27a/b have different roles even when they are co-expressed in the same cell. This can be exemplified by the diversity of their effector interactions in the same cell type that confers each Rab27 isoform its specific function (Singh et al., 2013). However, the functional roles of Rab27 effectors have not yet been fully elucidated and still require further investigations. Accordingly, the specific and distinct features of Rab27 effectors including cellular functions are described hereafter (see Table 1.3). In addition, details of Slp1, Slp2 and Slac2-a effectors described in the subsequent sections as they were used in this study.

Rab27 effector	Putative functions
Slp1/JFC1/Exophilin-7	• Regulation of the exocytosis of azurophilic granules by neutrophils (Brzezinska et al., 2008; Johnson et al., 2012; Munafo et al., 2007). • Control of lytic granule exocytosis by cytotoxic T lymphocytes via a Rab27a-dependent interaction (Holt et al., 2008). • Regulation of amylase secretion from pancreatic acinar cells via a Rab27b-dependent interaction (Saegusa et al., 2008).
Slp2-a/Exophilin-4	• Involvement in the targeting of glucagon containing granules to the plasma membrane via the C2A domain in the pancreatic α cells through Rab27a-dependent interaction manner (Yu et al., 2007). • The association of Slp2-a with Rab27a is involved in the regulation of exocytosis of lytic granules from cytotoxic T lymphocytes (Holt et al., 2008; Menasche et al., 2008). • Regulation of the trafficking of the signalling molecule podocalyxin-containing vesicles to the apical membrane in Madin–Darby canine kidney II (MDCK II) cells (Mrozowska and Fukuda, 2016; Yasuda et al., 2012). • Involvement in Schwann cell myelination via Rab27a interaction (Su et al., 2016).

Slp3-a/Exophilin-6	• The Rab27a-Slp3a complex regulates lytic granules trafficking towards the immune synapse of cytotoxic T lymphocytes by interaction of the linker domain of Slp3-a with kinesin-1 via the tetratricopeptide repeat of the kinesin-1 light chain (Kurowska et al., 2012). • Slp3 links kinesin-1 to Rab27b-containing secretory granules in mast cells via a phosphatidylinositol 3-kinase-depedent stimulation, thereby mediating mast cell degranulation (Munoz et al., 2016).
Slp4a/b/Granuphilin-a/b/Exophilin-2	• Involvement in the regulation of dense core secretory granules transport to the plasma membrane in MIN6 pancreatic β cells by interacting with Rab27a, thereby recruiting the brain-spliced isoform of myosin-Va (BR-MyoVa) motor protein to the plasma membrane by forming Slp4-a/b, Rab27a and BR-MyoVa tripartite complex (Brozzi et al., 2012). • Regulation of amylase secretion from rat parotid acinar cells by interaction with Syntaxin-2/3 via its linker domain in the presence of Munc18-2 via (Fukuda et al., 2005). • Slp4 association with Rab27b regulates pituitary hormones secretion in the pituitary endocrine AtT20 cells (Zhao et al., 2002). • Slp-4 promotes Weibel-Palade body exocytosis by interaction with syntaxin-binding protein 1 in a Rab27a-depedent interaction manner (van Breevoort et al., 2014). • Involvement in the regulation of stimulation-mediated release of receptor activator of NF-kB ligand (RANKL) in osteoblastic cells by interaction with Rab27/b (Kariya et al., 2011).
Slp5/Exophilin-9	• Negative regulation of the Rab27a-depedent inhibition of the epithelial sodium channel activity in HT-29 cells through C2A/C2B domains-dependent phospholipids binding activity (Saxena et al., 2006). • Overexpression of Slp5 promoted high KCl-induced NPY secretion by PC12 cells (Tsuboi and Fukuda, 2006b).

Rabphilin3a/Exophilin-1	• Participation in maintaining N-methyl-D-aspartate receptors (NMDARs) stabilization at synaptic sites by forming a ternary complex with GluN2A and PSD-95 (Stanic et al., 2015). • Overexpression of rabphilin negatively regulates the high KCl-induced NPY secretion in PC12 cells through a Rab27a-dependent interaction, suggesting that rabphilin controls dense-core vesicle exocytosis in PC12 cells (Fukuda et al., 2004).
Slac2-a/Melanophilin/Exophilin-3	• Regulation of Rab27a-dependent melanosome transport via interaction with myosin-Va (Hume et al., 2007). • The Rab27a/Slac2-a/myosin-Va complex has a distinct inhibitory role in mast cell degranulation by regulating the integrity of cortical F-actin (Singh et al., 2013).
Slac2-b/Exophilin-5	• Slac2-b has a significant role in the regulation of keratinocyte adhesion and it has been shown to co-localise with Rab27b and β4 integrin in normal keratinocytes (McGrath et al., 2012).
Slac2-c/Myosin-VIIa and Rab27 interacting protein (MyRIP)/Exophilin-8	• Regulation of Rab27a-dependent melanosome trafficking in the retinal pigment epithelium via interaction with myosin-VIIa (El-Amraoui et al., 2002). • Involvement in the regulation of amylase secretion from rat parotid acinar cells (Imai et al., 2009; Imai et al., 2004). • Rab27a-Slac2-c complex associates with secretory granules in PC12 cells, linking secretory granules to F-actin and regulating their transport along actin cortex (Desnos et al., 2003). • Rab27a-Slac2-c complex has been implicated in the regulation of insulin exocytosis in pancreatic β cells by mediating the association of secretory granules with cortical actin (Mizuno et al., 2011; Waselle et al., 2003).
Noc2	• Regulation of dense-core vesicle exocytosis in PC12 cells via specific interaction with Rab27a (Fukuda et al., 2004; Handley and Burgoyne, 2008). • Noc2 association with Rab27a is involved in the regulation of pancreatic β cells exocytosis, possibly through Noc2

	interaction with Munc13 (Cheviet et al., 2004).
Munc13-4	• Regulation of the exocytosis of matrix metalloproteinase (MMP)-9-containing granules in neutrophils (Brzezinska et al., 2008; Pivot-Pajot et al., 2008). • Munc13-4 and Rab27a have been suggested to be involved in mediating lipopolysaccharide-dependent exocytosis in neutrophils (Johnson et al., 2011). • Involvement in late endosomal maturation in neutrophils by interacting with SNARE proteins, syntaxin 7 and vesicle-associated membrane protein (VAMP)-8 in a calcium-dependent manner (He et al., 2016). • Munc13-4 plays an essential role with Rab27b and to a lesser extent Rab27a in enhancing mast cell degranulation in murine bone marrow-derived mast cells by mediating F-actin-dependent granule docking (Singh et al., 2013). • Involvement in the in vitro regulation of dense core granule exocytosis in platelets in a Rab27a-depedent manner (Shirakawa et al., 2004).

Table 1.3. Putative functions of Rab27 effectors.

1.4.1.1 Slp1/JFC1/Exophilin-7

Similar to other members of the Slp family, Slp1 has the N-terminal conserved SHD domains and the C-terminal tandem C2 domains, but lacks the zinc finger motif. The phosphatidylinositol 3,4,5-trisphosphate and, to a lesser extent, the phosphatidylinositol 3,4-diphosphate preferentially interact with the tandem C2 domains (McAdara Berkowitz et al., 2001). Apparently, the C2A domain is responsible for binding the 3'-phosphorylated phosphoinositides, and also contributes to the membrane binding activity of Slp1 (Catz et al., 2002b). Interestingly, Slp1 is endogenously phosphorylated by the protein kinase Akt at serine 241, mediating Slp1 membrane disassociation and re-directing Slp1 to the cytosol, while maintaining Rab27a binding activity (Johnson et al., 2005b).

The cooperation of the mammalian sterile 20–like kinase 1 (MST1) with Slp1 regulates the trafficking of VLA-3 and VLA-6 containing vesicles to the neutrophil surface (Kurz et al., 2016). In the neuron axon terminus, Rab27b mediates the interaction of Slp1 with the neurotrophin receptor TrkB, also

collapsing response mediator protein-2 (CRMP-2) interacts with Slp1, connecting Slp1 to kinesin-1 and linking TrkB to Kinesin-1, thereby regulating the anterograde transport of TrkB (Arimura et al., 2009). Intriguingly, the interaction of Slp1 with the GTPase-activating protein Rap1GAP2 via its C2A domain and with Rab27 forms a trimeric complex, regulating the secretion of dense granules in the platelets (Neumuller et al., 2009).

1.4.1.2 Slp2-a/Exophilin-4

Like Slp1, Slp2-a has the N-terminal conserved SHD domains and the C-terminal tandem C2 domains, and also lacks the zinc finger motif. The 3D structure of Slp2-a in complex with Rab27a has been identified (Chavas et al., 2008). The structure of the Slp2-a binding domain to Rab27a consists of the long N-terminal α1 helix, SHD1 region (10-39 residues) and SHD2 region comprising the short α2 (42-50 residues) and α3 (51-56 residues) helices. The hydrophobic face of SHD1 region forms tight contacts with the Rab27a inter-switch domain (β2 and β3 strands), containing RabF1 and RabF2 and the switch II domain (α2 helix), containing RabF3. In addition, the highly conserved charged residues in SHD2 region are involved in the interaction with Rab27a by forming electrostatic interactions, surrounding the interface. Interestingly, M49 in Slp2-a can compensate for the lack of the zinc finger motif by packing the aromatic ring of Y8 in Rab27a, thereby connecting α1, α2 and α3 helices to the Rab27a RabSF1 and RabSF4 motifs (Chavas et al., 2008). For further details see (Figure 1.16) and (Chavas et al., 2008).

It has been reported that Slp2-a co-localises with Rab27a at the melanosomes of melanoma cells and both Rab27a and Slp2-a distribute to cell periphery, especially at the dendritic tips in the B16-F1 melanoma cells (wild type), whilst they re-distribute to the perinuclear region in the melanosome transport-defective S91/Cloudman melanoma cells, indicating that Rab27a-Slp2-a complex plays additional role with Slac2-a (see section 1.4.1.3) in the regulation of melanosome transport in melanocytes (Kuroda et al., 2002a). Further research revealed that Slp2-a is required for melanosomes anchoring to the plasma membrane via its C2A phospholipids binding domain (by interacting mainly with phosphatidylserine), thereby maintaining peripheral melanosome distribution (Kuroda and Fukuda, 2004).

It has also been shown that Slp2-a is abundantly expressed at the apical region of mouse gastric-surface mucous cells and SLP2-A deficient KO mice displayed defects in mucus granules docking to the apical plasma membrane, with an accompanying reduction in the number of mucus granules and in gastric mucus secretion in those cells (Saegusa et al., 2006). Interestingly, Slp2-a together with Rab27a play an essential role in HIV assembly in HIV-infected Jurkat cells by participating in the generation of phosphatidylinositol 4-phosphate and a pool of phosphatidylinositol 4,5-bisphosphate via mediating phosphatidylinositol 4-kinase type 2α and $CD63^{+}$ endosomes transport towards the plasma membrane (Gerber et al., 2015).

Finally, Slp2-a has functions independent from association with Rab27, for instance it regulates renal cell size by interacting with Rap1GAP2 via a C2B domain-dependent manner (Yasuda and Fukuda, 2014). Furthermore, Slp2-a participates in the inactivation of ezrin in MDCK II cells by interacting with protein phosphatase 1 via its linker domain (which connects the SHD and C2 domains), thereby localising protein phosphatase 1 to the plasma membrane and inactivating ezrin by protein phosphatase 1 (Yasuda et al., 2015a).

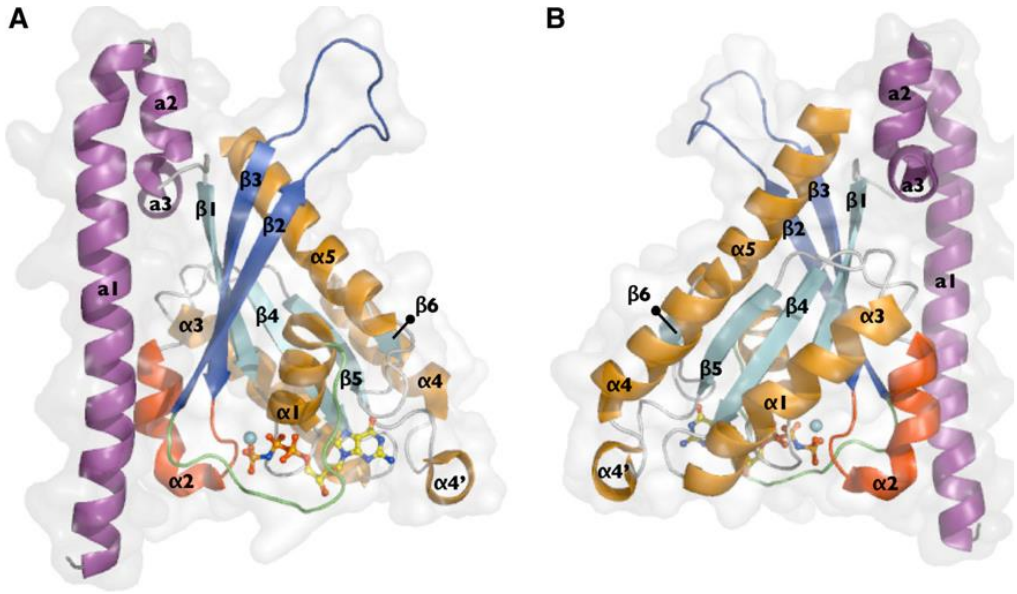


Figure 1.16. Structure of Rab27a in complex with Slp2-a. Ribbon diagram representation of the 3D structure of Rab27a (orange/cyan)-Slp2-a (purple) complex: A and B represent front and back views, respectively. The green, blue

and red highlighted regions represent the switch I, inter-switch and switch II domains, respectively. GppNHp (GTP analogue) and Mg^{2+} are displayed as ball-and-stick and space-filling models, respectively. Reproduced from (Chavas et al., 2008).

1.4.1.3 Slac2-a/Melanophilin/Exophilin-3

As a member of the Slac family, Slac2-a consists of the N-terminal SHD1/2 domains separated by the zinc finger motif, but lacks the C2 tandem domains. Notably, the 3D structure of Slac2-a in complex with the constitutively active form of Rab27b (Q78L) has been identified (Kukimoto-Niino et al., 2008). The structure of the Slac2-a binding domain to Rab27b consists of the SHD1 (α1 helix) and SHD2 (α3- α5 helices) regions surrounding the zinc finger motif (β1-β4 strands, L1–L5 loops and α1, η1, η2 helices). In addition, a coiled coil is formed between α1 and α3-α5 helices, thereby mediating intramolecular interaction of SHD1 with SHD2. The Rab27b binding interface consists of three contact areas: the coiled-coil regions of Slac2-a comprising the first and second contact areas, whereas the third contact area lies in the zinc finger motif which confers specificity for Rab27 binding. The first contact area of Slac2-a binding interface comprises residues 6–9 from RabCDRs, part of the switch and inter-switch regions of Rab27b. The second contact area consists of a cavity in the RabCDRs that harbours the side chains of the residues in the 117-SLEWYY-122 motif of Slac2-a. The third contact area comprises the prominent β2- β3 loop in Rab27b and the L5 loop of the zinc finger motif in Slac2-a. Those interactive residues with slac2-a are highly conserved between Rab27a/b. For further details see (Figure 1.17) and (Kukimoto-Niino et al., 2008).

In addition, the L84, F88 and D91 amino acid residues in the switch II region of Rab27a are specifically recognised by the Slac2-a SHD, and those residues are not conserved in the Rab3 or Rab8 isoforms. Therefore, this might explain the Slac2-a SHD specificity to bind Rab27a rather than Rab3 or Rab8 (Fukuda, 2002b). Interestingly, the Rab3a-(F19Y, I87L, Y91F, G94D) mutant containing the equivalent Rab27a residues can bind Slac2-a, but to a lesser extent than Rab27a, suggesting that these residues confer some degree of specificity to Slac2-a binding (Kukimoto-Niino et al., 2008) (see also sections 1.4 and 1.4.2). It has also been reported that the first 150 residues of Slac2-a are essential for

Rab27a binding as they contain the SHD1/2 domains and the zinc finger motif (Hume et al., 2006).

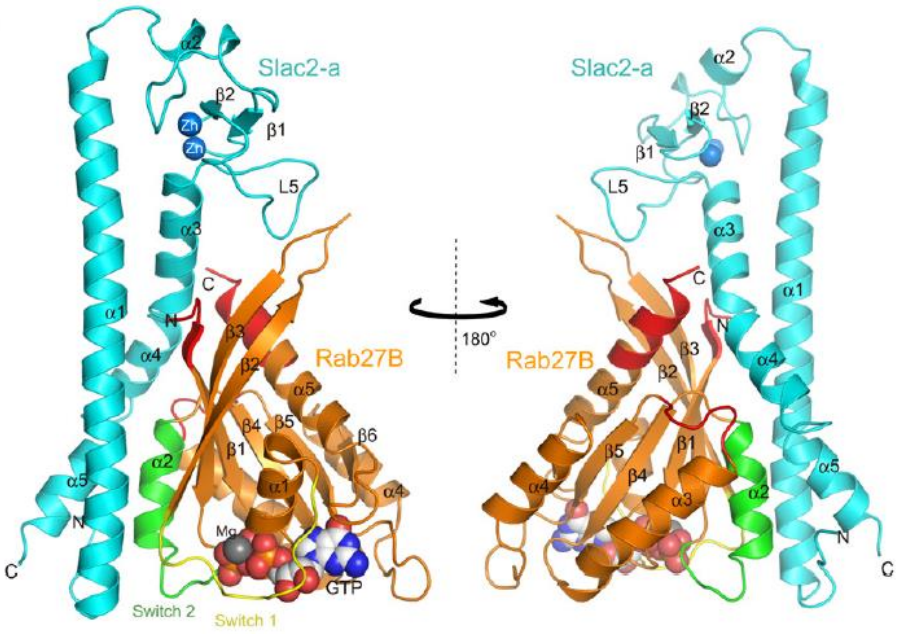


Figure 1.17. Structure of Rab27b in a complex with Slac2-a. Ribbon diagram representation of the 3D structure of Rab27b (orange)-Slac2-a (cyan) complex. The two models represent 180^0 rotation around the vertical axis. The switch 1, switch 2 and RabCDRs regions of Rab27b are highlighted in yellow, green and red, respectively. The spheres represent GTP, Mg^{2+} and Zn^{2+}. Reproduced from (Kukimoto-Niino et al., 2008).

It has been shown that slac2-a binds to the globular tail of myosin-Va motor protein through its C-terminus half (Fukuda et al., 2002). In addition, Strom and colleagues found that Slac2-a (full length) and the truncations: 1–400, 150–590, 367–590, 367–467 and 367–400 were able to interact with the tail of myosin-Va, whereas Slac2-a truncations: 1–266, 150–338 and 467–590 were not able to interact, suggesting that amino acids 367–400 of Slac2-a represent the minimal determinant of myosin-Va-binding domain (Strom et al., 2002). It has also been demonstrated that D378, E380, E381 and E382 residues in the myosin-Va binding domain (MBD) and K493, R495, R496 and K497 residues in the actin binding domain (ABD) are required for binding to myosin-Va and actin, respectively (Kuroda et al., 2003). Additionally, it has been shown that the exon F-binding domain (EFBD) (300-400 aa) within the MBD of Slac2-a is required for recruiting myosin-Va to the melanosomes, whereas the globular tail-binding

domain (GTBD) (150-246 aa) of Slac2-a has no role in this respect and it might function to stabilise the interaction with myosin-Va. Notably, a coiled-coil domain within the ABD (in the C-terminus) of Slac2-a potentially contributes to the interaction with myosin-Va (Hume et al., 2006). It has also been demonstrated that the GTBD region of Slac2-a activates the myosin-Va ATPase activity, thus promoting its motor activity (Li et al., 2005). For further details of Slac2-a structure see Figure 1.18.

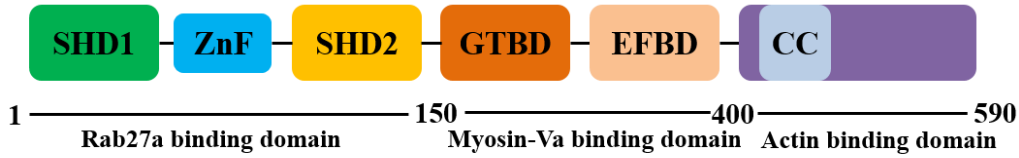


Figure 1.18. Structure of Slac2-a domains. Slac2-a consists of 1) A Rab27a binding domain (1-150 aa) comprising SHD1/2 and zinc finger motif (ZnF). 2) A myosin-Va binding domain (151-400 aa) which contains GTBD and EFBD subdomains. 3) An actin binding domain (401-590 aa) which includes the coiled-coil (CC) region. Adapted from (Hume et al., 2006).

Rab27a-Slac2-a-myosin-Va tripartite complex plays significant role in the regulation of melanosome transport in melanocytes as described below. It is thought that intracellular transport of organelles is mediated by microtubules and actin filaments which are responsible for long- and short- range transport, respectively (Langford, 1995). It has been suggested that mature melanosomes are transported bi-directionally from the perinuclear area along microtubules to the melanocyte cell periphery via kinesin and dynein motor proteins. Then at the cell periphery, mature melanosomes under go short-distance unidirectional transport along actin-filaments utilising Rab27a, Slac2-a and myosin-Va tripartite complex, where Rab27a associated-melanosomes interact with myosin-Va motor protein via Slac2-a-dependent interaction, thereby mediating melanosome transport towards the peripheral dendrites (Barral and Seabra, 2004; Bennett and Lamoreux, 2003; Hume et al., 2007; Marks and Seabra, 2001; Wu et al., 1998b); for further details see Figure 1.19. Disruption of the tripartite complex causes perinuclear clustering of melanosomes by abolishing Rab27a-

dependent melanosome transport (Fukuda and Kuroda, 2004; Hume et al., 2002; Hume et al., 2001; Hume et al., 2006; Hume et al., 2007; Kuroda and Fukuda, 2004; Matesic et al., 2001; Robinson et al., 2017; Wu et al., 1998b). Recently, it has been argued that the anterograde transport of melanosomes occurs mainly along actin filaments via myosin-Va, whereas the retrograde transport occurs along microtubules via kinesin motor protein, suggesting that the actin filaments-dependent transport is crucial for melanosomes trafficking in melanocytes (Evans et al., 2014). In addition, by using immunoelectron microscopy, it was found that GFP-Rab27a associates mainly with intermediate to mature melanosomes in the tips of the dendrites of primary human epidermal melanocytes, suggesting that Rab27a is involved mainly in the regulation of actin-based trafficking of mature melanosomes (Jordens et al., 2006).

It has also been suggested that Slac2-a association with the microtubule plus-end tracking protein EB1 orients melanosome transfer from microtubules towards actin (Wu et al., 2005b). In addition, Slac2-a binding to myosin-Va reduces the speed of transfer of myosin-Va, while prolonging the run-length of the motor along actin filaments, thus promoting melanosomes transfer to the adjacent keratinocyte (Sckolnick et al., 2013). Notably, Slac2-a inhibits the association of the globular tail domain and the head of myosin-Va, thereby promoting motor activity (Yao et al., 2015). Interestingly, the in vitro protein kinase A (PKA)-dependent phosphorylation of the Slac2-a C-terminal ABD domain favours binding to actin instead of microtubules (Oberhofer et al., 2017).

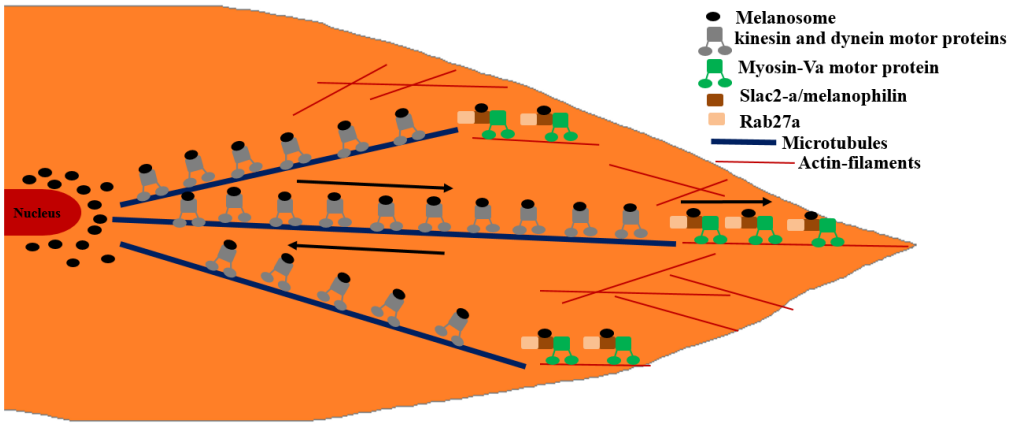


Figure 1.19. Cellular transport of melanosomes in epidermal melanocytes. Mature melanosomes are distributed in the perinuclear area of melanocytes, then transported along the microtubules in a bidirectional way to the cell periphery via kinesin and dynein motor proteins. At the cell periphery, melanosomes are transported along actin filaments in a unidirectional way to the peripheral dendrites via Rab27a, Slac2-a and myosin-Va tripartite complex.

1.4.2 Rab27-effector protein interaction disrupting mutations

A lot of research has been conducted to identify mutations that can disrupt Rab27-effector protein interactions. For instance, Kukimoto-Niino and colleagues tested the Slac2-a binding ability of different Rab27a mutants based on sequence alignment of Rab27 with Rab3a and the equivalent Rab3a residues were substituted in Rab27a. They found that Slac2-a binding was completely abolished by introducing the Y6F mutation and to a lesser extent by the D91G mutation. This might be caused by disrupting the specific hydrogen bonding between Rab27a and Slac2-a. In addition, the Rab27a-Slac2-a interaction was completely abolished by introducing the Y6F, L84I, F88Y and D91G mutations, suggesting that tyrosine-6 in the RabCDRs, leucine-84, phenylalanine-88 and aspartic acid-91 in the switch II of Rab27 are the key determinants of Slac2-a binding (Kukimoto-Niino et al., 2008). In contrast, rabphilin retains the ability to interact with the (D91G) and (L84I, F88Y, D91G) Rab27a mutants (Fukuda, 2002b).

Notably, the Rab27a (Y6F) mutant had no effect on Rab27a binding to Slac2-c, rabphilin3a, Slp1, Slp2, Slp3, Slp4, Slp5 and Munc13-4 (Tarafder et al., 2011). Furthermore, the (E48V), (Y122W, C123W) and (C188S) Rab27a mutants do not affect Slac2-a binding significantly (Fukuda, 2002b). It has also been shown

that the Rab27a (L9M), (I10F) and (F12I) mutants and substitution of the RabSF2 residues (NSKFIT) in Rab27a corresponding to that of the Rab5a (HEFQES) had no effect on Rab27a binding to Slac2-a, Slac2-c, rabphilin3a, Slp1, Slp2, Slp3, Slp4, Slp5 and Munc13-4. Moreover, substitution of the FFRDAM Rab27a residues in the RabF4 motif by the corresponding residues in Rab3a (YYRGAM) abrogated the binding to Slac2-a, Slac2-c, rabphilin3a, Slp3 and Munc13-4, but had no effect on the binding to Slp1, Slp2, Slp4 and Slp5 (Tarafder et al., 2011). Interestingly, the (K22R) Rab27a mutant does not have the ability to bind Slac2-a, Slp2-a and Slp4-a, but can interact with Munc13-4, whilst the I44T mutation in Rab27a resulted in disrupting Slac2-a binding ability and reducing the interaction with Slp2-a and Munc13-4, but can bind to Slp4-a in vitro (Ohbayashi et al., 2010).

In addition, mutating tyrosine-122 of Rab27a into alanine dramatically abrogated the interaction with Slp2-a, since Rab27a-Slp2a binding requires stacking of Rab27a-tyrosine-122 with Slp2-a-phenylalanine-54 (Chavas et al., 2008).

It was found that the introduction of the (E50A, I54A) and (E51A, I55A) mutations into rabphilin and Noc2, respectively completely abolished the interaction with Rab27a (Fukuda et al., 2004). Notably, replacement of cysteine 138 and 141 within the zinc finger motif with serine or mutating tryptophan-154, phenylalanine-155 and tyrosine-156 within the Rab27-binding domain to alanines, completely abrogated Noc2 interaction with both Rab27 and Rab3 (Cheviet et al., 2004). As expected, the GDP-bound Rab27b-(T23N) and Rab27b-(N133I) (low affinity for both GTP and GDP) mutants lack the interaction activity with granuphilin (Zhao et al., 2002). It has also been reported that the A87P mutation in Rab27a disrupts its binding to Munc13-4 and the L403P mutation in Munc13-4 inhibits its binding to Rab27a in vitro (Zur Stadt et al., 2006). Interestingly, Munc13-4 can interact with the Rab27a-(W73G) mutant but to a lesser extent than with the wild-type Rab27a (Neeft et al., 2005). In addition, introduction of alanine point mutations into Munc13-4-(F80, Q81, L82) and Munc13-4-(I83, H84, K85) reduced 80% of their Rab27a binding activity (Elstak et al., 2011). (For further details see sections 1.4, 1.4.1.3 and 1.3.3).

In conclusion, these Rab27-effector interaction disrupting mutations can be utilised to identify candidate small molecule inhibitors of Rab27 interactions by focusing on the pockets of interaction of the wild residues.

1.5 Rab27-related cancer cell invasion and proliferation

Although a lot of research has been conducted, the Rab27-related cancer signalling pathways has not yet been fully investigated. Early research conducted by Ostrowski and colleagues revealed that short hairpin RNA (shRNA) silencing of RAB27A and RAB27B resulted in reducing exosome secretion and multivesicular endosomes docking to the plasma membrane in HeLa B6H4 tumour cell line stably expressing the transactivator CIITA, also shRNA silencing of SLP4 and SLAC2B resulted in reducing exosome secretion and changing the distribution of multivesicular endosomes in a similar way to that produced by RAB27A and RAB27B silencing, respectively (Ostrowski et al., 2010). This suggests that Rab27a/b and their downstream effectors play a potential role in exosome secretion and exocytosis, thus promoting cancer cell invasion, metastasis and proliferation [for review see (Hendrix and De Wever, 2013; Hendrix and Hume, 2011)]. In addition, shRNA silencing of RAB27A significantly reduced cell proliferation in WM1385 and WM1960 human melanoma short-term cultures highly expressing Rab27a relative to cell lines with lower Rab27a expression (Akavia et al., 2010).

It has also been reported that Rab27b overexpression in human MCF-7 breast cancer cells resulted in increasing invasive tumour growth and proliferation and promoting HSP90α secretion (Hendrix et al., 2010b). HSP90α acts as an active regulator of proinvasive growth and MMP-2 activator (Eustace et al., 2004). Extracellular HSP90a might also mediate MMP-2 activation by chaperoning pro-MMP-2 and MT1-MMP complex (Hendrix et al., 2010c). Thus, activated MMP-2 degrades the extracellular matrix, releasing growth factors. HSP90α also facilitates the interaction of growth factors with their receptors, thereby mediating G1 to S phase transition, increasing cyclin A and E expression (positive cell cycle regulators) and reducing p27 expression (negative cell cycle regulator) (Hendrix et al., 2010b). Notably, CLIC3 has been implicated in the recycling of MT1-MMP in MDA-MB-231 breast cancer cell line, thus

promoting MT1-MMP-dependent invasion. Interestingly, Rab27a/b silencing resulted in reducing MT1-MMP recycling in a similar way to that of CLIC3 silencing (Macpherson et al., 2014). This suggests that Rab27a/b have substantial role in the regulation of MT1-MMP recycling, thereby promoting cancer cell invasion and metastasis. Furthermore, Rab8 drives MT1-MMP trafficking towards the plasma membrane extensions, thereby mediating cancer cell invasion (Bravo-Cordero et al., 2007); for further details see Figure 1.20.

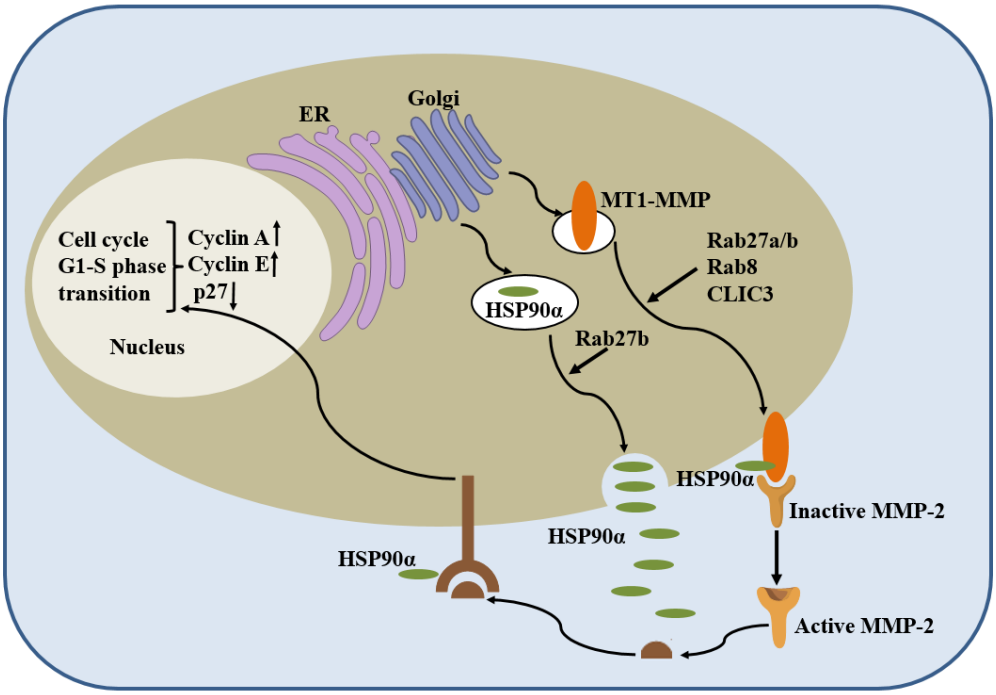


Figure 1.20. A schematic representation of Rab27-regulated exocytosis in invasive cancers. Rab27b mediates the exocytosis of HSP90α-containing vesicles in the cancer cell. Rab27a/b, Rab8 and CLIC3 mediates MT1-MMP transport towards the plasma membrane, HSP90α then acts on MT1-MMP, leading to activation of MMP-2. Activated MMP-2 degrades extracellular matrix, releasing growth factors (brown semicircles). HSP90α then facilitates the binding of growth factors to their receptors, thus promoting G1 to S phase transition, increasing cyclin A and E expression and reducing p27 expression.

Interestingly, selective inhibition of vacuolar H(+)-ATPase (V-ATPase) using bafilomycin A1 and siRNA silencing of V-ATPase V0a1 or V0d1 subunits in MCF-7 cells stably expressing Rab27b resulted in reducing Rab27b-dependent invasive growth, decreasing HSP90α and MMP-2 secretion with an accompanying reduction in cyclin A and cyclin E positive cell cycle regulators, whilst p27 expression is increased, suggesting that selective targeting of V-

ATPase activity represents an effective strategy to inhibit Rab27b-dependent oestrogen-receptor positive breast cancers (Hendrix et al., 2013).

In addition, it has been found that Rab27b is highly expressed in oestrogen receptor-positive MCF-7 cells, whereas Rab27a is highly expressed in oestrogen receptor-negative MDA-MB-231 cells, suggesting that Rab27b can be used as a biomarker to determine the progression of oestrogen receptor-positive breast cancers (Hendrix et al., 2010a). In line with that, Zhang et al. found that the expression level of Rab27b is increased in human breast cancer and can be used as an indicator of the degree of lymph node metastasis and breast cancer progression, prognosis and oestrogen receptor dependency (Zhang et al., 2012). Furthermore, by using 18 primary invasive breast cancer cell lines, it has been shown that mRNA expression of RAB27B and SYTL5 encoding Slp5 is higher in oestrogen receptor-α positive breast cancer cells than in oestrogen receptor-α negative breast cancer cells (Wright et al., 2009).

It was found that shRNA silencing of RAB27A in TS/A and 4T1 mammary carcinoma cell lines resulted in reducing secretion of exosomes and MMP-9 in both cell lines, but tumour growth is only impaired in 4T1 cells (Bobrie et al., 2012). In another study, the nanoparticle tracking analysis revealed that inhibition of RAB27A/B by using shRNA significantly reduced exosome secretion in MDA-MB-231 breast cancer cells (Zheng et al., 2013). Intriguingly, in MDA-MB-231 breast cancer cells, Rab27a has been implicated in the regulation of matrix degradation by controlling the late-endocytic transport of MT1-MMP through interaction with VPS39, an essential component of the post-endocytic HOPS complex. It has also been shown to be involved in the regulation of Golgi-dependent trafficking of E-cadherin, thus promoting tumour invasiveness in breast cancer cells (Kajiho et al., 2016).

It has also been reported that the degree of Rab27b expression is significantly correlated with tumour size in patients with gastrointestinal tumour and can be used as a prognostic marker for this type of cancer (Wang et al., 2014). Although knocking down of RAB27B resulted in reducing the exocytosis of miR23b microRNA (which has tumour-suppressor functions) in FL3 bladder carcinoma cells, intracellular (mature) miR23b, but not pri-miR23b is increased in parental

cells, thereby reducing cancer cell invasion and metastasis (Ostenfeld et al., 2014).

Interestingly, it has been reported that the nuclear factor-κB (NF-κB) transcriptionally activates Slp1 in the presence of tumour necrosis factor α (TNFα), thereby increasing promoter activity and protein expression of Slp1 in PC-3 prostate carcinoma cell line (Catz et al., 2002a). Furthermore, Slp1 regulates the androgen-dependent secretory machinery of the prostate-specific antigen and the prostatic-specific acid phosphatase in human LNCaP prostate carcinoma cells in a Rab27a-depedent manner, suggesting that Slp1 plays a significant role in prostate cancer metastasis (Catz, 2008; Johnson et al., 2005a). Similarly, the NF-κB signalling pathway acts on Rab27a promoter activity in HT29 colon cancer cells, increasing $CD44^+$ proportion, facilitating transition from G0 and G1 to S phase and stimulating secretion of vascular endothelial growth factor and transforming growth factor-β, thus promoting tumour progression in colon cancer cells (Feng et al., 2016). Notably, Slp1 is transcriptionally targeted by MEIS1, a TALE-class homeoprotein, mediating the activation of Slp1 effector protein which in turn promotes the activation of the CXCL12/CXCR4 axis, stimulating leukemogenesis and leukemic cell homing in H9M1 cells (Yokoyama et al., 2016).

In pancreatic cancer, high Rab27b protein expression is significantly correlated with vascular invasion and pancreatic cancer metastasis, suggesting that Rab27b inhibition can be used as a novel strategy to treat pancreatic cancers (Zhao et al., 2016). Remarkably, microarray and proteomics analysis showed that RAB27B gene is upregulated by K-Ras oncogene in lung adenomas of K-Ras transgenic mice (Lee et al., 2009). It has been reported that shRNA silencing of RAB27A in human lung adenocarcinoma A549 cells resulted in a significant reduction in exosome secretion, suggesting that that Rab27a might be a specific target for inhibition of cancer metastasis in lung adenocarcinoma (Li et al., 2014b).

Exosome release has also been inhibited by RAB27A silencing in mouse astrocytes using RAB27A siRNA, also RAB27A/B shRNA silencing resulted in reducing $TSG101^+$ and $CD63^+$ exosomes secretion in mouse brain parenchyma (Zhang et al., 2015). In addition, siRNA knockdown of RAB27a in B16-F10 and

SK-Mel-28 melanoma cell lines caused 50% reduction in exosome secretion with an accompanying decrease in the secretion of placental growth factor 2, platelet-derived growth factor A chain homodimer and osteopontin (the primary tumour growth and metastasis were decreased as well). (Peinado et al., 2012).

It has also been shown that exosome secretion was inhibited by 82% through selective Rab27a knockdown using ribozyme transgenes in Du145 prostate cancer cells, abolishing differentiation of stromal myofibroblasts (Webber et al., 2015). In addition, it has been reported that Rab27b is involved in the progression and metastasis of hepatocellular carcinoma (Yang et al., 2017), rectal adenocarcinoma (Hua et al., 2017), ovarian cancer (Ren et al., 2016) and colorectal cancer (Bao et al., 2014).

Notably, VAMP-2, a protein implicated in the exocytosis of human neutrophils specific and tertiary granules (Mollinedo et al., 2003), co-localises with Rab27a and Slp1 (Munafo et al., 2007) and with Rab27b (Johnson et al., 2010a). In addition, shRNA silencing of SLP5 reduced CXCL12- and CCL2-dependent migration in human SupT1 cells (T cell lymphoma cells) and THP-1 cells (human monocytic leukemia cells), respectively indicating that Slp5 positively regulates chemokines involved in leukocyte cell migration (Colvin et al., 2010). Accordingly, these studies suggest that inhibition of Rab27-effector interactions might be an effective strategy for treating inflammatory diseases in the future.

Accordingly, the interaction of Rab27a/b with their effector proteins plays an essential role in cancer growth, progression, invasion and metastasis. Therefore, by blocking those interactions, the subsequent signalling pathways promoting cancer cell proliferation, invasion and metastasis might be inhibited.

1.6 Inhibitors of small GTPases protein-protein interactions

Although the identification of inhibitors of small GTPases protein-protein interactions is still a challenging goal, many attempts succeeded in producing inhibitors of these interactions. For instance, by performing NMR-based screening, several small molecule inhibitors with a unique binding pocket between α2 helix and β1–β3 sheets of K-Ras were identified, thereby inhibiting the interaction with son of sevenless (SOS), a guanine nucleotide exchange factor (Maurer et al., 2012). Similarly, Sun and colleagues succeeded in identifying small molecule inhibitors of K-Ras interaction with SOS by binding between switch I and switch II regions (Sun et al., 2012).

In addition, small molecule inhibitors of the oncogenic mutant K-Ras (G12C) were identified using a fragment-based screening. It was found that these small molecules can bind to K-Ras (G12C) via a specific pocket below the switch II region, disrupting GTP binding ability, thereby impairing the interaction with its effector Raf (Ostrem et al., 2013). Furthermore, in silico virtual screening in the libraries for inhibitors of H-Ras by targeting the surface pockets of the Ras:GTP conformation resulted in identifying Kobe0065 and its analogue Kobe2602 small molecules, inhibiting H-Ras interaction with its effector c-Raf-1 both in vivo and in vitro (Shima et al., 2013).

Interestingly, anti-K-Ras (G12V) cell-permeable bicyclic peptide was identified by screening in a bicyclic peptide library, which had in vitro blocking effects on Ras-Raf interaction, thereby inhibiting Ras-regulated tumour growth in different cancer cell lines (Trinh et al., 2016).

Recently, targeting of multiple sites at the switch I and switch II regions of K-Ras (G12D) resulted in identifying the small molecule inhibitor 3144, which can bind to K-Ras (G12D), K-Ras, H-Ras and N-Ras, and exhibited inhibitory effects on tumour growth in different cancer cell lines (Welsch et al., 2017).

In conclusion, these findings suggest that small GTPases protein-protein interactions are potential druggable targets that can be inhibited by identifying unique binding pockets on their structures.

1.7 Aims and objectives

Rab27a/b proteins regulate trafficking and exocytosis of various intracellular organelles including secretory granules, thereby controlling exosomes secretion, tumour growth, cancer cell invasion and metastasis. This suggests that blocking of Rab27-regulated tumour growth pathways by disrupting Rab27-effector protein interactions might be an effective strategy to treat cancers and prevent cancer metastasis. The main aims of this study were as follows:

- Identification of the key determinants of Rab27-effector interactions using:

a) In vitro fluorescent GST-pull down protein-protein interaction assay. m.Cherry-Rab27b and either GST-Slp1 or GST-Slp2 were used as interacting partners.

b) In vitro fluorescence resonance energy transfer (FRET)-based protein-protein interaction assay. m.Cherry-Rab27a/b and either GFP-Slp1 or GFP-Slp2 were used as interacting components. Note that the conditions of these two assays were optimised. In addition the specificity of them were confirmed using unlabelled Rab27a and Rab27b as competitive inhibitors of Rab27-effector interactions. These assays were used to determine the binding affinity of Slp1 and Slp2 to Rab27.

c) Cellular melanosome clustering (transport) assay in which the effect on Rab27-Slac2-a interaction-dependent melanosome transport in melan-a murine melanocytes was considered as a read-out for Rab27-effector interaction.

- Identification of candidate inhibitors of Rab27-effector protein interactions: Slp2 super-effectors and small molecule inhibitors using the in vitro FRET-based protein-protein interaction assay and the cellular melanosome clustering assay. Those candidate inhibitors can be tested in the future using cancer cell lines.

Chapter 2

Methods

2.1 Molecular Biology techniques

2.1.1 Plasmid DNA preparation Techniques

2.1.1.1 Simple polymerase chain reactions (PCR)

All the PCR primers were synthesised by Sigma-Aldrich; the PCR primers were designed according to the specifications of the cDNA of interest to be used for PCR amplification (specifically described later for each PCR product). To ensure high fidelity and accurate PCR amplification, Pfu DNA Polymerase was used in the subsequent PCR and site-directed mutagenesis reaction mixtures. For a simple PCR amplification, a standard PCR reaction mixture (50µl) was made in the following order using a 200µl PCR tube: 31µl Milli-Q water, 5µl 10x Pfu DNA polymerase reaction buffer (Promega), 4µl dNTPs mix (2.5mM each) (Promega), 4µl forward primer (10µM), 4µl reverse primer (10µM), 1µl (50 ng/µl) cDNA template, 1µl (2 units) Pfu DNA polymerase enzyme (Promega). The PCR mixture was gently pipetted (to ensure homogenous mixing), centrifuged at 2,000 rpm for 1 min. Sensoquest thermocycler was used for all the simple PCR and site-directed mutagenesis reactions. The following PCR cycles were followed (Table 2.1):

Stage	Temperature (ºC)	Time (min)	Cycles
Denaturation	95	1	1
Denaturation	95	1	30
Annealing	55	1	30
Extension	72	1.5	30
Extension	72	10	1

Table 2.1. Simple PCR reaction Conditions.

The PCR products were then purified using a NucleoSpin gel and PCR clean-up kit (MACHERY-NAGEL) as per manufacturer's instructions. This involved adding 2 volumes of NTI binding buffer per 1 volume of PCR mixture and about 700µl of this mixture was loaded into the NucleoSpin gel and PCR clean-up column (DNA binding column) which was already placed into a collection tube. To bind the DNA onto the column, the DNA binding column was centrifuged for 30 seconds at 11,000 g, the flow-through was discarded and this process was repeated to load the remaining sample. A washing NT3 buffer (ethanol containing) was loaded into the column, followed by centrifugation for 1 min at 11,000 g. To ensure complete removal of ethanol, an additional centrifugation

for 1 min at 11,000 g was performed. Finally, to elute the DNA, 15–30µl NE buffer was added and the mixture was incubated at room temperature for 1 min and then centrifuged for 1 min at 11,000 g. To collect the DNA, the collection tube was replaced by a new Eppendorf tube, the column was then centrifuged for 1 min at 11,000 g and the DNA was collected. The following PCR primers were used to amplify DNA inserts that were sub-cloned into vectors (Table 2.2):

PCR product	**Primers sequences**	**Restriction sites**
Human (h) Rab27b-(1-218; T23N)	5'ACTTGCGGCCGCGATGACCGATGGAGACTATGAT3' 5'AAGTGCGGCCGCCTAGCAGATACATTTCTTCTC3'	5'NotI/3'NotI
Mouse (m) Slp2-(3-80)	5'CGTACAGGATCCGACTTAAGTTTCCTGACAGAG3' 5'GCATGAGAATTCCTACTTCTTCCTTCTCATGGATGC3'	5'BamHI/3'EcoRI
Green fluorescent protein (GFP)-mSlp2-(3-80)	5'CGTACAGGATCCGATGGTGACAAGGGCGAGGAG3' 5'GCATGAGCGGCCGCCTACTTCTTCCTTCTCATGGATGC3'	5'BamHI/3'NotI
mSlp2-(3-80)	5'CGTACAGGATCCGGACTTAAGTTTCCTGACAGAG−3' 5'GCATGAGCGGCCGCCTACTTCTTCCTTCTCATGGATGC3'	5'BamHI/3'NotI
mSlp2-(3-80)	5'CGTACAGAATTCGACTTAAGTTTCCTGACAGAG3' 5'GCATGAGGATCCCTACTTCTTCCTTCTCATGGATGC3'	5'EcoRI/3'BamHI
mSlp1-(1-116)	5'CGTACAGAATTCATGCCCCAGAGAGGCCACCCA3' 5'GCATGAGGATCCCTATTGGTCCCCCTTTGGGCTCTT3'	5'EcoRI/3'BamHI
mSlp2-(10-41)	5'CGTACAGAATTCGAGGAGCAAGACGCCATCTTA3' 5'GCATGAGGATCCCTACTTAATTTTTTCAGGCAGATG3'	5'EcoRI/3'BamHI
mSlp2-(10-50)	5'CGTACAGAATTCGAGGAGCAAGACGCCATCTTA3' 5'GCATGAGGATCCCTAACTCATATTCTTTAGTTGTTG3'	5'EcoRI/3'BamHI
mSlp2-(10-56)	5'CGTACAGAATTCGAGGAGCAAGACGCCATCTTA3' 5'GCATGAGGATCCCTATTCATAAAACCATTGGCCACT3'	5'EcoRI/3'BamHI

mSlp2-(10-56; K26R, A28R, Q44R, N48I)	5'CGTACAGAATTCGAGGAGCA AGACGCCATCTTA3' 5'GCATGAGGATCCCTACTTCTT CCTTCTCATGGATGC3'	5'EcoRI/3' BamHI
mSlp2-(10-56; K26R, A28R, Q44R, N48I, E56F)	5'CGTACAGAATTCGAGGAGCA AGACGCCATCTTA3' 5'GCATGAGGATCCCTACTTCTT CCTTCTCATGGATGC3'	5'EcoRI/3' BamHI
mSlp2-(10-56; K26R, A28R, Q44R, N48I, G51L, E56F)	5'CGTACAGAATTCGAGGAGCA AGACGCCATCTTA3' 5'GCATGAGGATCCCTACTTCTT CCTTCTCATGGATGC3'	5'EcoRI/3' BamHI
mSlp1-(1-74)	5'CGTACAGAATTCATGCCCCAG AGAGGCCACCCA3' 5'GCATGAGGATCCCTACCAGG GGTCTTCCAGGGAGGC3'	5'EcoRI/3' BamHI
mSlp1-(70-116)	5'CGTACAGAATTCCTGGAAGA CCCCTGGCAGCTG3' 5'GCATGAGGATCCCTATTGGTC CCCCTTTGGGCTCTT3'	5'EcoRI/3' BamHI
m.Cherry	5'CGTACAACCGGTACCATGGT GAGCAAGGGCGAGGAG3' 5'GCATGAGAATTCCTTGTACAG CTCGTCCATGCC3'	5'AgeI/3' EcoRI
mSlp2-(10-67)	5'CGTACAGAATTCGAGGAGCA AGACGCCATCTTA3' 5'GCATGAGGATCCCTACTTCTT CCTTCTCATGGATGC3'	5'EcoRI/3' BamHI
mSlp2-(10-67; K26R, A28R, Q44R, N48I)	5'CGTACAGAATTCGAGGAGCA AGACGCCATCTTA3' 5'GCATGAGGATCCCTACTTCTT CCTTCTCATGGATGC3'	5'EcoRI/3' BamHI
mSlp2-(10-67; K26R, A28R, Q44R, N48I, E56F, H62R, R63F)	5'CGTACAGAATTCGAGGAGCA AGACGCCATCTTA3' 5'GCATGAGGATCCCTACTTCTT CCTTCTCATGGATGC3'	5'EcoRI/3' BamHI
mSlp2-(10-67; K26R, A28R, Q44R, N48I, G51L, E56F, H62R, R63F)	5'CGTACAGAATTCGAGGAGCA AGACGCCATCTTA3' 5'GCATGAGGATCCCTACTTCTT CCTTCTCATGGATGC3'	5'EcoRI/3' BamHI

Table 2.2. List of PCR primers used to perform simple PCR in this study. Restriction enzyme sites, stop codons and parts of Kozak consensus sequence highlighted in green, red and blue, respectively. Inserted nucleotide(s) is in bold to avoid a stop codon.

2.1.1.2 Site directed mutagenesis

A standard site-directed mutagenesis protocol was followed, this involved designing of the appropriate primers to mutate a maximum of 2 amino acids or 4 base pairs (BP). To ensure complete annealing of the designed primers, 21 BP were included in the coding sequence in both sides of the mutated BPs, unless otherwise indicated. The standard PCR reaction mixture was followed as described in section 2.1.1.1 except of using 100 ng/µl cDNA template instead. The following PCR cycles were followed (Table 2.3):

Stage	Temperature (ºC)	Time (min)	Cycles
Denaturation	95	0.5	1
Denaturation	95	0.5	18
Annealing	55	1	18
Extension	72	1.5/kb	18
Extension	72	10	1

Table 2.3. Site-directed mutagenesis reaction Conditions.

To digest any dam methylated DNA (template), a DpnI restriction enzyme digestion was performed using17µl PCR product mixed with 2µl CutSmart buffer (NEB) and 1µl (20 units) DpnI (NEB) enzyme. The mixture was then incubated for 1 hour at 37ºC followed by DpnI enzyme heat inactivation for 20 mins at 80ºC. This was followed by transformation of the linear PCR product into DH5α *E. coli* competent cells as described in section 2.1.2.2 [*E. coli* cells were generated and maintained as described by (Chung et al., 1989)]. DNA amplification and purification was then performed as described in section 2.1.2.3. Details of primers used to perform site-directed mutagenesis reactions described in Table 2.4:

Construct produced	Primers sequences
pETDuet-1-m.Cherry-hRab27a	5'ATGGACGAGCTGTACAAGGCGGCCGCGTCGGATGGAGATTATGA3' 5'TCATAATCTCCATCCGACGCGGCCGCCTTGTACAGCTCGTCCAT3'
pETDuet-1-m.Cherry-hRab27b-(1-218)	5'TGTGTATCTATAAAGAAATGTTGTCTTCCCCACCCCTGAATCCC3' 5'GGGATTCAGGGGTGGGGAAGACAACATTTCTTTATAGATACACA3'
pETDuet-1-m.Cherry-	5'CAGCTTTGGGACACTGCGGGACTAGAGCGGTTCCGGAGTCTCACC3'

hRab27b-(1-218; Q78L)	5'GGTGAGACTCCGGAACCGCTCTAGTCCCGCAGTG TCCCAAAGCTG3'
pETDuet-1-m.Cherry-hRab27b-(1-200)	5'ATCCCTGATACTGTCAATGGTTGAAATTCTGGAAA CTTGGAT3' 5'ATCCAAGTTTCCAGAATTTCAACCATTGACAGTAT CAGGGAT3'
pGEX-4T1-mSlp2-(3-41)	5'CATCTGCCTGAAAAAATTAAGTAGGACCAACAAC TAAAGAATATG3' 5'CATATTCTTTAGTTGTTGGTCCTACTTAATTTTTTC AGGCAGATG3'
pGEX-4T1-mSlp2-(3-56)	5'AGTGGCCAATGGTTTTATGAATAGAAGGCAAAAA GACACAGGGAC3' 5'GTCCCTGTGTCTTTTTGCCTTCTATTCATAAAACCA TTGGCCACT3'
pETDuet-1-GFP-mSlp1-(1-116)	5'CCAAAGGGGGACCAATGATTCGAATTCTGCAGT3' 5'ACTGCAGAATTCGAATCATTGGTCCCCCTTTGG3'
pETDuet-1-GFP	5'GGCATGGACGAGCTGTACAAGTGAGGAATGCCCC AGAGAGGCC3' 5'GGCCTCTCTGGGGCATTCCTCACTTGTACAGCTCG TCCATGCC3'
pETDuet-1-mSlp2-(3-80; K26R, A28R)	5'CTGCAGAGGGATGCTGCCCTGAGGAGGCGTGAAG AGGAGAGAGTCAGACAT3' 5'ATGTCTGACTCTCTCCTCTTCACGCCTCCTCAGGG CAGCATCCCTCTGCAG3'
pETDuet-1-mSlp2-(3-80; K26R, A28R, Q44R)	5'CCTGAAAAAATTAAGGATGACCGACAACTAAAGA ATATGAGTGGC3' 5'GCCACTCATATTCTTTAGTTGTCGGTCATCCTTAA TTTTTTCAGG3'
pETDuet-1-mSlp2-(3-80; K26R, A28R, Q44R, N48I)	5'AAGGATGACCGACAACTAAAGATTATGAGTGGCC AATGGTTTTAT3' 5'ATAAAACCATTGGCCACTCATAATCTTTAGTTGTC GGTCATCCTT3'
pETDuet-1-mSlp2-(3-56)	5'AGTGGCCAATGGTTTTATGAATAGAAGGCAAAAA GACACAGGGAC3' 5'GTCCCTGTGTCTTTTTGCCTTCTATTCATAAAACCA TTGGCCACT3'
pETDuet-1-mSlp2-(3-56; K26R, A28R, Q44R, N48I)	5'AGTGGCCAATGGTTTTATGAATAGAAGGCAAAAA GACACAGGGAC3' 5'GTCCCTGTGTCTTTTTGCCTTCTATTCATAAAACCA TTGGCCACT3'
pETDuet-1-mSlp2-(3-67)	5'AGACACAGGGACAAAATCCACTGAGCTGACATCA TCAGAGCATCC3' 5'GGATGCTCTGATGATGTCAGCTCAGTGGATTTTGT CCCTGTGTCT3'
pENTR-EGFP-C2-mSlp2-(3-80; D3A)	5'CGAGCTCAAGCTTCGAATTCGCCTTAAGTTTCCTG ACAGAGGA3' 5'TCCTCTGTCAGGAAACTTAAGGCGAATTCGAAGC TTGAGCTCG3'

pENTR-EGFP-C2-mSlp2-(3-80; R32W)	5'CTGAAGAGGGCTGAAGAGGAGTGGGTCAGACATC TGCCTGAAAAA3' 5'TTTTTCAGGCAGATGTCTGACCCACTCCTCTTCAG CCCTCTTCAG3'
pENTR-EGFP-C2-mSlp2-(3-79)	5'AGAGCATCCATGAGAAGGAAGTAGTAGGGATCCA CCGGATCTA3' 5'TAGATCCGGTGGATCCCTACTACTTCCTTCTCATG GATGCTCT3'
pENTR-EGFP-C2-mSlp2-(3-80; K58A)	*5'GGTTTTATGAAGCTGCGGCAAAAAGACACAGGG AC3' *5'GTCCCTGTGTCTTTTTGCCGCAGCTTCATAAAAC C3'
pENTR-EGFP-C2-mSlp2-(3-80; R61A)	*5'GAAGCTAAGGCAAAAGCACACAGGGACAAAATC C3' *5'GGATTTTGTCCCTGTGTGCTTTTGCCTTAGCTTC3'
pENTR-EGFP-C2-mSlp2-(3-80; H62A)	*5'GCTAAGGCAAAAAGAGCCAGGGACAAAATCCAC G3' *5'CGTGGATTTTGTCCCTGGCTCTTTTTGCCTTAGC3'
pENTR-EGFP-C2-mSlp2-(3-80; G68I)	*5'GACACAGGGACAAAATCCACATCGCTGACATCA TCAGAGCATC3' *5'GATGCTCTGATGATGTCAGCGATGTGGATTTTGT CCCTGTGTC3'
pENTR-EGFP-C2-mSlp2-(3-80; D70A)	*5'CAAAATCCACGGTGCTGCCATCATCAGAGCATCC 3' *5'GGATGCTCTGATGATGGCAGCACCGTGGATTTTG 3'
pENTR-EGFP-C2-mSlp2-(3-80; I71A)	*5'AATCCACGGTGCTGACGCCATCAGAGCATCCATG 3' *5'CATGGATGCTCTGATGGCGTCAGCACCGTGGATT 3'
pENTR-EGFP-C2-mSlp2-(3-80; R73A)	*5'CGGTGCTGACATCATCGCAGCATCCATGAGAAG G3' *5'CCTTCTCATGGATGCTGCGATGATGTCAGCACCG 3'
pENTR-EGFP-C2-mSlp2-(3-80; S75A)	*5'GACATCATCAGAGCAGCCATGAGAAGGAAGAAG T3' *5'ACTTCTTCCTTCTCATGGCTGCTCTGATGATGTC3'
pENTR-EGFP-C2-mSlac2-a-(1-146)	5'GGTCTCTCTGTGGGCGGCTGCAGTGAGGAGGTGG ATCTGAGCCAAGCTT3' 5'AAGCTTGGCTCAGATCCACCTCCTCACTGCAGCCG CCCACAGAGAGACC3'
pENTR-EGFP-C2-mSlp2-(3-41)	5'CATCTGCCTGAAAAAATTAAGTAGGACCAACAAC TAAAGAATATG3' 5'CATATTCTTTAGTTGTTGGTCCTACTTAATTTTTTC AGGCAGATG3'

pENTR-EGFP-C2-mSlp2-(3-56)	5'AGTGGCCAATGGTTTTATGAATAGAAGGCAAAAAGACACAGGGAC3' 5'GTCCCTGTGTCTTTTTGCCTTCTATTCATAAAACCATTGGCCACT3'
pENTR-EGFP-C2-mSlp2-(3-56; K26R)	5'CTGCAGAGGGATGCTGCCCTGAGGAGGGCTGAAGAGGAGAGAGTCAGACAT3' 5'ATGTCTGACTCTCTCCTCTTCAGCCCTCCTCAGGGCAGCATCCCTCTGCAG3'
pENTR-EGFP-C2-mSlp2-(3-56; A28R)	5'CTGCAGAGGGATGCTGCCCTGAAGAGGCGTGAAGAGGAGAGAGTCAGACAT3' 5'ATGTCTGACTCTCTCCTCTTCACGCCTCTTCAGGGCAGCATCCCTCTGCAG3'
pENTR-EGFP-C2-mSlp2-(3-56; K26R, A28R)	5'CTGCAGAGGGATGCTGCCCTGAGGAGGCGTGAAGAGGAGAGAGTCAGACAT3' 5'ATGTCTGACTCTCTCCTCTTCACGCCTCCTCAGGGCAGCATCCCTCTGCAG3'
pENTR-EGFP-C2-mSlp2-(3-56; K26R, A28R, Q44R)	5'CCTGAAAAAATTAAGGATGACCGACAACTAAAGAATATGAGTGGC3' 5'GCCACTCATATTCTTTAGTTGTCGGTCATCCTTAATTTTTTCAGG3'
pENTR-EGFP-C2-mSlp2-(3-56; Q44R)	5'CCTGAAAAAATTAAGGATGACCGACAACTAAAGAATATGAGTGGC3' 5'GCCACTCATATTCTTTAGTTGTCGGTCATCCTTAATTTTTTCAGG3'
pENTR-EGFP-C2-mSlp2-(3-56; K26R, A28R, Q44R, N48I)	5'AAGGATGACCGACAACTAAAGATTATGAGTGGCCAATGGTTTTAT3' 5'ATAAAACCATTGGCCACTCATAATCTTTAGTTGTCGGTCATCCTT3'
pENTR-EGFP-C2-mSlp2-(3-56; N48I)	5'AAGGATGACCAACAACTAAAGATTATGAGTGGCCAATGGTTTTAT3' 5'ATAAAACCATTGGCCACTCATAATCTTTAGTTGTTGGTCATCCTT3'
pENTR-EGFP-C2-mSlp2-(3-56; Q44R, N48I)	5'AAGGATGACCGACAACTAAAGATTATGAGTGGCCAATGGTTTTAT3' 5'ATAAAACCATTGGCCACTCATAATCTTTAGTTGTCGGTCATCCTT3'
pENTR-EGFP-C2-mSlp2-(3-56; K26R, A28R, Q44R, N48I, G51L)	5'CGACAACTAAAGATTATGAGTCTCCAATGGTTTTATGAATAGAAG3' 5'CTTCTATTCATAAAACCATTGGAGACTCATAATCTTTAGTTGTCG3'
pENTR-EGFP-C2-mSlp2-(3-56; K26R, A28R, Q44R, N48I, G51L, E56F)	5'ATGAGTCTCCAATGGTTTTATTTCTAGAAGGCAAAAAGACACAGG3' 5'CCTGTGTCTTTTTGCCTTCTAGAAATAAAACCATTGGAGACTCAT3'

pENTR-EGFP-C2-mSlp2-(3-56; K26R, A28R, Q44R, N48I, E56F)	5'AAGGATGACCGACAACTAAAGATTATGAGTGGCC AATGGTTTTAT3' 5'ATAAAACCATTGGCCACTCATAATCTTTAGTTGTC GGTCATCCTT3'
pENTR-EGFP-C2-mSlp2-(3-67)	5'AGACACAGGGACAAAATCCACTGAGCTGACATCA TCAGAGCATCC3' 5'GGATGCTCTGATGATGTCAGCTCAGTGGATTTTGT CCCTGTGTCT3'
pENTR-EGFP-C2-mSlp2-(3-67; K26R, A28R)	5'CTGCAGAGGGATGCTGCCCTGAGGAGGCGTGAAG AGGAGAGAGTCAGACAT3' 5'ATGTCTGACTCTCTCCTCTTCACGCCTCCTCAGGG CAGCATCCCTCTGCAG3'
pENTR-EGFP-C2-mSlp2-(3-67; K26R, A28R, Q44R)	5'CCTGAAAAAATTAAGGATGACCGACAACTAAAGA ATATGAGTGGC3' 5'GCCACTCATATTCTTTAGTTGTCGGTCATCCTTAA TTTTTTCAGG3'
pENTR-EGFP-C2-mSlp2-(3-67; K26R, A28R, Q44R, N48I)	5'AAGGATGACCGACAACTAAAGATTATGAGTGGCC AATGGTTTTAT3' 5'ATAAAACCATTGGCCACTCATAATCTTTAGTTGTC GGTCATCCTT3'
pENTR-EGFP-C2-mSlp2-(3-67; K26R, A28R, Q44R, N48I, G51L)	5'CGACAACTAAAGATTATGAGTCTCCAATGGTTTTA TGAATAGAAG3' 5'CTTCTATTCATAAAACCATTGGAGACTCATAATCT TTAGTTGTCG3'
pENTR-EGFP-C2-mSlp2-(3-67; K26R, A28R, Q44R, N48I, G51L, E56F)	5'ATGAGTCTCCAATGGTTTTATTTCGCTAAGGCAAA AAGACACAGG3' 5'CCTGTGTCTTTTTGCCTTAGCGAAATAAAACCATT GGAGACTCAT3'
pENTR-EGFP-C2-mSlp2-(3-67; K26R, A28R, Q44R, N48I, G51L, E56F, H62R, R63F)	5'TATTTCGCTAAGGCAAAAAGACGCTTCGACAAAA TCCACTGAGCTGAC3' 5'GTCAGCTCAGTGGATTTTGTCGAAGCGTCTTTTTG CCTTAGCGAAATA3'

Table 2.4. List of PCR primers used to perform site-directed mutagenesis in this study. Mutagenic base-pairs highlighted in red.* refers to primers which were kind gifts from Dr Alistair Hume.

2.1.1.3 Restriction endonuclease digestion protocol

Restriction enzymes along with their buffers were purchased from either NEB or Promega. The following restriction enzymes and their buffers were used (Table 2.5):

Enzyme	Source	10x Buffer
BamHI	NEB	NEBuffer 3.1
BamHI-HF	NEB	CutSmart
EcoRI	NEB	NEBuffer 2.1
EcoRI-HF	NEB	CutSmart
NotI	NEB	NEBuffer 3.1
NotI-HF	NEB	CutSmart
AgeI	NEB	NEBuffer 1.1
Thermosensitive alkaline phosphatase (TSAP)	Promega	Multi-Core
PacI	NEB	CutSmart

Table 2.5. A list of the restriction enzymes and buffers used in this study.

For a single or double restriction enzyme digestion, the following protocol was used: 2µl appropriate10x buffer (as recommended by the manufacturer), up to 1µg plasmid or insert DNA, unless otherwise indicated, 1µl of each restriction enzyme, in a final volume of 20µl with Milli-Q water. The reaction mixture was incubated for between 1-16 hours at 37ºC as per manufacturer's instructions. This was followed by a heat in-activation step according to the manufacturer's instructions. Note that a CutSmart buffer was used for both BamHI-EcoRI and BamHI-NotI double restriction enzyme digestion. NEBuffer 1.1 was used for AgeI-EcoRI double restriction enzyme digestion (as recommended by the manufacturer). To prevent singly digested vectors from re-ligating, the reaction mixture (20µl) was then dephosphorylated using 1µl (1 unit) Alkaline Phosphatase enzyme (to remove the 5′ phosphate groups from DNA), 2.5µl appropriate10x buffer (as recommended by the manufacturer) and 1.5µl Milli-Q water. The reaction mixture was then incubated at 37ºC for 15 mins, and heat inactivated at 74ºC for 15 mins. The efficacy of the restriction enzyme digestion was then assessed by electrophoresis of 10% of the reaction volume on 1% agarose gel (see section 2.1.1.5). A further purification step was then carried out using a NucleoSpin gel and PCR clean-up kit (MACHERY-NAGEL) as described in section 2.1.1.1. This was performed to remove any impurities or small DNA fragments from DNA vectors, thus preventing the vector from

ligation with itself and increasing the ligation efficacy. In addition, upon DNA purification, a more accurate DNA concentration will be obtained as the impurities and small DNA fragments might affect the sensitivity of the Nanodrop spectrophotometer (accurate DNA concentrations are required to ensure higher ligation efficacy to obtain 3:1 insert/vector molar ratio as described in section 2.1.1.4).

2.1.1.4 Ligation of restriction endonuclease digested DNA fragments

DNA ligation reactions were performed using T4 DNA Ligase enzyme (Promega). In these reactions, digested insert and vector were mixed in a 3:1 molar ratio using a ligation calculator tool (http://www.insilico.uni-duesseldorf.de/Lig_Input.html): 150 ±10 ng digested vector was used, 1µl (1unit) T4 DNA ligase enzyme, 2µl T4 DNA ligase buffer and made up to a total volume of 20µl with MilliQ water. The ligation reaction mixture was then incubated at 16ºC for 16-18 hours. This was followed by transformation into DH5α *E. coli* competent cells, amplification and purification as described in sections 2.1.2.2 and 2.1.2.3. In order to assess the ligation efficacy, a diagnostic restriction enzyme digestion was carried out using the appropriate restriction enzymes as described in section 2.1.1.3, followed by performing 1% agarose gel electrophoresis to visualize the bands of interest as described in section 2.1.1.5.

2.1.1.5 Agarose gel electrophoresis

An ethidium bromide stained 1% (w/v) Tris-HCl/Borate/EDTA (ethylenediaminetetraacetic acid) [TBE] agarose gel was used to separate and visualize DNA bands. To prepare 1% (w/v) TBE agarose gel, the appropriate amount of agarose (to make 1% w/v gel) was added to 1x TBE buffer (1.08% w/v Tris base, 0.55% w/v boric acid, 0.0585% EDTA w/v in dH2O, adjusted to pH8.0), mixed gently in 500ml conical flask, followed by heating in a microwave for 30 seconds (repeated 3 times). The mixture was then moved into a fume hood and cooled down to about 50ºC, followed by adding ethidium bromide (0.5µg/ml). The agarose gel mixture was then poured into an appropriate casting tray, ensuring that the gel was 5-7mm thick. A comb was then inserted to make the wells and the mixture was left at room temperature until solid (15-30 mins). A gel tank was then filled with 1x TBE buffer, after removal of gel comb, the casting tray (containing the gel) was then placed into the tank. For DNA loading,

10µl DNA was added to 2µl 6x DNA loading buffer (40% sucrose, 0.25% bromophenol blue in Milli-Q water), pipetted gently and 10µl DNA mixture was then loaded into each well. Either 1 Kb Plus DNA Ladder Thermo Fisher Scientific; #10787018 or 1 Kb DNA Ladder NEB; #N3232S were used as molecular weight standards. Agarose gel electrophoresis was continued at 75mA until complete separation of the molecular weight standards (the lowest band in the marker reached the end of the gel), then visualised using a Gel Doc (Syngene).

2.1.1.6 DNA quantification

DNA concentrations were measured using the ThermoScientific NanoDrop 2000 spectrophotometer. Briefly, the upper and lower optical pedestal surfaces were cleaned using 2µl HPLC water and wiped using dry lab wipes. 2µl HPLC water was dispensed into the lower optical pedestal surface which was considered as a blank, the pedestal surfaces were wiped and dried again. 2µl DNA sample was then dispensed into the lower optical pedestal surface to be measured. DNA was considered as pure for a value of 1.8-2 using the 260/280nm sample purity ratios.

2.1.1.7 DNA sequencing

DNA sequencing was performed by Source BioScience; a 5µl plasmid DNA (100ng/µl) along with 10µl (3.2pmol/µl) primer were sent per reaction. Otherwise, appropriate primers from Source BioScience primers stock were used wherever possible. The sequencing data were then translated into the corresponding protein amino acid sequence and compared with protein databases as described in section 2.7.

2.1.1.8 Generating vector maps

SnapGene Viewer 3.2.1 software was used to create vector maps.

2.1.2 Bacterial cell culture techniques

2.1.2.1 Preparation of lysogeny broth (LB) medium and agar plates

To prepare LB bacterial growth medium, the following components were used: 10g tryptone, 5g yeast extract and 10g sodium chloride were mixed and dissolved in a final volume of 1L with distilled water and autoclaved to be used for the subsequent experiments. LB agar plates were prepared using 1.5% w/v agar in LB medium, this was followed by autoclaving of the whole mixture,

cooling to approximately 50ºC, the appropriate antibiotic(s) concentration (100µg/ml ampicillin, 35µg/ml chloramphenicol, 50µg/ml kanamycin) was then added and mixed to ensure complete distribution of the antibiotic. Agar medium was then poured into petridish plates to be stored at 4ºC.

2.1.2.2 Transformation of *E. coli* competent cells

To perform DNA bacterial transformation, thawing of 50µl DH5α *E. coli* competent cells was performed on ice for 30 mins, 2µl plasmid DNA (50-100ng/µl) was then added and gently mixed. The cells-DNA mixture was incubated on ice for 30 mins, and then heat shocked at 42ºC for 60 seconds using a heat plate, followed by incubation on ice for 5 mins. Autoclaved LB medium (800µl) was then added and the cells were incubated at 37ºC for 60 mins with continuous agitation at 175 rpm. For all transformation reactions followed ligation reactions, transformation of the digested vector and insert was performed as a negative control and to ensure that complete digestion of the vector was performed and the cut insert did not contain any undigested remnant of the original vector (the vector used for PCR amplification of the insert). Finally, the cells were pelleted by centrifugation (5,000-6,000 rpm for 5 mins), re-suspended in 100µl LB, spread on LB agar plates containing the appropriate antibiotic(s) concentration and incubated at 37ºC for approximately 16 hours. "Note that" ampicillin was used for transformation of pETDuet-1, pGEX-4T1 and pAd/PL-DEST vectors, whereas kanamycin was used for pENTR vectors as they contain those antibiotic resistance genes.

2.1.2.3 Plasmid DNA amplification, isolation and purification from *E. coli* competent cells

For plasmid DNA amplification, 5-10ml LB medium containing the appropriate antibiotic concentration was poured into a sterile Sterilin tube, followed by picking of single colonies from agar plate and inoculating into the LB medium. Subsequently, bacterial cell cultures were incubated at 37ºC with continuous agitation (175-200 rpm) for 16-18 hours (to ensure sufficient bacterial growth and efficient DNA amplification). For plasmid DNA isolation and purification, NucleoSpin plasmid DNA purification kit (MACHERY- NAGEL) was used as per manufacturer's instructions. The overnight cultures were centrifuged (using an Eppendorf 5804 swinging-bucket centrifuge) at 4,000 rpm for 5 mins, the

supernatant was discarded and the cell pellets were re-suspended in 250µl chilled A1 buffer containing RNase enzyme (to catalyse bacterial RNA degradation), then transferred into 1,500µl micro-centrifuge tubes, followed by lysis of bacterial cells using 250µl A2 lysis buffer, the mixture was then gently inverted 6-8 times and incubated at room temperature for 5 mins. For DNA binding, 300µl A3 binding buffer was added, followed by centrifugation for 5 mins at 11,000 g, then the supernatant was loaded into NucleoSpin Plasmid / Plasmid (NoLid) column (DNA binding column) which was already placed into a collection tube. To bind the DNA onto the column, the DNA binding column was centrifuged for 1 min at 11,000 g and the flow-through was discarded. A washing step was performed using 500µl AW buffer (preheated to 50ºC), then the column was centrifuged for 1 min at 11,000 g and washed with 600µl A4 buffer (supplemented with ethanol) and centrifuged for 1 min at 11,000 g. Further centrifugation step for 2 min at 11,000 g was performed to ensure complete removal of ethanol. For elution of DNA, 50µl AE buffer was added and the mixture was incubated for 1 min at room temperature. For DNA collection, the collection tube was replaced by a new Eppendorf tube, the column was then centrifuged for 1 min at 11,000 g and the DNA was collected.

2.1.3 Generating plasmid DNA constructs

2.1.3.1 Generating m.Cherry-hRab27b expressing vectors

To produce m.Cherry-hRab27b expressing vectors, pETDuet-1-m.Cherry-hRab27b vectors were generated as described below.

A PCR amplification of hRab27b-(1-218; T23N) cDNA using a pEGFP-hRab27b-(1-218; T23N) mammalian expression vector (was a kind gift from Dr Alistair Hume) was performed to incorporate NotI restriction sites into the 5' and 3' ends of hRab27b cDNA (as described in section 2.1.1.1). PCR clean-up was performed as described in section 2.1.1.1.

A site-directed mutagenesis (as described in section 2.1.1.2) was performed using the pETDuet-1-m.Cherry-hRab27a vector (was a kind gift from Dr Alistair Hume) in order to incorporate a NotI restriction site into the 5' end of hRab27a; this vector originally contained a NotI restriction site at the 3' end of hRab27a. The digested PCR product (using NotI restriction enzyme) was then sub-cloned

into the digested pETDuet-1-m.Cherry vector (as described in sections 2.1.1.3 and 2.1.1.4). DNA transformation into DH5α *E. coli* competent cells and subsequent amplification were performed using the indicated concentration of ampicillin, followed by subsequent DNA isolation and purification (as described in sections 2.1.2.2 and 2.1.2.3). A diagnostic restriction enzyme digestion was performed with NotI restriction enzyme as described in sections 2.1.1.3 and 2.1.1.5; NotI digestion confirmed the sub-cloning of hRab27b into the digested vector. Subsequently, this vector was sequenced (as described in section 2.1.1.7) using a forward primer generously given by Dr Alistair Hume to amplify m.Cherry: 5'GCGCGGATCCGCATGGTGAGCAAGGGCGAG3' and the Duet Down1 reverse primer from Source BioScience primers stock to amplify hRab27b: 5'GATTATGCGGCCGTGTACAA3'. "Note" that all the sequencing data obtained in this project were translated into the corresponding protein amino acid sequence and compared with protein databases as described in section 2.1.1.7.

In order to produce a wild hRab27b (to remove the T23N mutation), the newly generated vector was site-directed mutagenized (as described in section 2.1.1.2) DNA transformation, amplification and purification steps were performed as described in sections 2.1.2.2 and 2.1.2.3. A diagnostic restriction enzyme digestion was performed with NotI restriction enzyme (as described in sections 2.1.1.3 and 2.1.1.5), followed by sequencing of the vector (as described in section 2.1.1.7) using the forward and reverse primers utilised before for hRab27b PCR amplification. To produce the constitutively active GTPase deficient form of Rab27b, a Q78L mutant was generated. To this end, a site-directed mutagenesis was performed (as described in section 2.1.1.2) using the newly generated vector as a template. This was followed by performing the subsequent DNA transformation, amplification and purification steps as described in sections 2.1.2.2 and 2.1.2.3. A diagnostic restriction enzyme digestion was performed with NotI restriction enzyme as described in sections 2.1.1.3 and 2.1.1.5, followed by sequencing of the vector (as described in section 2.1.1.7) using the Duet Down1 reverse primer from Source BioScience primers stock.

In order to obtain a more purified m.Cherry-hRab27b protein, a C-terminus truncated hRab27b protein was produced (the reasons behind producing a C-terminus truncated hRab27b protein discussed in section 3.3.1.2). To this end, a site directed mutagenesis reaction was performed using the pETDuet-1-m.Cherry-hRab27b-(1-218) vector as a template (as described in section 2.1.1.2). Plasmid DNA transformation, amplification and purification steps were then performed as described in sections 2.1.2.2 and 2.1.2.3. A diagnostic restriction enzyme digestion was performed with NotI restriction enzyme as described in sections 2.1.1.3 and 2.1.1.5. The newly generated vector was then sequenced using the Duet Down1 reverse primer from Source BioScience primers stock as described in section 2.1.1.7.

2.1.3.2 Generating 6x histidine-Rab expressing vectors

pET-14b-rat (r) Rab27a-(1-221) (Seabra et al., 1995), pET-15b-hRab27b-(1-218) (Chen et al., 1997) and pET-14b-hRab5a-(1-216) (Farnsworth et al., 1994; Strom et al., 2002) were obtained generously from Dr Alistair Hume. In order to confirm the molecular weight of these vectors, BamHI restriction enzyme digests of these vectors were loaded into agarose gel as described in sections 2.1.1.3 and 2.1.1.5. Also, these vectors were sequenced using the T7 promoter (F) primer (5'TAATACGACTCACTATAGGG3') from Source BioScience primers stock as described in section 2.1.1.7.

2.1.3.3 Generating Glutathione-S-Transferase (GST)-mSlp1 and GST-mSlp2 expressing vectors

pGEX-4T1-mSlp1-(1-201) vector was obtained generously from Dr Alistair Hume. A diagnostic restriction enzyme digestion was performed using BamHI and EcoRI restriction enzymes as described in sections 2.1.1.3 and 2.1.1.5. This vector was then sequenced (as described in section 2.1.1.7) using the following primers: the PGEX 5' forward primer 5'GGGCTGGCAAGCCACGTTTGGTG3' and the PGEX 3' reverse primer 5'CCGGGAGCTGCATGTGTCAGAGG3' from Source BioScience primers stock.

In addition, mSlp2 was produced as GST-tagged protein using the pGEX-4T1 vector. Note that A isoform of mSlp2 was used in all experiments in this project.

The mSlp2 expressing vector was generated as follows: mSlp2-(3-80) was PCR amplified (as described in section 2.1.1.1) using pEGFP-mSlp2-(1-133) vector (was a kind gift from Dr Alistair Hume); BamHI and EcoRI restriction enzyme sites were introduced into the 5' and 3' ends of mSlp2 cDNA, respectively. PCR clean-up was performed as described in section 2.1.1.1. 5' BamHI and 3' EcoRI restriction enzyme sites in the pGEX-4T1 vector (obtained generously from Dr Alistair Hume) were used to ligate the digested insert and vector as described in sections 2.1.1.3 and 2.1.1.4, followed by transformation into DH5α *E. coli* competent cells, DNA amplification and isolation as described in sections 2.1.2.2 and 2.1.2.3. A diagnostic restriction enzyme digestion was performed using BamHI and EcoRI restriction enzymes as described in sections 2.1.1.3 and 2.1.1.5. This vector was then sequenced (as described in section 2.1.1.7) using the PGEX 5' forward primer and the PGEX 3' reverse primer from Source BioScience primers stock.

Furthermore, pGEX-4T1-mSlp2-(3-41) and pGEX-4T1-mSlp2-(3-56) vectors were generated by site-directed mutagenesis of the pGEX-4T1-mSlp2-(3-80) vector as described in section 2.1.1.2. A subsequent DNA transformation into DH5α *E. coli* competent cells, DNA amplification and isolation were performed as described in sections 2.1.2.2 and 2.1.2.3. A diagnostic restriction enzyme digestion was performed using BamHI and EcoRI restriction enzymes as described in sections 2.1.1.3 and 2.1.1.5. Subsequently, these vectors were sequenced as described in section 2.1.1.7 using the PGEX 5' forward primer from Source BioScience primers stock.

2.1.3.4 Generating GFP-mSlp1, GFP-mSlp2 and GFP expressing vectors

pETDuet-1-GFP-mSlp1-(1-116) vector was generated by site-directed mutagenesis (as described in section 2.1.1.2) of the pETDuet-GFP-mSlp1-(1-116)-m.Cherry-hRab27a vector (was kind gift from Dr Alistair Hume). This vector was sequenced using the EGFP C F primer from Source BioScience primers stock as described in section 2.1.1.7: 5'CATGGTCCTGCTGGA GTTCGTG3'). "Note" that GFP refers to the enhanced GFP (EGFP) variant and not wild GFP. The primers used to perform the site-directed mutagenesis reaction were obtained generously from Dr Alistair Hume. This was followed by performing DNA transformation into DH5α *E. coli* competent cells and

subsequent DNA amplification and isolation steps as described in sections 2.1.2.2 and 2.1.2.3.

In addition, the pETDuet-1-GFP-mSlp2-(3-80) vector was generated by PCR amplification of GFP-mSlp2-(3-80) cDNA (as described in section 2.1.1.1) using the pENTR-EGFP-mSlp2-(3-80) vector (the generation steps of this vector described in section 2.1.3.6.1). BamHI and NotI restriction enzyme sites were introduced into the 5' and 3' ends of GFP-mSlp2-(3-80) cDNA, respectively. PCR clean-up was performed as described in section 2.1.1.1. The digested GFP-mSlp2-(3-80) (insert) was then sub-cloned into the pETDuet-1 vector (Novagen; obtained generously from Dr Alistair Hume) using the 5' BamHI and 3' NotI restriction sites as described in sections 2.1.1.3 and 2.1.1.4. This was followed by transformation into DH5α *E. coli* competent cells and subsequent DNA amplification and isolation were performed as described in sections 2.1.2.2 and 2.1.2.3. The pETDuet-1-GFP vector was then generated using the pETDuet-1-GFP-mSlp1-(1-116) vector (mentioned before) as a template to perform a site-directed mutagenesis reaction (as described in section 2.1.1.2). Subsequent DNA transformation into DH5α *E. coli* competent cells, DNA amplification and isolation steps were performed as described in sections 2.1.2.2 and 2.1.2.3.

A diagnostic restriction enzyme digestion (for vectors mentioned before) was performed using BamHI and NotI restriction enzyme sites as described in sections 2.1.1.3 and 2.1.15, followed by DNA sequencing using the EGFP CF primer from Source BioScience primers stock as described in section 2.1.1.7.

2.1.3.5 Generating 6x Histidine-mSlp2 expressing vectors

To generate 6x Histidine-mSlp2 expressing vectors, mSlp2-(3-80) cDNA was first PCR amplified (as described in section 2.1.1.1) using pGEX-4T1-mSlp2-(3-80) vector (the generation steps of this vector described in section 2.1.3.3). BamHI and NotI restriction sites were introduced into the 5' and 3' ends of mSlp2-(3-80). PCR clean-up was performed as described in section 2.1.1.1. mSlp2-(3-80) cDNA was then sub-cloned into the pETDuet-1 vector (Novagen) using 5' BamHI and 3' NotI restriction sites to generate the pETDuet-1-mSlp2-(3-80) vector as described in sections 2.1.1.3 and 2.1.1.4. This was followed by transformation into DH5α *E. coli* competent cells and subsequent DNA

amplification and isolation as described in sections 2.1.2.2 and 2.1.2.3. A diagnostic restriction enzyme digestion was performed using BamHI and NotI restriction enzymes as described in sections 2.1.1.3 and 2.1.1.5. This vector was then sequenced using the Duet Down1 reverse primer from Source BioScience primers stock as described in section 2.1.1.7.

To generate the pETDuet-1-mSlp2-(3-56; K26R, A28R, Q44R, N48I) vector, a sequential site-directed mutagenesis (as described in section 2.1.1.2) was performed using the pETDuet-1-mSlp2-(3-80) vector as a template. Firstly, a site-directed mutagenesis was performed using the pETDuet-1-mSlp2-(3-80) vector as a template to generate the pETDuet-1-mSlp2-(3-80; K26R, A28R) vector. Secondly, a site-directed mutagenesis was then performed using the pETDuet-1-mSlp2-(3-80; K26R, A28R) vector as a template to generate the pETDuet-1-mSlp2-(3-80; K26R, A28R, Q44R) vector. Thirdly, the pETDuet-1-mSlp2-(3-80; K26R, A28R, Q44R) vector was then used as a template to perform site-directed mutagenesis to generate the pETDuet-1-mSlp2-(3-80; K26R, A28R, Q44R, N48I) vector.

To generate the pETDuet-1-mSlp2-(3-56) and the pETDuet-1-mSlp2-(3-56; K26R, A28R, Q44R, N48I) vectors, site-directed mutagenesis was performed (as described in section 2.1.1.2) using the pETDuet-1-mSlp2-(3-80) and the pETDuet-1-mSlp2-(3-80; K26R, A28R, Q44R, N48I) vectors as templates, respectively. In addition, the pETDuet-1-mSlp2-(3-67) vector was generated by site-directed mutagenesis of the pETDuet-1-mSlp2-(3-80) vector.

These vectors were transformed into DH5α *E. coli* competent cells and subsequent DNA amplification and purification were performed as described in sections 2.1.2.2 and 2.1.2.3. A diagnostic restriction enzyme digestion was performed using BamHI and NotI restriction enzymes as described in sections 2.1.1.3 and 2.1.1.5. This was followed by sequencing of these vectors using the Duet Down1 reverse primer from Source BioScience primers stock as described in section 2.1.1.7.

2.1.3.6 Generating adenoviral vectors

Initially, to generate adenoviral vectors, the gene of interest was PCR amplified from the appropriate vector using the appropriate primers containing the required

restriction enzyme sites. The digested PCR product was then sub-cloned into the pENTR vector (ThermoFisher Scientific) using the appropriate restriction enzyme sites and both the insert and vector were ligated using DNA ligase enzyme as described in sections 2.1.1.3 and 2.1.1.4. Note that Kozak consensus sequence was included in all of the inserts used in this study to ensure proper initiation of the translation process in mammalian cells (Kozak, 1990; Kozak, 1991). This was followed by DNA transformation, amplification, purification and sequencing as described in sections 2.1.2.2, 2.1.2.3 and 2.1.1.7. Next, a recombination reaction with pAd/PL-DEST (Invitrogen) destination vector was performed in order to transpose the gene of interest into this vector. This involved incubation of 150ng entry clone (pENTR-gene of interest vector) with150ng destination vector (pAd/PL-DEST vector; obtained generously from Dr Alistair Hume) in a total volume of 8µl using Tris/EDTA (TE) buffer, pH 8.0 (1M Tris-HCl, 0.5M EDTA in MilliQ water). LR Clonase II enzyme (Invitrogen) was thawed in ice for about 2 mins with vortexing, 2µl LR Clonase II enzyme was then added to the mixture with incubation at 25ºC for 1 hour (preferably overnight to ensure successful recombination reaction results). To terminate the reaction, 1µl Proteinase K enzyme was then added to the mixture and incubated at 37ºC for 10 mins. 3-5µl was then transformed into DH5α *E. coli* competent cells, as described in section 2.1.2.2, followed by DNA amplification and purification as described in section 2.1.2.3. DNA sequencing was performed (using EGFP CF primer mostly from Source BioScience primers stock) as described in section 2.1.1.7 to ensure successful transposition of the gene of interest into the pAd/PL-DEST vector without any mutation(s). This was followed by transfection of HEK293A cells using the generated pAd/PL-DEST vectors as described in section 2.4.2.

2.1.3.6.1 Generating GFP-mSlp2-(3-80), GFP-mSlp1-(1-116) and GFP-mSlac2-a-(1-146) expressing adenoviral vectors

In order to produce GFP-mSlp2-(3-80) expressing adenoviral vector, pENTR-EGFP-C2-mSlp2-(3-80) vector was generated; the generation steps were as follows. mSlp2-(3-80) was PCR amplified (as described in section 2.1.1.1) using the pGEX-4T1-mSlp2-(3-80) vector (the generation steps of this vector described in section 2.1.3.3). EcoRI and BamHI restriction enzyme sites were

introduced into the 5' and 3' ends of mSlp2 cDNA, respectively. PCR clean-up was performed as described in section 2.1.1.1. The PCR product and the pENTR-EGFP-C2 vector (was a kind gift from Dr Alistair Hume) were then digested using EcoRI and BamHI restriction enzymes as described in section 2.1.1.3. 5' EcoRI and 3' BamHI restriction enzyme sites were then used to ligate the digested insert and vector as described in section 2.1.1.4, followed by transformation into DH5α *E. coli* competent cells and subsequent DNA amplification and isolation as described in sections 2.1.2.2 and 2.1.2.3. "Note" that for all the pENTR-EGFP-C2 vectors, a subsequent diagnostic restriction enzyme digestion was performed using EcoRI and BamHI restriction enzymes (as described in sections 2.1.1.3 and 2.1.1.5), followed by sequencing using the EGFP C F forward primer from Source BioScience primers stock as described in section 2.1.1.7, unless otherwise indicated.

Site-directed mutagenesis reactions using this newly generated vector were performed to generate the pENTR-EGFP-C2-mSlp2-(3-80; D3A), pENTR-EGFP-C2-mSlp2-(3-80; R32W) and pENTR-EGFP-C2-mSlp2-(3-79) vectors.

Plasmid DNA was then transformed into DH5α *E. coli* competent cells and subsequent DNA amplification and isolation steps were performed as described in sections 2.1.2.2 and 2.1.2.3. The pENTR-EGFP-C2-mSlp2-(3-80; D3A) and the pENTR-EGFP-C2-mSlp2-(3-79) vectors were then sequenced utilising the forward primer used to generate the D3A mutant of mSlp2 and the reverse primer used to generate mSlp2-(3-79).

Furthermore, different mutations: K58A, R61A, H62A, G68I, D70A, I71A, R73A and S75A were individually introduced into the pENTR-EGFP-C2-mSlp2-(3-80) vector. Accordingly, the pENTR-EGFP-C2-mSlp2-(3-80) vector was used as a template to perform site-directed mutagenesis (as described in section 2.1.1.2).

Subsequently, DNA was transformed into DH5α *E. coli* competent cells, followed by DNA amplification and isolation steps as described in sections 2.1.2.2 and 2.1.2.3.

To produce GFP-mSlp1-(1-116) expressing adenoviral vector, pENTR-EGFP-C2-mSlp1-(1-116) was generated. mSlp1-(1-116) was PCR amplified (as described in section 2.1.1.1) using the pGEX-4T1-mSlp1-(1-201) vector (mentioned in section 2.1.3.3). EcoRI and BamHI restriction enzyme sites were introduced into the 5' and 3' ends of mSlp1-(1-116) cDNA, respectively. PCR clean-up was performed as described in section 2.1.1.1. 5' EcoRI and 3' BamHI restriction enzyme sites in pENTR-EGFP-C2 vector were used to ligate the digested insert and vector as described in sections 2.1.1.3 and 2.1.1.4, followed by transformation into DH5α *E. coli* competent cells and subsequent DNA amplification and purification as described in sections 2.1.2.2 and 2.1.2.3.

In order to generate the GFP-mSlac2-a-(1-146) expressing adenoviral vector, pENTR-EGFP-C2-mSlac2-a-(1-266) vector (was a kind gift from Dr Alistair Hume) was used as a template to perform site-directed mutagenesis (as described in section 2.1.1.2). Subsequently, this vector was transformed into DH5α *E. coli* competent cells, amplified and purified as described in sections 2.1.2.2 and 2.1.2.3.

To produce the entire adenoviral vectors, recombination reactions were then performed using these pENTR-C2 vectors and the pAd/PL-DEST vector as described in section 2.1.3.6.

2.1.3.6.2 Generating GFP-mSlp2-(10-41), GFP-mSlp2-(10-50) and GFP-mSlp2-(10-56) expressing adenoviral vectors

In order to generate pENTR-EGFP-C2-mSlp2-(10-41), pENTR-EGFP-C2-mSlp2-(10-50) and pENTR-EGFP-C2-mSlp2-(10-56) vectors, mSlp2 cDNA was PCR amplified (as described in section 2.1.1.1) using the pENTR-EGFP-C2-Slp2-(3-80) vector (the generation steps of this vector described in section 2.1.3.6.1) in order to introduce EcoRI and BamHI restriction enzyme sites at the 5' and 3' ends of mSlp2 cDNA, respectively. PCR clean-up was then performed as described in section 2.1.1.1. The digested inserts were then sub-cloned into the digested pENTR-EGFP-C2 vector using 5' EcoRI and 3' BamHI restriction enzyme sites as described in sections 2.1.1.3 and 2.1.1.4, followed by plasmid DNA transformation into DH5α *E. coli* competent cells and subsequent DNA amplification and purification as described in sections 2.1.2.2 and 2.1.2.3.

To generate pENTR-EGFP-C2-Slp2-(10-56) vectors containing (K26R, A28R, Q44R, N48I), (K26R, A28R, Q44R, N48I, E56F) and (K26R, A28R, Q44R, N48I, G51L, E56F) mutations, the following vectors were used as templates to perform PCR amplification of these mSlp2 cDNAs (to introduce EcoRI and BamHI restriction enzyme sites at the 5' and 3' ends of mSlp2 cDNA, respectively) as described in section 2.1.1.1: pENTR-EGFP-C2-mSlp2-(3-56; K26R, A28R, Q44R, N48I), pENTR-EGFP-C2-mSlp2-(3-56; K26R, A28R, Q44R, N48I, E56F) and pENTR-EGFP-C2-mSlp2-(3-56; K26R, A28R, Q44R, N48I, G51L, E56F); the generation steps of these vectors described in section 2.1.3.6.3. PCR clean-up was then performed as described in section 2.1.1.1. The digested inserts were then sub-cloned into the digested pENTR-EGFP-C2 vector using 5' EcoRI and 3' BamHI restriction enzyme sites as described in sections 2.1.1.3 and 2.1.1.4. Subsequently, plasmid DNA transformation into DH5α E. coli competent cells, DNA amplification and purification were performed as described in sections 2.1.2.2 and 2.1.2.3.

Next, the entire adenoviral vectors were generated by performing recombination reactions using these pENTR-EGFP-C2 vectors and the pAd/PL-DEST as described in section 2.1.3.6.

2.1.3.6.3 Generating GFP-mSlp2-(3-41), GFP-mSlp2-(3-56), GFP-mSlp1-(1-74), GFP-mSlp1-(70-116) and m.Cherry-mSlp1-(1-74) expressing adenoviral vectors

In order to generate GFP-mSlp2-(3-41) and GFP-mSlp2-(3-56) expressing vectors, a site-directed mutagenesis was performed (as described in section 2.1.1.2) using the pENTR-EGFP-C2-mSlp2-(3-80) vector as a template (the generation steps of this vector described in section 2.1.3.6.1). These vectors were then transformed into DH5α *E. coli* competent cells, amplified and purified as described in sections 2.1.2.2 and 2.1.2.3.

Next, the pENTR-EGFP-C2-mSlp2-(3-56) vector was used as a template to perform a sequential site-directed mutagenesis (as described in section 2.1.1.2) as follows: a site-directed mutagenesis was performed using this vector as a template to generate the pENTR-EGFP-C2-mSlp2-(3-56; K26R) and pENTR-EGFP-C2-mSlp2-(3-56; A28R) vectors.

In addition, the pENTR-EGFP-C2-mSlp2-(3-56) vector was used as a template to perform site-directed mutagenesis reaction in order to produce the pENTR-EGFP-C2-mSlp2-(3-56; K26R, A28R) vector. These vectors were then transformed into DH5α *E. coli* competent cells, amplified and purified as described in sections 2.1.2.2 and 2.1.2.3.

The pENTR-EGFP-C2-mSlp2-(3-56; K26R, A28R) and the pENTR-EGFP-C2-mSlp2-(3-56) vectors were then used as templates to perform site-directed mutagenesis reactions to generate the pENTR-EGFP-C2-mSlp2-(3-56; K26R, A28R, Q44R) and the pENTR-EGFP-C2-mSlp2-(3-56; Q44R) vectors, respectively. Subsequent plasmid DNA transformation into DH5α *E. coli* competent cells, amplification and purification were performed as described in sections 2.1.2.2 and 2.1.2.3.

Subsequently, the newly generated pENTR-EGFP-C2-mSlp2-(3-56; K26R, A28R, Q44R) vector was used as a template to perform site-directed mutagenesis in order to produce the pENTR-EGFP-C2-mSlp2-(3-56; K26R, A28R, Q44R, N48I) vector. Furthermore, the pENTR-EGFP-C2-mSlp2-(3-56) vector was used as a template to perform site-directed mutagenesis in order to produce the pENTR-EGFP-C2-mSlp2-(3-56; N48I) vector.

In addition, the pENTR-EGFP-C2-mSlp2-(3-56; Q44R) vector was used as a template to perform site-directed mutagenesis reaction in order to generate the pENTR-EGFP-C2-mSlp2-(Q44R, N48I) vector. To generate the pENTR-EGFP-C2-mSlp2-(3-56; K26R, A28R, Q44R, N48I, G51L) vector, a site-directed mutagenesis was performed using the pENTR-EGFP-C2-mSlp2-(3-56; K26R, A28R, Q44R, N48I) vector as a template. Plasmid DNA transformation into DH5α *E. coli* competent cells was then performed, followed by DNA amplification and purification as described in sections 2.1.2.2 and 2.1.2.3.

The newly generated pENTR-EGFP-C2-mSlp2-(3-56; K26R, A28R, Q44R, N48I, G51L) vector was then used to perform site-directed mutagenesis reaction in order to produce the pENTR-EGFP-C2-mSlp2-(3-56; K26R, A28R, Q44R, N48I, G51L, E56F) vector. Subsequent plasmid DNA transformation into DH5α *E. coli* competent cells, amplification and purification steps were performed as described in sections 2.1.2.2 and 2.1.2.3.

To generate the pENTR-EGFP-C2-mSlp2-(3-56; K26R, A28R, Q44R, N48I, E56F) vector (to remove the G51L mutation), the pENTR-EGFP-C2-mSlp2-(3-56; K26R, A28R, Q44R, N48I, G51L, E56F) vector was then used as a template to perform site-directed mutagenesis reaction. Plasmid DNA transformation into DH5α *E. coli* competent cells was then performed, followed by DNA amplification and purification as described in sections 2.1.2.2 and 2.1.2.3.

To generate the pENTR-EGFP-C2-mSlp1-(1-74) and the pENTR-EGFP-C2-mSlp1-(70-116) vectors, mSlp1-(1-74) and mSlp1-(70-116) were PCR amplified (as described in section 2.1.1.1) using the pGEX-4T1-mSlp1-(1-201) vector (mentioned in section 2.1.3.3). To PCR amplify mSlp1-(1-74) and mSlp1-(70-116), EcoRI and BamHI restriction enzyme sites were introduced into the 5' and 3' ends of mSlp1 cDNA, respectively. PCR clean-up was performed as described in section 2.1.1.1. The digested inserts were then sub-cloned into the digested pENTR-EGFP-C2 vector using 5' EcoRI and 3' BamHI restriction enzyme sites as described in sections 2.1.1.3 and 2.1.1.4, followed by transformation into DH5α *E. coli* competent cells and subsequent DNA amplification and isolation as described in sections 2.1.2.3 and 2.1.2.4.

In order to generate the pENTR-m.Cherry-mSlp1-(1-74) vector, m.Cherry cDNA was PCR amplified (as described in section 2.1.1.1) using the pETDuet-1-m.Cherry-hRab27b vector (mentioned in section 2.1.3.1). AgeI and EcoRI restriction sites were introduced into the 5' and 3' ends of m.Cherry cDNA, respectively. PCR clean-up was then performed as described in section 2.1.1.1. The digested insert was then sub-cloned into the digested pENTR-EGFP-C2-mSlp1-(1-74) vector (the generation steps of this vector described before) using 5' AgeI and 3' EcoRI restriction enzyme sites as described in sections 2.1.1.3 and 2.1.1.4 (by digesting this vector, EGFP was removed and replaced by m.Cherry), followed by transformation into DH5α *E. coli* competent cells and subsequent DNA amplification and isolation as described in sections 2.1.2.3 and 2.1.2.4. This vector was then sequenced using the forward primer utilised before to amplify m.Cherry as described in section 2.1.1.7.

Next, recombination reactions were performed using these pENTR-C2 vectors and the pAd/PL-DEST vector as described in section 2.1.3.6.

2.1.3.6.4 Generating GFP-mSlp2-(3-67) and GFP-mSlp2-(10-67) expressing adenoviral vectors

In order to generate the pENTR-EGFP-C2-mSlp2-(3-67) vector, a site directed mutagenesis reaction (as described in section 2.1.1.2) was performed using the pENTR-EGFP-C2-mSlp2-(3-80) vector as a template (mentioned in section 2.1.3.6.1). Subsequently, plasmid DNA was transformed into DH5α *E. coli* competent cells, amplified and purified as described in sections 2.1.2.3 and 2.1.2.4.

Furthermore, sequential site-directed mutagenesis reactions (as described in section 2.1.1.2) were performed using this newly generated vector as an initial template to produce the following mSlp2-(3-67) mutants: (K26R, A28R), (K26R, A28R, Q44R), (K26R, A28R, Q44R, N48I) and (K26R, A28R, Q44R, N48I, G51L). Subsequently, plasmid DNA was transformed into DH5α *E. coli* competent cells, amplified and purified as described in sections 2.1.2.3 and 2.1.2.4. In addition, to generate the pENTR-EGFP-C2-mSlp2-(3-67; K26R, A28R, Q44R, N48I, G51L, E56F) vector, a site-directed mutagenesis (as described in section 2.1.1.2) was performed using the pENTR-EGFP-C2-mSlp2-(3-67; K26R, A28R, Q44R, N48I, G51L) vector as a template. Subsequently, plasmid DNA was transformed into DH5α *E. coli* competent cells, amplified and purified as described in sections 2.1.2.3 and 2.1.2.4. This newly generated vector was then used as a template to perform further site-directed mutagenesis reaction (as described in section 2.1.1.2) in order to produce the mSlp2-(3-67; K26R, A28R, Q44R, N48I, G51L, E56F, H62R, R63F) mutant. Subsequently, plasmid DNA was transformed into DH5α *E. coli* competent cells, amplified and purified as described in sections 2.1.2.3 and 2.1.2.4.

In order to generate the following vectors: pENTR-EGFP-C2-mSlp2-(10-67), pENTR-EGFP-C2-mSlp2-(10-67; K26R, A28R, Q44R, N48I), pENTR-EGFP-C2-mSlp2-(10-67; K26R, A28R, Q44R, N48I, E56F, H62R, R63F) and pENTR-EGFP-C2-mSlp2-(10-67; K26R, A28R, Q44R, N48I, G51L, E56F, H62R, R63F), mSlp2-(10-67) cDNAs containing the specified mutations were PCR amplified (as described in section 2.1.1.1). The following vectors were used to perform the PCR amplification: pENTR-EGFP-C2-mSlp2-(3-67), pENTR-EGFP-C2-mSlp2-(3-67; K26R, A28R, Q44R, N48I), pENTR-EGFP-C2-mSlp2-

(3-67; K26R, A28R, Q44R, N48I, E56F) and pENTR-EGFP-C2-mSlp2-(3-67; K26R, A28R, Q44R, N48I, G51L, E56F); the generation steps of these vectors described before. PCR clean-up was then performed as described in section 2.1.1.1. The digested inserts were then sub-cloned into the digested pENTR-EGFP-C2 vector using 5' EcoRI and 3' BamHI restriction enzyme sites as described in sections 2.1.1.3 and 2.1.1.4, followed by transformation into DH5α *E. coli* competent cells and subsequent DNA amplification and purification as described in sections 2.1.2.3 and 2.1.2.4. The entire adenoviral vectors were then produced by performing recombination reactions using these pENTR-C2 vectors and the pAd/PL-DEST vector as described in section 2.1.3.6.

2.2 Protein production and purification techniques

2.2.1 Small-scale protein production

Small scale protein induction was performed to optimise the protein induction conditions; such as the incubation time and temperature and the optimum isopropyl β-D-1-thiogalactopyranoside (IPTG) concentration, whenever required (for example, if the protein was produced for the first time or problems happened during the large-scale protein production). Details of protein production described below in section 2.2.2.

2.2.2 Large-scale protein production

To produce and purify recombinant proteins, DNA transformation into Rosetta *E. coli* competent cells was performed as described in section 2.1.2.2, then 5-10ml LB medium containing the appropriate antibiotics concentration (100μg/ml ampicillin and 35μg/ml chloramphenicol) was poured into a sterile Sterilin tube, followed by picking of single colonies from agar plate and inoculating into the LB medium. Bacterial cell cultures were then incubated at 37ºC with continuous agitation (175-200 rpm) for 16-18 hours (to ensure sufficient bacterial growth). Subsequently, the 5-10ml bacterial medium was further grown using 125ml LB medium containing the appropriate antibiotics concentration (in a 500ml autoclaved conical flask) at 37ºC with continuous agitation (175-200 rpm) for 16-18 hours. This was followed by inoculation of 4L LB medium containing the appropriate antibiotics concentration with 100ml of bacterial culture (25ml/L; using four 2L autoclaved conical flasks). Bacterial

growth was performed under the specified conditions until reaching an optical density$_{600}$ (OD_{600}) value of 0.4-0.6 at 600nm (normally 1-2 hours; depending on the rate of bacterial growth and concentration). At this point, protein production was induced using 0.5Mm IPTG (Sigma) at 37°C with continuous agitation at 175 rpm for 2-3 hours. Subsequently, bacterial cells were harvested by centrifugation at 5,000 rpm for 20 mins at 4°C using ThermoScientific Sorvall RC3BP Plus centrifuge. The cell pellets were then re-suspended in ice-cold 1x Phosphate buffered saline (PBS) (Lonza) (20ml/pellet ≈ 1g), harvested by centrifugation at 5,000 rpm for 10 mins at 4°C (using an Allegra 64R; Beckman Coulter centrifuge) and stored at -80°C to be used for subsequent protein purification.

2.2.3 Purification of recombinant proteins

2.2.3.1 Purifying poly histidine-tagged recombinant proteins

The induced cell pellets (prepared as described in section 2.2.2) were re-suspended in ice cold lysis buffer (20ml/pellet ≈ 1g): 50mM Tris-HCl pH 7.5, 150mM sodium chloride, 5mM magnesium chloride, 1mM β-mercaptoethanol (BME) (Sigma) and one protease inhibitor cocktail tablet/10ml (Roche). Tris-HCl was added to regulate the acidity and keep the buffer in the 7.5-9.0 pH range, sodium chloride was included in the buffer to provide the required ionic strength, BME was working as a reducing agent by breaking disulphide bonds, magnesium chloride was added to maintain stabilisation of the nucleotides. The cell lysates were further lysed mechanically at 35 kilo-pound-force per square inch (Kpsi) using high pressure cell disruptor (CONSTANT SYSTEMS Ltd), followed by centrifugation (using SW 41 Ti Rotor; Beckman Coulter) at 100,000 g for 1 hour at 4°C using a 10ml centrifuge tubes. The supernatant was then adjusted to 500mM sodium chloride and purified using the immobilized metal affinity chromatography (IMAC) system. In this system, the supernatant was mixed with a thoroughly washed nickel sepharose beads (using a 50ml Falcon tube) in dialysis buffer (50mM Tris-HCl pH 7.5, 500mM sodium chloride, 5mM magnesium chloride and 1mM BME) and incubated with rotation at 4°C for 2-16 hours. The principle of the purification process was based on the affinity interaction between Ni^{2+} and the 6x histidine residues in the 6x histidine-tagged

proteins [by binding of the electron donor groups of the imidazole ring of histidine to Nickel (Bornhorst and Falke, 2000)].

The nickel sepharose beads were prepared as follows: 5-10ml chelating sepharose fast flow (GE Healthcare Life Sciences) was poured into a sterile 50ml Falcon tube, centrifuged (using an Eppendorf 5804 swinging-bucket centrifuge) at 2,000 rpm for 3 mins, re-suspended in 25-50ml distilled water, centrifuged at 2,000 rpm for 3 mins, re-suspended in 5-10ml of 250mM nickel sulphate and incubated for 1 hour at room temperature. Subsequently, the nickel-sepharose beads mixture was centrifuged at 2,000 rpm for 3 mins, re-suspended in 25-50ml distilled water, centrifuged at 2,000 rpm for 3 mins, re-suspended in 25-50ml acetate buffer pH 4 (41ml of 0.1M acetic acid mixed with 9ml sodium acetate in a final volume of 100ml with distilled water at pH 4) and centrifuged at 2,000 rpm for 3 mins. Finally, the Nickel-sepharose beads mixture was washed several times (2-3 times) by re-suspending in 25-50ml dialysis buffer and centrifugation at 2,000 rpm for 3 mins.

The supernatant-nickel sepharose beads mixture was then centrifuged (using an Allegra 64R; Beckman Coulter centrifuge) at 2,000 rpm for 3 mins at 4°C and washed with dialysis buffer; this was repeated at least 3 times. The supernatant-nickel sepharose beads mixture was then re-suspended in a sufficient volume of dialysis buffer, poured into a poly-prep chromatography column (Bio-Rad). The column was then washed several times with dialysis buffer to discard the non-specifically bound proteins to the nickel column; the flow-through was collected and kept to be analysed later. Subsequently, increasing concentrations of imidazole (20, 50, 100, 200 and 250 mM) in dialysis buffer at pH 8 (to maintain protein stability) were used to displace protein from binding to nickel beads (the flow-through using 20mM imidazole was discarded to remove low affinity bound proteins). The eluates were then collected and the presence of proteins was tested by adding 5µl of eluate/60µl of Coomassie protein assay reagent (ThermoScientific)/ using a 96-well plate (blue colour was considered as an indicator for the presence of the proteins). The successful protein eluates were then dialysed using 12–14 or 3.5KDa (based on protein molecular weight) molecular weight cut off visking dialysis tubing (Medicellmembranes) in a 2L dialysis buffer at 4°C with continuous stirring for 16-18 hours. To purify Rab

proteins, 0.21g GDP (Alfa Aesar) was added to the dialysis buffer to keep them in the GDP-bound inactive state as they possess intrinsic GTPase activity; i.e. stabilising them (Rybin et al., 1996). A further dialysis step was then performed using a new 2L dialysis buffer for 4 hours under the same conditions (without adding GDP). The purified protein was then collected from the dialysis tube and quantified using the NanoDrop 2000 spectrophotometer as described in section 2.2.7. In addition, the protein was then analysed as described in sections 2.2.4.1 and 2.2.4.2.

2.2.3.2 Purifying GST-fused recombinant proteins

The induced cell pellets (prepared as described in section 2.2.2) were re-suspended in ice cold lysis buffer (20ml/pellet ≈ 1g): 50mM Tris-HCl pH 7.5, 150mM sodium chloride, 5mM magnesium chloride, 1mM dithiothreitol (DTT) (Sigma) and one protease inhibitor cocktail tablet/10 ml 'Roche'; DTT was working as a reducing agent by breaking disulphide bonds. The cell lysates were additionally lysed mechanically at 35 Kpsi using high pressure cell disruptor (CONSTANT SYSTEMS Ltd), followed by centrifugation (using SW 41 Ti Rotor; Beckman Coulter) at 100,000 g for 1 hour at 4°C using a 10ml centrifuge tubes. The supernatant was then added (using a 50ml Falcon tube) to an extensively washed reduced glutathione (GSH)-sepharose beads (GE Healthcare Life Sciences) in dialysis buffer (the same contents of the lysis buffer without adding the protease inhibitor) and incubated with rotation at 4°C for 2-16 hours. The beads were prepared by washing with dialysis buffer as follows: 5-10ml GSH-sepharose beads were poured into a sterile 50ml Falcon tube and washed several times (2-3 times) by re-suspending in 25-50ml cold ice dialysis buffer and centrifugation at 2,000 rpm for 3 mins at 4°C. The principle of the purification process using this system was based on the interaction between GSH and GST in the GST-fused proteins. The supernatant-GSH beads mixture was then centrifuged (using an Allegra 64R; Beckman Coulter centrifuge) at 2,000 rpm for 3 mins at 4°C and washed by dialysis buffer; this was repeated at least 3 times. The supernatant-GSH beads mixture was then re-suspended in a sufficient volume of dialysis buffer and poured into a poly-prep chromatography column (Bio-Rad). The column was then washed several times with dialysis buffer to discard the non-specifically bound proteins to the GSH beads (the flow-through

was collected and kept to be analysed later. This was followed by protein displacement from binding to GSH beads using increasing concentrations of free reduced GSH (Sigma) in dialysis buffer (10, 20, 100mM at pH 7). The flow-through using 10mM free glutathione was discarded to remove low affinity bound proteins. The eluates were then collected and tested for the presence of proteins by adding 5µl of eluate/60µl of Coomassie protein assay reagent (ThermoScientific)/ using a 96-well plate (blue colour was considered as an indicator for the presence of the proteins). The successful protein eluates were then dialysed using 12–14 molecular weight cut off visking dialysis tubing (Medicellmembranes) in a 2L dialysis buffer at 4°C with continuous stirring for 16-18 hours. A further dialysis step was performed using a new 2L dialysis buffer for 4 hours under the same conditions. The purified protein was then collected from the dialysis tube and quantified using the NanoDrop 2000 spectrophotometer as described in section 2.2.7. In addition, the protein was then analysed as described in section 2.2.4.1.

2.2.4 Electrophoresis

2.2.4.1 Sodium dodecyl sulphate-polyacrylamide gel electrophoresis (SDS-PAGE)

To separate medium- to large- molecular weight proteins (greater than 20KDa), 10% (v/v) SDS-PAGE gel was prepared using the components outlined below (Table 2.6); ammonium persulfate (APS) (Fisher Scientific) was freshly prepared at the time of use.

Separating Gel (10ml)	
ddH2O	4.8ml
40% acrylamide	2.5ml
1.5M Tris-HCl pH 8.8	2.5ml
10% APS	100µl
10% SDS	100µl
N,N,N,N'-tetramethyethylene-diamine (TEMED)	4µl
Stacking Gel (5ml)	
ddH2O	3.65ml
40% acrylamide	625µl
1M Tris-HCl pH 6.8	625µl
10% APS	50µl
10% SDS	50µl
TEMED	5µl

Table 2.6. Components of 10% (v/v) SDS-PAGE gel.

Gels were casted using the Mini-PROTEAN Tetra Cell (BioRad) system (1.5mm spacer plates were used) and placed in the Mini-PROTEAN Tetra Cell tank (BioRad) using SDS-PAGE running buffer (25mM Tris-HCl, 192mM glycine, 0.1% (w/v) SDS). Protein samples were prepared by mixing with protein loading buffer (5x buffer: 0.3M Tris-HCl pH 6.8, 10% (w/v) SDS, 40% (v/v) glycerol, 0.02% (w/v) bromophenol blue and 10% (v/v) BME) by multiple pipetting of the mixture, then boiled at 100ºC for 5-10 mins, mixed and centrifuged for 1 min at 10,000 g. Protein samples were then loaded into 10% (v/v) SDS-PAGE gel and electrophoresed at 40mA per gel until complete separation of the molecular weight standards (the lowest band in the marker reached the bottom edge of the gel). 5µl of BLUeye Prestained Protein Ladder (Geneflow; # 94964) was used as a molecular weight standard and run alongside protein samples. This was followed by either transferring into polyvinylidene difluoride (PVDF) membrane for western blot analysis (as described in section 2.2.5) or staining with Instant Blue Protein Stain (Expedeon). The staining involved washing the gel gently with water then incubation using Instant Blue Protein Stain at room temperature by placing the gel in a tray with continuous agitation for 1-2 hours, this was followed by incubation in water for 2-16 hours, followed by 2-3 washes with water to be visualised later as described in section 2.2.6.

2.2.4.2 Protein SDS-PAGE pre-cast-gel

To achieve better separation of low-molecular weight proteins (less than 20KDa), the Invitrogen NuPAGE 4-12% Bis-Tris pre-cast gel system was used. Almost the same steps for loading protein samples using the 10% SDS-PAGE gel was followed. In this system, the comb and tape of the gel were removed carefully, the wells of the gel were then washed with water and well spacers were re-aligned using a gel-loader-tip. The Invitrogen LDS-NuPAGE (4x stock to make 1x final concentration) loading buffer was used for loading samples (0.5M DTT; 10x stock was made to 1x in loading buffer at time of preparation; used as a reducing agent). The following running buffer was used: 20ml running buffer (Invitrogen Tris-MES-SDS) was combined with 20ml running-buffer-diluent (5g SDS and 1.5g EDTA in 0.5L water) in a final volume of 800ml with ddH2O. 5µl of Novex Sharp Pre-Stained protein marker (ThermoFisherScientific) was used as a molecular weight standards. Protein samples were then electrophoresed at 200V for 60-75 mins (until complete separation of the protein). This was followed by either transferring into PVDF membrane for western blot analysis (as described in section 2.2.5) or staining with Coomassie blue. To stain protein gels with Coomassie blue, the gel was rinsed with water in a clean tray for 2-3 times and placed in a clean tray. 20-50ml Blue-Silver stain (Candiano et al., 2004) was then added and agitated at room temperature for between 1 to 16 hours. The Blue-Silver stain was prepared as follows: Reagent (A) was prepared by adding 118mL (85%) phosphoric acid to 500ml water with continuous mixing, followed by adding 100g ammonium sulphate and made up to 800ml with water. Reagent (B) was prepared by dissolving 1.2g Coomassie Blue G-250 (BIO-RAD) in 200ml methanol. To prepare 1x Blue-Silver stain, 4 parts of reagent (A) were added to 1 part of reagent (B) immediately before use. The gel was then rinsed 2-3 times with water, placed in a clean tray with water and agitated at room temperature for between 1 to 16 hours to be visualised later as described in section 2.2.6. Note that all the reagents used for Protein SDS-PAGE pre-cast-gel system were prepared by and obtained generously from Dr David Tooth with the required technical support.

2.2.5 Western blot analysis

To transfer medium- to large- molecular weight proteins (greater than 20KDa), immobilon-P PVDF transfer membrane (0.45μm) was used; whereas for low-molecular weight proteins (less than 20KDa), MACHEREY-NAGEL-Porablot PVDF (0.2μm) was used to avoid the over-transfer of the transferred proteins. The PVDF membrane was pre-soaked in 100% methanol for 15-30 seconds, then incubated in transfer buffer (25mM Tris-HCl, 192mM glycine, 20% methanol) for 2-5 mins at room temperature. The gel was then placed in the transfer sandwich using the following order: (two pieces of 7 x 9 cm 3mm filter paper, PVDF transfer membrane, the gel and two pieces of filter paper) and immersed in transfer buffer (air bubbles were avoided as much as possible by rolling and socking with transfer buffer). The transfer sandwich was placed in the Geneflow cassette (Geneflow wet transfer system). The cassette was then placed in a tank filled with ice cold transfer buffer. The PVDF membrane was faced to the cathode and transferred at 4ºC using either 150V for 3 hours, or 30V for 18 hours. The same steps were followed for transfer of low-molecular weight proteins except of using of Novex wet transfer system instead and proteins were transferred at 25V for 90 mins.

After transfer completion, the membrane was then blocked with 1x PBS, 0.1% Tween-20 and 5% skimmed milk for 1 hour at room temperature to block the non-specific binding to the primary antibody. This was followed by incubation with primary antibody using1x PBS and 0.1% Tween-20 for 16 hours at 4ºC. The membrane was then washed 3x with 1x PBS and 0.1% Tween-20 as follows: the membrane was placed in a clean tray filled with 1x PBS and 0.1% Tween-20 and agitated for 10 mins, followed by rinsing and the process was repeated 3 times. Subsequently, the membrane was incubated with the appropriate secondary antibody in 1x PBS and 0.1% Tween-20 for 1 hour at room temperature. The washing steps for the primary antibody were repeated except of using 5 mins instead. Details of antibody used are described below in Table 2.7.

Primary Antibody	**Source**	**Dilution**	**Catalogue no.**
Goat anti-m.Cherry	Sicgen	1:1,000	AB0040-200
Mouse anti-poly-histidine	Sigma-Aldrich	1:1,000	H1029
Goat anti-GFP	Sicgen	1:1,000	A0020-200
Secondary Antibody	**Source**	**Dilution**	**Catalogue no.**
Donkey anti-Goat IR800	Licor	1:30,000	P/N 926-32214
Donkey anti-Mouse IR680	Licor	1:10,000	P/N 926-68072

Table 2.7. A list of the antibodies used in this study.

2.2.6 Imaging

The Licor Odyssey instrument was used to visualise SDS-PAGE gels and PVDF membranes. The PVDF membrane or gels were placed facing the glass scanning area of the instrument; air bubbles were avoided as much as possible by wetting the glass surface with 1x PBS. Image Studio Ver 3.1 software was used to acquire images by applying the following settings: resolution; 84µm, quality; high, offset; 0.5mm, intensity; 5.

2.2.7 Determination of protein concentrations

Protein concentrations were measured using the ThermoScientific NanoDrop 2000 spectrophotometer. The same steps for DNA quantification described in section 2.1.1.6 were followed for protein quantification. The absorbance measurements for the purified proteins were performed at 280nm using the molecular weight and extinction coefficient of the quantified proteins which were measured using the expasy online tool for protein molecular weight determination (http://web.expasy.org/protparam/). The concentration of the purified protein was then measured by quantifying the band of interest from SDS-PAGE gel using ImageJ software. This was performed by measuring the intensity of the whole well, the background and the band of interest; then the percentage of the band of interest from the total signal of the well was calculated accordingly. The concentration of the purified protein was then calculated by multiplying the percentage of the band of interest by the already measured protein concentration using the NanoDrop 2000 spectrophotometer.

2.2.8 Mass spectrometry analysis

Proteomic analysis using mass spectrometry was performed by Dr David Tooth (Centre for Biomolecular Sciences, University of Nottingham). This involved separation of the purified protein using 10% SDS-PAGE gel, the bands of interest were then excised and proteomic analysis was performed. In this method of analysis, the protein was digested using trypsin (trypsin catalyses protein degradation at the carboxylic side of lysine or arginine, unless followed by proline), the resulted smaller peptides were then analysed by mass spectrometer to identify the amino acid residues of these peptides. The identified amino acid residues were then compared with protein databases to determine amino acid sequence homology.

2.3 Protein-protein interaction assays

2.3.1 Fluorescent GST-pull down protein-protein interaction assay experiments

The fluorescent GST-pull down assay had been used to measure the binding affinity of m.Cherry-hRab27b recombinant protein (fluorescent protein) to GST-mSlp1-(1-201) and GST-mSlp2-(3-80) recombinant proteins. Furthermore, this assay can be used to determine the inhibitory activity of the proposed blockers for these interactions (Rab27-effector protein interactions) in the future. In this assay, the fluorescence of m.Cherry-hRab27b protein was considered as a read-out for the bound fraction of Rab27b. The procedure of the fluorescent GST-pull down assay was as follows:

The glutathione magnetic beads (GE Healthcare Life Sciences) were poured into sterile Eppendorf tubes (1,000-1,500µl/tube) and washed several times (2-3 times) with 1x dilution buffer (50mM Tris-HCl pH 7.5, 150mM sodium chloride, 1mM DTT and 1 % bovine serum albumin; BSA) using a special magnet (ThermoFisherScientific; #12321D) (Figure 2.1) to collect the glutathione magnetic beads at the bottom and sides of the Eppendorf tube. The reaction mixture consisted of: m.Cherry-hRab27b, 0.5µM GST-mSlp1-(1-201) or GST-mSlp2-(3-80) , 3mM GTP (GE Healthcare Life Sciences), 10% glutathione magnetic beads and 5x dilution buffer (diluted to 1x) in a total volume of 200µl. In addition, another set of reactions contained the same components except of

using 0.5μM GST instead of GST-mSlp1-(1-201) or GST-mSlp2-(3-80) to normalise the data and served as a negative control for reactions. The reaction mixture was then incubated at room temperature for 2 hours using a 96-well microplate (ThermoFisherScientific; # 611F96; clear, flat bottom) with gentle agitation (100 rpm). This step was followed by transferring the supernatant (100μl) using a special magnetic stand (ThermoFisherScientific; # 12027) (Figure 2.2) into a new 96-well microplate. The fluorescence of the supernatant was considered as read-out for the unbound fraction and used indirectly to calculate the bound fraction as described below. The fluorescence of the 96 well microplate was then measured using the CLARIOstar (BMG Labtech) microplate reader (mostly) by exciting m.Cherry-hRab27b at 562.5-577.5nm and the emission was measured at 610-630nm. In addition, the PHERAstar (BMG Labtech) microplate reader was used to measure the fluorescence of the 96 well microplate by exciting m.Cherry-hRab27b at 570nm and the emission was measured at 610nm. Note that by using the CLARIOstar microplate reader, the range of the excitation and emission wave length can be increased, whereas only constant excitation and emission wave length can be used with the PHERAstar microplate reader.

The corrected fluorescence was measured in arbitrary units (a.u.) by subtracting the fluorescence of the supernatant of either the GST-mSlp1-(1-201) or GST-mSlp2-(3-80) included reactions from the average of the fluorescence of the supernatant of the GST included reactions for each specific m.Cherry-hRab27b concentration; i.e. the corrected fluorescence was considered as an indirect read-out of the m.Cherry-Rab27b bound fraction and GST was used to normalise the data and served as a negative control; for further details see the following equation:

Corrected fluorescence = (fluorescence of m.Cherry-hRab27b-GST reaction mixture – (fluorescence of m.Cherry-hRab27b-GST-effector reaction mixture) (2.1)

Accordingly, the EC50 values of m.Cherry-hRab27b for binding GST-mSlp1-(1-201) and GST-mSlp2-(3-80) were determined.

In the competition-binding experiments, unlabelled rRab27a and hRab27b were used as typical competitive inhibitors (hRab5a was used as a negative control) and tested in terms of disrupting the interaction between a constant concentration of m.Cherry-hRab27b (double the EC50 values were used to saturate the binding of hRab27b with either mSlp1 or mSlp2) and 0.5µM GST-mSlp1-(1-201) or GST-mSlp2-(3-80). This was performed in order to investigate the specificity of the fluorescent GST-pull down assay in terms of testing the inhibitory effects of candidate inhibitors of Rab27-effector protein interactions in the future.

Note that the dimensions of the 96-microplate were requested from the supplier and customised accordingly using the attached software of the microplate reader. The following settings were used: 40 flashes per well and the gain was set to 40%. The control software was used to interface with the CLARIOstar or the PHERAstar microplate readers and the MARS Data Analysis Software was used to acquire the data.



Figure 2.1. Magnet used to collect glutathione magnetic beads using Eppendorf tubes.



Figure 2.2. Magnet used to collect glutathione magnetic beads using a 96-well microplate.

2.3.2 FRET-based protein-protein interaction assay experiments

Another in vitro protein-protein interaction assay utilising the FRET principle was used to determine the binding affinity of different Rab27-effector proteins (mSlp1 and mSlp2) to hRab27a/b, therefore it can be used to test and determine the inhibitory effects of the candidate inhibitors of these interactions in the future. GFP-mSlp1-(1-116) and GFP-mSlp2-(3-80) recombinant proteins were used as donor fluorophores, whereas m.Cherry-hRab27a/b recombinant proteins were used as acceptor fluorophores.

This assay involved incubating the reaction mixture (the donor and the acceptor fluorophores) in a total reaction volume of 100µl at room temperature for 2 hours using a 96-well microplate (ThermoFisherScientific # 611F96; clear, flat bottom, the dimensions of this plate were customised accordingly using the attached software). The same dilution buffer used in the fluorescent GST-pull down assay (section 2.3.1) and 3mM GTP were used in these reactions. In addition, another set of reactions containing the donor and acceptor fluorophores as individual components were incubated using the same conditions and the FRET was calculated as described below. In order to quench the effect of GTP and BSA fluorescence on the FRET signals, another set of reactions was

incubated using the same reaction conditions without using any fluorophore (as described below).

The fluorescence of the wells of the 96-well microplate was then measured using the following settings: 40 flashes per well and the gain was set to 40%, samples were excited at 470-490nm (excitation wave length of the donor fluorophore; GFP-Rab27 effector protein) and the emission of light was measured at 600-610nm (the emission wave length of the acceptor fluorophore; m.Cherry-hRab27a/b). The control software was used to interface with the CLARIOstar microplate reader and the MARS Data Analysis Software was used to acquire the data.

The corrected fluorescence was measured by subtracting the average of the fluorescence of the individual components of the mixture (GFP and m.Cherry recombinant proteins) from the fluorescence of the total mixture. Note that the corrected fluorescence was considered as an indirect read-out of the net FRET. In addition, the fluorescence of the whole 96-well plate was normalised against the fluorescence of BSA and GTP by subtracting the fluorescence of the buffer and GTP mixture from each well; for further details see the following equation:

Corrected fluorescence = [fluorescence of m.Cherry-hRab27b-GFP-effector reaction mixture] – [(fluorescence of m.Cherry-hRab27b) + (fluorescence of GFP-effector)] (2.2)

Accordingly, the EC50 values of GFP-mSlp1-(1-116) and GFP-mSlp2-(3-80) for binding m.Cherry-hRab27a/b were determined and double that concentrations were used in the competition-binding experiments (to saturate the binding with m.Cherry-hRab27). Unlabelled rRab27a and hRab27b were used as typical competitive inhibitors (hRab5a was used as a negative control) to disrupt the binding between m.Cherry-hRab27b and either GFP-mSlp1-(1-116) or GFP-mSlp2-(3-80); i.e. fixed concentrations of both the donor and acceptor fluorophores were used in these competition experiments. This was performed to investigate the specificity and fidelity of this assy. The same reaction conditions of competition experiments were used to test and determine the inhibitory effects of different small molecule and peptide inhibitors of Rab27-effector protein interactions.

2.4 Tissue culture and microscopy techniques

2.4.1 Maintenance of growth of mammalian cell lines

2.4.1.1 Melan-a melanocytes

Murine melan-a melanocytes (Bennett et al., 1987) were maintained at 37ºC with 10% (v/v) CO2 using Roswell park memorial institute (RPMI) 1640 (+L-Glutamine) medium (Sigma), supplemented with 10% (v/v) foetal bovine serum (FBS) (Gibco), 100 units penicillin/ml (Sigma), 172µM streptomycin (Sigma) and 200nM Phorbol-1,2-myristate 1,3-acetate (PMA).

Melan-a melanocytes were grown until become 80-90% confluent, at this stage, the cells were passaged by detaching them using 0.05% trypsin and 0.02% EDTA (Sigma) in 1x PBS (Lonza) at 37ºC with 10% (v/v) CO2 for 2-5 mins. This was followed by gentle agitation of the flask, addition of complete RPMI-1640 medium to quench trypsin and performing multiple pipetting steps to collect the cell suspension (details of volumes used mentioned in Table 2.8). The cell suspension was then transferred to a sterile 25ml Sterilin tube and centrifuged at 1300 g using a Heraeus Biofuge Primo centrifuge (Thermo Scientific) for 5 mins. The cell pellets were re-suspended using 5-10ml complete RPMI-1640 medium. This was followed by splitting the cells into either T25 (Nunc) or T75 (Corning) filter cap flasks using 5ml or 10ml complete RPMI-1640 medium, respectively.

Flask/Plate	1x Trypsin/EDTA	RPMI/ DMEM
T-25 (Nunclon)	1.5ml	2ml
T-75 (Corning)	4ml	5ml
6-well (Nunclon)	1ml	1.5ml
24-well (Nunclon)	0.5ml	1ml
10cm dish (Corning)	4ml	5ml

Table 2.8. Volumes used for passaging melan-a and HEK293A cells.

2.4.1.2 HEK293A cells

Human embryonic kidney (HEK) 293A cells were maintained at 37ºC with 10% (v/v) CO2 using Dulbecco's modified Eagle's medium (DMEM) (+L-Glutamine) (Sigma), supplemented with 10% (v//v) FBS, 100 units penicillin/ml and 172µM streptomycin. HEK293A cells were passaged as described in section 2.4.1.1.

2.4.1.3 Freezing and thawing cell stocks

Melan-a melanocytes and HEK293A cells were (90-100% confluent cells) trypsinised, centrifuged and re-suspended in complete medium (as described in section 2.4.1.1) containing 7.5% dimethyl sulphoxide (DMSO). The cells were then then aliquoted into 1ml stocks using cryovials (Thermo Scientific), stored at -80ºC for 7-14 days using a cryogenic freezing container (Thermo Scientific) filled with isopropyl alcohol (to prevent the formation of ice crystals) and transferred into liquid nitrogen for long-term storage.

To re-grow cell stocks, the cryogenically frozen cell stocks were thawed by placing them in a 37ºC water bath for 2-5 mins (until the cells mixture was completely defrosted). The cells mixture was then transferred to a 25ml Sterilin tube and 5ml complete medium was added. The cells mixture was then centrifuged and the pellet re-suspended in complete medium as described in section 2.4.1.1. This was followed by transferring the cells mixture to a T25 filter cap flask and incubating them at 37ºC in 10% CO2 for 24 hours. The cells were then washed in 1x PBS to remove any dead cells and the cells were grown again using fresh complete medium until becoming 80-90% confluent. After which time the cells were ready to be transfected by either plasmids or viruses.

2.4.2 Generating adenoviruses and transfection of HEK 293A cells using adenoviral vectors

Plasmid DNA (5µg pAd/PL-DEST vector containing gene of interest) was digested using PacI enzyme as described in section 2.1.1.3 [to expose the left and right viral inverted terminal repeats (ITRs) and remove bacterial sequences such as pUC origin and ampicillin resistance gene] and heat inactivated as instructed by the manufacturer. HEK293A cells were trypsinized, counted and plated at 5×10^5 cells per well using a 6-well plate (Corning) in 2ml of complete DMEM medium containing the appropriate concentrations of ampicillin and streptomycin (as described in sections 2.4.1.1 and 2.4.1.2) and left to grow overnight. To perform transfection, OptiMEM (Gibco) medium was used to dilute Fugene 6 (Promega) transfection agent using an Eppendorf tube in the proportion of 4.5µl transfection agent/900µl OptiMEM medium without serum, the mixture was inverted for at least 3 times to ensure homogeneity and incubated at room temperature for 5 mins. This was followed by addition of the

digested plasmid DNA, mixing, inverting the mixture and incubation at room temperature for 15 mins (to allow the formation of the DNA-transfection agent complex). The DMEM medium was then removed from cells by aspiration and replaced with the DNA-transfection agent mixture. This was followed by incubation of cells at 37ºC with 10% CO2 for between 3 and 16 hours. Subsequently, the DNA-transfection agent mixture was removed and replaced with the original growth medium; i.e. DMEM medium containing ampicillin and streptomycin. To ensure complete expression of plasmid DNA, cells were further grown for between 24 and 72 hours. To check the success of the transfection process, the transfected HEK293A cells were then examined using a Zeiss AxioVert S100 inverted fluorescence microscope as described in section 2.4.4; this was performed to ensure that the cells were expressing the indicated fluorescent tag using the appropriate fluorescent channel (GFP or m.Cherry channel). At this point, the cells were mechanically detached from the plastic by multiple pipetting of the medium over them and the cell-medium mixture was transferred to a 10cm sterile dish and made up to10ml with complete DMEM. The cells were grown as described in section 2.4.1.2 and the medium was changed every 2-3 days until plaques formed (after about 10 days). The death of cells was tested visually and microscopically (the cells rounded up and detached from plastic); this was a strong indicator of adenovirus formation and complete infection of HEK293A cells caused by viruses. Subsequently, the cells were mechanically detached as described in section 2.4.1.1 and the cell-medium mixture was transferred to a 15ml Falcon tube. To prepare a crude viral stock, the cell-medium mixture was subjected to several freezing/thawing cycles to lyse the cells and release of adenoviral particles. Briefly, this involved freezing the mixture at -80ºC for 30 mins, followed by incubation at 37ºC (in water bath) for 15 mins; these freezing/thawing cycles were repeated twice. Finally, to pellet cell debris, the cell lysates were centrifuged at 3,000 rpm for 15 mins at room temperature using an Eppendorf 5804 swinging-bucket centrifuge. The supernatant was then harvested under sterile conditions and transferred into Eppendorf tubes and stored at -80ºC.

In order to generate a highest adenoviral titer, amplification of the crude viral stock was performed. To accomplish this, 100-1,000µl of the crude adenoviral

stock was then used to infect an 80% confluent HEK293A cells (3×10^6 cells) using a 10cm sterile dish and 10ml DMEM medium (grown and maintained as described in section 2.4.1.2). Typically, amplification of the original adenoviral stock was detected 2-3 days post- infection and this was confirmed by visual and microscopical detection as described before. The same steps (described before) for lysis of the cells and release of adenoviral particles were repeated. The amplified adenoviral stocks were then titrated by infecting HEK293A cells using different adenoviral concentrations until obtaining 90% protein expression which was detected by visualising HEK293A cells using a Zeiss AxioVert S100 inverted fluorescence microscope as described in section 2.4.4. GFP and m.Cherry protein expression was considered as a read-out for recombinant protein expression. The amplified adenoviral stocks were then used to infect melan-a melanocytes as described in section 2.4.3. Note that GFP and GFP-mSlac2-a-(1-266) adenoviruses were kind gifts from Dr Alistair Hume.

2.4.3 Infection of melan-a melanocytes using adenoviruses

Melan-a melanocytes were plated 12-24 hours prior to infection with adenoviruses using 24-well (Nunc) at 3×10^4cells/well as described in section 2.4.1.1. After which time, the cells were tested microscopically to ensure that $\geq$ 95% of melan-a cells had dispersed melanosome distribution, different concentrations of the amplified adenoviral stock were used to infect melan-a cells and the optimum concentration of the virus was titrated accordingly to ensure that 80-90% of melan-a cells were infected. The cells were then visualised 24-72 hours post-infection using a Zeiss AxioVert S100 inverted fluorescence microscope as described in section 2.4.4.

2.4.4 Live-cell Microscopy

The cells were seeded using the appropriate plate where indicated and visualised using a Zeiss AxioVert S100 inverted fluorescence microscope. AxioVision rel 4.8 software was used to acquire cell images. The fluorescent protein was coloured white; the brightfield and the fluorescent protein images were overlaid using ImageJ software.

2.4.5 The cellular melanosome clustering assay

Cell images were taken as described in section 2.4.4, the cells were manually scored as either clustered or dispersed based on melanosome distribution (Figure 2.3) and counted using ImageJ software. The images of the infected cells (4 images/experiment) had been chosen randomly from three independent experiments. Cells with more than 50% clustered melanosomes around the nucleus were considered as clustered; for further details see (Hume et al., 2001). The percentage of the clustered cells per image was then calculated and data were presented as mean ± standard error of the mean (SEM).

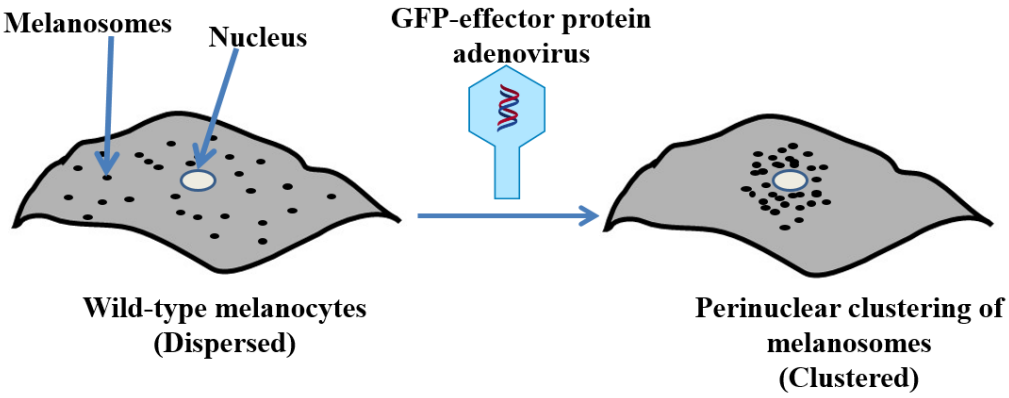


Figure 2.3. A schematic representation of the dispersed and clustered melanocyte phenotypes. Infection of wild-type melanocyte using GFP-effector protein encoding adenovirus causes perinuclear clustering of melanosomes, this is caused by competing with Slac2-a for Rab27a binding, resulting in blocking the trafficking of melanosomes in the cytosol.

2.5 Molecular dynamics simulation of Rab27-Slp2-a effector protein interaction

Molecular dynamics simulation (MDS) of Rab27a-Slp2-a effector protein interaction studies were performed by Mohammed Tumbi under supervision of Dr Charles Laughton (The University of Nottingham, Centre for Biomolecular Sciences). Briefly, the identified crystal structure of the Rab27a-Slp2-a complex interface: Protein Data Bank (PDB) accession code; 3BC1) (Chavas et al., 2008) was used to perform MDS of the Rab27a-Slp2-a complex interaction. As the Slp2-a-(5-56) binding interface was identified, MDS and energy contribution of these residues were calculated as described below.

The crystal structure of the Rab27a-Slp2-a complex was processed using the ambpdb utility of the Amber14 Molecular Dynamics Package. The generated PDB files were then opened with Xleap programme of Amber14 using ff14SB force field. To neutralise the simulation systems and made them isotonic, appropriate number of counter ions was added. These systems were then solvated using a TIP3P water box ensuring that at least 10 Å of the solvent exists around every atom of the protein. Under these conditions, the parameter topology and input coordinates files were generated. The MDS was performed using the PMEMD.cuda_SPFP program in AMBER14 package. The temperature of the systems was controlled using Langevin dynamics; a time step of 2fs was used to heat the systems gradually during the first 50 ps. The solute atoms were subjected to a position restraint; the position restraint was gradually reduced (from 10 to 0 kcal/mol-$Å^2$) at equilibration. The Shake algorithm was then used to constrain the bond lengths. For the non-bonded interactions, a 9 Å cutoff was chosen to be used. Finally, the systems were processed using 20ns MDS (with different initial velocities).

MMPBSA.py script (Miller et al., 2012) in the AmberTools14 package was used to perform the MMGBSA calculations and per residue decomposition analysis. In addition, the custom Python scripts were used to analyse each MDS replicate.

To visualise and perform structural and energetic analyses of the trajectories, PyMOL software (Delano, 2002), VMD (Visual Molecular Dynamics) software (Humphrey et al., 1996) and ptraj utility of Amber14 software were used. For further details of the methods used for performing MDS, see (Garton and Laughton, 2013).

In order to accomplish MDS for larger Slp2 fragment, *homology modelling* was performed using the identified crystal structure of the Rab27b-Slac2-a complex interface (PDB accession code; 2ZET) (Kukimoto-Niino et al., 2008). Therefore, based on sequence alignment between Slac2-a and Slp2-a, the corresponding Slp2-a residues were deposited into the crystal structure of the Rab27b-Slac2-a complex interface. These substituted residues were then added to the previously identified Rab27a-Slp2-a complex interface (to the crystal structure) to generate the crystal structure of the extra Slp2-a residues. Molecular dynamics simulation

for the Rab27a-Slp2-a-(10-78) interaction was then performed as described before.

2.6 Small molecule inhibitors

Two candidate small molecule inhibitors of Rab27-effector protein interaction were tested in this study (hesperidin and BMD-20). Hesperidin (M.W 610.54 g/mol) was bought from ACROS Organics (≠123460050) and BMD-20 (M.W 314 g/mol) was synthesised and analysed chemically by Dr Michael Stocks (The University of Nottingham, Centre for Biomolecular Sciences) (Figure 2.4). To use them, stock solutions of 1,000μM were prepared by dissolving them in DMSO (sigma) and stored at 4ºC (maximum one week; as hesperidin is hygroscopic) to be used later.

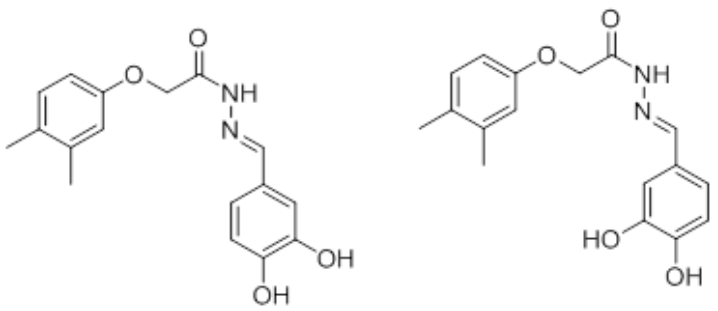


Figure 2.4. BMD-20 chemical structure. BMD-20 exists as 2 isomers in a 1:1 ratio; chemical formula: C17H18N2O4; molecular weight: 314.34; the HPLC purity was >98% pure and mass spectrum was m/z 315.1 (M+H)+.

2.7 Sequence alignments

CLC Sequence Viewer 7.7.1 was used to generate protein amino acid sequence alignments. In addition, the blastx tool in the NCBI site (https://blast.ncbi.nlm.nih.gov/Blast.cgi?PROGRAM=blastx&PAGE_TYPE=BlastSearch&LINK_LOC=blasthome) was used to translate nucleotide sequences into the corresponding protein amino acid sequences to be compared with protein databases.

2.8 Statistical analysis

Statistical data analysis was performed using Microsoft excel-2013 and GraphPad Prism-7. Unpaired t-test and both one and two-way analysis of

variance (ANOVA) were used to test significant differences where indicated. The non-linear regression was used to generate dose-response sigmoid curves and pEC50 (-logEC50) values were calculated accordingly. pIC50 (-log IC50) values were calculated by setting the bottom and top constraints to constant values of 0.0 and 100.0, respectively unless otherwise indicated; this was performed to accurately compare the pIC50 values. Statistical differences were determined as follows: $^{ns}P>0.05$ was considered as non-significant, $*P \leq 0.05$, $**P \leq 0.01$, $***P \leq 0.001$ and $****P \leq 0.0001$.

Chapter 3

Development of the fluorescent GST-pull down assay as an in vitro measure of the binding affinity of Rab27 to its effectors

3.1 Introduction

The current literature suggests that Rab27a/b proteins control cancer cell invasion and proliferation in different tumours (Hannafon et al., 2015; Harris et al., 2015; Huang and Feng, 2016; Miller and Grunewald, 2015; Ostenfeld et al., 2014) (as described in section 1.6). Rab27a/b small GTPases play an essential role in the regulation of exocytosis of various secretory vesicles or granules in the cell by interacting with their cognate effectors, preferentially in their GTP-bound state, thereby exerting their specific functions (Hume et al., 2002; Izumi et al., 2003; Ostermeier and Brunger, 1999; Stenmark, 2009). Accordingly, the interaction of Rab27a/b with their effectors might play a considerable role in cancer cell progression and metastasis and by inhibition of those interactions, the subsequent signalling pathways that might regulate cancer cell invasion and proliferation can be blocked. For these reasons, the focus of this project was to identify candidate inhibitors of Rab27-effector interactions in order to block the cancer regulating intracellular signalling pathways.

Although, a lot of research and efforts have been performed in this area, the identification of Rab27 inhibitors is still an early and promising approach for the treatment of cancer. Therefore, there is a necessity to develop and design in vitro and cellular assays to determine the Rab27-effector interactions which can be used further for testing the effects of the candidate inhibitors of these interactions. For instance, one of the early approaches to test the effects of the candidate Rab27 inhibitors was based on the use of the already established cellular melanosome clustering assay (Joung et al., 2014) (see section 6.3.4). In another study, the identification of Rab27-effector interaction inhibitors was based on developing a time resolved FRET assay (Johnson et al., 2016). Furthermore, the early studies to determine the binding of different Rab27 effectors were based on using the co-immunoprecipitation assays and simple GST-pull down techniques (Fukuda, 2006). The problem with these techniques is that the accuracy depends on the specificity of the used antibodies and some of the bound proteins are lost during multiple experimental steps. In addition, these techniques require performing SDS-PAGE electrophoresis and western blot analysis of protein complexes. Therefore, these techniques might be considered as effective qualitative rather than accurate quantitative measures of

the protein-protein interactions. This provokes the identification and development of an assay that can be used in determining Rab27-effector interactions, both quantitatively and qualitatively, which can be utilised further in testing the effects of the candidate inhibitors of those interactions.

As mentioned previously, there are 11 Rab27 effectors in human and mouse (Fukuda, 2005; Fukuda, 2013). Two of Rab27 effectors (Slp1 and Slp2) were chosen to be produced and tested in terms of binding to Rab27 as the 3D structure of the interface of interaction between Slp2 and Rab27a has been identified (Chavas et al., 2008) and both Slp1/Slp2-a effectors are structurally related (Fukuda and Mikoshiba, 2001).

To this end, a fluorescent GST-pull down assay was established and developed to be used as an in vitro measure of the Rab27-effector interactions (by determining the EC50 of binding). In addition, it can be used for testing the effects of the candidate inhibitors of these interactions (by measuring the IC50 of the candidate inhibitors).

The early attempts to produce a red fluorescent protein was performed in 1999 using the drFP583 protein (also called DsRED) from Discosoma, giving orange-red fluorescence (Matz et al., 1999). Then more mature variants of the DsRED with less green emission and brighter red fluorescence were produced; such as DsRed.T1, DsRed.T3 and DsRed.T4 (Bevis and Glick, 2002). Furthermore, a monomeric red fluorescent protein 1 (mRFP1) was generated using the DsRed protein; mRFP1 maturation is faster than DsRed, but the photo-stability is lower (Campbell et al., 2002). These continuous efforts based on performing mutagenesis and substitutions on mRFP1 succeeded in producing a monomeric fluorescent protein named m.Cherry; m.Cherry has faster maturation than mRFP1 with ten folds phot-stability higher than mRFP1 (Shaner et al., 2004). Therefore, hRab27b was produced as m.Cherry recombinant protein and used as a fluorescent protein in the fluorescent GST-pull down assay experiments. In addition, mSlp1 and mSlp2 were produced as GST-recombinant proteins. In these experiments, the binding affinity of hRab27b to mSlp1 and mSlp2 was determined as described in the subsequent sections (for further details of the

advantages of the fluorescent GST-pull down assay over the co-immunoprecipitation assays see Figure 3.1).

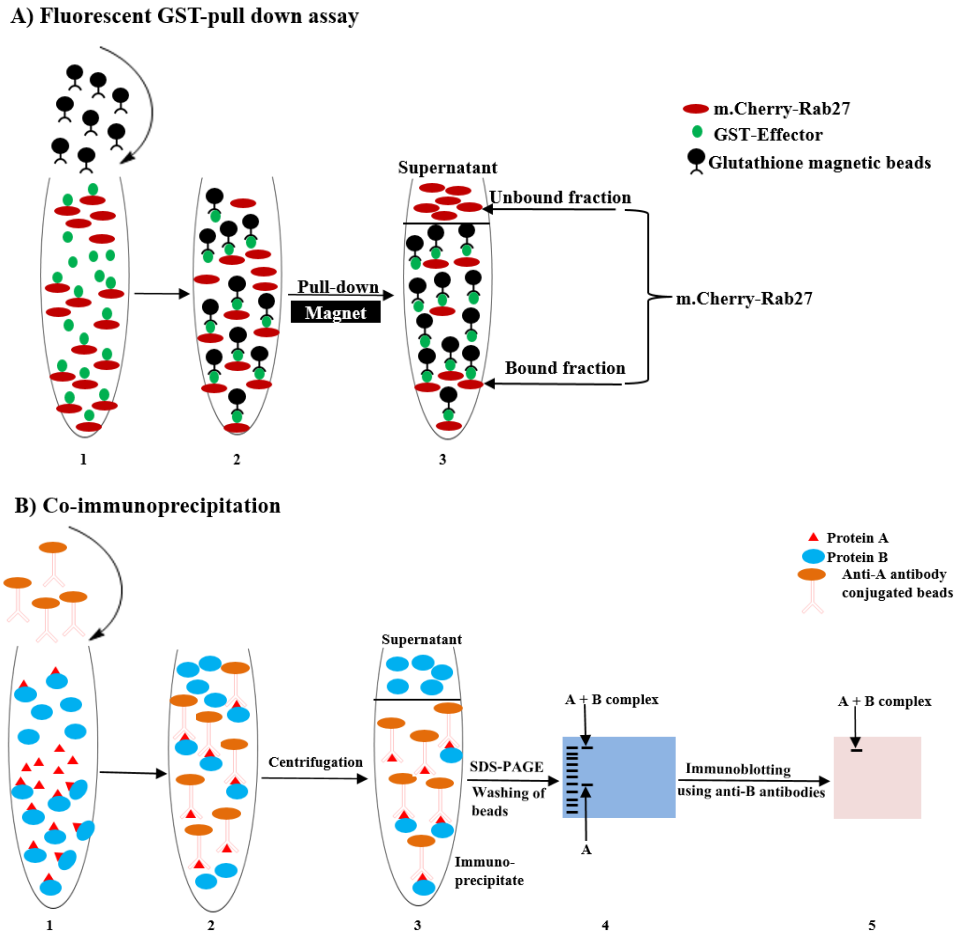


Figure 3.1. Comparison of the fluorescent GST-pull down and co-immunoprecipitation assays. A) A schematic representation of the fluorescent GST-pull down assay. Upon binding of Rab27 and its effector protein, a complex will be formed consisting of GST-effector-m.Cherry-Rab27. Glutathione magnetic beads then bind to this complex by interacting with GST, leading to pull-down of the bound fraction of m.Cherry-Rab27 (using a magnet). By measuring the fluorescence of the supernatant, the bound fraction can be calculated indirectly. B) A schematic representation of the co-immunoprecipitation assay. Upon interaction of the binding partners (A and B proteins), a complex will be formed. Anti-A antibody conjugated beads are then added to the reaction mixture and by centrifugation, the A-B proteins complex can be pulled down. Multiple washing steps of the beads are then performed to remove the unbound fraction of protein B. This is followed by SDS-PAGE gel electrophoresis and immunoblotting (using anti-B antibodies) to quantify the A-B proteins complex.

3.2 Aims

The premier aims of these experiments were to establish an in vitro assay for determining the Rab27-effector protein interactions which can be used further for testing the effects of the candidate inhibitors of these interactions in future studies. Accordingly, the conditions of the fluorescent GST-pull down experiments were optimised and the specificity of this assay was investigated.

3.3 Results

3.3.1 Generation of 6x Histidine-m.Cherry-hRab27b recombinant proteins

A preliminary study was performed by Dr Alistair Hume and Deborah Briggs to test Rab27a binding to Slp1 using m.Cherry-hRab27a recombinant protein (data not shown). Based on this, a fluorescent hRab27b protein was produced by fusing hRab27b to the C-terminus of m.Cherry to be used later for determining the binding affinity of hRab27b to mSlp1 and mSlp2 effector proteins using the fluorescent GST-pull down assay.

In these in vitro binding affinity experiments, Rab27b was used in the majority of experiments and in the cellular melanosome clustering assay (see chapter 5 and 6) the functional effects of different Rab27 effectors fragments and candidate inhibitors on Rab27a-Slac2-a interaction-dependent melanosome transport were tested. Therefore, the effects of the candidate inhibitors against Rab27a-dependent functions and Rab27b-effector interactions can be tested so that high-affinity and robust inhibitors for these interactions can be identified.

To produce 6x Histidine-m.Cherry-hRab27b recombinant protein, the concentration of IPTG to induce protein expression in Rosetta *E. coli* competent cells was optimised. Therefore, a small scale protein production was induced with different IPTG concentrations (0.5, 2.0 and 10.0 mM) using the pETDuet-1-m.Cherry-hRab27b-(1-218; T23N) vector (see section 2.1.3.1) for 3 hours at 37ºC as described in section 2.2.2. Analysis of lysates from the uninduced and induced bacterial cell cultures using instant blue stained 10% SDS-PAGE gel demonstrated that abundant protein bands were produced at the expected molecular weight (55.3KDa) for the 6x Histidine-m.Cherry-hRab27b (1-218; T23N) recombinant protein in the IPTG induced bacterial cultures using all the tested concentrations, whereas this band was absent from the uninduced bacterial cell lysates (Figure 3.2), indicating that induction of protein production using 0.5mM IPTG for 3 hours at 37ºC was successful and sufficient to produce abundant amount of protein. Accordingly, induction of protein production was performed using 0.5mM IPTG for 3 hours at 37ºC in the subsequent experiments. Notably, Rab27 protein co-localises with fusion vesicles, (Chen et al., 1997; Chen et al., 2003), this makes its subcellular distribution in the

cytoplasm mostly, thus the production and purification of this protein is easier than the plasma membrane associated proteins.

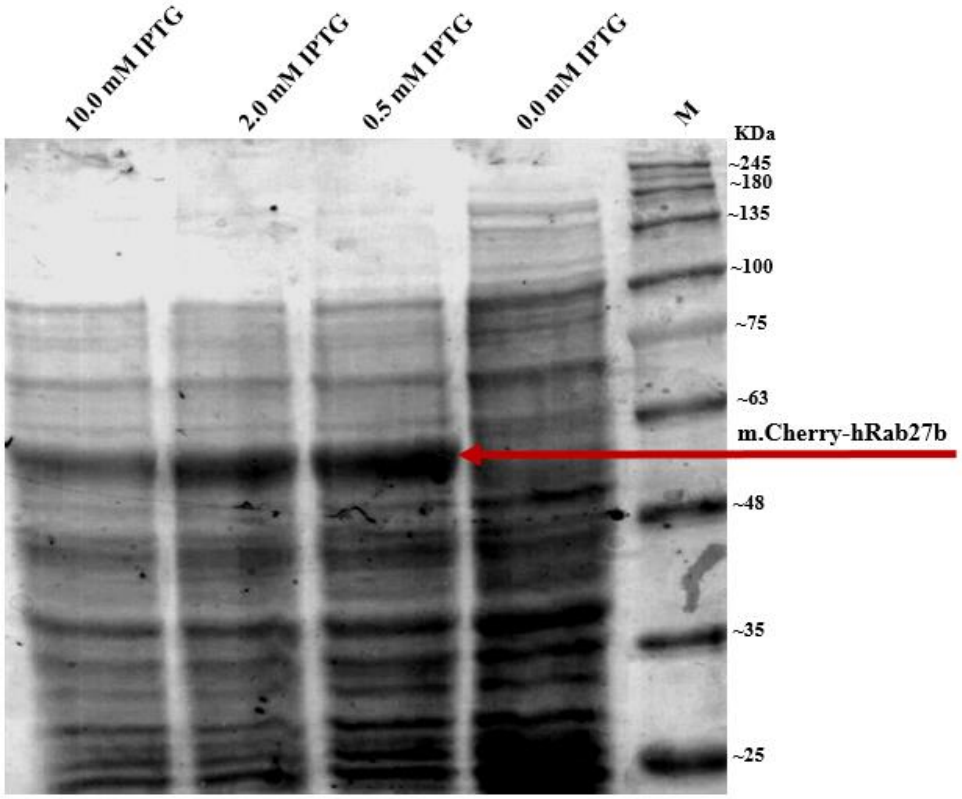


Figure 3.2. Small scale induction of the 6x Histidine-m.Cherry-hRab27b (1-218; T23N) recombinant protein production. Rosetta *E. coli* competent cells were transformed with the pETDuet-1-m.Cherry-hRab27b-(T23N) vector and small scale protein production was induced with different IPTG concentrations (0.0, 0.5, 2.0 and 10.0mM) for 3 hours at 37ºC. Bacterial cultures were pelleted and the cell lysate extracts were then analysed using instant blue stained 10% SDS-PAGE gel. Abundant protein bands (the arrow indicated bands) were produced at the expected molecular weight (55.208KDa) for the 6x Histidine-m.Cherry-hRab27b-(1-218; T23N) recombinant protein in the IPTG induced bacterial cultures using all the tested IPTG concentrations (M; molecular weight standards).

To produce 6x Histidine-m.Cherry-hRab27b (1-218; T23N) GDP-bound form (Menasche et al., 2003a), 6x Histidine-m.Cherry-hRab27b (1-218) and 6x Histidine-m.Cherry-hRab27b (1-218; Q78L) GTPase deficient form (Menasche et al., 2003a) recombinant proteins, the pETDuet-1-m.Cherry-hRab27b-(1-218; T23N), pETDuet-1-m.Cherry-hRab27b-(1-218) and pETDuet-1-m.Cherry-hRab27b-(1-218; Q78L) vectors were transformed into Rosetta *E. coli*

competent cells and protein production was induced with 0.5mM IPTG as described in section 2.2.2, this was followed by performing protein purification using the IMAC system as described in section 2.2.3.1. The purified protein, uninduced and induced cell lysates and protein samples from various protein purification steps were then analysed using instant blue stained 10% SDS-PAGE gel (see Figure 3.3 as an example). An abundant protein band was detected at the expected molecular weight of 55.3KDa.

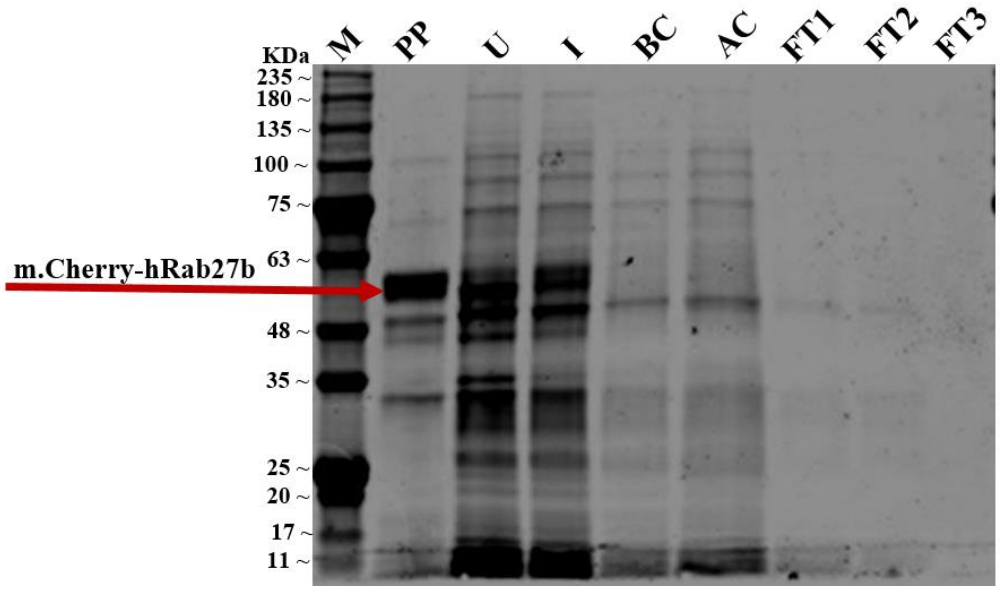


Figure 3.3. Production and purification profile of the 6x Histidine-m.Cherry-hRab27b-(1-218; T23N) recombinant protein. Rosetta *E. coli* competent cells were transformed with the pETDuet-1-m.Cherry-hRab27b-(1-218; T23N) vector and protein production was induced using 0.5mM IPTG for 3 hours at 37ºC. An instant blue stained 10% SDS-PAGE gel showing the analysis of the protein production and purification steps: M; molecular weight standards, PP; purified protein, U, I; uninduced and induced *E. coli* cell extracts, BC; cell lysates before centrifugation, AC; supernatant after centrifugation, FT1, 2, 3; 1st, 2nd and 3rd flow-through from nickel column after several washes with the dialysis buffer. An abundant protein band (the arrow indicated band) was detected at the predicted molecular weight for the 6x Histidine-m.Cherry-hRab27b-(1-218; T23N) recombinant protein (55.3KDa).

To further assess the produced proteins, a western blot analysis using anti-m.Cherry primary antibodies (Figure 3.4) was performed to determine whether the abundant protein bands detected previously using the SDS-PAGE gel electrophoresis were m.Cherry-tagged or not. This demonstrated that two abundant m.Cherry-tagged protein bands were produced, and the upper bands were detected at the predicted molecular weights for the transferred proteins (55.3KDa), indicating that protein induction was successful.

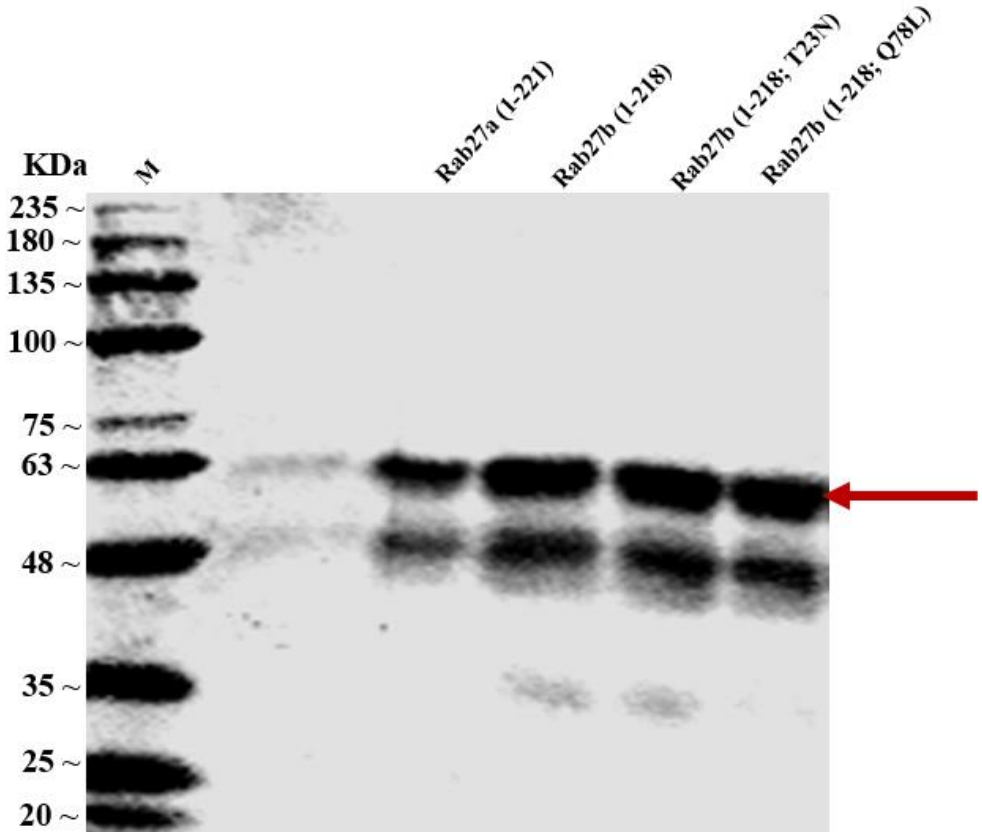


Figure 3.4. Western blot analysis of different 6x Histidine-m.Cherry-hRab27b recombinant proteins. The 6x Histidine-m.Cherry-hRab27b- [(1-218), (1-218; T23N), (1-218; Q78L)] and 6x Histidine-m.Cherry-hRab27a-(1-221) (as a positive control; obtained generously from Dr Alistair Hume) recombinant proteins were loaded into 10% SDS-PAGE gel, transferred into PVDF membrane (0.45µm) and immunoblotted with anti-m.Cherry antibody. All the analysed proteins expressed two bands (m.Cherry fused proteins). However, abundant protein bands (the arrow indicated bands) were detected at the predicted molecular weights for the transferred proteins (55.3KDa) (M; molecular weight standards).

Therefore, a proteomic analysis (see section 2.2.8) using mass spectrometry was performed by analysing these two bands (the upper and lower bands for the 6x Histidine-m.Cherry-hRab27b-1-218). This was performed to determine whether the purified protein was N- or C- terminal truncated hRab27b protein. The proteomic analysis (Appendix: Figure 8.9) revealed that the lower band is a C-terminal truncated hRab27b protein (1-200). Accordingly, in order to obtain a more homogenous preparation of protein, a C-terminal truncated 6x Histidine-m.Cherry-hRab27b (1-200) recombinant protein was produced and purified as described in sections 2.2.2 and 2.2.3.1. Analysis of this protein using 10% SDS-PAGE gel (data not shown) demonstrated that two abundant protein bands of different molecular weights were again produced and the C-terminal truncated protein production strategy was not efficient to produce a more homogenous preparation of protein, thus a full length hRab27b protein was used in the subsequent experiments. In addition, for this reason and to resemble the normal physiological conditions, the wild-type m.Cherry-hRab27b-(1-218) recombinant protein was only used in the subsequent binding affinity experiments of this study.

3.3.2 Generation of 6x Histidine-Rab recombinant proteins

In order to disrupt the interaction between hRab27b protein and their effectors, unlabelled Rab27a/b and Rab5 proteins were produced and purified. Those proteins were used later to assess the specificity of the developed binding assay (as described in the subsequent sections).

3.3.2.1 Protein production and purification of 6x Histidine-Rab recombinant proteins

To produce 6x Histidine-rRab27a, 6x Histidine-hRab27b and 6x Histidine-hRab5 recombinant proteins, pET-14b-rRab27a, pET-15b-hRab27b, and pET-14b-hRab5a vectors were transformed into Rosetta *E. coli* competent cells and protein production was induced with 0.5mM IPTG as described in section 2.2.2, followed by performing protein purification steps using the IMAC system as described in section 2.2.3.1.

Analysis of these proteins using 10% SDS-PAGE gel demonstrated that abundant protein bands were produced at the expected molecular weights of

28.85KDa, 28.38KDa and 27.20KDa for the 6x Histidine-rRab27a-(1-221) (see Figure 3.5), 6x Histidine-hRab27b-(1-218) (data not shown) and the 6x Histidine-hRab5a-(1-216) (data not shown) recombinant proteins, respectively. Furthermore, a western blot analysis using anti-histidine antibodies confirmed that those proteins were induced successfully at the expected molecular weights (Figure 3.6).

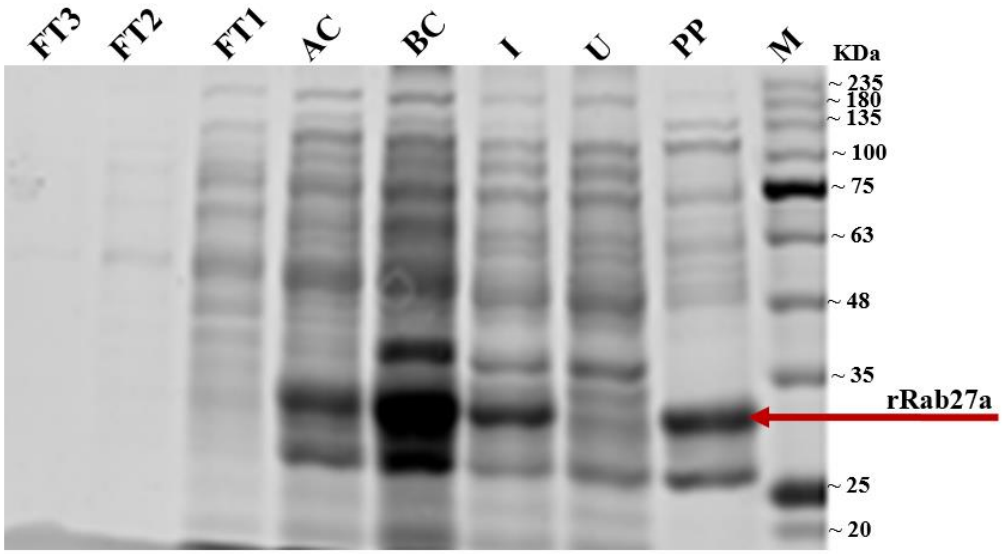


Figure 3.5. Production and purification profile of the 6x Histidine-rRab27a-(1-221) recombinant protein. Rosetta *E. coli* competent cells were transformed with the pET-14b-rRab27a-(1-221) vector and protein production was induced using 0.5mM IPTG for 3 hours at 37ºC. Protein production and purification steps were analysed using an instant blue stained 10% SDS-PAGE gel: M; molecular weight standards, PP; purified protein, U, I; uninduced and induced *E. coli* cell extracts, BC; cell lysates before centrifugation, AC; supernatant after centrifugation, FT1, 2, 3; 1st, 2nd and 3rd flow-through from nickel column after several washes with the dialysis buffer. An abundant protein band (the arrow indicated band) was detected at the predicted molecular weight for the 6x Histidine-rRab27a (1-221) recombinant protein (28.85KDa).

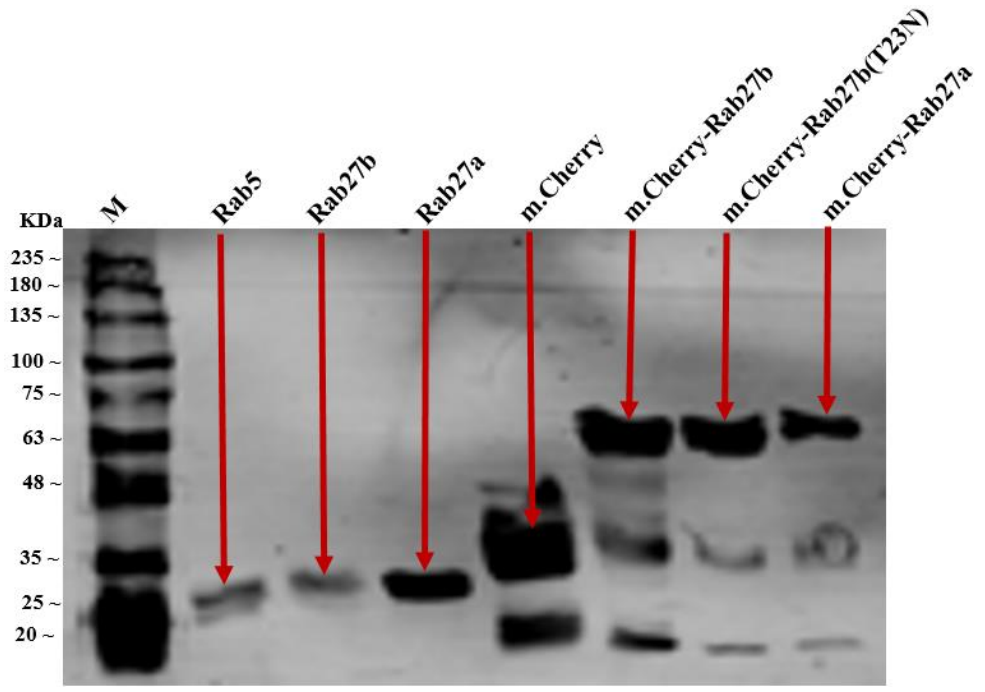


Figure 3.6. Western blot analysis profile of different 6x Histidine-Rab recombinant proteins. 6x Histidine-hRab5a (27.20KDa), 6x Histidine-hRab27b (28.38KDa), 6x Histidine-rRab27a (28.85KDa), 6x Histidine-m.Cherry (obtained generously from Dr Alistair Hume) (30.86KDa), 6x Histidine-m.Cherry-hRab27b (55.3KDa), 6x Histidine-m.Cherry-hRab27b-(T23N) (55.3KDa) and 6x Histidine-m.Cherry-hRab27a (55.3KDa) recombinant proteins were loaded into 10% SDS-PAGE gel, transferred into PVDF membrane (0.45µm) and immunoblotted with monoclonal anti-poly-Histidine antibody. Abundant protein bands (the arrow indicated bands) were detected at the predicted molecular weights for the transferred proteins (M; molecular weight standards).

3.3.3 Generation of GST-mSlp1 and GST-mSlp2 recombinant proteins

In order to test the binding affinity of Rab27 to different effector proteins, GST-mSlp1/mSlp2 recombinant proteins were produced to be used later in the fluorescent GST-pull down assay experiments.

To produce GST, GST-mSlp1-(1-201) and GST-mSlp2-(3-80) proteins, The pGEX-4T1, pGEX-4T1-mSlp1-(1-201) and pGEX-4T1-mSlp2-(3-80) vectors (section 2.1.3.3) were transformed into Rosetta *E. coli* competent cells and protein production was induced with 0.5mM IPTG as described in section 2.2.2, this was followed by performing protein purification steps using an affinity interaction with reduced glutathione (GSH)-sepharose beads as described in section 2.2.3.2).

Analysis of the purification profile of GST (27.5KDa) (see Figure 3.7), GST-mSlp1-(1-201) (50.77KDa) (data not shown) and GST-mSlp2-(3-80) (38.1KDa) (data not shown) proteins using 10% SDS-PAGE gel demonstrated that abundant protein bands were detected at the predicted molecular weights for these proteins.

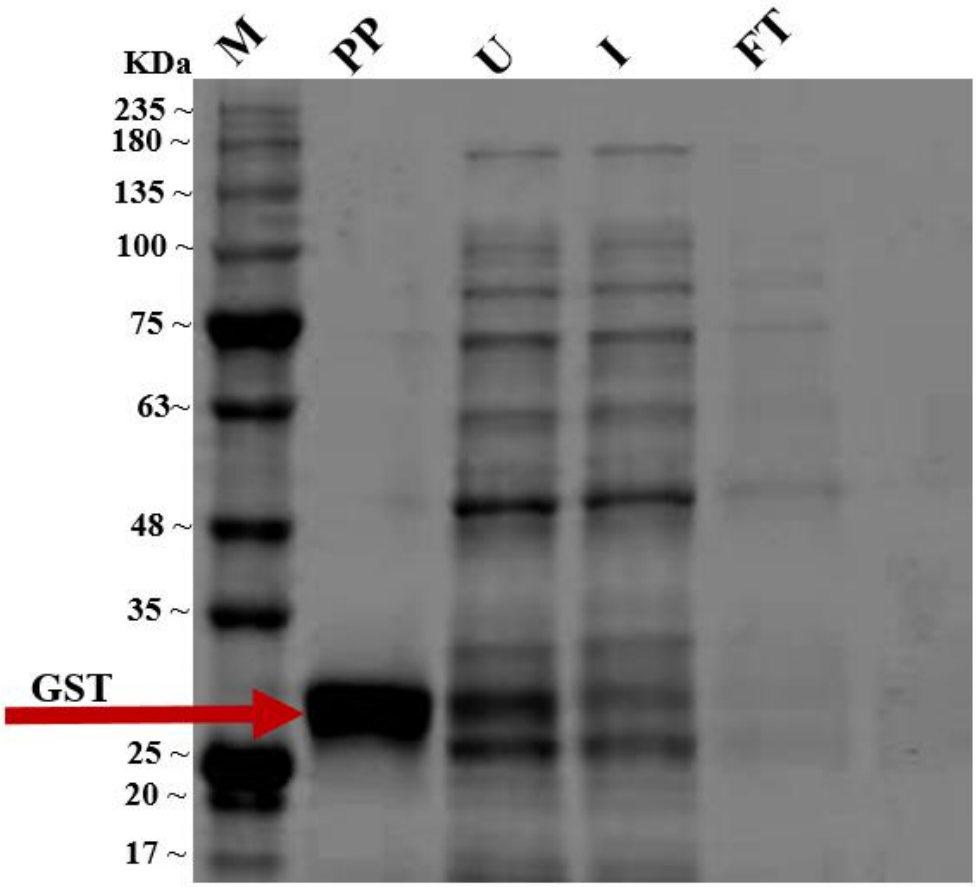


Figure 3.7. Production and purification profile of the GST protein. Rosetta *E. coli* competent cells were transformed with the pGEX-4T1 vector protein production was induced using 0.5mM IPTG for 3 hours at 37ºC. Protein production and purification steps were analysed using an instant blue stained 10% SDS-PAGE gel: M; molecular weight standards, PP; purified protein, U, I; uninduced and induced *E. coli* cell extracts, FT; flow-through from GSH column after several washes with the dialysis buffer. An abundant protein band (the arrow indicated band) was detected at the predicted molecular weight for the GST protein (27.5KDa).

3.3.4 Optimising the conditions of the fluorescent GST-pull down assay experiments

In order to determine the binding affinity of Rab27 protein to different Rab27 effectors, a fluorescence-based GST-pull down assay was established and optimised. In this assay, different concentrations of m.Cherry-hRab27b were used to saturate the binding with fixed concentrations of either GST-mSlp1-(1-201) or GST-mSlp2-(3-80) effectors (for further details of the principle of this assay see Figure 3.1). As described previously (see section 3.1), glutathione magnetic beads were used to bind the GST-effector-m.Cherry-hRab27b complex by interacting with GST, and the corrected fluorescence was calculated as described in section 2.3.1 by normalising the data using GST-included reactions (instead of GST-effector). The optimisation approaches of this assay will be discussed in detail thereafter.

3.3.4.1 Determining the optimum concentration of GTP, glutathione magnetic beads and incubation time

As the main aim of this assay was to determine the Rab27b binding affinity to mSlp1 and mSlp2 effectors, a constant concentration (0.5μM) of either GST-mSlp1-(1-201) or GST-mSlp2-(3-80) recombinant proteins was used in the subsequent Rab27b binding affinity experiments.

To optimise the conditions of the fluorescent GST-pull down assay, different reaction conditions were used to determine the binding between 4.5μM m.Cherry-hRab27b (this concentration was used in order to saturate the interaction with GST-mSlp1 as much as possible) and 0.5μM GST-mSlp1 (1-201). Thus, different incubation times (1, 2 and 4 hour) and GTP concentrations (0, 1, 2 and 3 mM) were tested using different concentrations of glutathione magnetic beads (5%, 10% and 15%). The findings of these experiments suggested that 1 or 2 hour incubation time at room temperature was enough to obtain maximum binding as the interactions using these incubation times were not significantly different from that of 4 hour incubation (data not shown). In addition, using of 3mM GTP was optimum to obtain higher binding fractions than using of 1mM or 2mM GTP (see Figure 3.8).

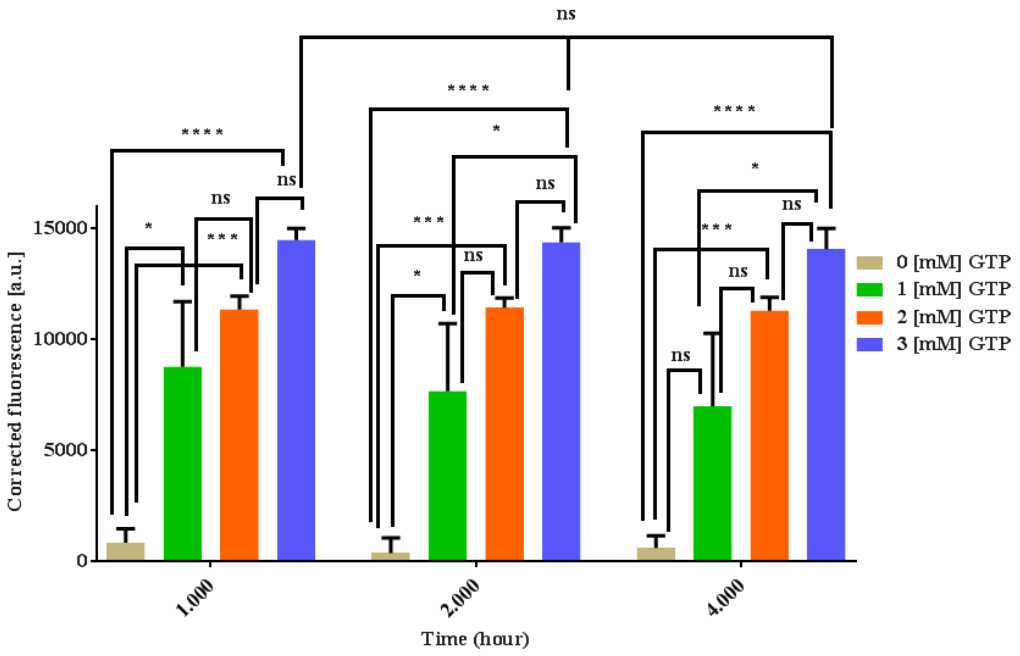


Figure 3.8. Effect of incubation time and GTP concentration on the binding between m.Cherry-hRab27b and GST-mSlp1-(1-201). Different incubation times (1, 2 and 4 hour) and GTP concentrations (0, 1, 2 and 3mM) using 10% glutathione magnetic beads concentration were used to test the binding of 4.5µM m.Cherry-hRab27b for 0.5µM GST-mSlp1-(1-20. Data points represent mean ± SEM of 3 independent experiments performed in quadruplicates. Two-way ANOVA: $^{ns}P > 0.05$; *$P \leq 0.05$; **$P \leq 0.01$; ***$P \leq 0.001$;****$P \leq 0.0001$.

Although the effect of using of 10% glutathione magnetic beads was not statistically different from that of using 5% and 15 % glutathione magnetic beads, higher binding was obtained using this concentration, indicating that 10% glutathione magnetic beads was enough to obtain optimum binding results (see Figure 3.9). Altogether, the findings of these experiments indicated that consistent and reliable binding affinity results can be obtained by using 3mM GTP, 10% glutathione magnetic beads and 2 hours incubation.

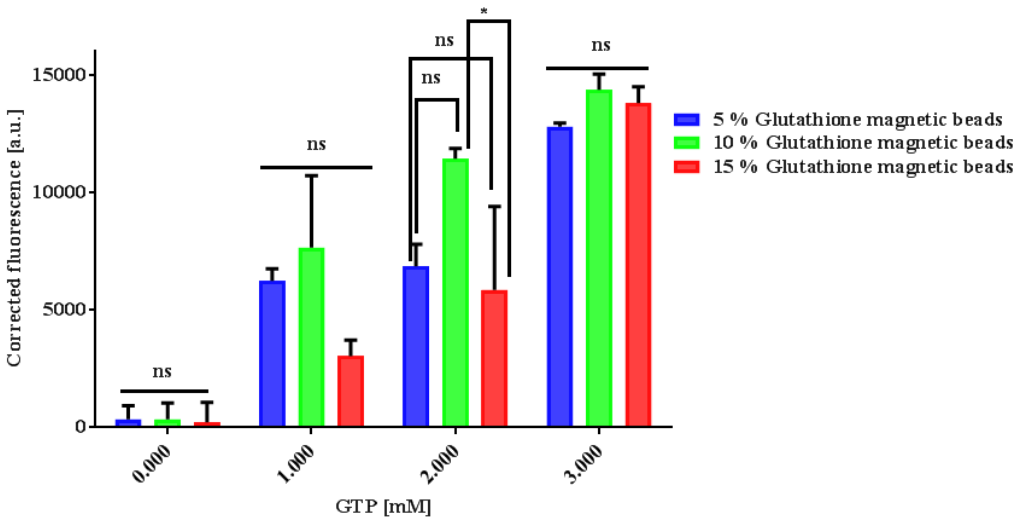


Figure 3.9. Effect of GTP and glutathione magnetic beads concentration on the binding between m.Cherry-hRab27b and GST-mSlp1-(1-201). Different GTP concentrations (0, 1, 2, and 3mM) and glutathione magnetic beads concentrations (5%, 10% and 15%) after 2 hours incubation were used to test the binding of 4.5µM m.Cherry-hRab27b for 0.5µM GST-mSlp1-(1-201) at room temperature. Data points represent mean ± SEM of 3 independent experiments performed in quadruplicates. Two- way ANOVA: $^{ns}P > 0.05$; *P ≤ 0.05; **P ≤ 0.01.

To further investigate these findings, different GTP concentrations (3, 6 and 9 mM) were tested using10% glutathione magnetic beads and 2 hours incubation. All the tested GTP concentrations were not statistically different (Figure 3.10). Consequently, 3mM GTP, 10% glutathione magnetic beads and 2 hours incubation time at room temperature (reaction conditions) were used in the subsequent Rab27b-effector binding affinity experiments. Typically, GTP concentration in human cells is 0.305mM (Traut, 1994). In addition, in GST-pull down experiments performed by other group, 0.5mM GTPγS was used to prepare GTP-loaded Rab27a (Kuroda et al., 2002b), indicating that 3mM GTP was enough to saturate Rab27-GTP binding site.

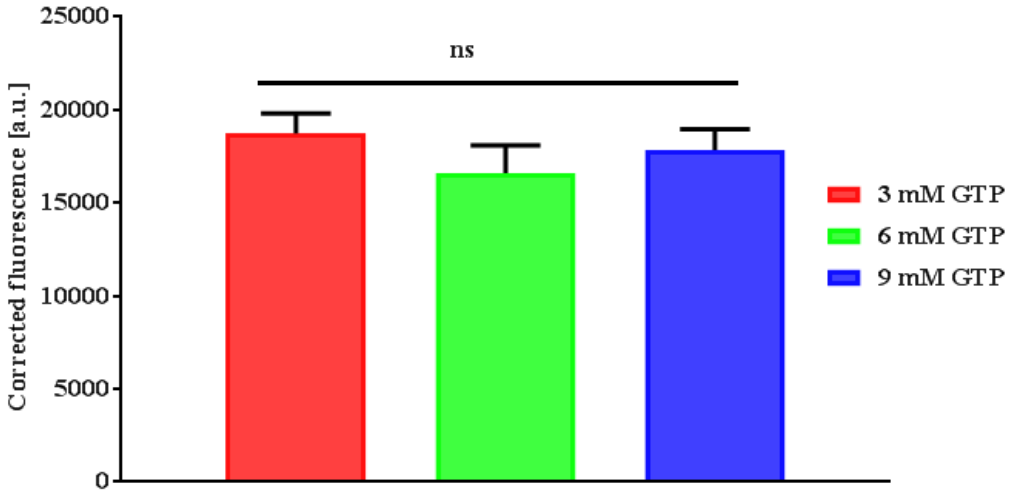


Figure 3.10. Effect of using different GTP concentrations on the binding between m.Cherry-hRab27b and GST-mSlp1-(1-201). The binding between 4.5µM m.Cherry-hRab27b and 0.5µM GST-mSlp1-(1-201) was tested using different GTP concentrations (3, 6 and 9mM), 10% glutathione magnetic beads and 2 hours incubation. Data points represent mean ± SEM of 3 independent experiments performed in quadruplicates. One-way ANOVA: $^{ns}P > 0.05$.

3.3.4.2 Comparing the binding of full length and C-terminal truncated hRab27b protein

To further optimise the conditions of the fluorescent GST-pull down assay, the binding of the full length (1-218) and C-terminal truncated (1-200) hRab27b to mSlp1 effector protein was tested. The results of these experiments (Figure 3.11) demonstrated that the binding of the full length Rab27b to mSlp1 was slightly higher that of the C-terminal truncated hRab27b and they were significantly different. Consequently, the full length hRab27b-(1-218) was used in the subsequent binding affinity experiments.

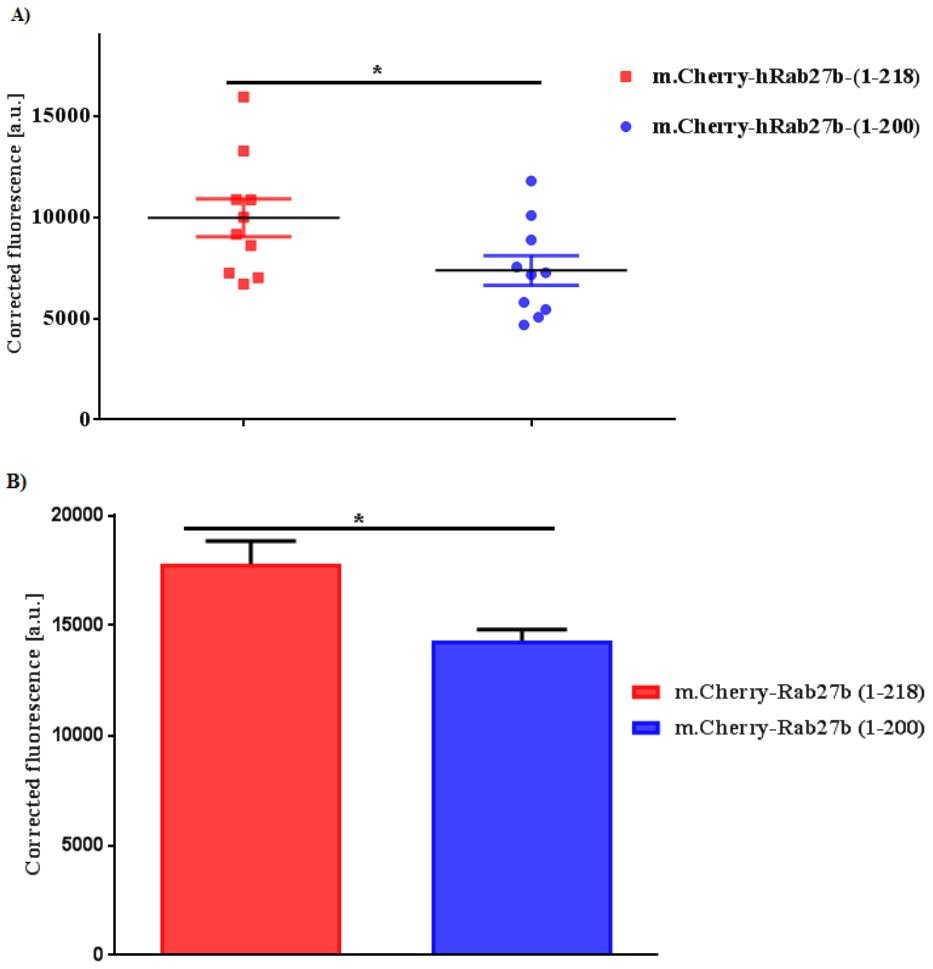


Figure 3.11. Comparison of the binding of the full length and C-terminal truncated hRab27b to mSlp1 effector protein (1-201). A) The binding between 1µM m.Cherry-hRab27b (full length, 1-218; C-terminal truncated, 1-200) and 0.5µM GST-mSlp1-(1-201) was tested. Data points represent mean ± SEM (n=10). B) The binding between 4.5µM m.Cherry-hRab27b (full length, 1-218; C-terminal truncated, 1-200) and 0.5µM GST-mSlp1-(1-201) was tested. Data points represent mean ± SEM of 3 independent experiments performed in quadruplicates. Unpaired t-test: *P ≤ 0.05.

3.3.5 Determination of Rab27b binding affinity to mSlp1 and mSlp2 effector proteins using the fluorescent GST-pull down assay

To determine the binding affinity of hRab27b to mSlp1 and mSlp2 effectors, different concentrations of m.Cherry-hRab27b (0.0, 0.05, 0.15, 0.5, 1.5, 4.5 and 6.0 µM) were incubated with 0.5µM of either GST-mSlp1-(1-201) or GST-mSlp2-(3-80). These experiments demonstrated that m.Cherry-hRab27b pEC50 value to bind GST-mSlp2-(3-80) (6.38M) was slightly higher than that for interaction with GST-mSlp1-(1-201) (6.16M), suggesting that hRab27b binding

affinity to mSlp2 was slightly higher than that to mSlp1 (Figure 3.12). These findings were investigated further using the FRET-based protein-protein interaction assay in chapter 4 (see section 4.3.3.2).

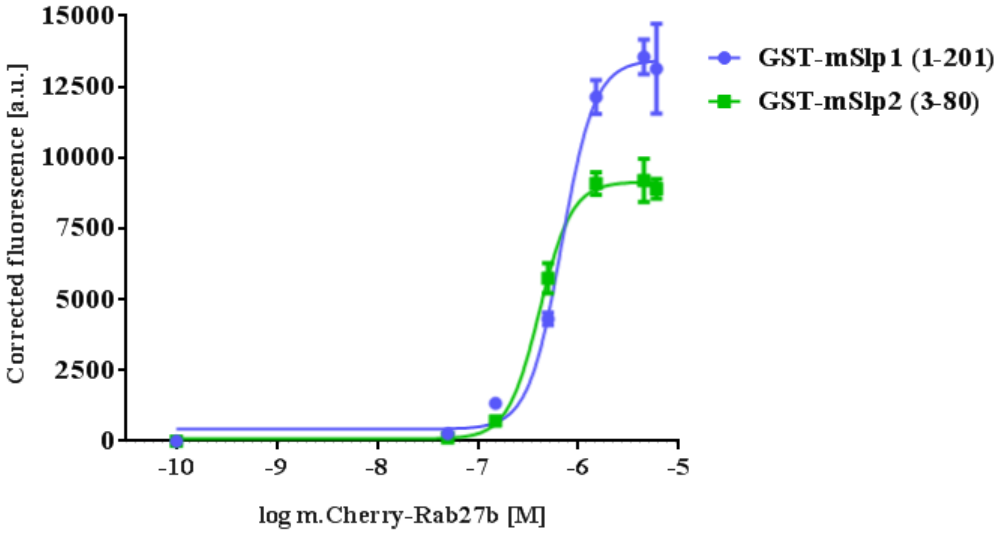


Figure 3.12. The binding affinity profile of hRab27b to mSlp1 and mSlp2 effector proteins. Different concentrations (0.0, 0.05, 0.15, 0.5, 1.5, 4.5 and 6.0 µM) of m.Cherry-hRab27b were used to determine the binding affinity to 0.5µM GST-mSlp1-(1-201) and 0.5µM GST-mSlp2-(3-80) using the fluorescent GST-pull down assay. The pEC50 values of m.Cherry-hRab27b to bind GST-mSlp1-(1-201) and GST-mSlp2-(3-80) were 6.16M and 6.38M, respectively. Data points represent mean ± SEM of 3 independent experiments performed in quadruplicates.

3.3.6 Disruption of Rab27b-effector protein binding using unlabelled Rab27a/b

In order to determine the specificity of the fluorescent GST-pull down assay, different unlabelled (non-fluorescent, His-tagged) Rab proteins were produced and used as competitive inhibitors. To this end, unlabelled Rab27a/b were used as typical competitive inhibitors for Rab27-effector protein interactions and Rab5 was used as a negative control. In addition, sequence alignment of Rab27a/b proteins (Figure 3.13) demonstrated that these proteins share high amino acid sequence similarity, especially at the N-terminus which is essential for Rab27a/b interaction with their effectors (Kukimoto-Niino et al., 2008). Since the N-terminal Rab27-effector interacting residues are conserved between Rab27a and Rab27b, it was supposed that they might exhibit the same binding

affinity to their effectors and can be used interchangeably when testing the binding affinity of different Rab27 effectors, therefore they used as typical competitive inhibitors to investigate the specificity of this assay.

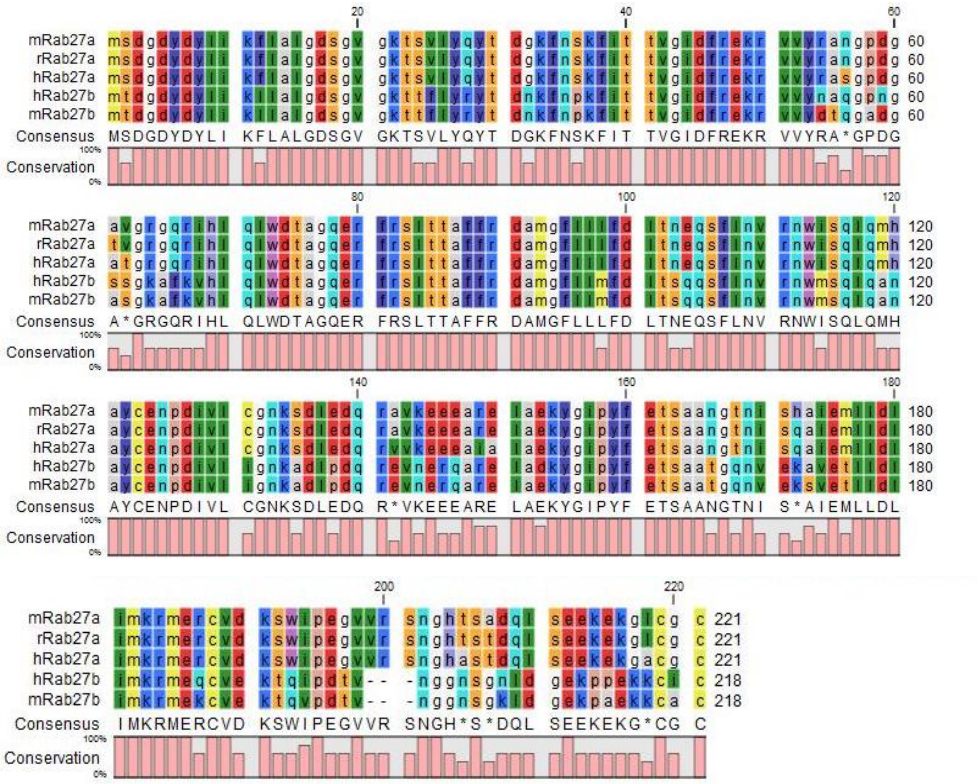


Figure 3.13. Amino acid sequence alignment of Rab27a/b proteins. Sequence alignment of mRab27a; GenBank: AAG24638.1, rRab27a; NCBI Reference Sequence: NP_059013.1, hRab27a; GenBank: CAG38735.1, hRab27b; GenBank: AAK11243.1 and mRab27b; GenBank: BAF02885.1 was performed with CLC sequence viewer 7.8.1. The sequence alignment is highlighted based on the degree of sequence homology, * stands for low sequence homology and the degree of conservation is presented as bar plots from 0 to 100%. Most of the amino acid residues in the N-terminus are conserved among these proteins.

To disrupt the binding between hRab27b and mSlp1 effector protein, a constant concentration of GST-mSlp1 (0.5μM) and 1.4μM m.Cherry-hRab27b (double the calculated EC50; to saturate the binding with mSlp1 completely) were incubated and different concentrations (0.0, 0.03, 0.1, 0.3, 1.0, 3.0 and 4.5 μM) of unlabelled rRab27a, hRab27b and hRab5 were used to test the possibility of

disrupting the interaction of hRab27b with mSlp1 (Figure 3.14: A). Both unlabelled Rab27a (pIC50; 6.86M) and Rab27b (pIC50; 6.84M) succeeded in disrupting the interaction between hRab27b and mSlp1 (evidenced by pIC50 values), whereas Rab5 (pIC50; 3.97M) failed to disrupt the interaction. In addition, Rab5 failed to produce an inhibitory sigmoid curve, whereas by using Rab27a/b inhibitory sigmoid curves were obtained.

Next, to better determine the specificity of this assay, unlabelled rRab27a, hRab27b and hRab5 were used again to test the possibility of disrupting the interaction between hRab27b (0.82μM m.Cherry-hRab27b; double the calculated EC50) and mSlp2 (0.5μM GST-mSlp2) (Figure 3.14: B). Again, the interaction between hRab27b and mSlp2 was completely disrupted using unlabelled rRab27a (pIC50; 6.67M) and hRab27b (pIC50; 6.78M), whereas hRab5 (pIC50; 4.10M) failed to disrupt the interaction.

Overall, the findings of these experiments showed that comparable results were obtained using the unlabelled Rab27a, Rab27b and Rab5 in disrupting the interaction of hRab27b with either mSlp1 or mSlp2. Based on this, the fluorescent GST-pull down assay can be used in the future to test and determine the effects of the candidate inhibitors of Rab27-effector interactions.

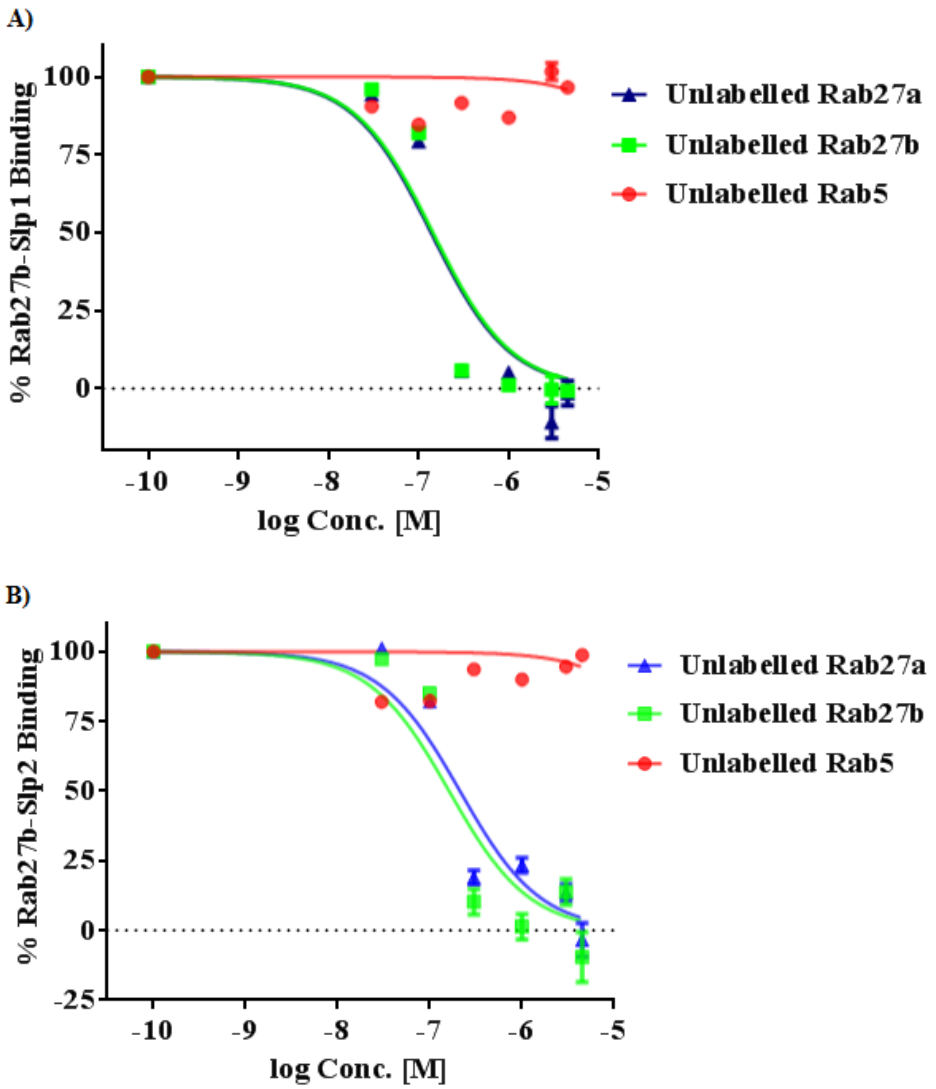


Figure 3.14. Disrupting hRab27b binding to either mSlp1 or mSlp2 effector proteins. Different concentrations (0.0, 0.03, 0.1, 0.3, 1.0, 3.0 and 4.5 µM) of unlabelled rRab27a and hRab27b; hRab5 (was used as a negative control) were used to disrupt the binding between: A) 1.4µM m.Cherry-hRab27b and 0.5µM GST-mSlp1-(1-201). The calculated pIC50 values were 6.86M, 6.84M and 3.97M for unlabelled rRab27a, hRab27b and hRab5, respectively. B) 0.82µM m.Cherry-hRab27b and 0.5µM GST-mSlp2-(3-80). The calculated pIC50 values were 6.67M, 6.78M and 4.10M for unlabelled rRab27a, hRab27b and hRab5, respectively. Data points represent mean ± SEM of 3 independent experiments performed in quadruplicates.

3.4 Discussion

This chapter has been focused on establishing and optimising a fluorescent-based protein-protein interaction assay utilising the GST-pull down strategy to be used for determining the in vitro binding affinity of Rab27b to different Rab27 effectors (mSlp1 and mSlp2).

In the classical GST-pull down assays, the specificity of protein-protein interactions can be tested i.e. they serve as qualitative measures for protein binding and to a lesser extent these assays can work as sensitive quantitative measures for protein-protein interactions. These assays involve performing multiple experimental steps, including: binding of the GST-fused proteins to GSH, washing off the unbound protein fractions, elution of the bound proteins, separation of the bound proteins using SDS-PAGE and analysing them by western blot which occasionally requires high quality specific antibodies (Casanova, 2012; Luo et al., 2014; Schechtman et al., 2003; Wang and Zeng, 2000). This suggests that some bound proteins might be lost during performing those steps, thus affecting the sensitivity of those assays. In addition, accurate measures of the binding affinity cannot be obtained, for instance it is difficult to measure the EC50 values of the protein-protein interactions and the IC50 values for the candidate inhibitors as binding affinity sigmoid curves cannot be established accurately. Therefore, a fluorescent GST-pull down assay was optimised to be used as an in vitro read-out for the Rab27-effector interactions.

Initial experiments aimed to optimise the conditions of this assay and, therefore m.Cherry-hRab27b was produced along with GST-mSlp1-(1-201) and GST-mSlp2 (3-80). The conditions of the reaction mixture were optimised including the concentration of GTP and glutathione magnetic beads and the incubation time. According to the results of the optimisation experiments, 3mM GTP, 10% glutathione magnetic beads and 2 hours incubation at room temperature were optimum to determine Rab27-effector binding (Figures 3.8, 3.9 and 3.10).

In addition, comparison of the binding of full length and C-terminal truncated hRab27b protein to mSlp1 effector protein demonstrated that the binding of the full length hRab27b was higher than that of the C-terminal truncated hRab27b

and they were significantly different. Thus, the full length hRab27b was used in the fluorescent-GST pull down assay experiments (Figure 3.11).

These reaction conditions were then used to establish and determine the binding affinity of hRab27b to mSlp1 and mSlp2 effector proteins and the EC50 values for binding to mSlp1and mSlp2 were determined accordingly. The binding affinity experiments (Figure 3.12) demonstrated that the EC50 for binding to mSlp2 (pEC50; 6.38M) was lower than that for binding to mSlp1 (pEC50; 6.16M), suggesting that the binding affinity of hRab27b to mSlp2 is slightly higher than that to mSlp1. In agreement with this finding, the Rab27a binding affinity to different effector proteins was determined using immunoprecipitation assay in COS-7 cells; the descending order of the binding affinity was found to be as follows: rabphilin > Slp2-a > Slp1 > Slp5 > Slp4-a > Slac2-b > Noc2 > Slac2-a > Slac2-c > Slp3-a. Accordingly, rabphilin, Slp2-a, Slp1, Slp5, Slp4-a, Slac2-b and Noc2 effectors were considered as a high affinity binding group for Rab27a, whereas Slac2-a, Slac2-c and Slp3-a were considered as a low affinity binding group (Fukuda, 2006).These findings provided the basis for focusing on mSlp2 when developing Rab27-effector interaction inhibitors (see chapter 5 and 6) as the Rab27 binding affinity for Slp2 was higher than that to Slp1.

In order to determine the specificity of this assay in terms of testing the effects of the candidate inhibitors of Rab27-effector interactions, unlabelled rRab27a and hRab27b (hRab5 was used as a negative control) were used as typical competitive inhibitors to disrupt the interaction between m.Cherry-hRab27b and either GST-mSlp1 or GST-mSlp2. The results of these experiments demonstrated that both unlabelled Rab27a and Rab27b were able to disrupt the interaction of hRab27b with either mSlp1 or mSlp2 ((Figure 3.14), assuring the specificity of this assay in terms of testing the effects of the candidate inhibitors of Rab27-effector interactions.

In conclusion, the fluorescent GST-pull down assay serves as an indirect read-out of Rab27 interaction with its effectors in vitro (both qualitatively and quantitatively) and can be used in the future to test the effects of the candidate inhibitors.

3.5 Conclusions

According to the current results of these experiments, the fluorescent GST-pull down assay is a valuable and reliable quantitative and qualitative read-out for the Rab27-effector interactions, since the EC50 for these interactions and the IC50 of the candidate inhibitors can be determined. In addition, this assay has many advantages over the classical GST-pull down assays as it involves performing fewer experimental steps and does not require using of high quality specific antibodies, thereby it functions as an effective and sensitive measure for Rab27-effector interactions. This suggests that this assay can be used in the future for testing the effects of the candidate inhibitors of Rab27-effector interactions.

Chapter 4

Determining the Rab27-effector protein binding affinity using a FRET-based assay

4.1 Introduction

As described previously in chapter 3, there is a continuous necessity to establish and develop a convenient in vitro assay for measuring Rab27-effector interactions which can be used later for identifying and determining the effects of the candidate small molecule or peptide inhibitors of these interactions. In addition, there are some limitations to the use of the fluorescent GST-pull down assay. These include: multiple pipetting steps, the use of the glutathione magnetic beads and related problems of stickiness and volume variability as the beads were reconstituted in the dilution buffer and contamination of the supernatant (unbound fraction) with glutathione beads which might affect the accuracy of the results. Therefore, an alternative approach was established and developed to determine Rab27-effector interactions. To achieve this goal, the principle of the FRET was exploited and used to establish and develop a protein-protein interaction assay. By definition, the FRET involves excitation of a donor fluorophore, this is followed by non-radiative energy transfer from the donor to the acceptor fluorophore; the excitation wave length of the acceptor should be within the emission wave length of the donor (Förster, 1947; Förster, 1948). The transfer of energy occurs by dipole-dipole interaction between the donor and acceptor when they come in close proximity to each other (1–10nm) (Banterle and Lemke, 2016) (Wu and Brand, 1994) without involving transfer of photons (Ma et al., 2014; Stryer, 1978). In general, FRET can be classified into two types: the intermolecular and intramolecular FRET. The intermolecular FRET occurs when the acceptor and donor fluorophores are attached to the interacting components separately; in this case the FRET is directly dependent on the binding between the interacting components and upon dissociation of these components, FRET signals are almost diminished. The intramolecular FRET occurs when the donor and acceptor fluorophores are attached to the interacting components in a complex form, thus the FRET is not always specific and directly related to the binding between the interacting components as they are already found in a complex form. It is more dependent on protein conformational changes than depending on direct protein-protein interaction, thus requiring further optimisation experiments in order to obtain specific FRET signals

(Miyawaki, 2011). Therefore, in this project, intermolecular FRET strategy was used and optimised as described thereafter.

Better selection of the donor and acceptor fluorophores is a key determinant of the FRET assay efficacy and specificity. Fluorescent proteins, organic dyes, and quantum dots represent the main fluorophore classes that can be used in FRET assays. The main advantage of the fluorescent proteins over organic dyes and quantum dots is that the fluorescent proteins are easily genetically engineered and attached to the interacting components without involving chemical labelling or antibodies (Bajar et al., 2016; Masharina et al., 2012). In addition, using of the fluorescent proteins ensures that both the fluorophore and the host protein are found in 1:1 ratio and more consistent results could be obtained, whereas upon chemical labelling of the interacting proteins, a uniform chemical labelling cannot always be assured (Ratner et al., 2002) which affects the consistency and accuracy of the results.

FRET-based assays have been used for many years for determining protein-protein interactions in cells using fluorescent recombinant proteins (Zaccolo, 2004). In addition, many protein-protein interactions have been determined in vitro using FRET-based techniques, for example excitation of Cy3-labelled Annexin A2 (donor), a $Ca2^{+}$ and phospholipids-binding protein and its binding protein Cy5-labelled S100A10 (acceptor) at 488nm resulted in producing significant FRET signals at 670nm, thereby determining the binding affinity (Li et al., 2010).

To establish a FRET-based protein-protein interaction assay, GFP-Rab27 effector proteins (mSlp1 and mSlp2) were used as donor fluorophores, whereas m.Cherry-hRab27a/b (hRab27b was used mostly) recombinant proteins were used as acceptor fluorophores. The excitation-emission spectra of these fluorophores overlap, thus they were appropriate and efficient FRET fluorophores as described below. GFP wild protein was first discovered in Aequorea jellyfish by Shimomura and colleagues in 1961, it is expressed along with aequorin protein (Shimomura, 2005; Shimomura et al., 1962). Then in 1974, GFP was successfully purified and crystallized (Morise et al., 1974). The structure of the chromophore of Aequorea GFP was then partially resolved in

1979 (Shimomura, 1979) and completely identified by Cody and colleagues (Cody et al., 1993). This protein was successfully expressed in *E. coli* and the excitation-emission spectra were comparable to that of the native Aequorea GFP protein (Inouye and Tsuji, 1994). This was followed by identification of the 3D structure of GFP protein (Yang et al., 1996a). Furthermore, different GFP variants were produced and the excitation-emission spectra were examined (Cubitt et al., 1995; Heim and Tsien, 1996). In this study, the enhanced GFP protein (F64L, S65T GFP variant) was used instead of the wild-type GFP as the fluorescence intensity of this GFP variant is 30-fold higher than the wild-type GFP and these mutations increase protein expression, folding and solubility in bacteria over the wild type (Cormack et al., 1996; Yang et al., 1996b).

In addition, the excitation-emission spectra analysis of the enhanced GFP protein demonstrated that maximum excitation and emission occur at 470-475nm and 509nm, respectively with an additional shoulder at 550nm (Patterson et al., 2001). In the current FRET-based assay experiments, m.Cherry protein was used as an acceptor fluorophore due to its high photostability and fluorescence intensity advantages over many acceptor fluorophores (Seefeldt et al., 2008) (for further details see section 3.1). Furthermore, excitation of m.Cherry at 450-625nm (maximum at 575nm) resulted in an emission at 575-700nm (maximum at 610nm) (Albertazzi et al., 2009). Accordingly, it was supposed that FRET could occur upon excitation of m.Cherry at 562.5-577.5nm. GFP emission spectrum overlaps with m.Cherry excitation spectrum at the shoulder of GFP emission spectrum as the excitation wave length of m.Cherry is within this range. Therefore, GFP-fused effector proteins were used as donor fluorophores (GFP-mSlp1and GFP-mSlp2) and m.Cherry-hRab27a/b recombinant proteins were used as acceptor fluorophores (for further details see Figure 4.1).

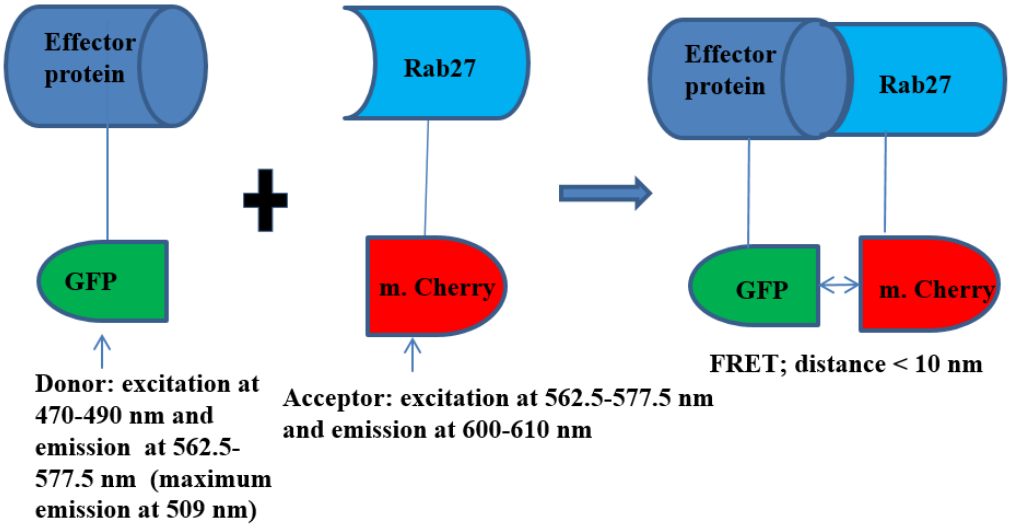


Figure 4.1. A schematic representation of the FRET-based protein-protein interaction assay. Upon binding of GFP-effector protein and m.Cherry-Rab27, a complex will be formed (GFP-effector protein-m.Cherry-Rab27 complex). Then, upon excitation of the donor fluorophore GFP-effector protein at 470-490nm, emission of light occurs at 562.5-577.5nm, this excites the acceptor fluorophore (m.Cherry-Rab27) (if the binding components come close to each other and the distance between them is less than 10nm) at this wave length which in turn emits light at 600-610nm, indicating FRET occurrence (transfer of energy from the donor fluorophore to the acceptor fluorophore.

4.2 Aims

As a preliminary study performed by Wenhua Zhou and Dr Alistair Hume (data not shown) demonstrated that FRET can occur using GFP and m.Cherry as donor and acceptor fluorophores, respectively. The main aims of these experiments were to confirm this finding, validate and optimise the conditions of the FRET-based protein-protein interaction assay. These involved choosing the appropriate fluorescence microplate reader, optimising the concentration of GTP, incubation time and fixing the concentration of the acceptor protein. In addition, to confirm the specificity of the assay, unlabelled Rab27a/b were used as typical competitive inhibitors for Rab27-effector protein interaction. Accordingly, this assay was used to determine the binding affinity of mSlp1 and mSlp2 effector proteins. This provides the basis for identifying and testing the effects of the candidate inhibitors of Rab27-effector protein interactions in the future, including small molecule and peptide inhibitors by comparing the IC50 values of those candidate inhibitors.

4.3 Results

4.3.1 Generation of 6x Histidine-[GFP-mSlp1-(1-116), GFP-mSlp2-(3-80) and GFP] recombinant proteins

GFP-mSlp1-(1-116) and GFP-mSlp2-(3-80) chimeric proteins were expressed in *E. coli* and used as donor fluorophores in the FRET-based protein-protein interaction assay. In addition, GFP protein was produced to be used as a negative control for establishing this assay.

To optimise the conditions of protein expression in *E. coli*, a small scale protein production was performed with different IPTG concentrations (0.5, 2.0 and 5.0mM) using different conditions: induction for 3 and 20 hours at 37ºC and 20ºC, respectively using the pETDuet-1-GFP-mSlp1-(1-116) vector (section 2.1.3.4) as described in section 2.2.2. Analysis of lysates from the uninduced and induced bacterial cell cultures using 10% SDS-PAGE instant blue staining demonstrated that abundant protein bands were produced at the expected molecular weight (43.97KDa) for the 6x Histidine-GFP-mSlp1-(1-116) recombinant protein in the IPTG induced bacterial cultures using all the tested IPTG concentrations and conditions, whereas this band was absent from the uninduced bacterial cell lysates (Figure 4.2). This indicates that induction of protein production using 0.5mM IPTG for 3 hours at 37ºC was successful and sufficient to produce abundant amount of protein. Accordingly, induction of protein production was performed using 0.5mM IPTG for 3 hours at 37ºC in the subsequent experiments.

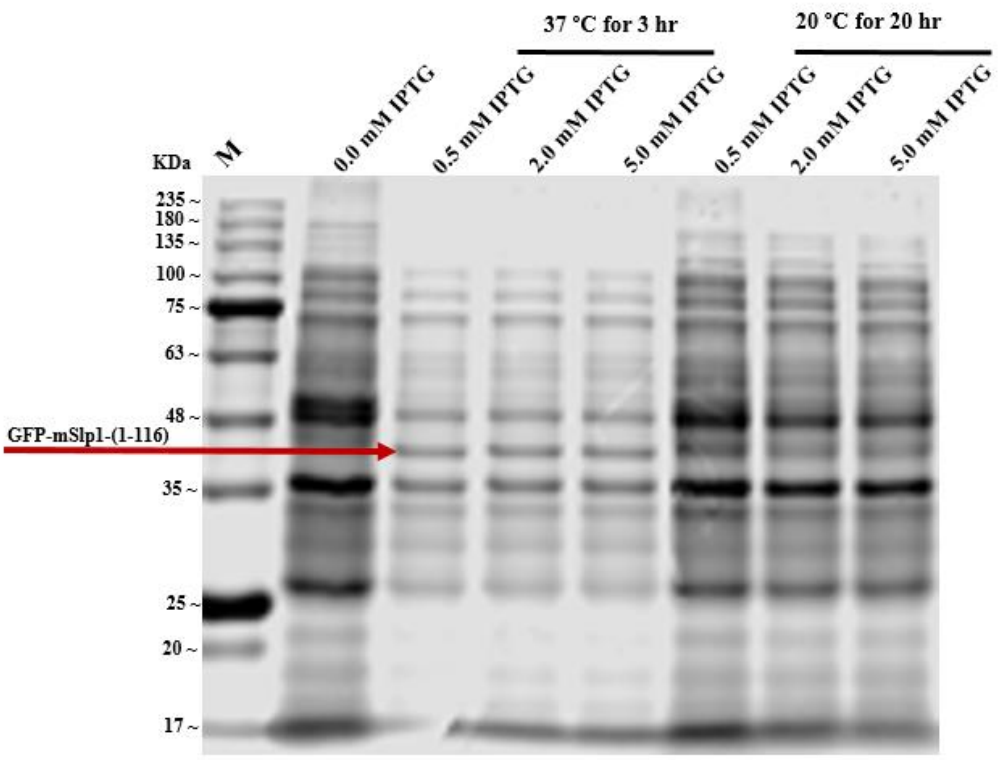


Figure 4.2. Small scale induction of the 6x Histidine-GFP-mSlp1-(1-116) recombinant protein production. Rosetta *E. coli* competent cells were transformed with the pETDuet-1-GFP-mSlp1-(1-116) vector and small scale protein production was induced with different IPTG concentrations (0.0, 0.5, 2.0 and 5.0mM) for 3 and 20 hours at 37ºC and 20ºC, respectively. Bacterial cultures were pelleted and the cell lysate extracts were then analysed using instant blue stained 10% SDS-PAGE gel. Abundant protein bands (the arrow indicated bands) were produced at the expected molecular weight (43.97KDa) for the 6x Histidine-GFP-mSlp1-(1-116) recombinant protein in the IPTG induced bacterial cultures using all the tested IPTG concentrations and conditions.

The pETDuet-1-GFP-mSlp1-(1-116), pETDuet-1-GFP and pETDuet-1-GFP-mSlp2-(3-80) vectors (section 2.1.3.4) were then transformed into Rosetta *E. coli* competent cells and protein production was induced with 0.5mM IPTG as described in section 2.2.2, this was followed by performing protein purification steps using the IMAC system (see section 2.2.3.1). Analysis of these proteins using 10% SDS-PAGE gel demonstrated that abundant protein bands were detected at the expected molecular weights of 43.97KDa, 41.33KDa and 30.034KDa for the 6x Histidine-GFP-mSlp1-(1-116), 6x Histidine-GFP and 6x Histidine-GFP-mSlp2-(3-80) (data not shown) recombinant proteins,

respectively. Furthermore, a western blot analysis using anti-GFP primary antibodies confirmed that the 6x Histidine-GFP-mSlp1-(1-116) (Figure 4.3) and 6x Histidine-GFP-mSlp2-(3-80) (data not shown) recombinant proteins were induced successfully at the expected molecular weights.

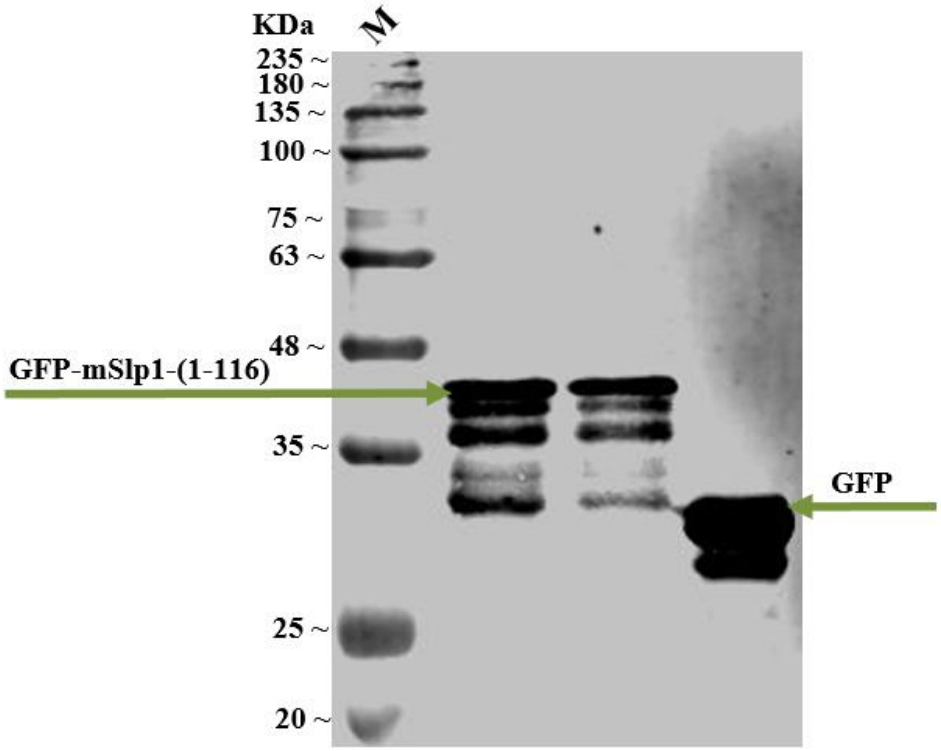


Figure 4.3. Western blot analysis of the 6x Histidine-GFP-mSlp1-(1-116) recombinant protein. 6x Histidine-GFP-mSlp1-(1-116) recombinant protein (different protein batches) and 6x Histidine-GFP protein (as a positive control) were loaded into 10% SDS-PAGE gel, transferred into PVDF membrane (0.45 um) and immunoblotted with anti-GFP antibody. Abundant protein bands (the arrow indicated bands) were detected at the predicted molecular weights for the 6x Histidine-GFP-mSlp1-(1-116) (43.97KDa) and 6x Histidine-GFP (30.03KDa) (M; molecular weight standards).

4.3.2 Establishing and optimising the FRET-based protein-protein interaction assay experiments

In order to measure and determine the binding affinity of different Rab27 effectors to Rab27 protein, a FRET-based protein-protein interaction assay was

established and optimised. As described previously, in this assay GFP-fused effector proteins were used as donor fluorophores [(GFP-mSlp1-(1-116) and GFP-mSlp2-(3-80)] and m.Cherry-hRab27a/b recombinant proteins were used as acceptor fluorophores. In these experiments, different concentrations of GFP-mSlp1 and GFP-mSlp2 were used to saturate the binding with fixed concentration of m.Cherry-hRab27a/b (for further details of the principle of this assay see Figure 4.1).

Preliminary studies were performed by Wenhua Zhou and Dr Alistair Hume to test the possibility of FRET occurrence using GFP and m.Cherry as donor and acceptor fluorophores, respectively (data not shown). These studies demonstrated that inter-molecular FRET signals were detected due to the interaction between mSlp1-(1-116)-GFP and mCherry-hRab27a. In addition, these preliminary experiments demonstrated that the detected intra-molecular FRET signals in COS7 cells using GFP-mSlp1-(1-116)-m.Cherry-hRab27a probe were higher than that of mSlp1-(1-116)-GFP-m.Cherry-hRab27a probe. Therefore, Rab27 effector proteins (Slp1 and Slp2) were fused to the C-terminus of GFP protein in these FRET-based assay experiments (instead of fusing them to the N-terminus of GFP). In addition, as the N-terminal domains of Slp1 and Slp2 are the main binding sites for Rab27 protein (Fukuda et al., 2001) (as described in section 1.4), fusing of GFP to the C-terminus of these effector proteins might affect their Rab27 binding activity by changing protein conformation and constraining the N-terminal domains from interacting with Rab27, thus decreasing Rab27-effector interaction and reducing the possibility of FRET occurrence between m.Cherry and GFP.

To investigate the occurrence of FRET, the interaction between GFP-mSlp1-(1-116) and m.Cherry-hRab27b was tested using the same conditions described in section 3.3.4; i.e. the same dilution buffer contents, GTP concentration and incubation temperature and time. As negative control reactions, the occurrence of FRET was tested using [GFP and m.Cherry-hRab27b] and [(GFP-mSlp1-(1-116) and m.Cherry] reaction mixtures. The corrected flourescence was calculated by subtracting the fluorescence of the individual components from the fluorescence of the whole mixture which was considered as an indirect read-out

of the bound fraction of mSlp1-(1-116) for -hRab27b (Figure 4.4). Overall, the findings of these experiments demonstrated that specific and significant FRET signals were detected as a result of direct binding between Rab27b and Slp1 rather than binding of these interacting components to m.Cherry or GFP proteins. This provided the basis for determining the Rab27-effector binding affinity using mSlp1 and mSlp2 effectors in the subsequent experiments.

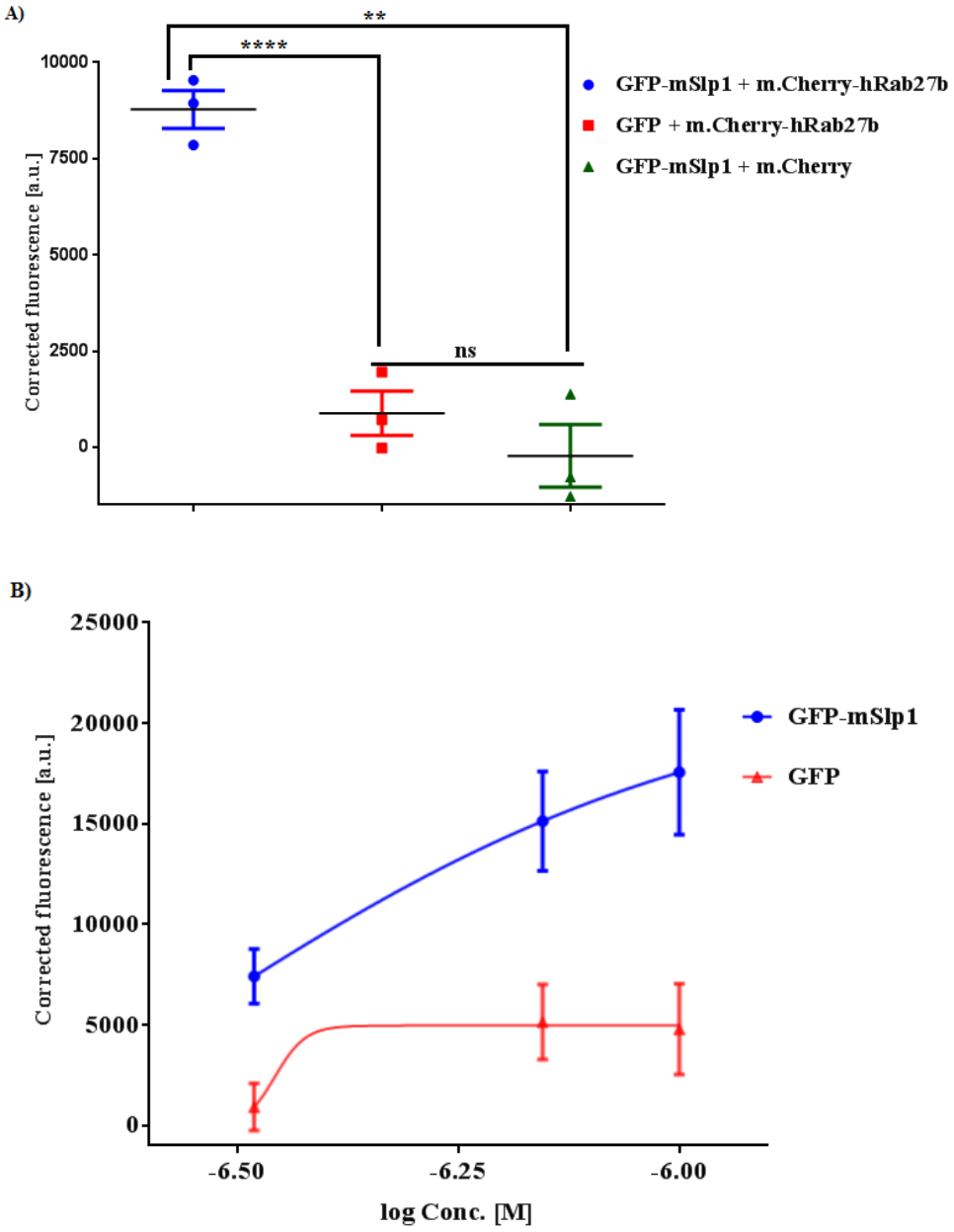


Figure 4.4. FRET profile of m.Cherry-hRab27b and GFP-mSlp1 binding. A) 0.5µM GFP-Slp1-(1-116) was incubated with either 0.3µM m.Cherry-hRab27b or 0.3µM m.Cherry as a negative control. In addition, 0.5µM GFP was incubated with 0.3µM m.Cherry-hRab27b and used as a negative control. Data points represent mean ± SEM performed in triplicates. B) The binding

affinity of different concentrations of GFP-mSlp1 and GFP (0.33, 0.7 and 1.0 μM) to 0.3μM m.Cherry-hRab27b was tested using the FRET assay. Data points represent mean ± SEM performed in quadruplicates. One-way ANOVA: $^{ns}P > 0.05$; $^{**}P \leq 0.01$; $^{***}P \leq 0.001$.

4.3.2.1 Determining the optimum incubation time and GTP concentration to be used in the FRET-based protein-protein interaction assay

To optimise the conditions of the FRET-based protein-protein interaction assay, the effect of different reaction conditions on the binding between 0.15μM m.Cherry-hRab27b and 0.35μM GFP-mSlp1-(1-116) was tested. Thus, different incubation times (0, 1, 2 and 4 hour) and GTP concentrations (0, 1, 3 and 9 mM) were used for testing the binding between these interacting components.

The findings of these experiments demonstrated that the interaction between hRab27b and mSlp1 of the GTP loaded reactions was higher than the interaction of the GTP unloaded reactions (data not shown). In addition, the use of different GTP concentrations (1, 3, 9 mM) did not affect the pattern of interaction between hRab27b and mSlp1 as the interactions using these GTP concentrations were not significantly different at different incubation times (data not shown) (see Figure 4.5 as an example).

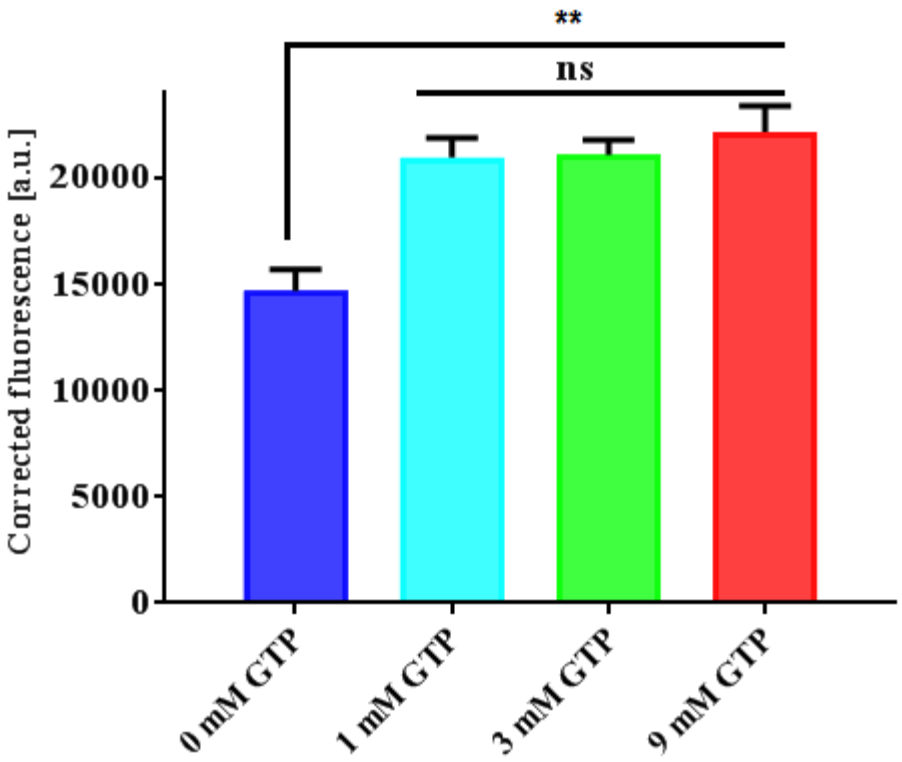


Figure 4.5. Effect of GTP concentration on the binding between GFP-mSlp1-(1-116) and m.Cherry-hRab27b after 2 hours incubation. Different GTP concentrations (0, 1, 3 and 9 mM) were used to test the binding between 0.35µM GFP-mSlp1-(1-116) and 0.15µM m.Cherry-hRab27b after 2 hours incubation. The corrected fluorescence was used as an indirect read-out for the bound fraction. Data points represent mean ± SEM of 3 independent experiments performed in quadruplicates. One-way ANOVA: $^{ns}P > 0.05$; $^{**}P \leq 0.01$, $^{***}P \leq 0.001$.

Although the effects of the used incubation times were not significantly different in terms of affecting the interaction between hRab27b and mSlp1, the binding using 3mM GTP was consistent. Furthermore, 2 and 4 hours incubation were comparable to each other in terms of obtaining sufficient binding (Figure 4.6). Accordingly, 2 hours incubation time at room temperature and 3mM GTP were used in the subsequent binding affinity experiments.

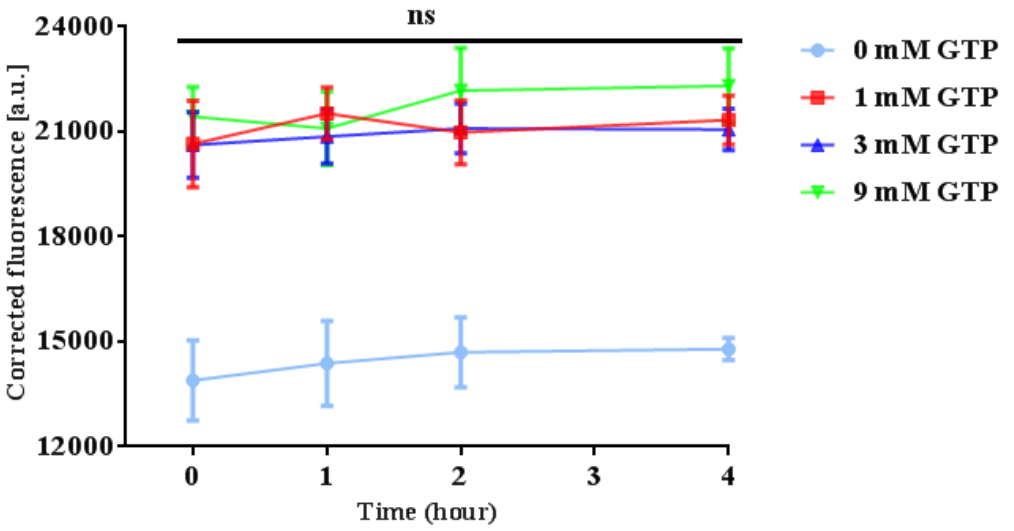


Figure 4.6. Effect of the incubation time on the binding between GFP-mSlp1-(1-116) and m.Cherry-hRab27b. Different incubation times (0, 1, 2, and 4 hour) were used to determine the binding between 0.35µM GFP-mSlp1-(1-116) and 0.15µM m.Cherry-hRab27b using different GTP concentrations (0, 1, 3 and 9 mM) at room temperature. Data points represent mean ± SEM of 3 independent experiments performed in quadruplicates. One-way ANOVA: $^{ns}P > 0.05$.

4.3.3 Slp1 and Slp2 have different binding affinities to Rab27

To determine the binding affinity of mSlp1 and mSlp2 effector proteins to Rab27b, the conditions of the FRET-based protein-protein interaction assay were optimised as described in section 4.3.2.1. In order to achieve this goal, different preliminary experiments were performed to optimise the concentration of m.Cherry-hRab27b recombinant protein that can be used in these binding affinity experiments (in order to use constant concentration).

Firstly, a constant concentration of m.Cherry-hRab27b (0.6µM) was chosen to be used for determining the binding affinity of different concentrations of GFP-mSlp1-(1-116) and GFP-mSlp2-(3-80). The pEC50 values of GFP-mSlp1-(1-116) and GFP-mSlp2-(3-80) binding to 0.6µM m.Cherry-hRab27b were 5.75M and 6.35M, respectively. Although a plateau or saturation kinetics was not reached, this suggested that the binding affinity of mSlp2 to Rab27b is higher than that of Slp1 (Figure 4.7).

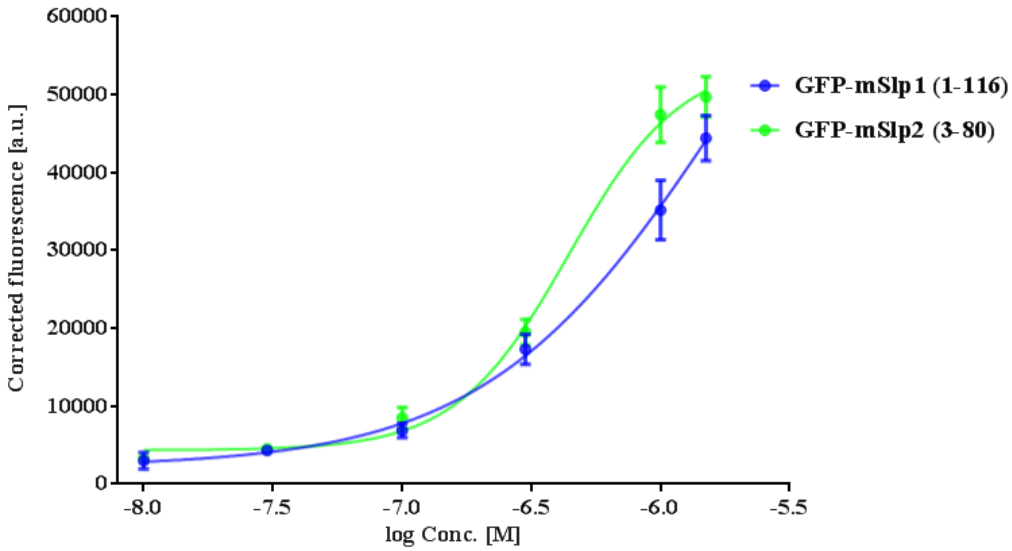


Figure 4.7. The binding affinity profile of mSlp1 and mSlp2 effector proteins to 0.6 µM hRab27b. The binding affinity of different concentrations (0.01, 0.03, 0.1, 0.3, 1.0 and 1.5 µM) of GFP-mSlp1-(1-116) and GFP-mSlp2-(3-80) to 0.6µM m.Cherry-hRab27b was determined using the FRET-based protein-protein interaction assay. The calculated pEC50 values were 5.75M and 6.35M for GFP-mSlp1 and GFP-mSlp2, respectively. Data points represent mean ± SEM performed in quadruplicates.

As saturation kinetics was not reached by using 0.6µM m.Cherry-hRab27b (the binding was not saturated completely) and to better determine the binding affinity of mSlp1 and mSlp2 to hRab27b, a lower concentration of 0.3µM instead of 0.6µM m.Cherry-hRab27b was used for determining the binding of these two Rab27 effector proteins. Recurrently, saturation kinetics was not reached. The pEC50 values of GFP-mSlp1-(1-116) and GFP-mSlp2-(3-80) binding to 0.3µM m.Cherry-hRab27b were 5.85M and 6.41M, respectively, suggesting again that the binding affinity of mSlp2 is higher than that of mSlp1 (Figure 4.8).

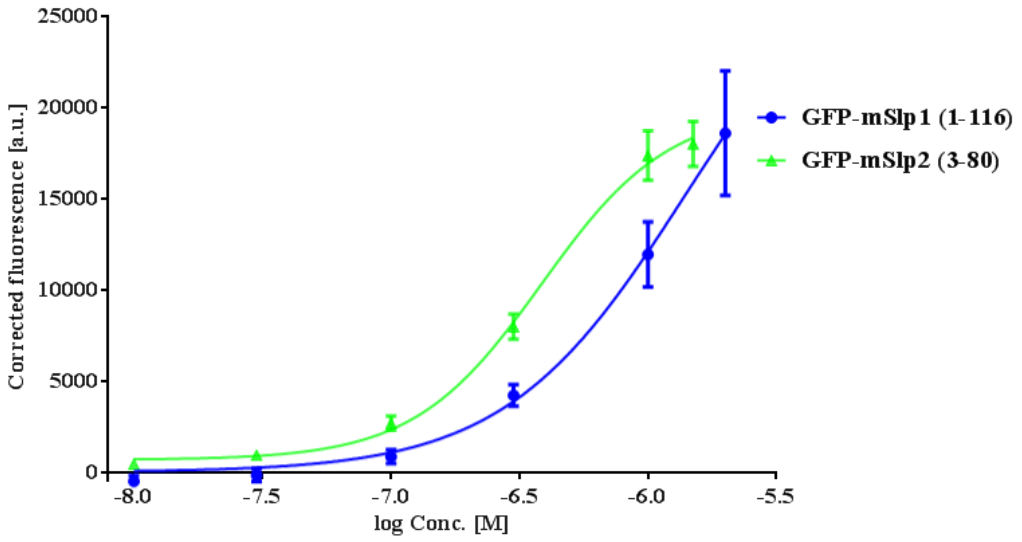


Figure 4.8. The binding affinity profile of mSlp1 and mSlp2 effector proteins to 0.3µM hRab27b. The binding affinity of different concentrations of GFP-mSlp1-(1-116) (0.01, 0.03, 0.1, 0.3, 1.0 and 2 µM) and GFP-mSlp2-(3-80) (0.01, 0.03, 0.1, 0.3, 1.0 and 1.5 µM) to 0.3µM m.Cherry-hRab27b was determined using the FRET-based protein-protein interaction assay. The calculated pEC50 values were 5.85M and 6.41M for GFP-mSlp1 and GFP-mSlp2, respectively. Data points represent mean ± SEM performed in quadruplicates.

Therefore, a lower concentration of m.Cherry-hRab27b (0.15µM) was used to determine the binding affinity of mSlp1 and mSlp2. Repeatedly, these experiments confirmed that the Rab27-binding affinity of mSlp2 (pEC50: 6.8M) is higher than that of mSlp1 (6.48M) (Figure 4.9). In addition, determination of mSlp1 and mSlp2 binding affinity using the FRET-assay was specific. This was evidenced by the pEC50 values of the negative control reactions: 1) GFP binding to m.Cherry-hRab27b (pEC50: 5.68M), 2) m.Cherry binding to GFP-mSlp1 (pEC50: 5.60M) and 3) m.Cherry binding to GFP-mSlp2 (pEC50: 4.17M) (Figure 4.9). These experiments demonstrated that the binding in the absence of one of the main interacting components (Rab27b, mSlp1 or mSlp2) was unspecific and not comparable to the binding affinity profile of GFP-mSlp1 or GFP-mSlp2 to m.Cherry-hRab27b recombinant protein.

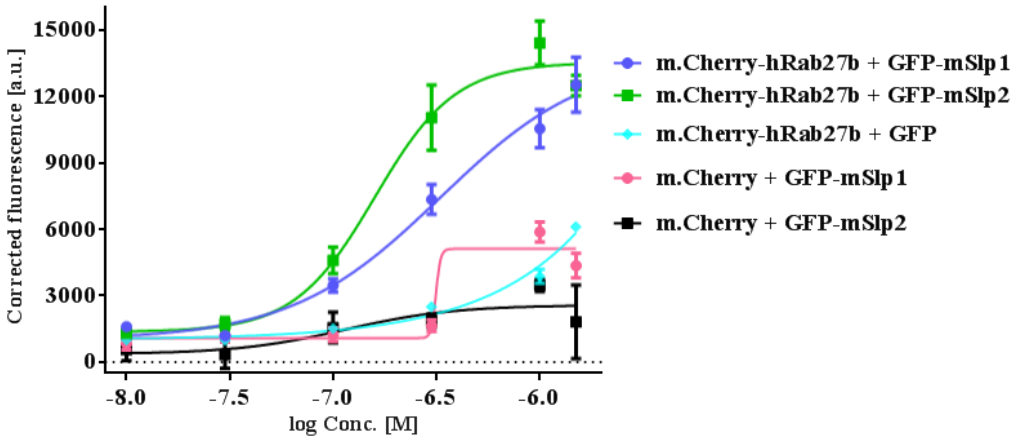


Figure 4.9. The binding affinity profile of mSlp1 and mSlp2 effector proteins to 0.15μM hRab27b. Different concentrations (0.01, 0.03, 0.1, 0.3, 1.0 and 1.5 μM) of GFP-mSlp1-(1-116), GFP-mSlp2-(3-80) and GFP were used to determine the binding affinity to 0.15μM m.Cherry-hRab27b. The calculated pEC50 values were 6.48M, 6.8M and 5.68M for GFP-mSlp1, GFP-mSlp2 and GFP, respectively. In addition, different concentrations (0.01, 0.03, 0.1, 0.3, 1.0 and 1.5 μM) of GFP-mSlp1-(1-116) and GFP-mSlp2-(3-80 were used to determine the binding affinity to 0.15μM m.Cherry. The calculated pEC50 values were 5.60M and 4.17M for GFP-mSlp1 and GFP-mSlp2, respectively. The FRET-based protein-protein interaction assay was used to determine the binding affinity in these experiments. Data points represent mean ± SEM of 3 independent experiments performed in quadruplicates.

Next, to further investigate the differences in the binding affinity to mSlp1 and mSlp2, the binding for the full length and C-terminal truncated hRab27b was tested. To this end, the binding of GFP-mSlp1-(1-116) and GFP-mSlp2-(3-80) to m.Cherry-hRab27b (full length; 1-218 and C-terminal truncated; 1-200) was tested by using constant concentrations of mSlp1 and mSlp2. Note that double the already determined EC50 values were used in order to saturate the binding; the calculated EC50 values were 0.35μM and 0.15μM for mSlp1 and mSlp2, respectively. Although the binding of mSlp1 and mSlp2 to hRab27b were not significantly different, the binding of mSlp2 for either full length or C-terminal truncated hRab27b was higher than that of mSlp1, since the used concentration of mSlp1 (0.7μM) was almost double the concentration of mSlp2 (0.3μM) (Figure 4.10).

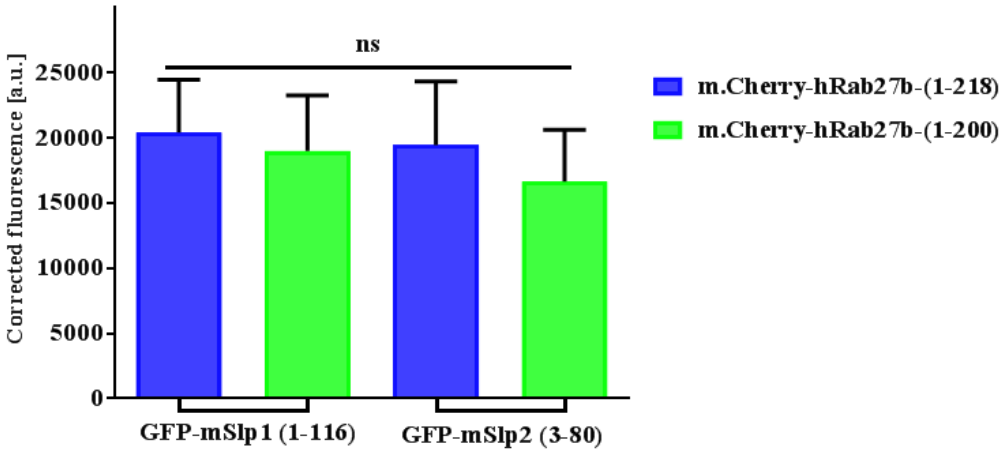


Figure 4.10. Comparison of the binding of mSlp1 and mSlp2 to the full length and C-terminal truncated hRab27b. The binding between 0.15µM m.Cherry-hRab27b (full length; 1-218 and C-terminal truncated; 1-200) and either 0.7µM GFP-mSlp1 (1-116) or 0.3µM GFP-mSlp2 (3-80) was tested using the FRET-based protein-protein interaction assay. Data points represent mean ± SEM of 3 independent experiments performed in quadruplicates. One-way ANOVA: $^{ns}P > 0.05$.

Moreover, the binding affinity of mSlp1 and mSlp2 to m.Cherry-hRab27a, another Rab27 isoform was determined using the same conditions and concentrations for m.Cherry-hRab27b. Again, these experiments demonstrated that the binding affinity of mSlp2 (pEC50: 6.69M) to Rab27a was slightly higher than that of mSlp1 (pEC50: 6.49M) (Figure 4.11). This indicates that the binding affinity of mSlp1 to Rab27a (pEC50: 6.49M) and Rab27b (pEC50: 6.48M) was similar, whereas the binding affinity of mSlp2 to Rab27b (pEC50: 6.8M) was slightly higher than to Rab27a (pEC50: 6.69M).

Overall, these experiments suggest that the binding affinity of mSlp2 to hRab27a/b was higher than that of mSlp1 which was evidenced by the pEC50 values differences as described above.

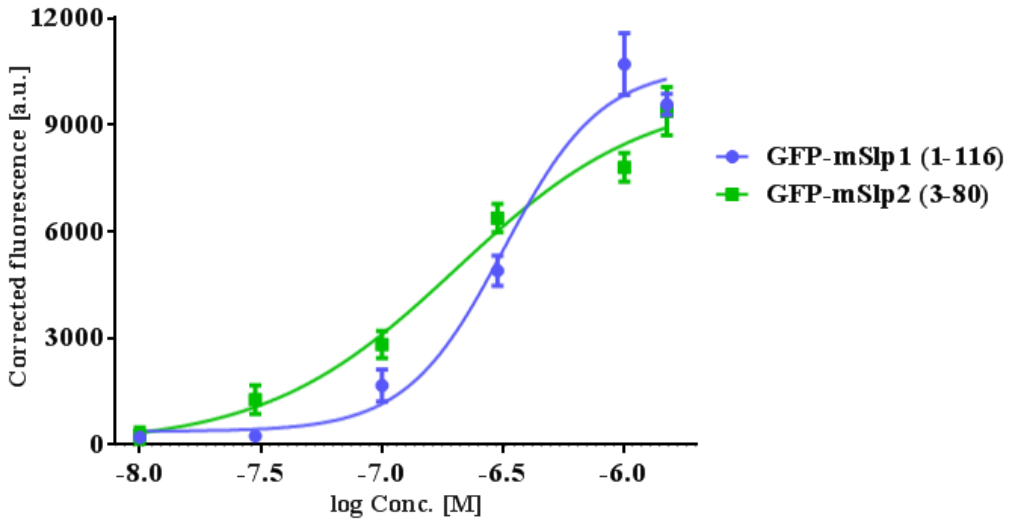


Figure 4.11. The binding affinity profile of mSlp1 and mSlp2 effector proteins to 0.15μM hRab27a. Different concentrations (0.01, 0.03, 0.1, 0.3, 1.0 and 1.5 μM) of GFP-mSlp1-(1-116) and GFP-mSlp2-(3-80) were used to determine the binding affinity to 0.15μM m.Cherry-hRab27a. The calculated pEC50 values were 6.49M and 6.69M for GFP-mSlp1 and GFP-mSlp2, respectively. The FRET-based protein-protein interaction assay was used to determine the binding affinity in these experiments. Data points represent mean ± SEM of 3 independent experiments performed in quadruplicates.

4.3.4 Specificity of the FRET based protein-protein interaction assay

By determining the Rab27-effector protein binding affinity using different Rab27 effectors (mSlp1 and mSlp2) as described in section 4.3.3, the EC50 values were measured for both mSlp1 and mSlp2 interactions with Rab27 and used to assess the specificity of the FRET assay in terms of testing the effects of the candidate inhibitors of Rab27-effector interactions in the future (including small molecule and peptide inhibitors). To achieve this goal, unlabelled rRab27a and hRab27b proteins were used as typical competitive inhibitors for Rab27-effector interactions. Therefore, unlabelled Rab27a/b and Rab5 (served as a negative control) were produced as 6x His-tagged Rab proteins as described in section 3.3.2.

In order to disrupt the interaction between hRab27b and mSlp1 effector protein, 0.15μM m.Cherry-hRab27b (as this concentration was used to determine the binding affinity of mSlp1 in the previous experiments) and 0.7μM GFP-mSlp1 (1-116) (double the calculated EC50; to saturate the binding with hRab27b) were

incubated and different concentrations (0.0, 0.03, 0.1, 0.3, 1.0, 3.0 and 4.5 μM) of unlabelled rRab27a, hRab27b and hRab5 were used as competitive inhibitors. The interaction between hRab27b and mSlp1 was completely disrupted using unlabelled Rab27a and Rab27b (evidenced by pIC50 values), whereas Rab5 failed to disrupt the interaction (Figure 4.12. A). The pIC50 values of unlabelled rRab27a and hRab27b were 7.45M and 7.57 M, respectively and higher than that of hRab5 (4.79M), indicating that the IC50 values of Rab27a/b were lower than that of Rab5. Also, Rab5 failed to produce an inhibitory sigmoid curve, whereas Rab27a/b succeeded in producing inhibitory sigmoid curves.

Next, to further investigate the specificity of this assay, the same concentrations of the previously described Rab proteins were used to test the possibility of disrupting the interaction between hRab27b and mSlp2 using 0.15μM m.Cherry-hRab27b and 0.3μM GFP-mSlp2-(3-80) (double the calculated EC50) (Figure 4.12: B). Repeatedly, the interaction between hRab27b and mSlp2 was completely disrupted using unlabelled rRab27a and hRab27b, whereas hRab5 failed to disrupt the interaction. This was evidenced by the pIC50 values of unlabelled rRab27a (7.07M) and hRab27b (6.71M) which were higher than that of hRab5 (5.04M), indicating that that the IC50 values of hRab27a/b were lower than that of hRab5. Consequently, the specificity of the FRET-based protein-protein interaction assay was confirmed and this indicates that this assay can be used in the future to test and determine the effects of the candidate inhibitors of Rab27-effector interactions.

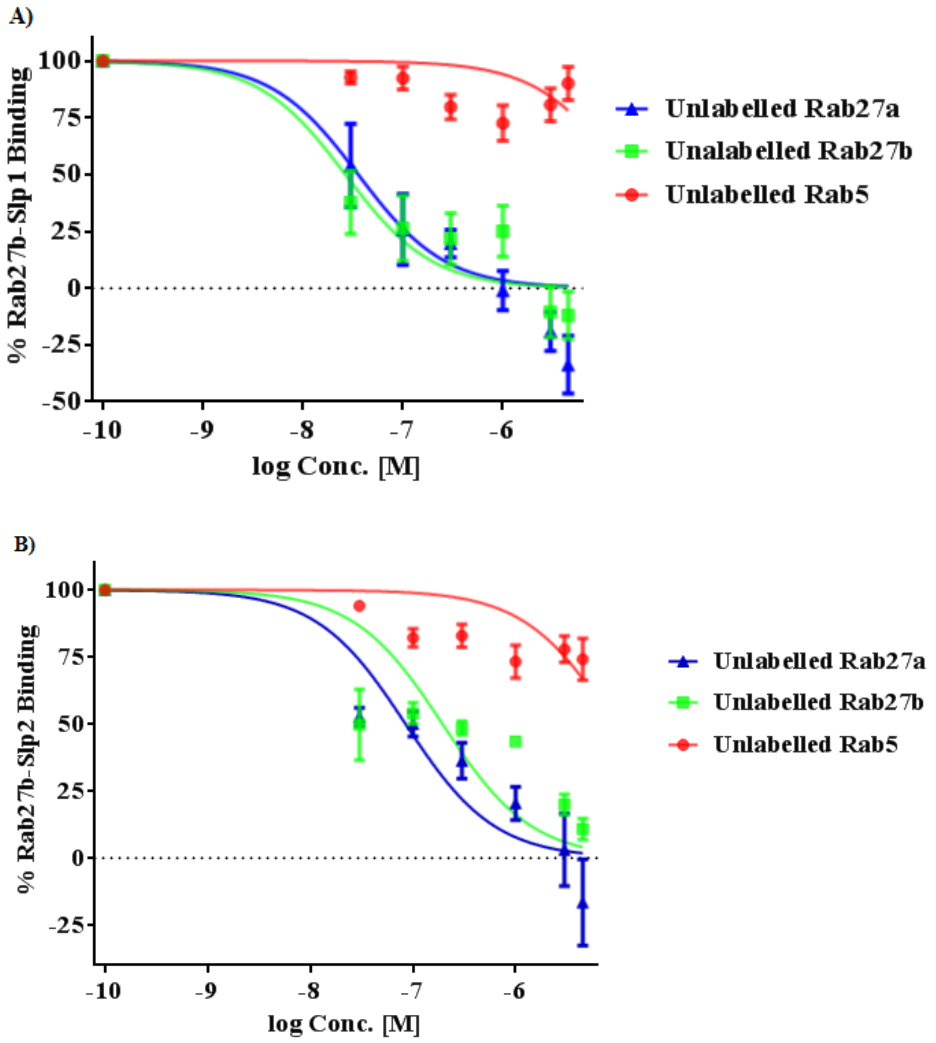


Figure 4.12. Disruption of hRab27b interaction with either mSlp1 or mSlp2 effector proteins using different unlabelled Rabs. Different concentrations (0.0, 0.03, 0.1, 0.3, 1.0, 3.0 and 4.5 µM) of unlabelled rRab27a and hRab27b; hRab5 (was used as a negative control) were used to disrupt the binding between: A) 0.15µM m.Cherry-hRab27b and 0.7µM GFP-mSlp1-(1-116). The calculated pIC50 values were 7.45M, 7.57M and 4.79M for unlabelled rRab27a, hRab27b and hRab5, respectively. B) 0.15µM m.Cherry-hRab27b and 0.3µM GFP-mSlp2-(3-80). The calculated pIC50 values were 7.07M, 6.71M and 5.04M for unlabelled rRab27a, hRab27b and hRab5, respectively. Data points represent mean ± SEM of 3 independent experiments performed in quadruplicates.

4.4 Discussion

Initially, this chapter experiments have mainly been focused on establishing and developing a robust FRET-based protein-protein interaction assay to be used as an in vitro measure of the binding affinity of Slp1 and Slp2 effector proteins to Rab2a/b proteins.

In order to obtain robust FRET signals, the acceptor and donor fluorophores with highest fluorescence intensity must be chosen to be used and their excitation-emission spectra should overlap (Piston and Kremers, 2007). Therefore, GFP-(mSlp1 or mSlp2) and m.Cherry-hRab27 recombinant proteins were chosen to used as donor and acceptor fluorophores, respectively. In addition, the fluorescence intensity of GFP and m.Cherry proteins are powerful and their excitation-emission spectra overlap as described in section 4.1. In the early stages, preliminary experiments were performed using the appropriate controls (GFP and m.Cherry proteins) to test the possibility of FRET occurrence between m.Cherry-hRab27b and GFP-mSlp1-(1-116) effector protein. These experiments demonstrated clearly that significant and specific FRET signals were obtained using those interacting components (Figure 4.4). In agreement with this, early FRET experiments using enhanced GFP-(donor)-DsRed-(acceptor) (the early discovered red fluorescent protein; for details see section 3.1) pair revealed that the critical distance (r_0) for FRET occurrence (when FRET efficiency is 50%) was 4.73nm (Patterson et al., 2000). Moreover, the calculated r_0 values of the enhanced GFP-(donor)-m.Cherry-(acceptor) (Akrap et al., 2010) and the enhanced ^{0}GFP-(donor)-m.Cherry-(acceptor) (Albertazzi et al., 2009) pairs were 5.24nm and 5.1nm, respectively. This suggests that GFP-mSlp1/2 and m.Cherry-hRab27 can produce significant FRET signals upon interaction of mSlp1/2 with hRab27, thus GFP and m.Cherry come close to each other, leading to FRET occurrence.

Together, the FRET evidence found in literature and preliminary data shown in Figure 4.4 provided the basis to perform further experiments and assured that this approach can be used to determine Rab27-effector protein interaction and optimisation of the assay was conducted accordingly.

In general, the FRET signals are not always powerful and detectable (Piston and Kremers, 2007), therefore the conditions of the FRET assay were optimised including optimisation of the concentration of GTP, the incubation time of the interacted components and using of the appropriate microplate reader with the proper fluorescence sensitivity. The binding increased dynamically within time until reaching saturation (after 2 hours incubation at room temperature) and 3mM GTP was optimum to obtain significant binding. This was evidenced by obtaining robust FRET signals using this GTP concentration which were not significantly different from that of using higher GTP concentrations as shown in Figures 4.5 and 4.6.

In addition, different concentrations of m.Cherry-hRab27b recombinant protein (0.6, 0.3 and 0.15 μM) were used to measure the FRET signals and fix the concentration of the acceptor protein as shown in Figures 4.7, 4.8 and 4.9. These experiments demonstrated that 0.15μM m.Cherry-hRab27 recombinant protein was optimum to obtain powerful FRET signals and saturate the binding with mSlp1 and mSlp2 effector proteins. Note that as the concentration of the acceptor (m.Cherry-hRab27) is increased, a wide range and higher concentrations of the donor (GFP-mSlp1 or GFP-mSlp2) should be used. Therefore, m.Cherry-hRab27 concentration was decreased and optimised as much as possible in order to use lower concentrations of the donor (due to volume limitations).

Accordingly, mSlp1 and mSlp2 binding affinity to hRab27b protein were determined and the pEC50 values were calculated accordingly. Negative control experiments were performed using the appropriate controls, these involved testing the interaction of: GFP with m.Cherry-hRab27b, m.Cherry with GFP-mSlp1-(1-116) and m.Cherry with GFP-mSlp2-(3-80). Altogether, the results of these control experiments demonstrated that the binding between m.Cherry-hRab27b and GFP-Slp1-(1-116) or GFP-mSlp2-(3-80) were specific and the binding affinity were not comparable to that of the negative control experiments. In addition, these experiments revealed that the binding affinity of mSlp2 to Rab27b is slightly higher than that of mSlp1. The slightly higher mSlp2 binding affinity over mSlp1 was further investigated by testing the binding of 0.7μM GFP-mSlp1-(1-116) and 0.3μM GFP-mSlp2 (3-80) to m.Cherry-hRab27b (full length, 1-218 and C-terminal truncated, 1-200) (Figure 4.10). The binding of

mSlp2 to either full length or C-terminal truncated Rab27b was slightly higher than that of mSlp1, since the used concentration of mSlp1 was almost double the concentration of mSlp2.

To further investigate this finding, the interaction of GFP-mSlp1-(1-116) and GFP-mSlp2-(3-80) with m.Cherry-hRab27a was tested (Figure 4.11). Recurrently, the binding affinity of mSlp2 to Rab27a was slightly higher than that of mSlp1.

As the binding affinity of mSlp2 is slightly higher than that of mSlp1 to either Rab27a or Rab27b, mSlp2 can be used as a typical Rab27 effector in this assay when testing the effects of the candidate inhibitors for these interactions.

To further assess the specificity of this assay in terms of using it to identify and determine the effects of the candidate inhibitors of Rab27-effector interactions, the information from the binding affinity experiments (the calculated EC50 values) was used to disrupt the interaction between Rab27b and Slp1/Slp2 using unlabelled Rab27a/b (as typical competitive inhibitors) and Rab5 was used as a negative control. The results of these experiments demonstrated that both unlabelled Rab27a/b were able to disrupt Rab27b-Slp1/2 interactions ((Figure 4.12).

Overall, both the binding affinity experiments using mSlp1 and mSlp2 effector proteins and the competition experiments using unlabelled Rab27a/b as typical competitive inhibitors confirmed the validity and fidelity of the FRET-based protein-protein interaction assay. This assured that this assay is powerful and robust in terms of determining Rab27-effector protein interaction and can be used to test the effects of the candidate small molecule and peptide inhibitors of these interactions in the future.

4.5 Conclusions

By optimisation of the FRET-based protein-protein interaction assay, significant and specific FRET signals were obtained. Therefore, this exquisite assay was utilised to determine the binding affinity of mSlp1 and mSlp2 to Rab27a/b and it was found that the binding affinity of mSlp2 is slightly higher than that of mSlp1 (evidenced by pEC50 differences). In addition, the specificity of this assay was confirmed using unlabelled Rab27a/b as typical competitive inhibitors and the pIC50 values for those inhibitors were determined. Accordingly, this assay can provide an in vitro read-out for Rab27-effector interactions and can be used in the future to identify candidate inhibitors of these interactions.

Chapter 5

Identification of the key determinants of the functional effects of Rab27-effector interactions on melanosome transport

5.1 Introduction

As mentioned earlier that the main aim of this project was to produce inhibitors of Rab27-effector interactions, therefore the key effector protein binding contacts of these interactions should be identified. To this end, a cellular melanosome clustering assay was used as a read-out for the functional effects of Rab27-effector interactions on melanosome transport in living cells (melan-a cells) (Hume et al., 2001; Strom et al., 2002).

Although a lot of work has been done to identify the key Rab27-effector binding contacts, many of the Rab27-effector interactions still need to be further investigated in order to identify the minimum effector protein fragments that can bind Rab27 protein. Accordingly, that information can be used to perform molecular dynamics simulation studies (by focusing on these fragments when performing these studies) in order to identify the key binding residues of these interactions, leading to production of Rab27-effector interaction inhibitors as described in chapter 6.

The crystal structure of Rab27 binding interface of only two Rab27 effectors (out of 11) is known as the 3D structure of Rab27a-Slp2 and Rab27b-Slac2-a binding interfaces have been determined (Chavas et al., 2008; Kukimoto-Niino et al., 2008). These structures provide the basis to test and investigate Rab27-effector interactions by focusing mainly on Slp1, Slp2 and Slac2-a effectors, since Slp1 and Slp2 are structurally related (Fukuda et al., 2001).

By using the melanosome clustering assay, successful candidate inhibitors of Rab27a-Slac2-a interaction-dependent melanosome transport can be identified by quantifying the induced perinuclear clustering of melanosomes. The melanosome clustering is caused by competing of those inhibitors with the endogenous Slac2-a for Rab27a interaction, thereby disrupting the Rab27a, Slac2-a and myosin-Va tripartite complex (Evans et al., 2014; Hume et al., 2001; Hume et al., 2006; Hume et al., 2007) (for further details see section 1.4.1.3). In addition, GFP expression was used as an indicator of gene and protein expression in cells (Chalfie et al., 1994).

Furthermore, the previously optimised FRET-based protein-protein interaction assay (see chapter 4) was used to test the effects of different mSlp2 fragments on Rab27-effector interaction, thereby comparing the results of the cellular and the in vitro assays.

5.2 Aims

The main aim of these experiments was to identify the key determinants of the functional effects of Rab27-effector interactions on melanosome transport in living cells, thereby indirectly determining the key binding contacts of Rab27-effector interactions. Accordingly, as a first step toward determining the key functional effects of mSlp1, mSlp2 and mSlac2-a on melanosome transport, different truncations of these effectors were tested. Furthermore, to identify the key Rab27 binding contacts and determine the minimum Rab27 binding fragments, the functional consequences of introducing different mutations into mSlp2 were tested. In parallel, different mSlp2 fragments were tested using the previously optimised FRET-based protein-protein interaction assay. That information was used to perform molecular dynamics simulation studies as described in chapter 6.

5.3 Results

5.3.1 Identifying the key determinants of Rab27a-Slac2-a interaction-dependent melanosome transport

In order to produce Rab27-effector interaction inhibitors, the cellular melanosome clustering assay (see section 2.4.5) was used as a read-out for Rab27a-Slac2-a interaction-dependent melanosome transport. Accordingly, adenoviruses expressing different mSlp1, mSlp2 and mSlac2-a effectors fragments were tested using this assay. Adenoviral-mediated infection was used in the those experiments, since this method is a highly efficient and convenient way to infect mammalian cells and can maintain stable gene expression (Kim and Eberwine, 2010). Melan-a melanocytes were infected with viruses expressing the indicated proteins as described in section 2.4.3 and examined using a Zeiss AxioVert S100 inverted fluorescence microscope (as described in section 2.4.4). In addition, GFP was used as a negative control in these experiments (differences in the shape of the dispersed and clustered melanosomes in melan-a melanocytes shown in Figure 5.1). Successful effector fragments induce perinuclear clustering of melanosomes by disrupting the interaction between Rab27a and endogenous mSlac2-a, thereby uncoupling melanosomes from actin in dendrites.

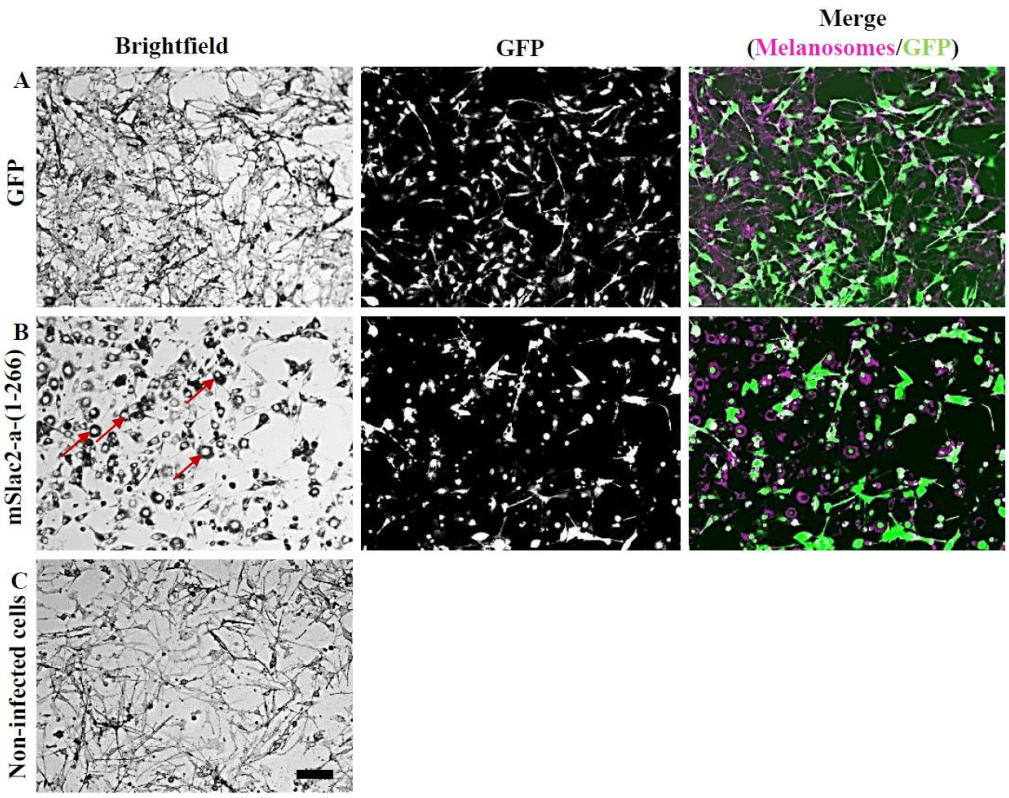


Figure 5.1. The cellular melanosome clustering assay as a read-out for Rab27a-Slac2-a interaction-dependent melanosome transport. Melan-a melanocytes were plated using 24-well (Nunc) plate. A) Melan-a melanocytes were infected with adenoviruses expressing GFP protein, the distribution of melanosomes was not affected (dispersed) as in the non-infected cells. B) Melan-a melanocytes were infected with adenoviruses expressing GFP-mSlac2-a-(1-266) protein, this resulted in inducing perinuclear clustering of melanosomes (the arrow indicated cells). C) Non-infected melan-a melanocytes showed dispersed distribution of melanosomes. In merge images, melanosomes are coloured magenta and GFP is coloured green. The cells were visualised (24-72 hours post-infection) using fluorescent microscopy. Scale bar represents 100µm.

5.3.2 mSlp2-(3-80) disrupts Rab27a-Slac2-a interaction-dependent melanosome transport

As a starting point to identify key determinants of Rab27a-Slac2-a interaction-dependent melanosome transport, mSlp2-(3-80) was chosen to be tested firstly, since this mSlp2 fragment encompasses all parts of Slp2 that are common with other Rab27 effectors. For instance, sequence alignment of different Rab27 effectors primarily demonstrated that mSlp2-a-(1-80) contains SHD1 and SHD2 regions for binding Rab27 (Fukuda et al., 2001). Furthermore, Kuroda et al. found that GST fused mSlp2-a-(1-87) can interact with FLAG tagged Rab27a

(GTP-bound) using a GST pull-down assay (Kuroda et al., 2002a). Also, the binding interface between Slac2-a and Rab27b was identified and sequence alignment of the binding interface of Slac2-a with Slp2 revealed that the crucial residues of Slp2 for Rab27 interaction lie between 1-80 aa (Kukimoto-Niino et al., 2008).

In this study, mouse Slp2 was used, therefore sequence alignment of human and mouse Slp2-(3-80) was performed to investigate whether the key Rab27 binding residues identified previously in the crystal structure of human Slp2-Rab27a complex (Chavas et al., 2008) are conserved between them or not. Sequence alignment clearly demonstrated that all the crucial Rab27 binding residues are conserved between them and sequence homology is 95%, suggesting that both human and mouse Slp2-(3-80) have similar Rab27 binding activities (Figure 5.2).

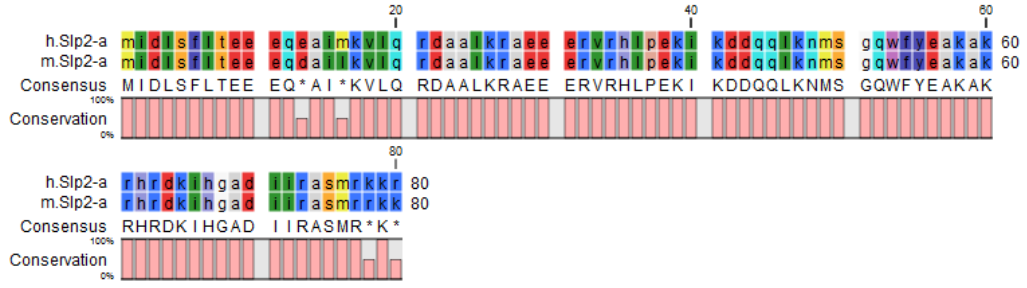


Figure 5.2. Amino acid sequence alignment of human and mouse Slp2-a. Sequence alignment of hSlp2-(3-80); NCBI Reference Sequence: NP_116561.1 and mSlp2-(3-80); GenBank: BAB41082.1 was performed with CLC sequence viewer 7.8.1. The degree of conservation is presented as bar plots from 0 to 100%; * stands for non-conserved residues. Sequence homology is 95%.

Accordingly, GFP-mSlp2-(3-80) was tested in terms of disrupting Rab27a-Slac2-a interaction-dependent melanosome transport in melan-a cells. As a positive control, GFP-mSlac2-a-(1-266) was used in these experiments (Strom et al., 2002). This fragment of Slac2-a contains the Rab27a binding domain (SHD1/2), but lacks the essential residues required to form stable interaction with myosin-Va motor protein, thus it competes with endogenous Slac2-a for Rab27a binding at the melanosome membrane, inducing perinuclear clustering of melanosomes by disrupting Rab27a-Slac2-a dependent melanosome transport

(Hume et al., 2006). The results of these experiments (Figure 5.3) demonstrated that mSlp2-(3-80) significantly disrupted Rab27a-Slac2-a interaction-dependent melanosome transport by inducing perinuclear clustering of melanosomes in 95.28% ±0.35 of expressing cells which was comparable to that of mSlac2-a-(1-266) (the positive control) as they were not significantly different. In comparison, GFP (the negative control) induced perinuclear clustering of melanosomes in 0.19% ±0.04 of expressing cells. This suggests that mSlp2-(3-80) exhibited this effect by competing with the endogenous mSlac2-a for Rab27a interaction, indicating that this mSlp2 fragment is able to stably interact with Rab27a in living cells.

Next, to identify the minimum mSlp2-Rab27a binding fragment and to further investigate whether mSlp2-(3-80) contains all the key contacts required for Rab27a binding, a point mutation was introduced at amino acid 3 of mSlp2 and 3-79 fragment of mSlp2 was tested. These mSlp2 fragments: mSlp2-(3-80; D3A) and mSlp2-(3-79) were able to induce perinuclear clustering of melanosomes in 94.42% ±0.55 and 95.13% ±0.63 of expressing cells, respectively (Figure 5.3). These effects were not significantly different from that induced by mSlp2-(3-80), suggesting that smaller mSlp2 fragments could disrupt Rab27a-Slac2-a interaction-dependent melanosome transport. Accordingly, further investigations were performed later in order to identify the key determinants of these effects as described in the subsequent sections.

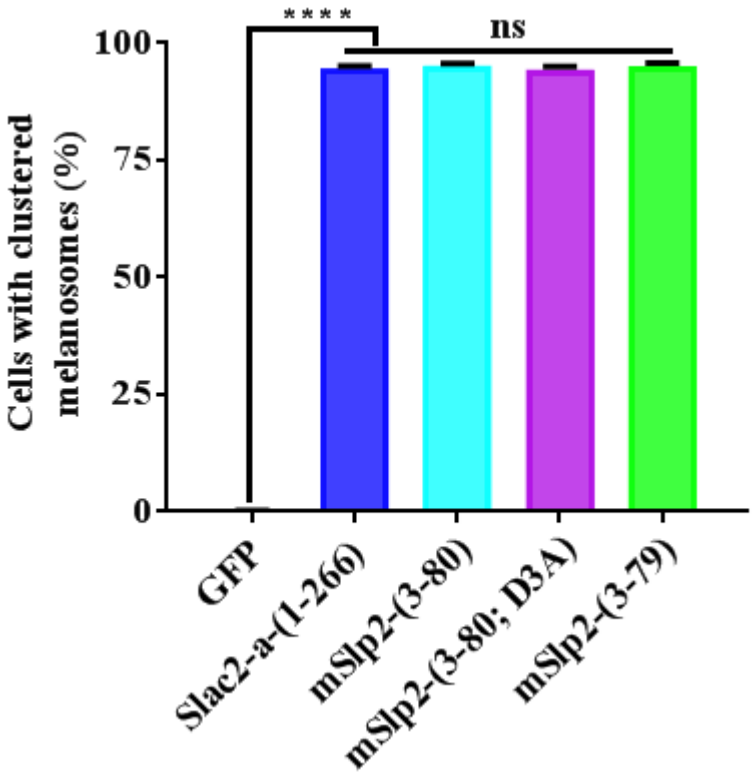


Figure 5.3. Effects of mSlp2-(3-80), mSlp2-(3-80; D3A) and mSlp2-(3-79) on Rab27a-Slac2-a interaction-dependent melanosome transport. Melan-a melanocytes were plated using 24-well (Nunc) plate and then infected using adenoviruses expressing the indicated proteins: GFP (as a negative control), GFP-mSlac2-a-(1-266) (as a positive control), GFP-mSlp2-(3-80), GFP-mSlp2-(3-80, D3A) and GFP-mSlp2-(3-79). The cells were visualised (24-72 hours post-infection) using fluorescent microscopy and cells with clustered melanosomes were then quantified. Data represent mean ± SEM of 3 independent experiments (4 images/experiment). One-way ANOVA: $^{ns}P > 0.05$; ****$P \leq 0.0001$.

5.3.3 Testing of the effects of introducing different point mutations into mSlp2-(3-80)

Next to further investigate and identify the functional effects of mSlp2 on Rab27a-Slac2-a interaction-dependent melanosome transport, different point mutations were introduced into mSlp2-(3-80). These mutations involved: K58A, R61A, H62A, G68I, D70A, I71A, R73A and S75A (see Figure 5.4). This was performed to investigate whether the introduction of any of these mutations into mSlp2-(3-80) could disrupt the induced perinuclear clustering of melanosomes, thus key contacts of Rab27a-Slp2 interaction can be identified.

The results of these experiments demonstrated that none of these mutations affected the induced perinuclear clustering of melanosomes in melan-a cells (Figure 5.5), since their effects were not significantly different from that of mSlp2-(3-80). This suggested that further investigations need to be performed to to identify key contacts of mSlp2-Rab27a interaction that can disrupt the induced perinuclear clustering of melanosomes. This was performed in the subsequent melanosome clustering assay experiments.

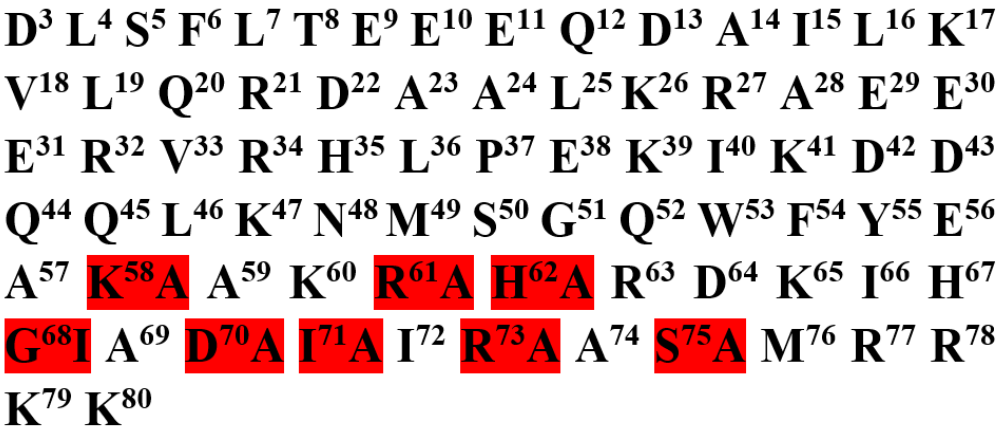


Figure 5.4. The introduced point mutations into mSlp2-(3-80). Different point mutations were introduced into mSlp2-(3-80) (highlighted in red).

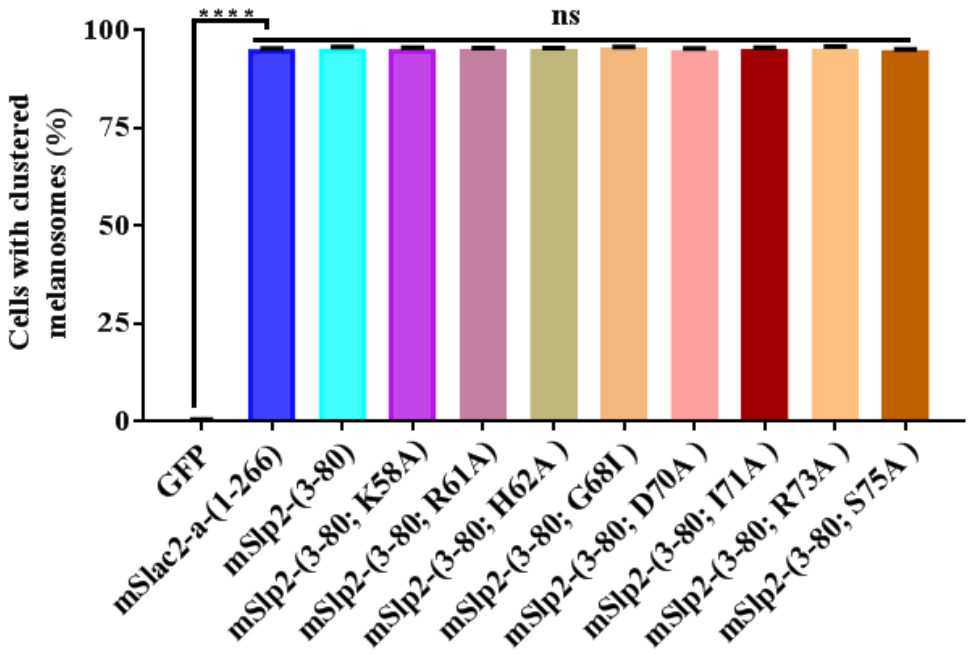


Figure 5.5. Introducing different point mutations into mSlp2-(3-80) does not affect the induced melanosome clustering. Melan-a melanocytes were plated using 24-well (Nunc) plate and then infected using adenoviruses expressing the indicated proteins: GFP (as a negative control), GFP-mSlac2-a-(1-266) (as a positive control), GFP-mSlp2-(3-80) (as a positive control), GFP-mSlp2-(3-80; K58A), GFP-mSlp2-(3-80; R61A), GFP-mSlp2-(3-80; H62A), GFP-mSlp2-(3-80; G68I), GFP-mSlp2-(3-80; D70A), GFP-mSlp2-(3-80; I71A), GFP-mSlp2-(3-80; R73A) and GFP-mSlp2-(3-80; S75A).The cells were visualised (24-72 hours post-infection) using fluorescent microscopy and cells with clustered melanosomes were then quantified. Data represent mean ± SEM of 3 independent experiments (4 images/experiment). One-way ANOVA: $^{ns}P > 0.05$; ****$P \leq 0.0001$.

5.3.4 mSlp2-(R32W) mutant partially disrupts Rab27a-Slac2-a interaction-dependent melanosome transport

In order to identify key contacts of Rab27-mSlp2 interaction, the R32W mutation was introduced into mSlp2-(3-80). The reasons behind choosing this mutation were as follows.

As the R35W mutation in Slac2-a causes GS type III (for further details see section 1.3.3) by disrupting Slac2-a binding to Rab27a, (Menasche et al., 2003b; Tomita and Suzuki, 2004), the equivalent mSlp2 residue was mutated by introducing the R32W mutation. In addition, R32 and R35 represent one of the

key residues of the binding interface of Rab27a-Slp2 and Rab27b-Slac2-a, respectively, since they make contacts with Y6 in Rab27a/b (Chavas et al., 2008; Kukimoto-Niino et al., 2008). Therefore, the R32W mutation in mSlp2 was chosen to be tested using the melanosome clustering assay.

The results of these experiments revealed that the introduction of this mutation into mSlp2-(3-80) induced perinuclear clustering of melanosomes in 53.03% ±2.83 of expressing cells compared with 95.29% ±0.08 using mSlp2-(3-80) (positive control), reducing 42% of its melanosome clustering inducing effects (Figure 5.6). This effect was significantly different from both the positive and negative controls. This indicates that this mutation partially inhibited the effects of mSlp2-(3-80) on melanosome transport, suggesting that R32 residue is one of the key Rab27 binding contacts that can be utilised when performing virtual screening of candidate small molecule inhibitors of Rab27-effector interactions.

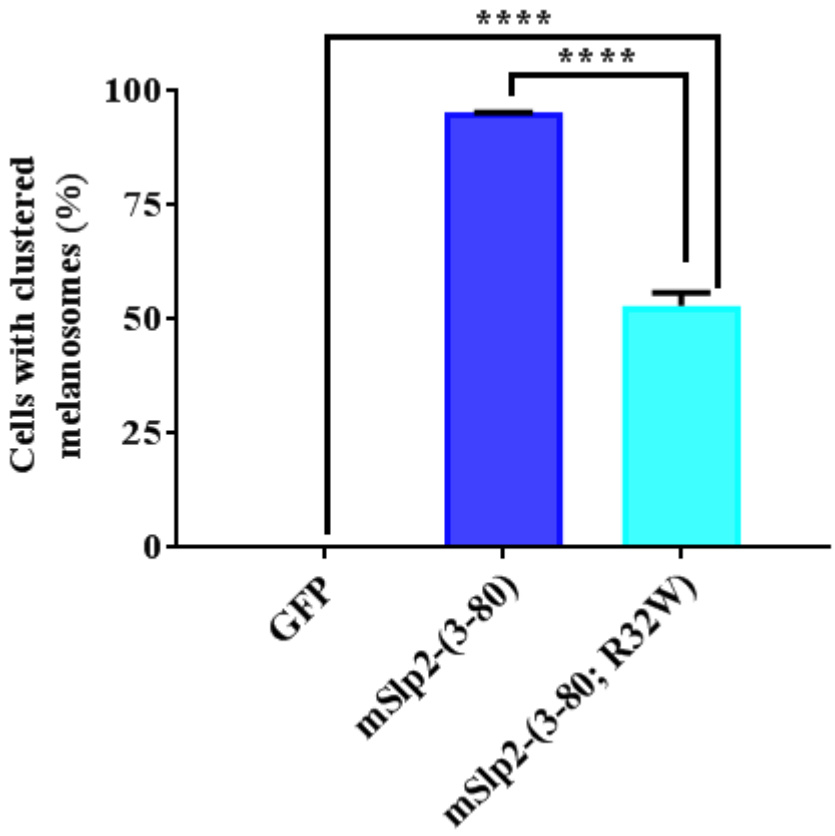


Figure 5.6. R32W mutation partially inhibits mSlp2-(3-80)-induced melanosome clustering. Melan-a melanocytes were plated using 24-well (Nunc) plate and then infected using adenoviruses expressing the indicated proteins: GFP (as a negative control), GFP-mSlp2-(3-80) (as a positive control) and GFP-

mSlp2-(3-80; R32W). The cells were visualised (24-72 hours post-infection) using fluorescent microscopy and cells with clustered melanosomes were then quantified. Data represent mean ± SEM of 3 independent experiments (4 images/experiment). One-way ANOVA: ****P ≤ 0.0001.

5.3.5 Testing of the inhibitory effects of different mSlp2 fragments on Rab27a-Slac2-a interaction-dependent melanosome transport

To further identify key contacts for interaction with Rab27a and to determine the minimum interacting fragment of mSlp2 that can disrupt Rab27a-dependent melanosome transport, different mSlp2 fragments were tested using the cellular melanosome clustering assay. These fragments were selected based on the identified 3-dimentional structure of the binding interface between Rab27a and Slp2 (Chavas et al., 2008). The binding interface comprises α1 (10-41 aa), α2 (42-50 aa) and α3 (51-56 aa) helices as shown in Figure 5.7 (α1 and α2-α3 represent SHD1 and SHD2 regions, respectively (for further details see sections 1.4 and 1.4.1.2).

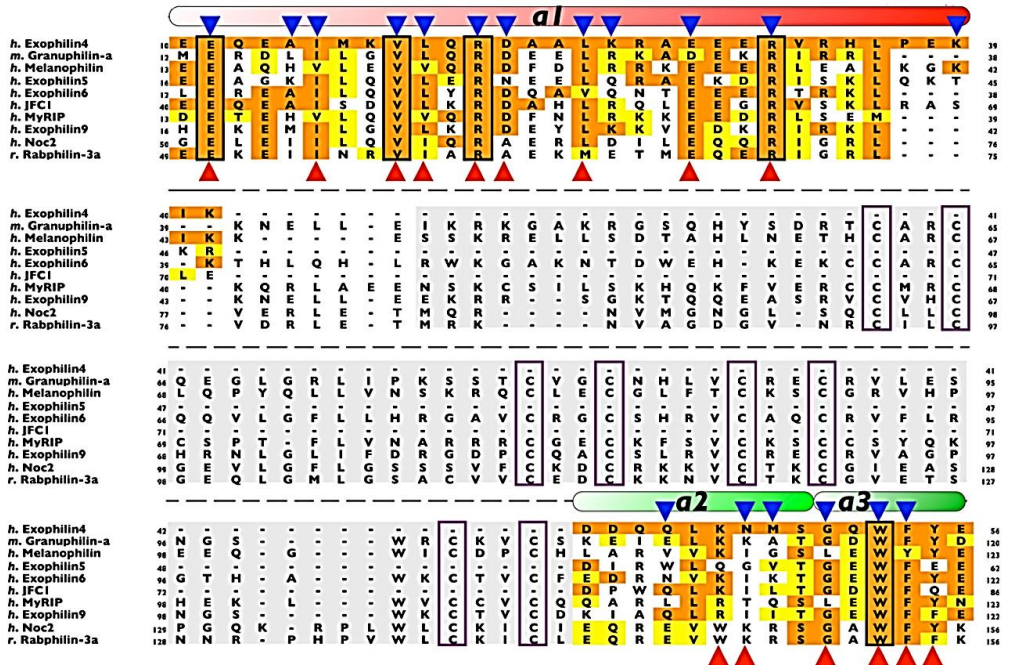


Figure 5.7. Sequence alignment of Slp2/Exophilin4-Rab27a binding interface with other Rab27 effector proteins. Black boxes represent highly conserved residues; red, green, and dark-green bars represent α1, α2 and α3 helices, respectively; grey-highlighted residues represent the zinc-finger motifs, purple boxes represent conserved cysteine residues. Slp2 and rabphilin-3a crucial binding residues for Rab27a and Rab3a presented as blue and red triangles, respectively. h; human, m; mouse, r; rat. Reproduced from (Chavas et al., 2008).

In order to investigate the effects of these helices (α1, α2 and α3) on melanosome transport, these Rab27 binding motifs were tested in an additive way; i.e. α1-(10-41), α1-α2-(10-50) and α1-α2-α3-(10-56). Surprisingly, none of these mSlp2 fragments succeeded in inducing significant perinuclear clustering of melanosomes as their effects were not significantly different from that of the negative control (GFP) (Figure 5.8), indicating that these fragments cannot stably interact with Rab27a and larger fragments required to be tested.

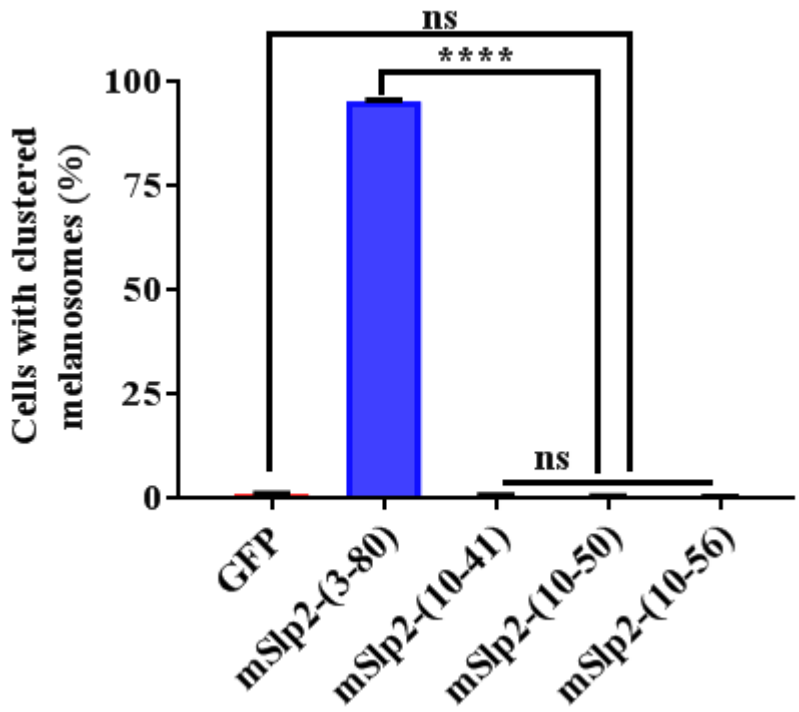


Figure 5.8. mSlp2-(10-41), mSlp2-(10-50) and mSlp2-(10-56) do not inhibit Rab27a-Slac2-a interaction-dependent melanosome transport. Melan-a melanocytes were plated using 24-well (Nunc) plate and then infected using adenoviruses expressing the indicated proteins: GFP (as a negative control), GFP-mSlp2-(3-80) (as a positive control), GFP-mSlp2-(10-41), GFP-mSlp2-(10-50) and GFP-mSlp2-(10-56). The cells were visualised (24-72 hours post-infection) using fluorescent microscopy and cells with clustered melanosomes were then quantified. Data represent mean ± SEM of 3 independent experiments (4 images/experiment). One-way ANOVA: $^{ns}P > 0.05$; ****$P \leq 0.0001$.

Accordingly, these mSlp2 fragments were extended at the N-terminal by testing the effects of mSlp2-(3-41) and mSlp2-(3-56) using the melanosome clustering assay (Figure 5.9). These experiments demonstrated that mSlp2-(3-41) effects were comparable to that of the negative control (GFP), whereas mSlp2-(3-56) induced perinuclear clustering of melanosomes in 36% ±0.74 of expressing cells compared with 95.10% ±0.32 using mSlp2-(2-3-80) (positive control). These effects were significantly different from that of mSlp2-(3-80), mSlp2-(3-41) and GFP. This suggests that mSlp2-(3-41) does not have the ability to disrupt Rab27a-Slac2-a interaction-dependent melanosome transport, whereas mSlp2-(3-56) had partial effects. This might be due to missing of some of the key Rab27 binding contacts (57-80 residues) in mSlp2-(3-56) which again suggested performing further investigations.

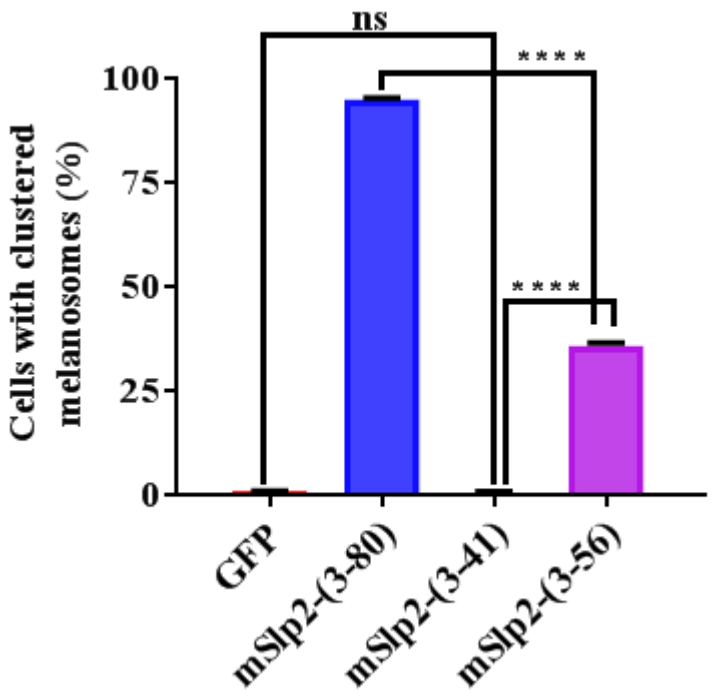


Figure 5.9. mSlp2-(3-56) partially inhibits Rab27a-Slac2-a interaction-dependent melanosome transport. Melan-a melanocytes were plated using 24-well (Nunc) plate and then infected using adenoviruses expressing the indicated proteins: GFP (as a negative control), GFP-mSlp2-(3-80) (as a positive control), GFP-mSlp2-(3-41) and GFP-mSlp2-(3-56).The cells were visualised (24-72 hours post-infection) using fluorescent microscopy and cells with clustered melanosomes were then quantified. Data represent mean ± SEM of 3 independent experiments (4 images/experiment). One-way ANOVA: $^{ns}P > 0.05$; ****$P \leq 0.0001$.

Parallel to the cellular melanosome clustering assay experiments and to better investigate the inhibitory effects of SHD1/2 of mSlp2, mSlp2-(3-41) and mSlp2-(3-56) fragments were tested using the FRET-based protein-protein interaction assay.

To this end, these mSlp2 fragments were produced as GST-fused recombinant proteins as described in section 5.3.9 (to be used as unlabelled competitive inhibitors; non-fluorescent) and tested using the FRET assay (the data were normalised using GST as a negative control). GST-mSlp2-(3-80) was used as a positive control to disrupt the interaction between hRab27b and mSlp1, since this fragment was used previously in the fluorescent GST-pull down assay as the main component for interaction with m.Cherry-Rab27b (see chapter 3). The findings of these competition experiments (Figure 5.10) demonstrated that mSlp2-(3-80) completely disrupted the interaction between hRab27b and mSlp1 evidenced by pIC50 (6.97M). In addition, these experiments showed that mSlp2-(3-41) and mSlp2-(3-56) were not comparable to mSlp2-(3-80) in terms of disrupting the interaction between hRab27b and mSlp1 evidenced by pIC50 differences [pIC50 mSlp2-(3-41); 6.57M, pIC50 mSlp2-(3-56); 6.47M]. Although these experiments demonstrated that none of these mSlp2 fragments were able to completely disrupt the interaction between hRab27b and mSlp1, mSlp2-(3-41) and mSlp2-(3-56) had partial inhibitory effects on hRab27b-mSlp1 interaction (evidenced by pIC50 values). This suggests that either mSlp2-(3-41) or mSlp2-(3-56) might provide initial platforms to develop Rab27-effector interaction inhibitors (see chapter 6).

In conclusion, testing of mSlp2-(3-41) and mSlp2-(3-56) using the cellular melanosome clustering and the FRET in vitro assays suggests that the in vitro results should always be confirmed by cellular or in vivo investigations and vice versa.

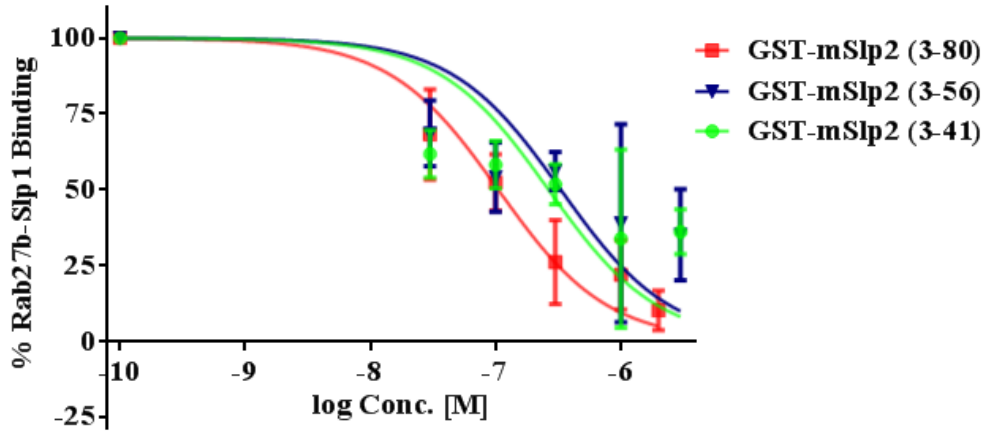


Figure 5.10. Testing the effects of GST-mSlp2-(3-41) and GST-mSlp2-(3-56) on hRab27b-mSlp1 interaction. Different GST-fused mSlp2 fragments were tested in terms of inhibiting the interaction between 0.15µM m.Cherry-hRab27b and 0.7µM GFP-mSlp1-(1-116). GST-mSlp2-(3-80) (0.0, 0.03, 0.1, 0.3, 1.0 and 2.0 µM) was used as a positive control; pIC50: 6.97M. The effects of GST-mSlp2-(3-41) and GST-mSlp2-(3-56) on the binding were tested using different concentrations (0.0, 0.03, 0.1, 0.3, 1.0 and 3.0 µM). pIC50 mSlp2-(3-41): 6.57M; pIC50 mSlp2-(3-56): 6.47M. The FRET based protein-protein interaction assay was used to determine the binding. Data points represent mean ± SEM of 3 independent experiments performed in quadruplicates.

5.3.6 mSlp2-(3-67) is comparable to mSlp2-(3-80) in terms of inducing melanosome clustering

As explained in section 5.3.5, mSlp2-(3-56) had partial melanosome clustering inducing effects, therefore larger fragment(s) required to be investigated. To this end, mSlp2-(3-67) was chosen to be tested using the melanosome clustering assay, since sequence alignment of mSlp2 with Rab27b-Slac2-a binding interface demonstrated that mSlp2-(3-67) encompasses all the equivalent Slac2-a residues required to interact with Rab27b in the 3D complex structure (the last essential residue for binding of Slac2-a to Rab27b is G133 in α5 helix which is equivalent to H67 in mSlp2 structure) (see Figure 5.11) (Kukimoto-Niino et al., 2008).

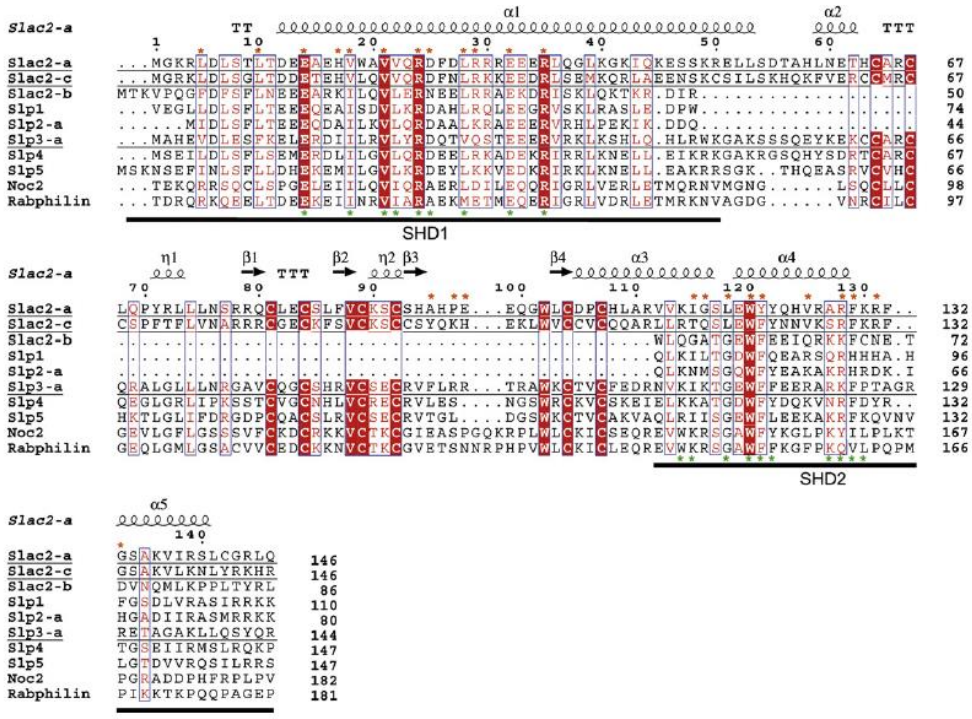


Figure 5.11. Sequence alignment of mSlac2-a-mRab27b binding interface with other Rab27 effector proteins. mSlac2-a and rabphilin crucial binding residues for Rab27b and Rab3a presented as red and green asterisks, respectively. Red boxes (white coloured residues) and red coloured residues represent highly conserved residues and less conserved residues, respectively. Reproduced from (Kukimoto-Niino et al., 2008).

mSlp2-(3-67) testing experiments revealed that mSlp2-(3-67) was comparable to mSlp2-(3-80) as it induced perinuclear clustering of melanosomes in 95.16% ±0.2 of expressing cells and this effect was not significantly different from that of mSlp2-(3-80), suggesting that mSlp2-(3-67) might be the minimum Rab27a binding fragment that contains all the essential interacting residues with Rab27a (Figure 5.12).

To better investigate this finding, a smaller mSlp2 fragment was tested (mSlp2-10-67). These experiments demonstrated that mSlp2-(10-67) partially induced perinuclear clustering of melanosomes in 72.75% ±0.9 of expressing cells compared with 95.43% ±0.11 and 1.02% ±0.12 using mSlp2-(3-80) and GFP, respectively (Figure 5.12). This effect was significantly different from that of mSlp2-(3-80), mSlp2-(3-67) and GFP. This indicates that mSlp2-(10-67) might partially inhibit Rab27a-Slac2-a binding by 72.75%, suggesting again that

mSlp2-(3-67) fragment might encompass all the key determinants of Rab27-Slp2 interactions.

These findings indicate that the deletion of the first (3-9) amino acids in the N-terminus of mSlp2 resulted in reducing the induced perinuclear clustering of melanosomes by 22.41%, since mSlp2-(10-67) induced melanosome clustering in 72.75% of expressing cells compared with 95.16% using mSlp2-(3-67), suggesting that the contribution of the 3-9 amino acids in the disruption of Rab27a-Slac2-a interaction-dependent melanosome transport is 22.41%. In addition, these experiments indicate that 57-67 residues of mSlp2 might be essential for Rab27a binding as extending mSlp2-(3-56) (see section 5.3.5) to mSlp2-(3-67) resulted in increasing the induced melanosome clustering by 59.16%, suggesting that 57-67 amino acids might contribute to 59.16% of the inhibitory effect on Rab27a-Slac2-a interaction-dependent melanosome transport.

These findings are supported by sequence alignment of mSlp2 with Rab27b-Slac2-a binding interface (Figure 5.11), since D3, L4, S5, L7, T8 and R61 mSlp2 residues are conserved between mSlp2 and Slac2-a, highlighting the importance of these residues in Rab27a binding.

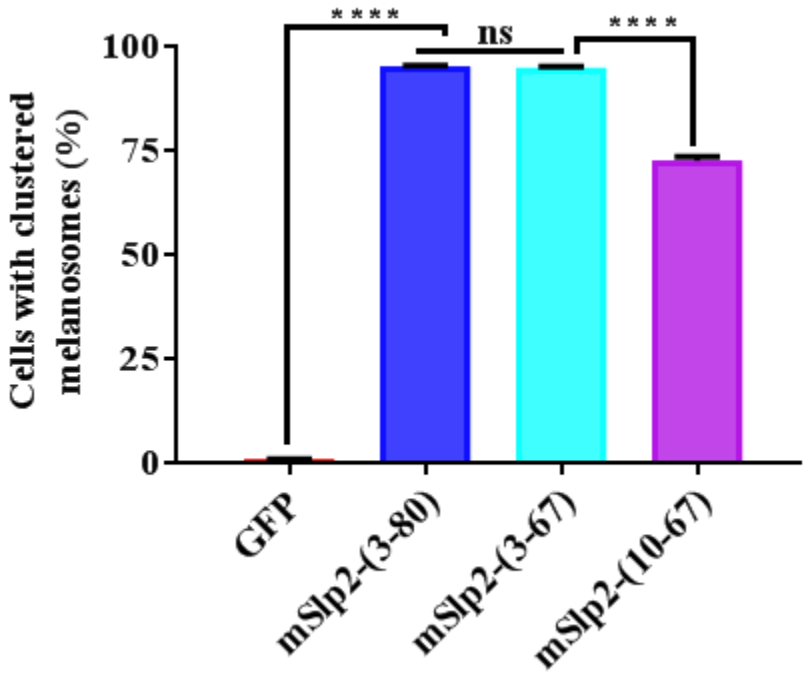


Figure 5.12. Testing of the inhibitory effects of mSlp2-(3-67) and mSlp2-(10-67) on Rab27a-Slac2-a interaction-dependent melanosome transport. Melan-a melanocytes were plated using 24-well (Nunc) plate and then infected using adenoviruses expressing the indicated proteins: GFP (as a negative control), GFP-mSlp2-(3-80) (as a positive control), GFP-mSlp2-(3-67) and GFP-mSlp2-(10-67). The cells were visualised (24-72 hours post-infection) using fluorescent microscopy and cells with clustered melanosomes were then quantified. Data represent mean ± SEM of 3 independent experiments (4 images/experiment). One-way ANOVA: $^{ns}P > 0.05$; ****$P \leq 0.0001$.

5.3.7 mSlp1-(1-116) disrupts Rab27a-Slac2-a interaction-dependent melanosome transport

mSlp1 was another Rab27 effector protein that was tested in this study as it is structurally related to mSlp2 and shares many of the Rab27 interacting residues with Slp2 and Slac2-a effector proteins (see sections 1.4, 1.4.1.1, 1.4.1.2 and 1.4.1.3)

According to sequence alignment of Slp1 with other Rab27 effector proteins, mSlp1-(1-116) contains SHD1/2 regions required for binding to Rab27 protein (Fukuda et al., 2001). This is in agreement with testing of this mSlp1 fragment using the GST pull-down assay, since GST fused mSlp1-(1-117) is able to interact with FLAG tagged Rab27a (GTP-bound) (Kuroda et al., 2002a).

In addition, sequence alignment with Rab27b-Slac2-a binding interface demonstrates that 1-74 (SHD1) and 75-116 (SHD2) Slp1 fragments contain all the essential Rab27 binding residues (Kukimoto-Niino et al., 2008; Kuroda et al., 2002a) (see Figure 5.11). That information in the literature called attention to test mSlp1-(1-116) using the melanosome clustering assay. Notably, sequence alignment of human and mouse Slp1-(1-116) demonstrated that most of the crucial Rab27 binding residues are conserved between them and sequence homology is 87% (Figure 5.13), suggesting that both human and mouse Slp1-(1-116) have similar Rab27 binding activities (this was performed as mouse Slp1 was used in this study).

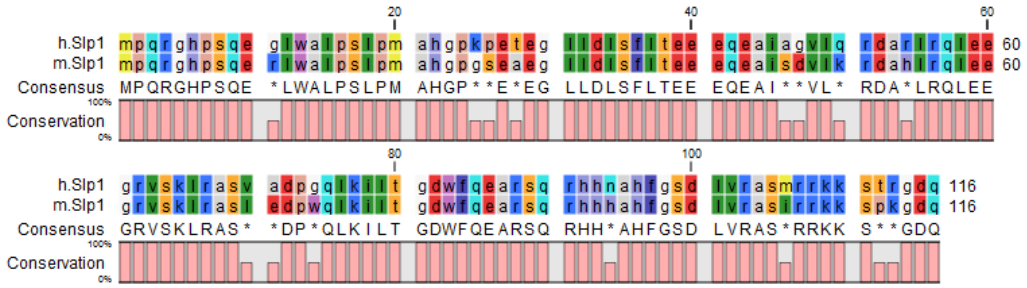


Figure 5.13. Amino acid sequence alignment of human and mouse Slp1. Sequence alignment of hSlp1-(1-116); GenBank: AAH35725.1 and mSlp1-(1-116); NCBI Reference Sequence: NP_113570.2 was performed with CLC sequence viewer 7.8.1. The degree of conservation is presented as bar plots from 0 to 100%; * stands for non-conserved residues. Sequence homology is 87%.

Accordingly, different mSlp1 fragments were tested in terms of inducing of perinuclear clustering of melanosomes in melan-a cells. These fragments comprised: mSlp1-(1-116), mSlp1-(1-74) (SHD1) and mSlp1-(70-116) (SHD2).

The results of these experiments demonstrated that mSlp1-(1-116) was comparable to mSlp2-(3-80) by inducing perinuclear clustering of melanosomes in 95.4% ±0.22 of expressing cells (Figure 5.14).

mSlp1-(1-74) induced perinuclear clustering of melanosomes in 18.33% ±0.94 of expressing cells, whereas mSlp1-(70-116) was comparable to the negative control (GFP), suggesting that SHD1 is more important than SHD2 for Rab27a binding (Figure 5.14). To investigate whether mSlp1-(1-74) and mSlp1-(70-116) could work additively or synergistically, a combination of both of them was tested. The combination of mSlp1-(1-74) and mSlp1-(70-116) induced perinuclear clustering of melanosomes in 20.11% ±2.56 of expressing cells; i.e. comparable to mSlp1-(1-74) alone (Figure 5.14). This indicates that the combination of both SHD1/2 was not sufficient to obtain comparable inhibitory effects to that of mSlp1-(1-116); i.e. the combination strategy is not effective in terms of producing comparable results, since splitting SHD regions might change protein conformation of the binding interface.

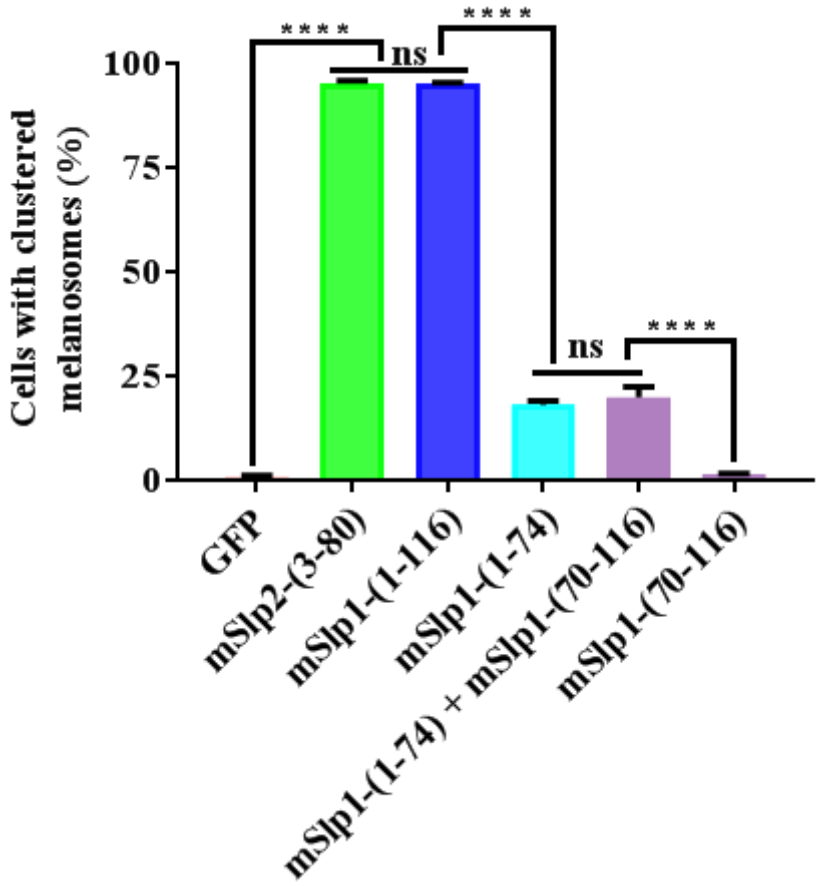


Figure 5.14. mSlp1-(1-116) is comparable to mSlp2-(3-80) in terms of disrupting Rab27a-Slac2-a interaction-dependent melanosome transport. Melan-a melanocytes were plated using 24-well (Nunc) plate and then infected using adenoviruses expressing the indicated proteins: GFP (as a negative control), GFP-mSlp2-(3-80) (as a positive control), GFP-mSlp1-(1-116), GFP-mSlp1-(1-74), GFP-mSlp1-(70-116) and combination of GFP-mSlp1-(1-74)/GFP-mSlp1-(70-116).The cells were visualised (24-72 hours post-infection) using fluorescent microscopy and cells with clustered melanosomes were then quantified. Data represent mean ± SEM of 3 independent experiments (4 images/experiment). One-way ANOVA: $^{ns}P > 0.05$; ****$P \leq 0.0001$.

Next, to further investigate that the combination of both SHD1/2 was not sufficient to disrupt Rab27a-Slac2-a interaction-dependent melanosome transport, mSlp1-(1-74) was produced as m.Cherry fused protein. This was performed to confirm that the obtained results were not related to insufficient protein expression (as both SHD1/2 were GFP fusion proteins in the previous experiments). Accordingly, a combination of both m.Cherry-mSlp1-(1-74) and

GFP-mSlp1-(70-116) were tested. Again, quantification of these data showed comparable results (data not shown).

In conclusion, these experiments demonstrated that mSlp1-(1-116) was comparable to mSlp2-(3-80) and the combination of SHD1/2 was not comparable to mSlp1-(1-116) (when SHD1/2 tested as a whole fragment), highlighting the importance of further investigating Slp1 (SHD1/2) in the future.

5.3.8 mSlac2-a-(1-146) is not comparable to mSlac2-a-(1-266) in terms of disrupting Rab27a-Slac2-a interaction-dependent melanosome transport

As the 3-dimentional structure of the binding interface between Slac2-a and Rab27b is known (Kukimoto-Niino et al., 2008), it was hypothesised that testing of Slac2-a might provide an initial platform to identify Rab27 key binding contacts. Based on the identified crystal structure of interaction with Rab27b, mSlac2-a-(146) was selected to be tested using the melanosome clustering assay, since it contains all the essential Rab27 binding residues as described in section 1.4.1.3 (see Figures 1.17 and 5.11).

In addition, sequence alignment of human and mouse Slac2-a-(1-146) demonstrated that all the essential Rab27 binding residues are conserved between them and sequence homology is 85.6% (Figure 5.15) (this was performed as mouse Slac2-a was used in this study).

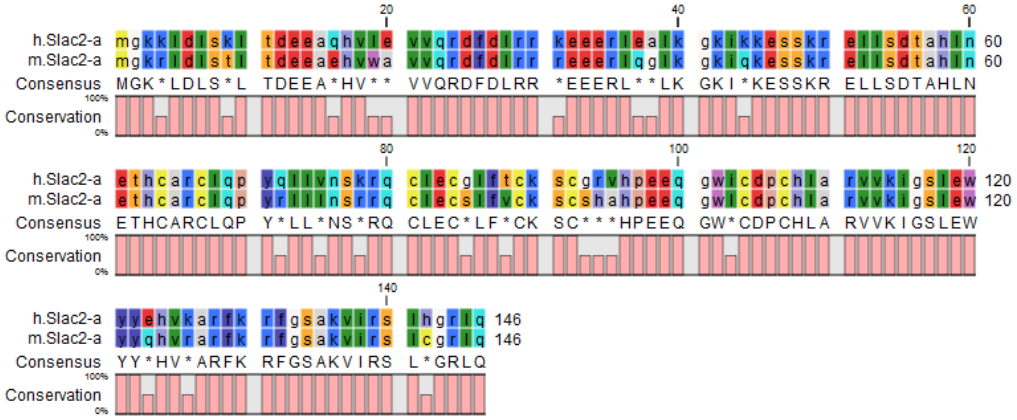


Figure 5.15. Amino acid sequence alignment of human and mouse Slac2-a. Sequence alignment of hSlac2-a-(1-146); GenBank: AAH51269.1 and mSlac2-a; NCBI Reference Sequence: NP_443748.2 was performed with CLC sequence

viewer 7.8.1. The degree of conservation is presented as bar plots from 0 to 100%; * stands for non-conserved residues. Sequence homology is 85.6%.

Testing of mSlac2-a-(1-146) using the melanosome clustering assay demonstrated that this fragment partially induced perinuclear clustering of melanosomes in 71.58% ±0.29 of expressing cells compared with 94.23% ±0.39 and 95.23% ±0.34 using mSlac2-a-(1-266) and mSlp2-(3-80), respectively (Figure 5.16). This suggests that this mSlac2-a fragment is not comparable to mSlac2-a-(1-266) or mSlp2-(3-80) in terms of inducing melanosome clustering and disrupting Rab27a interaction with endogenous Slac2-a.

Other studies suggest that Slac2-a-(1-153) encompasses SHD1 and SHD2 regions required for binding to Rab27 (based on sequence alignment with other Rab27 effectors) (Fukuda et al., 2001). In addition, by using GST pull-down assay, GST fused mSlac2-a-(1-153) interacts with FLAG tagged Rab27a (GTP-bound) (Kuroda et al., 2002a). This highlights the importance of testing larger Slac2-a fragments in the future.

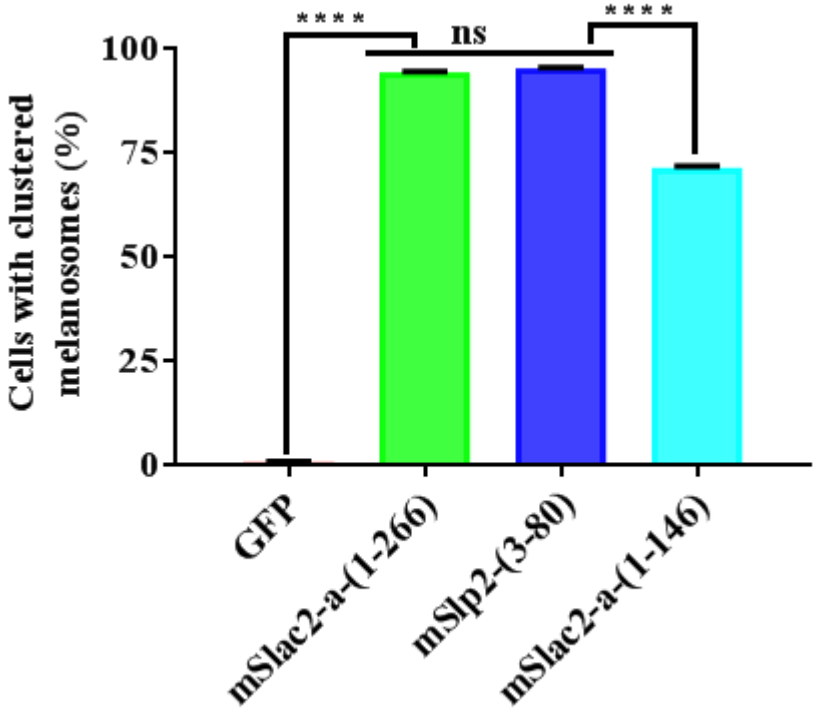


Figure 5.16. mSlac2-a-(1-146) does not completely disrupt Rab27a-Slac2-a interaction-dependent melanosome transport. Melan-a melanocytes were plated using 24-well (Nunc) plate and then infected using adenoviruses expressing the indicated proteins: GFP (as a negative control), GFP-mSlac2-a-(1-266) (as a positive control), GFP-mSlp2-(3-80) (as a positive control) and GFP-mSlac2-a-(1-146). The cells were visualised (24-72 hours post-infection) using fluorescent microscopy and cells with clustered melanosomes were then quantified. Data represent mean ± SEM of 3 independent experiments (4 images/experiment). One-way ANOVA: $^{ns}P > 0.05$; ****$P \leq 0.0001$.

5.3.9 Generation of GST-mSlp2-(3-41) and GST-mSlp2-(3-56) recombinant proteins

In order to produce GST-mSlp2-(3-41) and GST-mSlp2-(3-56) recombinant proteins (see section 5.3.5), the pGEX-4T1-mSlp2-(3-41) and pGEX-4T1 mSlp2-(3-56) vectors (see section 2.1.3.3) were transformed into Rosetta E. *coli* competent cells and protein production was induced with 0.5mM IPTG as described in section 2.2.2, this was followed by performing protein purification steps using an affinity interaction with reduced glutathione (GSH)-sepharose beads as described in section 2.2.3.2).

Analysis of the purified proteins using 10% SDS-PAGE gel electrophoresis confirmed that induction of protein production was successful and abundant protein bands were detected at the predicted molecular weights for GST-mSlp2-(3-41); 32.98KDa (Figure 5.17) and GST-mSlp2-(3-56); 35.08KDa (data not shown).

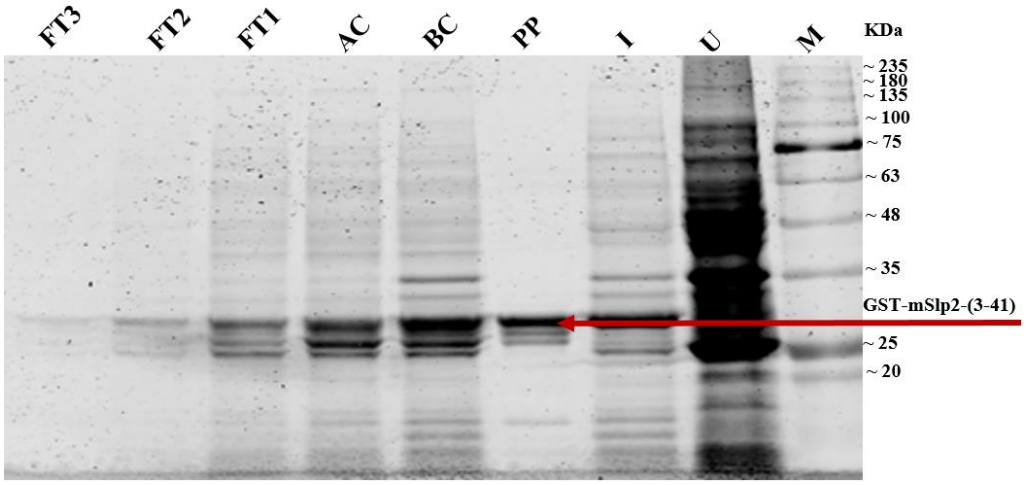


Figure 5.17. Production and purification profile of the GST-mSlp2-(3-41) recombinant protein. Rosetta *E. coli* competent cells were transformed with the pGEX-4T1-mSlp2-(3-41) vector, protein production was induced using 0.5mM IPTG for 3 hours at 37ºC. Protein production and purification steps were analysed using an instant blue stained 10% SDS-PAGE gel: M; molecular weight standards, U, I; uninduced and induced *E. coli* cell extracts, PP; purified protein, BC; cell lysates before centrifugation, AC; supernatant after centrifugation, FT1, 2, 3; 1st, 2nd and 3rd flow-through from GSH column after several washes with the dialysis buffer. An abundant protein band (the arrow indicated band) was detected at the predicted molecular weight for the GST-mSlp2-(3-41) recombinant protein (32.98KDa).

5.4 Discussion

Overall, the major findings of this chapter experiments were: First, mSlp2-(3-80), mSlp2-(3-67) and mSlp2-(1-116) were able to significantly inhibit Rab27a-Slac2-a interaction-dependent melanosome transport. Second, the introduction of the R32W mutation into mSlp2-(3-80) resulted in partial loss of its inhibitory activity. Third, testing of different mSlp2 truncations based on the crystal structure of the binding interface between Slp2 and Rab27a unexpectedly revealed that none of them succeeded in obtaining significant inhibitory effects in living cells, but partial inhibitory effects were obtained by using mSlp2-(3-56). Fourth, mSlp2-(3-41) and mSlp2-(3-56) had partial inhibitory effects on Rab27b-Slp1 interaction in vitro. Fifth, testing of different mSlp1 truncations containing either SHD1 or SHD2 regions failed in producing significant inhibitory effects in living cells. Sixth, Slac2-a-(1-146) had partial inhibitory effects in living cells (was tested based on the crystal structure of the binding interface between Slac2-a and Rab27b).

The melanosome clustering assay was used in this chapter experiments to investigate the functional effects of different Rab27 effectors on Rab27a-Slac2-a interaction-dependent melanosome transport. Thus this assay was considered as an indirect read-out for Rab27-effector interaction and was used to identify key contacts of these interactions.

mSlp2-(3-80) was firstly chosen to be tested and it had comparable effects to mSlac2-a-(1-266) (positive control) in terms of inducing perinuclear clustering of melanosomes by inhibiting Rab27a-Slac2-a interaction-dependent melanosome transport (Figure 5.3). This is in agreement with the results of testing this mSlp2 fragment using the fluorescent GST pull down and the FRET-based in vitro assays (see chapters 3 and 4).

Accordingly, to further investigate whether mSlp2-(3-80) was the minimum Rab27a binding fragment, mSlp2-(3-80; D3A) and mSlp2-(3-79) were tested. Again, infection of melan-a cells using these two mSlp2 fragments resulted in producing comparable effects to that of mSlp2-(3-80) (Figure 5.3). These experiments indicate that mSlp2-(3-80) was not the minimum Rab27 binding fragment and comparable effects might be obtained by testing smaller fragments,

suggesting that further investigations need to be performed. Therefore, different point mutations were introduced into mSlp2-(3-80 (Figure 5.4) to identify key contacts of Rab27-effector interactions. Repeatedly, these experiments failed in identifying Rab27 key contacts, suggesting that smaller fragments were required to be tested (Figure 5.5).

Moreover, the R32W mutation was introduced into mSlp2-(3-80) as this mutation equivalents to R35W mutation in Slac2-a (see sections 1.3.3 and 5.3.4). Upon introducing this mutation, the effect of mSlp2-(3-80) on the perinuclear clustering of melanosomes was decreased by 42% (Figure 5.6). Since the R residue is positively charged, replacement with W (which has bulky aliphatic chain; α-amino and α-carboxylic acid groups) might disrupt the interaction with Rab27a (Menasche et al., 2003b). Notably, overexpression of Slp2-a-(E11A, R32A) in melan-a cells did not induce perinuclear clustering of melanosomes, indicating that this Slp2-a mutant lacks the ability to interact with Rab27a and competes with Slac2-a for Rab27a binding (Kuroda and Fukuda, 2004). This suggests that E11A, R32A mutations might work synergistically or additively to disrupt the interaction with Rab27a. This assumption is in agreement with the results of this study, since the introduction of the R32W mutation partially induced perinuclear clustering of melanosomes. Accordingly, that information (the identification of the R32 residue as one of the key contacts of Rab27-Slp2 interaction) can be used to perform virtual screening to identify candidate small molecule inhibitors of Rab27-effector interactions in the future by focusing on the pocket of interaction of Rab27 with R32 residue in Slp2.

In addition, the already identified crystal structure of Rab27a-Slp2-(10-56) complex interface (Chavas et al., 2008) was investigated by testing the inhibitory effects of α1-(10-41), α1-α2-(10-50) and α1-α2-α3-(10-56); i.e. SHD1, SHD1+ α2 and SHD1/2. Unexpectedly, none of these mSlp2 fragments succeeded in inducing perinuclear clustering of melanosomes (Figure 5.8), indicating that the findings of this study were in disagreement with the results of the crystal structure of Slp2-Rab27a complex and mSlp2-(10-56) fragment does not encompass all the Rab27a binding interface. This suggested that additional key binding residues need to be investigated by testing larger fragments. In contrast, it has been found that the interaction of Slp4-a with the Q78L constitutively

active mutant (GTP-bound) of Rab27a requires SHD1 only, whereas the interaction with the T23N dominant negative (GDP-bound) mutant of Rab27a requires both SHD1 and SHD2, also the TGDWFY motif in SHD2 confers specificity for Rab27a-(T23N) binding (Fukuda, 2003b). Similarly, it has been shown that SHD1 domain of Noc2 is sufficient to interact with Rab27a (Fukuda et al., 2004). This might be related to the fact that SHD1 and SHD2 of Slp4-a and Noc2 are separated by zinc finger motif (unlike Slp2), thus SHD1 and SHD2 might exert independent Rab27 binding activities, whereas in Slp2 as both SHD1 and SHD2 are linked directly, their binding interfaces with Rab27 might overlap with each other, suggesting that both SHD1/2 of Slp2 are required for Rab27 binding.

Apparently, those mSlp2 α-helices were unable to stably interact with Rab27a. The problem with the use of mSlp2 α-helices as a hot spot binding sites might be related to the lack of helicity, thereby reducing or even abolishing their binding affinity (Zhao et al., 2017). Therefore, the N-terminus of these fragments were extended further. These experiments demonstrated that mSlp2-(3-41) negligibly induced perinuclear clustering of melanosomes. In comparison mSlp2-(3-56) partially induced perinuclear clustering of melanosomes (Figure 5.9). This highlights the importance of the N-terminus in stabilising the interaction with Rab27a.

In addition, the effects of SHD1/2 of mSlp2 on Rab27-effector interaction were tested in vitro using the FRET-based protein-protein interaction assay (Figure 5.10). mSlp2-(3-41) and mSlp2-(3-56) had partial inhibitory effects on hRab27b-mSlp1 interaction (evidenced by pIC50 differences). The inhibitory effect produced by mSlp2-(3-56) was in line with the results of testing this fragment using the cellular melanosome clustering assay, whereas testing mSlp2-(3-41) was inconsistent with the results of the melanosome clustering assay (see Figure 5.9). This suggests that mSlp2-(3-41) and mSlp2-(3-56) might contain essential contacts to interact with Rab27 which can be used to develop Rab27 inhibitors (see chapter 6).

The findings of the FRET-based and the cellular melanosome clustering assays suggest that in vitro results of protein-protein interactions are not always

consistent with the results from cellular assays, therefore in vitro findings of those interactions should always be confirmed by in vivo and/or cellular assays.

Next, mSlp2-(3-67) was chosen to be tested based on sequence alignment of mSlp2 with Rab27b-mSlac2-a binding interface as described in section 5.3.6. These experiments demonstrated that mSlp2-(3-67) was comparable to mSlp2-(3-80) in terms of inducing melanosome clustering (Figure 5.12). This suggested that comparable effects might be obtained using smaller mSlp2 fragment(s), therefore mSlp2-(10-67) was chosen to be tested and it was found that this fragment can partially induce melanosome clustering by 72.75% (Figure 5.12).

Altogether, these results suggest that the first 3-9 residues in the N-terminus of mSlp2 might contribute to 22.41% of the inhibitory effect on Rab27a-Slac2-a interaction-dependent melanosome transport. This is evidenced by comparing mSlp2-(10-67) and mSlp2-(3-67) melanosome clustering inducing effects. In comparison, 57-67 mSlp2 residues might account for 59.16% of the inhibitory effect; this is evidenced by comparing mSlp2-(3-56) and mSlp2-(3-67) melanosome clustering inducing effects. This suggests that the first 3-9 aa and the last 57-67 aa of mSlp2-(3-67) might stabilise the interaction with Rab27a which requires further investigations in the future. However, to the best of found knowledge, this is the first study that suggests that mSlp2-(3-67) is the minimum Rab27 interacting fragment that can give significant melanosome clustering effects comparable to that of mSlp2-(3-80). In previous studies, larger Slp2 fragments were tested, for instance Slp2-(1-87) was used to determine the binding to Rab27a using co-immunoprecipitation assays (Fukuda, 2006; Kuroda et al., 2002a).

To expand our understanding of the key contacts of Rab27-effector interactions, Slp1 effector protein was also chosen to be tested in this study. The results of these experiments (Figure 5.14) revealed that the inhibitory effect of mSlp1-(1-116) on melanosome transport was comparable to that of mSlp2-(3-80), indicating that testing of mSlp1-(1-116) using the cellular melanosome clustering assay is consistent with the results of the FRET-based in vitro assay (see chapter 4). In contrast, mSlp1-(1-74) induced melanosome clustering effects comparable to that of mSlp1-(1-74) and mSlp1-(70-116) combination. In line

with this, mSlp1-(70-116) was comparable to the negative control (GFP), indicating that the melanosome clustering effects exhibited by mSlp1-(1-74) and mSlp1-(70-116) combination was related to mSlp1-(1-74) only. This suggests that SHD1 contributes mainly to the binding and the addition of SHD2 might stabilise the interaction with Rab27a as it had negligible effects when tested alone; i.e. both SHD1/2 are essential for Rab27 binding activity. This finding is in agreement with the results of several studies that demonstrated that both SHD1 and SHD2 are essential for Rab27 binding (Fukuda, 2006; Kuroda and Fukuda, 2004; Kuroda et al., 2002a). Similar to Slp2, Slp1 lacks the zinc finger motif; i.e. SHD1 and SHD2 are linked directly (Fukuda, 2005; Fukuda et al., 2001), suggesting that SHD1/2 might adopt compact conformation upon binding to Rab27, thereby stabilising the interaction (for further details of Slp1 and Slp2 structures see section 1.4 and Figure 1.14).

In addition, mSlac2-a-(1-146) was chosen to be tested based on the already identified Rab27b-Slac2-a binding interface (Kukimoto-Niino et al., 2008). These experiments demonstrated that this fragment can partially inhibit Rab27a-Slac2-a interaction-dependent melanosome transport evidenced by inducing partial perinuclear clustering of melanosomes in 71.58% ±0.29 of expressing cells (Figure 5.16), suggesting that it is not comparable to mSlac2-a-(1-266) or mSlp2 (3-80) (positive controls). Although, mSlac2-a-(1-146) was enough to bind GTP-loaded Rab27a using in vitro co-immunoprecipitation assay (Fukuda, 2002b), the current results of the melanosome clustering assay suggest that this fragment might need to be further extended to obtain comparable inhibitory effect to that of mSlac2-a-(1-266). This highlights the importance of confirming in vitro findings by results from in vivo or cellular assays, especially for protein-protein interactions including Rab27-effector interactions as the reaction conditions using in vitro assays is controlled, whereas in cells various intracellular pathways can affect protein-protein interactions and many proteins can interact with each other.

In comparison, Kuroda et al. found that mSlac2-a-(1-153) was sufficient to induce perinuclear clustering of melanosomes in 86.5% ±2.5% of melan-a cells (Kuroda et al., 2003). This differences between the current results of this study (71.58% ±0.29) and Kuroda et al. experiments might be due to limited number

of expressing cells used to obtain their results (as they tested one dish/experiment from three independent experiments), whereas the current results were obtained randomly using 4 images per experiment from 3 independent experiments; i.e. 12 images. In addition, this difference might be related to the additional amino acids used in their experiments (1-153 instead of 1-146). This suggests that this finding requires further investigations using larger fragments, for instance testing mSlac2-a-(1-153) using the cellular melanosome clustering assay to confirm that this difference was related to these additional amino acids and not to variability in experimental conditions; such as protein expression of the infected viruses, endogenous Rab27a/Slac2-a protein expression and melanosomes number in melan-a cells.

5.5 Conclusions

Altogether, the results of this chapter suggest to focus mainly on mSlp2, especially 3-56 residues (as they had partial inhibitory effects on Rab27a-Slac2-a interaction-dependent melanosome transport) when developing Rab27-effector protein interaction inhibitors. In addition, the introduction of R32W mutation into mSlp2 resulted in decreasing the inhibitory effect by 42%, suggesting that R32 residue can be utilised to identify candidate small molecule inhibitors of Rab27-effector protein interactions when performing virtual screening in the libraries. In addition, mSlp2-(3-67) was able to dramatically induce perinuclear clustering of melanosomes in melan-a cells, suggesting that this mSlp2 fragment might encompass all the key Rab27 binding contacts.

Chapter 6

Designing and development of Rab27-effector protein interaction inhibitors

6.1 Introduction

Some work has already been done to develop and/or identify Rab27-effector protein interaction inhibitors by other groups. For instance, in one study, the identification of candidate small molecule inhibitors of Rab27-Slp1 interaction (to inhibit neutrophil exocytosis) was based on developing a high-throughput screening approach using two libraries of small molecule inhibitors for a total of 32,000 compounds. This resulted in discovery of neutrophil exocytosis inhibitor20 (Nexinhib20), 4,4-dimethyl-1-(3-nitrophenyl)-2-(1H-1,2,4-triazol-1-yl)pent-1-en-3-one (Johnson et al., 2016).

Another strategy is to inhibit Rab27 gene expression using microRNAs, since numerous cancer-related metastasis can be inhibited using specific microRNAs gene suppressors; such as in hepatocellular carcinoma (Xu et al., 2017), gastric cancer (Ni et al., 2017), glioma brain tumour (Zhi et al., 2017), non-small-cell lung cancer (Zhang et al., 2017a) and cervical cancer (Zhang et al., 2017b). For instance miR-134-3p as one of the microRNAs was used to silence RAB27A by binding to the 3′ untranslated region (3′-UTR) of RAB27A mRNA, resulted in inhibition of human ovarian cancer stem cells (Chang et al., 2017) [for review see (Rupaimoole and Slack, 2017)].

Although a lot of work has been done to identify the key Rab27 binding residues, many of the Rab27-effector protein interactions still need to be investigated. Here, molecular dynamics simulation studies were performed in order to identify the key Rab27 binding residues by calculating the free energy of binding to Rab27 for wild-type and mutated Slp2 residues. This information was then utilised to design Rab27 super-effectors which were considered as Rab27-effector protein interaction inhibitors. These candidate inhibitor(s) were tested later using the cellular melanosome clustering and the in vitro FRET-based assays as described thereafter.

6.2 Aims

The main aim of these experiments was to identify and develop candidate inhibitors of Rab27-effector protein interactions by performing molecular dynamics simulation studies. Furthermore, those developed inhibitors and candidate small molecule inhibitors found in the literature were tested using the cellular melanosome clustering and the FRET-based protein-protein interaction assays.

6.3 Results

6.3.1 Molecular dynamics simulation studies of Rab27-Slp2 interaction

Parallel to the previous experiments performed in chapter 5 and to identify the key Rab27 binding residues, molecular dynamics simulation of the Rab27a-Slp2-(5-56) interaction was performed as described in section 2.5 utilising the previously identified crystal structure of the Rab27a-Slp2 complex interface (Chavas et al., 2008). In addition, to perform molecular dynamics simulation of a larger Slp2 fragment, homology modelling was performed as described in section 2.5 using the already identified crystal structure of the Rab27b-Slac2-a complex interface (Kukimoto-Niino et al., 2008), thereby molecular dynamics simulation of Rab27a-Slp2-(10-78) interaction was performed.

By performing molecular dynamics simulation studies for Rab27a-Slp2-(5-56) and Rab27a-Slp2-(10-78) interactions, the free energy of binding of the wild-type Slp2 residues were calculated. "Note that" the binding affinity increases as the free energy of binding decreases, since this leads to formation of stable interactions (Du et al., 2016). Based on the free energy of binding calculations (Figure 6.1), residues that had relatively higher free energy of binding were identified; i.e. residues that had weak binding affinity. This suggested that those residues might be suitable candidates for substitution with proposed mutations, thereby increasing their binding affinities.

These simulation studies (Figure 6.1) demonstrated that 16 residues in Slp2-(5-56) had relatively higher free energy of binding (lower Rab27 binding affinity): Q12, E13, A14, K17, V18, L19, Q20, L25, K26, A28, E38, K39, Q44, N48, G51 and E56. In addition, 20 residues that also had relatively higher free energy of binding were identified in Slp2-(10-78). These residues comprised the previously mentioned residues (16 residues) in addition to H62, R63, K65 and H67. Therefore, to decrease the free energy of binding of these residues (to increase their binding affinity), 16 and 20 mutations were proposed to be introduced into Slp2-(5-56) and Slp2-(10-78), respectively by substituting the wild-type residues by those mutations (see Table 6.1). These mutations were tested by performing other molecular dynamics simulation studies of the mutated

Slp2-(5-56) and Slp2-(10-78), thereby the free energy of binding of these mutated residues were calculated (Figure 6.1).

Next, based on chemical interaction predictions (Table 6.2) and comparison of the free energy of binding (Figure 6.1) of the wild-type and the mutated residues, 6 mutations: K26R, A28R, Q44R, N48I, G51L and E56F (see Table 6.1) were proposed to be introduced into mSlp2-(3-56) and tested using the melanosome clustering assay. For instance, it was hypothesised that mutating lysine-26 to arginine could induce a salt bridge interaction between glutamine-71 in Rab27a and arginine-26 in Slp2. It was also supposed that substitution of asparagine-48 by isoleucine might result in decreasing steric clashes with the Rab27a binding region, also this substitution could increase the hydrophobic interactions with methionine-185 and tyrosine-8 hydrophobic residues in Rab27a, thus increasing the binding affinity to Rab27a. In addition, the free energy of binding of the K26 (wild-type) and the R26 (mutated) residues were +1.38Kcal/mol and –3.30Kcal/mol, respectively. This suggests that by mutating K26 into R26, the free energy of binding at this region could be greatly decreased, thus stabilising the interaction with Rab27a and increasing the binding affinity. The same applies on the Q44R mutation as the free energy of binding of the Q44 (wild-type) and the R44 (mutated) residues were –0.46Kcal/mol and –5.91Kcal/mol, respectively (see Figures 6.1, 6.2 and 6.3).

As demonstrated before, mSlp2-(3-56) had partial melanosome clustering inducing effects (for further details see section 5.3.5), therefore it was supposed that by introducing these mutations, the melanosome clustering inducing effects of this fragment could be increased; i.e. this could increase the Rab27 inhibitory activity and Slp2 super-effector could be produced to be used as an inhibitor of Rab27-effector interactions.

In addition, to better investigate the effects of this strategy, 8 mutations (K26R, A28R, Q44R, N48I, G51L, E56F, H62R, R63F) (see Tables 6.1 and 6.2) were proposed to be introduced into mSlp2-(3-67). The foremost aim for introducing these mutations into mSlp2-(3-67) was not to increase its melanosome clustering inducing effects as it dramatically induced perinuclear clustering of melanosomes in expressing cells (see section 5.3.6). Instead, it was supposed

that introduction of these mutations into mSlp2-(3-67) might lead to identification of key contacts of Rab27-effector interactions, since these mutations could also disrupt or decrease the interaction with Rab27a as described in section 6.3.2.

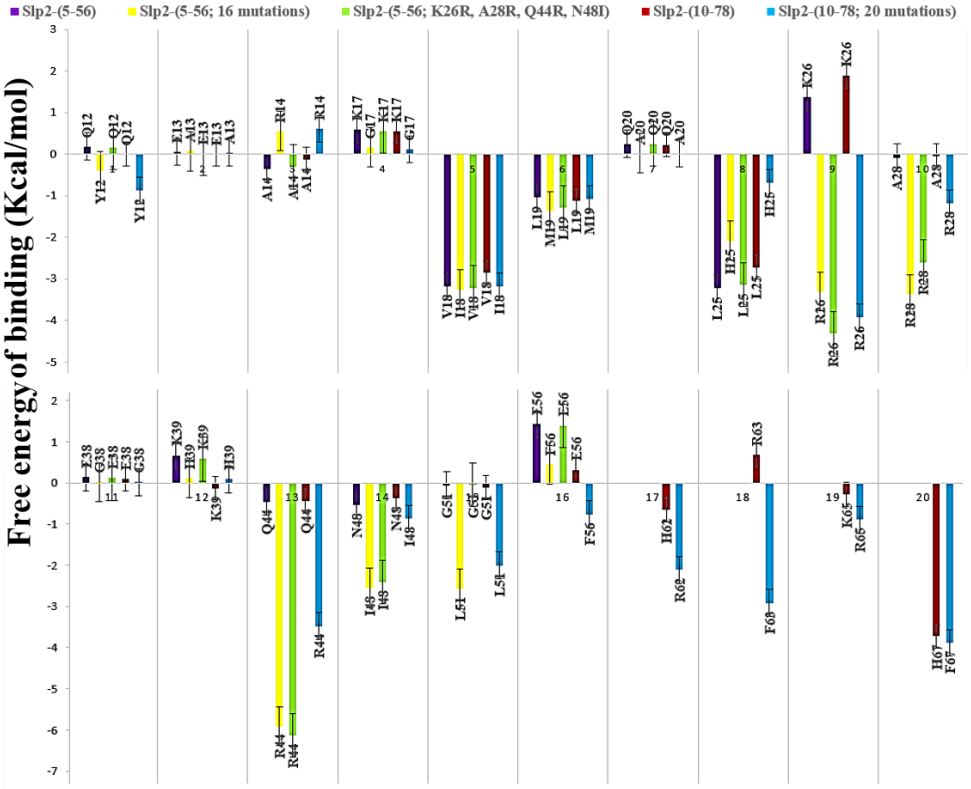


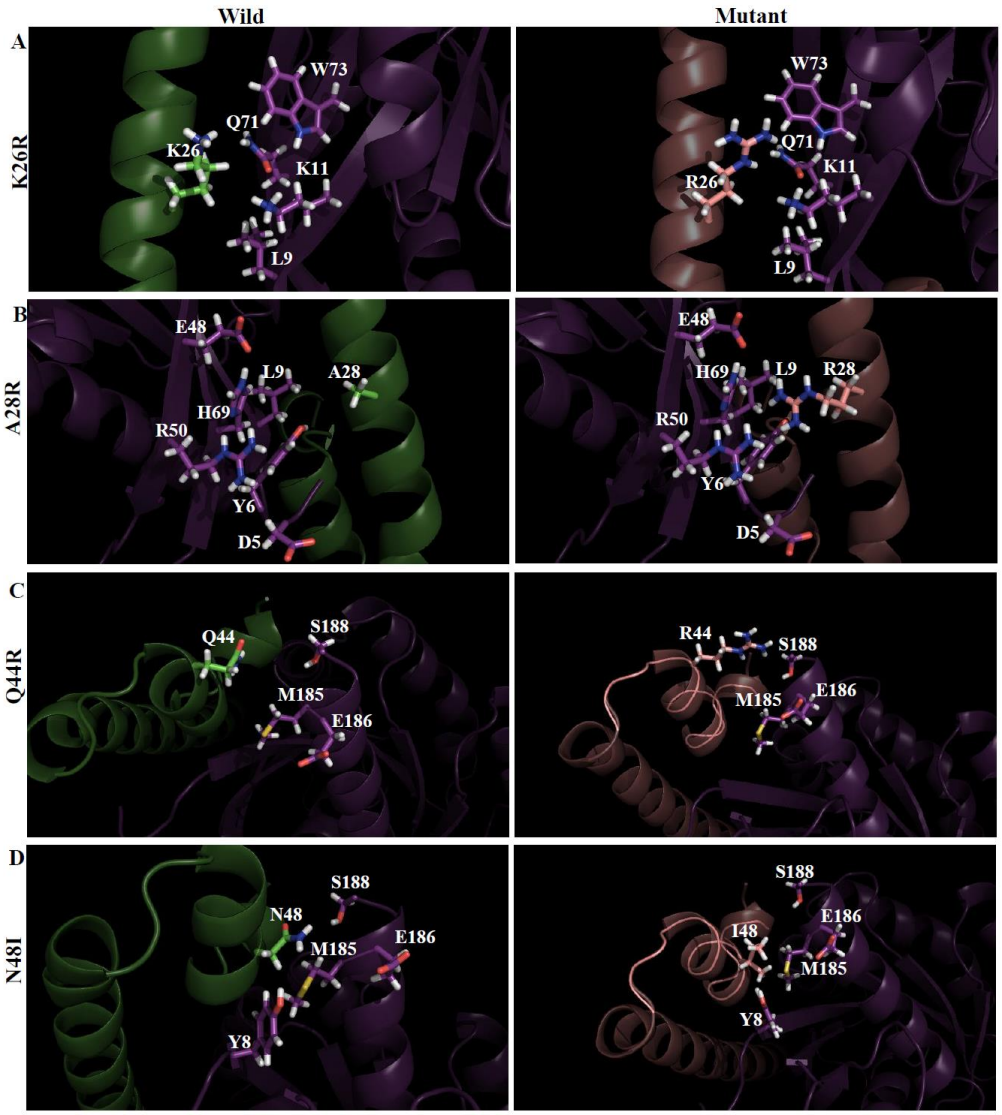
Figure 6.1. Free energy of binding of Rab27a-Slp2 interaction. Molecular dynamics simulation of Rab27a-Slp2-(5-56) (n=30), Rab27a-Slp2-(5-56; 16 mutations) (n=30), Rab27a-Slp2-(5-56; K26R, A28R, Q44R, N48I) (n=30), Rab27a-Slp2-(10-78) (n=6) and Rab27a-Slp2-(10-78; 20 mutations) (n=6) were performed as described section 2.5 and free energy of binding of the interacted residues was calculated accordingly. Details of the 16 and 20 mutations described in section 6.3.1. Data points represent mean ± SEM. Molecular dynamics simulation studies and subsequent data analysis were performed by Mohammed Tumbi.

Slp2 (16 mutations)	Slp2 (20 mutations)	Slp2 (8 mutations)	Slp2 (6 mutations)
Q12Y	Q12Y	Q12	Q12
E13A	E13A	E13	E13
A14R	A14R	A14	A14
K17G	K17G	K17	K17
V18I	V18I	V18	V18
L19M	L19M	L19	L19
Q20A	Q20A	Q20	Q20
L25H	L25H	L25	L25
K26R	K26R	K26R	K26R
A28R	A28R	A28R	A28R
E38G	E38G	E38	E38
K39H	K39H	K39	K39
Q44R	Q44R	Q44R	Q44R
N48I	N48I	N48I	N48I
G51L	G51L	G51L	G51L
E56F	E56F	E56F	E56F
	H62R	H62R	
	R63F	R63F	
	K65R	K65	
	H67F	H67	

Table 6.1. A list of Slp2 proposed mutations. Mutated residues highlighted in red. Mutations were proposed by Mohammed Tumbi under supervision of Dr Charles Laughton.

Mutation	Reason behind performing mutation
K26R	Mutating lysine-26 to arginine was proposed to induce a salt bridge interaction between glutamine-71 (Rab27a) and arginine-26 (Slp2).
A28R	Mutating alanine-28 to a larger amino acid like arginine (H-donor) might increase H-bonding with aspartic acid-5 (H-acceptor) and tyrosine-6 (contains H-donor and acceptor atoms).
Q44R	Mutating glutamine-44 to a larger amino acid like arginine might increase H-bonding with serine-188 (Rab27a) as serine has both hydrogen donor and acceptor atoms in its side chains.
N48I	Mutating asparagine-48 to isoleucine might decrease steric clashes with the Rab27a binding region, as isoleucine size is smaller than asparagine. In addition, mutating to isoleucine might increase the hydrophobic interactions with methionine-185 and tyrosine-8 (Rab27a), as these residues are hydrophobic.
G51L	Mutating glysine-51 to leucine might increase the hydrophobic interactions with methionine-93, methionine-185 and tyrosine-8 (Rab27a) as these residues are hydrophobic.
E56F	Mutating glutamic acid-56 to phenylalanine (hydrophobic amino acid) might induce pi-pi interactions with tyrosine-122 (Rab27a) as glutamic acid-56 is in close proximity (less than 5Å) to tyrosine-122.
H62R	Mutating histidine-62 to arginine was based on the assumption that arginine might interact with the nearby polar residues found in arginine-90, methionine-119, tyrosine-122 and glutamic acid-124 (Rab27a).
R63F	Mutating arginine-63 to phenylalanine was performed to decrease steric clashes with arginine-90 (Rab27a) (energy contribution = +0.63 kcal/mol), while maintaining hydrophobicity and probable pi-pi interactions.

Table 6.2. Reasons behind the proposed Slp2 mutations. Mutations were proposed by Mohammed Tumbi under supervision of Dr Charles Laughton.


Wild
Mutant
A
K26R
W73
Q71
K26
K11
L9
W73
Q71
K11
R26
L9
B
A28R
E48
L9
A28
H69
R50
Y6
D5
E48
H69
L9
R28
R50
Y6
D5
C
Q44R
Q44
S188
M185
E186
R44
S188
M185
E186
D
N48I
S188
N48
M185
E186
Y8
S188
E186
I48
M185
Y8

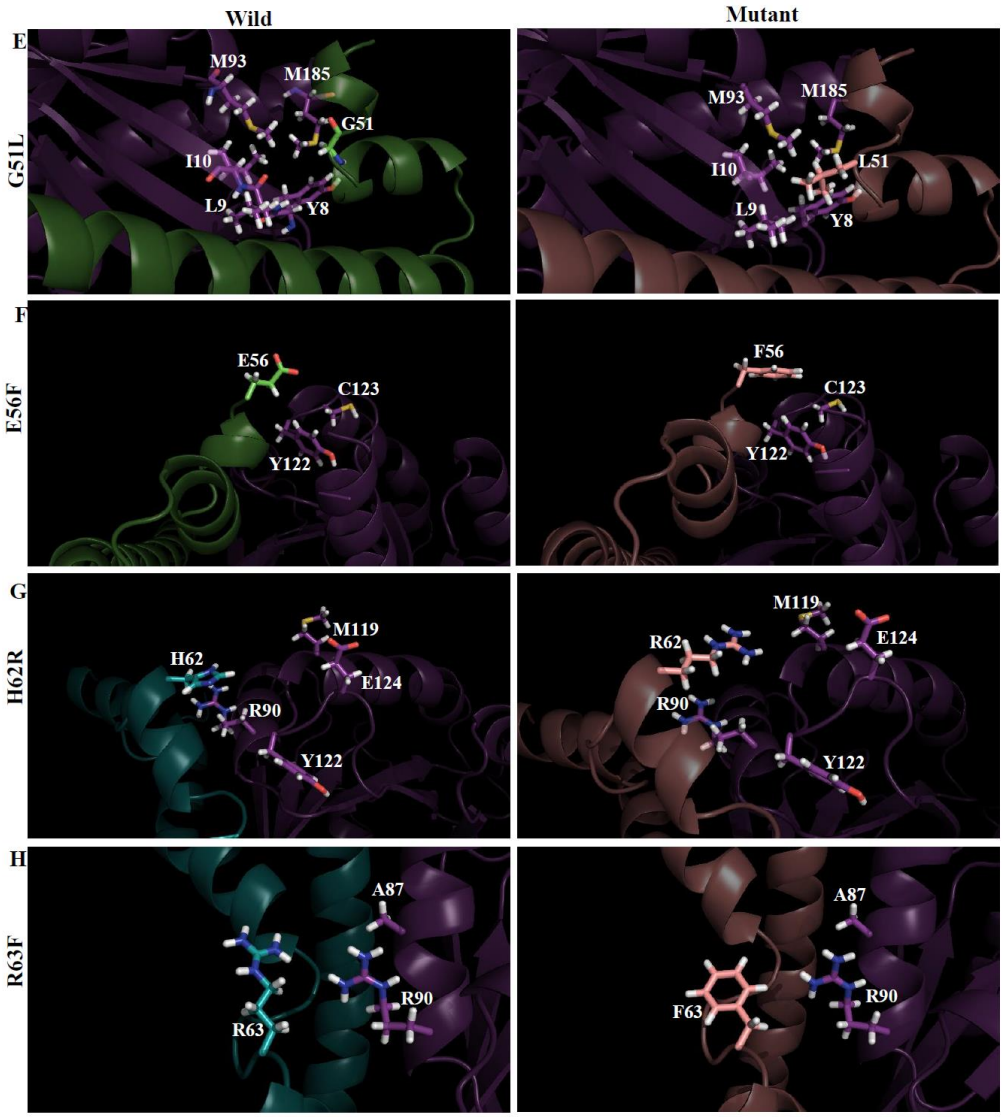
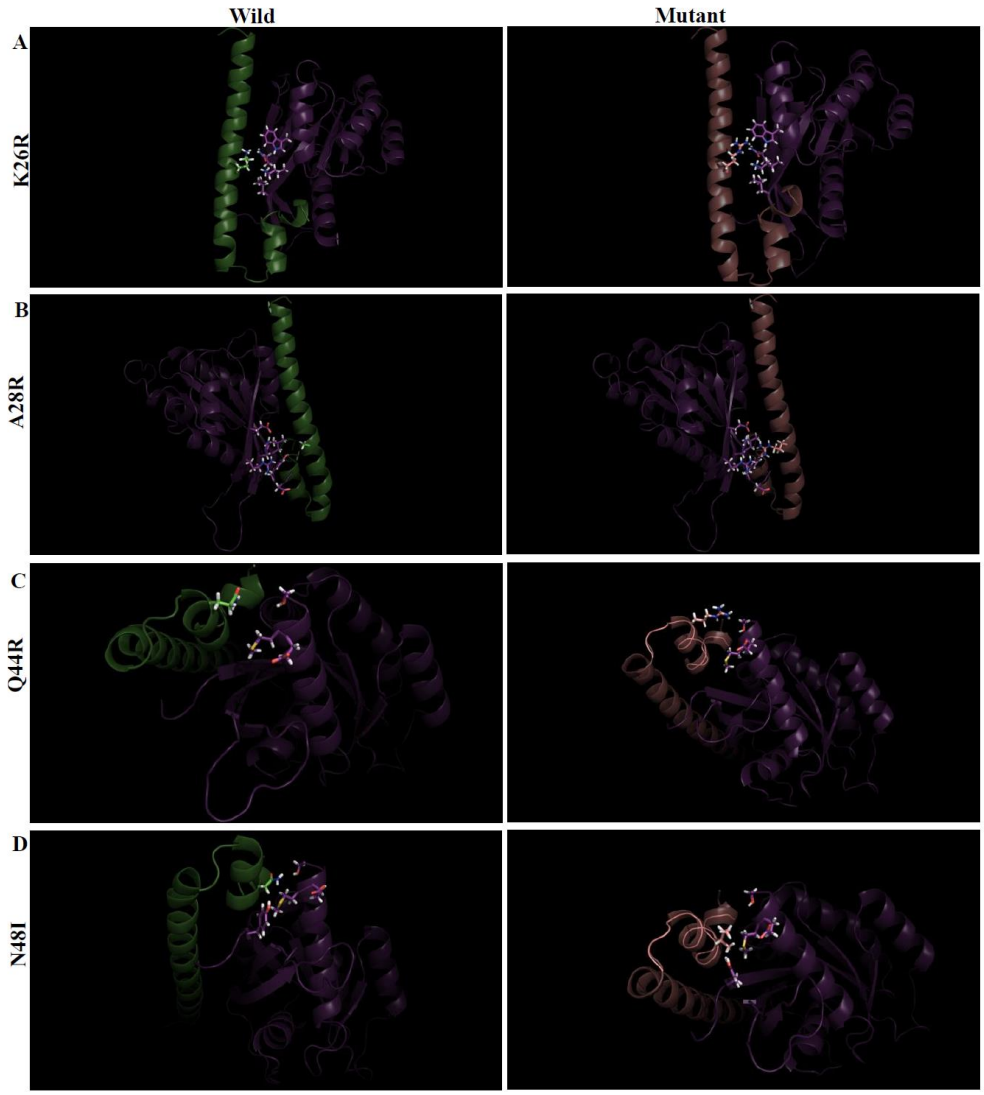


Figure 6.2. Three-dimensional structure of Rab27a-Slp2 proposed mutations. Different mutations were proposed to be introduced into Rab27a-Slp2. The proposed mutations were visualised using PyMOL software (Rab27a-Slp2 complex interface; PDB accession code: 3BC1). A) K26R, B) A28R, C) Q44R, D) N48I, E) G51L, F) E56F (using Rab27-Slp2 complex interface; PDB accession code:3BC1), G) H62R and H) R63F. Note that G and H were created using the crystal structure generated by performing homology modelling as described in section 2.5 (utilising Rab27b-Slac2-a; PDB accession code: 2ZET to add the extra residues). Oxygen, nitrogen and hydrogen atoms are depicted in red, blue and white, respectively. Rab27a, Slp2-(5-56; wild), Slp2-(10-78; wild) and Slp2-(mutant) (including Carbon molecules) are depicted in violet, green, dark green and light brown, respectively. Images were created by Mohammed Tumbi.


Wild
Mutant
A
K26R
B
A28R
C
Q44R
D
N481

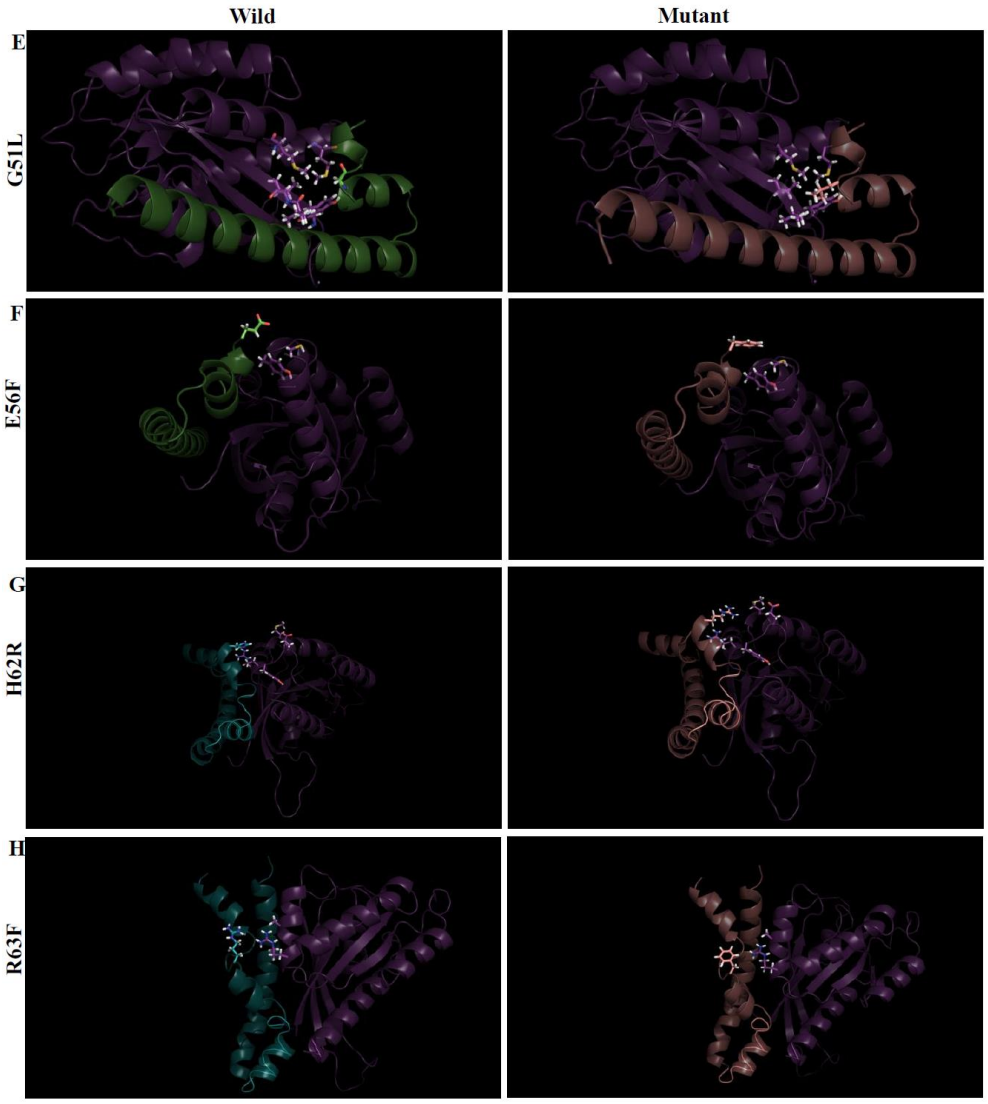


Figure 6.3. Full three-dimensional structure of Rab27a-Slp2 proposed mutations. Different mutations were proposed to be introduced into Rab27a-Slp2; the proposed mutations were visualised using PyMOL software: A) K26R, B) A28R, C) Q44R, D) N48I, E) G51L, F) E56F, G) H62R and H) R63F.Oxygen, nitrogen and hydrogen atoms are depicted in red, blue and white, respectively. Rab27a, Slp2-(5-56; wild), Slp2-(10-78; wild) and Slp2-(mutant) (including Carbon molecules) are depicted in violet, green, dark green and light brown, respectively. Images were created by Mohammed Tumbi.

6.3.2 Development of Rab27 super-effectors based on molecular dynamics simulation of Rab27-Slp2 effector protein interaction

In order to investigate the effects of the proposed mutations described in section 6.3.1, adenoviruses expressing the indicated proteins containing those mutations were used to infect melan-a cells and the melanosome clustering assay was used to test their effects (see chapter 5).

As described in section 6.3.1, the following mutations: K26R, A28R, Q44R, N48I, G51L and E56F were proposed to be introduced into mSlp2-(3-56). In addition, two additional mutations (H62R, R63F) were proposed to be introduced into mSlp2-(3-67). These mutations were introduced sequentially into mSlp2-(3-56) and mSlp2-(3-67) by adding the first two mutations using one site-directed mutagenesis reaction and the other mutations were added to this. In addition, the last two mutations (H62R, R63F) were introduced into mSlp2-(3-67) using one site-directed mutagenesis reaction.

Accordingly, the proposed mutations were sequentially tested using the cellular melanosome clustering assay as a read-out for Rab27a-Slac2-a interaction-dependent melanosomes transport (for further details see chapter 5). "Note that" GFP was used as a negative control, whereas mSlp2-(3-80) and mSlp2-(3-67) were used as positive controls in the subsequent experiments.

The results of these experiments (Figure 6.4) demonstrated that the introduction of the first two mutations (K26R, A28R) into mSlp2-(3-56) induced perinuclear clustering of melanosomes in 66.26% ±4.17 of expressing cells, compared with 32.15% ±3.87, 95.14% ±0.11 and 94.48% ±0.53 using mSlp2-(3-56), mSlp2-(3-80) and mSlp2-(3-67), respectively. The effects of introducing these mutations were significantly different from that of mSlp2-(3-56) and the positive controls, indicating that the introduction of these two mutations significantly increased the inhibitory effects of mSlp2-(3-56) on melanosome transport. In comparison, the introduction of the third mutation (Q44R) increased the perinuclear clustering of melanosomes into 71.90% ±1.15 of expressing cells, but this effect was not significantly different from that of introducing the first two mutations, and the inhibitory effects were less than that of the positive controls (Figure 6.4).

Interestingly, the introduction of the fourth mutation (N48I) succeeded in inducing perinuclear clustering of melanosomes in 94.02% ±0.53 of expressing cells. This effect was not significantly different from that of the positive controls, but was significantly different from that of introducing the (K26R, A28R) and the (K26R, A28R, Q44R) mutations. This indicates that the introduction of (K26R, A28R, Q44R, N48I) mutations into mSlp2-(3-56) produced significant inhibitory effects on Rab27a-Slac2-a interaction-dependent melanosomes transport comparable to that of either mSlp2-(3-80) or mSlp2-(3-67) (Figure 6.4).

Surprisingly, the introduction of the fifth mutation (G51L) almost completely disrupted the inhibitory effects caused by the first four mutations, by reducing the perinuclear clustering of melanosomes into 19.35% ±1.95 of expressing cells (Figure 6.4). This effect was significantly different form that of mSlp2-(3-56) (32.15% ±3.87), suggesting that this mutation had abolishing effects on Rab27a-Slac2-a interaction-dependent melanosomes transport as described below.

Introducing the sixth mutation (E56F) did not enhance the inhibitory effect as it induced perinuclear clustering of melanosomes in only 21.90% ±1.79 of expressing cells (Figure 6.4). The effect of introducing this mutation was not significantly different from that of mSlp2-(3-56), suggesting that this mutation had no or slightly effects on the interaction with Rab27a.

To better investigate the effects of introducing the G51L mutation on the binding between Rab27a and Slac2-a, the G51L mutation was deleted and only 5 mutations were tested; i.e. the K26R, A28R, Q44R, N48I and E56F mutations. The results of these experiments demonstrated that introducing these mutations into mSlp2-(3-56) resulted in inducing perinuclear clustering of melanosomes in 89.14% ±1.07 of expressing cells which was not significantly different from that of the positive controls (Figure 6.4). This indicates that the deletion of the G51L mutation restored the inhibitory effect of the first four mutations (K26R, A28R, Q44R, N48I) and the E56F mutation had no effect or even caused slight decrease in the inhibitory effects.

Notably, sequence alignment of Slp2 with other Rab27 effectors (see Figures 5.7 and 5.11) revealed that the G51 residue is highly conserved among all Rab27

effector proteins except Slac2-a and Slac2-c effectors (Chavas et al., 2008; Kukimoto-Niino et al., 2008). This might explain why this mutation disrupted the interaction between Rab27a and mSlp2, since this residue is highly conserved among many Rab27 effectors. This highlights the importance of the G51 residue in stabilising Rab27-effector interactions. Accordingly, the G51 residue can be considered as one of the key contacts of Rab27-effector interaction.

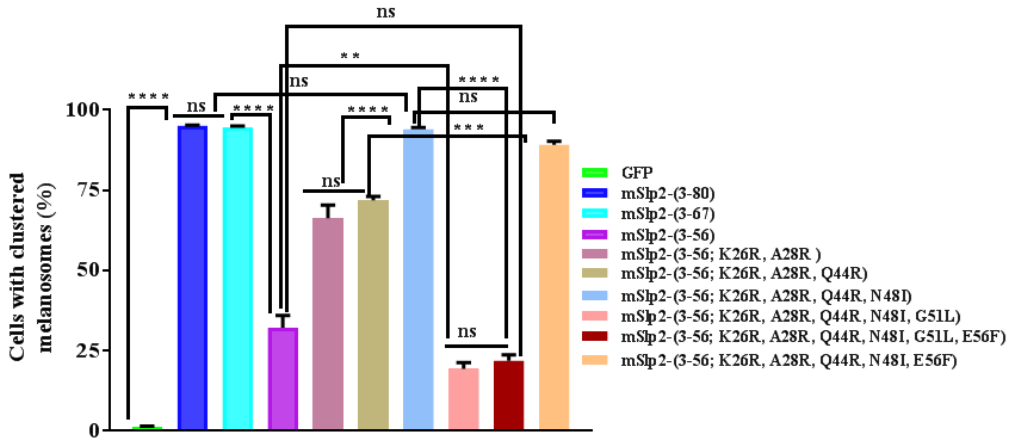


Figure 6.4. Effects of introducing different mutations into mSlp2-(3-56) on Rab27a-Slac2-a interaction-dependent melanosome transport. Melan-a melanocytes were plated using 24-well (Nunc) plate and then infected using adenoviruses expressing the indicated proteins: GFP (as a negative control), GFP-mSlp2-(3-80) (as a positive control), GFP-mSlp2-(3-67) (as a positive control, GFP-mSlp2-(3-56), GFP-mSlp2-(3-56; K26R, A28R), GFP-mSlp2-(3-56; K26R, A28R, Q44R), GFP-mSlp2-(3-56; K26R, A28R, Q44R, N48I), GFP-mSlp2-(3-56; K26R, A28R, Q44R, N48I, G51L), GFP-mSlp2-(3-56; K26R, A28R, Q44R, N48I, G51L, E56F) and GFP-mSlp2-(3-56; K26R, A28R, Q44R, N48I, E56F). The cells were visualised (24-72 hours post-infection) using fluorescent microscopy and cells with clustered melanosomes were then quantified. Data represent mean ± SEM of 3 independent experiments (4 images/experiment). One-way ANOVA: $^{ns}P > 0.05$; $**P \leq 0.01$, $***P \leq 0.001$, $****P \leq 0.0001$.

As mentioned in section 6.3.1, it was hypothesised that the introduction of K26R, A28R, Q44R, N48I, G51L, E56F, H62R and R63F mutations into mSlp2-(3-67) might identify key contacts of Rab27-effector interactions. To this end, these mutations were introduced into mSlp2-(3-67) sequentially as described before. The mSlp2-(3-67; K26R, A28R), mSlp2-(3-67; K26R, A28R, Q44R), mSlp2-(3-67; K26R, A28R, Q44R, N48I), mSlp2-(3-67; K26R, A28R, Q44R, N48I, G51L) and mSlp2-(3-67; K26R, A28R, Q44R, N48I, G51L, E56F, H62R, R63F) mutants induced comparable melanosome clustering effects to that of the positive controls (Figure 6.5). In addition, the mSlp2-(3-67; K26R, A28R, Q44R, N48I, G51L, E56F) mutant induced perinuclear clustering of melanosomes in 93.66% ±0.21 of expressing cells compared with 96% ±0.37 and 95.17% ±0.38 using mSlp2-(3-80) and mSlp2-(3-67), respectively (significantly different effect). This indicates that the introduction of the G51L and E56F mutations slightly decreased the melanosome clustering inducing effects and the presence of the extra residues (57-67) might compensate for the disruption of the binding caused by the G51L mutation (Figure 6.5). Again, these experiments support the previous findings that the G51 residue is one of the key contacts of Rab27-effector interactions and can be exploited in the future when performing virtual screening to identify candidate small molecule inhibitors of Rab27-effector interactions.

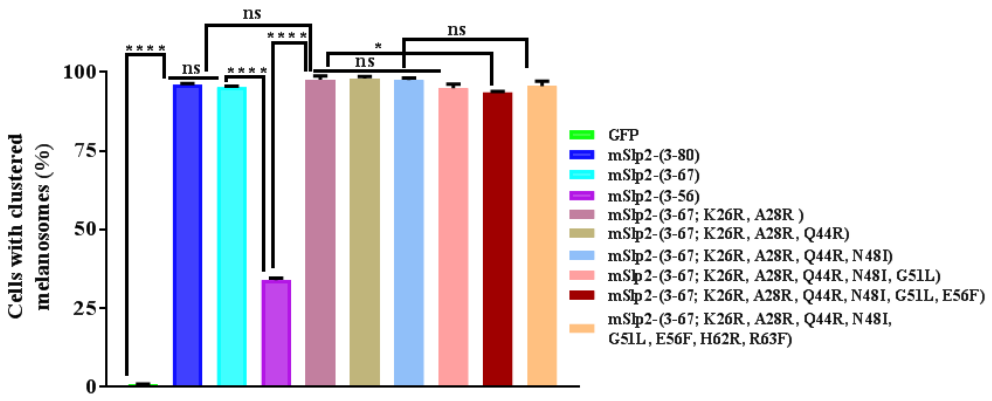


Figure 6.5. Effects of introducing different mutations into mSlp2-(3-67) on Rab27a-Slac2-a interaction dependent melanosome transport. Melan-a melanocytes were plated using 24-well (Nunc) plate and then infected using adenoviruses expressing the indicated proteins: GFP (as a negative control), GFP-mSlp2-(3-80) (as a positive control), GFP-mSlp2-(3-67) (as a positive control, GFP-mSlp2-(3-56), GFP-mSlp2-(3-67; K26R, A28R), GFP-mSlp2-(3-67; K26R, A28R, Q44R), GFP-mSlp2-(3-67; K26R, A28R, Q44R, N48I), GFP-mSlp2-(3-67; K26R, A28R, Q44R, N48I, G51L), GFP-mSlp2-(3-67; K26R, A28R, Q44R, N48I, G51L, E56F) and GFP-mSlp2-(3-67; K26R, A28R, Q44R, N48I, G51L, E56F, H62R, R63F). The cells were visualised (24-72 hours post-infection) using fluorescent microscopy and cells with clustered melanosomes were then quantified. Data represent mean ± SEM of 3 independent experiments (4 images/experiment). One-way ANOVA: $^{ns}P > 0.05$; *$P \leq 0.05$, ****$P \leq 0.0001$.

Next, these mutations were introduced into mSlp2-(10-56) and mSlp2-(10-67), since mSlp2-(10-56) had negligible effects on melanosome transport and mSlp2-(10-67) induced partial perinuclear clustering of melanosomes in melan-a cells (see sections 5.3.5 and 5.3.6. Therefore, it was supposed that by introducing these mutations into mSlp2-(10-56) and/or mSlp2-(10-67), the interaction with Rab27a can be stabilised, thus resulting in production of smaller Slp2 super-effectors in case of using mSlp2-(10-56) or improving the inhibitory effects of mSlp2-(10-67).

To achieve these goals, the mSlp2-(10-56; K26R, A28R, Q44R, N48I), mSlp2-(10-56; K26R, A28R, Q44R, N48I, E56F) and mSlp2-(10-56; K26R, A28R, Q44R, N48I, G51L, E56F) mutants were chosen to be tested. In addition, the

mSlp2-(10-67; K26R, A28R, Q44R, N48I), mSlp2-(10-67; K26R, A28R, Q44R, N48I, E56F, H62R, R63F) and mSlp2-(10-67; K26R, A28R, Q44R, N48I, G51L, E56F, H62R, R63F) mutants were also tested.

These experiments (Figure 6.6) demonstrated that the introduction of (K26R, A28R, Q44R, N48I, G51L, E56F), (K26R, A28R, Q44R, N48I, E56F) and (K26R, A28R, Q44R, N48I) mutations into mSlp2-(10-56) had no significant melanosome clustering inducing effects as their effects were not significantly different from that of the wild-type mSlp2-(10-56).

In contrast, the introduction of (K26R, A28R, Q44R, N48I, G51L, E56F, H62R, R63F) mutations into mSlp2-(10-67) reduced the perinuclear clustering of melanosomes into 8.63% ±1.59 of expressing cells compared with 70.60% ±5.58 using wild-type mSlp2-(10-67). This suggests that these mutations including the G51L mutation disrupted the binding with Rab27a when introduced into mSlp2-(10-67) (Figure 6.6).

Deletion of the G51L mutation by introducing the (K26R, A28R, Q44R, N48I, E56F, H62R, R63F) mutations into mSlp2-(10-67) significantly increased the perinuclear clustering of melanosomes into 36.80% ±6.39 of expressing cells compared with 8.63% ±1.59 using mSlp2-(10-67) with 8 mutations as mentioned before (Figure 6.6). However, this effect was significantly lower than that produced by the wild-type mSlp2-(10-67) (70.60% ±5.58) (Figure 6.6). Again, this points out the crucial effects of the G51 residue in stabilising the interaction with Rab27a. In addition, this suggests that the introduction of the H62R and R63F mutations into mSlp2-(10-67) might disrupt the interaction with Rab27a, thus reducing its inhibitory effects on Rab27a-Slac2-a interaction dependent melanosome transport. In case of mSlp2-(3-67), the 3-9 residues might compensate for the disruption effect caused by these 2 mutations.

Interestingly, the introduction of (K26R, A28R, Q44R, N48I) mutations into mSlp2-(10-67) induced perinuclear clustering of melanosomes in 95.34% ±0.54 of expressing cells. This effect was not significantly different from that of mSlp2-(3-80) (95.98% ±0.4) and mSlp2-(3-67) (95.42% ±0.37) (Figure 6.6). This suggests that the first four mutations (K26R, A28R, Q44R, N48I) had

essential functions in enhancing the inhibitory effects of either mSlp2-(3-56) or mSlp2-(10-67) on Rab27a-Slac2-a interaction dependent melanosome transport.

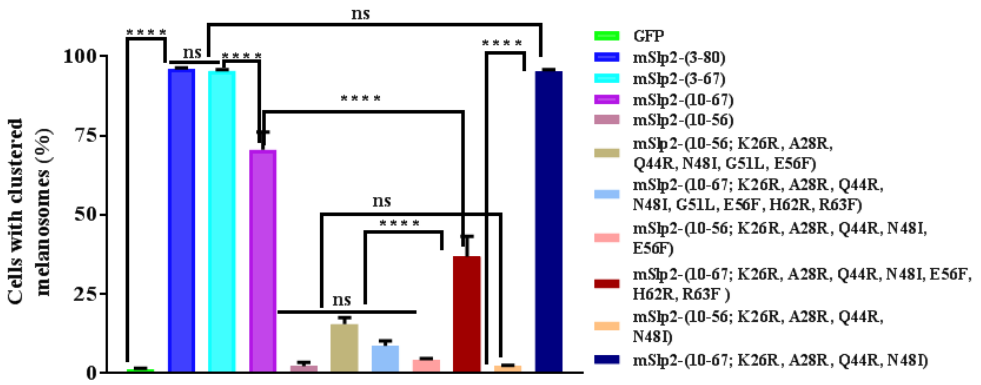


Figure 6.6. Effects of introducing different mutations into mSlp2-(10-56) and mSlp2-(10-67) on Rab27a-Slac2-a interaction-dependent melanosome transport. Melan-a melanocytes were plated using 24-well (Nunc) plate and then infected using adenoviruses expressing the indicated proteins: GFP (as a negative control), GFP-mSlp2-(3-80) (as a positive control), GFP-mSlp2-(3-67) (as a positive control, GFP-mSlp2-(10-67), GFP-mSlp2-(10-56), GFP-mSlp2-(10-56; K26R, A28R, Q44R, N48I, G51L, E56F), GFP-mSlp2-(10-67; K26R, A28R, Q44R, N48I, G51L, E56F, H62R, R63F), GFP-mSlp2-(10-56; K26R, A28R, Q44R, N48I, E56F), GFP-mSlp2-(10-67; K26R, A28R, Q44R, N48, E56F, H62R, R63F), GFP-mSlp2-(10-56; K26R, A28R, Q44R, N48I) and GFP-mSlp2-(10-67; K26R, A28R, Q44R, N48I).The cells were visualised (24-72 hours post-infection) using fluorescent microscopy and cells with clustered melanosomes were then quantified. Data represent mean ± SEM of 3 independent experiments (4 images/experiment). One-way ANOVA: $^{ns}P > 0.05$, ****$P \leq 0.0001$.

To better investigate the effects of the first four mutations on the binding and to define the superiority of these mutations to each other, single and double mutations were introduced into mSlp2-(3-56) (in addition to the already tested mutations) (Figure 6.7). These experiments demonstrated that the hierarchy of the inhibitory effects of these mutations in terms of inducing perinuclear clustering of melanosomes in expressing cells was as follows (% of cells with clustered melanosomes): (K26R, A28R, Q44R, N48I); 94.39% ±0.53, (K26R, A28R, Q44R); 77.71% ±1.23, (Q44R, N48I); 69.79% ±0.33, (K26R); 68.28% ±0.77, (K26R, A28R); 66.67% ±1.18, (Q44R); 49.89% ±0.14, (N48I); 41.63% ±3.57, (A28R); 29.74% ±3.33. Notably, the A28R mutation produced comparable effects to that of the wild-type mSlp2-(3-56); 31.93% ±3.75, suggesting that this mutation might be not essential for enhancing the interaction with Rab27a. The effects of introducing the (Q44R) and (N48I) mutations were not significantly different. In addition, the effects of introducing (K26R), (K26R, A28R) and (Q44R, N48I) mutations were not significantly different, but their effects were significantly different from that of (K26R, A28R Q44R). This suggests that the Q44R mutation had essential role in enhancing the inhibitory effects of mSlp2-(3-56) on melanosome transport. Furthermore, the effects of the (K26R, A28R, Q44R, N48I) and the (K26R, A28R Q44R) mutations were significantly different, indicating that the fourth mutation was essential to promote the inhibitory effects. The effects of introducing (K26R, A28R, Q44R, N48I) mutations were not significantly different from that of the positive controls: mSlp2-(3-80); 95.66% ±0.2 and mSlp2-(3-67); 94.94% ±0.05. Again, these findings confirmed that by introducing the (K26R, A28R, Q44R, N48I) mutations into mSlp2-(3-56), a novel Rab27 super-effector was produced. In addition, these results indicated that K26R was the most powerful single mutation and A28R was the least significant mutation. This points out that the introduction of three mutations (K26R, Q44R, N48I) might be able to produce comparable effects to that of four mutations which can be tested in the future.

In addition, to further investigate the effects of these four mutations on the interaction with Rab27a, other molecular dynamics simulation studies were performed. These studies demonstrated that the introduction of these mutations into mSlp2-(5-56) resulted in producing comparable effects to that of

introducing 16 or 20 mutations (Table 6.1) in terms of reducing the free energy of binding, thereby increasing the binding affinity to Rab27a (Figures 6.1 and 6.8). In addition, the introduction of these mutations into mSlp2-(5-56) resulted in reducing the free energy of binding compared with the wild-type mSlp2-(5-56) (Figures 6.1 and 6.8), thereby increasing the binding affinity.

Interestingly, sequence alignment with other Rab27 effectors (see Figures 5.7 and 5.11) (Chavas et al., 2008; Kukimoto-Niino et al., 2008) demonstrates that R26, R44 and I48 residues (mutated Slp2 residues) are in consensus with the corresponding arginine and isoleucine residues in different Rab27 effectors (are the most conserved residues) (see Table 6.3). Furthermore, the E56 (wild-type Slp2 residue) is highly conserved among Rab27 effector proteins except Slp4-a, Slac2-c, Noc2 and Rabphilin3-a, suggesting that this residue might be essential for the interaction with Rab27, even though mutating to phenylalanine in the absence of the G51L mutation had slightly effects on the induced melanosome clustering.

In conclusion, the findings of the molecular simulation studies and the results of the cellar melanosome clustering assay indicate that the mSlp2-(3-56; K26R, A28R, Q44R, N48I) mutant significantly induced perinuclear clustering of melanosomes and was comparable to mSlp2-(3-80) and mSlp2-(3-67), thereby increasing Rab27-interaction inhibitory effects.

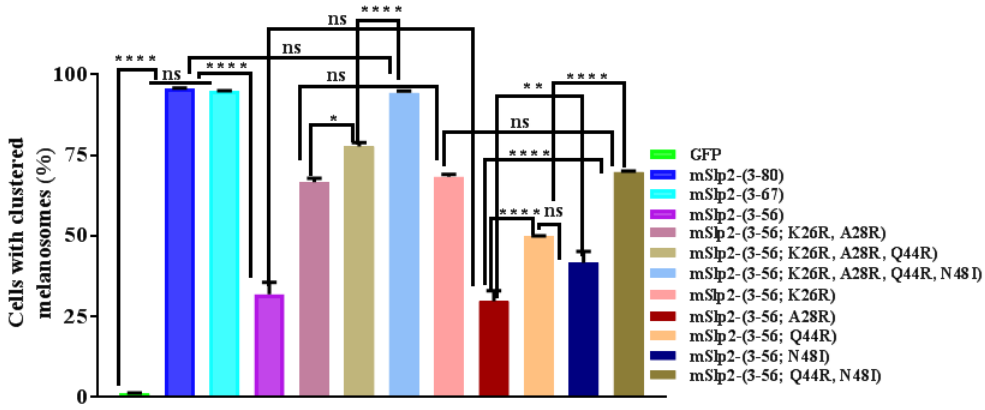


Figure 6.7. Effects of introducing single mutations into mSlp2-(3-56) on Rab27-Slac2-a interaction-dependent melanosome transport. Melan-a melanocytes were plated using 24-well (Nunc) plate and then infected using adenoviruses expressing the indicated proteins: GFP (as a negative control), GFP-mSlp2-(3-80) (as a positive control), GFP-mSlp2-(3-67) (as a positive control, GFP-mSlp2-(3-56), GFP-mSlp2-(3-56; K26R, A28R), GFP-mSlp2-(3-56; K26R, A28R, Q44R), GFP-mSlp2-(3-56; K26R, A28R, Q44R, N48I), GFP-mSlp2-(3-56; K26R), GFP-mSlp2-(3-56; A28R), GFP-mSlp2-(3-56; Q44R), GFP-mSlp2-(3-56; N48I,) and GFP-mSlp2-(3-56; Q44R, N48I).The cells were visualised (24-72 hours post-infection) using fluorescent microscopy and cells with clustered melanosomes were then quantified. Data represent mean ± SEM of 3 independent experiments (4 images/experiment). One-way ANOVA: $^{ns}P > 0.05$; $*P \leq 0.05$, $**P \leq 0.01$, $****P \leq 0.0001$.

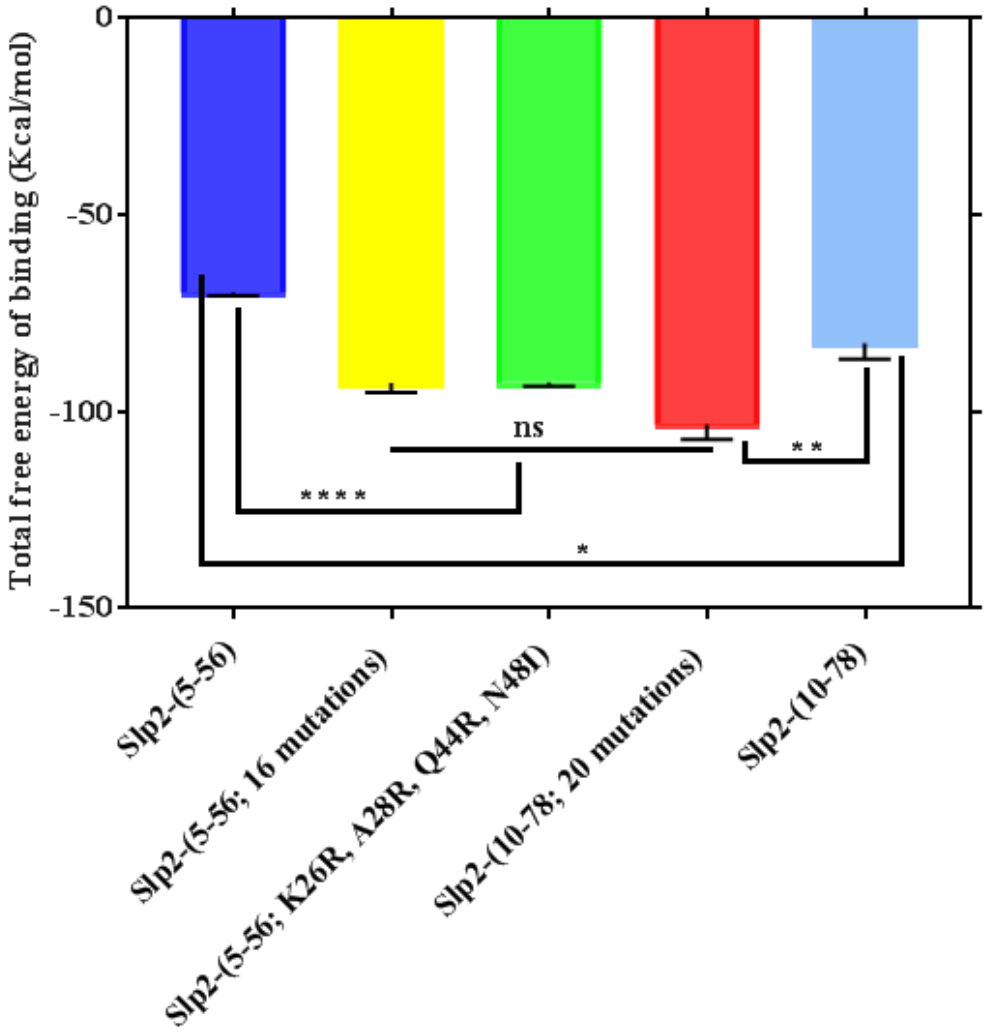


Figure 6.8. Molecular dynamics simulation studies of Rab27a-Slp2-(K26R, A28R, Q44R, N48I) interaction. Molecular dynamics simulation of Rab27a-Slp2-(5-56) (n=30), Rab27a-Slp2-(5-56; 16 mutations) (n=30), Rab27a-Slp2-(5-56; K26R, A28R, Q44R, N48I) (n=30), Rab27a-Slp2-(10-78; 20 mutations) (n=6) and Rab27a-Slp2-(10-78) (n=6) were performed as described in section 2.5 and free energy of binding of the interacted residues was calculated accordingly. Details of the 16 and 20 mutations described in section 6.3.1.Data points represent mean ± SEM. One-way ANOVA: $^{ns}P > 0.05$; *P ≤ 0. 05, **P ≤ 0.01, ****P ≤ 0.0001. Molecular dynamics simulation studies and subsequent data analysis were performed by Mohammed Tumbi.

Effector protein	Residue							
	*R26	R28	*R44	*I48	L51	F56	R62	F63
Slp1	+	-	-	+	-	-	-	-
Slp2-a	-	-	-	-	-	-	-	-
Slp3-a	-	-	+	+	-	-	-	-
Slp4-a	+	-	-		-	-	-	-
Slp5	-	-	-	+	-	-	-	-
Slac2-a	+	+	+	+	+	-	-	-
Slac2-b	+	-	+	-	+	-	-	-
Slac2-c	+	-	+	-	-	-	-	-
Noc2	-	-	+	-	-	-	-	-
Rabphilin	-	-	+	-	-	-	-	-

Table 6.3. Consensus of Slp2 proposed mutations with corresponding residues in other Rab27 effectors. * refers to the most conserved residues, + and – refer to the presence and absence of the indicated residues, respectively.

6.3.3 Testing the inhibitory effects of the mutated mSlp2-(3-56) super-effector protein using the FRET-based assay

Parallel to the melanosome clustering assay experiments (section 6.3.2), the inhibitory effects of the successful mSlp2-(3-56; K26R, A28R, Q44R, N48I) super-effector protein was tested using the FRET-based assay as described thereafter.

6.3.3.1 Generation of 6x Histidine-mSlp2 recombinant proteins

In order to test the inhibitory effects of the mutated mSlp2-(3-56; K26R, A28R, Q44R, N48I) super-effector protein using the FRET-based assay, this protein was produced as 6x Histidine recombinant protein. In addition, 6x Histidine-mSlp2-(3-56) recombinant protein was produced in order to investigate the effects of introducing the proposed mutations on this mSlp2 fragment as it had partial melanosome clustering inducing effects (see section 6.3.2). 6x Histidine-mSlp2-(3-80) and 6x Histidine-mSlp2-(3-67) recombinants proteins were produced in order to use one or both of them as positive control in the FRET assay experiments.

To produce 6x Histidine-mSlp2-(3-80) (M.W 11.70KDa), 6x Histidine-mSlp2-(3-56) (M.W 8.56KDa), 6x Histidine-mSlp2-(3-67) (M.W 9.90KDa) and 6x Histidine-mSlp2-(3-56; K26R, A28R, Q44R, N48I) (M.W 8.56KDa) recombinant proteins, pETDuet-1-mSlp2-(3-80), pETDuet-1-mSlp2-(3-56),

pETDuet-1-mSlp2-(3-67) and pETDuet-1-mSlp2-(3-56; K26R, A28R, Q44R, N48I) vectors (see section 2.1.3.5) were transformed into Rosetta *E. coli* competent cells and protein production was induced with 0.5mM IPTG as described in section 2.2.2, followed by protein purification steps using the IMAC system (see section 2.2.3.1). These proteins were then analysed using both 10% and 15% SDS-PAGE gel electrophoresis. 10% and 15% SDS-PAGE gel electrophoresis failed to resolve those proteins (data not shown) as they were low molecular weight proteins.

Therefore, for better separation of these low molecular weight proteins (less than 12.5KDa), the Invitrogen NuPAGE 4-12% Bis-Tris pre-cast gel system was used to analyse and separate these proteins as described in section 2.2.4.2. Analysis of the purified proteins using Invitrogen NuPAGE 4-12% Bis-Tris pre-cast gel system confirmed that the purified proteins were of the expected molecular weights (Figure 6.9).

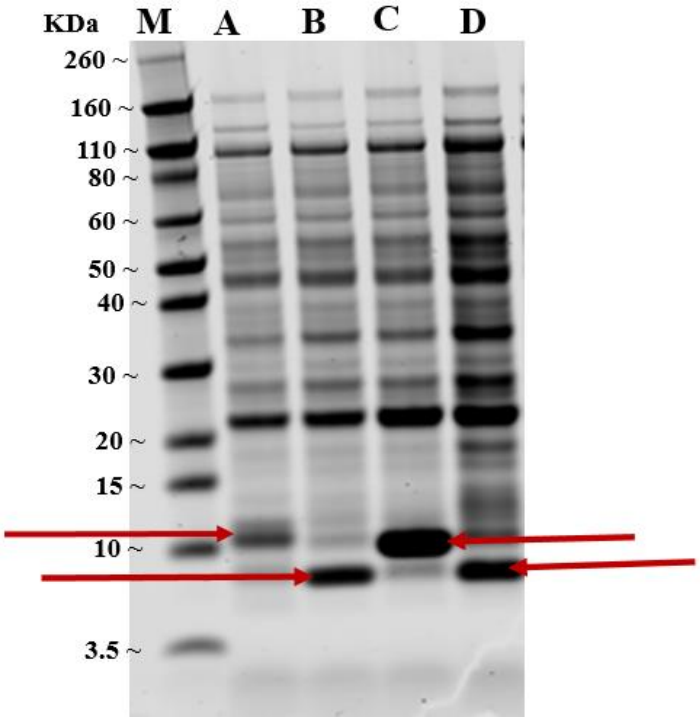


Figure 6.9. Separation profile of different 6x Histidine-mSlp2 recombinant proteins. Rosetta *E. coli* competent cells were transformed with the appropriate vectors, protein production was induced with 0.5mM IPTG for 3 hours at 37ºC. A Coomassie blue stained Invitrogen NuPAGE 4-12% Bis-Tris pre-cast gel was used to load the denatured purified protein samples (M; molecular weight standards). A) 6x Histidine-mSlp2-(3-80) (M.W 11.70KDa). B) 6x Histidine-mSlp2-(3-56) (M.W 8.56KDa). C) 6x Histidine-mSlp2-(3-67) (M.W 9.90KDa).

D) 6x Histidine-mSlp2-(3-56; K26R, A28R, Q44R, N48I) (M.W 8.56KDa). Abundant protein bands (the arrow indicated bands) were detected at the predicted molecular weights.

Next, to better confirm the specificity of the bands of interest, a western blot analysis using anti-histidine antibodies was also performed. 0.45 um PVDF transfer membrane was used and proteins were transferred at 4ºC using different conditions: 150V for 3 hours, 30V for 18 hours and 25V for 90 mins. Analysis of the western blots using those conditions failed in detecting protein bands (data not shown). This might be due to over-transfer of proteins from gel to membrane which is the most common problem during transfer of low molecular weight proteins, especially proteins with less than 12.5KDa molecular weight. Therefore, 0.2 um PVDF transfer membrane was used (instead of using 0.45 um PVDF) and proteins were transferred at 25V for 90 mins. Abundant protein bands were detected at the predicted molecular weights for these proteins (Figure 6.10), thereby confirming the specificity of protein bands detected previously using the Invitrogen NuPAGE 4-12% Bis-Tris pre-cast gel.

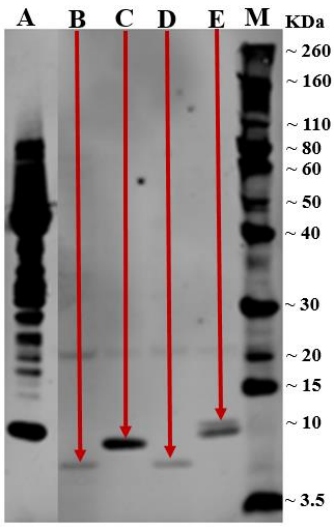


Figure 6.10. Western blot analysis profile of different 6x Histidine-mSlp2 recombinant proteins. Different 6x Histidine-mSlp2 recombinant proteins were loaded into 4-12% Bis-Tris pre-cast gel, transferred into PVDF membrane (0.2 µm) and immunoblotted with monoclonal anti-poly-Histidine antibody (M; molecular weight standards). A) 6x Histidine m.Cherry-Rab27b-(1-218) was used as a positive control. B) 6x Histidine-mSlp2-(3-56; K26R, A28R, Q44R, N48I) (M.W 8.56KDa). C) 6x Histidine-mSlp2-(3-67) (M.W 9.90KDa). D) 6x Histidine-mSlp2-(3-56) (M.W 8.56KDa). E) 6x Histidine-mSlp2-(3-80) (M.W 11.70KDa). Abundant protein bands (the arrow indicated bands) were detected

at the predicted molecular weights for these proteins. This western blot was cropped to remove unrelated proteins.

6.3.3.2 The inhibitory effect of the mutated mSlp2-(3-56) super-effector protein is comparable to that of mSlp2-(3-67)

As described in section 6.3.2, mSlp2-(3-56; K26R, A28R, Q44R, N48I) succeeded in producing comparable effects to that of mSlp2-(3-80) and mSlp2-(3-67) which were used as positive controls (by inducing perinuclear clustering of melanosomes and inhibiting Rab27a-Slac2-a interaction-dependent melanosome transport). Therefore, to better investigate the findings of the melanosome clustering assay, 6x Histidine-Slp2-(3-56; K26R, A28R, Q446, N48I) was produced and tested using the FRET-based protein-protein interaction assay.

To this end, different concentrations of mSlp2 mutant were used to disrupt the interaction between Rab27b and either Slp1 or Slp2. mSlp2-(3-56) and mSlp2-(3-67) were produced as 6x Histidine recombinant proteins and used as negative and positive controls, respectively (Figures 6.11 and 6.12). The calculated pIC50 values of the mutated mSlp2-(3-56), mSlp2-(3-56) and mSlp2-(3-67) for disrupting Rab27b-mSlp1 interaction were 7.37M, 5.21M and 7.59M, respectively. In comparison, the calculated pIC50 values of the mutated mSlp2-(3-56), mSlp2-(3-56) and mSlp2-(3-67) for disrupting Rab27b-mSlp2 interaction were 6.44M, 5.45M and 6.62M, respectively. Altogether, these experiments suggested that the inhibitory effects of the mutated mSlp2-(3-56) were comparable to that of mSlp2-(3-67) (positive control) (evidenced by pIC50 values), whereas the inhibitory effects of mSlp2-(3-56) (wild-type) were not comparable to that of the positive control or the mutated mSlp2-(3-56) (evidenced by pIC50 values).

According to these experiments, the introduction of these four mutations into mSlp2-(3-56) succeeded in producing a Rab27 super-effector. Thus, this novel Rab27 super-effector is an effective inhibitor of Rab27-effector interactions and can be tested later using breast cancer cell lines by examining its effects on reducing cancer cell invasion and metastasis.

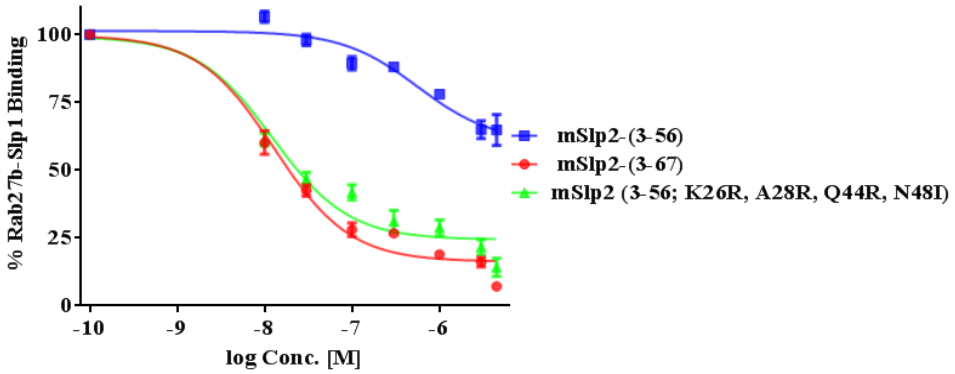


Figure 6.11. The inhibitory effect of the mutated mSlp2-(3-56) super-effector protein on hRab27b-mSlp1 effector interaction. Different 6x Histidine-mSlp2 fragments (0.0, 0.01, 0.03, 0.1, 0.3, 1.0, 3.0 and 4.5 µM) were used to disrupt the interaction between 0.15µM m.Cherry-hRab27b and 0.7µM GFP-mSlp1-(1-116). mSlp2-(3-56); pIC50: 5.21M. mSlp2-(3-67); pIC50: 7.59M. mSlp2-(3-56; K26R, A28R, Q446, N48I); pIC50: 7.37M. The FRET based protein-protein interaction assay was used to determine the binding. The pIC50 values were calculated by setting the bottom and top constraints to constant values of 0.0 and 100.0, respectively (no bottom and top constraints were used to create the dose-response sigmoid curve). Data points represent mean ± SEM of 4 independent experiments performed in quadruplicates.

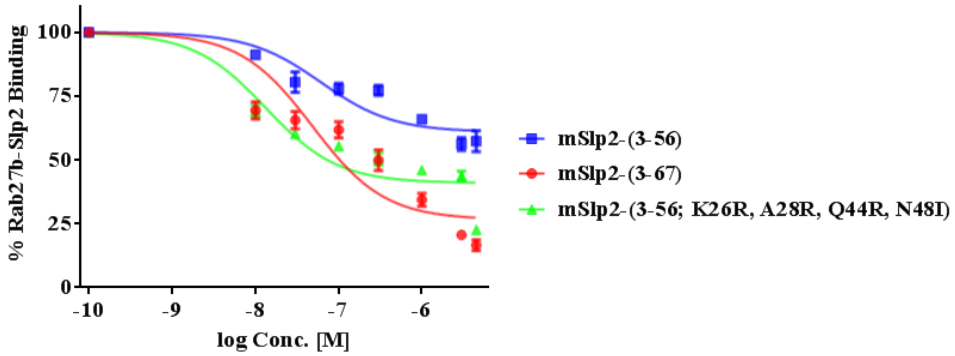


Figure 6.12. The inhibitory effect of the mutated mSlp2-(3-56) super-effector protein on hRab27b-mSlp2 effector interaction. Different 6x Histidine-mSlp2 fragments (0.0, 0.01, 0.03, 0.1, 0.3, 1.0, 3.0 and 4.5 µM) were used to disrupt the interaction between 0.15µM m.Cherry-hRab27b and 0.3µM GFP-mSlp2-(3-80). mSlp2-(3-56); pIC50: 5.45M. mSlp2-(3-67); pIC50: 6.62M. mSlp2-(3-56; K26R, A28R, Q446, N48I); pIC50: 6.44M. The FRET based protein-protein interaction assay was used to determine the binding. The pIC50 values were calculated by setting the bottom and top constraints to constant values of 0.0 and 100.0 respectively (only the top constraint was set to 100.0 to create the dose-response sigmoid curve). Data points represent mean ± SEM of 4 independent experiments performed in quadruplicates.

6.3.4 Testing of Hesperidin and BMD-20 as candidate small molecule inhibitors

Parallel to the experiments of testing the mutated mSlp2 in terms of inhibiting Rab27-effector protein interaction, searching in the literature identified two candidate small molecule inhibitors for Rab27a-Slac2-a interaction. The first compound was hesperidin, a natural citrus flavonoid found in orange peel. It was identified based on performing molecular docking studies on Slac2-a effector protein crystal structure (Kim et al., 2013). According to this docking study, hesperidin binds V21, D25, L28, R29, E32 and Y122 of Slac2-a (see Figure 6.13). Based on the identified binding interface between Rab27b and Slac2-a, these residues are essential for binding to Rab27b (Kukimoto-Niino et al., 2008). These interacting residues (V21, D25, L28, R29 and E32) of Slac2-a are also in consensus with the corresponding residues in Slp1 and Slp2 effector proteins (Kukimoto-Niino et al., 2008). Therefore, it was suggested that hesperidin might

be an effective inhibitor for interaction of Rab27 with either Slp1 or Slp2. Thus, this compound was chosen to be tested using the melanosome clustering and the FRET-based assays.

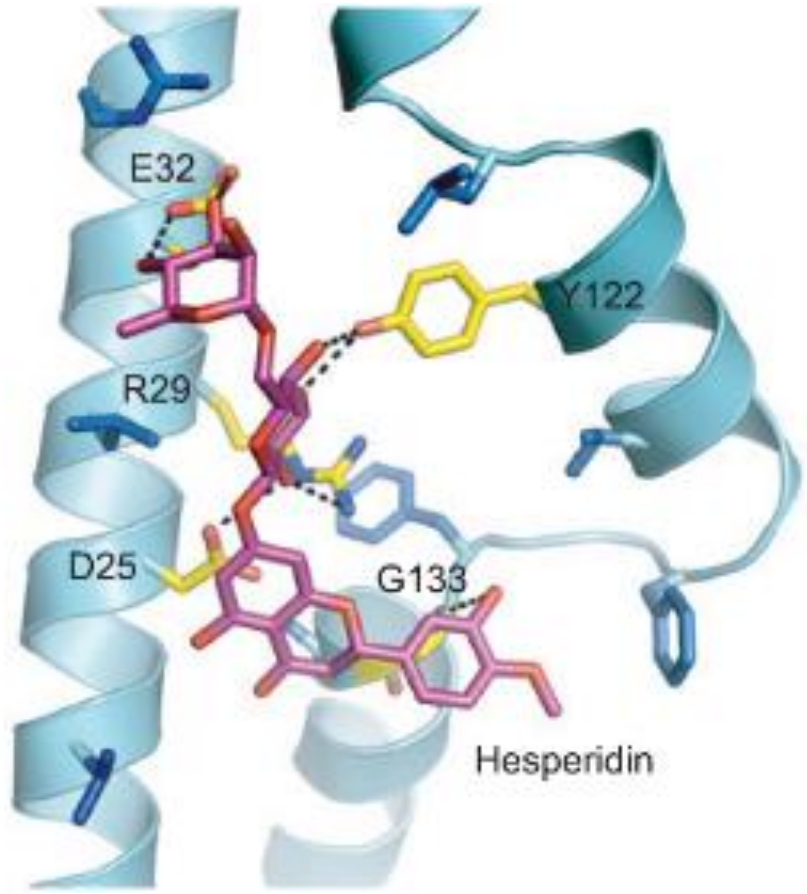


Figure 6.13. Model of hesperidin docking on Slac2-a structure. Yellow highlighted residues and black dashes represent interacting residues (between hesperidin and Slac2-a) and hydrogen bonds, respectively. Reproduced from (Kim et al., 2013).

The second compound was BMD-20 (Joung et al., 2014), this compound was identified by performing virtual screening for inhibitors of Slac2-a-Rab27 interaction based on the already identified 3-dimensional structure of Rab27b-Slac2-a complex (Kukimoto-Niino et al., 2008). Molecular docking of BMD-20 on Slac2-a structure showed that it can bind E32, R29, Y122 and G133 of Slac2-a (Figure 6.14) (based on the binding interface, these residues are essential for interaction with Rab27b). According to this, it was hypothesised that BMD-20

can inhibit the binding between Slac2-a and Rab27a (as mentioned before, E32 are conserved among Slac2-a, Slp1 and Slp2 effector proteins).

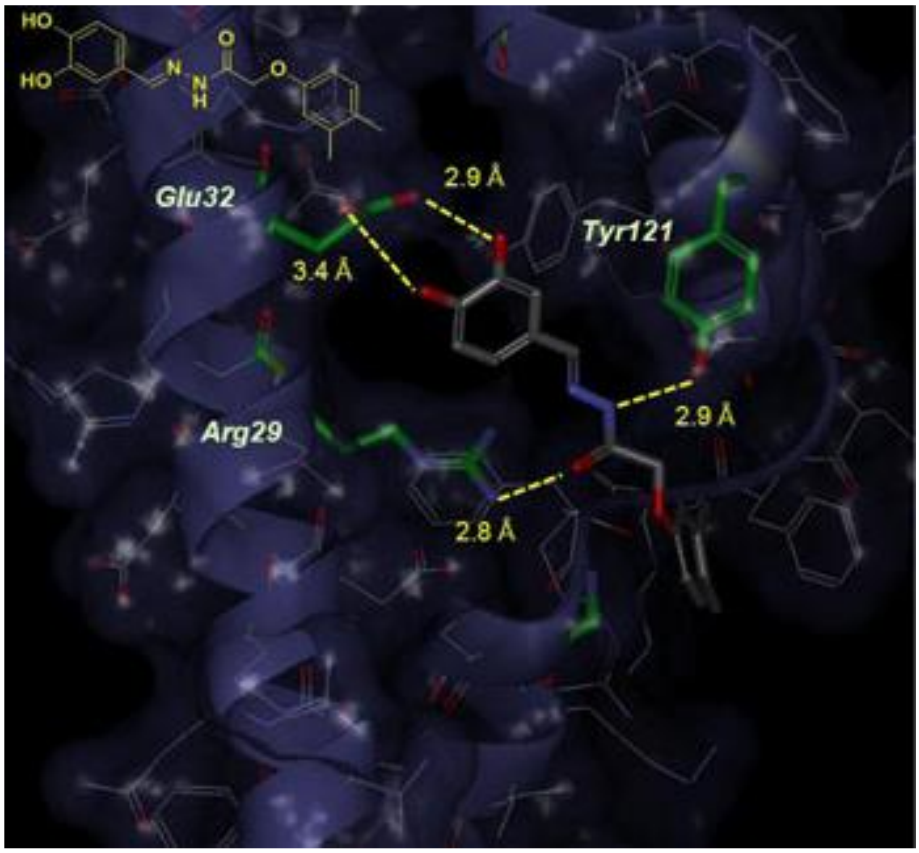


Figure 6.14. Proposed model of BMD-20 interaction with Slac2-a. The interaction model between BMD-20 and Slac2-a was generated based on the docking on Slac2-a structure. BMD-20 blocks the binding of E32, R29 and Y122 of Slac2-a with Rab27a. Reproduced from (Joung et al., 2014).

To test the veracity of these compounds as inhibitors of Rab27-effector interactions, different concentrations of either hesperidin or BMD-20 (0.0, 0.3, 1.0, 3.0, 10.0 and 30.0 μM) were used to investigate if they could disrupt the interaction between m.Cherry-hRab27b and either GFP-mSlp1-(1-116) or GFP-mSlp2-(3-80) (data were normalised against non-specific inhibition caused by DMSO). These two compounds failed to disrupt the interaction of Rab27b with either Slp1 or Slp2. pIC50 values of these two compounds were not determined as standard sigmoid curves could not be established (Figure 6.15).

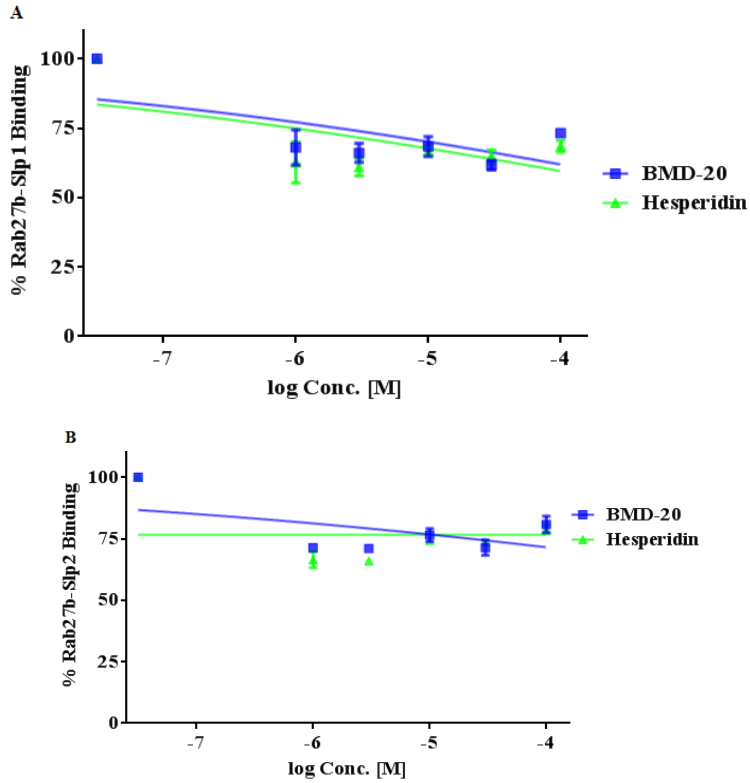


Figure 6.15. Testing the proposed inhibitory effects of BMD-20 and hesperidin on hRab27b-effector protein interaction. Different concentrations of BMD-20 and hesperidin (0.0, 0.3, 1.0, 3.0, 10.0, and 30.0 μM) were tested in terms of disrupting the interaction between: A) 0.15μM m.Cherry-hRab27b and 0.7μM GFP-mSlp1-(1-116). B) 0.15μM m.Cherry-hRab27b and 0.3μM GFP-mSlp2-(3-80). The FRET based protein-protein interaction assay was used to determine the binding. Data points represent mean ± SEM of 3 independent experiments performed in quadruplicates.

In addition, these compounds were also tested using the cellular melanosome clustering assay using different concentrations: 2.5, 5, 7.5, 10, 20 and 30μM. Again, the results of these experiments demonstrated that hesperidin and BMD-20 were not able to induce perinuclear clustering of melanosomes; i.e. they were not able to inhibit Rab27a-Slac2-a interaction. The quantification of the data demonstrated melanosome clustering pattern comparable to that of the negative control (data not shown). In these experiments, higher concentration (30μM) of both hesperidin and BMD-20 were used to investigate the proposed inhibitory effects (Kim et al. used 10μM hesperidin; Joung et al. used 2.5, 5 and 10μM BMD-20).

Those conflicting results in these two papers might be related to the method of quantifying the data, since this was done by counting the cells with clustered melanosomes without including the number of cells with dispersed melanosomes, followed by comparing with that of the negative control only (they did not calculate the percentage of cells with clustered melanosomes). In principle, the percentage of the clustered cells should be calculated and compared with reliable positive and negative controls (as performed in the current experiments when calculating the percentage of cells with clustered melanosomes), instead of counting the clustered cells and compare the absolute numbers with that of the negative control experiments only. Furthermore, the method of considering the cells as clustered was not accurate as some of the tested cells which were scored as clustered might be dead cells as shown in Figure 6.16.

In addition, no positive control for melanosome clustering was used in Kim et al. experiments, making it difficult to rely on the results of these experiments. Accordingly, hesperidin and BMD-20 cannot be considered as small molecule inhibitors of Rab27-effector protein interactions.

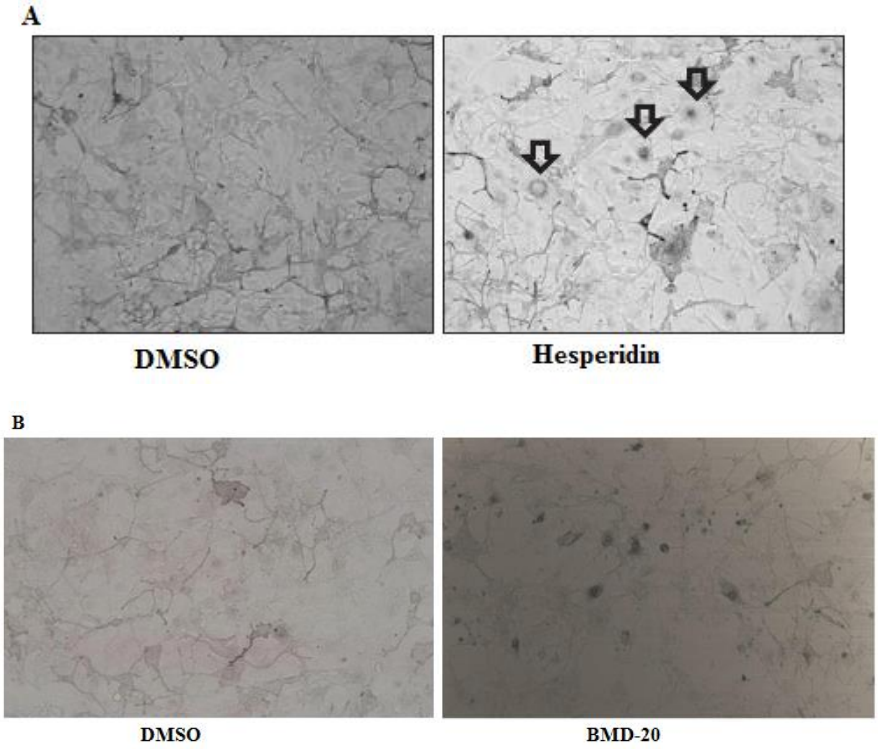


Figure 6.16. Hesperidin and BMD-20 treated cells. A) Hesperidin treated melan-a. B) BMD-20 treated melan-a. DMSO was used as a negative control in these experiments. Cell images reproduced from (Joung et al., 2014; Kim et al., 2013).

6.4 Discussion

Three major findings are presented here: First, the introduction of K26R, A28R, Q44R, N48I mutations into mSlp2-(3-56) resulted in producing significant inhibitory effects on Rab27a-Slac2-a interaction-dependent melanosome transport in living cells and on Rab27-Slp1/2 interaction in vitro by making mSlp2-(3-56) works as a Rab27 super-effector. Second, the introduction of the G51L mutation into the mSlp2-(3-56) super-effector significantly disrupted its melanosome clustering effects in living cells. Third, the production of Rab27 super-effectors might be an effective strategy to develop Rab27-effector interaction inhibitors in the future.

Early attempts to identify small molecule inhibitors of ras-effector protein interactions, identified sulindac sulphide as a probable inhibitor of interaction of p21 ras and its effector c-Raf (Herrmann et al., 1998). In addition, NMR analysis suggest that sulindac-derived compounds can inhibit Ras-Raf interaction by interacting with Ras at the switch I region (Muller et al., 2004; Waldmann et al., 2004). This suggests that molecular docking of sulindac-related compounds on Rab27 structure might reveal some binding hits within Rab27 protein.

Another approach to develop inhibitors of Rab27-effector interactions is by blocking the Rab27-GTP binding site, thus changing the conformation of Rab27 from GTP to GDP -bound state, inhibiting effector protein interactions (as Rab27 effector proteins bind Rab27 preferentially in its GTP-bound sate. For instance, the small molecule inhibitor, CID1067700 blocks GTP binding to Cdc42 (belongs to Rho GTPase family), Ras and Rab7, thereby inhibiting the signalling pathways related to GTP binding, including the interaction with their cognate effector proteins (Agola et al., 2012; Hong et al., 2015).

In this project, an alternative approach was utilised to produce Rab27 super-effectors which can be used as inhibitors of Rab27-effector protein interactions. Briefly, different mutations were proposed to be introduced into mSlp2-(3-56) and mSlp2-(3-67) based on performing molecular dynamics simulation studies of Rab27a-Slp2 complex interface and chemical interaction predictions as described in section in 6.3.1 (see Tables 6.1 and 6.2; Figures 6.1, 6.2 and 6.3).

These experiments (Figure 6.4) demonstrated that the introduction of the first four mutations (K26R, A28R, Q44R, N48I) into mSlp2-(3-56) resulted in an enhancement of the inhibitory effect in an additive way by inducing perinuclear clustering of melanosomes in 94.02% ±0.53 of expressing cells (was comparable to the positive control). Unexpectedly, upon introducing the fifth mutation (G51L), the inhibitory effect was almost completely abolished. In addition, upon introducing the sixth mutation (E56F), the inhibitory effect was not affected; i.e. it did not enhance the inhibitory effect. To investigate that, the G51L mutation was deleted, this resulted in restoring the inhibitory effect of the first four mutations (K26R, A28R, Q44R, N48I). In conclusion, the E56F mutation had no effect or even caused slight decrease in the inhibitory effect and the introduction of the first four mutations succeeded in producing a novel Rab27 super-effector which can be used as an effective Rab27-effector interaction inhibitor.

Interestingly, the G51 residue is highly conserved among most of the Rab27 effector proteins (Chavas et al., 2008; Kukimoto-Niino et al., 2008), suggesting that the G51 residue is crucial for Rab27 binding. Therefore, the G51 residue could be utilised in the future when performing virtual screening for candidate small molecule inhibitors of Rab27-effector protein interactions.

In comparison, the introduction of the proposed mutations into mSlp2-(3-67) revealed that the G51L and E56F mutations slightly reduced the melanosome clustering inducing effects compared with the positive controls (Figure 6.5), suggesting that 57-67 residues might compensate for the disruption of the binding caused by the G51L mutation and again highlighting the importance of the G51 residues as one of the key contacts of Rab27-effector interactions.

In addition, these mutations were further investigated using smaller mSlp2 fragments. Introducing (K26R, A28R, Q44R, N48I, G51L, E56F), (K26R, A28R, Q44R, N48I, E56F) and (K26R, A28R, Q44R, N48I) mutations into mSlp2-(10-56) did not improve the inhibitory effect (Figure 6.6), suggesting to focus mainly on mSlp2-(3-56) when developing Rab27-effector interaction inhibitors. This finding is in disagreement with the results of the crystal structure of Rab27a-Slp2 binding interface as it has been reported that mSlp2-(10-56)

represents the Rab27a binding interface and encompasses all the Rab27 binding contacts (Chavas et al., 2008) (see section 5.3.5).

In comparison, the (K26R, A28R, Q44R, N48I, G51L, E56F, H62R, R63F) mutations reduced the melanosome clustering inducing effects of mSlp2-(10-67); i.e. reducing its inhibitory effects on Rab27a-Slac2-a interaction-dependent melanosome transport (Figure 6.6). This suggests that this effect might be related to the G51L mutation, causing disruption of the binding to Rab27a. Deletion of the G51L mutation improved the inhibitory effect, indicating that G51 residue is essential for binding to Rab27a. Furthermore, introducing H62R, and R63F mutations might disrupt the binding, suggesting that 3-9 residues in mSlp2-(3-67) might compensate for this effect (Figure 6.6).

Intriguingly, introducing (K26R, A28R, Q44R, N48I) mutations into mSlp2-(10-67) improved the inhibitory effect (produced comparable effects to that of the positive controls) (Figure 6.6). Accordingly, the introduction of the first four mutations succeeded in promoting the inhibitory effects of either mSlp2-(3-56) or mSlp2-(10-67), making them Rab27 super-effectors.

In addition, by further investigating the effects of the first four proposed mutations on promoting mSlp2-(3-56) inhibitory effects (Figure 6.7), it was found that the K26R mutation was the most important mutation , whereas A28R was inferior to the other mutations. But, at least K26R, Q44R and N48I mutations were required to obtain comparable inhibitory effect to that of the positive controls. In agreement with that, molecular dynamics simulation studies suggested that introducing the first four mutations had comparable inhibitory effects to that of introducing 16 or 20 mutations (see section 6.3.1; Figures 6.1 and 6.8).

Notably, sequence alignment with other Rab27 effector proteins (Figure 5.7 and 5.11) (Chavas et al., 2008; Kukimoto-Niino et al., 2008) revealed that R26, R44 and I48 residues are the most conserved residues among Rab27 effectors (see Table 6.3), supporting the assumption that the introduction of only those three mutation might be enough to obtain comparable effects to that of introducing four mutations. This suggests that single K26R mutation and combination of

K26R and Q44R mutations can be introduced into mSlp2-(3-41) and mSlp2-(3-50), respectively and tested in the future.

Next, the successful mSlp2 super-effector, mSlp2-(3-56; K26R, A28R, Q446, N48I) was produced as 6x Histidine recombinant protein and its inhibitory effects was tested using the FRET-based protein-protein interaction assay (Figures 6.11 and 6.12). The inhibitory effects on Rab27b binding to Slp1/Slp2 were comparable to that of mSlp2-(3-67) (positive control). In contrast the inhibitory effect of mSlp2-(3-56) was not comparable to that of mSlp2-(3-67) or the mutated mSlp2. This suggests that those mutations might change protein conformation, making mSlp2-(3-56) stably interacts with Rab27. Notably, the binding ability of the constitutively active mutant of Rab27a/b-(Q78L) to Slp2-a, Slp4-a and Slac2-a is increased by replacement of cysteine-123 and cysteine-188 by serine, thereby inhibiting the intramolecular S-S bond formation between cysteine-123 and cysteine-188 (Chavas et al., 2008). Intriguingly, the introduction of the Y249V mutation into GDIβ protein resulted in gain of function toward Rab9 and Rab5, probably by inducing conformational changes in this protein, leading to increase its interaction with these Rab proteins (Shisheva et al., 1999). Accordingly, this supports the hypothesis that introduction of certain mutations into proteins might enhance their binding affinities by inducing conformal changes.

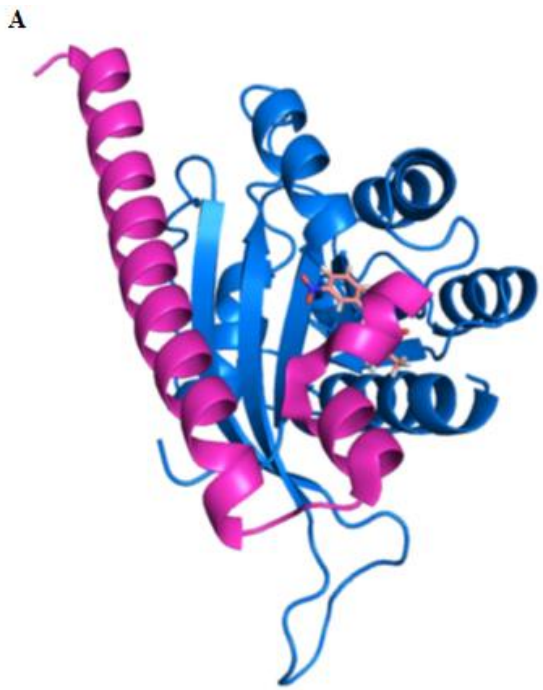
Overall, these experiments using the cellular melanosome clustering and the FRET-based assays demonstrated that the introduction of these mutations into mSlp2-(3-56) was a successful strategy to produce Rab27 super-effectors. This novel Rab27 super-effector can also be tested and used as a protein inhibitor in the future using cancer cell lines by investigating its effects on inhibiting/reducing cancer cell invasion and metastasis.

In addition, small molecule inhibitors found in literature were tested using the cellular melanosome clustering and the FRET-based assays, these included hesperidin and BMD-20. Surprisingly, none of them succeeded in disrupting the interaction between Rab27b and either Slp1 or Slp2 and dose-response sigmoid curve could not be established using the FRET-based assay (Figure 6.15). In agreement with that, testing of these two candidate inhibitors using the cellular

melanosome clustering assay demonstrated that none of them succeeded in producing significant melanosome clustering effects.

Consequently, these small molecules inhibitors failed to disrupt Rab27-effector protein interaction and cannot be considered as specific inhibitors for these interactions (see section 6.3.4). This suggests that they might work via other mechanisms other than inhibiting Rab27a-Slac2-a interactions.

Recently, molecular docking of Nexinhib20 on Rab27a structure (a novel Rab27a-Slp1 interaction inhibitor) (Johnson et al., 2016) based-on the already identified crystal structure of Rab27a-Slp2 complex (Chavas et al., 2008) demonstrated that tyrosine122 in Rab27a forms pi-pi stacking interactions with Nexinhib20 (for further details of Rab27 binding residues; see Figure 6.17). Interestingly, most of these Rab27-Nexinhib20 binding residues are crucial for Rab27a-Slp2 binding. Accordingly, Nexinhib20 could be used as a candidate inhibitor of Rab27-Slp2 interactions and tested using cancer cell lines in the future.



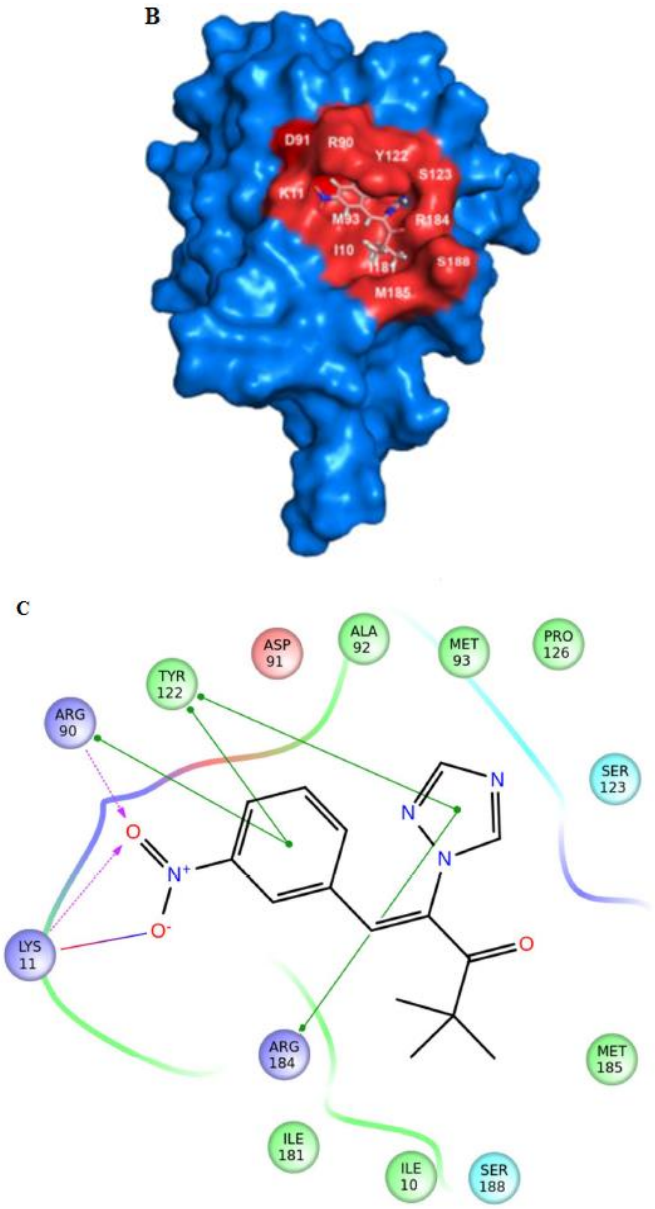


Figure 6.17. Molecular docking of Nexinhib20 on Rab27a structure. A) Crystal structure of Rab27a in complex with Nexinhib20 based on Rab27a-Slp2 complex interface (PDB: 3BC1), Rab27a and Slp2 depicted in blue and magenta, respectively. B) Rab27a-Nexinhib20 binding residues highlighted in red. C) Two- dimensional structure of Rab27a interaction with Nexinhib20 complex. Pi-pi interactions, hydrogen bonding, positively-charged, negatively-charged, polar and hydrophobic residues are depicted as green lines, purple arrows, blue, red, cyan and green circles, respectively. Reproduced from (Johnson et al., 2016).

6.5 Conclusions

Different candidate inhibitors, including small molecule and mSlp2-developed super-effectors were tested in terms of inhibiting Rab27-effector protein interactions. These competitions experiments revealed that the introduction of certain mutations into mSlp2-(3-56) was a successful strategy to produce and develop mSlp2 super-effectors. This can provide the basis for developing more peptide inhibitors, probably smaller peptide fragments which can be tested later using cellular and in vitro assays.

Chapter 7

Summary

The principal aim of this project was to characterise the key determinants of the Rab27-effector interactions, leading to identification of candidate inhibitors of these interactions, which can be tested later using in vitro and cellular assays. It has been reported that Rab27 proteins correlate with cancer cell invasion and proliferation signalling pathways (Hendrix and De Wever, 2013), therefore the main focus of this project was to design and develop inhibitors of Rab27-effector interactions which can be used not only to treat cancer, but also to cure Rab27-related inflammatory diseases. However, little research has been conducted to identify such Rab27 inhibitors and the research on this field is still limited, highlighting the importance of carrying out further research in this respect.

This project involved using and/or development of intra- and inter- disciplinary approaches, including the development of the in vitro florescent GST-pull down and FRET-based protein-protein interaction assays, using of the cellular melanosome clustering assay and related tissue culture techniques, construction of many DNA plasmids and adenoviral vectors and production of several recombinant proteins.

Initially, the conditions of the fluorescent GST-pull down assay were optimised and the specificity of this assay was investigated using unlabelled Rab27a/b as competitive inhibitors for Rab27-effector interactions. Classical GST pull down assays are not sensitive measures for determination of protein-protein interactions, since they involve performing multiple experimental steps, causing variability in the results. In this project, this assay was optimised in a way that the low sensitivity and the lack of consistent data were decreased. Overall, the fluorescent GST-pull down assay experiments demonstrated that the binding affinity of m.Cherry-Rab27b to GST-mSlp2-(3-80) is slightly higher than that to GST-mSlp1-(1-201). This assay might provide an in vitro advantageous and powerful quantitative and qualitative read-out for the Rab27-effector interactions, which can be used for testing the blocking effects of the candidate inhibitors in the future.

Next, to develop a more convenient, sensitive, fast and robust assay with fewer experimental steps, a FRET-based protein-protein interaction assay was set up to determine the binding affinity of mSlp1 and mSlp2 to Rab27a/b. By using this

assay, a large number of samples can be tested in a shorter period of time compared to the fluorescent GST-pull down assay, since the FRET assay requires fewer pipetting steps and there is no need to use the glutathione magnetic beads, thus reducing volume variability and contamination of samples with glutathione beads, indicating that more accurate results are obtained using this exquisite assay. The findings of the FRET-based assay experiments demonstrated that the binding affinity of GFP-mSlp2-(3-80) to m.Cherry-Rab27a/b is higher than that of GFP-mSlp1-(1-116) (consistent with the results of the GST-pull down assay), suggesting that mSlp2 is an appropriate candidate to focus on when developing protein inhibitors for Rab27-effector interactions. Additionally, building upon the binding affinity results, testing the effects of the candidate inhibitors on Rab27 interaction with Slp2 is superior to Slp1, since this can be considered as a more efficient indicator for the effectiveness and/or functional strength of the inhibitor. Moreover, as the conditions of the FRET-based assay were controlled including GTP concentration, incubation time and concentration of the interacting components, this assay can be considered as a specific in vitro measure for determining Rab27-effector interactions, and therefore can be used in the future to test the inhibitory effects of the candidate inhibitors.

Furthermore, a Rab27a-dependent melanosome transport assay was used as an indirect read-out of Rab27-effector interaction in melan-a murine melanocytes by testing the induced perinuclear clustering of melanosomes. Initial experiments aimed to identify the minimum mSlp2 binding fragment to Rab27a and the key determinants and/or contacts of Rab27-effector interactions by introducing different mutations into mSlp2-(3-80). These experiments demonstrated that mSlp2-(3-80) dramatically induced perinuclear clustering of melanosomes by competing with Slac2-a for Rab27a binding and none of the introduced mutations affected Rab27a-dependent melanosome transport, suggesting that smaller mSlp2 fragments were required to be investigated. In addition, introduction of the R32W mutation into mSlp2 equivalent to R35W mutation in Slac2-a (Menasche et al., 2003b; Tomita and Suzuki, 2004) resulted in partial loss of the induced melanosome clustering effects, suggesting that R32 residue is essential determinant of Rab27a-Slp2 interaction and can be targeted

when performing virtual screening for candidate small molecule inhibitors of Rab27-effector interactions.

Afterwards, based on the already identified crystal structures of the binding interface of Slp2-Rab27a and Slac2-a-Rab27b (Chavas et al., 2008; Kukimoto-Niino et al., 2008), different truncations at the N-terminal of mSlp1 and mSlp2 (by sequentially adding mSlp2 α helices) were performed, and also mSlac2-a-(1-146) was tested. These experiments revealed that the Slp2-Rab27a crystal structure findings do not correspond with the current results of the melanosome clustering assay, therefore larger Slp2 fragments were tested. Overall, these experiments revealed that mSlp2-(3-67) was comparable to mSlp2-(3-80) and might act as the minimum Rab27a binding fragment, whereas mSlp2-(3-56) partially induced perinuclear clustering of melanosomes. In addition, mSlp1-(1-116) was comparable to mSlp2-(3-80), whilst mSlac2-a-(1-146) was capable of partially inducing perinuclear clustering of melanosomes by about 71.58% which is not consistent with the Slac2-a-Rab27b crystal structure results, suggesting that larger mSlac2-a fragments need to be investigated in the future.

As described in section 5.4, mSlp2 α-helices were unable to induce significant perinuclear clustering of melanosomes; i.e. they could not form stable interactions with Rab27b and this might be due to loss of helicity. Therefore, as a future work, α helicity can be improved by using an appropriate alkyl linker or the hydrocarbon-stapled peptides strategy (Walensky and Bird, 2014) which can be exploited in the development of inhibitors with significant Rab27 binding activity using either α1 (10-41 aa), α2 (42-50 aa) or α3 (51-56 aa) mSlp2 helices, thus increasing α helicity. For instance, the stabilized α-helical domain of Rab6 interacting protein1-3 (StRIP3), a hydrocarbon-stapled peptide, was found to disrupt the interaction between Rab8a and its effector Lowe oculocerebrorenal syndrome protein1 (OCRL1) using a fluorescence polarization assay (Spiegel et al., 2014).

Next to better investigate the results of testing mSlp2 fragments using the melanosome clustering assay, the inhibitory effects of mSlp2-(3-41) and mSlp2-(3-56) fragments on hRab27b-mSlp1 interaction were tested using the FRET in vitro assay. These experiments demonstrated that mSlp2-(3-41 and 3-56) had

partial inhibitory effect, suggesting that the inhibitory effects of those mSlp2 fragments can be promoted using the hydrocarbon-stapled peptides approach as described before.

It might be difficult to identify candidate small molecule inhibitors of Rab27-Slp2 interaction as there are many key contacts between them which require to be blocked [for further details of Rab27a-Slp2 binding interface see (Chavas et al., 2008)]. Therefore, the design and development of Rab27 super-effectors strategy was used as an alternative approach to obtain inhibitors of Rab27-effector interactions. These experiments revealed that the sequential introduction of K26R, A28R, Q44R and N48I mutations into mSlp2-(3-56) worked progressively to enhance the Rab27 binding activity and profoundly promoted the inhibitory effects on Rab27a-dependent melanosome transport, achieving comparable effects to mSlp2-(3-80) and mSlp2-(3-67) using the melanosome clustering assay. Moreover, those results were investigated further using the FRET in vitro assay, again mSlp2-(3-56; K26R, A28R, Q44R, N48I) significantly inhibited hRab27b binding to mSlp1/mSlp2 and was comparable to mSlp2-(3-67). These mSlp2 mutants might adopt a gain of function conformation, leading to an incremental enhancement of binding to Rab27. This indicates that a novel Rab27 super-effector was effectively produced and this can provide the basis for the development of smaller peptide inhibitors. Noteworthy, proteins penetration into living cells can be enhanced by fusing them with cell-penetrating peptides (Gautam et al., 2016; Johnson et al., 2010b; Kristensen et al., 2016).

Furthermore, hesperidin and BMD-20, proposed small molecule inhibitors found in literature (Joung et al., 2014; Kim et al., 2013) were tested, but both of them failed to inhibit Rab27-effector interaction in vitro and in living cells, indicating that these small molecules cannot be considered as specific inhibitors and might work through mechanisms other than inhibiting Rab27-effector interactions.

As a future work, screening for small molecule inhibitors can also be performed in the future. The main advantage of screening for inhibitors using virtual libraries over traditional high-throughput, is that millions of compounds can be screened, leading to identification of inhibitors based on structure-activity

relationship rationale (Zhao et al., 2017). Furthermore, Rab27 proteins can be targeted by inhibiting RGGT enzyme, for instance 3-PEHPC, a phosphonocarboxylate analogue of risedronate acts as a negative regulator of Rab6 prenylation and induces apoptosis by inhibiting RGGT enzyme in human myeloma cells (Roelofs et al., 2006). In addition, numerous RGGT enzyme inhibitors have been identified and developed using a virtual high throughput screening (Stigter et al., 2012), but the lack of selectivity of these inhibitors (as they can work on wide range of Rab proteins) suggests the design and development of selective inhibitors which can be performed by targeting Rab27-effector interactions, especially those related to specific Rab27 effectors. Additionally, GEF inhibitors can be used as Rab27 inhibitors by inhibiting the cycling of Rab27 from GDP- to GTP- bound state, thus blocking Rab27-effector interaction. Interestingly, NSC-658497 has been identified as a small molecule inhibitor of the Ras GEF activity and found to inhibit Ras downstream signalling effects including downregulation of cell proliferation in murine fibroblasts (Evelyn et al., 2014), but again the lack of selectivity of those inhibitors might limit their clinical uses. Furthermore, the Rab GTPase intrinsic activity can be promoted by enhancing GAP enzyme activity, increasing Rab (GDP), and thus reducing Rab binding to its effectors, however development of GAP agonists is less promising target than identification of GEG antagonists (Vigil et al., 2010).

In conclusion, this study provides the basis for identifying Rab27-effector interaction inhibitors, but high thorough virtual screening for candidate small molecule inhibitors can be performed in the future. Furthermore, the newly developed in vitro fluorescent GST-pull down and FRET-based protein-protein interaction assays, and also the already established melanosome clustering cellular assay can be used to test the inhibitory effects of the candidate inhibitors in the future. Interestingly, the findings of this study suggest that the development of Slp2 super-effectors might be an effective strategy to produce Rab27-effector interaction protein inhibitors. Those protein inhibitors can be delivered into cells either by endocytosis from the medium or by microinjection to be tested further using cancer cell lines in terms of reducing cancer cell invasion and metastasis, for instance they can be tested in MCF7 breast cancer cells stably expressing Rab27.

Chapter 8

Appendix

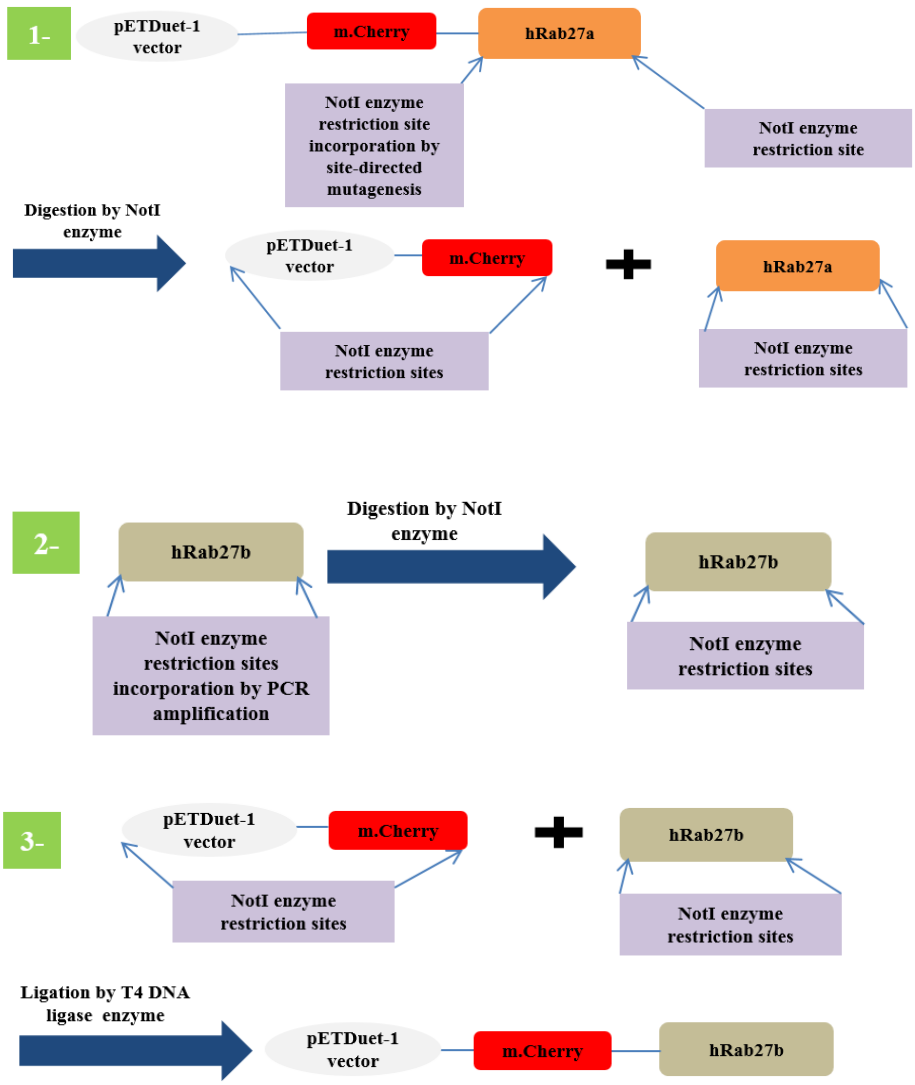


Figure 8.1. A schematic representation of the pETDuet-1-m.Cherry-hRab27b vector generation steps. The steps performed for generation of the pETDuet-1-m.Cherry-hRab27b-(1-218; T23N) vector involved: 1) A site-directed mutagenesis of the pETDuet-1-m.Cherry-hRab27b vector was performed and NotI enzyme restriction site was incorporated into the 5' end of hRab27a (this vector originally contained a NotI enzyme restriction site at the 3' end of hRab27a). This step was followed by NotI restriction enzyme digestion. 2) hRab27b-(1-218; T23N) cDNA was PCR amplified using the appropriate vector. 3) The digested vector and insert were then ligated to form the pETDuet-1-m.Cherry-hRab27b-(1-218; T23N) vector.

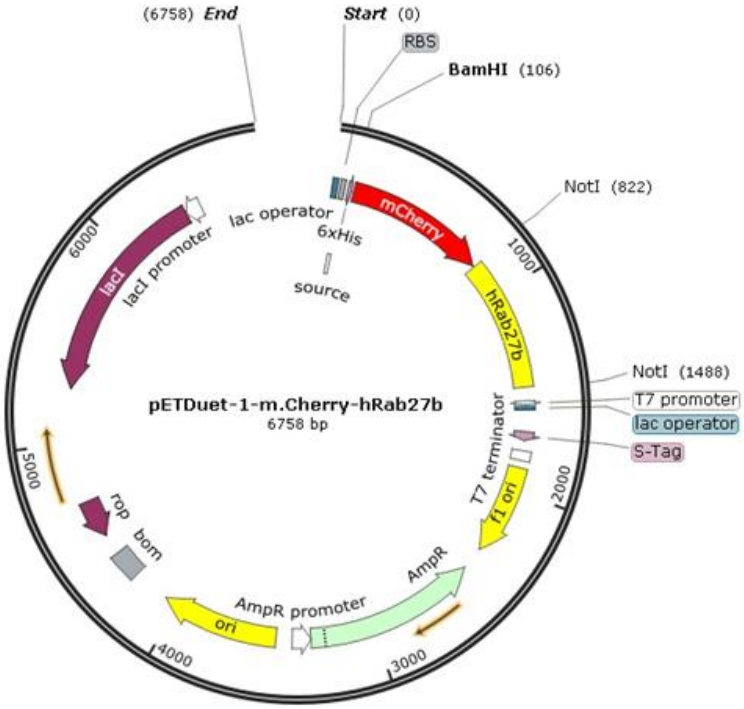


Figure 8.2. pETDuet-1-m.Cherry-hRab27b-(1-218; T23N) vector map. The pETDuet-1-m.Cherry-hRab27b-(1-218; T23N) vector contains 6x histidine at the 5' end of m.Cherry, two NotI restriction sites at the 5' and 3' ends of hRab27b and ampicillin resistance gene. The molecular weight of this vector is 6758BP; 6x Histidine, m.Cherry and hRab27b are in the same open reading frame to produce the 6x Histidine-m.Cherry-hRab27b recombinant protein.

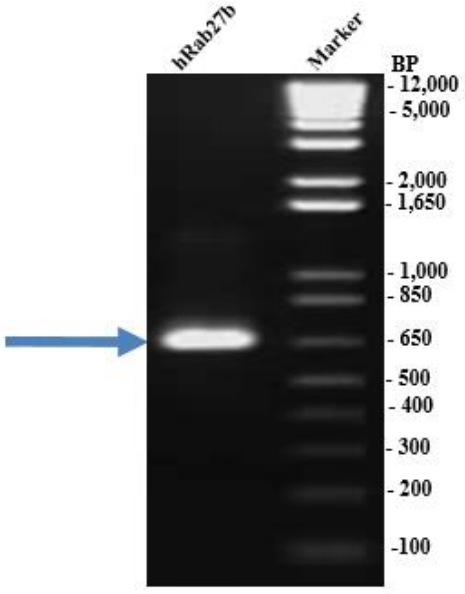


Figure 8.3. PCR amplification of hRab27b-(1-218; T23N). An ethidium bromide stained 1% (W/V) TBE agarose gel showing PCR amplification of hRab27b-(1-218; T23N) using the pEGFP-hRab27b-(T23N) vector. The molecular weight is 654BP (the arrow indicated band).

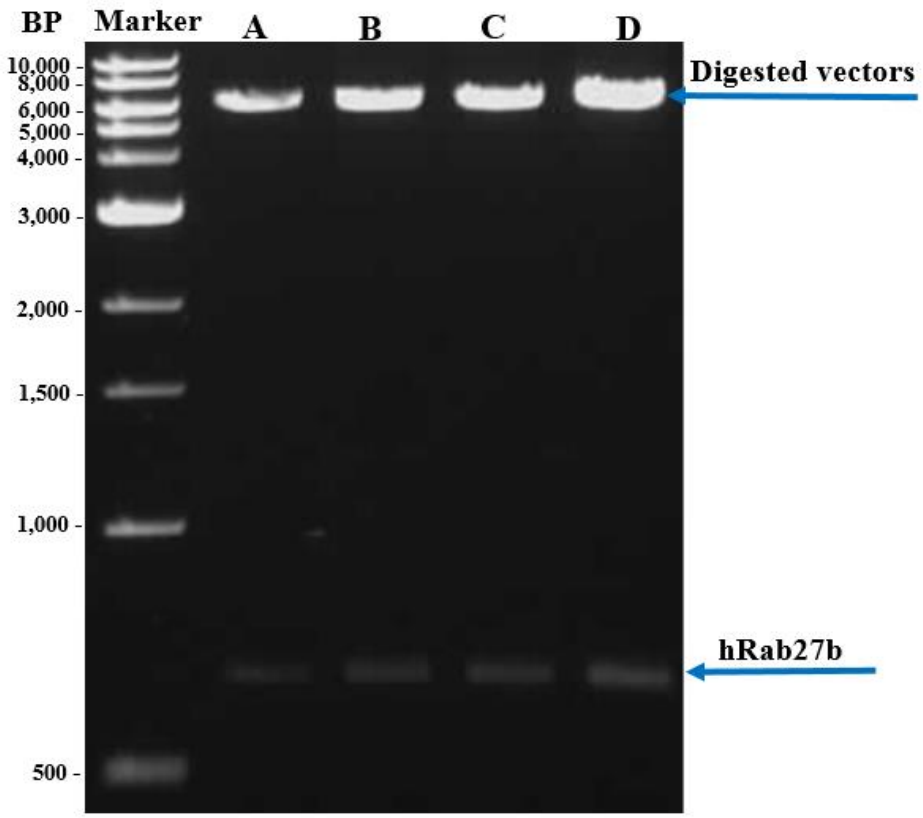


Figure 8.4. An ethidium bromide stained 1% TBE agarose gel showing NotI restriction enzyme digests of different pETDuet-1-m.Cherry-hRab27b vectors. A) pETDuet-1-m.Cherry-hRab27b-(1-218; T23N). B) pETDuet-1-m.Cherry-hRab27b-(1-218). C) pETDuet-1-m.Cherry-hRab27b-(1-218; Q78L). D) pETDuet-1-m.Cherry-hRab27b-(1-200). The molecular weights of the upper (digested vector) and lower (digested insert) arrow indicated bands are 6104BP and 654BP, respectively.

A

mCherry-6xHIS [Cloning vector pLM006-mCherry]

Sequence ID: ANF29839.1 Length: 249 Number of Matches: 1

▶ See 1 more title(s)

Range 1: 15 to 237 GenPept Graphics ▼ Next Match ▲ Previous Match

Score	Expect	Method	Identities	Positives	Gaps	Frame
432 bits(1112)	2e-149	Compositional matrix adjust.	221/223(99%)	222/223(99%)	0/223(0%)	+3

```
Query  24   EFMRFXVHMEGSVNghefeiegegegRPYEGTQTAKLKVTKGGPLPFAWDILSPQFMYGS  203
            EFMRF VHMEGSVNGHEFEIEGEGEGRPYEGTQTAKLKVTKGGPLPFAWDILSPQFMYGS
Sbjct  15   EFMRFKVHMEGSVNGHEFEIEGEGEGRPYEGTQTAKLKVTKGGPLPFAWDILSPQFMYGS  74

Query  204  KAYVKHPADIPDYLKLSFPEGFKWERVMNFEDGGVVTVTQDSSLQDGEFIYKVKLRGTNF  383
            KAYVKHPADIPDYLKLSFPEGFKWERVMNFEDGGVVTVTQDSSLQDGEFIYKVKLRGTNF
Sbjct  75   KAYVKHPADIPDYLKLSFPEGFKWERVMNFEDGGVVTVTQDSSLQDGEFIYKVKLRGTNF  134

Query  384  PSDGPVMQKKTMGWEASSERMYPEDGALKGEIKQRLKLKDGGHYDAEVKTTYKAKKPVQL  563
            PSDGPVMQKKTMGWEASSERMYPEDGALKGEIKQRLKLKDGGHYDAEVKTTYKAKKPVQL
Sbjct  135  PSDGPVMQKKTMGWEASSERMYPEDGALKGEIKQRLKLKDGGHYDAEVKTTYKAKKPVQL  194

Query  564  PGAYNVNIKLDITSHNEDYTIVEQYERAEGRHSTGGMDELYRA  692
            PGAYNVNIKLDITSHNEDYTIVEQYERAEGRHSTGGMDELYR+
Sbjct  195  PGAYNVNIKLDITSHNEDYTIVEQYERAEGRHSTGGMDELYRS  237
```

B

ras-related protein Rab-27B [Homo sapiens]

Sequence ID: NP_004154.2 Length: 218 Number of Matches: 1

▶ See 15 more title(s)

Range 1: 1 to 218 GenPept Graphics ▼ Next Match ▲ Previous Match

Score	Expect	Method	Identities	Positives	Gaps	Frame
455 bits(1171)	4e-158	Compositional matrix adjust.	217/218(99%)	217/218(99%)	0/218(0%)	-2

```
Query  689  MTDGDYDYLIKLLALGDSGVGKNTFLYRYTDNKFNPKFITTVGIDFREKRVVYNAQGPNG  510
            MTDGDYDYLIKLLALGDSGVGK TFLYRYTDNKFNPKFITTVGIDFREKRVVYNAQGPNG
Sbjct  1    MTDGDYDYLIKLLALGDSGVGKTTFLYRYTDNKFNPKFITTVGIDFREKRVVYNAQGPNG  60

Query  509  SSGKAFKVHLQLWDTAGQERFRSLTTAFFRDAMGFLLMFDLTSQQSFLNVRNWMSQLQAN  330
            SSGKAFKVHLQLWDTAGQERFRSLTTAFFRDAMGFLLMFDLTSQQSFLNVRNWMSQLQAN
Sbjct  61   SSGKAFKVHLQLWDTAGQERFRSLTTAFFRDAMGFLLMFDLTSQQSFLNVRNWMSQLQAN  120

Query  329  AYCENPDIVLIGNKADLPDQREVNERQARELADKYGIPYFETSAATGQNVEKAVETLLDL  150
            AYCENPDIVLIGNKADLPDQREVNERQARELADKYGIPYFETSAATGQNVEKAVETLLDL
Sbjct  121  AYCENPDIVLIGNKADLPDQREVNERQARELADKYGIPYFETSAATGQNVEKAVETLLDL  180

Query  149  IMKRMEQCVEKTQIPDTVNGGNSGNLDGEKPPEKKCIC  36
            IMKRMEQCVEKTQIPDTVNGGNSGNLDGEKPPEKKCIC
Sbjct  181  IMKRMEQCVEKTQIPDTVNGGNSGNLDGEKPPEKKCIC  218
```

Figure 8.5. Amino acid sequence alignment of the pETDuet-1-m.Cherry-hRab27b-(1-218; T23N) vector sequencing data. A) Using a forward primer for amplification of m.Cherry. B) Using the Duet Down1 reverse primer.

A

ras-related protein Rab-27B [Homo sapiens]

Sequence ID: NP_004154.2 Length: 218 Number of Matches: 1

▶ See 15 more title(s)

Range 1: 9 to 215 GenPept Graphics ▼ Next Match ▲ Previous Match

Score	Expect	Method	Identities	Positives	Gaps	Frame
428 bits(1101)	9e-149	Compositional matrix adjust.	206/207(99%)	206/207(99%)	0/207(0%)	+1

```
Query  10   LTKLLALGDSGVGKTTFLYRYTDNKFNPKFITTVGIDFREKRVVYNAQGPNGSSGKAFKV  189
            L KLLALGDSGVGKTTFLYRYTDNKFNPKFITTVGIDFREKRVVYNAQGPNGSSGKAFKV
Sbjct  9    LIKLLALGDSGVGKTTFLYRYTDNKFNPKFITTVGIDFREKRVVYNAQGPNGSSGKAFKV  68

Query  190  HLQLWDTAGQERFRSLTTAFFRDAMGFLLMFDLTSQQSFLNVRNWMSQLQANAYCENPDI  369
            HLQLWDTAGQERFRSLTTAFFRDAMGFLLMFDLTSQQSFLNVRNWMSQLQANAYCENPDI
Sbjct  69   HLQLWDTAGQERFRSLTTAFFRDAMGFLLMFDLTSQQSFLNVRNWMSQLQANAYCENPDI  128

Query  370  VLIGNKADLPDQREVNERQARELADKYGIPYFETSAATGQNVEKAVETLLDLIMKRMEQC  549
            VLIGNKADLPDQREVNERQARELADKYGIPYFETSAATGQNVEKAVETLLDLIMKRMEQC
Sbjct  129  VLIGNKADLPDQREVNERQARELADKYGIPYFETSAATGQNVEKAVETLLDLIMKRMEQC  188

Query  550  VEKTQIPDTVNGGNSGNLDGEKPPEKK  630
            VEKTQIPDTVNGGNSGNLDGEKPPEKK
Sbjct  189  VEKTQIPDTVNGGNSGNLDGEKPPEKK  215
```

B

ras-related protein Rab-27B [Homo sapiens]

Sequence ID: NP_004154.2 Length: 218 Number of Matches: 1

▸ See 15 more title(s)

Range 1: 1 to 212 GenPept Graphics ▼ Next Match ▲ Previous Match

Score	Expect	Method	Identities	Positives	Gaps	Frame
439 bits(1130)	3e-153	Compositional matrix adjust.	210/212(99%)	211/212(99%)	0/212(0%)	-2

```
Query  640  MTDGDYDYLIKLLALGDSGVGKTTFLYRYTDNKFNPKFITTVGIDFREKRVVYNAQGPNG  461
            MTDGDYDYLIKLLALGDSGVGKTTFLYRYTDNKFNPKFITTVGIDFREKRVVYNAQGPNG
Sbjct  1    MTDGDYDYLIKLLALGDSGVGKTTFLYRYTDNKFNPKFITTVGIDFREKRVVYNAQGPNG  60

Query  460  SSGKAFKVHLQLWDTAGQERFRSLTTAFFRDAMGFLLMFDLTSQQSFLNVRNWMSQLQAN  281
            SSGKAFKVHLQLWDTAGQERFRSLTTAFFRDAMGFLLMFDLTSQQSFLNVRNWMSQLQAN
Sbjct  61   SSGKAFKVHLQLWDTAGQERFRSLTTAFFRDAMGFLLMFDLTSQQSFLNVRNWMSQLQAN  120

Query  280  AYCENPDIVLIGNKADLPDQREVNERQARELADKYGIPYFETSAATGQNVEKAVETLLDL  101
            AYCENPDIVLIGNKADLPDQREVNERQARELADKYGIPYFETSAATGQNVEKAVETLLDL
Sbjct  121  AYCENPDIVLIGNKADLPDQREVNERQARELADKYGIPYFETSAATGQNVEKAVETLLDL  180

Query  100  IMKRMEQCVEKTQIPDTVNGGNSGNLDGKSPP  5
            IMKRMEQCVEKTQIPDTVNGGNSGNLDG+ PP
Sbjct  181  IMKRMEQCVEKTQIPDTVNGGNSGNLDGEKPP  212
```

Figure 8.6. Amino acid sequence alignment of the pETDuet-1-m.Cherry-hRab27b-(1-218) vector sequencing data. A) Using the forward primer for hRab27b PCR amplification. B) Using the reverse primer for hRab27b PCR amplification.

ras-related protein Rab-27B [Homo sapiens]

Sequence ID: NP_004154.2 Length: 218 Number of Matches: 1

▸ See 15 more title(s)

Range 1: 1 to 217 GenPept Graphics ▼ Next Match ▲ Previous Match

Score	Expect	Method	Identities	Positives	Gaps	Frame
452 bits(1163)	3e-158	Compositional matrix adjust.	216/217(99%)	216/217(99%)	0/217(0%)	-2

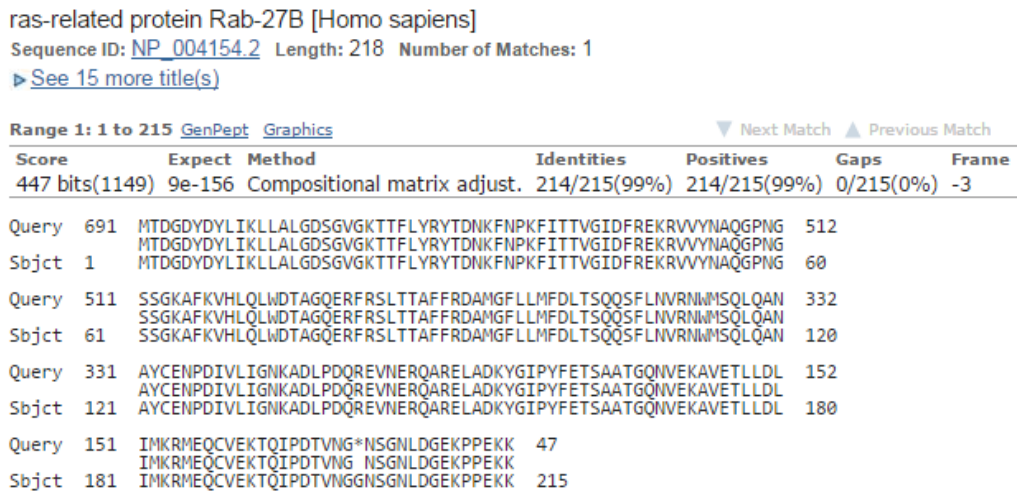
```
Query  696  MTDGDYDYLIKLLALGDSGVGKTTFLYRYTDNKFNPKFITTVGIDFREKRVVYNAQGPNG  517
            MTDGDYDYLIKLLALGDSGVGKTTFLYRYTDNKFNPKFITTVGIDFREKRVVYNAQGPNG
Sbjct  1    MTDGDYDYLIKLLALGDSGVGKTTFLYRYTDNKFNPKFITTVGIDFREKRVVYNAQGPNG  60

Query  516  SSGKAFKVHLQLWDTAGLERFRSLTTAFFRDAMGFLLMFDLTSQQSFLNVRNWMSQLQAN  337
            SSGKAFKVHLQLWDTAG ERFRSLTTAFFRDAMGFLLMFDLTSQQSFLNVRNWMSQLQAN
Sbjct  61   SSGKAFKVHLQLWDTAGQERFRSLTTAFFRDAMGFLLMFDLTSQQSFLNVRNWMSQLQAN  120

Query  336  AYCENPDIVLIGNKADLPDQREVNERQARELADKYGIPYFETSAATGQNVEKAVETLLDL  157
            AYCENPDIVLIGNKADLPDQREVNERQARELADKYGIPYFETSAATGQNVEKAVETLLDL
Sbjct  121  AYCENPDIVLIGNKADLPDQREVNERQARELADKYGIPYFETSAATGQNVEKAVETLLDL  180

Query  156  IMKRMEQCVEKTQIPDTVNGGNSGNLDGEKPPEKKCI  46
            IMKRMEQCVEKTQIPDTVNGGNSGNLDGEKPPEKKCI
Sbjct  181  IMKRMEQCVEKTQIPDTVNGGNSGNLDGEKPPEKKCI  217
```

Figure 8.7. Amino acid sequence alignment of the pETDuet-1-m.Cherry-hRab27b-(1-218; Q78L) vector sequencing data. The Duet Down1 reverse primer was used to sequence the vector.



ras-related protein Rab-27B [Homo sapiens]
Sequence ID: NP_004154.2 Length: 218 Number of Matches: 1
▶ See 15 more title(s)

Range 1: 1 to 215 GenPept Graphics ▼ Next Match ▲ Previous Match

Score	Expect	Method	Identities	Positives	Gaps	Frame
447 bits(1149)	9e-156	Compositional matrix adjust.	214/215(99%)	214/215(99%)	0/215(0%)	-3

```
Query  691  MTDGDYDYLIKLLALGDSGVGKTTFLYRYTDNKFNPKFITTVGIDFREKRVVYNAQGPNG  512
            MTDGDYDYLIKLLALGDSGVGKTTFLYRYTDNKFNPKFITTVGIDFREKRVVYNAQGPNG
Sbjct  1    MTDGDYDYLIKLLALGDSGVGKTTFLYRYTDNKFNPKFITTVGIDFREKRVVYNAQGPNG  60

Query  511  SSGKAFKVHLQLWDTAGQERFRSLTTAFFRDAMGFLLMFDLTSQQSFLNVRNWMSQLQAN  332
            SSGKAFKVHLQLWDTAGQERFRSLTTAFFRDAMGFLLMFDLTSQQSFLNVRNWMSQLQAN
Sbjct  61   SSGKAFKVHLQLWDTAGQERFRSLTTAFFRDAMGFLLMFDLTSQQSFLNVRNWMSQLQAN  120

Query  331  AYCENPDIVLIGNKADLPDQREVNERQARELADKYGIPYFETSAATGQNVEKAVETLLDL  152
            AYCENPDIVLIGNKADLPDQREVNERQARELADKYGIPYFETSAATGQNVEKAVETLLDL
Sbjct  121  AYCENPDIVLIGNKADLPDQREVNERQARELADKYGIPYFETSAATGQNVEKAVETLLDL  180

Query  151  IMKRMEQCVEKTQIPDTVNG*NSGNLDGEKPPEKK  47
            IMKRMEQCVEKTQIPDTVNG NSGNLDGEKPPEKK
Sbjct  181  IMKRMEQCVEKTQIPDTVNGGNSGNLDGEKPPEKK  215
```

Figure 8.8. Amino acid sequence alignment of the pETDuet-1-m.Cherry-hRab27b-(1-200) vector sequencing data. The Duet Down1 reverse primer was used to sequence the vector.

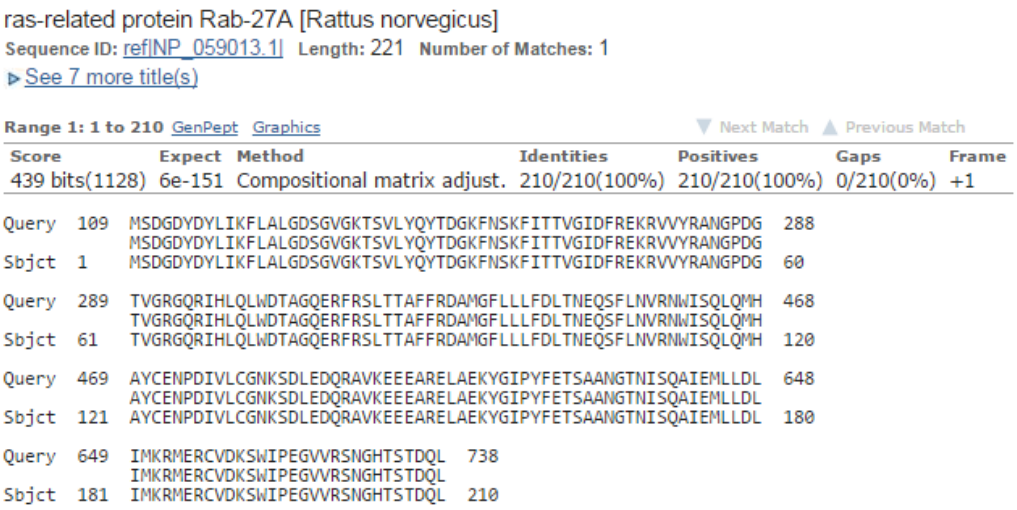
A

```
  1 MTDGDYDYLI KLLALGDSGV GKTTFLYRYT DNKFNPKFIT TVGIDFREKR
 51 VVYNAQGPNG SSGKAFKVHL QLWDTAGQER FRSLTTAFFR DAMGFLLMFD
101 LTSQQSFLNV RNWMSQLQAN AYCENPDIVL IGNKADLPDQ REVNERQARE
151 LADKYGIPYF ETSAATGQNV EKAVETLLDL IMKRMEQCVE KTQIPDTVNG
201 GNSGNLDGEK PPEKKCIC
```

B

```
  1 MTDGDYDYLI KLLALGDSGV GKTTFLYRYT DNKFNPKFIT TVGIDFREKR
 51 VVYNAQGPNG SSGKAFKVHL QLWDTAGQER FRSLTTAFFR DAMGFLLMFD
101 LTSQQSFLNV RNWMSQLQAN AYCENPDIVL IGNKADLPDQ REVNERQARE
151 LADKYGIPYF ETSAATGQNV EKAVETLLDL IMKRMEQCVE KTQIPDTVNG
201 GNSGNLDGEK PPEKKCIC
```

Figure 8.9. The proteomic analysis and amino acid sequence alignment of the 6x histidine m.Cherry-Rab27b-(1-218) recombinant protein. Induction of protein production of the 6x histidine m.Cherry-Rab27b-(1-218) recombinant protein using the appropriate vector resulted in production of two abundant proteins. Accordingly, a proteomic analysis using mass spectrometry was performed by analysing these two proteins; the upper (A) and lower (B) bands in 10% SDS-PAGE gel). The results of the proteomic analysis was then aligned with protein databases to detect the sequence homology with the already identified Rab27b protein sequences. The proteomic analysis revealed that the lower band is C-terminal truncated Rab27b protein (1-200). Matched peptides shown in bold red.



ras-related protein Rab-27A [Rattus norvegicus]
Sequence ID: ref|NP_059013.1| Length: 221 Number of Matches: 1
See 7 more title(s)

Range 1: 1 to 210 GenPept Graphics Next Match Previous Match

Score	Expect	Method	Identities	Positives	Gaps	Frame
439 bits(1128)	6e-151	Compositional matrix adjust.	210/210(100%)	210/210(100%)	0/210(0%)	+1

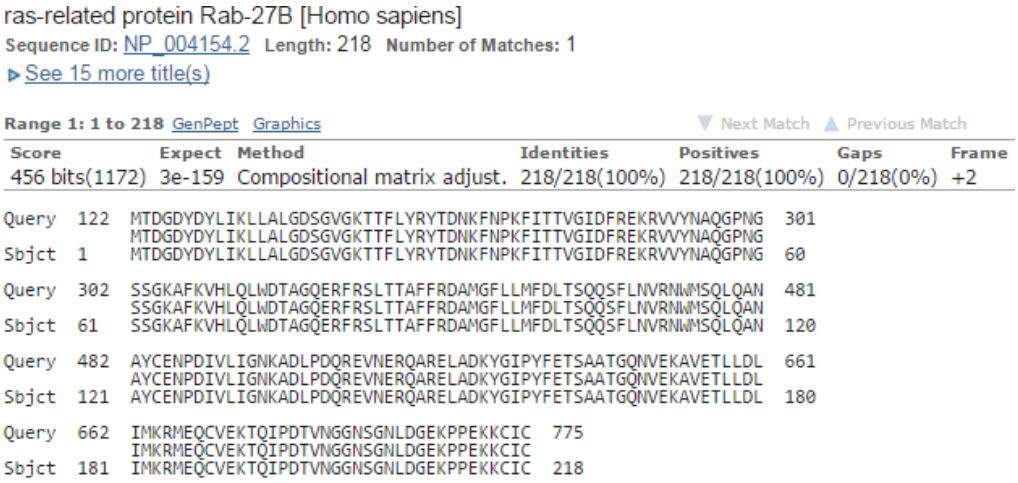
```
Query  109  MSDGDYDYLIKFLALGDSGVGKTSVLYQYTDGKFNSKFITTVGIDFREKRVVYRANGPDG  288
            MSDGDYDYLIKFLALGDSGVGKTSVLYQYTDGKFNSKFITTVGIDFREKRVVYRANGPDG
Sbjct  1    MSDGDYDYLIKFLALGDSGVGKTSVLYQYTDGKFNSKFITTVGIDFREKRVVYRANGPDG  60

Query  289  TVGRGQRIHLQLWDTAGQERFRSLTTAFFRDAMGFLLLFDLTNEQSFLNVRNWISQLQMH  468
            TVGRGQRIHLQLWDTAGQERFRSLTTAFFRDAMGFLLLFDLTNEQSFLNVRNWISQLQMH
Sbjct  61   TVGRGQRIHLQLWDTAGQERFRSLTTAFFRDAMGFLLLFDLTNEQSFLNVRNWISQLQMH  120

Query  469  AYCENPDIVLCGNKSDLEDQRAVKEEEARELAEKYGIPYFETSAANGTNISQAIEMLLDL  648
            AYCENPDIVLCGNKSDLEDQRAVKEEEARELAEKYGIPYFETSAANGTNISQAIEMLLDL
Sbjct  121  AYCENPDIVLCGNKSDLEDQRAVKEEEARELAEKYGIPYFETSAANGTNISQAIEMLLDL  180

Query  649  IMKRMERCVDKSWIPEGVVRSNGHTSTDQL  738
            IMKRMERCVDKSWIPEGVVRSNGHTSTDQL
Sbjct  181  IMKRMERCVDKSWIPEGVVRSNGHTSTDQL  210
```

Figure 8.10. Amino acid sequence alignment of the pET-14b-rRab27a-(1-221) vector sequencing data. The T7 promoter (F) primer was used to sequence the vector.



ras-related protein Rab-27B [Homo sapiens]
Sequence ID: NP_004154.2 Length: 218 Number of Matches: 1
See 15 more title(s)

Range 1: 1 to 218 GenPept Graphics Next Match Previous Match

Score	Expect	Method	Identities	Positives	Gaps	Frame
456 bits(1172)	3e-159	Compositional matrix adjust.	218/218(100%)	218/218(100%)	0/218(0%)	+2

```
Query  122  MTDGDYDYLIKLLALGDSGVGKTTFLYRYTDNKFNPKFITTVGIDFREKRVVYNAQGPNG  301
            MTDGDYDYLIKLLALGDSGVGKTTFLYRYTDNKFNPKFITTVGIDFREKRVVYNAQGPNG
Sbjct  1    MTDGDYDYLIKLLALGDSGVGKTTFLYRYTDNKFNPKFITTVGIDFREKRVVYNAQGPNG  60

Query  302  SSGKAFKVHLQLWDTAGQERFRSLTTAFFRDAMGFLLMFDLTSQQSFLNVRNWMSQLQAN  481
            SSGKAFKVHLQLWDTAGQERFRSLTTAFFRDAMGFLLMFDLTSQQSFLNVRNWMSQLQAN
Sbjct  61   SSGKAFKVHLQLWDTAGQERFRSLTTAFFRDAMGFLLMFDLTSQQSFLNVRNWMSQLQAN  120

Query  482  AYCENPDIVLIGNKADLPDQREVNERQARELADKYGIPYFETSAATGQNVEKAVETLLDL  661
            AYCENPDIVLIGNKADLPDQREVNERQARELADKYGIPYFETSAATGQNVEKAVETLLDL
Sbjct  121  AYCENPDIVLIGNKADLPDQREVNERQARELADKYGIPYFETSAATGQNVEKAVETLLDL  180

Query  662  IMKRMEQCVEKTQIPDTVNGGNSGNLDGEKPPEKKCIC  775
            IMKRMEQCVEKTQIPDTVNGGNSGNLDGEKPPEKKCIC
Sbjct  181  IMKRMEQCVEKTQIPDTVNGGNSGNLDGEKPPEKKCIC  218
```

Figure 8.11. Amino acid sequence alignment of the pET-15b-hRab27b-(1-218) vector sequencing data. The T7 promoter (F) primer was used to sequence the vector.

ras-related protein Rab-5A isoform 1 [Homo sapiens]
Sequence ID: NP_004153.2 Length: 215 Number of Matches: 1
▶ See 17 more title(s)

Range 1: 1 to 209 GenPept Graphics ▼ Next Match ▲ Previous Match

Score	Expect	Method	Identities	Positives	Gaps	Frame
436 bits(1121)	2e-151	Compositional matrix adjust.	209/209(100%)	209/209(100%)	0/209(0%)	+2

```
Query  110  MASRGATRPNGPNTGNKICQFKLVLLGESAVGKSSLVLRFVKGQFHEFQESTIGAAFLTQ  289
            MASRGATRPNGPNTGNKICQFKLVLLGESAVGKSSLVLRFVKGQFHEFQESTIGAAFLTQ
Sbjct  1    MASRGATRPNGPNTGNKICQFKLVLLGESAVGKSSLVLRFVKGQFHEFQESTIGAAFLTQ  60

Query  290  TVCLDDTTVKFEIWDTAGQERYHSLAPMYYRGAQAAIVVYDITNEESFARAKNWVKELQR  469
            TVCLDDTTVKFEIWDTAGQERYHSLAPMYYRGAQAAIVVYDITNEESFARAKNWVKELQR
Sbjct  61   TVCLDDTTVKFEIWDTAGQERYHSLAPMYYRGAQAAIVVYDITNEESFARAKNWVKELQR  120

Query  470  QASPNIVIALSGNKADLANKRAVDFQEAQSYADDNSLLFMETSAKTSMNVNEIFMAIAKK  649
            QASPNIVIALSGNKADLANKRAVDFQEAQSYADDNSLLFMETSAKTSMNVNEIFMAIAKK
Sbjct  121  QASPNIVIALSGNKADLANKRAVDFQEAQSYADDNSLLFMETSAKTSMNVNEIFMAIAKK  180

Query  650  LPKNEPQNPGANSARGRGVDLTEPTQPTR  736
            LPKNEPQNPGANSARGRGVDLTEPTQPTR
Sbjct  181  LPKNEPQNPGANSARGRGVDLTEPTQPTR  209
```

Figure 8.12. Amino acid sequence alignment of the pET-14b-hRab5a-(1-216) vector sequencing data. The T7 promoter (F) primer was used to sequence the vector.

A

Sytl1 protein [Mus musculus]
Sequence ID: AAH05623.1 Length: 308 Number of Matches: 1

Range 1: 1 to 201 GenPept Graphics ▼ Next Match ▲ Previous Match

Score	Expect	Method	Identities	Positives	Gaps	Frame
366 bits(939)	9e-123	Compositional matrix adjust.	200/201(99%)	200/201(99%)	0/201(0%)	+1

```
Query  46   MPQRGHPSQERLWALPSLPMAHGPGSEVEGLLDLSFLTEEEQEAISDVLKRDAHLRQLEE  225
            MPQRGHPSQERLWALPSLPMAHGPGSEVEGLLDLSFLTEEEQEAISDVLKRDAHLRQLEE
Sbjct  1    MPQRGHPSQERLWALPSLPMAHGPGSEVEGLLDLSFLTEEEQEAISDVLKRDAHLRQLEE  60

Query  226  GRVSKLRASLEDPWQLKILTGDWFQEARSQRHHHAHFGSDLVRASIRRKKSPKGDQALGS  405
            GRVSKLRASLEDPWQLKILTGDWFQEARSQRHHHAHFGSDLVRASIRRKKSPKGDQALGS
Sbjct  61   GRVSKLRASLEDPWQLKILTGDWFQEARSQRHHHAHFGSDLVRASIRRKKSPKGDQALGS  120

Query  406  DGEAEAAGEDTIEGEPESRVSIEVAAPERSTETQGPDLSSPYVPSKASegqeeepqdqec  585
            DGEAEAAGEDTIEGEPESRVSIEVAAPERSTETQGPDLSSPYVPSKASEGQEEEPQD EC
Sbjct  121  DGEAEAAGEDTIEGEPESRVSIEVAAPERSTETQGPDLSSPYVPSKASEGQEEEPQDHEC  180

Query  586  eleAPGEGGVQVAEADPELDP  648
            ELEAPGEGGVQVAEADPELDP
Sbjct  181  ELEAPGEGGVQVAEADPELDP  201
```

B

Sytl1 protein [Mus musculus]
Sequence ID: AAH05623.1 Length: 308 Number of Matches: 1

Range 1: 1 to 201 GenPept Graphics ▼ Next Match ▲ Previous Match

Score	Expect	Method	Identities	Positives	Gaps	Frame
365 bits(938)	3e-122	Compositional matrix adjust.	200/201(99%)	200/201(99%)	0/201(0%)	-3

```
Query  666  MPQRGHPSQERLWALPSLPMAHGPGSEVEGLLDLSFLTEEEQEAISDVLKRDAHLRQLEE  487
            MPQRGHPSQERLWALPSLPMAHGPGSEVEGLLDLSFLTEEEQEAISDVLKRDAHLRQLEE
Sbjct  1    MPQRGHPSQERLWALPSLPMAHGPGSEVEGLLDLSFLTEEEQEAISDVLKRDAHLRQLEE  60

Query  486  GRVSKLRASLEDPWQLKILTGDWFQEARSQRHHHAHFGSDLVRASIRRKKSPKGDQALGS  307
            GRVSKLRASLEDPWQLKILTGDWFQEARSQRHHHAHFGSDLVRASIRRKKSPKGDQALGS
Sbjct  61   GRVSKLRASLEDPWQLKILTGDWFQEARSQRHHHAHFGSDLVRASIRRKKSPKGDQALGS  120

Query  306  DGEAEAAGEDTIEGEPESRVSIEVAAPERSTETQGPDLSSPYVPSKASegqeeepqdqec  127
            DGEAEAAGEDTIEGEPESRVSIEVAAPERSTETQGPDLSSPYVPSKASEGQEEEPQD EC
Sbjct  121  DGEAEAAGEDTIEGEPESRVSIEVAAPERSTETQGPDLSSPYVPSKASEGQEEEPQDHEC  180

Query  126  eleAPGEGGVQVAEADPELDP  64
            ELEAPGEGGVQVAEADPELDP
Sbjct  181  ELEAPGEGGVQVAEADPELDP  201
```

Figure 8.13. Amino acid sequence alignment of pGEX-4T1-mSlp1-(1-201) vector sequencing data. A) Using the PGEX 5' forward primer. B) Using the PGEX 3' reverse primer.

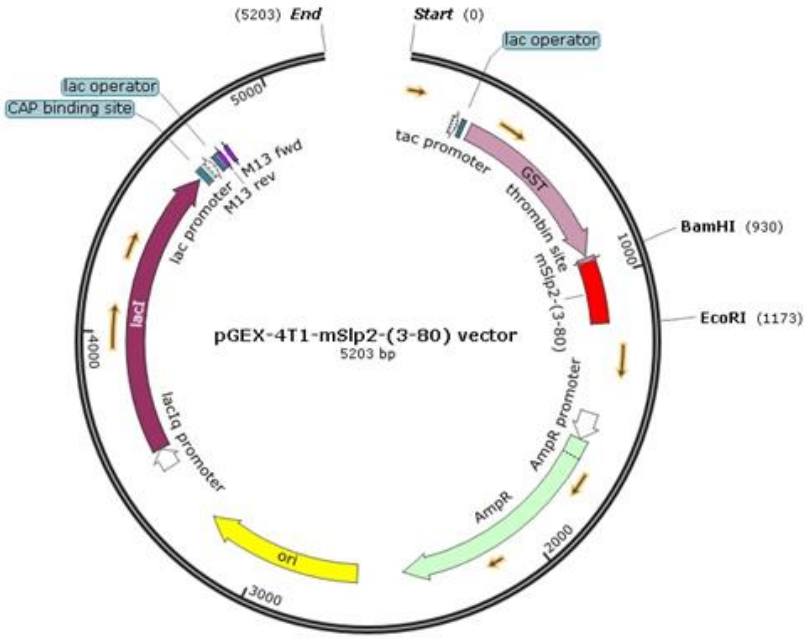


Figure 8.14. pGEX-4T1-mSlp2-(3-80) vector map. 5' BamHI and 3' EcoRI restriction enzyme sites were introduced into the 5' and 3' ends of mSlp2-(3-80) cDNA, mSlp2-(3-80) cDNA was then sub-cloned into the pGEX-4T1vector utilising 5' BamHI and 3' EcoRI enzyme restriction sites. This vector also contains ampicillin resistance gene (molecular weight: 5203BP).

A

Sytl2 protein, partial [Mus musculus]
Sequence ID: AAH64769.1 Length: 533 Number of Matches: 1

Range 1: 3 to 80 GenPept Graphics Next Match Previous Match

Score	Expect	Method	Identities	Positives	Gaps	Frame
163 bits(412)	3e-45	Compositional matrix adjust.	78/78(100%)	78/78(100%)	0/78(0%)	+1

```
Query  40   DLSFLTEEEQDAILKVLQRDAALKRAEEERVRHLPEKIKDDQQLKNMSGQWFYEAKAKRH  219
            DLSFLTEEEQDAILKVLQRDAALKRAEEERVRHLPEKIKDDQQLKNMSGQWFYEAKAKRH
Sbjct  3    DLSFLTEEEQDAILKVLQRDAALKRAEEERVRHLPEKIKDDQQLKNMSGQWFYEAKAKRH  62

Query  220  RDKIHGADIIRASMRRKK  273
            RDKIHGADIIRASMRRKK
Sbjct  63   RDKIHGADIIRASMRRKK  80
```

B

Sytl2 protein, partial [Mus musculus]
Sequence ID: AAH64769.1 Length: 533 Number of Matches: 1

Range 1: 3 to 80 GenPept Graphics Next Match Previous Match

Score	Expect	Method	Identities	Positives	Gaps	Frame
162 bits(409)	9e-45	Compositional matrix adjust.	78/78(100%)	78/78(100%)	0/78(0%)	-3

```
Query  308  DLSFLTEEEQDAILKVLQRDAALKRAEEERVRHLPEKIKDDQQLKNMSGQWFYEAKAKRH  129
            DLSFLTEEEQDAILKVLQRDAALKRAEEERVRHLPEKIKDDQQLKNMSGQWFYEAKAKRH
Sbjct  3    DLSFLTEEEQDAILKVLQRDAALKRAEEERVRHLPEKIKDDQQLKNMSGQWFYEAKAKRH  62

Query  128  RDKIHGADIIRASMRRKK  75
            RDKIHGADIIRASMRRKK
Sbjct  63   RDKIHGADIIRASMRRKK  80
```

Figure 8.15. Amino acid sequence alignment of the pGEX-4T1-mSlp2-(3-80) vector sequencing data. A) Using the PGEX 5' forward primer. B) Using the PGEX 3' reverse primer.

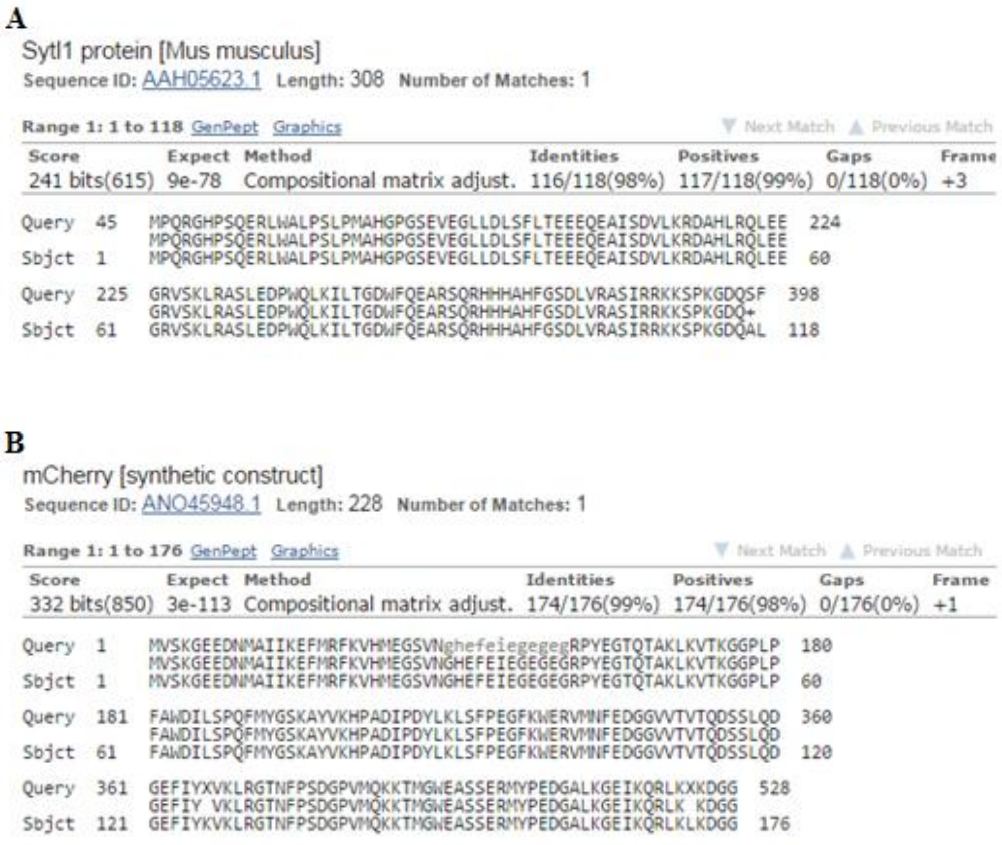


Figure 8.16. Amino acid sequence alignment of the pETDuet-1-GFP-mSlp1-(1-116)-m.Cherry-hRab27a-(1-221) vector sequencing data. The EGFP CF forward primer was used to sequence the vector. A) Amino acid sequence alignment of mSlp1-(1-116). B) Amino acid sequence alignment of m.Cherry.

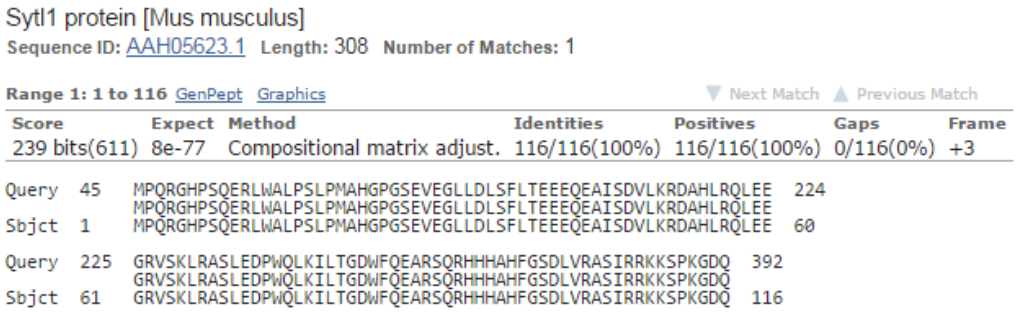


Figure 8.17. Amino acid sequence alignment of the pETDuet-1-GFP-mSlp1-(1-116) vector sequencing data. The EGFP CF forward primer was used to sequence the vector.

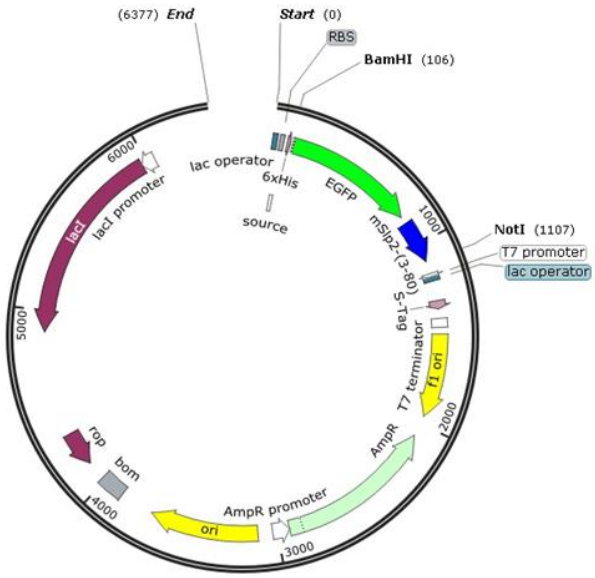


Figure 8.18. pETDuet-1-GFP-mSlp2-(3-80) vector map. 5' BamHI and 3' NotI restriction enzyme sites were introduced into GFP-mSlp2-(3-80) cDNA by performing PCR amplification using appropriate vector and primers, GFP-mSlp2-(3-80) cDNA was then sub-cloned into the pETDuet-1vector using 5' BamHI and 3' NotI enzyme restriction sites. This vector also contains ampicillin resistance gene (molecular weight: 6377BP).

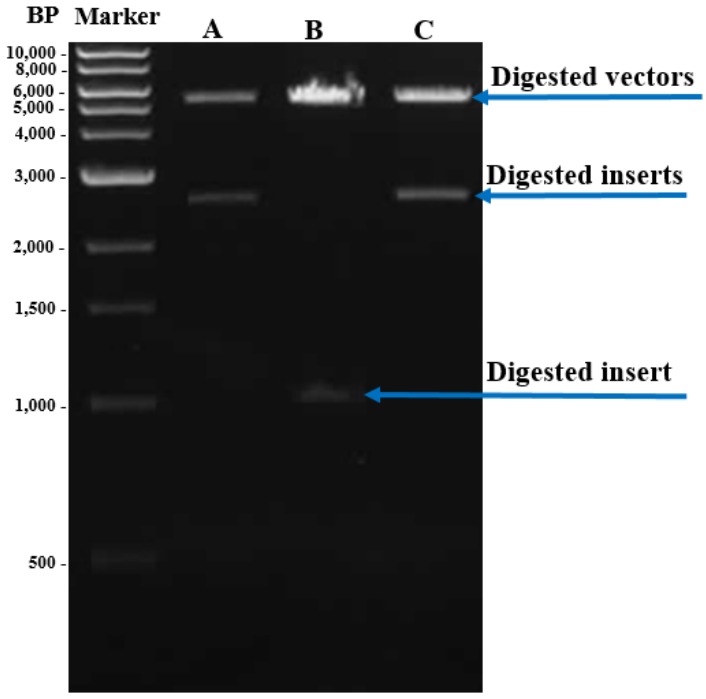


Figure 8.19. An ethidium bromide stained 1% TBE agarose gel showing BamHI and NotI digests of different pETDuet-1 vectors. A) pETDuet-1-GFP-mSlp1-(1-116) vector digest; the expected molecular weights of the arrow indicated upper (digested vector) and lower (GFP-mSlp1-(1-116)-m.Cherry-hRab27a) bands are 5369BP and 2460BP, respectively B) pETDuet-1-GFP-mSlp2-(3-80) vector digest; the expected molecular weights of the arrow

indicated upper (digested vector) and lower (GFP-mSlp2) bands are 5369BP and 1008BP, respectively. C) pETDuet-1-GFP vector digest; the expected molecular weights of the arrow indicated upper (digested vector) and lower (GFP-mSlp1-(1-116)-m.Cherry-hRab27a) bands are 5369BP and 2460BP, respectively.

Sytl2 protein, partial [Mus musculus]
Sequence ID: AAH52915.1 Length: 534 Number of Matches: 1

Range 1: 2 to 80 GenPept Graphics ▼ Next Match ▲ Previous Match

Score	Expect	Method	Identities	Positives	Gaps	Frame
164 bits(415)	1e-46	Compositional matrix adjust.	78/79(99%)	78/79(98%)	0/79(0%)	+3

```
Query  3    FDLSFLTEEEQDAILKVLQRDAALKRAEEERVRHLPEKIKDDQQLKNMSGQWFYEAKAKR  182
            DLSFLTEEEQDAILKVLQRDAALKRAEEERVRHLPEKIKDDQQLKNMSGQWFYEAKAKR
Sbjct  2    IDLSFLTEEEQDAILKVLQRDAALKRAEEERVRHLPEKIKDDQQLKNMSGQWFYEAKAKR  61

Query  183  HRDKIHGADIIRASMRRKK  239
            HRDKIHGADIIRASMRRKK
Sbjct  62   HRDKIHGADIIRASMRRKK  80
```

Figure 8.20. Amino acid sequence alignment of the pETDuet-1-GFP-mSlp2-(3-80) vector sequencing data. The EGFP CF forward primer was used to sequence the vector.

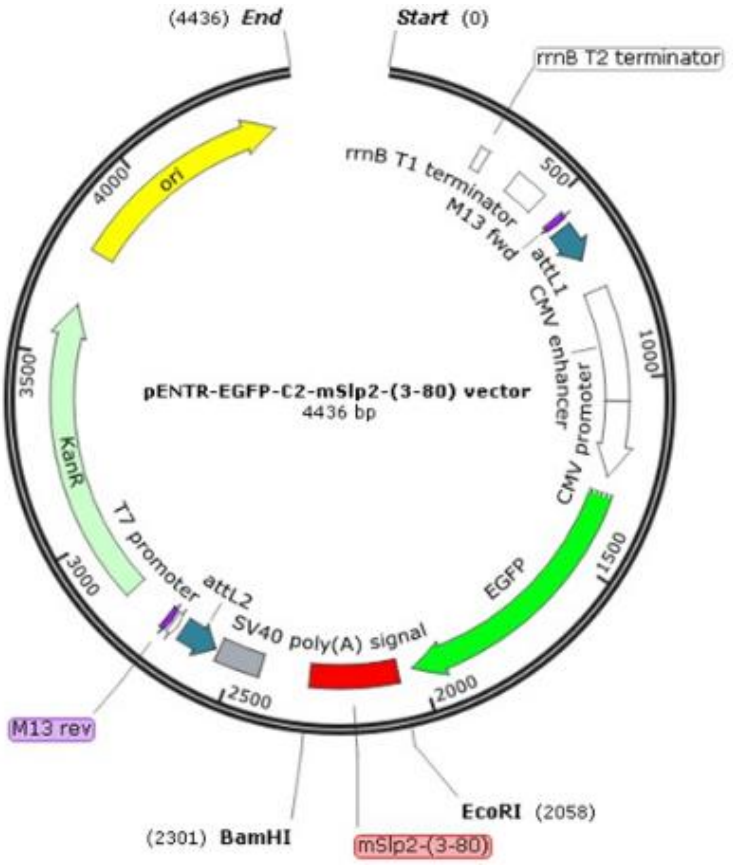


Figure 8.21. pENTR-EGFP-C2-mSlp2-(3-80) vector map. 5' EcoRI and 3' BamHI restriction enzyme sites were introduced into the 5' and 3' ends of mSlp2-(3-80) cDNA, mSlp2-(3-80) cDNA was then sub-cloned into the pENTR-EGFP-C2 vector which contains 5' EcoRI and 3' BamHI enzymes restriction sites. This vector also contains kanamycin resistance gene (molecular weight: 4436BP).

Sytl2 protein, partial [Mus musculus]
Sequence ID: AAH64769.1 Length: 533 Number of Matches: 1

Range 1: 3 to 80 GenPept Graphics Next Match Previous Match

Score	Expect	Method	Identities	Positives	Gaps	Frame
164 bits(414)	6e-46	Compositional matrix adjust.	78/78(100%)	78/78(100%)	0/78(0%)	+1

```
Query  1    DLSFLTEEEQDAILKVLQRDAALKRAEEERVRHLPEKIKDDQQLKNMSGQWFYEAKAKRH  180
            DLSFLTEEEQDAILKVLQRDAALKRAEEERVRHLPEKIKDDQQLKNMSGQWFYEAKAKRH
Sbjct  3    DLSFLTEEEQDAILKVLQRDAALKRAEEERVRHLPEKIKDDQQLKNMSGQWFYEAKAKRH  62

Query  181  RDKIHGADIIRASMRRKK  234
            RDKIHGADIIRASMRRKK
Sbjct  63   RDKIHGADIIRASMRRKK  80
```

Figure 8.22. Amino acid sequence alignment of the pENTR-EGFP-C2-mSlp2-(3-80) vector sequencing data. The EGFP CF forward primer was used to sequence the vector.

A)

Sytl2 protein, partial [Mus musculus]
Sequence ID: AAH52915.1 Length: 534 Number of Matches: 1

Range 1: 21 to 80 GenPept Graphics Next Match Previous Match

Score	Expect	Method	Identities	Positives	Gaps	Frame
127 bits(320)	7e-29	Compositional matrix adjust.	60/60(100%)	60/60(100%)	0/60(0%)	+2

```
Query  47   RDAALKRAEEERVRHLPEKIKDDQQLKNMSGQWFYEAKAKRHRDKIHGADIIRASMRRKK  226
            RDAALKRAEEERVRHLPEKIKDDQQLKNMSGQWFYEAKAKRHRDKIHGADIIRASMRRKK
Sbjct  21   RDAALKRAEEERVRHLPEKIKDDQQLKNMSGQWFYEAKAKRHRDKIHGADIIRASMRRKK  80
```

B)

Sytl2 protein, partial [Mus musculus]
Sequence ID: AAH64769.1 Length: 533 Number of Matches: 1

Range 1: 4 to 70 GenPept Graphics Next Match Previous Match

Score	Expect	Method	Identities	Positives	Gaps	Frame
142 bits(358)	1e-38	Compositional matrix adjust.	67/67(100%)	67/67(100%)	0/67(0%)	+1

```
Query  4    LSFLTEEEQDAILKVLQRDAALKRAEEERVRHLPEKIKDDQQLKNMSGQWFYEAKAKRHR  183
            LSFLTEEEQDAILKVLQRDAALKRAEEERVRHLPEKIKDDQQLKNMSGQWFYEAKAKRHR
Sbjct  4    LSFLTEEEQDAILKVLQRDAALKRAEEERVRHLPEKIKDDQQLKNMSGQWFYEAKAKRHR  63

Query  184  DKIHGAD  204
            DKIHGAD
Sbjct  64   DKIHGAD  70
```

Figure 8.23. Amino acid sequence alignment of the pENTR-EGFP-C2-mSlp2-(3-80; D3A) vector sequencing data. A) Using a forward primer for amplification of mSlp2. B) Using a reverse primer for amplification of mSlp2.

A)

Sytl2 protein, partial [Mus musculus]
Sequence ID: AAH64769.1 Length: 533 Number of Matches: 1

Range 1: 21 to 79 GenPept Graphics Next Match Previous Match

Score	Expect	Method	Identities	Positives	Gaps	Frame
126 bits(316)	5e-31	Compositional matrix adjust.	59/59(100%)	59/59(100%)	0/59(0%)	+2

```
Query  53   RDAALKRAEEERVRHLPEKIKDDQQLKNMSGQWFYEAKAKRHRDKIHGADIIRASMRRK  229
            RDAALKRAEEERVRHLPEKIKDDQQLKNMSGQWFYEAKAKRHRDKIHGADIIRASMRRK
Sbjct  21   RDAALKRAEEERVRHLPEKIKDDQQLKNMSGQWFYEAKAKRHRDKIHGADIIRASMRRK  79
```

B)

Sytl2 protein, partial [Mus musculus]
Sequence ID: AAH64769.1 Length: 533 Number of Matches: 1

Range 1: 3 to 70 GenPept Graphics ▼ Next Match ▲ Previous Match

Score	Expect	Method	Identities	Positives	Gaps	Frame
144 bits(363)	3e-39	Compositional matrix adjust.	68/68(100%)	68/68(100%)	0/68(0%)	+1

```
Query  1    DLSFLTEEEQDAILKVLQRDAALKRAEEERVRHLPEKIKDDQQLKNMSGQWFYEAKAKRH  180
            DLSFLTEEEQDAILKVLQRDAALKRAEEERVRHLPEKIKDDQQLKNMSGQWFYEAKAKRH
Sbjct  3    DLSFLTEEEQDAILKVLQRDAALKRAEEERVRHLPEKIKDDQQLKNMSGQWFYEAKAKRH  62

Query  181  RDKIHGAD  204
            RDKIHGAD
Sbjct  63   RDKIHGAD  70
```

Figure 8.24. Amino acid sequence alignment of the pENTR-EGFP-C2-mSlp2-(3-79) vector sequencing data. A) Using a forward primer for amplification of mSlp2. B) Using a reverse primer for amplification of mSlp2.

Sytl2 protein, partial [Mus musculus]
Sequence ID: AAH64769.1 Length: 533 Number of Matches: 1

Range 1: 3 to 80 GenPept Graphics ▼ Next Match ▲ Previous Match

Score	Expect	Method	Identities	Positives	Gaps	Frame
161 bits(407)	4e-45	Compositional matrix adjust.	77/78(99%)	77/78(98%)	0/78(0%)	+1

```
Query  1    DLSFLTEEEQDAILKVLQRDAALKRAEEEWVRHLPEKIKDDQQLKNMSGQWFYEAKAKRH  180
            DLSFLTEEEQDAILKVLQRDAALKRAEEE VRHLPEKIKDDQQLKNMSGQWFYEAKAKRH
Sbjct  3    DLSFLTEEEQDAILKVLQRDAALKRAEEERVRHLPEKIKDDQQLKNMSGQWFYEAKAKRH  62

Query  181  RDKIHGADIIRASMRRKK  234
            RDKIHGADIIRASMRRKK
Sbjct  63   RDKIHGADIIRASMRRKK  80
```

Figure 8.25. Amino acid sequence alignment of the pENTR-EGFP-C2-mSlp2-(3-80; R32W) vector sequencing data. The EGFP CF forward primer was used to sequence the vector.

Sytl2 protein, partial [Mus musculus]
Sequence ID: AAH52915.1 Length: 534 Number of Matches: 1

Range 1: 3 to 80 GenPept Graphics ▼ Next Match ▲ Previous Match

Score	Expect	Method	Identities	Positives	Gaps	Frame
162 bits(409)	2e-45	Compositional matrix adjust.	77/78(99%)	77/78(98%)	0/78(0%)	+1

```
Query  1    DLSFLTEEEQDAILKVLQRDAALKRAEEERVRHLPEKIKDDQQLKNMSGQWFYEAAAKRH  180
            DLSFLTEEEQDAILKVLQRDAALKRAEEERVRHLPEKIKDDQQLKNMSGQWFYEA AKRH
Sbjct  3    DLSFLTEEEQDAILKVLQRDAALKRAEEERVRHLPEKIKDDQQLKNMSGQWFYEAKAKRH  62

Query  181  RDKIHGADIIRASMRRKK  234
            RDKIHGADIIRASMRRKK
Sbjct  63   RDKIHGADIIRASMRRKK  80
```

Figure 8.26. Amino acid sequence alignment of the pENTR-EGFP-C2-mSlp2-(3-80; K58A) vector sequencing data. The EGFP CF forward primer was used to sequence the vector.

Sytl2 protein, partial [Mus musculus]
Sequence ID: AAH52915.1 Length: 534 Number of Matches: 1

Range 1: 3 to 80 GenPept Graphics ▼ Next Match ▲ Previous Match

Score	Expect	Method	Identities	Positives	Gaps	Frame
161 bits(407)	5e-45	Compositional matrix adjust.	77/78(99%)	77/78(98%)	0/78(0%)	+1

```
Query  1    DLSFLTEEEQDAILKVLQRDAALKRAEEERVRHLPEKIKDDQQLKNMSGQWFYEAKAKAH  180
            DLSFLTEEEQDAILKVLQRDAALKRAEEERVRHLPEKIKDDQQLKNMSGQWFYEAKAK H
Sbjct  3    DLSFLTEEEQDAILKVLQRDAALKRAEEERVRHLPEKIKDDQQLKNMSGQWFYEAKAKRH  62

Query  181  RDKIHGADIIRASMRRKK  234
            RDKIHGADIIRASMRRKK
Sbjct  63   RDKIHGADIIRASMRRKK  80
```

Figure 8.27. Amino acid sequence alignment of the pENTR-EGFP-C2-mSlp2-(3-80; R61A) vector sequencing data. The EGFP CF forward primer was used to sequence the vector.

Sytl2 protein, partial [Mus musculus]
Sequence ID: AAH52915.1 Length: 534 Number of Matches: 1

Range 1: 3 to 80 GenPept Graphics ▼ Next Match ▲ Previous Match

Score	Expect	Method	Identities	Positives	Gaps	Frame
160 bits(405)	8e-45	Compositional matrix adjust.	77/78(99%)	77/78(98%)	0/78(0%)	+3

```
Query  3    DLSFLTEEEQDAILKVLQRDAALKRAEEERVRHLPEKIKDDQQLKNMSGQWFYEAKAKRA  182
            DLSFLTEEEQDAILKVLQRDAALKRAEEERVRHLPEKIKDDQQLKNMSGQWFYEAKAKR
Sbjct  3    DLSFLTEEEQDAILKVLQRDAALKRAEEERVRHLPEKIKDDQQLKNMSGQWFYEAKAKRH  62

Query  183  RDKIHGADIIRASMRRKK  236
            RDKIHGADIIRASMRRKK
Sbjct  63   RDKIHGADIIRASMRRKK  80
```

Figure 8.28. Amino acid sequence alignment of the pENTR-EGFP-C2-mSlp2-(3-80; H62A) vector sequencing data. The EGFP CF forward primer was used to sequence the vector.

Sytl2 protein, partial [Mus musculus]
Sequence ID: AAH52915.1 Length: 534 Number of Matches: 1

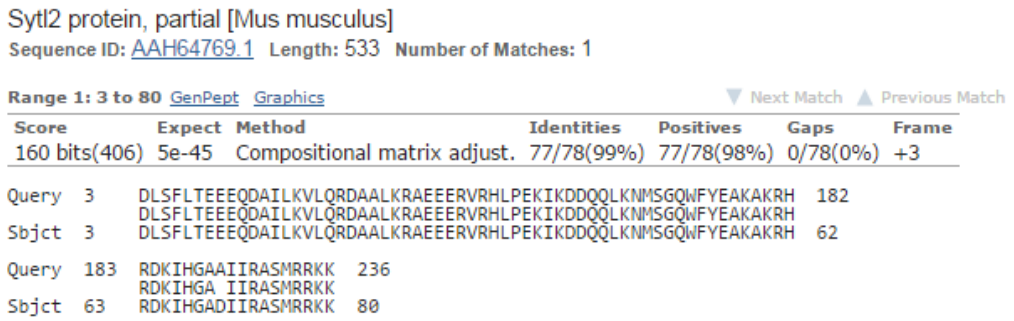
Range 1: 3 to 80 GenPept Graphics ▼ Next Match ▲ Previous Match

Score	Expect	Method	Identities	Positives	Gaps	Frame
160 bits(405)	9e-45	Compositional matrix adjust.	77/78(99%)	77/78(98%)	0/78(0%)	+1

```
Query  1    DLSFLTEEEQDAILKVLQRDAALKRAEEERVRHLPEKIKDDQQLKNMSGQWFYEAKAKRH  180
            DLSFLTEEEQDAILKVLQRDAALKRAEEERVRHLPEKIKDDQQLKNMSGQWFYEAKAKRH
Sbjct  3    DLSFLTEEEQDAILKVLQRDAALKRAEEERVRHLPEKIKDDQQLKNMSGQWFYEAKAKRH  62

Query  181  RDKIHIADIIRASMRRKK  234
            RDKIH ADIIRASMRRKK
Sbjct  63   RDKIHGADIIRASMRRKK  80
```

Figure 8.29. Amino acid sequence alignment of the pENTR-EGFP-C2-mSlp2-(3-80; G68I) vector sequencing data. The EGFP CF forward primer was used to sequence the vector.



Sytl2 protein, partial [Mus musculus]
Sequence ID: AAH64769.1 Length: 533 Number of Matches: 1

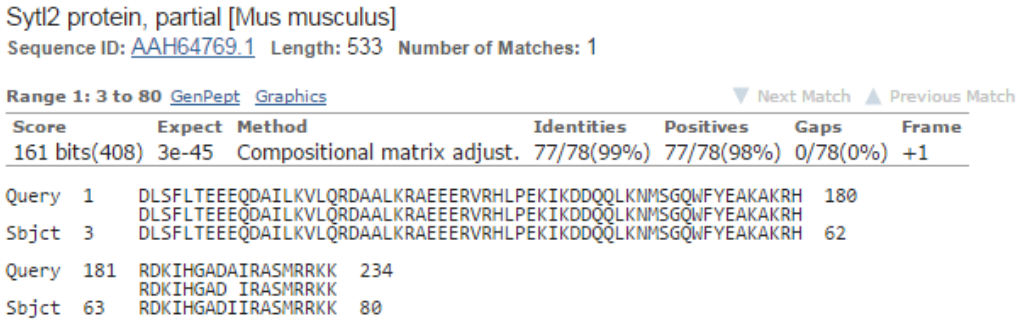
Range 1: 3 to 80 GenPept Graphics ▼ Next Match ▲ Previous Match

Score	Expect	Method	Identities	Positives	Gaps	Frame
160 bits(406)	5e-45	Compositional matrix adjust.	77/78(99%)	77/78(98%)	0/78(0%)	+3

```
Query  3    DLSFLTEEEQDAILKVLQRDAALKRAEEERVRHLPEKIKDDQQLKNMSGQWFYEAKAKRH  182
            DLSFLTEEEQDAILKVLQRDAALKRAEEERVRHLPEKIKDDQQLKNMSGQWFYEAKAKRH
Sbjct  3    DLSFLTEEEQDAILKVLQRDAALKRAEEERVRHLPEKIKDDQQLKNMSGQWFYEAKAKRH  62

Query  183  RDKIHGAAIIRASMRRKK  236
            RDKIHGA IIRASMRRKK
Sbjct  63   RDKIHGADIIRASMRRKK  80
```

Figure 8.30. Amino acid sequence alignment of the pENTR-EGFP-C2-mSlp2-(3-80; D70A) vector sequencing data. The EGFP CF forward primer was used to sequence the vector.



Sytl2 protein, partial [Mus musculus]
Sequence ID: AAH64769.1 Length: 533 Number of Matches: 1

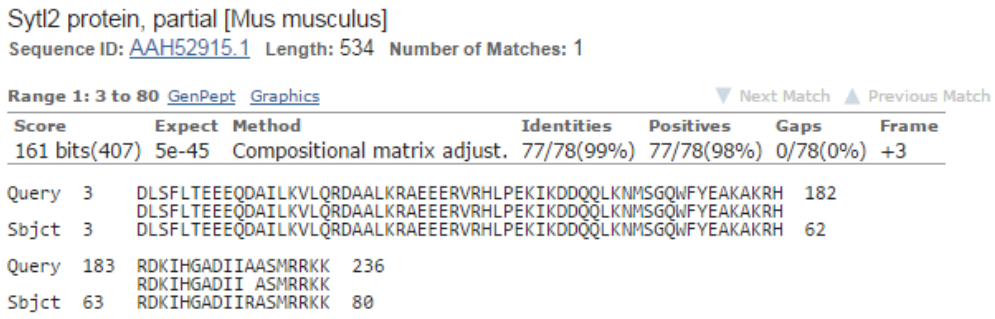
Range 1: 3 to 80 GenPept Graphics ▼ Next Match ▲ Previous Match

Score	Expect	Method	Identities	Positives	Gaps	Frame
161 bits(408)	3e-45	Compositional matrix adjust.	77/78(99%)	77/78(98%)	0/78(0%)	+1

```
Query  1    DLSFLTEEEQDAILKVLQRDAALKRAEEERVRHLPEKIKDDQQLKNMSGQWFYEAKAKRH  180
            DLSFLTEEEQDAILKVLQRDAALKRAEEERVRHLPEKIKDDQQLKNMSGQWFYEAKAKRH
Sbjct  3    DLSFLTEEEQDAILKVLQRDAALKRAEEERVRHLPEKIKDDQQLKNMSGQWFYEAKAKRH  62

Query  181  RDKIHGADAIRASMRRKK  234
            RDKIHGAD IRASMRRKK
Sbjct  63   RDKIHGADIIRASMRRKK  80
```

Figure 8.31. Amino acid sequence alignment of the pENTR-EGFP-C2-mSlp2-(3-80; I71A) vector sequencing data. The EGFP CF forward primer was used to sequence the vector.



Sytl2 protein, partial [Mus musculus]
Sequence ID: AAH52915.1 Length: 534 Number of Matches: 1

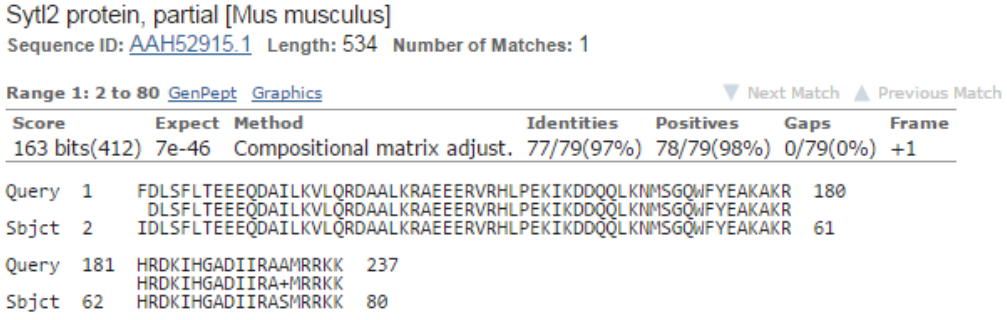
Range 1: 3 to 80 GenPept Graphics ▼ Next Match ▲ Previous Match

Score	Expect	Method	Identities	Positives	Gaps	Frame
161 bits(407)	5e-45	Compositional matrix adjust.	77/78(99%)	77/78(98%)	0/78(0%)	+3

```
Query  3    DLSFLTEEEQDAILKVLQRDAALKRAEEERVRHLPEKIKDDQQLKNMSGQWFYEAKAKRH  182
            DLSFLTEEEQDAILKVLQRDAALKRAEEERVRHLPEKIKDDQQLKNMSGQWFYEAKAKRH
Sbjct  3    DLSFLTEEEQDAILKVLQRDAALKRAEEERVRHLPEKIKDDQQLKNMSGQWFYEAKAKRH  62

Query  183  RDKIHGADIIAASMRRKK  236
            RDKIHGADII ASMRRKK
Sbjct  63   RDKIHGADIIRASMRRKK  80
```

Figure 8.32. Amino acid sequence alignment of the pENTR-EGFP-C2-mSlp2-(3-80; R73A) vector sequencing data. The EGFP CF forward primer was used to sequence the vector.



Sytl2 protein, partial [Mus musculus]
Sequence ID: AAH52915.1 Length: 534 Number of Matches: 1

Range 1: 2 to 80 GenPept Graphics ▼ Next Match ▲ Previous Match

Score	Expect	Method	Identities	Positives	Gaps	Frame
163 bits(412)	7e-46	Compositional matrix adjust.	77/79(97%)	78/79(98%)	0/79(0%)	+1

```
Query  1    FDLSFLTEEEQDAILKVLQRDAALKRAEEERVRHLPEKIKDDQQLKNMSGQWFYEAKAKR  180
             DLSFLTEEEQDAILKVLQRDAALKRAEEERVRHLPEKIKDDQQLKNMSGQWFYEAKAKR
Sbjct  2    IDLSFLTEEEQDAILKVLQRDAALKRAEEERVRHLPEKIKDDQQLKNMSGQWFYEAKAKR  61

Query  181  HRDKIHGADIIRAAMRRKK  237
            HRDKIHGADIIRA+MRRKK
Sbjct  62   HRDKIHGADIIRASMRRKK  80
```

Figure 8.33. Amino acid sequence alignment of the pENTR-EGFP-C2-mSlp2-(3-80; S75A) vector sequencing data. The EGFP CF forward primer was used to sequence the vector.

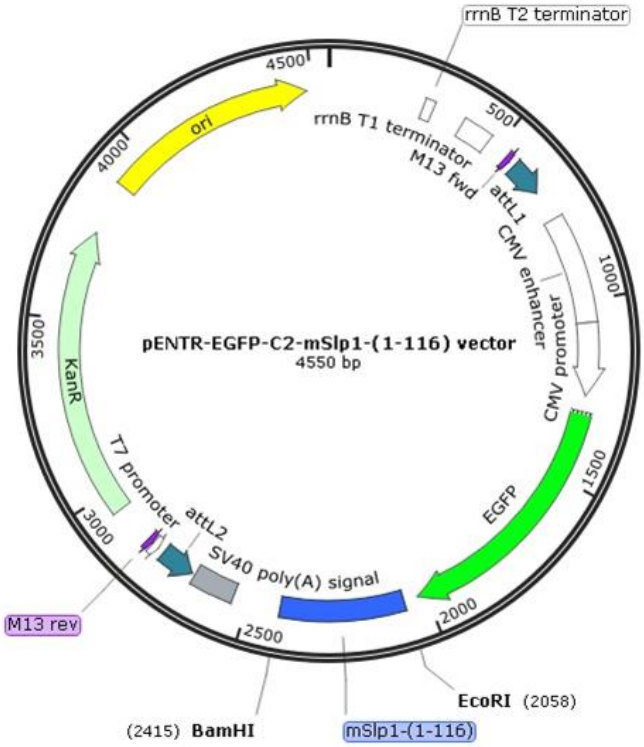


Figure 8.34. pENTR-EGFP-C2-mSlp1-(1-116) vector map. 5' EcoRI and 3' BamHI restriction enzyme sites were introduced into the 5' and 3' ends of mSlp1-(1-116) cDNA, mSlp1-(1-116) cDNA was then sub-cloned into the pENTR-EGFP-C2 vector which contains 5' EcoRI and 3' BamHI enzymes restriction sites. This vector also contains kanamycin resistance gene (molecular weight: 4550BP).

Sytl1 protein [Mus musculus]
Sequence ID: AAH05623.1 Length: 308 Number of Matches: 1

Range 1: 1 to 116 GenPept Graphics ▼ Next Match ▲ Previous Match

Score	Expect	Method	Identities	Positives	Gaps	Frame
241 bits(615)	2e-73	Compositional matrix adjust.	116/116(100%)	116/116(100%)	0/116(0%)	+2

```
Query  74   MPQRGHPSQERLWALPSLPMAHGPGSEVEGLLDLSFLTEEEQEAISDVLKRDAHLRQLEE  253
            MPQRGHPSQERLWALPSLPMAHGPGSEVEGLLDLSFLTEEEQEAISDVLKRDAHLRQLEE
Sbjct  1    MPQRGHPSQERLWALPSLPMAHGPGSEVEGLLDLSFLTEEEQEAISDVLKRDAHLRQLEE  60

Query  254  GRVSKLRASLEDPWQLKILTGDWFQEARSQRHHHAHFGSDLVRASIRRKKSPKGDQ  421
            GRVSKLRASLEDPWQLKILTGDWFQEARSQRHHHAHFGSDLVRASIRRKKSPKGDQ
Sbjct  61   GRVSKLRASLEDPWQLKILTGDWFQEARSQRHHHAHFGSDLVRASIRRKKSPKGDQ  116
```

Figure 8.35. Amino acid sequence alignment of the pENTR-EGFP-C2-mSlp1-(1-116) vector sequencing data. The EGFP CF forward primer was used to sequence the vector.

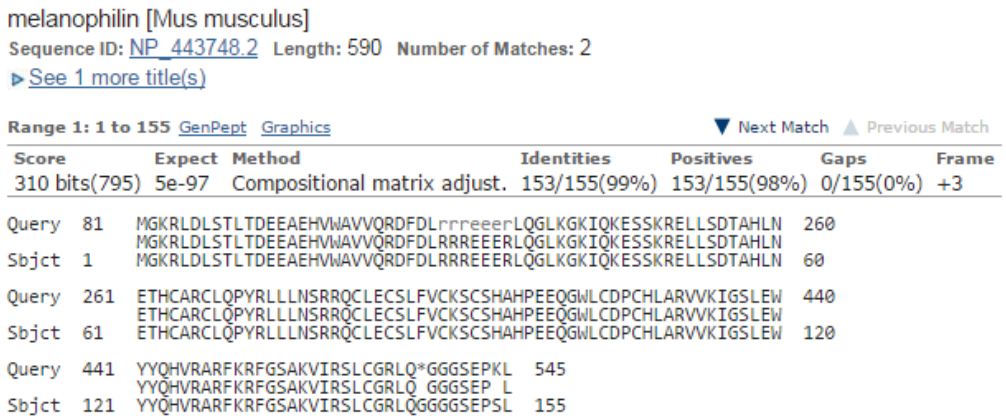


Figure 8.36. Amino acid sequence alignment of the pENTR-EGFP-C2-mSlac2-a-(1-146) vector sequencing data. The EGFP CF forward primer was used to sequence the vector.

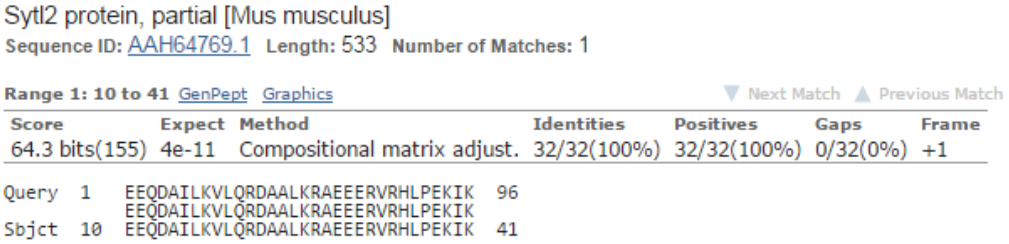


Figure 8.37. Amino acid sequence alignment of the pENTR-EGFP-C2-mSlp2-(10-41) vector sequencing data. The EGFP CF forward primer was used to sequence the vector.

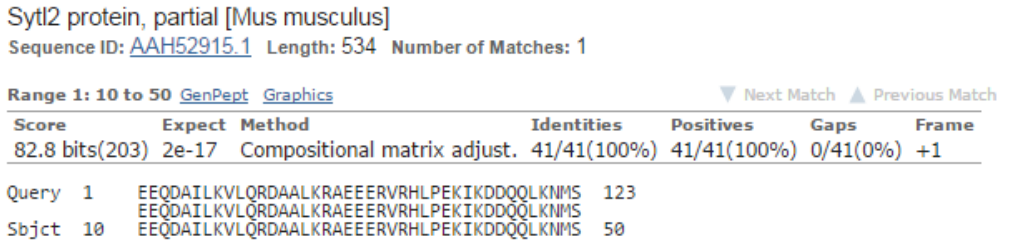


Figure 8.38. Amino acid sequence alignment of the pENTR-EGFP-C2-mSlp2-(10-50) vector sequencing data. The EGFP CF forward primer was used to sequence the vector.

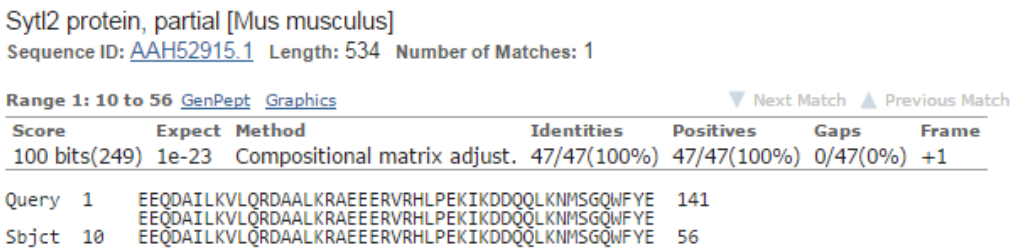
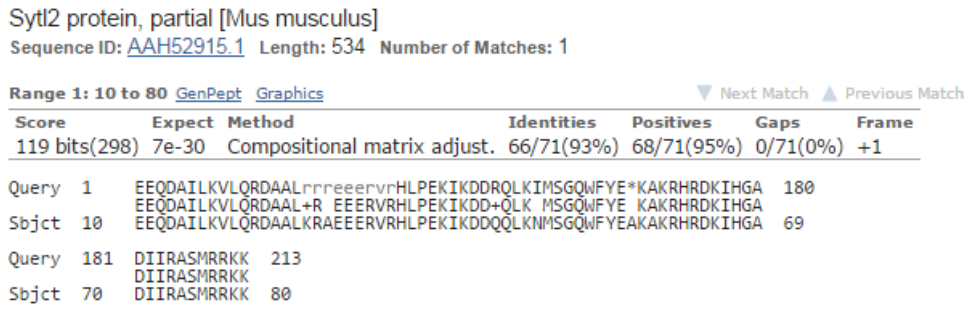


Figure 8.39. Amino acid sequence alignment of the pENTR-EGFP-C2-mSlp2-(10-56) vector sequencing data. The EGFP CF forward primer was used to sequence the vector.



Sytl2 protein, partial [Mus musculus]
Sequence ID: AAH52915.1 Length: 534 Number of Matches: 1

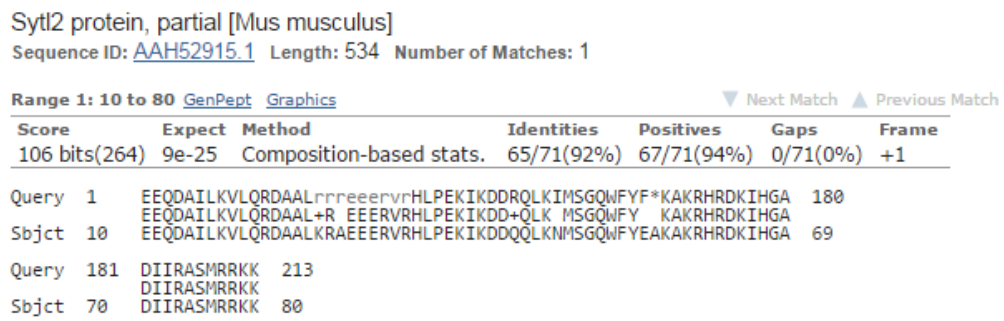
Range 1: 10 to 80 GenPept Graphics ▼ Next Match ▲ Previous Match

Score	Expect	Method	Identities	Positives	Gaps	Frame
119 bits(298)	7e-30	Compositional matrix adjust.	66/71(93%)	68/71(95%)	0/71(0%)	+1

```
Query  1    EEQDAILKVLQRDAALrrreeervrHLPEKIKDDRQLKIMSGQWFYE*KAKRHRDKIHGA  180
            EEQDAILKVLQRDAAL+R EEERVRHLPEKIKDD+QLK MSGQWFYE KAKRHRDKIHGA
Sbjct  10   EEQDAILKVLQRDAALKRAEEERVRHLPEKIKDDQQLKNMSGQWFYEAKAKRHRDKIHGA  69

Query  181  DIIRASMRRKK  213
            DIIRASMRRKK
Sbjct  70   DIIRASMRRKK  80
```

Figure 8.40. Amino acid sequence alignment of the pENTR-EGFP-C2-mSlp2-(10-56; K26R, A28R, Q44R, N48I) vector sequencing data. The EGFP CF forward primer was used to sequence the vector.



Sytl2 protein, partial [Mus musculus]
Sequence ID: AAH52915.1 Length: 534 Number of Matches: 1

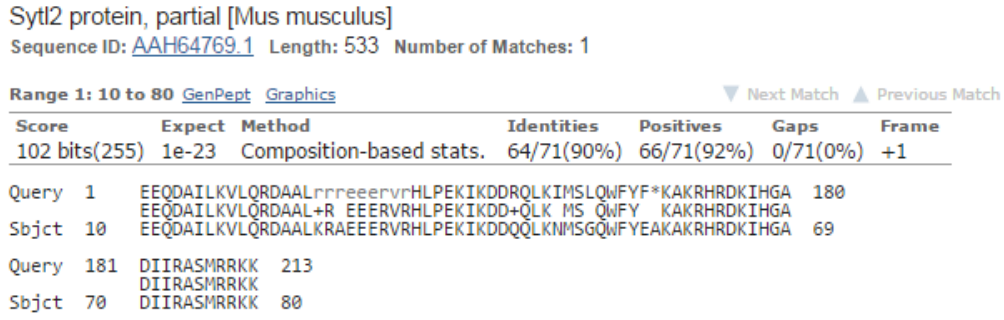
Range 1: 10 to 80 GenPept Graphics ▼ Next Match ▲ Previous Match

Score	Expect	Method	Identities	Positives	Gaps	Frame
106 bits(264)	9e-25	Composition-based stats.	65/71(92%)	67/71(94%)	0/71(0%)	+1

```
Query  1    EEQDAILKVLQRDAALrrreeervrHLPEKIKDDRQLKIMSGQWFYF*KAKRHRDKIHGA  180
            EEQDAILKVLQRDAAL+R EEERVRHLPEKIKDD+QLK MSGQWFY  KAKRHRDKIHGA
Sbjct  10   EEQDAILKVLQRDAALKRAEEERVRHLPEKIKDDQQLKNMSGQWFYEAKAKRHRDKIHGA  69

Query  181  DIIRASMRRKK  213
            DIIRASMRRKK
Sbjct  70   DIIRASMRRKK  80
```

Figure 8.41. Amino acid sequence alignment of the pENTR-EGFP-C2-mSlp2-(10-56; K26R, A28R, Q44R, N48I, E56F) vector sequencing data. The EGFP CF forward primer was used to sequence the vector.



Sytl2 protein, partial [Mus musculus]
Sequence ID: AAH64769.1 Length: 533 Number of Matches: 1

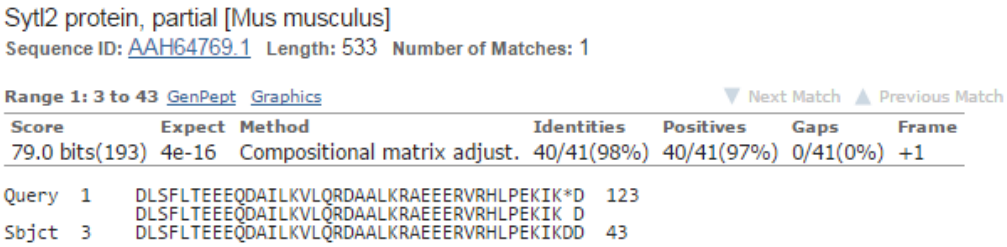
Range 1: 10 to 80 GenPept Graphics ▼ Next Match ▲ Previous Match

Score	Expect	Method	Identities	Positives	Gaps	Frame
102 bits(255)	1e-23	Composition-based stats.	64/71(90%)	66/71(92%)	0/71(0%)	+1

```
Query  1    EEQDAILKVLQRDAALrrreeervrHLPEKIKDDRQLKIMSLQWFYF*KAKRHRDKIHGA  180
            EEQDAILKVLQRDAAL+R EEERVRHLPEKIKDD+QLK MS QWFY  KAKRHRDKIHGA
Sbjct  10   EEQDAILKVLQRDAALKRAEEERVRHLPEKIKDDQQLKNMSGQWFYEAKAKRHRDKIHGA  69

Query  181  DIIRASMRRKK  213
            DIIRASMRRKK
Sbjct  70   DIIRASMRRKK  80
```

Figure 8.42. Amino acid sequence alignment of the pENTR-EGFP-C2-mSlp2-(10-56; K26R, A28R, Q44R, N48I, G51L, E56F) vector sequencing data. The EGFP CF forward primer was used to sequence the vector.



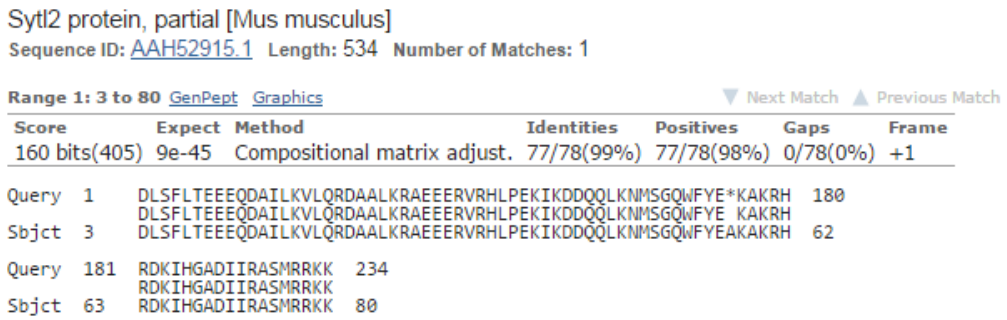
Sytl2 protein, partial [Mus musculus]
Sequence ID: AAH64769.1 Length: 533 Number of Matches: 1

Range 1: 3 to 43 GenPept Graphics ▼ Next Match ▲ Previous Match

Score	Expect	Method	Identities	Positives	Gaps	Frame
79.0 bits(193)	4e-16	Compositional matrix adjust.	40/41(98%)	40/41(97%)	0/41(0%)	+1

```
Query  1    DLSFLTEEEQDAILKVLQRDAALKRAEEERVRHLPEKIK*D  123
            DLSFLTEEEQDAILKVLQRDAALKRAEEERVRHLPEKIK D
Sbjct  3    DLSFLTEEEQDAILKVLQRDAALKRAEEERVRHLPEKIKDD  43
```

Figure 8.43. Amino acid sequence alignment of the pENTR-EGFP-C2-mSlp2-(3-41) vector sequencing data. The EGFP CF forward primer was used to sequence the vector.



Sytl2 protein, partial [Mus musculus]
Sequence ID: AAH52915.1 Length: 534 Number of Matches: 1

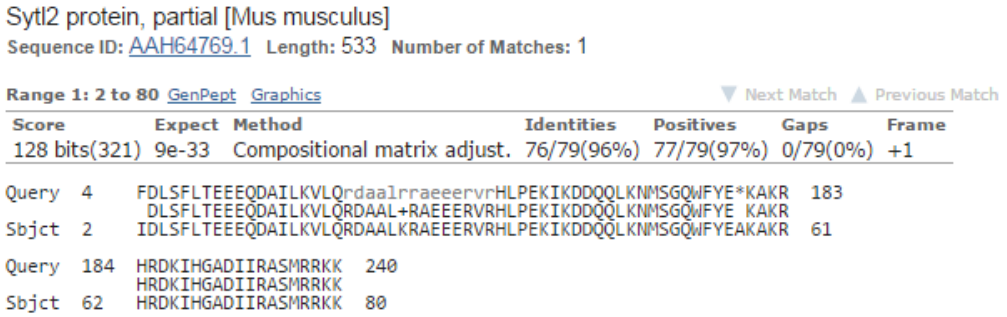
Range 1: 3 to 80 GenPept Graphics ▼ Next Match ▲ Previous Match

Score	Expect	Method	Identities	Positives	Gaps	Frame
160 bits(405)	9e-45	Compositional matrix adjust.	77/78(99%)	77/78(98%)	0/78(0%)	+1

```
Query  1    DLSFLTEEEQDAILKVLQRDAALKRAEEERVRHLPEKIKDDQQLKNMSGQWFYE*KAKRH  180
            DLSFLTEEEQDAILKVLQRDAALKRAEEERVRHLPEKIKDDQQLKNMSGQWFYE KAKRH
Sbjct  3    DLSFLTEEEQDAILKVLQRDAALKRAEEERVRHLPEKIKDDQQLKNMSGQWFYEAKAKRH  62

Query  181  RDKIHGADIIRASMRRKK  234
            RDKIHGADIIRASMRRKK
Sbjct  63   RDKIHGADIIRASMRRKK  80
```

Figure 8.44. Amino acid sequence alignment of the pENTR-EGFP-C2-mSlp2-(3-56) vector sequencing data. The EGFP CF forward primer was used to sequence the vector.



Sytl2 protein, partial [Mus musculus]
Sequence ID: AAH64769.1 Length: 533 Number of Matches: 1

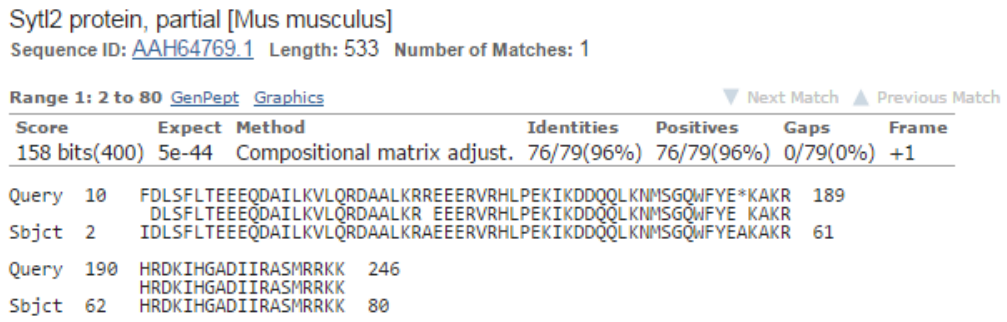
Range 1: 2 to 80 GenPept Graphics ▼ Next Match ▲ Previous Match

Score	Expect	Method	Identities	Positives	Gaps	Frame
128 bits(321)	9e-33	Compositional matrix adjust.	76/79(96%)	77/79(97%)	0/79(0%)	+1

```
Query  4    FDLSFLTEEEQDAILKVLQrdaalrraeeervrHLPEKIKDDQQLKNMSGQWFYE*KAKR  183
             DLSFLTEEEQDAILKVLQRDAAL+RAEEERVRHLPEKIKDDQQLKNMSGQWFYE KAKR
Sbjct  2    IDLSFLTEEEQDAILKVLQRDAALKRAEEERVRHLPEKIKDDQQLKNMSGQWFYEAKAKR  61

Query  184  HRDKIHGADIIRASMRRKK  240
            HRDKIHGADIIRASMRRKK
Sbjct  62   HRDKIHGADIIRASMRRKK  80
```

Figure 8.45. Amino acid sequence alignment of the pENTR-EGFP-C2-mSlp2-(3-56; K26R) vector sequencing data. The EGFP CF forward primer was used to sequence the vector.



Sytl2 protein, partial [Mus musculus]
Sequence ID: AAH64769.1 Length: 533 Number of Matches: 1

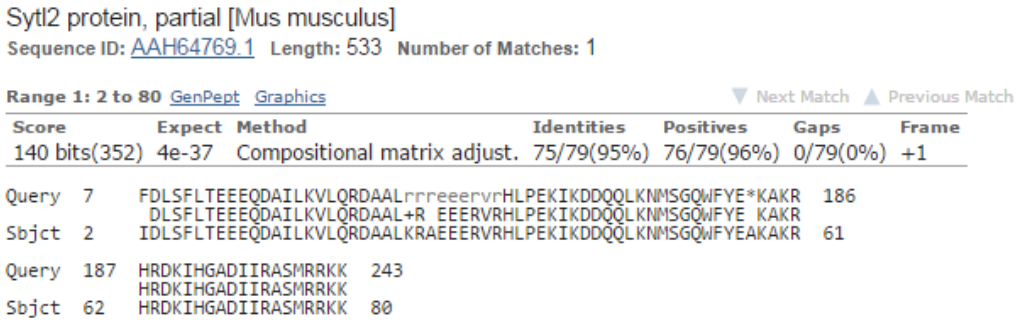
Range 1: 2 to 80 GenPept Graphics ▼ Next Match ▲ Previous Match

Score	Expect	Method	Identities	Positives	Gaps	Frame
158 bits(400)	5e-44	Compositional matrix adjust.	76/79(96%)	76/79(96%)	0/79(0%)	+1

```
Query  10   FDLSFLTEEEQDAILKVLQRDAALKRREEERVRHLPEKIKDDQQLKNMSGQWFYE*KAKR  189
            DLSFLTEEEQDAILKVLQRDAALKR EEERVRHLPEKIKDDQQLKNMSGQWFYE KAKR
Sbjct  2    IDLSFLTEEEQDAILKVLQRDAALKRAEEERVRHLPEKIKDDQQLKNMSGQWFYEAKAKR  61

Query  190  HRDKIHGADIIRASMRRKK  246
            HRDKIHGADIIRASMRRKK
Sbjct  62   HRDKIHGADIIRASMRRKK  80
```

Figure 8.46. Amino acid sequence alignment of the pENTR-EGFP-C2-mSlp2-(3-56; A28R) vector sequencing data. The EGFP CF forward primer was used to sequence the vector.



Sytl2 protein, partial [Mus musculus]
Sequence ID: AAH64769.1 Length: 533 Number of Matches: 1

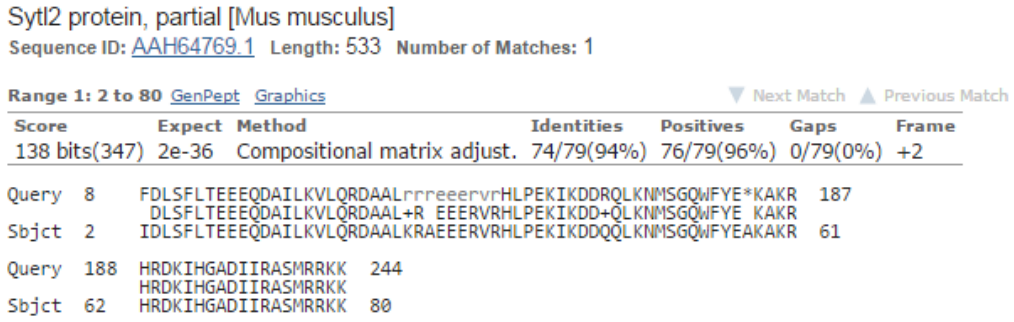
Range 1: 2 to 80 GenPept Graphics ▼ Next Match ▲ Previous Match

Score	Expect	Method	Identities	Positives	Gaps	Frame
140 bits(352)	4e-37	Compositional matrix adjust.	75/79(95%)	76/79(96%)	0/79(0%)	+1

```
Query  7    FDLSFLTEEEQDAILKVLQRDAALrrreeervrHLPEKIKDDQQLKNMSGQWFYE*KAKR  186
            DLSFLTEEEQDAILKVLQRDAAL+R EEERVRHLPEKIKDDQQLKNMSGQWFYE KAKR
Sbjct  2    IDLSFLTEEEQDAILKVLQRDAALKRAEEERVRHLPEKIKDDQQLKNMSGQWFYEAKAKR  61

Query  187  HRDKIHGADIIRASMRRKK  243
            HRDKIHGADIIRASMRRKK
Sbjct  62   HRDKIHGADIIRASMRRKK  80
```

Figure 8.47. Amino acid sequence alignment of the pENTR-EGFP-C2-mSlp2-(3-56; K26R, A28R) vector sequencing data. The EGFP CF forward primer was used to sequence the vector.



Sytl2 protein, partial [Mus musculus]
Sequence ID: AAH64769.1 Length: 533 Number of Matches: 1

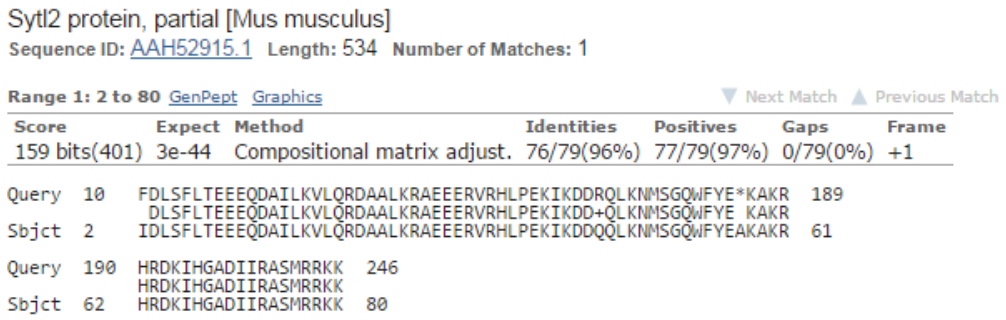
Range 1: 2 to 80 GenPept Graphics ▼ Next Match ▲ Previous Match

Score	Expect	Method	Identities	Positives	Gaps	Frame
138 bits(347)	2e-36	Compositional matrix adjust.	74/79(94%)	76/79(96%)	0/79(0%)	+2

```
Query  8    FDLSFLTEEEQDAILKVLQRDAALrrreeervrHLPEKIKDDRQLKNMSGQWFYE*KAKR  187
            DLSFLTEEEQDAILKVLQRDAAL+R EEERVRHLPEKIKDD+QLKNMSGQWFYE KAKR
Sbjct  2    IDLSFLTEEEQDAILKVLQRDAALKRAEEERVRHLPEKIKDDQQLKNMSGQWFYEAKAKR  61

Query  188  HRDKIHGADIIRASMRRKK  244
            HRDKIHGADIIRASMRRKK
Sbjct  62   HRDKIHGADIIRASMRRKK  80
```

Figure 8.48. Amino acid sequence alignment of the pENTR-EGFP-C2-mSlp2-(3-56; K26R, A28R, Q44R) vector sequencing data. The EGFP CF forward primer was used to sequence the vector.



Sytl2 protein, partial [Mus musculus]
Sequence ID: AAH52915.1 Length: 534 Number of Matches: 1

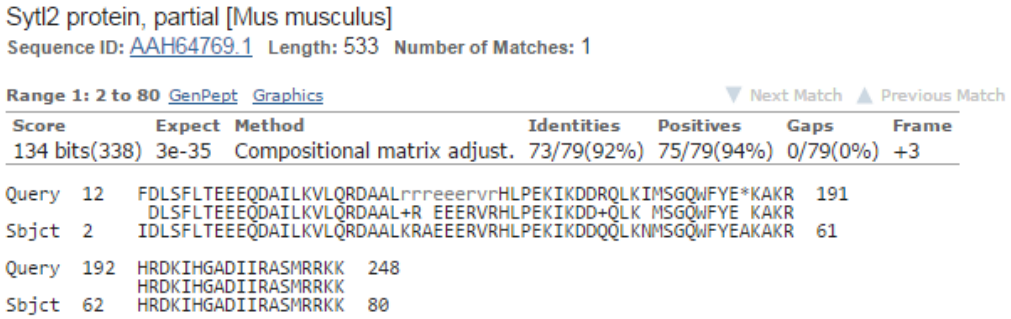
Range 1: 2 to 80 GenPept Graphics ▼ Next Match ▲ Previous Match

Score	Expect	Method	Identities	Positives	Gaps	Frame
159 bits(401)	3e-44	Compositional matrix adjust.	76/79(96%)	77/79(97%)	0/79(0%)	+1

```
Query  10   FDLSFLTEEEQDAILKVLQRDAALKRAEEERVRHLPEKIKDDRQLKNMSGQWFYE*KAKR  189
            DLSFLTEEEQDAILKVLQRDAALKRAEEERVRHLPEKIKDD+QLKNMSGQWFYE KAKR
Sbjct  2    IDLSFLTEEEQDAILKVLQRDAALKRAEEERVRHLPEKIKDDQQLKNMSGQWFYEAKAKR  61

Query  190  HRDKIHGADIIRASMRRKK  246
            HRDKIHGADIIRASMRRKK
Sbjct  62   HRDKIHGADIIRASMRRKK  80
```

Figure 8.49. Amino acid sequence alignment of the pENTR-EGFP-C2-mSlp2-(3-56; Q44R) vector sequencing data. The EGFP CF forward primer was used to sequence the vector.



Sytl2 protein, partial [Mus musculus]
Sequence ID: AAH64769.1 Length: 533 Number of Matches: 1

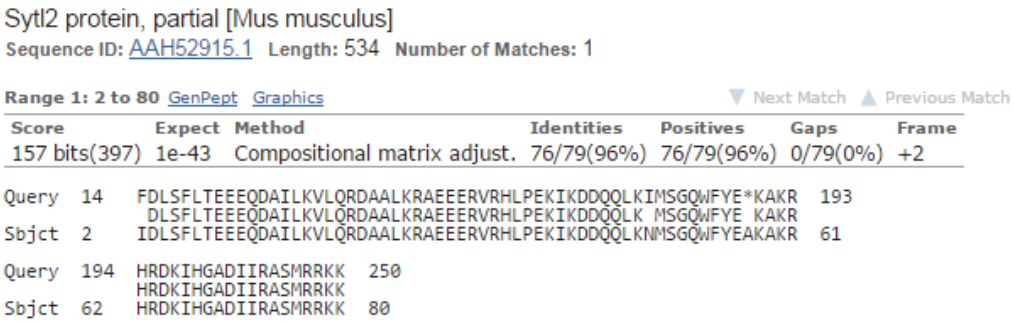
Range 1: 2 to 80 GenPept Graphics ▼ Next Match ▲ Previous Match

Score	Expect	Method	Identities	Positives	Gaps	Frame
134 bits(338)	3e-35	Compositional matrix adjust.	73/79(92%)	75/79(94%)	0/79(0%)	+3

```
Query  12   FDLSFLTEEEQDAILKVLQRDAALrrreeervrHLPEKIKDDRQLKIMSGQWFYE*KAKR  191
            DLSFLTEEEQDAILKVLQRDAAL+R EEERVRHLPEKIKDD+QLK MSGQWFYE KAKR
Sbjct  2    IDLSFLTEEEQDAILKVLQRDAALKRAEEERVRHLPEKIKDDQQLKNMSGQWFYEAKAKR  61

Query  192  HRDKIHGADIIRASMRRKK  248
            HRDKIHGADIIRASMRRKK
Sbjct  62   HRDKIHGADIIRASMRRKK  80
```

Figure 8.50. Amino acid sequence alignment of the pENTR-EGFP-C2-mSlp2-(3-56; K26R, A28R, Q44R, N48I) vector sequencing data. The EGFP CF forward primer was used to sequence the vector.



Sytl2 protein, partial [Mus musculus]
Sequence ID: AAH52915.1 Length: 534 Number of Matches: 1

Range 1: 2 to 80 GenPept Graphics ▼ Next Match ▲ Previous Match

Score	Expect	Method	Identities	Positives	Gaps	Frame
157 bits(397)	1e-43	Compositional matrix adjust.	76/79(96%)	76/79(96%)	0/79(0%)	+2

```
Query  14   FDLSFLTEEEQDAILKVLQRDAALKRAEEERVRHLPEKIKDDQQLKIMSGQWFYE*KAKR  193
            DLSFLTEEEQDAILKVLQRDAALKRAEEERVRHLPEKIKDDQQLK MSGQWFYE KAKR
Sbjct  2    IDLSFLTEEEQDAILKVLQRDAALKRAEEERVRHLPEKIKDDQQLKNMSGQWFYEAKAKR  61

Query  194  HRDKIHGADIIRASMRRKK  250
            HRDKIHGADIIRASMRRKK
Sbjct  62   HRDKIHGADIIRASMRRKK  80
```

Figure 8.51. Amino acid sequence alignment of the pENTR-EGFP-C2-mSlp2-(3-56; N48I) vector sequencing data. The EGFP CF forward primer was used to sequence the vector.

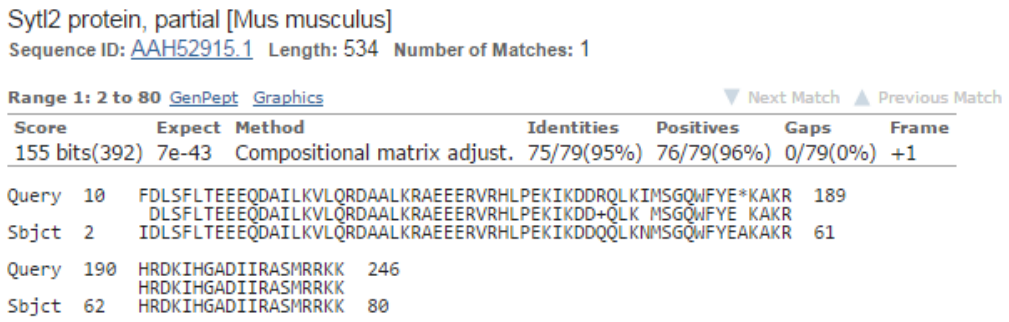


Figure 8.52. Amino acid sequence alignment of the pENTR-EGFP-C2-mSlp2-(3-56; Q44R, N48I) vector sequencing data. The EGFP CF forward primer was used to sequence the vector.

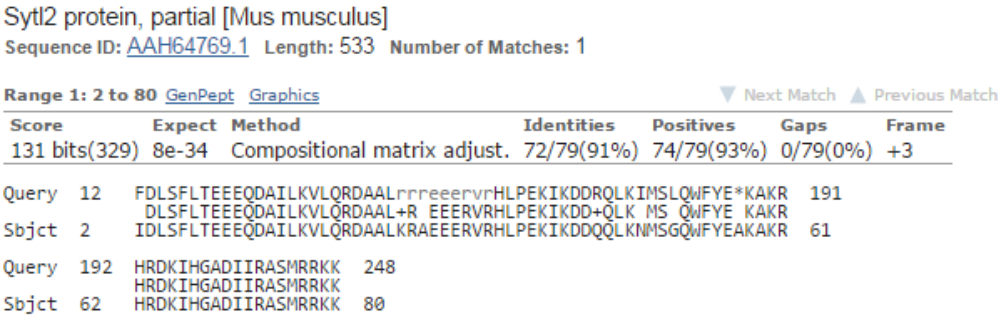


Figure 8.53. Amino acid sequence alignment of the pENTR-EGFP-C2-mSlp2-(3-56; K26R, A28R, Q44R, N48I, G51L) vector sequencing data. The EGFP CF forward primer was used to sequence the vector.

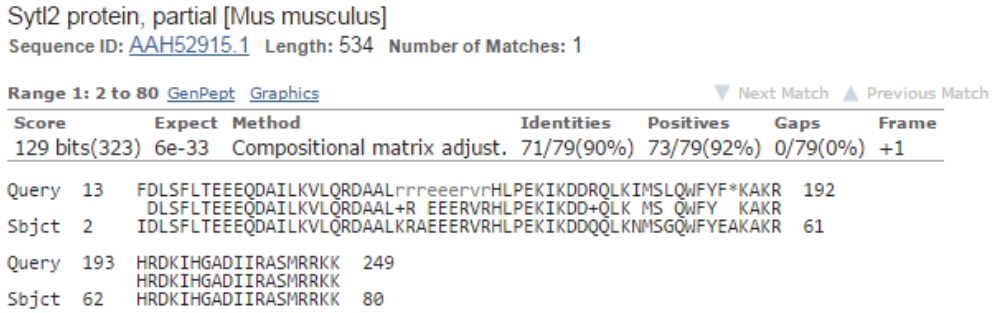


Figure 8.54. Amino acid sequence alignment of the pENTR-EGFP-C2-mSlp2-(3-56; K26R, A28R, Q44R, N48I, G51L, E56F) vector sequencing data. The EGFP CF forward primer was used to sequence the vector.

Sytl2 protein, partial [Mus musculus]
Sequence ID: AAH64769.1 Length: 533 Number of Matches: 1

Range 1: 12 to 80 GenPept Graphics ▼ Next Match ▲ Previous Match

Score	Expect	Method	Identities	Positives	Gaps	Frame
105 bits(261)	2e-24	Composition-based stats.	63/69(91%)	65/69(94%)	0/69(0%)	+1

```
Query  49   QDAILKVLQRDAALrrreeervrHLPEKIKDDRQLKIMSGQWFYF*KAKRHRDKIHGADI  228
            QDAILKVLQRDAAL+R EEERVRHLPEKIKDD+QLK MSGQWFY  KAKRHRDKIHGADI
Sbjct  12   QDAILKVLQRDAALKRAEEERVRHLPEKIKDDQQLKNMSGQWFYEAKAKRHRDKIHGADI  71

Query  229  IRASMRRKK  255
            IRASMRRKK
Sbjct  72   IRASMRRKK  80
```

Figure 8.55. Amino acid sequence alignment of the pENTR-EGFP-C2-mSlp2-(3-56; K26R, A28R, Q44R, N48I, E56F) vector sequencing data. The EGFP CF forward primer was used to sequence the vector.

Sytl1 protein [Mus musculus]
Sequence ID: AAH05623.1 Length: 308 Number of Matches: 1

Range 1: 1 to 74 GenPept Graphics ▼ Next Match ▲ Previous Match

Score	Expect	Method	Identities	Positives	Gaps	Frame
152 bits(384)	3e-43	Compositional matrix adjust.	74/74(100%)	74/74(100%)	0/74(0%)	+3

```
Query  45   MPQRGHPSQERLWALPSLPMAHGPGSEVEGLLDLSFLTEEEQEAISDVLKRDAHLRQLEE  224
            MPQRGHPSQERLWALPSLPMAHGPGSEVEGLLDLSFLTEEEQEAISDVLKRDAHLRQLEE
Sbjct  1    MPQRGHPSQERLWALPSLPMAHGPGSEVEGLLDLSFLTEEEQEAISDVLKRDAHLRQLEE  60

Query  225  GRVSKLRASLEDPW  266
            GRVSKLRASLEDPW
Sbjct  61   GRVSKLRASLEDPW  74
```

Figure 8.56. Amino acid sequence alignment of the pENTR-EGFP-C2-mSlp1-(1-74) vector sequencing data. The EGFP CF forward primer was used to sequence the vector.

Sytl1 protein [Mus musculus]
Sequence ID: AAH05623.1 Length: 308 Number of Matches: 1

Range 1: 70 to 116 GenPept Graphics ▼ Next Match ▲ Previous Match

Score	Expect	Method	Identities	Positives	Gaps	Frame
104 bits(260)	2e-25	Compositional matrix adjust.	47/47(100%)	47/47(100%)	0/47(0%)	+1

```
Query  76   LEDPWQLKILTGDWFQEARSQRHHHAHFGSDLVRASIRRKKSPKGDQ  216
            LEDPWQLKILTGDWFQEARSQRHHHAHFGSDLVRASIRRKKSPKGDQ
Sbjct  70   LEDPWQLKILTGDWFQEARSQRHHHAHFGSDLVRASIRRKKSPKGDQ  116
```

Figure 8.57. Amino acid sequence alignment of the pENTR-EGFP-C2-mSlp1-(70-116) vector sequencing data. The EGFP CF forward primer was used to sequence the vector.

mCherry [synthetic construct]
Sequence ID: ANO45948.1 Length: 228 Number of Matches: 1

Range 1: 10 to 217 GenPept Graphics ▼ Next Match ▲ Previous Match

Score	Expect	Method	Identities	Positives	Gaps	Frame
381 bits(978)	7e-133	Compositional matrix adjust.	199/208(96%)	199/208(95%)	0/208(0%)	+2

```
Query  8    MXXIKEFXRFKVHMEGSVNghefeiegegegRPYEGTQTAKLKVTKGGPLPFAWDILSPQ  187
            M  IKEF RFKVHMEGSVNGHEFEIEGEGEGRPYEGTQTAKLKVTKGGPLPFAWDILSPQ
Sbjct  10   MAIIKEFMRFKVHMEGSVNGHEFEIEGEGEGRPYEGTQTAKLKVTKGGPLPFAWDILSPQ  69

Query  188  FMYGSKAYVKHPADIPDYLKLSFPEGFKWERVMNFEDGGVVTVTQDSSLQDGEFIYKVKL  367
            FMYGSKAYVKHPADIPDYLKLSFPEGFKWERVMNFEDGGVVTVTQDSSLQDGEFIYKVKL
Sbjct  70   FMYGSKAYVKHPADIPDYLKLSFPEGFKWERVMNFEDGGVVTVTQDSSLQDGEFIYKVKL  129

Query  368  RGTNFPSDGPVMQKKTMGWEASSERMYPEDGALKGEIKQRLKLKDGGHYXAEVKTTYKAK  547
            RGTNFPSDGPVMQKKTMGWEASSERMYPEDGALKGEIKQRLKLKDGGHY AEVKTTYKAK
Sbjct  130  RGTNFPSDGPVMQKKTMGWEASSERMYPEDGALKGEIKQRLKLKDGGHYDAEVKTTYKAK  189

Query  548  XPVQLPGAYXVNIKLDXTSHXEDYTXVE  631
             PVQLPGAY VNIKLD TSH EDYT VE
Sbjct  190  KPVQLPGAYNVNIKLDITSHNEDYTIVE  217
```

Figure 8.58. Amino acid sequence alignment of the pENTR-m.Cherry-mSlp1-(1-74) vector sequencing data. A forward primer was used to sequence the vector.

Sytl2 protein, partial [Mus musculus]
Sequence ID: AAH64769.1 Length: 533 Number of Matches: 1

Range 1: 2 to 80 GenPept Graphics ▼ Next Match ▲ Previous Match

Score	Expect	Method	Identities	Positives	Gaps	Frame
160 bits(404)	1e-44	Compositional matrix adjust.	77/79(97%)	77/79(97%)	0/79(0%)	+1

```
Query  10   FDLSFLTEEEQDAILKVLQRDAALKRAEEERVRHLPEKIKDDQQLKNMSGQWFYEAKAKR  189
            DLSFLTEEEQDAILKVLQRDAALKRAEEERVRHLPEKIKDDQQLKNMSGQWFYEAKAKR
Sbjct  2    IDLSFLTEEEQDAILKVLQRDAALKRAEEERVRHLPEKIKDDQQLKNMSGQWFYEAKAKR  61

Query  190  HRDKIH*ADIIRASMRRKK  246
            HRDKIH ADIIRASMRRKK
Sbjct  62   HRDKIHGADIIRASMRRKK  80
```

Figure 8.59. Amino acid sequence alignment of the pENTR-EGFP-C2-mSlp2-(3-67) vector sequencing data. The EGFP CF forward primer was used to sequence the vector.

Sytl2 protein, partial [Mus musculus]
Sequence ID: AAH52915.1 Length: 534 Number of Matches: 1

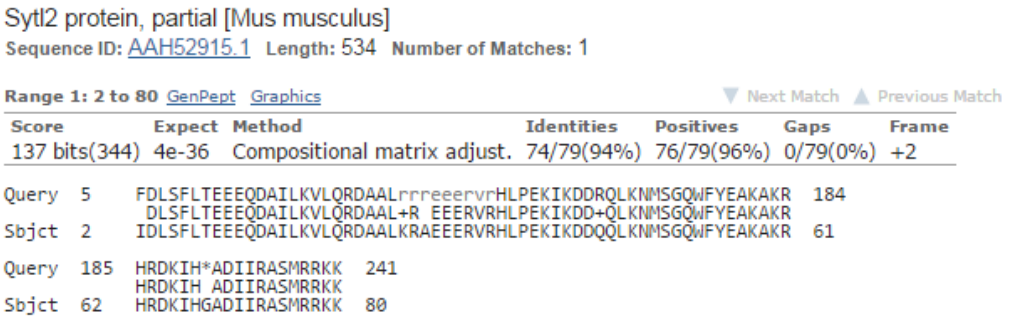
Range 1: 2 to 80 GenPept Graphics ▼ Next Match ▲ Previous Match

Score	Expect	Method	Identities	Positives	Gaps	Frame
139 bits(351)	5e-37	Compositional matrix adjust.	75/79(95%)	76/79(96%)	0/79(0%)	+3

```
Query  18   FDLSFLTEEEQDAILKVLQRDAALrrreeervrHLPEKIKDDQQLKNMSGQWFYEAKAKR  197
            DLSFLTEEEQDAILKVLQRDAAL+R EEERVRHLPEKIKDDQQLKNMSGQWFYEAKAKR
Sbjct  2    IDLSFLTEEEQDAILKVLQRDAALKRAEEERVRHLPEKIKDDQQLKNMSGQWFYEAKAKR  61

Query  198  HRDKIH*ADIIRASMRRKK  254
            HRDKIH ADIIRASMRRKK
Sbjct  62   HRDKIHGADIIRASMRRKK  80
```

Figure 8.60. Amino acid sequence alignment of the pENTR-EGFP-C2-mSlp2-(3-67; K26R, A28R) vector sequencing data. The EGFP CF forward primer was used to sequence the vector.



Sytl2 protein, partial [Mus musculus]
Sequence ID: AAH52915.1 Length: 534 Number of Matches: 1

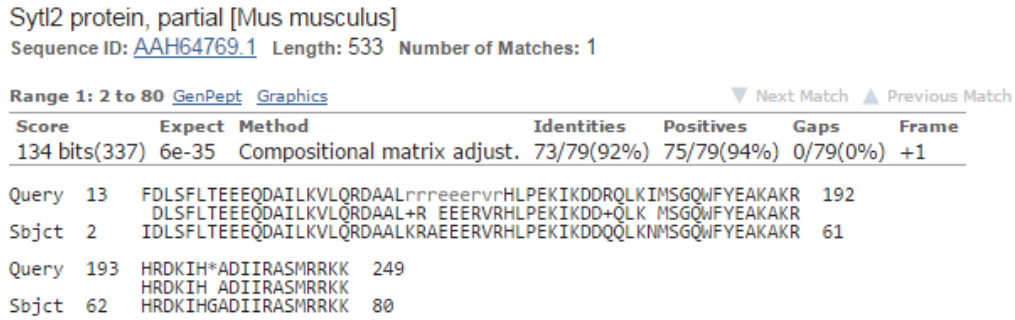
Range 1: 2 to 80 GenPept Graphics ▼ Next Match ▲ Previous Match

Score	Expect	Method	Identities	Positives	Gaps	Frame
137 bits(344)	4e-36	Compositional matrix adjust.	74/79(94%)	76/79(96%)	0/79(0%)	+2

```
Query  5    FDLSFLTEEEQDAILKVLQRDAALrrreeervrHLPEKIKDDRQLKNMSGQWFYEAKAKR  184
            DLSFLTEEEQDAILKVLQRDAAL+R EEERVRHLPEKIKDD+QLKNMSGQWFYEAKAKR
Sbjct  2    IDLSFLTEEEQDAILKVLQRDAALKRAEEERVRHLPEKIKDDQQLKNMSGQWFYEAKAKR  61

Query  185  HRDKIH*ADIIRASMRRKK  241
            HRDKIH ADIIRASMRRKK
Sbjct  62   HRDKIHGADIIRASMRRKK  80
```

Figure 8.61. Amino acid sequence alignment of the pENTR-EGFP-C2-mSlp2-(3-67; K26R, A28R, Q44R) vector sequencing data. The EGFP CF forward primer was used to sequence the vector.



Sytl2 protein, partial [Mus musculus]
Sequence ID: AAH64769.1 Length: 533 Number of Matches: 1

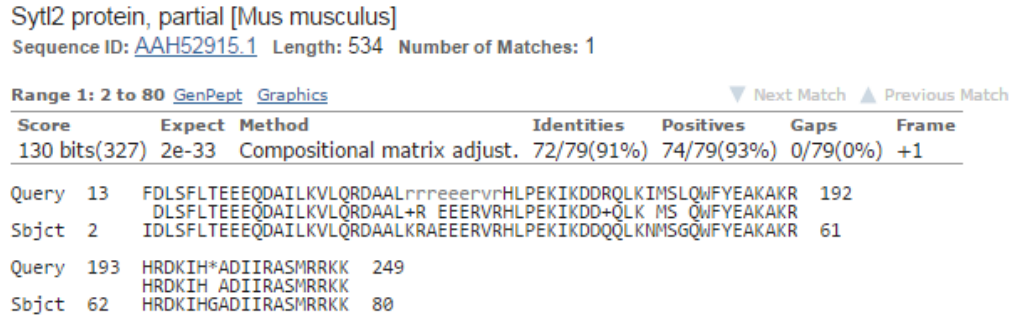
Range 1: 2 to 80 GenPept Graphics ▼ Next Match ▲ Previous Match

Score	Expect	Method	Identities	Positives	Gaps	Frame
134 bits(337)	6e-35	Compositional matrix adjust.	73/79(92%)	75/79(94%)	0/79(0%)	+1

```
Query  13   FDLSFLTEEEQDAILKVLQRDAALrrreeervrHLPEKIKDDRQLKIMSGQWFYEAKAKR  192
            DLSFLTEEEQDAILKVLQRDAAL+R EEERVRHLPEKIKDD+QLK MSGQWFYEAKAKR
Sbjct  2    IDLSFLTEEEQDAILKVLQRDAALKRAEEERVRHLPEKIKDDQQLKNMSGQWFYEAKAKR  61

Query  193  HRDKIH*ADIIRASMRRKK  249
            HRDKIH ADIIRASMRRKK
Sbjct  62   HRDKIHGADIIRASMRRKK  80
```

Figure 8.62. Amino acid sequence alignment of the pENTR-EGFP-C2-mSlp2-(3-67; K26R, A28R, Q44R, N48I) vector sequencing data. The EGFP CF forward primer was used to sequence the vector.



Sytl2 protein, partial [Mus musculus]
Sequence ID: AAH52915.1 Length: 534 Number of Matches: 1

Range 1: 2 to 80 GenPept Graphics ▼ Next Match ▲ Previous Match

Score	Expect	Method	Identities	Positives	Gaps	Frame
130 bits(327)	2e-33	Compositional matrix adjust.	72/79(91%)	74/79(93%)	0/79(0%)	+1

```
Query  13   FDLSFLTEEEQDAILKVLQRDAALrrreeervrHLPEKIKDDRQLKIMSLQWFYEAKAKR  192
            DLSFLTEEEQDAILKVLQRDAAL+R EEERVRHLPEKIKDD+QLK MS QWFYEAKAKR
Sbjct  2    IDLSFLTEEEQDAILKVLQRDAALKRAEEERVRHLPEKIKDDQQLKNMSGQWFYEAKAKR  61

Query  193  HRDKIH*ADIIRASMRRKK  249
            HRDKIH ADIIRASMRRKK
Sbjct  62   HRDKIHGADIIRASMRRKK  80
```

Figure 8.63. Amino acid sequence alignment of the pENTR-EGFP-C2-mSlp2-(3-67; K26R, A28R, Q44R, N48I, G51L) vector sequencing data. The EGFP CF forward primer was used to sequence the vector.

Sytl2 protein, partial [Mus musculus]
Sequence ID: AAH64769.1 Length: 533 Number of Matches: 1

Range 1: 2 to 80 GenPept Graphics ▼ Next Match ▲ Previous Match

Score	Expect	Method	Identities	Positives	Gaps	Frame
128 bits(321)	1e-32	Compositional matrix adjust.	71/79(90%)	73/79(92%)	0/79(0%)	+3

```
Query  15   FDLSFLTEEEQDAILKVLQRDAALrrreeervrHLPEKIKDDRQLKIMSLQWFYFAKAKR  194
            DLSFLTEEEQDAILKVLQRDAAL+R EEERVRHLPEKIKDD+QLK MS QWFY AKAKR
Sbjct  2    IDLSFLTEEEQDAILKVLQRDAALKRAEEERVRHLPEKIKDDQQLKNMSGQWFYEAKAKR  61

Query  195  HRDKIH*ADIIRASMRRKK  251
            HRDKIH ADIIRASMRRKK
Sbjct  62   HRDKIHGADIIRASMRRKK  80
```

Figure 8.64. Amino acid sequence alignment of the pENTR-EGFP-C2-mSlp2-(3-67; K26R, A28R, Q44R, N48I, G51L, E56F) vector sequencing data. The EGFP CF forward primer was used to sequence the vector.

Sytl2 protein, partial [Mus musculus]
Sequence ID: AAH64769.1 Length: 533 Number of Matches: 1

Range 1: 2 to 80 GenPept Graphics ▼ Next Match ▲ Previous Match

Score	Expect	Method	Identities	Positives	Gaps	Frame
122 bits(305)	2e-30	Compositional matrix adjust.	69/79(87%)	71/79(89%)	0/79(0%)	+2

```
Query  14   FDLSFLTEEEQDAILKVLQRDAALrrreeervrHLPEKIKDDRQLKIMSLQWFYFAKAKR  193
            DLSFLTEEEQDAILKVLQRDAAL+R EEERVRHLPEKIKDD+QLK MS QWFY AKAKR
Sbjct  2    IDLSFLTEEEQDAILKVLQRDAALKRAEEERVRHLPEKIKDDQQLKNMSGQWFYEAKAKR  61

Query  194  RFDKIH*ADIIRASMRRKK  250
              DKIH ADIIRASMRRKK
Sbjct  62   HRDKIHGADIIRASMRRKK  80
```

Figure 8.65. Amino acid sequence alignment of the pENTR-EGFP-C2-mSlp2-(3-67; K26R, A28R, Q44R, N48I, G51L, E56F, H62R, R63F) vector sequencing data. The EGFP CF forward primer was used to sequence the vector.

Sytl2 protein, partial [Mus musculus]
Sequence ID: AAH64769.1 Length: 533 Number of Matches: 1

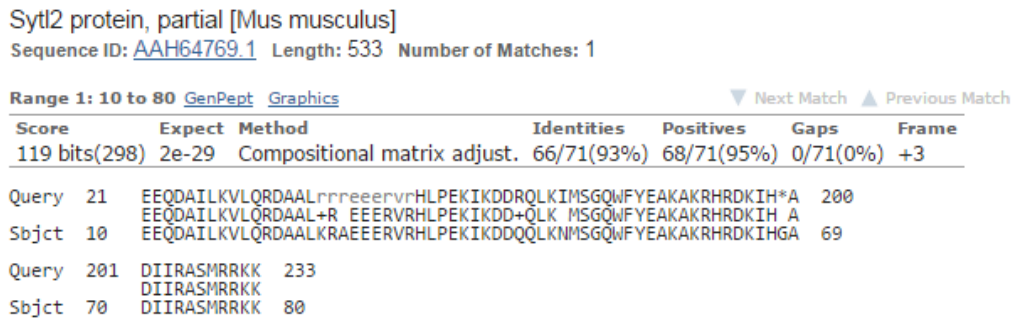
Range 1: 10 to 80 GenPept Graphics ▼ Next Match ▲ Previous Matc

Score	Expect	Method	Identities	Positives	Gaps	Frame
145 bits(365)	5e-39	Compositional matrix adjust.	70/71(99%)	70/71(98%)	0/71(0%)	+2

```
Query  17   EEQDAILKVLQRDAALKRAEEERVRHLPEKIKDDQQLKNMSGQWFYEAKAKRHRDKIH*A  196
            EEQDAILKVLQRDAALKRAEEERVRHLPEKIKDDQQLKNMSGQWFYEAKAKRHRDKIH A
Sbjct  10   EEQDAILKVLQRDAALKRAEEERVRHLPEKIKDDQQLKNMSGQWFYEAKAKRHRDKIHGA  69

Query  197  DIIRASMRRKK  229
            DIIRASMRRKK
Sbjct  70   DIIRASMRRKK  80
```

Figure 8.66. Amino acid sequence alignment of the pENTR-EGFP-C2-mSlp2-(10-67) vector sequencing data. The EGFP CF forward primer was used to sequence the vector.



Sytl2 protein, partial [Mus musculus]
Sequence ID: AAH64769.1 Length: 533 Number of Matches: 1

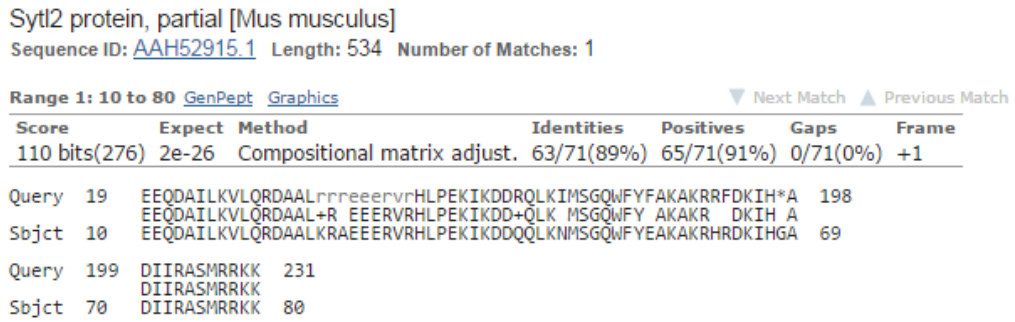
Range 1: 10 to 80 GenPept Graphics ▼ Next Match ▲ Previous Match

Score	Expect	Method	Identities	Positives	Gaps	Frame
119 bits(298)	2e-29	Compositional matrix adjust.	66/71(93%)	68/71(95%)	0/71(0%)	+3

```
Query  21   EEQDAILKVLQRDAALrrreeervrHLPEKIKDDRQLKIMSGQWFYEAKAKRHRDKIH*A  200
            EEQDAILKVLQRDAAL+R EEERVRHLPEKIKDD+QLK MSGQWFYEAKAKRHRDKIH A
Sbjct  10   EEQDAILKVLQRDAALKRAEEERVRHLPEKIKDDQQLKNMSGQWFYEAKAKRHRDKIHGA  69

Query  201  DIIRASMRRKK  233
            DIIRASMRRKK
Sbjct  70   DIIRASMRRKK  80
```

Figure 8.67. Amino acid sequence alignment of the pENTR-EGFP-C2-mSlp2-(10-67; K26R, A28R, Q44R, N48I) vector sequencing data. The EGFP CF forward primer was used to sequence the vector.



Sytl2 protein, partial [Mus musculus]
Sequence ID: AAH52915.1 Length: 534 Number of Matches: 1

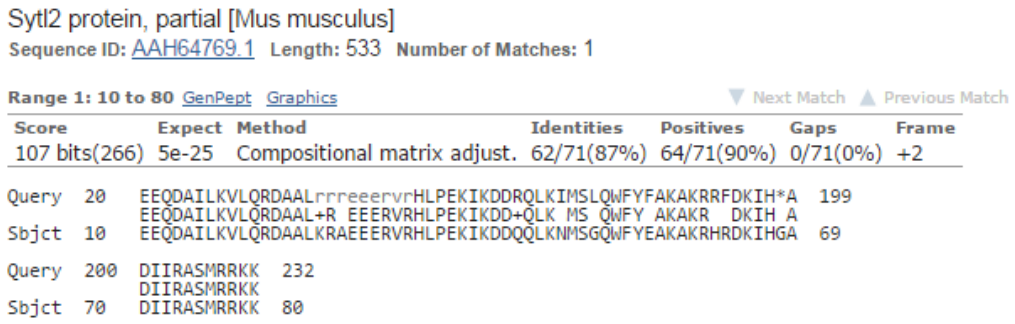
Range 1: 10 to 80 GenPept Graphics ▼ Next Match ▲ Previous Match

Score	Expect	Method	Identities	Positives	Gaps	Frame
110 bits(276)	2e-26	Compositional matrix adjust.	63/71(89%)	65/71(91%)	0/71(0%)	+1

```
Query  19   EEQDAILKVLQRDAALrrreeervrHLPEKIKDDRQLKIMSGQWFYFAKAKRRFDKIH*A  198
            EEQDAILKVLQRDAAL+R EEERVRHLPEKIKDD+QLK MSGQWFY AKAKR  DKIH A
Sbjct  10   EEQDAILKVLQRDAALKRAEEERVRHLPEKIKDDQQLKNMSGQWFYEAKAKRHRDKIHGA  69

Query  199  DIIRASMRRKK  231
            DIIRASMRRKK
Sbjct  70   DIIRASMRRKK  80
```

Figure 8.68. Amino acid sequence alignment of the pENTR-EGFP-C2-mSlp2-(10-67; K26R, A28R, Q44R, N48I, E56F, H62R, R63F) vector sequencing data. The EGFP CF forward primer was used to sequence the vector.



Sytl2 protein, partial [Mus musculus]
Sequence ID: AAH64769.1 Length: 533 Number of Matches: 1

Range 1: 10 to 80 GenPept Graphics ▼ Next Match ▲ Previous Match

Score	Expect	Method	Identities	Positives	Gaps	Frame
107 bits(266)	5e-25	Compositional matrix adjust.	62/71(87%)	64/71(90%)	0/71(0%)	+2

```
Query  20   EEQDAILKVLQRDAALrrreeervrHLPEKIKDDRQLKIMSLQWFYFAKAKRRFDKIH*A  199
            EEQDAILKVLQRDAAL+R EEERVRHLPEKIKDD+QLK MS QWFY AKAKR  DKIH A
Sbjct  10   EEQDAILKVLQRDAALKRAEEERVRHLPEKIKDDQQLKNMSGQWFYEAKAKRHRDKIHGA  69

Query  200  DIIRASMRRKK  232
            DIIRASMRRKK
Sbjct  70   DIIRASMRRKK  80
```

Figure 8.69. Amino acid sequence alignment of the pENTR-EGFP-C2-mSlp2-(10-67; K26R, A28R, Q44R, N48I, G51L, E56F, H62R, R63F) vector sequencing data. The EGFP CF forward primer was used to sequence the vector.

Sytl2 protein, partial [Mus musculus]
Sequence ID: AAH64769.1 Length: 533 Number of Matches: 1

Range 1: 3 to 80 GenPept Graphics ▼ Next Match ▲ Previous Match

Score	Expect	Method	Identities	Positives	Gaps	Frame
160 bits(404)	2e-44	Compositional matrix adjust.	77/78(99%)	77/78(98%)	0/78(0%)	+1

```
Query  1    DLSFLTEEEQDAILKVLQRDAALKRAEEERVRHLPEKIK*DQQLKNMSGQWFYEAKAKRH  180
            DLSFLTEEEQDAILKVLQRDAALKRAEEERVRHLPEKIK DQQLKNMSGQWFYEAKAKRH
Sbjct  3    DLSFLTEEEQDAILKVLQRDAALKRAEEERVRHLPEKIKDDQQLKNMSGQWFYEAKAKRH  62

Query  181  RDKIHGADIIRASMRRKK  234
            RDKIHGADIIRASMRRKK
Sbjct  63   RDKIHGADIIRASMRRKK  80
```

Figure 8.70. Amino acid sequence alignment of the pGEX-4T1-mSlp2-(3-41) vector sequencing data. The PGEX 5' forward primer was used to sequence the vector.

Sytl2 protein, partial [Mus musculus]
Sequence ID: AAH52915.1 Length: 534 Number of Matches: 1

Range 1: 3 to 80 GenPept Graphics ▼ Next Match ▲ Previous Match

Score	Expect	Method	Identities	Positives	Gaps	Frame
160 bits(405)	7e-45	Compositional matrix adjust.	77/78(99%)	77/78(98%)	0/78(0%)	+1

```
Query  1    DLSFLTEEEQDAILKVLQRDAALKRAEEERVRHLPEKIKDDQQLKNMSGQWFYE*KAKRH  180
            DLSFLTEEEQDAILKVLQRDAALKRAEEERVRHLPEKIKDDQQLKNMSGQWFYE KAKRH
Sbjct  3    DLSFLTEEEQDAILKVLQRDAALKRAEEERVRHLPEKIKDDQQLKNMSGQWFYEAKAKRH  62

Query  181  RDKIHGADIIRASMRRKK  234
            RDKIHGADIIRASMRRKK
Sbjct  63   RDKIHGADIIRASMRRKK  80
```

Figure 8.71. Amino acid sequence alignment of the pGEX-4T1-mSlp2-(3-56) vector sequencing data. The PGEX 5' forward primer was used to sequence the vector.

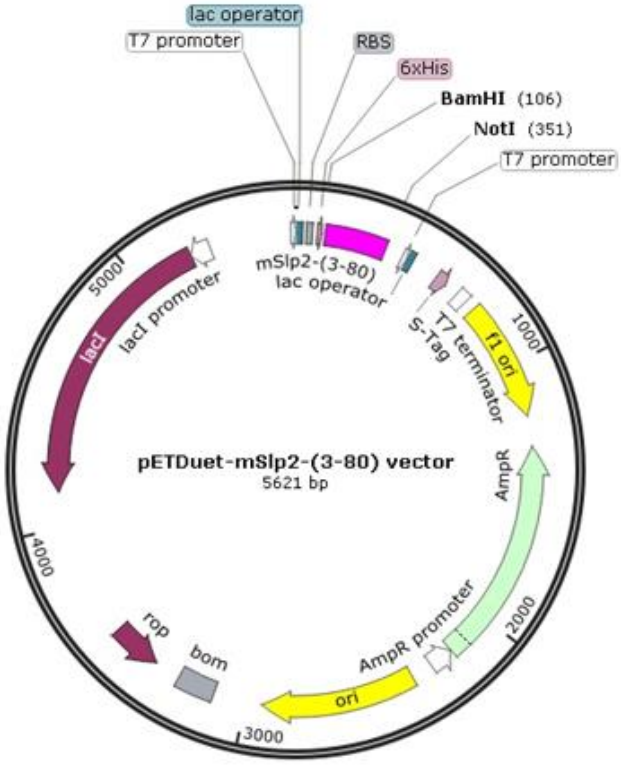


Figure 8.72. pETDuet-1- mSlp2-(3-80) vector map. 5' BamHI and 3' NotI restriction enzyme sites were introduced into the 5' and 3' ends of mSlp2-(3-80) cDNA, mSlp2-(3-80) cDNA was then sub-cloned into the pETDuet-1vector which contains 5' BamHI and 3' NotI enzyme restriction sites. This vector also contains ampicillin resistance gene (molecular weight: 5621BP).

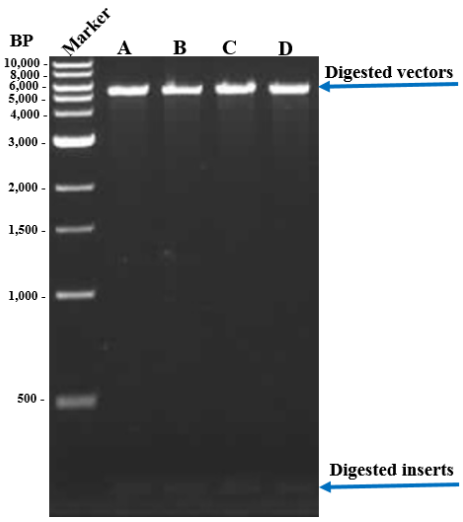


Figure 8.73. BamHI and NotI digests of the pETDuet-1-mSlp2-(3-80) vector. An ethidium bromide stained 1% TBE agarose gel showing different BamHI and NotI digests of the pETDuet-1-mSlp2-(3-80) vector. A) pETDuet-1-mSlp2-(3-80) vector. B) pETDuet-1-mSlp2-(3-80; K26R, A28R) vector. C) pETDuet-1-mSlp2-(3-80; K26R, A28R, Q44R) vector. D) pETDuet-1-mSlp2-(3-80; K26R, A28R, Q44R, N48I) vector. The molecular weights of the upper (vector) and lower (insert) bands are 5387BP and 234BP, respectively.

Sytl2 protein, partial [Mus musculus]
Sequence ID: AAH52915.1 Length: 534 Number of Matches: 1

Range 1: 3 to 80 GenPept Graphics ▼ Next Match ▲ Previous Match

Score	Expect	Method	Identities	Positives	Gaps	Frame
162 bits(411)	6e-45	Compositional matrix adjust.	78/78(100%)	78/78(100%)	0/78(0%)	+1

```
Query  202  DLSFLTEEEQDAILKVLQRDAALKRAEEERVRHLPEKIKDDQQLKNMSGQWFYEAKAKRH  381
            DLSFLTEEEQDAILKVLQRDAALKRAEEERVRHLPEKIKDDQQLKNMSGQWFYEAKAKRH
Sbjct  3    DLSFLTEEEQDAILKVLQRDAALKRAEEERVRHLPEKIKDDQQLKNMSGQWFYEAKAKRH  62

Query  382  RDKIHGADIIRASMRRKK  435
            RDKIHGADIIRASMRRKK
Sbjct  63   RDKIHGADIIRASMRRKK  80
```

Figure 8.74. Amino acid sequence alignment of the pETDuet-1-mSlp2-(3-80) vector sequencing data. The Duet Down1 reverse primer was used to sequence the vector.

Sytl2 protein, partial [Mus musculus]
Sequence ID: AAH64769.1 Length: 533 Number of Matches: 1

Range 1: 3 to 80 GenPept Graphics ▼ Next Match ▲ Previous Match

Score	Expect	Method	Identities	Positives	Gaps	Frame
142 bits(359)	1e-37	Compositional matrix adjust.	76/78(97%)	77/78(98%)	0/78(0%)	+3

```
Query  138  DLSFLTEEEQDAILKVLQRDAALrrreeervrHLPEKIKDDQQLKNMSGQWFYEAKAKRH  317
            DLSFLTEEEQDAILKVLQRDAAL+R EEERVRHLPEKIKDDQQLKNMSGQWFYEAKAKRH
Sbjct  3    DLSFLTEEEQDAILKVLQRDAALKRAEEERVRHLPEKIKDDQQLKNMSGQWFYEAKAKRH  62

Query  318  RDKIHGADIIRASMRRKK  371
            RDKIHGADIIRASMRRKK
Sbjct  63   RDKIHGADIIRASMRRKK  80
```

Figure 8.75. Amino acid sequence alignment of the pETDuet-1-mSlp2-(3-80; K26R, A28R) vector sequencing data. The Duet Down1 reverse primer was used to sequence the vector.

Sytl2 protein, partial [Mus musculus]
Sequence ID: AAH52915.1 Length: 534 Number of Matches: 1

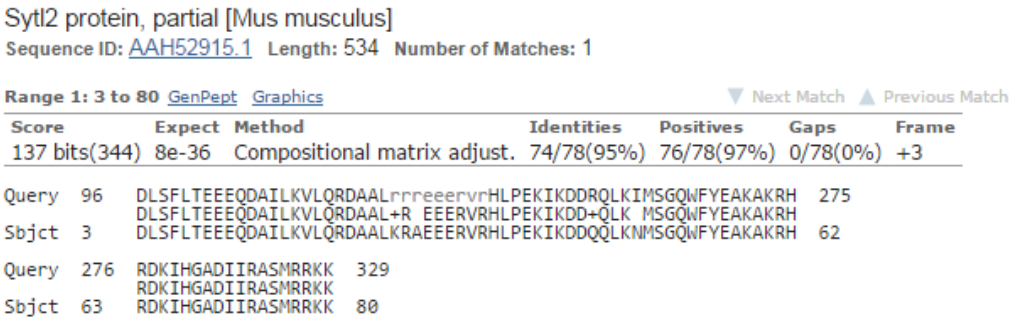
Range 1: 3 to 80 GenPept Graphics ▼ Next Match ▲ Previous Match

Score	Expect	Method	Identities	Positives	Gaps	Frame
140 bits(353)	4e-37	Compositional matrix adjust.	75/78(96%)	77/78(98%)	0/78(0%)	+3

```
Query  102  DLSFLTEEEQDAILKVLQRDAALrrreeervrHLPEKIKDDRQLKNMSGQWFYEAKAKRH  281
            DLSFLTEEEQDAILKVLQRDAAL+R EEERVRHLPEKIKDD+QLKNMSGQWFYEAKAKRH
Sbjct  3    DLSFLTEEEQDAILKVLQRDAALKRAEEERVRHLPEKIKDDQQLKNMSGQWFYEAKAKRH  62

Query  282  RDKIHGADIIRASMRRKK  335
            RDKIHGADIIRASMRRKK
Sbjct  63   RDKIHGADIIRASMRRKK  80
```

Figure 8.76. Amino acid sequence alignment of the pETDuet-1-mSlp2-(3-80; K26R, A28R, Q44R) vector sequencing data. The Duet Down1 reverse primer was used to sequence the vector.



Sytl2 protein, partial [Mus musculus]
Sequence ID: AAH52915.1 Length: 534 Number of Matches: 1

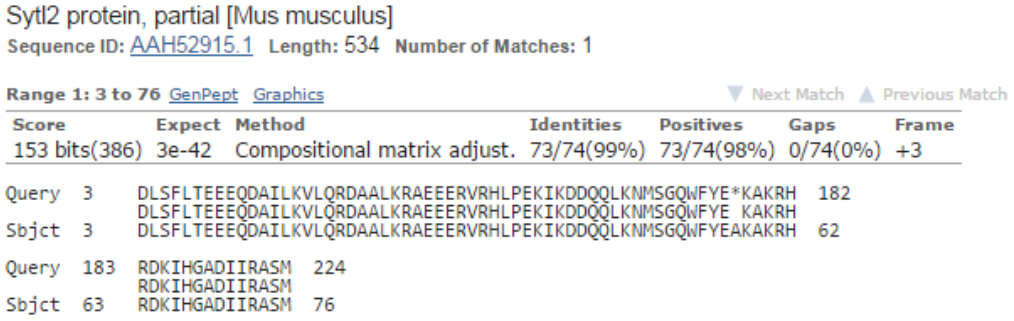
Range 1: 3 to 80 GenPept Graphics ▼ Next Match ▲ Previous Match

Score	Expect	Method	Identities	Positives	Gaps	Frame
137 bits(344)	8e-36	Compositional matrix adjust.	74/78(95%)	76/78(97%)	0/78(0%)	+3

```
Query  96   DLSFLTEEEQDAILKVLQRDAALrrreeervrHLPEKIKDDRQLKIMSGQWFYEAKAKRH  275
            DLSFLTEEEQDAILKVLQRDAAL+R EEERVRHLPEKIKDD+QLK MSGQWFYEAKAKRH
Sbjct  3    DLSFLTEEEQDAILKVLQRDAALKRAEEERVRHLPEKIKDDQQLKNMSGQWFYEAKAKRH  62

Query  276  RDKIHGADIIRASMRRKK  329
            RDKIHGADIIRASMRRKK
Sbjct  63   RDKIHGADIIRASMRRKK  80
```

Figure 8.77. Amino acid sequence alignment of the pETDuet-1-mSlp2-(3-80; K26R, A28R, Q44R, N48I) vector sequencing data. The Duet Down1 reverse primer was used to sequence the vector.



Sytl2 protein, partial [Mus musculus]
Sequence ID: AAH52915.1 Length: 534 Number of Matches: 1

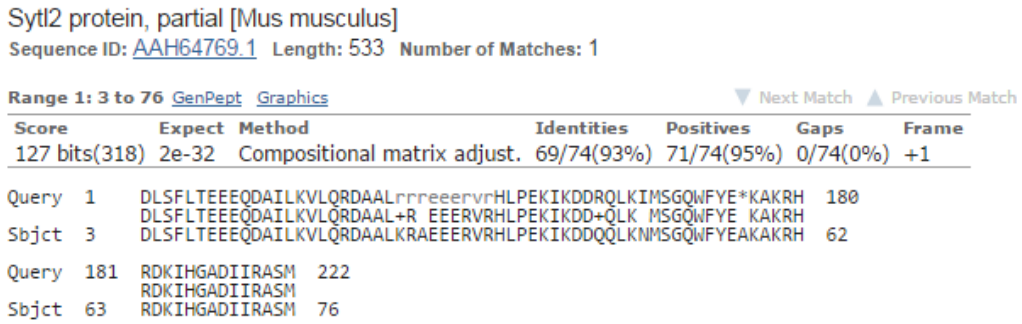
Range 1: 3 to 76 GenPept Graphics ▼ Next Match ▲ Previous Match

Score	Expect	Method	Identities	Positives	Gaps	Frame
153 bits(386)	3e-42	Compositional matrix adjust.	73/74(99%)	73/74(98%)	0/74(0%)	+3

```
Query  3    DLSFLTEEEQDAILKVLQRDAALKRAEEERVRHLPEKIKDDQQLKNMSGQWFYE*KAKRH  182
            DLSFLTEEEQDAILKVLQRDAALKRAEEERVRHLPEKIKDDQQLKNMSGQWFYE KAKRH
Sbjct  3    DLSFLTEEEQDAILKVLQRDAALKRAEEERVRHLPEKIKDDQQLKNMSGQWFYEAKAKRH  62

Query  183  RDKIHGADIIRASM  224
            RDKIHGADIIRASM
Sbjct  63   RDKIHGADIIRASM  76
```

Figure 8.78. Amino acid sequence alignment of the pETDuet-1-mSlp2-(3-56) vector sequencing data. The Duet Down1 reverse primer was used to sequence the vector.



Sytl2 protein, partial [Mus musculus]
Sequence ID: AAH64769.1 Length: 533 Number of Matches: 1

Range 1: 3 to 76 GenPept Graphics ▼ Next Match ▲ Previous Match

Score	Expect	Method	Identities	Positives	Gaps	Frame
127 bits(318)	2e-32	Compositional matrix adjust.	69/74(93%)	71/74(95%)	0/74(0%)	+1

```
Query  1    DLSFLTEEEQDAILKVLQRDAALrrreeervrHLPEKIKDDRQLKIMSGQWFYE*KAKRH  180
            DLSFLTEEEQDAILKVLQRDAAL+R EEERVRHLPEKIKDD+QLK MSGQWFYE KAKRH
Sbjct  3    DLSFLTEEEQDAILKVLQRDAALKRAEEERVRHLPEKIKDDQQLKNMSGQWFYEAKAKRH  62

Query  181  RDKIHGADIIRASM  222
            RDKIHGADIIRASM
Sbjct  63   RDKIHGADIIRASM  76
```

Figure 8.79. Amino acid sequence alignment of the pETDuet-1-mSlp2-(3-56; K26R, A28R, Q44R, N48I) vector sequencing data. The Duet Down1 reverse primer was used to sequence the vector.

Sytl2 protein, partial [Mus musculus]
Sequence ID: AAH64769.1 Length: 533 Number of Matches: 1

Range 1: 3 to 76 GenPept Graphics ▼ Next Match ▲ Previous Match

Score	Expect	Method	Identities	Positives	Gaps	Frame
152 bits(383)	6e-42	Compositional matrix adjust.	73/74(99%)	73/74(98%)	0/74(0%)	+3

```
Query  3    DLSFLTEEEQDAILKVLQRDAALKRAEEERVRHLPEKIKDDQQLKNMSGQWFYEAKAKRH  182
            DLSFLTEEEQDAILKVLQRDAALKRAEEERVRHLPEKIKDDQQLKNMSGQWFYEAKAKRH
Sbjct  3    DLSFLTEEEQDAILKVLQRDAALKRAEEERVRHLPEKIKDDQQLKNMSGQWFYEAKAKRH  62

Query  183  RDKIH*ADIIRASM  224
            RDKIH ADIIRASM
Sbjct  63   RDKIHGADIIRASM  76
```

Figure 8.80. Amino acid sequence alignment of the pETDuet-1-mSlp2-(3-67) vector sequencing data. The Duet Down1 reverse primer was used to sequence the vector.

References

Agola, J.O., L. Hong, Z. Surviladze, O. Ursu, A. Waller, J.J. Strouse, D.S. Simpson, C.E. Schroeder, T.I. Oprea, J.E. Golden, J. Aube, T. Buranda, L.A. Sklar, and A. Wandinger-Ness. 2012. A competitive nucleotide binding inhibitor: in vitro characterization of Rab7 GTPase inhibition. *ACS chemical biology*. 7:1095-1108.

Aivazian, D., R.L. Serrano, and S. Pfeffer. 2006. TIP47 is a key effector for Rab9 localization. *The Journal of cell biology*. 173:917-926.

Akavia, U.D., O. Litvin, J. Kim, F. Sanchez-Garcia, D. Kotliar, H.C. Causton, P. Pochanard, E. Mozes, L.A. Garraway, and D. Pe'er. 2010. An integrated approach to uncover drivers of cancer. *Cell*. 143:1005-1017.

Akrap, N., T. Seidel, and B.G. Barisas. 2010. Forster distances for fluorescence resonant energy transfer between mCherry and other visible fluorescent proteins. *Analytical biochemistry*. 402:105-106.

Albertazzi, L., D. Arosio, L. Marchetti, F. Ricci, and F. Beltram. 2009. Quantitative FRET analysis with the EGFP-mCherry fluorescent protein pair. *Photochemistry and photobiology*. 85:287-297.

Alexandrov, K., H. Horiuchi, O. Steele-Mortimer, M.C. Seabra, and M. Zerial. 1994. Rab escort protein-1 is a multifunctional protein that accompanies newly prenylated rab proteins to their target membranes. *The EMBO journal*. 13:5262-5273.

Alexandrov, K., I. Simon, V. Yurchenko, A. Iakovenko, E. Rostkova, A.J. Scheidig, and R.S. Goody. 1999. Characterization of the ternary complex between Rab7, REP-1 and Rab geranylgeranyl transferase. *European journal of biochemistry*. 265:160-170.

Ali, B.R., C. Wasmeier, L. Lamoreux, M. Strom, and M.C. Seabra. 2004. Multiple regions contribute to membrane targeting of Rab GTPases. *Journal of cell science*. 117:6401-6412.

Alory, C., and W.E. Balch. 2000. Molecular basis for Rab prenylation. *The Journal of cell biology*. 150:89-103.

Alory, C., and W.E. Balch. 2003. Molecular evolution of the Rab-escort-protein/guanine-nucleotide-dissociation-inhibitor superfamily. *Molecular biology of the cell*. 14:3857-3867.

An, Y., Y. Shao, C. Alory, J. Matteson, T. Sakisaka, W. Chen, R.A. Gibbs, I.A. Wilson, and W.E. Balch. 2003. Geranylgeranyl switching regulates GDI-Rab GTPase recycling. *Structure*. 11:347-357.

Anant, J.S., L. Desnoyers, M. Machius, B. Demeler, J.C. Hansen, K.D. Westover, J. Deisenhofer, and M.C. Seabra. 1998. Mechanism of Rab geranylgeranylation: formation of the catalytic ternary complex. *Biochemistry*. 37:12559-12568.

Andres, D.A., M.C. Seabra, M.S. Brown, S.A. Armstrong, T.E. Smeland, F.P.M. Cremers, and J.L. Goldstein. 1993. Cdna Cloning of Component-a of Rab Geranylgeranyl Transferase and Demonstration of Its Role as a Rab Escort Protein. *Cell*. 73:1091-1099.

Anikster, Y., M. Huizing, P.D. Anderson, D.L. Fitzpatrick, A. Klar, E. Gross-Kieselstein, Y. Berkun, G. Shazberg, W.A. Gahl, and H. Hurvitz. 2002. Evidence that Griscelli syndrome with neurological involvement is caused by mutations in RAB27A, not MYO5A. *American journal of human genetics*. 71:407-414.

Araki, K., H. Nakanishi, H. Hirano, M. Kato, T. Sasaki, and Y. Takai. 1995. Purification and characterization of Rab GDI beta from rat brain. *Biochemical and biophysical research communications*. 211:296-305.

Arimura, N., T. Kimura, S. Nakamuta, S. Taya, Y. Funahashi, A. Hattori, A. Shimada, C. Menager, S. Kawabata, K. Fujii, A. Iwamatsu, R.A. Segal, M. Fukuda, and K. Kaibuchi. 2009. Anterograde transport of TrkB in axons is mediated by direct interaction with Slp1 and Rab27. *Developmental cell*. 16:675-686.

Arnold, T.R., R.E. Stephenson, and A.L. Miller. 2017. Rho GTPases and Actomyosin: partners in regulating epithelial cell-cell junction structure and function. *Experimental cell research*.

Bahadoran, P., R. Busca, C. Chiaverini, W. Westbroek, J. Lambert, K. Bille, G. Valony, M. Fukuda, J.M. Naeyaert, J.P. Ortonne, and R. Ballotti. 2003. Characterization of the molecular defects in Rab27a, caused by RAB27A missense mutations found in patients with Griscelli syndrome. *The Journal of biological chemistry*. 278:11386-11392.

Bajar, B.T., E.S. Wang, S. Zhang, M.Z. Lin, and J. Chu. 2016. A Guide to Fluorescent Protein FRET Pairs. *Sensors (Basel, Switzerland)*. 16.

Banterle, N., and E.A. Lemke. 2016. Nanoscale devices for linkerless long-term single-molecule observation. *Current opinion in biotechnology*. 39:105-112.

Bao, J., Y. Ni, H. Qin, L. Xu, Z. Ge, F. Zhan, H. Zhu, J. Zhao, X. Zhou, X. Tang, and L. Tang. 2014. Rab27b is a potential predictor for metastasis and prognosis in colorectal cancer. *Gastroenterology research and practice*. 2014:913106.

Baron, R.A., and M.C. Seabra. 2008. Rab geranylgeranylation occurs preferentially via the pre-formed REP-RGGT complex and is regulated by geranylgeranyl pyrophosphate. *The Biochemical journal*. 415:67-75.

Barr, F., and D.G. Lambright. 2010. Rab GEFs and GAPs. *Curr Opin Cell Biol*. 22:461-470.

Barral, D.C., J.S. Ramalho, R. Anders, A.N. Hume, H.J. Knapton, T. Tolmachova, L.M. Collinson, D. Goulding, K.S. Authi, and M.C. Seabra. 2002. Functional redundancy of Rab27 proteins and the pathogenesis of Griscelli syndrome. *The Journal of clinical investigation*. 110:247-257.

Barral, D.C., and M.C. Seabra. 2004. The melanosome as a model to study organelle motility in mammals. *Pigment cell research / sponsored by the European Society for Pigment Cell Research and the International Pigment Cell Society*. 17:111-118.

Bennett, D.C., P.J. Cooper, and I.R. Hart. 1987. A line of non-tumorigenic mouse melanocytes, syngeneic with the B16 melanoma and requiring a tumour promoter for growth. *International journal of cancer. Journal international du cancer*. 39:414-418.

Bennett, D.C., and M.L. Lamoreux. 2003. The color loci of mice--a genetic century. *Pigment cell research / sponsored by the European Society for Pigment Cell Research and the International Pigment Cell Society*. 16:333-344.

Bevis, B.J., and B.S. Glick. 2002. Rapidly maturing variants of the Discosoma red fluorescent protein (DsRed). *Nature biotechnology*. 20:83-87.

Blom, M., K. Reis, J. Heldin, J. Kreuger, and P. Aspenstrom. 2017. The atypical Rho GTPase RhoD is a regulator of actin cytoskeleton dynamics and directed cell migration. *Experimental cell research*. 352:255-264.

Bobrie, A., S. Krumeich, F. Reyal, C. Recchi, L.F. Moita, M.C. Seabra, M. Ostrowski, and C. Thery. 2012. Rab27a supports exosome-dependent and -independent mechanisms that modify the tumor microenvironment and can promote tumor progression. *Cancer research*. 72:4920-4930.

Bock, J.B., H.T. Matern, A.A. Peden, and R.H. Scheller. 2001. A genomic perspective on membrane compartment organization. *Nature*. 409:839-841.

Bolasco, G., D.C. Tracey-White, T. Tolmachova, A.J. Thorley, T.D. Tetley, M.C. Seabra, and A.N. Hume. 2011. Loss of Rab27 function results in abnormal lung epithelium structure in mice. *American journal of physiology. Cell physiology*. 300:C466-476.

Bornhorst, J.A., and J.J. Falke. 2000. Purification of proteins using polyhistidine affinity tags. *Methods in enzymology*. 326:245-254.

Boucher, J.M., R.P. Clark, D.C. Chong, K.M. Citrin, L.A. Wylie, and V.L. Bautch. 2017. Dynamic alterations in decoy VEGF receptor-1 stability regulate angiogenesis. *Nature communications*. 8:15699.

Bourne, H.R., D.A. Sanders, and F. McCormick. 1991. The GTPase superfamily: conserved structure and molecular mechanism. *Nature*. 349:117-127.

Bravo-Cordero, J.J., R. Marrero-Diaz, D. Megias, L. Genis, A. Garcia-Grande, M.A. Garcia, A.G. Arroyo, and M.C. Montoya. 2007. MT1-MMP proinvasive activity is regulated by a novel Rab8-dependent exocytic pathway. *The EMBO journal*. 26:1499-1510.

Brozzi, F., F. Diraison, S. Lajus, S. Rajatileka, T. Philips, R. Regazzi, M. Fukuda, P. Verkade, E. Molnar, and A. Varadi. 2012. Molecular mechanism of myosin Va recruitment to dense core secretory granules. *Traffic*. 13:54-69.

Brzezinska, A.A., J.L. Johnson, D.B. Munafo, K. Crozat, B. Beutler, W.B. Kiosses, B.A. Ellis, and S.D. Catz. 2008. The Rab27a effectors JFC1/Slp1 and Munc13-4 regulate exocytosis of neutrophil granules. *Traffic*. 9:2151-2164.

Bucci, C., M. Chiariello, D. Lattero, M. Maiorano, and C.B. Bruni. 1999. Interaction cloning and characterization of the cDNA encoding the human prenylated rab acceptor (PRA1). *Biochemical and biophysical research communications*. 258:657-662.

Campbell, R.E., O. Tour, A.E. Palmer, P.A. Steinbach, G.S. Baird, D.A. Zacharias, and R.Y. Tsien. 2002. A monomeric red fluorescent protein. *Proceedings of the National Academy of Sciences of the United States of America*. 99:7877-7882.

Candiano, G., M. Bruschi, L. Musante, L. Santucci, G.M. Ghiggeri, B. Carnemolla, P. Orecchia, L. Zardi, and P.G. Righetti. 2004. Blue silver: a very sensitive colloidal Coomassie G-250 staining for proteome analysis. *Electrophoresis*. 25:1327-1333.

Cantalupo, G., P. Alifano, V. Roberti, C.B. Bruni, and C. Bucci. 2001. Rab-interacting lysosomal protein (RILP): the Rab7 effector required for transport to lysosomes. *The EMBO journal*. 20:683-693.

Carroll, K.S., J. Hanna, I. Simon, J. Krise, P. Barbero, and S.R. Pfeffer. 2001. Role of Rab9 GTPase in facilitating receptor recruitment by TIP47. *Science (New York, N.Y.)*. 292:1373-1376.

Casalou, C., A. Faustino, and D.C. Barral. 2016. Arf proteins in cancer cell migration. *Small GTPases*. 7:270-282.

Casanova, J.E. 2012. Advantages and limitations of cell-based assays for GTPase activation and regulation. *Cellular logistics*. 2:147-150.

Casey, P.J., and M.C. Seabra. 1996. Protein prenyltransferases. *The Journal of biological chemistry*. 271:5289-5292.

Catz, S.D. 2008. Characterization of Rab27a and JFC1 as constituents of the secretory machinery of prostate-specific antigen in prostate carcinoma cells. *Methods in enzymology*. 438:25-40.

Catz, S.D., B.M. Babior, and J.L. Johnson. 2002a. JFC1 is transcriptionally activated by nuclear factor-kappaB and up-regulated by tumour necrosis factor alpha in prostate carcinoma cells. *The Biochemical journal*. 367:791-799.

Catz, S.D., J.L. Johnson, and B.M. Babior. 2002b. The C2A domain of JFC1 binds to 3'-phosphorylated phosphoinositides and directs plasma membrane association in living cells. *Proceedings of the National Academy of Sciences of the United States of America*. 99:11652-11657.

Cazares, V.A., A. Subramani, J.J. Saldate, W. Hoerauf, and E.L. Stuenkel. 2014. Distinct actions of Rab3 and Rab27 GTPases on late stages of exocytosis of insulin. *Traffic*. 15:997-1015.

Cetica, V., Y. Hackmann, S. Grieve, E. Sieni, B. Ciambotti, M.L. Coniglio, D. Pende, K. Gilmour, P. Romagnoli, G.M. Griffiths, and M. Arico. 2015. Patients with Griscelli syndrome and normal pigmentation identify RAB27A mutations that selectively disrupt MUNC13-4 binding. *The Journal of allergy and clinical immunology*. 135:1310-1318 e1311.

Chaineau, M., M.S. Ioannou, and P.S. McPherson. 2013. Rab35: GEFs, GAPs and effectors. *Traffic*. 14:1109-1117.

Chalfie, M., Y. Tu, G. Euskirchen, W.W. Ward, and D.C. Prasher. 1994. Green fluorescent protein as a marker for gene expression. *Science (New York, N.Y.)*. 263:802-805.

Chang, C., T. Liu, Y. Huang, W. Qin, H. Yang, and J. Chen. 2017. MicroRNA-134-3p is a novel potential inhibitor of human ovarian cancer stem cells by targeting RAB27A. *Gene*. 605:99-107.

Chavas, L.M., K. Ihara, M. Kawasaki, S. Torii, T. Uejima, R. Kato, T. Izumi, and S. Wakatsuki. 2008. Elucidation of Rab27 recruitment by its effectors: structure of Rab27a bound to Exophilin4/Slp2-a. *Structure*. 16:1468-1477.

Chavrier, P., J.P. Gorvel, E. Stelzer, K. Simons, J. Gruenberg, and M. Zerial. 1991. Hypervariable C-terminal domain of rab proteins acts as a targeting signal. *Nature*. 353:769-772.

Chavrier, P., and B. Goud. 1999. The role of ARF and Rab GTPases in membrane transport. *Curr Opin Cell Biol*. 11:466-475.

Chen, D., J. Guo, T. Miki, M. Tachibana, and W.A. Gahl. 1997. Molecular cloning and characterization of rab27a and rab27b, novel human rab proteins shared by melanocytes and platelets. *Biochemical and molecular medicine*. 60:27-37.

Chen, X., C. Li, T. Izumi, S.A. Ernst, P.C. Andrews, and J.A. Williams. 2004. Rab27b localizes to zymogen granules and regulates pancreatic acinar exocytosis. *Biochemical and biophysical research communications*. 323:1157-1162.

Chen, Y., X. Guo, F.M. Deng, F.X. Liang, W. Sun, M. Ren, T. Izumi, D.D. Sabatini, T.T. Sun, and G. Kreibich. 2003. Rab27b is associated with fusiform vesicles and may be involved in targeting uroplakins to urothelial apical membranes. *Proceedings of the National Academy of Sciences of the United States of America*. 100:14012-14017.

Cherfils, J., and M. Zeghouf. 2013. Regulation of small GTPases by GEFs, GAPs, and GDIs. *Physiol Rev*. 93:269-309.

Cheviet, S., T. Coppola, L.P. Haynes, R.D. Burgoyne, and R. Regazzi. 2004. The Rab-binding protein Noc2 is associated with insulin-containing secretory granules and is essential for pancreatic beta-cell exocytosis. *Molecular endocrinology (Baltimore, Md.)*. 18:117-126.

Chiang, L., S. Karvar, and S.F. Hamm-Alvarez. 2012. Direct imaging of RAB27B-enriched secretory vesicle biogenesis in lacrimal acinar cells reveals origins on a nascent vesicle budding site. *PloS one*. 7:e31789.

Chiang, L., J. Ngo, J.E. Schechter, S. Karvar, T. Tolmachova, M.C. Seabra, A.N. Hume, and S.F. Hamm-Alvarez. 2011. Rab27b regulates exocytosis of

secretory vesicles in acinar epithelial cells from the lacrimal gland. *American journal of physiology. Cell physiology*. 301:C507-521.

Christoforidis, S., H.M. McBride, R.D. Burgoyne, and M. Zerial. 1999. The Rab5 effector EEA1 is a core component of endosome docking. *Nature*. 397:621-625.

Chung, C.T., S.L. Niemela, and R.H. Miller. 1989. One-step preparation of competent Escherichia coli: transformation and storage of bacterial cells in the same solution. *Proceedings of the National Academy of Sciences of the United States of America*. 86:2172-2175.

Cody, C.W., D.C. Prasher, W.M. Westler, F.G. Prendergast, and W.W. Ward. 1993. Chemical structure of the hexapeptide chromophore of the Aequorea green-fluorescent protein. *Biochemistry*. 32:1212-1218.

Colicelli, J. 2004. Human RAS superfamily proteins and related GTPases. *Science's STKE : signal transduction knowledge environment*. 2004:RE13.

Colvin, R.A., T.K. Means, T.J. Diefenbach, L.F. Moita, R.P. Friday, S. Sever, G.S. Campanella, T. Abrazinski, L.A. Manice, C. Moita, N.W. Andrews, D. Wu, N. Hacohen, and A.D. Luster. 2010. Synaptotagmin-mediated vesicle fusion regulates cell migration. *Nature immunology*. 11:495-502.

Cormack, B.P., R.H. Valdivia, and S. Falkow. 1996. FACS-optimized mutants of the green fluorescent protein (GFP). *Gene*. 173:33-38.

Cremers, F.P., S.A. Armstrong, M.C. Seabra, M.S. Brown, and J.L. Goldstein. 1994. REP-2, a Rab escort protein encoded by the choroideremia-like gene. *The Journal of biological chemistry*. 269:2111-2117.

Cremers, F.P., C.M. Molloy, D.J. van de Pol, J.A. van den Hurk, I. Bach, A.H. Geurts van Kessel, and H.H. Ropers. 1992. An autosomal homologue of the choroideremia gene colocalizes with the Usher syndrome type II locus on the distal part of chromosome 1q. *Human molecular genetics*. 1:71-75.

Cubitt, A.B., R. Heim, S.R. Adams, A.E. Boyd, L.A. Gross, and R.Y. Tsien. 1995. Understanding, improving and using green fluorescent proteins. *Trends in biochemical sciences*. 20:448-455.

Del Nery, E., S. Miserey-Lenkei, T. Falguieres, C. Nizak, L. Johannes, F. Perez, and B. Goud. 2006. Rab6A and Rab6A' GTPases play non-overlapping roles in membrane trafficking. *Traffic*. 7:394-407.

Delano, W.L. 2002. The PyMOL Molecular Graphics System.

Deneka, M., M. Neeft, and P. van der Sluijs. 2003. Regulation of membrane transport by rab GTPases. *Critical reviews in biochemistry and molecular biology*. 38:121-142.

Desnos, C., J.S. Schonn, S. Huet, V.S. Tran, A. El-Amraoui, G. Raposo, I. Fanget, C. Chapuis, G. Menasche, G. de Saint Basile, C. Petit, S. Cribier, J.P. Henry, and F. Darchen. 2003. Rab27A and its effector MyRIP link secretory granules to F-actin and control their motion towards release sites. *The Journal of cell biology*. 163:559-570.

Desnoyers, L., J.S. Anant, and M.C. Seabra. 1996. Geranylgeranylation of Rab proteins. *Biochemical Society transactions*. 24:699-703.

Desnoyers, L., and M.C. Seabra. 1998. Single prenyl-binding site on protein prenyl transferases. *Proceedings of the National Academy of Sciences of the United States of America*. 95:12266-12270.

Dessinioti, C., A.J. Stratigos, D. Rigopoulos, and A.D. Katsambas. 2009. A review of genetic disorders of hypopigmentation: lessons learned from the biology of melanocytes. *Experimental dermatology*. 18:741-749.

Detter, J.C., Q. Zhang, E.H. Mules, E.K. Novak, V.S. Mishra, W. Li, E.B. McMurtrie, V.T. Tchernev, M.R. Wallace, M.C. Seabra, R.T. Swank, and S.F. Kingsmore. 2000. Rab geranylgeranyl transferase alpha mutation in the gunmetal mouse reduces Rab prenylation and platelet synthesis. *Proceedings of the National Academy of Sciences of the United States of America*. 97:4144-4149.

Dey, S., G. Banker, and K. Ray. 2017. Anterograde Transport of Rab4-Associated Vesicles Regulates Synapse Organization in Drosophila. *Cell reports*. 18:2452-2463.

Diekmann, Y., E. Seixas, M. Gouw, F. Tavares-Cadete, M.C. Seabra, and J.B. Pereira-Leal. 2011. Thousands of rab GTPases for the cell biologist. *PLoS computational biology*. 7:e1002217.

Dirac-Svejstrup, A.B. 1995. Rab GDP Dissociation Inhibitor: Putting Rab GTPases in the Right Place. *Journal of Biological Chemistry*. 270:17057-17059.

Dirac-Svejstrup, A.B., T. Sumizawa, and S.R. Pfeffer. 1997. Identification of a GDI displacement factor that releases endosomal Rab GTPases from Rab-GDI. *The EMBO journal*. 16:465-472.

Donaldson, J.G., and C.L. Jackson. 2011. ARF family G proteins and their regulators: roles in membrane transport, development and disease. *Nature reviews. Molecular cell biology*. 12:362-375.

Donaldson, J.G., D.L. Johnson, and D. Dutta. 2016. Rab and Arf G proteins in endosomal trafficking and cell surface homeostasis. *Small GTPases*. 7:247-251.

Dozynkiewicz, M.A., N.B. Jamieson, I. Macpherson, J. Grindlay, P.V. van den Berghe, A. von Thun, J.P. Morton, C. Gourley, P. Timpson, C. Nixon, C.J. McKay, R. Carter, D. Strachan, K. Anderson, O.J. Sansom, P.T. Caswell, and J.C. Norman. 2012. Rab25 and CLIC3 collaborate to promote integrin recycling from late endosomes/lysosomes and drive cancer progression. *Developmental cell*. 22:131-145.

Du, X., Y. Li, Y.L. Xia, S.M. Ai, J. Liang, P. Sang, X.L. Ji, and S.Q. Liu. 2016. Insights into Protein-Ligand Interactions: Mechanisms, Models, and Methods. *International journal of molecular sciences*. 17.

Dumas, J.J., Z. Zhu, J.L. Connolly, and D.G. Lambright. 1999. Structural basis of activation and GTP hydrolysis in Rab proteins. *Structure*. 7:413-423.

Ehrhardt, A., G.R. Ehrhardt, X. Guo, and J.W. Schrader. 2002. Ras and relatives--job sharing and networking keep an old family together. *Experimental hematology*. 30:1089-1106.

El-Amraoui, A., J.S. Schonn, P. Kussel-Andermann, S. Blanchard, C. Desnos, J.P. Henry, U. Wolfrum, F. Darchen, and C. Petit. 2002. MyRIP, a novel Rab effector, enables myosin VIIa recruitment to retinal melanosomes. *EMBO reports*. 3:463-470.

Elstak, E.D., M. Neeft, N.T. Nehme, J. Voortman, M. Cheung, M. Goodarzifard, H.C. Gerritsen, P.M. van Bergen En Henegouwen, I. Callebaut, G. de Saint Basile, and P. van der Sluijs. 2011. The munc13-4-rab27 complex is specifically required for tethering secretory lysosomes at the plasma membrane. *Blood*. 118:1570-1578.

Eustace, B.K., T. Sakurai, J.K. Stewart, D. Yimlamai, C. Unger, C. Zehetmeier, B. Lain, C. Torella, S.W. Henning, G. Beste, B.T. Scroggins, L. Neckers, L.L. Ilag, and D.G. Jay. 2004. Functional proteomic screens reveal an essential extracellular role for hsp90 alpha in cancer cell invasiveness. *Nature cell biology*. 6:507-514.

Eva, R., E. Dassie, P.T. Caswell, G. Dick, C. ffrench-Constant, J.C. Norman, and J.W. Fawcett. 2010. Rab11 and its effector Rab coupling protein contribute to the trafficking of beta 1 integrins during axon growth in adult dorsal root ganglion neurons and PC12 cells. *The Journal of neuroscience : the official journal of the Society for Neuroscience*. 30:11654-11669.

Evans, R.D., C. Robinson, D.A. Briggs, D.J. Tooth, J.S. Ramalho, M. Cantero, L. Montoliu, S. Patel, E.V. Sviderskaya, and A.N. Hume. 2014. Myosin-Va and dynamic actin oppose microtubules to drive long-range organelle transport. *Current biology : CB*. 24:1743-1750.

Evelyn, C.R., X. Duan, J. Biesiada, W.L. Seibel, J. Meller, and Y. Zheng. 2014. Rational design of small molecule inhibitors targeting the Ras GEF, SOS1. *Chemistry & biology*. 21:1618-1628.

Farnsworth, C.C., M.C. Seabra, L.H. Ericsson, M.H. Gelb, and J.A. Glomset. 1994. Rab geranylgeranyl transferase catalyzes the geranylgeranylation of adjacent cysteines in the small GTPases Rab1A, Rab3A, and Rab5A. *Proceedings of the National Academy of Sciences of the United States of America*. 91:11963-11967.

Feldmann, J., I. Callebaut, G. Raposo, S. Certain, D. Bacq, C. Dumont, N. Lambert, M. Ouachee-Chardin, G. Chedeville, H. Tamary, V. Minard-Colin, E. Vilmer, S. Blanche, F. Le Deist, A. Fischer, and G. de Saint Basile. 2003. Munc13-4 is essential for cytolytic granules fusion and is mutated in a form of familial hemophagocytic lymphohistiocytosis (FHL3). *Cell*. 115:461-473.

Feng, F., Y. Jiang, H. Lu, X. Lu, S. Wang, L. Wang, M. Wei, W. Lu, Z. Du, Z. Ye, G. Yang, F. Yuan, Y. Ma, X. Lei, and Z. Lu. 2016. Rab27A mediated by NF-kappaB promotes the stemness of colon cancer cells via up-regulation of cytokine secretion. *Oncotarget*. 7:63342-63351.

Figueiredo, A.C., C. Wasmeier, A.K. Tarafder, J.S. Ramalho, R.A. Baron, and M.C. Seabra. 2008. Rab3GEP is the non-redundant guanine nucleotide exchange factor for Rab27a in melanocytes. *The Journal of biological chemistry*. 283:23209-23216.

Förster, T. 1947. Ein Beitrag zur theorie der Photosynthese. *Zeitschrift für Naturforschung B*. 2:174-182.

Förster, T. 1948. Zwischenmolekulare Energiewanderung und Fluoreszenz. *Annalen der Physik*. 437:55-75.

Fukuda, M. 2002a. The C2A domain of synaptotagmin-like protein 3 (Slp3) is an atypical calcium-dependent phospholipid-binding machine: comparison with the C2A domain of synaptotagmin I. *The Biochemical journal*. 366:681-687.

Fukuda, M. 2002b. Synaptotagmin-like protein (Slp) homology domain 1 of Slac2-a/melanophilin is a critical determinant of GTP-dependent specific binding to Rab27A. *The Journal of biological chemistry*. 277:40118-40124.

Fukuda, M. 2003a. Distinct Rab binding specificity of Rim1, Rim2, rabphilin, and Noc2. Identification of a critical determinant of Rab3A/Rab27A recognition by Rim2. *The Journal of biological chemistry*. 278:15373-15380.

Fukuda, M. 2003b. Slp4-a/granuphilin-a inhibits dense-core vesicle exocytosis through interaction with the GDP-bound form of Rab27A in PC12 cells. *The Journal of biological chemistry*. 278:15390-15396.

Fukuda, M. 2005. Versatile role of Rab27 in membrane trafficking: focus on the Rab27 effector families. *Journal of biochemistry*. 137:9-16.

Fukuda, M. 2006. Distinct Rab27A binding affinities of Slp2-a and Slac2-a/melanophilin: Hierarchy of Rab27A effectors. *Biochemical and biophysical research communications*. 343:666-674.

Fukuda, M. 2008. Regulation of secretory vesicle traffic by Rab small GTPases. *Cellular and molecular life sciences : CMLS*. 65:2801-2813.

Fukuda, M. 2011. TBC proteins: GAPs for mammalian small GTPase Rab? *Bioscience reports*. 31:159-168.

Fukuda, M. 2013. Rab27 effectors, pleiotropic regulators in secretory pathways. *Traffic*. 14:949-963.

Fukuda, M., A. Imai, T. Nashida, and H. Shimomura. 2005. Slp4-a/granuphilin-a interacts with syntaxin-2/3 in a Munc18-2-dependent manner. *The Journal of biological chemistry*. 280:39175-39184.

Fukuda, M., E. Kanno, and A. Yamamoto. 2004. Rabphilin and Noc2 are recruited to dense-core vesicles through specific interaction with Rab27A in PC12 cells. *The Journal of biological chemistry*. 279:13065-13075.

Fukuda, M., and T.S. Kuroda. 2002. Slac2-c (synaptotagmin-like protein homologue lacking C2 domains-c), a novel linker protein that interacts with Rab27, myosin Va/VIIa, and actin. *The Journal of biological chemistry*. 277:43096-43103.

Fukuda, M., and T.S. Kuroda. 2004. Missense mutations in the globular tail of myosin-Va in dilute mice partially impair binding of Slac2-a/melanophilin. *Journal of cell science*. 117:583-591.

Fukuda, M., T.S. Kuroda, and K. Mikoshiba. 2002. Slac2-a/melanophilin, the missing link between Rab27 and myosin Va: implications of a tripartite protein complex for melanosome transport. *The Journal of biological chemistry*. 277:12432-12436.

Fukuda, M., and K. Mikoshiba. 2001. Synaptotagmin-like protein 1-3: a novel family of C-terminal-type tandem C2 proteins. *Biochemical and biophysical research communications*. 281:1226-1233.

Fukuda, M., C. Saegusa, and K. Mikoshiba. 2001. Novel splicing isoforms of synaptotagmin-like proteins 2 and 3: identification of the Slp homology domain. *Biochemical and biophysical research communications*. 283:513-519.

Gallegos, M.E., S. Balakrishnan, P. Chandramouli, S. Arora, A. Azameera, A. Babushekar, E. Bargoma, A. Bokhari, S.K. Chava, P. Das, M. Desai, D. Decena, S.D. Saramma, B. Dey, A.L. Doss, N. Gor, L. Gudiputi, C. Guo, S. Hande, M. Jensen, S. Jones, N. Jones, D. Jorgens, P. Karamchedu, K. Kamrani, L.D. Kolora, L. Kristensen, K. Kwan, H. Lau, P. Maharaj, N. Mander, K. Mangipudi, H. Menakuru, V. Mody, S. Mohanty, S. Mukkamala, S.A. Mundra, S. Nagaraju, R. Narayanaswamy, C. Ndungu-Case, M. Noorbakhsh, J. Patel, P. Patel, S.V. Pendem, A. Ponakala, M. Rath, M.C. Robles, D. Rokkam, C. Roth, P. Sasidharan, S. Shah, S. Tandon, J. Suprai, T.Q. Truong, R. Uthayaruban, A. Varma, U. Ved, Z. Wang, and Z. Yu. 2012. The C. elegans rab family: identification, classification and toolkit construction. *PloS one*. 7:e49387.

Ganley, I.G., K. Carroll, L. Bittova, and S. Pfeffer. 2004. Rab9 GTPase regulates late endosome size and requires effector interaction for its stability. *Molecular biology of the cell*. 15:5420-5430.

Garcia, I.A., H.E. Martinez, and C. Alvarez. 2011. Rab1b regulates COPI and COPII dynamics in mammalian cells. *Cellular logistics*. 1:159-163.

Garton, M., and C. Laughton. 2013. A comprehensive model for the recognition of human telomeres by TRF1. *Journal of molecular biology*. 425:2910-2921.

Gautam, A., J.S. Nanda, J.S. Samuel, M. Kumari, P. Priyanka, G. Bedi, S.K. Nath, G. Mittal, N. Khatri, and G.P. Raghava. 2016. Topical Delivery of Protein and Peptide Using Novel Cell Penetrating Peptide IMT-P8. *Scientific reports*. 6:26278.

Gerber, P.P., M. Cabrini, C. Jancic, L. Paoletti, C. Banchio, C. von Bilderling, L. Sigaut, L.I. Pietrasanta, G. Duette, E.O. Freed, G. de Saint Basile, C.F. Moita, L.F. Moita, S. Amigorena, P. Benaroch, J. Geffner, and M. Ostrowski. 2015. Rab27a controls HIV-1 assembly by regulating plasma membrane levels of phosphatidylinositol 4,5-bisphosphate. *The Journal of cell biology*. 209:435-452.

Gomes, A.Q., B.R. Ali, J.S. Ramalho, R.F. Godfrey, D.C. Barral, A.N. Hume, and M.C. Seabra. 2003. Membrane targeting of Rab GTPases is

influenced by the prenylation motif. *Molecular biology of the cell*. 14:1882-1899.

Gomi, H., K. Mori, S. Itohara, and T. Izumi. 2007. Rab27b is expressed in a wide range of exocytic cells and involved in the delivery of secretory granules near the plasma membrane. *Molecular biology of the cell*. 18:4377-4386.

Goody, R.S., M.P. Muller, and Y.W. Wu. 2017. Mechanisms of action of Rab proteins, key regulators of intracellular vesicular transport. *Biological chemistry*. 398:565-575.

Grigoriev, I., D. Splinter, N. Keijzer, P.S. Wulf, J. Demmers, T. Ohtsuka, M. Modesti, I.V. Maly, F. Grosveld, C.C. Hoogenraad, and A. Akhmanova. 2007. Rab6 regulates transport and targeting of exocytotic carriers. *Developmental cell*. 13:305-314.

Griscelli, C., A. Durandy, D. Guy-Grand, F. Daguillard, C. Herzog, and M. Prunieras. 1978. A syndrome associating partial albinism and immunodeficiency. *The American journal of medicine*. 65:691-702.

Grosshans, B.L., A. Andreeva, A. Gangar, S. Niessen, J.R. Yates, 3rd, P. Brennwald, and P. Novick. 2006a. The yeast lgl family member Sro7p is an effector of the secretory Rab GTPase Sec4p. *The Journal of cell biology*. 172:55-66.

Grosshans, B.L., and P. Novick. 2008. Identification and verification of Sro7p as an effector of the Sec4p Rab GTPase. *Methods in enzymology*. 438:95-108.

Grosshans, B.L., D. Ortiz, and P. Novick. 2006b. Rabs and their effectors: achieving specificity in membrane traffic. *Proceedings of the National Academy of Sciences of the United States of America*. 103:11821-11827.

Guerra, F., and C. Bucci. 2016. Multiple Roles of the Small GTPase Rab7. *Cells*. 5.

Hales, C.M., J.P. Vaerman, and J.R. Goldenring. 2002. Rab11 family interacting protein 2 associates with Myosin Vb and regulates plasma membrane recycling. *The Journal of biological chemistry*. 277:50415-50421.

Hammer, J.A., and X.F.S. Wu. 2002. Rabs grab motors: defining the connections between Rab GTPases and motor proteins. *Curr Opin Cell Biol*. 14:69-75.

Handley, M.T., and R.D. Burgoyne. 2008. The Rab27 effector Rabphilin, unlike Granuphilin and Noc2, rapidly exchanges between secretory granules

and cytosol in PC12 cells. *Biochemical and biophysical research communications*. 373:275-281.

Hannafon, B.N., K.J. Carpenter, W.L. Berry, R. Janknecht, W.C. Dooley, and W.Q. Ding. 2015. Exosome-mediated microRNA signaling from breast cancer cells is altered by the anti-angiogenesis agent docosahexaenoic acid (DHA). *Molecular cancer*. 14:133.

Hanono, A., D. Garbett, D. Reczek, D.N. Chambers, and A. Bretscher. 2006. EPI64 regulates microvillar subdomains and structure. *The Journal of cell biology*. 175:803-813.

Harris, D.A., S.H. Patel, M. Gucek, A. Hendrix, W. Westbroek, and J.W. Taraska. 2015. Exosomes released from breast cancer carcinomas stimulate cell movement. *PloS one*. 10:e0117495.

Haugsten, E.M., A. Brech, K. Liestol, J.C. Norman, and J. Wesche. 2014. Photoactivation approaches reveal a role for Rab11 in FGFR4 recycling and signalling. *Traffic*. 15:665-683.

He, J., J.L. Johnson, J. Monfregola, M. Ramadass, K. Pestonjamasp, G. Napolitano, J. Zhang, and S.D. Catz. 2016. Munc13-4 interacts with syntaxin 7 and regulates late endosomal maturation, endosomal signaling, and TLR9-initiated cellular responses. *Molecular biology of the cell*. 27:572-587.

Heim, R., and R.Y. Tsien. 1996. Engineering green fluorescent protein for improved brightness, longer wavelengths and fluorescence resonance energy transfer. *Current Biology*. 6:178-182.

Hendrix, A., G. Braems, M. Bracke, M. Seabra, W. Gahl, O. De Wever, and W. Westbroek. 2010a. The secretory small GTPase Rab27B as a marker for breast cancer progression. *Oncotarget*. 1:304-308.

Hendrix, A., and O. De Wever. 2013. Rab27 GTPases distribute extracellular nanomaps for invasive growth and metastasis: implications for prognosis and treatment. *International journal of molecular sciences*. 14:9883-9892.

Hendrix, A., and A.N. Hume. 2011. Exosome signaling in mammary gland development and cancer. *The International journal of developmental biology*. 55:879-887.

Hendrix, A., K. Lambein, W. Westbroek, M.C. Seabra, V. Cocquyt, P. Pauwels, M. Bracke, C. Gespach, and O. De Wever. 2012. An immunohistochemical analysis of Rab27B distribution in fetal and adult tissue. *The International journal of developmental biology*. 56:363-368.

Hendrix, A., D. Maynard, P. Pauwels, G. Braems, H. Denys, R. Van den Broecke, J. Lambert, S. Van Belle, V. Cocquyt, C. Gespach, M. Bracke, M.C. Seabra, W.A. Gahl, O. De Wever, and W. Westbroek. 2010b. Effect of the secretory small GTPase Rab27B on breast cancer growth, invasion, and metastasis. *Journal of the National Cancer Institute*. 102:866-880.

Hendrix, A., R. Sormunen, W. Westbroek, K. Lambein, H. Denys, G. Sys, G. Braems, R. Van den Broecke, V. Cocquyt, C. Gespach, M. Bracke, and O. De Wever. 2013. Vacuolar H+ ATPase expression and activity is required for Rab27B-dependent invasive growth and metastasis of breast cancer. *International journal of cancer. Journal international du cancer*. 133:843-854.

Hendrix, A., W. Westbroek, M. Bracke, and O. De Wever. 2010c. An ex(o)citing machinery for invasive tumor growth. *Cancer research*. 70:9533-9537.

Herrero-Turrion, M.J., J. Calafat, H. Janssen, M. Fukuda, and F. Mollinedo. 2008. Rab27a regulates exocytosis of tertiary and specific granules in human neutrophils. *Journal of immunology (Baltimore, Md. : 1950)*. 181:3793-3803.

Herrmann, C., C. Block, C. Geisen, K. Haas, C. Weber, G. Winde, T. Moroy, and O. Muller. 1998. Sulindac sulfide inhibits Ras signaling. *Oncogene*. 17:1769-1776.

Hokanson, D.E., and A.P. Bretscher. 2012. EPI64 interacts with Slp1/JFC1 to coordinate Rab8a and Arf6 membrane trafficking. *Molecular biology of the cell*. 23:701-715.

Holt, O., E. Kanno, G. Bossi, S. Booth, T. Daniele, A. Santoro, M. Arico, C. Saegusa, M. Fukuda, and G.M. Griffiths. 2008. Slp1 and Slp2-a localize to the plasma membrane of CTL and contribute to secretion from the immunological synapse. *Traffic*. 9:446-457.

Hong, L., Y. Guo, S. BasuRay, J.O. Agola, E. Romero, D.S. Simpson, C.E. Schroeder, P. Simons, A. Waller, M. Garcia, M. Carter, O. Ursu, K. Gouveia, J.E. Golden, J. Aube, A. Wandinger-Ness, and L.A. Sklar. 2015. A Pan-GTPase Inhibitor as a Molecular Probe. *PloS one*. 10:e0134317.

Hou, Y., X. Chen, T. Tolmachova, S.A. Ernst, and J.A. Williams. 2013. EPI64B acts as a GTPase-activating protein for Rab27B in pancreatic acinar cells. *The Journal of biological chemistry*. 288:19548-19557.

Hou, Y., S.A. Ernst, S.I. Lentz, and J.A. Williams. 2016. Genetic deletion of Rab27B in pancreatic acinar cells affects granules size and has inhibitory

effects on amylase secretion. *Biochemical and biophysical research communications*. 471:610-615.

Hou, Y., S.A. Ernst, E.L. Stuenkel, S.I. Lentz, and J.A. Williams. 2015. Rab27A Is Present in Mouse Pancreatic Acinar Cells and Is Required for Digestive Enzyme Secretion. *PloS one*. 10:e0125596.

Hsu, C., Y. Morohashi, S. Yoshimura, N. Manrique-Hoyos, S. Jung, M.A. Lauterbach, M. Bakhti, M. Gronborg, W. Mobius, J. Rhee, F.A. Barr, and M. Simons. 2010. Regulation of exosome secretion by Rab35 and its GTPase-activating proteins TBC1D10A-C. *The Journal of cell biology*. 189:223-232.

Hua, Y., X. Ma, X. Liu, X. Yuan, H. Qin, and X. Zhang. 2017. Identification of the potential biomarkers for the metastasis of rectal adenocarcinoma. *APMIS : acta pathologica, microbiologica, et immunologica Scandinavica*. 125:93-100.

Huang, Z., and Y. Feng. 2016. Exosomes derived from hypoxic colorectal cancer cells promotes angiogenesis through Wnt4 induced beta-catenin signaling in endothelial cells. *Oncology research*.

Huber, S.K., and A.J. Scheidig. 2005. High resolution crystal structures of human Rab4a in its active and inactive conformations. *FEBS letters*. 579:2821-2829.

Hume, A.N., L.M. Collinson, C.R. Hopkins, M. Strom, D.C. Barral, G. Bossi, G.M. Griffiths, and M.C. Seabra. 2002. The leaden gene product is required with Rab27a to recruit myosin Va to melanosomes in melanocytes. *Traffic*. 3:193-202.

Hume, A.N., L.M. Collinson, A. Rapak, A.Q. Gomes, C.R. Hopkins, and M.C. Seabra. 2001. Rab27a regulates the peripheral distribution of melanosomes in melanocytes. *The Journal of cell biology*. 152:795-808.

Hume, A.N., A.K. Tarafder, J.S. Ramalho, E.V. Sviderskaya, and M.C. Seabra. 2006. A coiled-coil domain of melanophilin is essential for Myosin Va recruitment and melanosome transport in melanocytes. *Molecular biology of the cell*. 17:4720-4735.

Hume, A.N., D.S. Ushakov, A.K. Tarafder, M.A. Ferenczi, and M.C. Seabra. 2007. Rab27a and MyoVa are the primary Mlph interactors regulating melanosome transport in melanocytes. *Journal of cell science*. 120:3111-3122.

Humphrey, W., A. Dalke, and K. Schulten. 1996. VMD: visual molecular dynamics. *Journal of molecular graphics*. 14:33-38, 27-38.

Hutagalung, A.H., and P.J. Novick. 2011. Role of Rab GTPases in membrane traffic and cell physiology. *Physiol Rev*. 91:119-149.

Imai, A., M. Fukuda, S. Yoshie, T. Nashida, and H. Shimomura. 2009. Redistribution of Rab27-specific effector Slac2-c, but not Slp4-a, after isoproterenol-stimulation in rat parotid acinar cells. *Archives of oral biology*. 54:361-368.

Imai, A., M. Ishida, M. Fukuda, T. Nashida, and H. Shimomura. 2013. MADD/DENN/Rab3GEP functions as a guanine nucleotide exchange factor for Rab27 during granule exocytosis of rat parotid acinar cells. *Archives of biochemistry and biophysics*. 536:31-37.

Imai, A., S. Yoshie, K. Ishibashi, M. Haga-Tsujimura, T. Nashida, H. Shimomura, and M. Fukuda. 2011. EPI64 protein functions as a physiological GTPase-activating protein for Rab27 protein and regulates amylase release in rat parotid acinar cells. *The Journal of biological chemistry*. 286:33854-33862.

Imai, A., S. Yoshie, T. Nashida, H. Shimomura, and M. Fukuda. 2004. The small GTPase Rab27B regulates amylase release from rat parotid acinar cells. *Journal of cell science*. 117:1945-1953.

Inouye, S., and F.I. Tsuji. 1994. Aequorea green fluorescent protein. Expression of the gene and fluorescence characteristics of the recombinant protein. *FEBS letters*. 341:277-280.

Ishibashi, K., E. Kanno, T. Itoh, and M. Fukuda. 2009. Identification and characterization of a novel Tre-2/Bub2/Cdc16 (TBC) protein that possesses Rab3A-GAP activity. *Genes to cells : devoted to molecular & cellular mechanisms*. 14:41-52.

Ishida, M., S.P. Arai, N. Ohbayashi, and M. Fukuda. 2014. The GTPase-deficient Rab27A(Q78L) Mutant Inhibits Melanosome Transport in Melanocytes through Trapping of Slac2-a/melanophilin in their Cytosol: Development of a Novel Melanosome-targeting Tag. *The Journal of biological chemistry*.

Isikay, S. 2014. Cerebellar involvement of Griscelli syndrome type 2. *BMJ case reports*. 2014.

Itoh, T., and M. Fukuda. 2006. Identification of EPI64 as a GTPase-activating protein specific for Rab27A. *The Journal of biological chemistry*. 281:31823-31831.

Itzen, A., and R.S. Goody. 2008. Key determinants of Rab specificity. *Structure*. 16:1437-1439.

Iwanami, N., Y. Nakamura, T. Satoh, Z. Liu, and A.K. Satoh. 2016. Rab6 Is Required for Multiple Apical Transport Pathways but Not the Basolateral Transport Pathway in Drosophila Photoreceptors. *PLoS genetics*. 12:e1005828.

Izumi, T. 2007. Physiological roles of Rab27 effectors in regulated exocytosis. *Endocrine journal*. 54:649-657.

Izumi, T., H. Gomi, K. Kasai, S. Mizutani, and S. Torii. 2003. The roles of Rab27 and its effectors in the regulated secretory pathways. *Cell structure and function*. 28:465-474.

Jackson, C.L., and S. Bouvet. 2014. Arfs at a glance. *Journal of cell science*. 127:4103-4109.

Johansson, M., N. Rocha, W. Zwart, I. Jordens, L. Janssen, C. Kuijl, V.M. Olkkonen, and J. Neefjes. 2007. Activation of endosomal dynein motors by stepwise assembly of Rab7-RILP-p150Glued, ORP1L, and the receptor betalll spectrin. *The Journal of cell biology*. 176:459-471.

Johnson, J.L., A.A. Brzezinska, T. Tolmachova, D.B. Munafo, B.A. Ellis, M.C. Seabra, H. Hong, and S.D. Catz. 2010a. Rab27a and Rab27b regulate neutrophil azurophilic granule exocytosis and NADPH oxidase activity by independent mechanisms. *Traffic*. 11:533-547.

Johnson, J.L., B.A. Ellis, D. Noack, M.C. Seabra, and S.D. Catz. 2005a. The Rab27a-binding protein, JFC1, regulates androgen-dependent secretion of prostate-specific antigen and prostatic-specific acid phosphatase. *The Biochemical journal*. 391:699-710.

Johnson, J.L., H. Hong, J. Monfregola, W.B. Kiosses, and S.D. Catz. 2011. Munc13-4 restricts motility of Rab27a-expressing vesicles to facilitate lipopolysaccharide-induced priming of exocytosis in neutrophils. *The Journal of biological chemistry*. 286:5647-5656.

Johnson, J.L., J. Monfregola, G. Napolitano, W.B. Kiosses, and S.D. Catz. 2012. Vesicular trafficking through cortical actin during exocytosis is regulated by the Rab27a effector JFC1/Slp1 and the RhoA-GTPase-activating protein Gem-interacting protein. *Molecular biology of the cell*. 23:1902-1916.

Johnson, J.L., G. Napolitano, J. Monfregola, C.J. Rocca, S. Cherqui, and S.D. Catz. 2013. Upregulation of the Rab27a-dependent trafficking and secretory mechanisms improves lysosomal transport, alleviates endoplasmic reticulum stress, and reduces lysosome overload in cystinosis. *Mol Cell Biol*. 33:2950-2962.

Johnson, J.L., S. Pacquelet, W.S. Lane, B. Eam, and S.D. Catz. 2005b. Akt regulates the subcellular localization of the Rab27a-binding protein JFC1 by phosphorylation. *Traffic*. 6:667-681.

Johnson, J.L., M. Ramadass, J. He, S.J. Brown, J. Zhang, L. Abgaryan, N. Biris, E. Gavathiotis, H. Rosen, and S.D. Catz. 2016. Identification of Nexinhibs, small-molecule inhibitors of neutrophil exocytosis and inflammation. Druggability of the small GTPase Rab27a. *The Journal of biological chemistry*.

Johnson, L.N., S.M. Cashman, S.P. Read, and R. Kumar-Singh. 2010b. Cell penetrating peptide POD mediates delivery of recombinant proteins to retina, cornea and skin. *Vision research*. 50:686-697.

Jordens, I., M. Fernandez-Borja, M. Marsman, S. Dusseljee, L. Janssen, J. Calafat, H. Janssen, R. Wubbolts, and J. Neefjes. 2001. The Rab7 effector protein RILP controls lysosomal transport by inducing the recruitment of dynein-dynactin motors. *Current biology : CB*. 11:1680-1685.

Jordens, I., W. Westbroek, M. Marsman, N. Rocha, M. Mommaas, M. Huizing, J. Lambert, J.M. Naeyaert, and J. Neefjes. 2006. Rab7 and Rab27a control two motor protein activities involved in melanosomal transport. *Pigment cell research / sponsored by the European Society for Pigment Cell Research and the International Pigment Cell Society*. 19:412-423.

Joung, J.Y., H.Y. Lee, J. Park, J.Y. Lee, B.H. Chang, K.T. No, K.Y. Nam, and J.S. Hwang. 2014. Identification of novel rab27a/melanophilin blockers by pharmacophore-based virtual screening. *Applied biochemistry and biotechnology*. 172:1882-1897.

Kajiho, H., Y. Kajiho, E. Frittoli, S. Confalonieri, G. Bertalot, G. Viale, P.P. Di Fiore, A. Oldani, M. Garre, G.V. Beznoussenko, A. Palamidessi, M. Vecchi, P. Chavrier, F. Perez, and G. Scita. 2016. RAB2A controls MT1-MMP endocytic and E-cadherin polarized Golgi trafficking to promote invasive breast cancer programs. *EMBO reports*. 17:1061-1080.

Kariya, Y., M. Honma, A. Hanamura, S. Aoki, T. Ninomiya, Y. Nakamichi, N. Udagawa, and H. Suzuki. 2011. Rab27a and Rab27b are involved in stimulation-dependent RANKL release from secretory lysosomes in osteoblastic cells. *Journal of bone and mineral research : the official journal of the American Society for Bone and Mineral Research*. 26:689-703.

Kasai, K., M. Ohara-Imaizumi, N. Takahashi, S. Mizutani, S. Zhao, T. Kikuta, H. Kasai, S. Nagamatsu, H. Gomi, and T. Izumi. 2005. Rab27a mediates the tight docking of insulin granules onto the plasma membrane during glucose stimulation. *The Journal of clinical investigation*. 115:388-396.

Kawakami, T., J. He, H. Morita, K. Yokoyama, H. Kaji, C. Tanaka, S. Suemori, K. Tohyama, and Y. Tohyama. 2014. Rab27a is essential for the formation of neutrophil extracellular traps (NETs) in neutrophil-like differentiated HL60 cells. *PloS one*. 9:e84704.

Kelly, E.E., C.P. Horgan, B. Goud, and M.W. McCaffrey. 2012. The Rab family of proteins: 25 years on. *Biochemical Society transactions*. 40:1337-1347.

Kesari, A., M. Fukuda, S. Knoblach, R. Bashir, G.A. Nader, D. Rao, K. Nagaraju, and E.P. Hoffman. 2008. Dysferlin deficiency shows compensatory induction of Rab27A/Slp2a that may contribute to inflammatory onset. *The American journal of pathology*. 173:1476-1487.

Khosravi-Far, R., R.J. Lutz, A.D. Cox, L. Conroy, J.R. Bourne, M. Sinensky, W.E. Balch, J.E. Buss, and C.J. Der. 1991. Isoprenoid modification of rab proteins terminating in CC or CXC motifs. *Proceedings of the National Academy of Sciences of the United States of America*. 88:6264-6268.

Kim, B., J.Y. Lee, H.Y. Lee, K.Y. Nam, J. Park, S.M. Lee, J.E. Kim, J.D. Lee, and J.S. Hwang. 2013. Hesperidin Suppresses Melanosome Transport by Blocking the Interaction of Rab27A-Melanophilin. *Biomolecules & therapeutics*. 21:343-348.

Kim, T.K., and J.H. Eberwine. 2010. Mammalian cell transfection: the present and the future. *Analytical and bioanalytical chemistry*. 397:3173-3178.

Kimura, T., Y. Kaneko, S. Yamada, H. Ishihara, T. Senda, A. Iwamatsu, and I. Niki. 2008. The GDP-dependent Rab27a effector coronin 3 controls endocytosis of secretory membrane in insulin-secreting cell lines. *Journal of cell science*. 121:3092-3098.

Kimura, T., and I. Niki. 2011. Rab27a, actin and beta-cell endocytosis. *Endocrine journal*. 58:1-6.

Kimura, T., S. Taniguchi, and I. Niki. 2010. Actin assembly controlled by GDP-Rab27a is essential for endocytosis of the insulin secretory membrane. *Archives of biochemistry and biophysics*. 496:33-37.

Kohnke, M., C. Delon, M.L. Hastie, U.T. Nguyen, Y.W. Wu, H. Waldmann, R.S. Goody, J.J. Gorman, and K. Alexandrov. 2013. Rab GTPase prenylation hierarchy and its potential role in choroideremia disease. *PloS one*. 8:e81758.

Kondo, H., R. Shirakawa, T. Higashi, M. Kawato, M. Fukuda, T. Kita, and H. Horiuchi. 2006. Constitutive GDP/GTP exchange and secretion-

dependent GTP hydrolysis activity for Rab27 in platelets. *The Journal of biological chemistry*. 281:28657-28665.

Kozak, M. 1990. Downstream secondary structure facilitates recognition of initiator codons by eukaryotic ribosomes. *Proceedings of the National Academy of Sciences of the United States of America*. 87:8301-8305.

Kozak, M. 1991. An analysis of vertebrate mRNA sequences: intimations of translational control. *The Journal of cell biology*. 115:887-903.

Kristensen, M., D. Birch, and H. Morck Nielsen. 2016. Applications and Challenges for Use of Cell-Penetrating Peptides as Delivery Vectors for Peptide and Protein Cargos. *International journal of molecular sciences*. 17.

Kucera, A., M. Borg Distefano, A. Berg-Larsen, F. Skjeldal, U. Repnik, O. Bakke, and C. Progida. 2016. Spatiotemporal Resolution of Rab9 and CI-MPR Dynamics in the Endocytic Pathway. *Traffic*. 17:211-229.

Kukimoto-Niino, M., A. Sakamoto, E. Kanno, K. Hanawa-Suetsugu, T. Terada, M. Shirouzu, M. Fukuda, and S. Yokoyama. 2008. Structural basis for the exclusive specificity of Slac2-a/melanophilin for the Rab27 GTPases. *Structure*. 16:1478-1490.

Kummel, D., and C. Ungermann. 2014. Principles of membrane tethering and fusion in endosome and lysosome biogenesis. *Curr Opin Cell Biol*. 29:61-66.

Kuroda, T.S., H. Ariga, and M. Fukuda. 2003. The actin-binding domain of Slac2-a/melanophilin is required for melanosome distribution in melanocytes. *Mol Cell Biol*. 23:5245-5255.

Kuroda, T.S., and M. Fukuda. 2004. Rab27A-binding protein Slp2-a is required for peripheral melanosome distribution and elongated cell shape in melanocytes. *Nature cell biology*. 6:1195-1203.

Kuroda, T.S., M. Fukuda, H. Ariga, and K. Mikoshiba. 2002a. The Slp homology domain of synaptotagmin-like proteins 1-4 and Slac2 functions as a novel Rab27A binding domain. *The Journal of biological chemistry*. 277:9212-9218.

Kuroda, T.S., M. Fukuda, H. Ariga, and K. Mikoshiba. 2002b. Synaptotagmin-like protein 5: a novel Rab27A effector with C-terminal tandem C2 domains. *Biochemical and biophysical research communications*. 293:899-906.

Kurowska, M., N. Goudin, N.T. Nehme, M. Court, J. Garin, A. Fischer, G. de Saint Basile, and G. Menasche. 2012. Terminal transport of lytic granules to the immune synapse is mediated by the kinesin-1/Slp3/Rab27a complex. *Blood*. 119:3879-3889.

Kurz, A.R., M. Pruenster, I. Rohwedder, M. Ramadass, K. Schafer, U. Harrison, G. Gouveia, C. Nussbaum, R. Immler, J.R. Wiessner, A. Margraf, D.S. Lim, B. Walzog, S. Dietzel, M. Moser, C. Klein, D. Vestweber, R. Haas, S.D. Catz, and M. Sperandio. 2016. MST1-dependent vesicle trafficking regulates neutrophil transmigration through the vascular basement membrane. *The Journal of clinical investigation*. 126:4125-4139.

Langford, G.M. 1995. Actin- and microtubule-dependent organelle motors: interrelationships between the two motility systems. *Curr Opin Cell Biol*. 7:82-88.

Laufman, O., A. Kedan, W. Hong, and S. Lev. 2009. Direct interaction between the COG complex and the SM protein, Sly1, is required for Golgi SNARE pairing. *The EMBO journal*. 28:2006-2017.

Lawe, D.C., A. Chawla, E. Merithew, J. Dumas, W. Carrington, K. Fogarty, L. Lifshitz, R. Tuft, D. Lambright, and S. Corvera. 2002. Sequential roles for phosphatidylinositol 3-phosphate and Rab5 in tethering and fusion of early endosomes via their interaction with EEA1. *The Journal of biological chemistry*. 277:8611-8617.

Lee, S., J. Kang, M. Cho, E. Seo, H. Choi, E. Kim, J. Kim, H. Kim, G.Y. Kang, K.P. Kim, Y.H. Park, D.Y. Yu, Y.N. Yum, S.N. Park, and D.Y. Yoon. 2009. Profiling of transcripts and proteins modulated by K-ras oncogene in the lung tissues of K-ras transgenic mice by omics approaches. *Int J Oncol*. 34:161-172.

Lee, S.H., K. Baek, and R. Dominguez. 2008. Large nucleotide-dependent conformational change in Rab28. *FEBS letters*. 582:4107-4111.

Lehman, K., G. Rossi, J.E. Adamo, and P. Brennwald. 1999. Yeast homologues of tomosyn and lethal giant larvae function in exocytosis and are associated with the plasma membrane SNARE, Sec9. *The Journal of cell biology*. 146:125-140.

Leung, K.F., R. Baron, and M.C. Seabra. 2006. Thematic review series: lipid posttranslational modifications. geranylgeranylation of Rab GTPases. *Journal of lipid research*. 47:467-475.

Li, C., T.R. Reddy, P.M. Fischer, and L.V. Dekker. 2010. A Cy5-labeled S100A10 tracer used to identify inhibitors of the protein interaction with annexin A2. *Assay and drug development technologies*. 8:85-95.

Li, F., L. Yi, L. Zhao, A. Itzen, R.S. Goody, and Y.W. Wu. 2014a. The role of the hypervariable C-terminal domain in Rab GTPases membrane targeting. *Proceedings of the National Academy of Sciences of the United States of America*. 111:2572-2577.

Li, G., and M.C. Marlin. 2015. Rab family of GTPases. *Methods in molecular biology (Clifton, N.J.)*. 1298:1-15.

Li, W., Y. Hu, T. Jiang, Y. Han, G. Han, J. Chen, and X. Li. 2014b. Rab27A regulates exosome secretion from lung adenocarcinoma cells A549: involvement of EPI64. *APMIS : acta pathologica, microbiologica, et immunologica Scandinavica*.

Li, X.D., R. Ikebe, and M. Ikebe. 2005. Activation of myosin Va function by melanophilin, a specific docking partner of myosin Va. *The Journal of biological chemistry*. 280:17815-17822.

Liu, D., T. Meckel, and E.O. Long. 2010. Distinct role of rab27a in granule movement at the plasma membrane and in the cytosol of NK cells. *PloS one*. 5:e12870.

Liu, L., J.E. Mellerio, A.E. Martinez, J.R. McMillan, S. Aristodemou, M. Parsons, and J.A. McGrath. 2014. Mutations in EXPH5 result in autosomal recessive inherited skin fragility. *The British journal of dermatology*. 170:196-199.

Loirand, G., V. Sauzeau, and P. Pacaud. 2013. Small G proteins in the cardiovascular system: physiological and pathological aspects. *Physiol Rev*. 93:1659-1720.

Lombardi, D., T. Soldati, M.A. Riederer, Y. Goda, M. Zerial, and S.R. Pfeffer. 1993. Rab9 functions in transport between late endosomes and the trans Golgi network. *The EMBO journal*. 12:677-682.

Luan, P., A. Heine, K. Zeng, B. Moyer, S.E. Greasely, P. Kuhn, W.E. Balch, and I.A. Wilson. 2000. A new functional domain of guanine nucleotide dissociation inhibitor (alpha-GDI) involved in Rab recycling. *Traffic*. 1:270-281.

Luo, L., N.P. King, J.C. Yeo, A. Jones, and J.L. Stow. 2014. Single-step protease cleavage elution for identification of protein-protein interactions from GST pull-down and mass spectrometry. *Proteomics*. 14:19-23.

Lurick, A., J. Gao, A. Kuhlee, E. Yavavli, L. Langemeyer, A. Perz, S. Raunser, and C. Ungermann. 2017. Multivalent Rab interactions determine tether-mediated membrane fusion. *Molecular biology of the cell*. 28:322-332.

Ma, L., F. Yang, and J. Zheng. 2014. Application of fluorescence resonance energy transfer in protein studies. *Journal of molecular structure*. 1077:87-100.

Macpherson, I.R., E. Rainero, L.E. Mitchell, P.V. van den Berghe, C. Speirs, M.A. Dozynkiewicz, S. Chaudhary, G. Kalna, J. Edwards, P. Timpson, and J.C. Norman. 2014. CLIC3 controls recycling of late endosomal MT1-MMP and dictates invasion and metastasis in breast cancer. *Journal of cell science*. 127:3893-3901.

Magee, A.I., and M.C. Seabra. 2003. Are prenyl groups on proteins sticky fingers or greasy handles? *The Biochemical journal*. 376:e3-4.

Malchin, N., O. Sarig, M. Grafi-Cohen, S. Geller, I. Goldberg, A. Shani, A. Gat, E. Sprecher, and J. Mashiah. 2016. A novel homozygous deletion in EXPH5 causes a skin fragility phenotype. *Clinical and experimental dermatology*. 41:915-918.

Mamishi, S., M.H. Modarressi, B. Pourakbari, B. Tamizifar, F. Mahjoub, A. Fahimzad, S. Alyasin, M.H. Bemanian, A.A. Hamidiyeh, M.R. Fazlollahi, M.R. Ashrafi, A. Isaeian, G. Khotaei, M. Yeganeh, and N. Parvaneh. 2008. Analysis of RAB27A gene in griscelli syndrome type 2: novel mutations including a deletion hotspot. *Journal of clinical immunology*. 28:384-389.

Marks, M.S., and M.C. Seabra. 2001. The melanosome: membrane dynamics in black and white. *Nature reviews. Molecular cell biology*. 2:738-748.

Martinez, O., C. Antony, G. Pehau-Arnaudet, E.G. Berger, J. Salamero, and B. Goud. 1997. GTP-bound forms of rab6 induce the redistribution of Golgi proteins into the endoplasmic reticulum. *Proceedings of the National Academy of Sciences of the United States of America*. 94:1828-1833.

Masharina, A., L. Reymond, D. Maurel, K. Umezawa, and K. Johnsson. 2012. A fluorescent sensor for GABA and synthetic GABA(B) receptor ligands. *Journal of the American Chemical Society*. 134:19026-19034.

Masri, A., F.G. Bakri, M. Al-Hussaini, A. Al-Hadidy, R. Hirzallah, G. de Saint Basile, and H. Hamamy. 2008. Griscelli syndrome type 2: a rare and lethal disorder. *Journal of child neurology*. 23:964-967.

Matanis, T., A. Akhmanova, P. Wulf, E. Del Nery, T. Weide, T. Stepanova, N. Galjart, F. Grosveld, B. Goud, C.I. De Zeeuw, A. Barnekow, and C.C. Hoogenraad. 2002. Bicaudal-D regulates COPI-independent Golgi-ER transport by recruiting the dynein-dynactin motor complex. *Nature cell biology*. 4:986-992.

Matesic, L.E., R. Yip, A.E. Reuss, D.A. Swing, T.N. O'Sullivan, C.F. Fletcher, N.G. Copeland, and N.A. Jenkins. 2001. Mutations in Mlph, encoding a member of the Rab effector family, cause the melanosome transport defects observed in leaden mice. *Proceedings of the National Academy of Sciences of the United States of America*. 98:10238-10243.

Matz, M.V., A.F. Fradkov, Y.A. Labas, A.P. Savitsky, A.G. Zaraisky, M.L. Markelov, and S.A. Lukyanov. 1999. Fluorescent proteins from nonbioluminescent Anthozoa species. *Nature biotechnology*. 17:969-973.

Maurer, T., L.S. Garrenton, A. Oh, K. Pitts, D.J. Anderson, N.J. Skelton, B.P. Fauber, B. Pan, S. Malek, D. Stokoe, M.J. Ludlam, K.K. Bowman, J. Wu, A.M. Giannetti, M.A. Starovasnik, I. Mellman, P.K. Jackson, J. Rudolph, W. Wang, and G. Fang. 2012. Small-molecule ligands bind to a distinct pocket in Ras and inhibit SOS-mediated nucleotide exchange activity. *Proceedings of the National Academy of Sciences of the United States of America*. 109:5299-5304.

McAdara Berkowitz, J.K., S.D. Catz, J.L. Johnson, J.M. Ruedi, V. Thon, and B.M. Babior. 2001. JFC1, a novel tandem C2 domain-containing protein associated with the leukocyte NADPH oxidase. *The Journal of biological chemistry*. 276:18855-18862.

McGrath, J.A., K.L. Stone, R. Begum, M.A. Simpson, P.J. Dopping-Hepenstal, L. Liu, J.R. McMillan, A.P. South, C. Pourreyron, W.H. McLean, A.E. Martinez, J.E. Mellerio, and M. Parsons. 2012. Germline Mutation in EXPH5 Implicates the Rab27B Effector Protein Slac2-b in Inherited Skin Fragility. *American journal of human genetics*. 91:1115-1121.

Menasche, G., J. Feldmann, A. Houdusse, C. Desaymard, A. Fischer, B. Goud, and G. de Saint Basile. 2003a. Biochemical and functional characterization of Rab27a mutations occurring in Griscelli syndrome patients. *Blood*. 101:2736-2742.

Menasche, G., C.H. Ho, O. Sanal, J. Feldmann, I. Tezcan, F. Ersoy, A. Houdusse, A. Fischer, and G. de Saint Basile. 2003b. Griscelli syndrome restricted to hypopigmentation results from a melanophilin defect (GS3) or a MYO5A F-exon deletion (GS1). *The Journal of clinical investigation*. 112:450-456.

Menasche, G., M.M. Menager, J.M. Lefebvre, E. Deutsch, R. Athman, N. Lambert, N. Mahlaoui, M. Court, J. Garin, A. Fischer, and G. de Saint Basile. 2008. A newly identified isoform of Slp2a associates with Rab27a in cytotoxic T cells and participates to cytotoxic granule secretion. *Blood*. 112:5052-5062.

Menasche, G., E. Pastural, J. Feldmann, S. Certain, F. Ersoy, S. Dupuis, N. Wulffraat, D. Bianchi, A. Fischer, F. Le Deist, and G. de Saint Basile. 2000. Mutations in RAB27A cause Griscelli syndrome associated with haemophagocytic syndrome. *Nat Genet*. 25:173-176.

Mercer, J.A., P.K. Seperack, M.C. Strobel, N.G. Copeland, and N.A. Jenkins. 1991. Novel myosin heavy chain encoded by murine dilute coat colour locus. *Nature*. 349:709-713.

Merithew, E., S. Hatherly, J.J. Dumas, D.C. Lawe, R. Heller-Harrison, and D.G. Lambright. 2001. Structural plasticity of an invariant hydrophobic triad in the switch regions of Rab GTPases is a determinant of effector recognition. *The Journal of biological chemistry*. 276:13982-13988.

Merrins, M.J., and E.L. Stuenkel. 2008. Kinetics of Rab27a-dependent actions on vesicle docking and priming in pancreatic beta-cells. *The Journal of physiology*. 586:5367-5381.

Miller, B.R., 3rd, T.D. McGee, Jr., J.M. Swails, N. Homeyer, H. Gohlke, and A.E. Roitberg. 2012. MMPBSA.py: An Efficient Program for End-State Free Energy Calculations. *Journal of chemical theory and computation*. 8:3314-3321.

Miller, I.V., and T.G. Grunewald. 2015. Tumour-derived exosomes: Tiny envelopes for big stories. *Biology of the cell / under the auspices of the European Cell Biology Organization*. 107:287-305.

Mills, I.G., S. Urbe, and M.J. Clague. 2001. Relationships between EEA1 binding partners and their role in endosome fusion. *Journal of cell science*. 114:1959-1965.

Mishra, K., S. Singla, S. Sharma, R. Saxena, and V.V. Batra. 2014. Griscelli syndrome type 2: a novel mutation in RAB27A gene with different clinical features in 2 siblings: a diagnostic conundrum. *Korean journal of pediatrics*. 57:91-95.

Mitin, N., K.L. Rossman, and C.J. Der. 2005. Signaling interplay in Ras superfamily function. *Current biology : CB*. 15:R563-574.

Miyawaki, A. 2011. Development of probes for cellular functions using fluorescent proteins and fluorescence resonance energy transfer. *Annual review of biochemistry*. 80:357-373.

Mizuno, K., J.S. Ramalho, and T. Izumi. 2011. Exophilin8 transiently clusters insulin granules at the actin-rich cell cortex prior to exocytosis. *Molecular biology of the cell*. 22:1716-1726.

Mollinedo, F., B. Martin-Martin, J. Calafat, S.M. Nabokina, and P.A. Lazo. 2003. Role of vesicle-associated membrane protein-2, through Q-soluble N-ethylmaleimide-sensitive factor attachment protein receptor/R-soluble N-ethylmaleimide-sensitive factor attachment protein receptor interaction, in the exocytosis of specific and tertiary granules of human neutrophils. *Journal of immunology (Baltimore, Md. : 1950)*. 170:1034-1042.

Moore, I., J. Schell, and K. Palme. 1995. Subclass-specific sequence motifs identified in Rab GTPases. *Trends in biochemical sciences*. 20:10-12.

Moores, S.L., M.D. Schaber, S.D. Mosser, E. Rands, M.B. O'Hara, V.M. Garsky, M.S. Marshall, D.L. Pompliano, and J.B. Gibbs. 1991. Sequence dependence of protein isoprenylation. *The Journal of biological chemistry*. 266:14603-14610.

Morise, H., O. Shimomura, F.H. Johnson, and J. Winant. 1974. Intermolecular energy transfer in the bioluminescent system of Aequorea. *Biochemistry*. 13:2656-2662.

Mrozowska, P.S., and M. Fukuda. 2016. Regulation of podocalyxin trafficking by Rab small GTPases in epithelial cells. *Small GTPases*. 7:231-238.

Muller, M.P., and R.S. Goody. 2017. Molecular control of Rab activity by GEFs, GAPs and GDI. *Small GTPases*:1-17.

Muller, O., E. Gourzoulidou, M. Carpintero, I.M. Karaguni, A. Langerak, C. Herrmann, T. Moroy, L. Klein-Hitpass, and H. Waldmann. 2004. Identification of potent Ras signaling inhibitors by pathway-selective phenotype-based screening. *Angewandte Chemie (International ed. in English)*. 43:450-454.

Munafo, D.B., J.L. Johnson, B.A. Ellis, S. Rutschmann, B. Beutler, and S.D. Catz. 2007. Rab27a is a key component of the secretory machinery of azurophilic granules in granulocytes. *The Biochemical journal*. 402:229-239.

Munoz, I., L. Danelli, J. Claver, N. Goudin, M. Kurowska, I.K. Madera-Salcedo, J.D. Huang, A. Fischer, C. Gonzalez-Espinosa, G. de Saint Basile, U. Blank, and G. Menasche. 2016. Kinesin-1 controls mast cell degranulation and anaphylaxis through PI3K-dependent recruitment to the granular Slp3/Rab27b complex. *The Journal of cell biology*. 215:203-216.

Nagai, H., S. Yasuda, Y. Ohba, M. Fukuda, and T. Nakamura. 2013. All members of the EPI64 subfamily of TBC/RabGAPs also have GAP activities towards Ras. *Journal of biochemistry*. 153:283-288.

Neeft, M., M. Wieffer, A.S. de Jong, G. Negroiu, C.H. Metz, A. van Loon, J. Griffith, J. Krijgsveld, N. Wulffraat, H. Koch, A.J. Heck, N. Brose, M. Kleijmeer, and P. van der Sluijs. 2005. Munc13-4 is an effector of rab27a and controls secretion of lysosomes in hematopoietic cells. *Molecular biology of the cell*. 16:731-741.

Netter, P., S.K. Chan, P.P. Banerjee, L. Monaco-Shawver, L.M. Noroski, I.C. Hanson, L.R. Forbes, E.M. Mace, J. Chinen, H.B. Gaspar, P. Sleiman, H. Hakonarson, C. Klein, M.S. Ehlayel, and J.S. Orange. 2016. A novel Rab27a mutation binds melanophilin, but not Munc13-4, causing immunodeficiency without albinism. *The Journal of allergy and clinical immunology*. 138:599-601 e593.

Neumuller, O., M. Hoffmeister, J. Babica, C. Prelle, K. Gegenbauer, and A.P. Smolenski. 2009. Synaptotagmin-like protein 1 interacts with the GTPase-activating protein Rap1GAP2 and regulates dense granule secretion in platelets. *Blood*. 114:1396-1404.

Ni, J., Y. Yang, D. Liu, H. Sun, S. Jin, and J. Li. 2017. MicroRNA-429 inhibits gastric cancer migration and invasion through the downregulation of specificity protein 1. *Oncology letters*. 13:3845-3849.

Nishimura, N., H. Nakamura, Y. Takai, and K. Sano. 1994. Molecular cloning and characterization of two rab GDI species from rat brain: brain-specific and ubiquitous types. *The Journal of biological chemistry*. 269:14191-14198.

Nouriel, A., J. Zisquit, A.M. Helfand, Y. Anikster, and S. Greenberger. 2015. Griscelli Syndrome Type 3: Two New Cases and Review of the Literature. *Pediatric dermatology*. 32:e245-248.

Novak, E.K., R. Gautam, M. Reddington, L.M. Collinson, N.G. Copeland, N.A. Jenkins, M.P. McGarry, and R.T. Swank. 2002. The regulation of platelet-dense granules by Rab27a in the ashen mouse, a model of Hermansky-Pudlak and Griscelli syndromes, is granule-specific and dependent on genetic background. *Blood*. 100:128-135.

Novak, E.K., M. Reddington, L. Zhen, P.E. Stenberg, C.W. Jackson, M.P. McGarry, and R.T. Swank. 1995. Inherited thrombocytopenia caused by reduced platelet production in mice with the gunmetal pigment gene mutation. *Blood*. 85:1781-1789.

Oberhofer, A., P. Spieler, Y. Rosenfeld, W.L. Stepp, A. Cleetus, A.N. Hume, F. Mueller-Planitz, and Z. Okten. 2017. Myosin Va's adaptor protein melanophilin enforces track selection on the microtubule and actin networks in vitro. *Proceedings of the National Academy of Sciences of the United States of America*.

Ohbayashi, N., S. Mamishi, K. Ishibashi, Y. Maruta, B. Pourakbari, B. Tamizifar, M. Mohammadpour, M. Fukuda, and N. Parvaneh. 2010. Functional characterization of two RAB27A missense mutations found in Griscelli syndrome type 2. *Pigment cell & melanoma research*. 23:365-374.

Omerovic, J., A.J. Laude, and I.A. Prior. 2007. Ras proteins: paradigms for compartmentalised and isoform-specific signalling. *Cellular and molecular life sciences : CMLS*. 64:2575-2589.

Ostenfeld, M.S., D.K. Jeppesen, J.R. Laurberg, A.T. Boysen, J.B. Bramsen, B. Primdal-Bengtson, A. Hendrix, P. Lamy, F. Dagnaes-Hansen, M.H. Rasmussen, K.H. Bui, N. Fristrup, E.I. Christensen, I. Nordentoft, J.P. Morth, J.B. Jensen, J.S. Pedersen, M. Beck, D. Theodorescu, M. Borre, K.A. Howard, L. Dyrskjot, and T.F. Orntoft. 2014. Cellular disposal of miR23b by RAB27-dependent exosome release is linked to acquisition of metastatic properties. *Cancer research*. 74:5758-5771.

Ostermeier, C., and A.T. Brunger. 1999. Structural basis of Rab effector specificity: crystal structure of the small G protein Rab3A complexed with the effector domain of rabphilin-3A. *Cell*. 96:363-374.

Ostrem, J.M., U. Peters, M.L. Sos, J.A. Wells, and K.M. Shokat. 2013. K-Ras(G12C) inhibitors allosterically control GTP affinity and effector interactions. *Nature*. 503:548-551.

Ostrowski, M., N.B. Carmo, S. Krumeich, I. Fanget, G. Raposo, A. Savina, C.F. Moita, K. Schauer, A.N. Hume, R.P. Freitas, B. Goud, P. Benaroch, N. Hacohen, M. Fukuda, C. Desnos, M.C. Seabra, F. Darchen, S. Amigorena, L.F. Moita, and C. Thery. 2010. Rab27a and Rab27b control different steps of the exosome secretion pathway. *Nature cell biology*. 12:19-30; sup pp 11-13.

Oxford, G., and D. Theodorescu. 2003. Ras superfamily monomeric G proteins in carcinoma cell motility. *Cancer letters*. 189:117-128.

Pan, X., S. Eathiraj, M. Munson, and D.G. Lambright. 2006. TBC-domain GAPs for Rab GTPases accelerate GTP hydrolysis by a dual-finger mechanism. *Nature*. 442:303-306.

Pastural, E., F.J. Barrat, R. Dufourcq-Lagelouse, S. Certain, O. Sanal, N. Jabado, R. Seger, C. Griscelli, A. Fischer, and G. de Saint Basile. 1997. Griscelli disease maps to chromosome 15q21 and is associated with mutations in the myosin-Va gene. *Nat Genet*. 16:289-292.

Patterson, G., R.N. Day, and D. Piston. 2001. Fluorescent protein spectra. *Journal of cell science*. 114:837-838.

Patterson, G.H., D.W. Piston, and B.G. Barisas. 2000. Forster distances between green fluorescent protein pairs. *Analytical biochemistry*. 284:438-440.

Peinado, H., M. Aleckovic, S. Lavotshkin, I. Matei, B. Costa-Silva, G. Moreno-Bueno, M. Hergueta-Redondo, C. Williams, G. Garcia-Santos, C. Ghajar, A. Nitadori-Hoshino, C. Hoffman, K. Badal, B.A. Garcia, M.K. Callahan, J. Yuan, V.R. Martins, J. Skog, R.N. Kaplan, M.S. Brady, J.D. Wolchok, P.B. Chapman, Y. Kang, J. Bromberg, and D. Lyden. 2012. Melanoma exosomes educate bone marrow progenitor cells toward a pro-metastatic phenotype through MET. *Nature medicine*. 18:883-891.

Pereira-Leal, J.B., A.N. Hume, and M.C. Seabra. 2001. Prenylation of Rab GTPases: molecular mechanisms and involvement in genetic disease. *FEBS letters*. 498:197-200.

Pereira-Leal, J.B., and M.C. Seabra. 2000. The mammalian Rab family of small GTPases: definition of family and subfamily sequence motifs suggests a mechanism for functional specificity in the Ras superfamily. *Journal of molecular biology*. 301:1077-1087.

Pereira-Leal, J.B., and M.C. Seabra. 2001. Evolution of the Rab family of small GTP-binding proteins. *Journal of molecular biology*. 313:889-901.

Pfeffer, S.R. 2001. Rab GTPases: specifying and deciphering organelle identity and function. *Trends in cell biology*. 11:487-491.

Pfeffer, S.R. 2005. Structural clues to Rab GTPase functional diversity. *The Journal of biological chemistry*. 280:15485-15488.

Pfeffer, S.R. 2013. Rab GTPase regulation of membrane identity. *Curr Opin Cell Biol*. 25:414-419.

Pfeffer, S.R., A.B. Dirac-Svejstrup, and T. Soldati. 1995. Rab GDP dissociation inhibitor: putting rab GTPases in the right place. *The Journal of biological chemistry*. 270:17057-17059.

Piston, D.W., and G.J. Kremers. 2007. Fluorescent protein FRET: the good, the bad and the ugly. *Trends in biochemical sciences*. 32:407-414.

Pivot-Pajot, C., F. Varoqueaux, G. de Saint Basile, and S.G. Bourgoin. 2008. Munc13-4 regulates granule secretion in human neutrophils. *Journal of immunology (Baltimore, Md. : 1950)*. 180:6786-6797.

Ponting, C.P., and P.J. Parker. 1996. Extending the C2 domain family: C2s in PKCs delta, epsilon, eta, theta, phospholipases, GAPs, and perforin. *Protein science : a publication of the Protein Society*. 5:162-166.

Prakash, P., and A.A. Gorfe. 2016. Membrane orientation dynamics of lipid-modified small GTPases. *Small GTPases*:1-10.

Pylypenko, O., and B. Goud. 2012. Posttranslational modifications of Rab GTPases help their insertion into membranes. *Proceedings of the National Academy of Sciences of the United States of America*. 109:5555-5556.

Pylypenko, O., A. Rak, T. Durek, S. Kushnir, B.E. Dursina, N.H. Thomae, A.T. Constantinescu, L. Brunsveld, A. Watzke, H. Waldmann, R.S. Goody, and K. Alexandrov. 2006. Structure of doubly prenylated Ypt1:GDI complex and the mechanism of GDI-mediated Rab recycling. *The EMBO journal*. 25:13-23.

Pylypenko, O., A. Rak, R. Reents, A. Niculae, V. Sidorovitch, M.D. Cioaca, E. Bessolitsyna, N.H. Thoma, H. Waldmann, I. Schlichting, R.S. Goody, and K. Alexandrov. 2003. Structure of Rab escort protein-1 in complex with Rab geranylgeranyltransferase. *Molecular cell*. 11:483-494.

Rajalingam, K., R. Schreck, U.R. Rapp, and S. Albert. 2007. Ras oncogenes and their downstream targets. *Biochimica et biophysica acta*. 1773:1177-1195.

Rak, A., O. Pylypenko, A. Niculae, K. Pyatkov, R.S. Goody, and K. Alexandrov. 2004. Structure of the Rab7 : REP-1 complex: Insights into the mechanism of rab prenylation and choroideremia disease. *Cell*. 117:749-760.

Ramalho, J.S., T. Tolmachova, A.N. Hume, A. McGuigan, C.Y. Gregory-Evans, C. Huxley, and M.C. Seabra. 2001. Chromosomal mapping, gene structure and characterization of the human and murine RAB27B gene. *BMC genetics*. 2:2.

Ratner, V., E. Kahana, M. Eichler, and E. Haas. 2002. A general strategy for site-specific double labeling of globular proteins for kinetic FRET studies. *Bioconjugate chemistry*. 13:1163-1170.

Reiner, D.J., and E.A. Lundquist. 2016. Small GTPases. *WormBook : the online review of C. elegans biology*:1-99.

Reiss, Y., J.L. Goldstein, M.C. Seabra, P.J. Casey, and M.S. Brown. 1990. Inhibition of purified p21ras farnesyl:protein transferase by Cys-AAX tetrapeptides. *Cell*. 62:81-88.

Ren, P., X.Q. Yang, X.L. Zhai, Y.Q. Zhang, and J.F. Huang. 2016. Overexpression of Rab27B is correlated with distant metastasis and poor prognosis in ovarian cancer. *Oncology letters*. 12:1539-1545.

Reuther, G.W., and C.J. Der. 2000. The Ras branch of small GTPases: Ras family members don't fall far from the tree. *Curr Opin Cell Biol*. 12:157-165.

Riederer, M.A., T. Soldati, A.D. Shapiro, J. Lin, and S.R. Pfeffer. 1994. Lysosome biogenesis requires Rab9 function and receptor recycling from endosomes to the trans-Golgi network. *The Journal of cell biology*. 125:573-582.

Robinson, C.L., R.D. Evans, D.A. Briggs, J.S. Ramalho, and A.N. Hume. 2017. Deficiency in kinesin-1 recruitment to melanosomes precludes it from facilitating their centrifugal transport. *Journal of cell science*.

Roelofs, A.J., P.A. Hulley, A. Meijer, F.H. Ebetino, R.G. Russell, and C.M. Shipman. 2006. Selective inhibition of Rab prenylation by a phosphonocarboxylate analogue of risedronate induces apoptosis, but not S-phase arrest, in human myeloma cells. *International journal of cancer. Journal international du cancer*. 119:1254-1261.

Rojas, R., T. van Vlijmen, G.A. Mardones, Y. Prabhu, A.L. Rojas, S. Mohammed, A.J. Heck, G. Raposo, P. van der Sluijs, and J.S. Bonifacino. 2008. Regulation of retromer recruitment to endosomes by sequential action of Rab5 and Rab7. *The Journal of cell biology*. 183:513-526.

Rupaimoole, R., and F.J. Slack. 2017. MicroRNA therapeutics: towards a new era for the management of cancer and other diseases. *Nature reviews. Drug discovery*. 16:203-222.

Rush, M.G., G. Drivas, and P. D'Eustachio. 1996. The small nuclear GTPase Ran: how much does it run? *BioEssays : news and reviews in molecular, cellular and developmental biology*. 18:103-112.

Rybin, V., O. Ullrich, M. Rubino, K. Alexandrov, I. Simon, M.C. Seabra, R. Goody, and M. Zerial. 1996. GTPase activity of Rab5 acts as a timer for endocytic membrane fusion. *Nature*. 383:266-269.

Saegusa, C., E. Kanno, S. Itohara, and M. Fukuda. 2008. Expression of Rab27B-binding protein Slp1 in pancreatic acinar cells and its involvement in amylase secretion. *Archives of biochemistry and biophysics*. 475:87-92.

Saegusa, C., T. Tanaka, S. Tani, S. Itohara, K. Mikoshiba, and M. Fukuda. 2006. Decreased basal mucus secretion by Slp2-a-deficient gastric surface mucous cells. *Genes to cells : devoted to molecular & cellular mechanisms*. 11:623-631.

Sakisaka, T., T. Meerlo, J. Matteson, H. Plutner, and W.E. Balch. 2002. Rab-alphaGDI activity is regulated by a Hsp90 chaperone complex. *The EMBO journal*. 21:6125-6135.

Saxena, S.K., H. Horiuchi, and M. Fukuda. 2006. Rab27a regulates epithelial sodium channel (ENaC) activity through synaptotagmin-like protein (SLP-5) and Munc13-4 effector mechanism. *Biochemical and biophysical research communications*. 344:651-657.

Schafer, J.C., N.W. Baetz, L.A. Lapierre, R.E. McRae, J.T. Roland, and J.R. Goldenring. 2014. Rab11-FIP2 interaction with MYO5B regulates movement of Rab11a-containing recycling vesicles. *Traffic*. 15:292-308.

Schalk, I., K. Zeng, S.K. Wu, E.A. Stura, J. Matteson, M. Huang, A. Tandon, I.A. Wilson, and W.E. Balch. 1996. Structure and mutational analysis of Rab GDP-dissociation inhibitor. *Nature*. 381:42-48.

Schechtman, D., D. Mochly-Rosen, and D. Ron. 2003. Glutathione S-transferase pull-down assay. *Methods in molecular biology (Clifton, N.J.)*. 233:345-350.

Sckolnick, M., E.B. Krementsova, D.M. Warshaw, and K.M. Trybus. 2013. More than just a cargo adapter, melanophilin prolongs and slows processive runs of myosin Va. *The Journal of biological chemistry*. 288:29313-29322.

Seabra, M.C. 1996. Nucleotide dependence of Rab geranylgeranylation. Rab escort protein interacts preferentially with GDP-bound Rab. *The Journal of biological chemistry*. 271:14398-14404.

Seabra, M.C., M.S. Brown, C.A. Slaughter, T.C. Sudhof, and J.L. Goldstein. 1992a. Purification of component A of Rab geranylgeranyl transferase: possible identity with the choroideremia gene product. *Cell*. 70:1049-1057.

Seabra, M.C., J.L. Goldstein, T.C. Sudhof, and M.S. Brown. 1992b. Rab geranylgeranyl transferase. A multisubunit enzyme that prenylates GTP-binding proteins terminating in Cys-X-Cys or Cys-Cys. *The Journal of biological chemistry*. 267:14497-14503.

Seabra, M.C., Y.K. Ho, and J.S. Anant. 1995. Deficient geranylgeranylation of Ram/Rab27 in choroideremia. *The Journal of biological chemistry*. 270:24420-24427.

Seabra, M.C., E.H. Mules, and A.N. Hume. 2002. Rab GTPases, intracellular traffic and disease. *Trends in molecular medicine*. 8:23-30.

Seabra, M.C., Y. Reiss, P.J. Casey, M.S. Brown, and J.L. Goldstein. 1991. Protein farnesyltransferase and geranylgeranyltransferase share a common alpha subunit. *Cell*. 65:429-434.

Seefeldt, B., R. Kasper, T. Seidel, P. Tinnefeld, K.J. Dietz, M. Heilemann, and M. Sauer. 2008. Fluorescent proteins for single-molecule fluorescence applications. *Journal of biophotonics*. 1:74-82.

Segev, N. 2001. Ypt and Rab GTPases: insight into functions through novel interactions. *Curr Opin Cell Biol*. 13:500-511.

Shaner, N.C., R.E. Campbell, P.A. Steinbach, B.N. Giepmans, A.E. Palmer, and R.Y. Tsien. 2004. Improved monomeric red, orange and yellow fluorescent proteins derived from Discosoma sp. red fluorescent protein. *Nature biotechnology*. 22:1567-1572.

Shapiro, A.D., M.A. Riederer, and S.R. Pfeffer. 1993. Biochemical analysis of rab9, a ras-like GTPase involved in protein transport from late endosomes to the trans Golgi network. *The Journal of biological chemistry*. 268:6925-6931.

Shen, F., and M.C. Seabra. 1996. Mechanism of digeranylgeranylation of Rab proteins. Formation of a complex between monogeranylgeranyl-Rab and Rab escort protein. *The Journal of biological chemistry*. 271:3692-3698.

Shima, F., Y. Ijiri, S. Muraoka, J. Liao, M. Ye, M. Araki, K. Matsumoto, N. Yamamoto, T. Sugimoto, Y. Yoshikawa, T. Kumasaka, M. Yamamoto, A. Tamura, and T. Kataoka. 2010. Structural basis for conformational dynamics of GTP-bound Ras protein. *The Journal of biological chemistry*. 285:22696-22705.

Shima, F., Y. Yoshikawa, M. Ye, M. Araki, S. Matsumoto, J. Liao, L. Hu, T. Sugimoto, Y. Ijiri, A. Takeda, Y. Nishiyama, C. Sato, S. Muraoka, A. Tamura, T. Osoda, K. Tsuda, T. Miyakawa, H. Fukunishi, J. Shimada, T. Kumasaka, M. Yamamoto, and T. Kataoka. 2013. In silico discovery of small-molecule Ras inhibitors that display antitumor activity by blocking the Ras-effector interaction. *Proceedings of the National Academy of Sciences of the United States of America*. 110:8182-8187.

Shimada-Sugawara, M., E. Sakai, K. Okamoto, M. Fukuda, T. Izumi, N. Yoshida, and T. Tsukuba. 2015. Rab27A regulates transport of cell surface receptors modulating multinucleation and lysosome-related organelles in osteoclasts. *Scientific reports*. 5:9620.

Shimomura, O. 1979. Structure of the chromophore of Aequorea green fluorescent protein. *FEBS letters*. 104:220-222.

Shimomura, O. 2005. The discovery of aequorin and green fluorescent protein. *Journal of microscopy*. 217:1-15.

Shimomura, O., F.H. Johnson, and Y. Saiga. 1962. Extraction, purification and properties of aequorin, a bioluminescent protein from the luminous hydromedusan, Aequorea. *Journal of cellular and comparative physiology*. 59:223-239.

Shinde, S.R., and S. Maddika. 2017. Post translational modifications of Rab GTPases. *Small GTPases*:1-8.

Shirakawa, R., T. Higashi, A. Tabuchi, A. Yoshioka, H. Nishioka, M. Fukuda, T. Kita, and H. Horiuchi. 2004. Munc13-4 is a GTP-Rab27-binding protein regulating dense core granule secretion in platelets. *The Journal of biological chemistry*. 279:10730-10737.

Shisheva, A., J. Buxton, and M.P. Czech. 1994. Differential intracellular localizations of GDP dissociation inhibitor isoforms. Insulin-dependent redistribution of GDP dissociation inhibitor-2 in 3T3-L1 adipocytes. *The Journal of biological chemistry*. 269:23865-23868.

Shisheva, A., S.R. Chinni, and C. DeMarco. 1999. General role of GDP dissociation inhibitor 2 in membrane release of Rab proteins: modulations of its functional interactions by in vitro and in vivo structural modifications. *Biochemistry*. 38:11711-11721.

Simonsen, A., J.M. Gaullier, A. D'Arrigo, and H. Stenmark. 1999. The Rab5 effector EEA1 interacts directly with syntaxin-6. *The Journal of biological chemistry*. 274:28857-28860.

Simonsen, A., R. Lippe, S. Christoforidis, J.M. Gaullier, A. Brech, J. Callaghan, B.H. Toh, C. Murphy, M. Zerial, and H. Stenmark. 1998. EEA1 links PI(3)K function to Rab5 regulation of endosome fusion. *Nature*. 394:494-498.

Singh, R.K., R.C. Furze, M.A. Birrell, S.M. Rankin, A.N. Hume, and M.C. Seabra. 2014. A role for Rab27 in neutrophil chemotaxis and lung recruitment. *BMC cell biology*. 15:39.

Singh, R.K., W. Liao, D. Tracey-White, C. Recchi, T. Tolmachova, S.M. Rankin, A.N. Hume, and M.C. Seabra. 2012. Rab27a-mediated protease release regulates neutrophil recruitment by allowing uropod detachment. *Journal of cell science*. 125:1652-1656.

Singh, R.K., K. Mizuno, C. Wasmeier, S.T. Wavre-Shapton, C. Recchi, S.D. Catz, C. Futter, T. Tolmachova, A.N. Hume, and M.C. Seabra. 2013. Distinct and opposing roles for Rab27a/Mlph/MyoVa and

Rab27b/Munc13-4 in mast cell secretion. *The FEBS journal*. 280:892-903.

Sivars, U., D. Aivazian, and S. Pfeffer. 2005. Purification and properties of Yip3/PRA1 as a Rab GDI displacement factor. *Methods in enzymology*. 403:348-356.

Sivars, U., D. Aivazian, and S.R. Pfeffer. 2003. Yip3 catalyses the dissociation of endosomal Rab-GDI complexes. *Nature*. 425:856-859.

Soldati, T., M.A. Riederer, and S.R. Pfeffer. 1993. Rab GDI: a solubilizing and recycling factor for rab9 protein. *Molecular biology of the cell*. 4:425-434.

Spiegel, J., P.M. Cromm, A. Itzen, R.S. Goody, T.N. Grossmann, and H. Waldmann. 2014. Direct targeting of Rab-GTPase-effector interactions. *Angewandte Chemie (International ed. in English)*. 53:2498-2503.

Stanic, J., M. Carta, I. Eberini, S. Pelucchi, E. Marcello, A.A. Genazzani, C. Racca, C. Mulle, M. Di Luca, and F. Gardoni. 2015. Rabphilin 3A retains NMDA receptors at synaptic sites through interaction with GluN2A/PSD-95 complex. *Nature communications*. 6:10181.

Stein, M., M. Pilli, S. Bernauer, B.H. Habermann, M. Zerial, and R.C. Wade. 2012. The interaction properties of the human Rab GTPase family--comparative analysis reveals determinants of molecular binding selectivity. *PloS one*. 7:e34870.

Stenmark, H. 2009. Rab GTPases as coordinators of vesicle traffic. *Nature reviews. Molecular cell biology*. 10:513-525.

Stenmark, H., and V.M. Olkkonen. 2001. The Rab GTPase family. *Genome Biology*. 2:reviews3007.3001-reviews3007.3007.

Stenmark, H., A. Valencia, O. Martinez, O. Ullrich, B. Goud, and M. Zerial. 1994. Distinct structural elements of rab5 define its functional specificity. *The EMBO journal*. 13:575-583.

Stigter, E.A., Z. Guo, R.S. Bon, Y.W. Wu, A. Choidas, A. Wolf, S. Menninger, H. Waldmann, W. Blankenfeldt, and R.S. Goody. 2012. Development of selective, potent RabGGTase inhibitors. *Journal of medicinal chemistry*. 55:8330-8340.

Storrie, B., M. Micaroni, G.P. Morgan, N. Jones, J.A. Kamykowski, N. Wilkins, T.H. Pan, and B.J. Marsh. 2012. Electron tomography reveals Rab6 is essential to the trafficking of trans-Golgi clathrin and COPI-coated

vesicles and the maintenance of Golgi cisternal number. *Traffic*. 13:727-744.

Strom, M., A.N. Hume, A.K. Tarafder, E. Barkagianni, and M.C. Seabra. 2002. A family of Rab27-binding proteins. Melanophilin links Rab27a and myosin Va function in melanosome transport. *The Journal of biological chemistry*. 277:25423-25430.

Stryer, L. 1978. Fluorescence energy transfer as a spectroscopic ruler. *Annual review of biochemistry*. 47:819-846.

Su, W.F., Y. Gu, Z.Y. Wei, Y.T. Shen, Z.H. Jin, Y. Yuan, X.S. Gu, and G. Chen. 2016. Rab27a/Slp2-a complex is involved in Schwann cell myelination. *Neural regeneration research*. 11:1830-1838.

Sultana, A., Y. Jin, C. Dregger, E. Franklin, L.S. Weisman, and A.R. Khan. 2011. The activation cycle of Rab GTPase Ypt32 reveals structural determinants of effector recruitment and GDI binding. *FEBS letters*. 585:3520-3527.

Sun, Q., J.P. Burke, J. Phan, M.C. Burns, E.T. Olejniczak, A.G. Waterson, T. Lee, O.W. Rossanese, and S.W. Fesik. 2012. Discovery of small molecules that bind to K-Ras and inhibit Sos-mediated activation. *Angewandte Chemie (International ed. in English)*. 51:6140-6143.

Suvorova, E.S., R. Duden, and V.V. Lupashin. 2002. The Sec34/Sec35p complex, a Ypt1p effector required for retrograde intra-Golgi trafficking, interacts with Golgi SNAREs and COPI vesicle coat proteins. *The Journal of cell biology*. 157:631-643.

Swank, R.T., S.Y. Jiang, M. Reddington, J. Conway, D. Stephenson, M.P. McGarry, and E.K. Novak. 1993. Inherited abnormalities in platelet organelles and platelet formation and associated altered expression of low molecular weight guanosine triphosphate-binding proteins in the mouse pigment mutant gunmetal. *Blood*. 81:2626-2635.

Tarafder, A.K., C. Wasmeier, A.C. Figueiredo, A.E. Booth, A. Orihara, J.S. Ramalho, A.N. Hume, and M.C. Seabra. 2011. Rab27a targeting to melanosomes requires nucleotide exchange but not effector binding. *Traffic*. 12:1056-1066.

Thoma, N.H., A. Iakovenko, R.S. Goody, and K. Alexandrov. 2001a. Phosphoisoprenoids modulate association of Rab geranylgeranyltransferase with REP-1. *The Journal of biological chemistry*. 276:48637-48643.

Thoma, N.H., A. Iakovenko, A. Kalinin, H. Waldmann, R.S. Goody, and K. Alexandrov. 2001b. Allosteric regulation of substrate binding and product release in geranylgeranyltransferase type II. *Biochemistry*. 40:268-274.

Thoma, N.H., A. Niculae, R.S. Goody, and K. Alexandrov. 2001c. Double prenylation by RabGGTase can proceed without dissociation of the mono-prenylated intermediate. *The Journal of biological chemistry*. 276:48631-48636.

Tolmachova, T., M. Abrink, C.E. Futter, K.S. Authi, and M.C. Seabra. 2007. Rab27b regulates number and secretion of platelet dense granules. *Proceedings of the National Academy of Sciences of the United States of America*. 104:5872-5877.

Tolmachova, T., R. Anders, J. Stinchcombe, G. Bossi, G.M. Griffiths, C. Huxley, and M.C. Seabra. 2004. A general role for Rab27a in secretory cells. *Molecular biology of the cell*. 15:332-344.

Tomita, Y., and T. Suzuki. 2004. Genetics of pigmentary disorders. *American journal of medical genetics. Part C, Seminars in medical genetics*. 131C:75-81.

Touchot, N., P. Chardin, and A. Tavitian. 1987. Four additional members of the ras gene superfamily isolated by an oligonucleotide strategy: molecular cloning of YPT-related cDNAs from a rat brain library. *Proceedings of the National Academy of Sciences of the United States of America*. 84:8210-8214.

Traut, T.W. 1994. Physiological concentrations of purines and pyrimidines. *Molecular and cellular biochemistry*. 140:1-22.

Trinh, T.B., P. Upadhyaya, Z. Qian, and D. Pei. 2016. Discovery of a Direct Ras Inhibitor by Screening a Combinatorial Library of Cell-Permeable Bicyclic Peptides. *ACS combinatorial science*. 18:75-85.

Tsuboi, T., and M. Fukuda. 2006a. Rab3A and Rab27A cooperatively regulate the docking step of dense-core vesicle exocytosis in PC12 cells. *Journal of cell science*. 119:2196-2203.

Tsuboi, T., and M. Fukuda. 2006b. The Slp4-a linker domain controls exocytosis through interaction with Munc18-1.syntaxin-1a complex. *Molecular biology of the cell*. 17:2101-2112.

Turcan, I., A.M. Pasmooij, P.C. Van den Akker, H. Lemmink, R.J. Sinke, and M.F. Jonkman. 2016. Association of Epidermolysis Bullosa Simplex

With Mottled Pigmentation and EXPH5 Mutations. *JAMA dermatology*. 152:1137-1141.

Ueno, H., X. Huang, Y. Tanaka, and N. Hirokawa. 2011. KIF16B/Rab14 molecular motor complex is critical for early embryonic development by transporting FGF receptor. *Developmental cell*. 20:60-71.

Ullrich, O., H. Stenmark, K. Alexandrov, L.A. Huber, K. Kaibuchi, T. Sasaki, Y. Takai, and M. Zerial. 1993. Rab GDP dissociation inhibitor as a general regulator for the membrane association of rab proteins. *The Journal of biological chemistry*. 268:18143-18150.

van Breevoort, D., A.P. Snijders, N. Hellen, S. Weckhuysen, K.W. van Hooren, J. Eikenboom, K. Valentijn, M. Fernandez-Borja, B. Ceulemans, P. De Jonghe, J. Voorberg, M. Hannah, T. Carter, and R. Bierings. 2014. STXBP1 promotes Weibel-Palade body exocytosis through its interaction with the Rab27A effector Slp4-a. *Blood*. 123:3185-3194.

Vetter, I.R. 2014. The Structure of the G Domain of the Ras Superfamily. *In* Ras Superfamily Small G Proteins: Biology and Mechanisms 1: General Features, Signaling. A. Wittinghofer, editor. Springer Vienna, Vienna. 25-50.

Vetter, I.R., and A. Wittinghofer. 2001. The guanine nucleotide-binding switch in three dimensions. *Science (New York, N.Y.)*. 294:1299-1304.

Vigil, D., J. Cherfils, K.L. Rossman, and C.J. Der. 2010. Ras superfamily GEFs and GAPs: validated and tractable targets for cancer therapy? *Nature reviews. Cancer*. 10:842-857.

Wada, M., H. Nakanishi, A. Satoh, H. Hirano, H. Obaishi, Y. Matsuura, and Y. Takai. 1997. Isolation and characterization of a GDP/GTP exchange protein specific for the Rab3 subfamily small G proteins. *The Journal of biological chemistry*. 272:3875-3878.

Waldmann, H., I.M. Karaguni, M. Carpintero, E. Gourzoulidou, C. Herrmann, C. Brockmann, H. Oschkinat, and O. Muller. 2004. Sulindac-derived Ras pathway inhibitors target the Ras-Raf interaction and downstream effectors in the Ras pathway. *Angewandte Chemie (International ed. in English)*. 43:454-458.

Walensky, L.D., and G.H. Bird. 2014. Hydrocarbon-Stapled Peptides: Principles, Practice, and Progress: Miniperspective. *Journal of medicinal chemistry*. 57:6275-6288.

Wang, H., R. Ishizaki, J. Xu, K. Kasai, E. Kobayashi, H. Gomi, and T. Izumi. 2013. The Rab27a effector exophilin7 promotes fusion of secretory

granules that have not been docked to the plasma membrane. *Molecular biology of the cell*. 24:319-330.

Wang, H., and X. Zeng. 2000. Analysing protein–protein interactions using a GST-fusion protein to pull down the interacting target from the cell lysate. *Technical Tips Online*. 5:26-30.

Wang, M., and P.J. Casey. 2016. Protein prenylation: unique fats make their mark on biology. *Nature reviews. Molecular cell biology*. 17:110-122.

Wang, W., Q. Ni, H. Wang, S. Zhang, and H. Zhu. 2014. Prognostic value of Rab27B nuclear expression in gastrointestinal stromal tumors. *Disease markers*. 2014:942181.

Wang, Z., G. Miao, X. Xue, X. Guo, C. Yuan, Z. Wang, G. Zhang, Y. Chen, D. Feng, J. Hu, and H. Zhang. 2016. The Vici Syndrome Protein EPG5 Is a Rab7 Effector that Determines the Fusion Specificity of Autophagosomes with Late Endosomes/Lysosomes. *Molecular cell*. 63:781-795.

Waselle, L., T. Coppola, M. Fukuda, M. Iezzi, A. El-Amraoui, C. Petit, and R. Regazzi. 2003. Involvement of the Rab27 binding protein Slac2c/MyRIP in insulin exocytosis. *Molecular biology of the cell*. 14:4103-4113.

Webber, J.P., L.K. Spary, A.J. Sanders, R. Chowdhury, W.G. Jiang, R. Steadman, J. Wymant, A.T. Jones, H. Kynaston, M.D. Mason, Z. Tabi, and A. Clayton. 2015. Differentiation of tumour-promoting stromal myofibroblasts by cancer exosomes. *Oncogene*. 34:290-302.

Welsch, M.E., A. Kaplan, J.M. Chambers, M.E. Stokes, P.H. Bos, A. Zask, Y. Zhang, M. Sanchez-Martin, M.A. Badgley, C.S. Huang, T.H. Tran, H. Akkiraju, L.M. Brown, R. Nandakumar, S. Cremers, W.S. Yang, L. Tong, K.P. Olive, A. Ferrando, and B.R. Stockwell. 2017. Multivalent Small-Molecule Pan-RAS Inhibitors. *Cell*. 168:878-889 e829.

Wennerberg, K., K.L. Rossman, and C.J. Der. 2005. The Ras superfamily at a glance. *Journal of cell science*. 118:843-846.

Westbroek, W., A. Klar, A.R. Cullinane, S.G. Ziegler, H. Hurvitz, A. Ganem, K. Wilson, H. Dorward, M. Huizing, H. Tamimi, I. Vainshtein, Y. Berkun, M. Lavie, W.A. Gahl, and Y. Anikster. 2012. Cellular and clinical report of new Griscelli syndrome type III cases. *Pigment cell & melanoma research*. 25:47-56.

Westbroek, W., M. Tuchman, B. Tinloy, O. De Wever, T. Vilboux, J.M. Hertz, H. Hasle, C. Heilmann, A. Helip-Wooley, R. Kleta, and W.A. Gahl. 2008. A novel missense mutation (G43S) in the switch I region of

Rab27A causing Griscelli syndrome. *Molecular genetics and metabolism*. 94:248-254.

Wilson, S.M., R. Yip, D.A. Swing, T.N. O'Sullivan, Y. Zhang, E.K. Novak, R.T. Swank, L.B. Russell, N.G. Copeland, and N.A. Jenkins. 2000. A mutation in Rab27a causes the vesicle transport defects observed in ashen mice. *Proceedings of the National Academy of Sciences of the United States of America*. 97:7933-7938.

Wright, L.P., and M.R. Philips. 2006. Thematic review series: lipid posttranslational modifications. CAAX modification and membrane targeting of Ras. *Journal of lipid research*. 47:883-891.

Wright, P.K., F.E. May, S. Darby, R. Saif, T.W. Lennard, and B.R. Westley. 2009. Estrogen regulates vesicle trafficking gene expression in EFF-3, EFM-19 and MCF-7 breast cancer cells. *International journal of clinical and experimental pathology*. 2:463-475.

Wu, M., T. Wang, E. Loh, W. Hong, and H. Song. 2005a. Structural basis for recruitment of RILP by small GTPase Rab7. *The EMBO journal*. 24:1491-1501.

Wu, P., and L. Brand. 1994. Resonance energy transfer: methods and applications. *Analytical biochemistry*. 218:1-13.

Wu, S.K., P. Luan, J. Matteson, K. Zeng, N. Nishimura, and W.E. Balch. 1998a. Molecular role for the Rab binding platform of guanine nucleotide dissociation inhibitor in endoplasmic reticulum to Golgi transport. *The Journal of biological chemistry*. 273:26931-26938.

Wu, S.K., K. Zeng, I.A. Wilson, and W.E. Balch. 1996. Structural insights into the function of the Rab GDI superfamily. *Trends in biochemical sciences*. 21:472-476.

Wu, X., B. Bowers, K. Rao, Q. Wei, and J.A. Hammer, 3rd. 1998b. Visualization of melanosome dynamics within wild-type and dilute melanocytes suggests a paradigm for myosin V function In vivo. *The Journal of cell biology*. 143:1899-1918.

Wu, X., K. Rao, M.B. Bowers, N.G. Copeland, N.A. Jenkins, and J.A. Hammer, 3rd. 2001. Rab27a enables myosin Va-dependent melanosome capture by recruiting the myosin to the organelle. *Journal of cell science*. 114:1091-1100.

Wu, X.S., K. Rao, H. Zhang, F. Wang, J.R. Sellers, L.E. Matesic, N.G. Copeland, N.A. Jenkins, and J.A. Hammer, 3rd. 2002. Identification of an organelle receptor for myosin-Va. *Nature cell biology*. 4:271-278.

Wu, X.S., G.L. Tsan, and J.A. Hammer, 3rd. 2005b. Melanophilin and myosin Va track the microtubule plus end on EB1. *The Journal of cell biology*. 171:201-207.

Wu, Y.W., K.T. Tan, H. Waldmann, R.S. Goody, and K. Alexandrov. 2007. Interaction analysis of prenylated Rab GTPase with Rab escort protein and GDP dissociation inhibitor explains the need for both regulators. *Proceedings of the National Academy of Sciences of the United States of America*. 104:12294-12299.

Xu, Y., K. Ge, J. Lu, J. Huang, W. Wei, and Q. Huang. 2017. MicroRNA-493 suppresses hepatocellular carcinoma tumorigenesis through down-regulation of anthrax toxin receptor 1 (ANTXR1) and R-Spondin 2 (RSPO2). *Biomedicine & pharmacotherapy = Biomedecine & pharmacotherapie*. 93:334-343.

Yamamoto, K., E. Ishii, M. Sako, S. Ohga, K. Furuno, N. Suzuki, I. Ueda, M. Imayoshi, S. Yamamoto, A. Morimoto, H. Takada, T. Hara, S. Imashuku, T. Sasazuki, and M. Yasukawa. 2004. Identification of novel MUNC13-4 mutations in familial haemophagocytic lymphohistiocytosis and functional analysis of MUNC13-4-deficient cytotoxic T lymphocytes. *Journal of medical genetics*. 41:763-767.

Yamaoka, M., T. Ishizaki, and T. Kimura. 2015. GTP- and GDP-Dependent Rab27a Effectors in Pancreatic Beta-Cells. *Biological & pharmaceutical bulletin*. 38:663-668.

Yan, X., M. Yan, Y. Guo, G. Singh, Y. Chen, M. Yu, D. Wang, C.A. Hillery, and A.M. Chan. 2015. R-Ras Regulates Murine T Cell Migration and Intercellular Adhesion Molecule-1 Binding. *PloS one*. 10:e0145218.

Yang, C., V.I. Slepnev, and B. Goud. 1994. Rab proteins form in vivo complexes with two isoforms of the GDP-dissociation inhibitor protein (GDI). *The Journal of biological chemistry*. 269:31891-31899.

Yang, F., L.G. Moss, and G.N. Phillips, Jr. 1996a. The molecular structure of green fluorescent protein. *Nature biotechnology*. 14:1246-1251.

Yang, T.T., L. Cheng, and S.R. Kain. 1996b. Optimized codon usage and chromophore mutations provide enhanced sensitivity with the green fluorescent protein. *Nucleic acids research*. 24:4592-4593.

Yang, X., X. Ye, L. Sun, F. Gao, Y. Li, X. Ji, X. Wang, Y. Feng, and X. Wang. 2017. Downregulation of serum RAB27B confers improved prognosis and is associated with hepatocellular carcinoma progression through PI3K-AKT-P21 signaling. *Oncotarget*.

Yao, L.L., Q.J. Cao, H.M. Zhang, J. Zhang, Y. Cao, and X.D. Li. 2015. Melanophilin Stimulates Myosin-5a Motor Function by Allosterically Inhibiting the Interaction between the Head and Tail of Myosin-5a. *Scientific reports*. 5:10874.

Yasuda, T., and M. Fukuda. 2014. Slp2-a controls renal epithelial cell size through regulation of Rap-ezrin signaling independently of Rab27. *Journal of cell science*. 127:557-570.

Yasuda, T., Y. Homma, and M. Fukuda. 2015a. Slp2-a inactivates ezrin by recruiting protein phosphatase 1 to the plasma membrane. *Biochemical and biophysical research communications*. 460:896-902.

Yasuda, T., P.S. Mrozowska, and M. Fukuda. 2015b. Functional analysis of Rab27A and its effector Slp2-a in renal epithelial cells. *Methods in molecular biology (Clifton, N.J.)*. 1298:127-139.

Yasuda, T., C. Saegusa, S. Kamakura, H. Sumimoto, and M. Fukuda. 2012. Rab27 effector Slp2-a transports the apical signaling molecule podocalyxin to the apical surface of MDCK II cells and regulates claudin-2 expression. *Molecular biology of the cell*. 23:3229-3239.

Yi, Z., H. Yokota, S. Torii, T. Aoki, M. Hosaka, S. Zhao, K. Takata, T. Takeuchi, and T. Izumi. 2002. The Rab27a/Granuphilin Complex Regulates the Exocytosis of Insulin-Containing Dense-Core Granules. *Molecular and Cellular Biology*. 22:1858-1867.

Yokoyama, T., M. Nakatake, T. Kuwata, A. Couzinet, R. Goitsuka, S. Tsutsumi, H. Aburatani, P.J. Valk, R. Delwel, and T. Nakamura. 2016. MEIS1-mediated transactivation of synaptotagmin-like 1 promotes CXCL12/CXCR4 signaling and leukemogenesis. *The Journal of clinical investigation*. 126:1664-1678.

Yu, M., K. Kasai, K. Nagashima, S. Torii, H. Yokota-Hashimoto, K. Okamoto, T. Takeuchi, H. Gomi, and T. Izumi. 2007. Exophilin4/Slp2-a targets glucagon granules to the plasma membrane through unique Ca2+-inhibitory phospholipid-binding activity of the C2A domain. *Molecular biology of the cell*. 18:688-696.

Yuen, H.F., K.K. Chan, A. Platt-Higgins, H. Dakir el, K.B. Matchett, Y.A. Haggag, P.V. Jithesh, T. Habib, A. Faheem, F.A. Dean, R. Morgan, P.S. Rudland, and M. El-Tanani. 2016. Ran GTPase promotes cancer progression via Met recepto-rmediated downstream signaling. *Oncotarget*. 7:75854-75864.

Zaccolo, M. 2004. Use of chimeric fluorescent proteins and fluorescence resonance energy transfer to monitor cellular responses. *Circulation research*. 94:866-873.

Zerial, M., and H. McBride. 2001. Rab proteins as membrane organizers. *Nature Reviews*. 2:107-119.

Zhang, G., H. Zheng, G. Zhang, R. Cheng, C. Lu, Y. Guo, and G. Zhao. 2017a. MicroRNA-338-3p suppresses cell proliferation and induces apoptosis of non-small-cell lung cancer by targeting sphingosine kinase 2. *Cancer cell international*. 17:46.

Zhang, H., M.C. Seabra, and J. Deisenhofer. 2000. Crystal structure of Rab geranylgeranyltransferase at 2.0 A resolution. *Structure*. 8:241-251.

Zhang, J.X., X.X. Huang, M.B. Cai, Z.T. Tong, J.W. Chen, D. Qian, Y.J. Liao, H.X. Deng, D.Z. Liao, M.Y. Huang, Y.X. Zeng, D. Xie, and S.J. Mai. 2012. Overexpression of the secretory small GTPase Rab27B in human breast cancer correlates closely with lymph node metastasis and predicts poor prognosis. *Journal of translational medicine*. 10:242.

Zhang, L., S. Zhang, J. Yao, F.J. Lowery, Q. Zhang, W.C. Huang, P. Li, M. Li, X. Wang, C. Zhang, H. Wang, K. Ellis, M. Cheerathodi, J.H. McCarty, D. Palmieri, J. Saunus, S. Lakhani, S. Huang, A.A. Sahin, K.D. Aldape, P.S. Steeg, and D. Yu. 2015. Microenvironment-induced PTEN loss by exosomal microRNA primes brain metastasis outgrowth. *Nature*. 527:100-104.

Zhang, P., F. Kong, X. Deng, Y. Yu, C. Hou, T. Liang, and L. Zhu. 2017b. MicroRNA-326 suppresses the proliferation, migration and invasion of cervical cancer cells by targeting ELK1. *Oncology letters*. 13:2949-2956.

Zhao, H., Q. Wang, X. Wang, H. Zhu, S. Zhang, W. Wang, Z. Wang, and J. Huang. 2016. Correlation Between RAB27B and p53 Expression and Overall Survival in Pancreatic Cancer. *Pancreas*. 45:204-210.

Zhao, S., S. Torii, H. Yokota-Hashimoto, T. Takeuchi, and T. Izumi. 2002. Involvement of Rab27b in the regulated secretion of pituitary hormones. *Endocrinology*. 143:1817-1824.

Zhao, W., M. Jamshidiha, T. Lanyon-Hogg, C. Recchi, E. Cota, and E.W. Tate. 2017. Direct Targeting of the Ras GTPase Superfamily Through Structure- Based Design. *Current topics in medicinal chemistry*. 17:16-29.

Zheng, Y., E.C. Campbell, J. Lucocq, A. Riches, and S.J. Powis. 2013. Monitoring the Rab27 associated exosome pathway using nanoparticle tracking analysis. *Experimental cell research*. 319:1706-1713.

Zhi, T., K. Jiang, C. Zhang, X. Xu, W. Wu, E. Nie, T. Yu, X. Zhou, Z. Bao, X. Jin, J. Zhang, Y. Wang, and N. Liu. 2017. MicroRNA-1301 inhibits proliferation of human glioma cells by directly targeting N-Ras. *American journal of cancer research*. 7:982-998.

Zur Stadt, U., K. Beutel, S. Kolberg, R. Schneppenheim, H. Kabisch, G. Janka, and H.C. Hennies. 2006. Mutation spectrum in children with primary hemophagocytic lymphohistiocytosis: molecular and functional analyses of PRF1, UNC13D, STX11, and RAB27A. *Human mutation*. 27:62-68.